Modelling Transient Air-water Flows in Civil and Environmental Engineering

François Kerger

Dissertation submitted to the University of Liège in fulfillment of the requirements for the degree of « Docteur en Sciences de l'Ingénieur »

University of Liège

Faculty of Applied Science

Department of Architecture, Geology, Environment and Construction

Hydrology, Applied Hydrodynamics and Hydraulic Constructions

Modelling Transient Air-water Flows in Civil and Environmental Engineering

François Kerger

Dissertation submitted to the University of Liège in fulfillment of the requirements for the degree of « Docteur en Sciences de l'Ingénieur »

2010, August

This dissertation details the original results of a research carried out by:

François Kerger
FNRS-F.R.S Research Fellow
Ingénieur des Arts et Manufactures (Ecole Centrale Paris)
Ingénieur Civil en Construction (University of Liège)
University of Liège
ArGenCo Department – Architecture, Geology, Environment & Construction
Building B52/3
Chemin des Chevreuils, 1
4000 – Liège – Belgium
e-mail: fkerger@ulg.ac.be

This research was financed by:

Fonds de la Recherche Scientifique – FNRS
(Funds for Scientific Research – FNRS-F.R.S.)
Rue d'Egmont, 5
1000 Bruxelles – Belgium

Citation: Kerger, F., 2010, Modelling Transient Air-water Flows in Civil and Environmental Engineering, PhD Thesis. University of Liège, Faculty of Applied Science, Liège, Belgium, pp 315

Summary

Facing voluminous waterfalls makes anybody conscious of the power and the beauty of water in motion. The energy contained in flowing water constitutes both an opportunity and a thread. Harnessing water streams remains indeed complex because the flow behavior is affected by many sources of uncertainties like transient phenomena and air-water. For that reason, scientists and engineers have been devoting a lot of effort to understand and predict natural and anthropogenic flows.

The present thesis aims at improving the understanding and description of air-water interactions in transient flows. A particular emphasis is set on phenomena relevant in civil and environmental engineering, like rivers, pipe networks, and hydraulic structures. These situations are indeed crucial for economical, ecological, and safety reasons.

Organized in ten chapters, this text investigates the description and modelling of both pure water flows and air-water flows in open channel and closed pipes. The traditional distinction between free surface and pressurized flows is questioned in order to create a unified framework for all kinds of flows relevant in civil and environmental engineering. For both single- and multi-phase situations, original mathematical models are developed, innovative numerical schemes are used to discretize them, and associated computational codes are implemented and applied to validation and practical cases.

Theoretical results of the doctoral research may be summarized in two main propositions. First, it is shown that any mathematical model for free surface flows could be extended to pressurized flows by modifying the expression of the pressure gradient. Second, the drift-flux theory is proven an adequate alternative to Navier-Stokes equations in order to derive mid- and large-scale multiphase models. Such models provide an improved description of environmental flows affected by air entrainment. These two propositions underpin the development of two original one-dimensional mathematical models for mixed flows, one single-phase and one multi-phase. Thanks to suitable numerical methods, the discretised forms of these equations are implemented into two modelling systems, WOLF1D and WOLF IMPack. Once validated, these computational codes are successfully applied to practical cases: a low-pressure sewer network, a gravity drainage system, and a dam bottom gallery.

Original concepts applied with success on air-water flows in this thesis pave the way for further research on environmental flows. In particular, the multiphase drift-flux model constitutes an elegant framework to investigate multidimensional flows affected by transport phenomena (pollutants, sediments) and heterogeneous interactions (vegetation, rough bed).

Preface

"Anybody who has been seriously engaged in scientific work of any kind realizes that over the entrance to the gates of the temple of science are written the words: *Ye must have faith*. It is a quality which the scientist cannot dispense with" [246]. In this respect, producing a thesis certainly assimilates to a serious scientific work. Nevertheless, I hope that the present thesis meets all the other aspects of a serious scientific work such that its results are valuable for the scientific community.

This text provides the results of a three-year long research about the understanding and description of air-water transient flows. A particular attention is paid to one-dimensional phenomena relevant to civil and environmental engineering. This mainly includes large-scale flows in open channels and closed conduits.

From a scientific point of view, many of the mechanisms altering such flows are still poorly understood. It is particularly true for the mechanisms governing air-water interactions and the effects of air entrainment on the flow dynamics. From an engineering point of view, these shortcomings are aggravated by the lack of methods for predicting and describing air-water flows in practical applications.

In this thesis, original methods and concepts provide elements of answer to this actual dilemma that occupies many scientists and engineers active in hydraulics. The approach that I investigate relies on the establishment of mathematical models describing the flow dynamics and on their solving with computers.

The first step of my procedure relies on the continuum mechanics for deriving mathematical models. In particular, I investigate the problem from two different points of view. First, I neglect air-water interactions and develop an original single-phase theory for one-dimensional mixed flows. Second, I develop an original multiphase counterpart to the single-phase model. It is proven to enhance the fidelity of the description of the flow.

The second step is the concern of the Computational Fluid Mechanics. Based on the mathematical models, I discretised equations in an algebraic form. Subsequently, I implement them into algorithms for an easy resolution with computers. In this thesis, it results in two computational codes. First, WOLF1D simulates pure water flows. Second, WOLF IMPack integrates the effect of air-water interactions. Both codes are original tools developed by the HACH.

Before getting into the heart of the matter, I would like to bring to the attention of the reader a series of remarks that shed light on this text. They concern its form, its context and its output.

This text summarizes my research and gives the sufficient elements for assessing its validity and originality. In various ways, I tried to make these 300 pages the most readable possible. First, I separate the results found in the literature from my original contributions to the field. In particular, I concentrate the conclusions of my literature review in Chapter 2. Second, all the important results and summaries of each section are framed with a blue box, while blue backgrounds emphasize conclusions of each chapter. For hurried readers, it seems possible to get the substance of the text by reading only these paragraphs.

Being a fundamental researcher in applied science has certain similarities with the act of building a bridge. This wonderful activity consists indeed in facing a gap between a phenomenon of interest and its technical harnessing for economical or security purpose. Building the bridge between the phenomenon and its practical application requires excelling in very different operations. This constitutes the challenge of fundamental research in applied science. First, the natural mechanisms involved must be understood in all their relevant aspects. Second, a model describing these mechanisms must be set up and validated. Third, a way to use (or solve) this model must be developed. Finally, a tool adapted to the practical application must synthesize the model and its solving method. Without being presumptuous, I think this thesis provides a particular bridge between air-water flows and a better employment of them in civil and environmental engineering.

In order to maximize the impact of my work on the scientific community, I have communicated at the maximum about my research. Even if this thesis constitutes the most complete transcription of the results of this doctoral research, I submitted the original results in various journals and conferences. A book published on editor's demand describes the theoretical multiphase approach [175]. Two book chapters relates also some elements of this thesis [169, 172]. Four peer-reviewed journal papers [5-8] have been published (or accepted). Five other papers are currently under reviewing/preparation for submission [155, 156, 161, 162, 170]. Finally, ten conference papers complement this output [91, 152, 153, 155, 158, 160-163, 168].

Finally, I would like to acknowledge several people that give me help and support during the last three years. First, I thank the Belgian Fund for Scientific Research for the four-year funding that it provides me. Second, my advisor, Prof. M. Pirotton, is greatly thanked for the opportunity and support that he provides me during my PhD. Third, I am grateful to all the members of the Jury for the honor they give me to judge this thesis. Fourth, I thank all my collaborators within the HACH, namely Benjamin, Pierre, Sébastien, Sylvain, Julien, Raphaël, Damien, Nicolas, Bruno, Olivier, Arnaud, and François. Finally, this thesis would never be possible without the moral support of my parents and Catherine. I thank all of them sincerely.

Table of Contents

Chapter 1 Introduction

Fluid Mechanics and Engineering are born a long time before the development of the mathematical background required to describe all the observed phenomena. The recourse to images has occupied a privileged position since the inception of this science field in the ancient Greece and Rome. Granted, charcoal drawings have been replaced by modern techniques such as Particle Image Velocimetry (PIV). However, the utmost importance of images in Fluid Mechanics is still true nowadays. Consequently, it seems natural to me to open my PhD thesis dealing with transient air-water flows by referring to the work of an artist of the Renaissance, Leonardo da Vinci (1452-1519). In 1505, he proposed the first scientific account of the interactions between air and water under the form of a drawing called: ”Studies of water movement” (Figure 1). 400 years prior the development of corresponding mathematical theories, da Vinci prefigured in this drawing the now famous Reynolds turbulence decomposition and the air entrainment. In particular, he shows remarkable insight into the chaotic and unsteady nature of flows. Since the Renaissance, works on transient aerated flows have been continually intensifying.

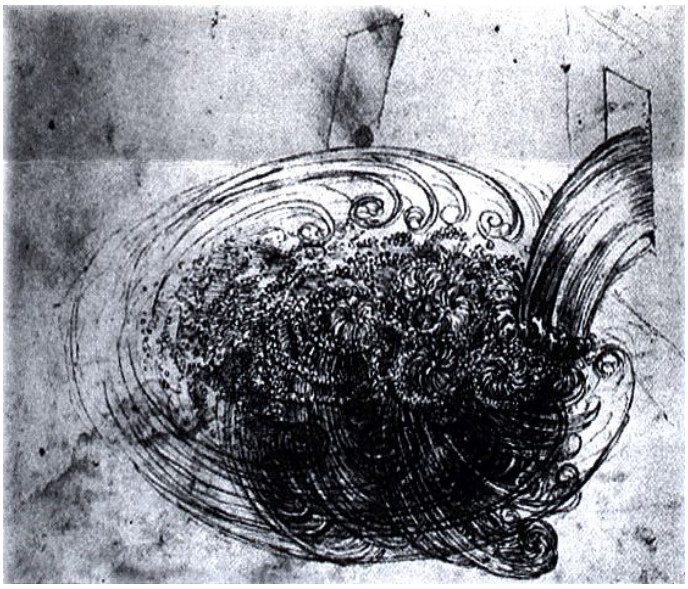

Figure 1: “Studies of Water Movement” by Leonardo da Vinci represents the vortices and bubbles that appear when water is poured into a reservoir

There is nothing surprising about this curiosity of many researchers about air-water flows since they crop up in many situations of daily live. Anyone who has already admired a waterfall, opened its water tap, or observed a public fountain was the involuntary witness to a two-phase phenomenon.

The present thesis fits into this scheme of improvement of the understanding/description of air-water interactions in transient flows, with a particular emphasis on phenomena relevant to civil and environmental engineering. The three years of research result in:

- a new mathematical model for single-phase mixed flows;
- its equivalent for multiphase flows;
- their implementation into computational codes;
- their validation and application on practical cases.

Including three sections, this introduction chapter gives a full description of the problem treated in this thesis, and already introduces the results of the research. In section 1.1, I propose to the reader a reminder about the context of the study. Next, the importance of air-water flows in civil and environmental engineering is underlined (section 1.2). In section 1.3, I anticipate on the rest of the text. First, I state the strengths and shortcomings that I have identified in the literature review (subsection 1.3.1). Second, I establish the research objectives that I derived from this analysis of available results (subsection 1.3.2). Finally, I already assert the main results this thesis lead to (subsection 1.3.3).

1.1 CONTEXT OF THE STUDY

A scientific work cannot be beneficial if its object is treated without reference to the context of the research. This consideration is especially true for applied science and water-related issues. Consequently, I always kept in mind the fundamental aspects of modern hydraulic engineering in carrying out my doctoral research.

As detailed in this section, I have maximized the impact of my research by correlating my fundamental work with its context, which includes six main dimensions:

- a necessity of sustainable development;
- an added value in competitive economical environment;
- a compliance to risk management policy;
- an adequacy to technological means at disposal;
- a high scientific level as required by the FNRS;
- an adequacy with the skills and know-how available within my research unit (HACH).

Degradation of the natural environment prompts all scientists and researchers, especially in civil and environmental engineering, to face new challenges and provide sustainable solutions. Since the XVII's century, the industrial exploitation of natural resources has been causing damages to the biotope (green-house effects, soil pollution,…), depletion of stocks in energy sources,…. Progress has had detrimental effects that we are now responsible for fixing and attenuating. It has also modified climatic conditions so that old natural and human structures need to be re-assessed and modernized. In many cases, solutions to these new problems are not straightforward, require research and funds, constitute a challenge. On the other hand, all the facets of the collective and personal way of life are now deemed by the yardstick of its sustainability, i.e. its ability to curb the negative impacts of human involvement and to preserve the earth's potential for maintaining human wellbeing. This new demand has been considerably modifying the field of engineering by prompting a reorganization of living conditions (sustainable cities), by inducing a re-appraisal of economic sector (green building), or work practices (sustainable architecture), and finally by creating a new field of application for science under the form of Green Technology. The topic of this thesis inscribes naturally itself in this fresh impetus for both preservation of environmental flows from the human impact and sustainable design of hydraulic structures.

Anglo-Saxons used to say that "green is gold". Even if this mantra seems exaggerated, one cannot forget that innovation is a major strategic issue in the globalized economical competition. Any research should aim, at least partly, at creating a competitive advantage and results in the creation of new markets, in quality improvements, in cost reductions,… There is no better way to ensure the best impact for the results of a research. As the following pages highlight it, the topic of my PhD matters to industrials active in the construction sector and the town and country planning. In addition, the new proposed models enable to optimize and improve the design of hydraulic structures.

The notion of risk, which previously was a wooly concept, has been widely investigated and can be now quantified, analyzed, prioritized and even managed. Probabilistic methods naturally occupy a first-rate place in the tools used in risk management. However, physically based methods as presented in this writing offer another valuable point of view in order to assess and quantify potential risks for the structure or the environment. This tool will never replace the expert in this task but surely provides an efficient support.

Modern technological tools give the opportunity to complement the classical analytical and experimental methodologies with numerical approaches. The ongoing increase in the performance of computers as well as the continuous decrease of their cost has been enabling a more frequent use of the Computational Fluid Dynamics (CFD) in designing hydraulic structures, and in analyzing environmental flows. In this case, computers are used to perform the millions of computation required to simulate the flow behavior. If many 3D mathematical models are well known now, the computational effort to solve them remains often too costly for practical applications. Simplified models are then of current use. The biggest part of this study is devoted to develop such a simplified model to describe air-water flows. An adapted numerical scheme is then used to solve the model on practical applications. In this process, I try to find a compromise between the sufficient complexity to describe accurately air-water flows and the necessary simplicity to remain applicable in civil and environmental engineering.

The Belgian Fund for Scientific Research FNRS-F.R.S funded this study about air-water flows. The organism is known not only for the quality of its researchers, but also for maintaining the scientific content of the financed projects at a state-of-the-art level in the globalized research. It goes through a strong involvement in international scientific networks, the diffusion of the results by means of peer-reviewed publications, edition of books, conference presentations, and through the choice of high-potential topics of research. The number and impact of publications coming from the present doctoral research show my ambition to fit my work into this scheme. Notably, I have paid particular attention to the fact that today's works pave the way for valuable research tomorrow (as it will be pointed at in the last section of the thesis).

Finally, daily activities took place at the University of Liège (Belgium), within the Unit of Hydrology, Applied Hydraulics, and Hydraulic Structures (HACH). HACH unit has been making research since the 90's in the field of civil and environmental engineering. The philosophy of the unit is based on a fruitful collaboration between experimental investigations within its laboratory, fieldwork on actual hydraulic structures and natural flows, and theoretical research. Activities of the unit range from a high-level fundamental research in fluid mechanics to the exploitation of results on practical applications. In particular, two decades of research gave birth to a modelling system named WOLF.

1.2 TOPIC OF THE RESEARCH

Hydraulic engineering treats of the conveyance of fluids in natural or anthropogenic environments. Hydraulics is intimately linked with the fields of civil, environmental and sanitary engineering. Common topics of design for hydraulic engineers include hydraulic structures (dams, channels, canals, elevators and levees), water supply networks, drainage networks, storm water management, natural rivers, and tanks, sediment transport, pollutant transfers,…

In this section, I review the flows that are likely to occur in civil and environmental engineering applications. I also identify their main features: unsteadiness and air-water interactions. For the sake of simplicity, I classify all these flows into four basic types, namely free surface flows, stratified flows, pressurized flows, and mixed flows. As pointed in Figure 2, the simultaneous occurrence of free surface and pressurized flows characterizes the "mixed flows" category. The overview underlines the importance of transient air-water flows for civil and environmental engineers. Considering the effect of the air phase on the water flow also blurs the classical distinction between free surface and pressurized flows.

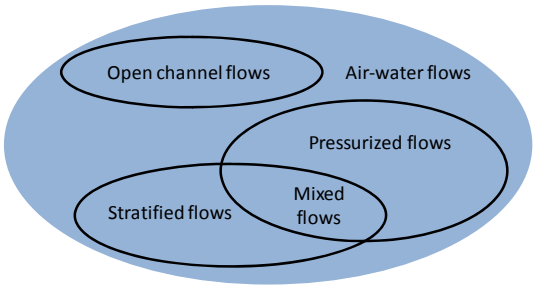

Figure 2: Classification of air-water flows into 4 categories: free surface, stratified, pressurized and mixed flows

In many of the situations summarized in Figure 2, a strong interaction is likely to develop between the water flow and the surrounding air. As pointed in the classic reference written by Falvey [100], "sometimes the interaction produces beneficial effects. However, more often than not, these effects are not beneficial and the remedial action required to reduce the effects can be costly". In both cases, an accurate consideration of the effect of air is thus an industrial necessity, from both an economic and security point of view.

In hydraulic engineering, a traditional distinction is made between steady flows, for which there is no change in conditions at a point with time, and unsteady flows, for which flow velocity and pressure are changing with time. Such a distinguo is clearly academic since a steady flow is the macroscopic result of a microscopic equilibrium of moving particles. The classification remains however very useful in practice, especially for numerical considerations. Furthermore, we define a transient flow as an unsteady flow whose parameters are highly variable over the time. Transient flows usually refer to dam break flows and water hammer phenomena, as I will show in the next pages.

1.2.1 FREE SURFACE FLOWS

A free surface flow can be a waterway, a canal, a river, a lake, an estuary, or the sea. In fact, it designates any liquid flow presenting a free surface. It includes both natural and anthropogenic streams (Figure 3). In the nature, large rivers, mountain torrents, lakes, and ponds constitute examples of free surface flows. In the same category, human-made structures may be channels, dams, spillways,…

Two different velocities characterize a free surface flow, namely the fluid velocity and the wave celerity. The fluid velocity is the velocity of the fluid particles at a given point of the space. On the other hand, the wave celerity is the velocity of a surface wave. To put it another way, the wave celerity is the speed at which the information of pressure propagates in the medium. In free surface flows, both speeds are usually limited to 10m/s. If the wave celerity is greater than the fluid velocity, any perturbation of the flow (topography modification, clutter in the flow,…) may propagate both upstream and downstream. In other words, information may go upstream and the flow behavior adapts itself upstream of the cause of the perturbation. Such a situation is called subcritical flow or fluvial flow. If the wave celerity is lower than the fluid velocity, information propagates only downstream. A perturbation of the river stream affects the flow only downstream its cause. This situation is usually named supercritical flow or torrential flow. Critical flow designates the case for which fluid velocity and wave celerity equalize. A correct representation of the propagation of information is a necessity to assess the behavior of the stream.

Figure 3: Examples of natural free surface streams – a large river (top left) and an underground river (top right) – as well as anthropogenic free surface flows - a dam reservoir (bottom right), and a human-made channel or lock (bottom left)

Surely the most impressive structures in hydraulic engineering, dams are affected by various flow regimes ranging from steady flows to highly transient streams (Figure 4). Flows in the reservoir and downstream the dam are indeed free surface flows. In normal conditions, such flows vary very slowly if they are not simply steady. In the case of dam failure, a transient wave propagates downstream the dam and raises the depth abruptly. Simultaneously, another wave travels upstream into the deep-water region and has the effect of reducing the free surface height. The dam break problem is of utmost importance in hydraulic engineering for two reasons. First, dam failures are generally catastrophic with important casualties. Second, it constitutes an academic problem difficult to solve because of the discontinuity of the flow. The dam break problem is thus a current topic of research. Another case of transience in free surface flows, object of intense research, is the propagation of waves in natural environment. Tidal waves, tsunamis, and storm surges are indeed of particular interest for hydraulic engineers.

Figure 4: Flow over the Contra&Hongrin Dam in Switzerland (Left) and over an ogee-crest spillway (Right)- the flow is divided into a region of clear water and a region of white water characteristic of air entrainment.

In observing natural and anthropogenic high velocity streams one can often identify a region of clear water and a region of milky appearance. This “white water” mostly appear in high velocity flows over a spillway or in a chute (Figure 4). A region of clear water is observed where the water enters the chute or spillway. At some distance downstream, the water takes a milky appearance. “White water” is a phenomenon due to air entrainment or free surface aeration. It is defined as “the entrainment/entrapment of undissolved air bubbles and air pockets that are carried away within the flowing fluid”[44]. As pointed out in Figure 4, the resulting fluid is a mixture of air-water which exhibits a stratified structure [100]:

- An upper zone of drops of water ejected from the free surface in the surrounding air; the distance at which the particles can rise may be considerable.
- A mixing zone where the water surface is continuous but highly fluctuant (surface waves of random amplitudes and frequencies). A good knowledge of this layer is important for two reasons. First, all the air exchange between the water and the air

occurs in this area. Second, maximum heights of the waves determine the height of the open channel side walls.

- An underlying zone where bubbles are diffused within the water body. The concentration of air in this layer is conditioned by the equilibrium between the number and size of the bubbles and the turbulence intensity.
- An air free zone that exists only if the aeration is not fully developed.

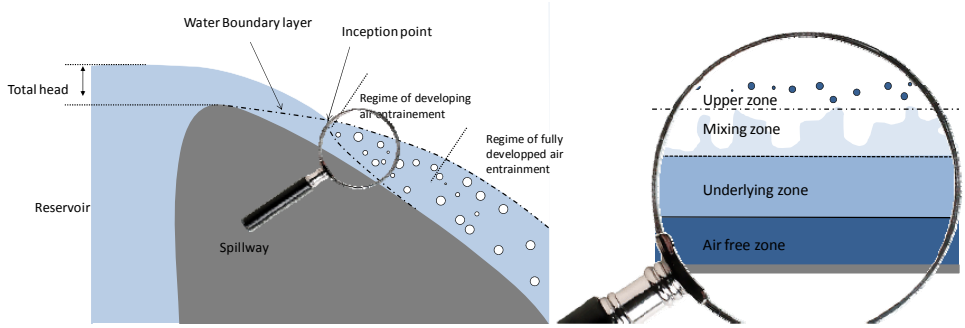

Figure 5: An air-water flow over a spillway presents a longitudinal and a stratified structure

Evidence suggests that air entrainment is intimately linked to turbulence fluctuations in the neighborhood of the free surface. Air is continuously trapped and released through the free surface. It is a dynamic process. The point in the flow where the turbulence level is sufficient to entrain air is called inception point (Figure 5, Figure 6). According to classification of Falvey [100], this point separates a first region called “regime of no air entrainment” from the second region named “regime of developing air-entrainment”. This last one is characterized by a changing air concentration profile along the flow. It is followed by a third region, the “regime of fully developed air entrainment, in which the air concentration profile is constant with distance”. It is commonly admitted that the inception point is localized at the intersection point between the water surface and the boundary layer from the bottom. On the side walls, the boundary layers also generate air-entrainment (Figure 6).

Figure 6: Spillway of the Oldman Dam (USA) [2] - air entrainment on side walls is created by the intersection of the free surface with the side-walls boundary layers

Figure 7: Saint Anthony Falls on the Mississippi River shows a pronounced Hydraulic jump

Hydraulic jump is another phenomenon frequently observed in free surface flows. Both air-entrainment (Figure 7) and transience of the flow parameters affect hydraulic jumps. This phenomenon occurs when a liquid at high velocity (super-critical flow) discharges into an area of lower velocity (sub-critical flow). The transition takes the form of an abrupt rise of the free surface (Figure 8). The Hydraulic jump is characterized by a huge dissipation of energy in large-scale turbulence, waves, and sprays. The macro-scale vortices that develop in the jump roller interact with the free surface and lead to air entrapment, and droplets formation. It results in a two-phase region that cannot be accurately described with a pure hydrodynamic model. According to Chanson [45], "air bubbles and air packets are entrapped at the impingement of the upstream jet flow with the roller. The air packets are broken up in very small air bubbles as they are entrained in the shear region which is characterized by large air contents and maximum bubble count rates. Once the entrained bubbles are advected into regions of lesser shear, bubble collisions, and coalescence lead to larger air entities (bubbles, pockets) that are driven towards the free surface by a combination of buoyancy and turbulent advection." Figure 8 shows the air entrainment in the hydraulic jump.

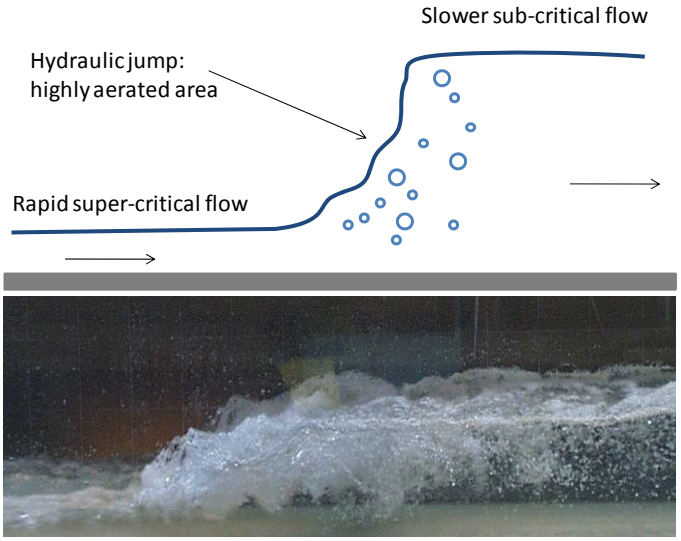

Figure 8: Hydraulic Jump entrapped air at the impingement of the upstream jet flow - Photograph taken at the Laboratory of Construction Hydraulics (University of Liège-HACH)

1.2.2 STRATIFIED FLOWS

A stratified flow is a free surface flow that occurs in a closed section. The considerable role played by the air layer above the free surface justifies the distinction with the previous flow pattern. Such stratified flows often appear in irrigation or sewage schemes that make use of steep pipes or conduits designed to operate at free surface. Often used in dams, bottom outlets, headrace and tailrace tunnels are other hydraulic structures in which stratified flows occur (Figure 9). Their role is essential in controlling the level in the reservoir and the discharge in the hydroelectric stations. Finally, spillway tunnels (Figure 9) also convey a free surface flow from the reservoir to the bottom of the dam. All these structures are designed in such a way that both super-critical and sub-critical flows occur in the pipe with a visible free surface. Computation of the pipe dimension usually does not take into account the case of pressurization. Consequently, pressurization must be avoided at all costs. It requires predicting all the transient phenomena that may occur during the pipe life and accounting for the air-water interactions that are likely to appear. Transient events in stratified flows are the same as those described for free surface flows. We refer the interested reader to the previous section. On the other hand, the question of air entrainment in such partially filled pipelines has recently gained importance. Experimental research and field investigations have indeed underlined the strength of the air/water interactions and the necessity to consider them in designing hydraulic structures affected by stratified flows.

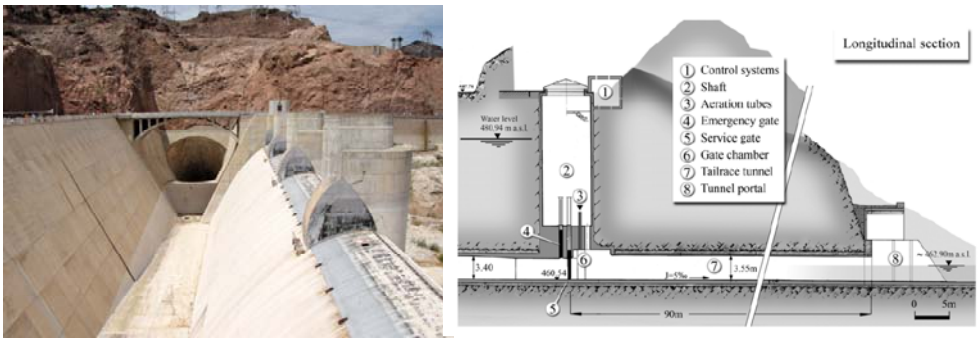

Figure 9: The spillway tunnel of the Hoover Dam in the USA (left) and tailrace tunnel of the Mühleberg bottom outlet (right - according to Keller[165]) present stratified flows in normal operation

Literature [5-7] reports two types of air-water interactions in partially filled pipes, namely self-aeration process (already depicted in the previous section) and air motion in the upper layer (Figure 10). In the second case, the water flowing in the lower layer interacts with the air enclosed above the free surface. The interaction is due to both the interfacial friction and the air pressure variation induced by the free surface motion. It induces instabilities of the free surface. Waves and ripples appear at the interface between the upper and lower layer. Such a mechanism is known as Kelvin-Helmholtz instabilities [329]. Both kinds of air-water interactions enhance the risk of pressurization of the pipe and the potential damages it may cause. Furthermore, the presence of air affects the celerity at which information propagates in the pipe. On the one hand, the air dispersed in the water diminishes the wave celerity. On the other hand, motion of the interface creates perturbations of the pressure in the air layer that travels at a higher celerity (~330 m/s). This pressure wave in

the air interacts with the lower layer and provokes the motion of the interface. These antagonistic phenomena significantly alter the dynamics of the flow.

Two tasks enable to prevent unexpected air-water interactions. First, it requires assessing the demand in air and designing adequate air vents. Second, it is necessary to describe accurately the effect of this amount of air on the behavior of the water flow. A key point in this respect is the influence of the air supply system. The quantity of air entering in the closed conduit may indeed affect considerably the water dynamics.

Figure 10: Stratified flows present a water lower layer and an air upper layer separated by a free surface

1.2.3 PRESSURIZED FLOWS

Water distribution networks, low-pressure sewer systems, hydroelectric plants, cooling systems, and forced pipes in dams are all devices that aim at conveying water under pressure. The importance of such structures is vital. Consequently, pressurized flows, aka pipe flows, are of utmost importance in many engineering problems. This importance is heightened because of the environmental dimension of the involved implication and the inherent risks to maintain conduits under pressure.

When the fluid in motion in the pipe is forced to stop or change direction suddenly, a pressure surge occurs. This water hammer propagates at high velocity along the pipeline. The pressure wave celerity depends on the pipe characteristics, the compressibility of the fluid, and the level of pressure. For water in rigid pipes, its value is about 1400 m/s. Water hammer commonly occurs when a valve is suddenly closed at the end of a pipeline system or upon the starting of a pump. This pressure wave can cause major problems, from noise and vibration to pipe collapse. For this reason, most of the structures are equipped with hydraulic devices that aim at attenuating the surge intensity. ARAA Balloon, water towers, air valves, bypasses are examples of mitigating measures. In any case, taking into account the water hammer is a necessity in most hydraulic engineering problems.

Sub-atmospheric pressures may appear in the pipe. Water hammer or very high velocity in low points of the pipe usually explains such a negative pressure. It results in the dilatation of the water and the contraction of the pipe without apparition of a free surface. Sub-atmospheric pressurized flows may only appear if the aeration device does not supply enough air to enable the apparition of a free surface. In the cases where the pressure drops below the liquid vapor pressure, cavitation is likely to appear. Cavitation is the formation of vapor bubbles inside the fluid. Since shock waves formed by the implosion of cavitation bubbles may severely damage the pipe, pipelines design should absolutely prevent the apparition of sub-atmospheric pressures.

The entry, control, and release of air from pipelines are major concern in designing such hydraulic structures. Air in lines comes from different sources. During its filling, a pipeline is full of air. If adequate systems of air release (valves, vents…) are not disposed, air pockets may remain at high points. Air also enters through mechanical and hydraulic equipments such as pumps, valves, gates, dropshafts… Finally, water contains always over 2% of air. Dissolved air may transform into free gas phase when the pressure drops.

Air in pipes may have both beneficial and detrimental effects. In first approximation, one can say that the presence of air in pipes is a problem for three reasons [98]:

- Air pockets reduce the effective pipe cross-section and increase head losses. It results in a decrease in pipe capacity.
- Bulk properties of the fluid (air-water mixture) are changed. It modifies the dynamics of hydraulic transients, notably by reducing the pressure wave celerity.
- Air accumulations may lead to disruptions of the flow such as blowbacks or blowouts. This leads to vibrations and structural damages or even geysers (Figure 14).

On the other hand, free air may be beneficial for cavitation prevention. Presence of free air is known to diminish the impact of the implosion of cavitation bubbles.

1.2.4 Mixed Flows

Mixed flow is defined in literature as the simultaneous occurrence of free surface and pressurized flows. Such a flow displays a hybrid behavior, as the motion is governed mainly by gravity in the free surface part and by pressure in the pressurized part. Consequently, the wave celerity ranges from about 1m/s to about 1000m/s in mixed flows. In particular, the celerity varies very rapidly at the transition point. Hydraulic engineers frequently encounter mixed flows in sewer systems, storm-water storage pipes, flushing galleries, bottom outlets, and even in river networks.

Figure 11: Mixed flows are defined as the simultaneous occurrence of free surface and pressurized flows

Some hydraulic structures are designed to combine free surface and pressurized sections. For instance, water intake is a hydraulic device built to divert water from a reservoir into an irrigation network or a hydroelectric plant. Most of them consist in a pipe under pressure connected to an open-channel flow and constitute thus a mixed flow. Another example is the bottom outlet of a dam. It is used to draw down the reservoir level or to flush the sediments that accumulate into the reservoir. At the building stage, a bottom outlet can also serve as temporary channel for the river. According to the type of control gates and the position of the outflow in relation to the tailwater, they operate either under pressure or under free surface over part of their length. Recently, the need for additional flexibility in the hydraulic electricity production and the re-assessment of existing hydraulic structures justified a relaxing of the “no-pressurization rule” in many situations. New guidelines for sewer systems, water intakes, and tailrace tunnels allow partial pressurization.

Many hydraulic structures are designed for conveying only free surface flow. It means the conduit is able to convey a pre-determined discharge in free surface flow conditions. The design criteria depend on the return period of the inflow. However, an unexpected change in the boundary conditions may cause a rapid pressurization of the flow. Evocative examples of such situations are the sudden rises of water level in a manhole or a dropshaft caused by an extreme water inflow, the rapid closure of a gate, the failure of a pumping system, or the starting of a pump. This transition may happen gradually. The flow depth arises progressively and eventually reaches the pipe crown. It also may take place abruptly under the form of a dynamic pipe-filling bore that propagates along the pipe at a very high velocity.

Figure 12: Tailrace tunnel of the Rankine Generating Station in Niagara Falls [149]

During the transition from free surface to pressurized flows, air/water interactions may arise, particularly at the transition bore [301] (defined as the discontinuity where the free surface flow get pressurized). The water inflow squeezes the air phase initially present within the pipe. Literature gives the name of “air cushioning” to this air pressurization. Air cushioning is known to reduce the velocity of the pipe-filling bore, to create transience in the conduit,… In addition, the transition bore entraps air that is then transported and diffused within the pressurized flow.

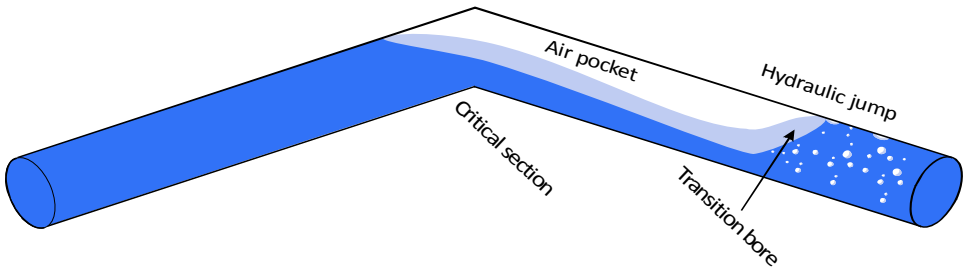

Figure 13: Large air pockets may accumulate at high points in pipelines

In water networks and pipelines, large air pockets may accumulate at high points of the pipe [98]. It is thus important to place air removal systems in such points. Even though air valves have been placed, air pockets may appear due to the change in pipe slope. For instance, the high point may be a critical section. An air pocket is thus entrapped between the control section and a hydraulic jump (Figure 13). The hydraulic jump entrains air under the form of small bubbles. It creates a mixed flow with strong air-water interactions.

Finally, Vasconcelos [298, 300, 303] underlined that flow regime transitions caused a number of serious operational problems in storm water drainage systems. According to him, strong rain events caused damages to drainage systems. Damages were mainly due to pressure peaks as air pockets were expelled through vertical shafts or manholes. The apparition of geysers in storm water storage pipes is an example of such an accident. Many cities in the USA complement their combined sewage system by an underground tunnel for inline storage. The goal of such a storm-water storage tunnel is to prevent the overflow of the sewage system if the flow rate exceeds the capacity of the treatment system. The tunnel is used to store waters during the storm events. Storm water are later pumped to the treatment plant during dry weather [135]. Under extreme inflow conditions, entrapped air pockets in such inline tunnels may result in the development of large pressure forces due to air pocket compression and water hammer caused by a sudden air expulsion. In particular, Vasconcelos [298] reports the occurrence of a geyser in such a tunnel recorded by a security camcorder in St. Paul, Minnesota. It is now admitted that such a geyser is produced by the evacuation of a large air pocket entrapped in the storm-water storage networks below the road. When evacuating the pipe, the air pocket entrains a large amount of water that creates a column of water. Figure 14 represents different snapshots taken out of a video. In the first and second pictures, the geyser starts. In the other pictures, the geyser is fully developed and it reaches several meters in height. A large amount of water overflows the road. The phenomenon lasts barely 20 seconds. The last picture shows the state of the road at the end of the geyser. The car gives a good idea of the scale of the phenomenon. It is worthwhile noting that the manhole plug has been blown out and “New-Jersey” barricades have been displaced.

Figure 14: Storm-water storage tunnel - Chicago TARP

1.2.5 Multi-phase Classification of Flows

In contrast with hydraulic engineering, multiphase theory classifies flows according to the internal phase distribution or “pattern” instead of the distinction pressurized/free surface flows. The flow patterns that develop depend upon the relative rates of both air and water flows as well as upon the slope of the pipe. In horizontal and near-horizontal conduits, literature [98, 100, 264] reports five different patterns of interest in this research.

Bubbly pressurized flow presents air bubbles that form at the upper surface of the pipe. The bubbles and water velocities are about equal. Bubbly flow pattern occurs at relatively large water discharge, with little airflow.

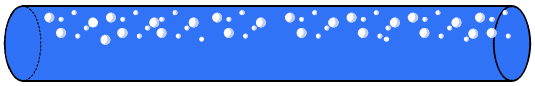

Figure 15: Bubbly pressurized flow

For increased air rate the bubbles coalesce to form an air pocket called plug. In such *plug flows* the main water flow entrains these pockets. At a given point of the pipe, we observe alternatively a moving plug of water or a moving plug of air. Dynamics and celerity of plug flows remain those of a pressurized flow.

Figure 16: Plug flow

Stratified smooth flow presents a distinct horizontal interface that separates the air and water flows. The rates of both water and air are in this case relatively small. In particular, the upper air phase hardly affects the behavior of the water phase.

Figure 17: Stratified smooth flow

As the airflow increases, interactions amplify between the air and water phases in the neighborhood of the interface. Surface waves appear on the stratified flow interface. It forms a *stratified wavy flow*. The previously smooth interface becomes rippled and wavy.

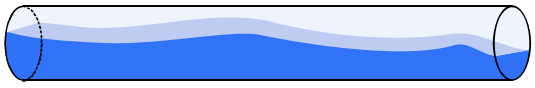

Figure 18: Stratified wavy flow

Finally, the amplitude of the surface waves becomes large enough to reach the pipe crown and seal the conduit. It results in a *slug flow* characterized by travelling slugs whose velocity is bigger than the average water velocity. What is more, the slug entraps a small amount of air under the form of small bubbles. Dynamics and celerity of slug flows remain however those of a free surface flow.

Figure 19: Slug flow

Slug and plug flows are called *intermittent flows* because the flow parameters present large time fluctuations even in steady conditions. The transition from slug to plug flow is also very gradual. At a certain point, it is even difficult to say if the flow is pressurized or free surface.

In conclusion, the present section provides a brief overview of the flow frequently encountered in civil and environmental engineering. In particular, I emphasized on both transient cases and situations exhibiting strong air-water interactions. This outline should convince the reader of the importance of transient air-water flows for people involved in applied hydraulics, namely engineers, scientists, practitioners,… Moreover, the comparison of the flow classifications in single and multi-phase theories shows that the distinction between free surface and pressurized flows is somewhat blurred when considering the effect of air on the water flow.

1.3 SCOPE OF THE THESIS

Civil and environmental engineers make frequent use of mathematical models (and their numerical solutions) to handle problems related to environmental flows and hydraulic structures like those presented in section 1.2. In this respect, the need of consistent models has never been more pressing. The acuteness of the situation is prompted by growing concerns about environmental issues. It also results from the increase in the number and in the technical nature of civil engineering works related to hydraulic structures, transportation means as well as town and country planning. In addition, economic and commercial objectives urge engineers to use more accurate design methods. Finally, the development of the Computational Fluid Dynamics combined with the expansion of personal computers give a new field of application for mathematical models.

In this section, I anticipate on the rest of the text by briefly stating the foremost content of Chapter 2 to Chapter 10. First, the strong background of results available in fluid mechanics is reviewed. More specifically, I identify several shortcomings in single-phase models frequently used in civil and environmental engineering. I also underline that the use of multiphase models in hydraulics remains in its infancy. Based on these shortcomings of classical methods, I state the objective of this research: developing a unified mathematical and numerical model for simulating a wide range of air-water flows. Finally, I summarize the major innovations of this research in three propositions and two computational codes. These are the findings of my doctoral research.

1.3.1 LITERATURE REVIEW AND SHORTCOMINGS OF CLASSICAL METHODS

Current section summarizes and interprets the results of the literature review presented in Chapter 2. This chapter is indeed dedicated to reminding state-of-the-art results in Computational Fluid Dynamic (CFD) for environmental and civil engineering. Since CFD is a highly interdisciplinary activity, I successively review the fundamentals of continuum fluid mechanics, the mathematical models for single- and multi-phase flows, the numerical methods for hyperbolic problems, and the homemade modelling system WOLF.

Making basic assumptions about the fluid flow is a prerequisite to deriving a mathematical model from real world observations. In this respect, the continuum assumption, the continuity principle, and the law of momentum conservation have been proven effective in fluid mechanics. These assumptions, applied to multiphase flows, give the Local Instant Formulation (LIF). The LIF includes field and constitutive equations for each single-phase sub-region. Jump conditions link single-phase regions with each other. LIF constitutes a reliable basis to develop efficient models.

Hydraulic engineers mostly recourse to single-phase models coupled with an advection-diffusion equation when dealing with environmental flows. In the three-dimensional framework, Reynolds-averaged Navier-Stokes (RANS) equations describe the evolution of

both the velocity field and the pressure in the pure water. For essentially one-dimensional applications, the Saint-Venant equations govern the evolution of the flow cross-section and the velocity component along the mainstream. An advection-diffusion equation for passive scalars complements both models and describes the evolution of the concentration in dispersed phase. What is more, various forms of the pressure term accommodate free surface equations to pressurized flows as well. Close scrutiny of these models reveals however weaknesses in their mathematical formulation. In particular, equations fail to describe rigorously the impact of the dispersed phase on the water flow, to characterize the mechanism of dispersion within the water flow, and to give an unambiguous definition of the concentration. Finally, mixed flow formulations are unable to account for the presence of air in the pressurized flow and present spurious oscillations at the transition bore.

The use of multiphase flow theories in civil and environmental engineering has remained circumscribed to very few attempts. If it gives interesting preliminary results, the theory is still in its infancy. A more thorough two-phase theory originates from chemical and mechanical engineering. In particular, the drift-flux model is a three-dimensional macroscopic model frequently used in these fields. It is derived by time-integrating the LIF. In my opinion, it constitutes a reliable alternative to RANS equations. Drift-flux model addresses indeed most of the shortcomings identified in the single-phase approach. Nevertheless, it has never been used in the field of environmental and civil engineering.

Since its inception, Computational Fluid Mechanics has been developing at an outstanding high rate and has met success in numerous fields of application. Examination of basic discretisation techniques available in literature underlines the performance of “numerical shock-capturing” schemes over structured grid, and the ability of the Finite Volume Method to handle discontinuities and to ensure conservation of the physical quantities. For a first order of accuracy, both Godunov methods and Flux Vector Splitting have their own advantages and shortcomings. Extension to higher order of accuracy requires using Total Variation Diminishing schemes for ensuring the stability of the method.

Development of both the mathematical model and the numerical scheme must aim at facilitating the integration of results into the modelling system WOLF. Researchers from the HACH unit have been developing this software for the last twenty years. WOLF is an integrated package of various computational schemes for pure water and sediment flows [73, 79, 81, 95, 97]. Its one-dimensional module relies on the Saint-Venant equations as well as a finite volume scheme coupled with an original Flux-Vector splitting.

1.3.2 OBJECTIVES

The precise objective of this thesis is to develop a unified mathematical and numerical model for simulating a wide range of air-water flows. Particular emphasis is placed on flows relevant to civil and environmental engineering. Shortcomings of traditional methods motivate the use of a multiphase theory (the drift-flux model). Seven conditions are sought in the development of the model. Equations must:

- account for the multiphase character of flows;
- handle transient features of the flow;
- account for the scale heterogeneities in time and space;
- unify the description of pressurized and free surface flows;
- remain affordable from a computational point of view;
- be implementable under the form of a computational code;
- be validated on academic problems and applied on real cases.

As already mentioned, the new model has to take into account the presence of air with a sufficient fidelity. In particular, it should describe efficiently the interaction of the water flow with the dispersed air and the external environment. Examples of hydraulic structures and environmental flows presented in section 1.2 underlined indeed this necessity to describe correctly the effect of the air in many practical applications. For this purpose, I aim at applying multiphase flow theories in the field of civil and environmental engineering.

Second, the model has to capture adequately the unsteadiness, and even the transience, that is likely to appear in pipes and channels. As shown in section 1.2, this is a necessity in designing hydraulic structures. Particularly, the role of the engineers is to attenuate the pressure variations for security reasons.

Practical applications and mechanisms encountered in free surface hydraulics present scale heterogeneities in time and space. The set of equations must handle correctly this disparity that may be important. Indeed, the spatial scale of typical situations encountered in civil and environmental engineering ranges from country-scale river networks to localized hydraulic structures such as manholes, valves, or gates. Intermediate applications include sewer systems, channels, dams, levees, water intakes, spillways… In a similar manner, the typical time scale of hydrodynamic flow ranges from steady flows that are not affected by time variation to highly transient phenomena such as wave propagation and turbulent instabilities. Finally, even in a single application, the space scale of mechanisms involved ranges from the macro-scale gravity force to the Kolmogorov micro-scale turbulent dissipation. In a similar manner, the time scale varies greatly with the kind of phenomenon observed. For instance, flood wave propagation in a river has a typical timescale of a few minutes or hours. However, sedimentation phenomena in the same river have a longer characteristic time scale, spanning over years or decades. All these mechanisms are linked with each other such that none of them can be neglected without causing a significant uncertainty. Still today, taking into account scale dissimilarities remains challenging.

ext, there is a need to overcome the traditional opposition between free surface and pressurized flows in order to create a unified framework of simulation. The dynamics of free surface flow is indeed mainly governed by gravity, which is the driving force of the fluid motion. It results in a hydrostatic distribution of pressure over the flow depth. In pressurized flows, the driving force is the pressure itself, which is assumed constant over the flow cross-section. Taking into account the air phase blurs this distinction, to such an extent that it loses any sense.

Computational effort to solve the model has to remain sufficiently affordable in order to create a computational code that is usable for classical engineering problems. Granted, it requires developing an optimized algorithm. But simplifications may already be applied to the mathematical model. For instance, judicious practice of time and area-averaging methods lead to a simplified 1D model whose applicability is partially extended to 3D flows by enriching the vertical profile of the flow parameters.

Usefulness of mathematical models would be very limited without disposing of the required tools to apply the equations to practical cases. Computational Fluid Dynamics (CFD) provides the set of necessary methods to perform computation. Indeed, CFD enables to treat continuous fluids, described by continuous equations, in a discretised fashion on a computer. Consequently, the problem of the discretization is also addressed in this thesis. The resulting algorithm must be able to treat all the engineering problems presented in section 1.2 and to preserve the fundamental features of the mathematical model, in particular the five conditions presented here above.

In order to prove the validity of both the mathematical model and its implementation in a discretised manner, I perform validation on a large number of benchmarks. Finally, interest of the results is exemplified by application of the developed algorithm on real engineering problems.

1.3.3 Propositions and Original Results

In the current section, I already introduce the innovations of my doctoral research. For this purpose, I state three propositions, namely a first, a second, and a corollary proposition. The development of these three propositions relies on a solid background of research and publications (see the literature review presented in chapter 2).

The **first proposition** queries the traditional distinction between free surface and pressurized flows. A rigorous analysis of both the mathematical formulation of the equations and the physical behavior of natural flows shows that:

> Any one-dimensional set of equations describing free surface flows can be extended to pressurized and mixed flows by modifying the pressure term. The unified formulation depends on the pipe characteristics, the flow area, and the aeration rate of the pipe.

This aspect of the doctoral research is treated in Chapter 3 for single-phase flows and in chapter 7 for air-water flows. It results in an original formulation of the pressure term that extends the applicability of traditional mixed flows models to sub-atmospheric pressures and air-water flows.

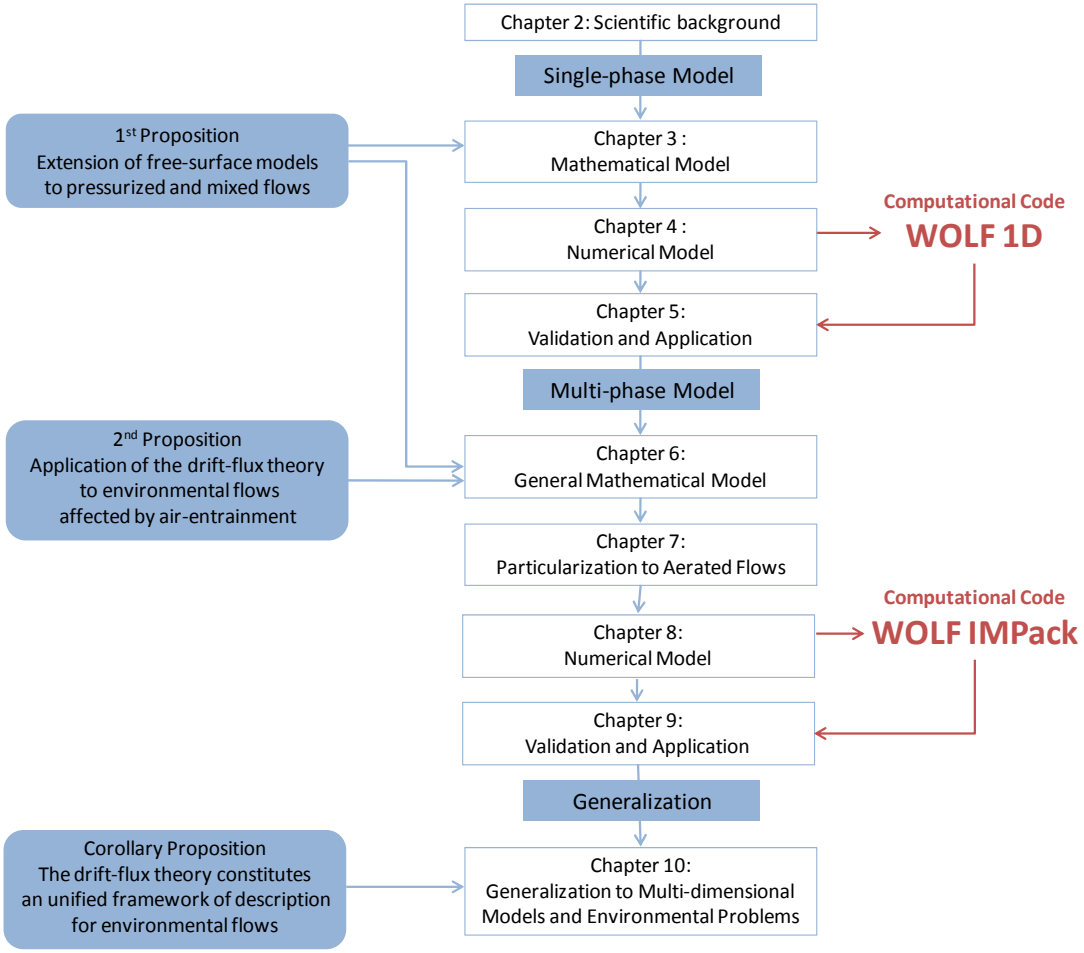

Figure 20: General map of the text - Part, chapters, propositions, and computational codes

An adequate discretization of the equations and the development of an efficient algorithm are a prerequisite to the validation and practical applications of the new model. Because of its ability to both ensure the strict conservation of mass and momentum and handle discontinuous solutions, the finite volume method is used here to solve the partial differential equations. In chapter 4 and 5, performances of various numerical fluxes are compared in view of their ability to treat transient single-phase flows. Pros and cons of each method are listed. Evidence argues in favor of the Flux Vector Splitting originally developed within the HACH for the modeling system WOLF. The resulting algorithm is implemented within the module WOLF 1D such that its applicability is extended to pressurized and mixed flows as well. Validity of WOLF1D is assessed by comparison with analytical, numerical, and experimental data. The module is then applied to two practical cases: the design of a sewer system, and of a city low-pressure sewer network.

The **second proposition** concerns the opportunity to use multiphase theories in order to enhance the fidelity of models used in civil and environmental engineering. Particular attention is brought to the description of free surface flows and air-water interactions. It can be formulated as follows:

> Originating from chemical and mechanical engineering, up-to-now principally applied to small-scale pressurized flows, the drift-flux theory constitutes an adequate alternative to Navier-Stokes equations in order to derive mid- and large-scale free surface multiphase models. Such models provide an improved description of free surface environmental flows affected by air entrainment.

The following pages address this proposition from both a theoretical and practical point of view. Chapter 2 exposes the basics of multiphase theories. The review arguments in favor of the drift-flux model as a valuable answer to our query. Chapter 6 proposes an original Eulerian cross-sectional integration of the 3D drift-flux model over a general flow cross-section. It results in an innovative one-dimensional drift-flux model that accounts for the free surface, for two phases, and for a multi-layer behavior. Next, chapter 7 presents a particularization of the previous model to air-water flows. This original drift-flux model includes two layers and three phases: water, dispersed air and pure air above the free surface.

In chapter 8, I discretize the new multiphase model by using an extension of the flux-vector splitting chosen for single-phase flows. The original algorithm is then implemented into a new research modeling system called **WOLF IMPack** (**I**ntegrated **M**ulti-**P**hase **PACK**). Both performance and validity of the model are assessed on various benchmarks and applied to different practical cases (Chapter 9).

Finally, I anticipate the next steps of the research by widening the object of my doctoral research to other multidimensional environmental flows with transport of a dispersed phase. It is the **corollary proposition** that states that:

> The drift-flux model developed in this thesis to describe one-dimensional air-water flows may be extended to many other phenomena of interest in civil and environmental engineering. It constitutes a unified framework of description for environmental flows.

Chapter 10 summarizes the discussion on the extension of this model to sediment and pollutant transport, to multidimensional problems, and to rough- and vegetated-roughness. In 2006, Dewals' PhD thesis [75] paved indeed the way for a unification of the flows simulation and their interactions with various constituents; while the present PhD thesis provides an adequate mathematical formulation to this objective. This topic has been partly treated in a book [174] published in 2010.

Summary and conclusions

Sections 1.1 and 1.2 of this chapter defined the context and topic of the research. Precisely, the topic section specified what I mean by “transient air-water flows in civil and environmental engineering”. In particular, I underlined the industrial and scientific interest to improve the description of such flows. On account of this necessity to improve the understanding of air-water flows, I chose the develop a unified mathematical and numerical model as the main objective of this thesis. The associated computational code must meet seven conditions presented in section 1.3.

In order to meet this objective, I orient my research on methods to unify the description of pressurized and free surface flows as well as on multiphase theories originating from chemical and mechanical engineering. This research results in three propositions that summarize innovations proposed in this thesis. It also gives birth to two computational codes: WOLF1D for pure water flows and WOLF IMPack for aerated flows.

In the next chapters, theoretical arguments will prove the soundness and efficiency of the three propositions. Validations and practical applications will also exhibit performance of the new computational codes. In particular, all these original results rely on a solid background of research and publications that I briefly summarize in the following chapter.

Chapter 2 Scientific Background

This chapter aims at:

- ✓ establishing the scientific background of the research;
- ✓ identifying the knowledge gap that is proposed to be filled.

Design and innovations in hydraulics date back to the ancient and medieval era in the Hellenistic, Roman and Islamic worlds. Maybe the most famous hydraulic structure from this period is the “Pont du Gard”, an aqueduct in the South of France (Figure 21). Romans designed the bridge to carry water across the small Gardon River valley. It was part of a 50km long aqueduct that brought water from the Fontaines d'Eure springs near Uzès to the Castellum in the Roman city of Nemausus (Nîmes). In view of the size and durability of the aqueduct, Romans must already have mastered the basis of hydraulics and they had at hand various methods of design.

Figure 21: "Pont du Gard” is one of the most famous hydraulic structures from the ancient era.

Historically, the design of hydraulic structures has been relying on experimental methods, under the form of both guidelines and scale models in a laboratory (Figure 22). Simple and small engineering projects make frequent use of guidelines for design. Guidelines usually rely on systematic experimental researches on a particular structure or on common practice reputed to be safe and efficient. On the other hand, scale models are more precise and reliable but also more expensive. Resorting to such a method is then restricted to larger and more complex engineering problems. In any case, a first step of design based on guidelines is necessary before assessing the validity of the solution with a scale model.

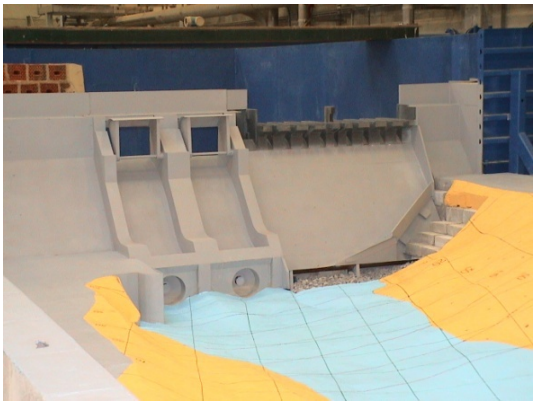

Figure 22: Classical hydraulic design relies on scale models – Example of a PKW spillway [211] built in the Laboratory of Engineering Hydraulics (ULG-HACH)

Using an analytical solution is another predictive tool that is useful in science and engineering. Historically, such methods appeared later than experimental methods because it relies on a mathematical model describing the problem, the form, and origin of which depend on the particular field of study. Since governing equations of fluid flows are often complex (e.g. a multidimensional system of partial differential equations along with a complex domain of computation), analytical solutions are obtainable only if sufficient simplifications can reasonable be made. Applicability of analytical methods is thus limited. According to Toro [286], the process of using these methods remains however useful in a number of ways. First, finding an analytical solution to a physical problem requires the development of a relatively good understanding of the phenomenon. Second, analytical solutions may be very valuable in assessing the interrelation between various aspects of the problem.

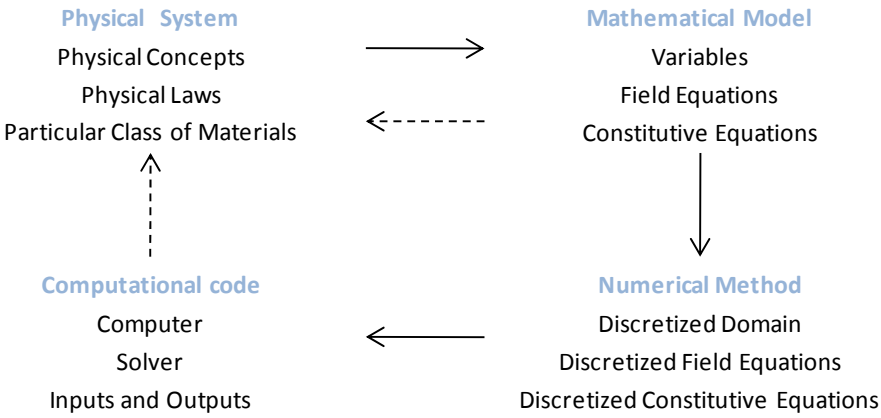

Figure 23: The classical method to solve a problem in CFD includes four interdependent stages

Computational Fluid Dynamics (CFD) has found its own place between the two traditional methods (analytical and experimental methods) as a valuable alternative to design hydraulic structures and simulate environmental flows. Its boom is intimately linked to both the increase in computational capacity of computers and the improvement of mathematical models. In fact, CFD has a common starting point with analytical methods: a mathematical model. Instead of seeking a simplified continuous solution to the model, CFD solves the

governing equations in a discretised fashion on a computer. The method requires a discretised form of the equation (aka numerical scheme) and a discretization of the spatial and temporal domains. Theoretically, this feature enables to apply CFD to every practical cases encountered in civil and environmental engineering. In practice, first codes only dates back to the sixties. Many ongoing researches still aim at improving the accuracy of CFD codes and extending their applicability to the widest range of applications. This doctoral research takes part in this global quest.

CFD is a highly interdisciplinary activity involving theoretical concepts of fluid mechanics, a strong background of mathematical results and a comprehensive use of computer science (Figure 23). In this respect, I do not start from scratch and my research relies on a strong background of results. Consequently, this chapter is dedicated to a brief reminder of state-of-the-art results in CFD for environmental and civil engineering. This chapter is naturally not an exhaustive review of the literature in CFD. Rather, its purpose is to situate my research within material already published and to identify knowledge gaps in the simulation of transient air-water flows. I also aim at providing the sufficient knowledge to assess the scope and validity of original works presented in chapters 3-10.

In this respect, the standard approach to simulate the transport of a dispersed phase consists in coupling pure water models with an advection-diffusion equation for the concentration. As pointed in this section, such models fail in describing accurately the behavior of the dispersed phase and its interaction with the water flow. On the opposite, mechanical and chemical engineering provides a consistent description of a dispersed phase behavior and accurately accounts for interactions between the water and the dispersed phase. These multiphase models are widespread for small-scale applications involving pressurized flows. However, their application remains in its infancy for mid- and large-scale applications in civil and environmental engineering. Particularly, one-dimensional multiphase models do not describe free surface and mixed flows. Next, the finite volume method is proven an efficient methodology to discretize and implement such models into a computational code. In conclusion, available single- and multi-phase models are not sufficient to describe transient air-water flows. Consequently, creating a computational code requires additional research on both the mathematical description of such phenomena and its implementation into a code.

This literature review is subdivided in four sections summarizing main results about:

- the fundamentals of continuum fluid mechanics;
- the mathematical models for single-phase flows;
- the mathematical models for multi-phase flows;
- the numerical models for hyperbolic problems.

2.1 Continuum Fluid Mechanics for Single and Multi-phase Flows

In natural science and engineering, describing and understanding a system can be tackled by developing a model, which is "a representation of the essential aspects of an existing system (or a system to be constructed) which presents knowledge of that system in usable form" [99]. In engineering, this usable form is most often a mathematical model. In order to derive such a mathematical model from the real world, some basic assumptions about the fluid flow are needed.

In this respect, common assumptions in fluid mechanics are the continuum assumption and the laws of conservation. From these assumptions, a unified mathematical model that describes both single and multi-phase flows was derived: the Local Instant Formulation (LIF). This model constitutes a reliable basis to derive models applicable to practical cases.

2.1.1 Fundamental assumptions

The continuum assumption is proven to produce extremely accurate results when applied to fluid mechanics [38, 152]. This hypothesis states that the matter in the body is continuously distributed and fills the entire region of space it occupies. In other words, both fluids can be continually sub-divided into infinitesimal elements with properties being those of the bulk material. Fluids involved in this research, namely liquids and gases, accord with this definition of continuum mean. Granted, both fluids are composed of molecules separated by empty space. However, approximating the fluid as a continuum is widely accepted and proven in fluid mechanics. This assumption supports the majority of studies since the 18th century.

In this thesis, I do not consider any thermodynamic relations because the research focuses only on the mechanics of air-water systems. In addition to the continuum assumption, I make the hypothesis that every fluid obeys:

- The law of mass conservation or continuity principle [11, 75, 288]: the mass of a closed system remains constant, regardless of the processes acting inside the system. An equivalent statement is that matter cannot be created/destroyed, although it may be rearranged.
- The law of momentum conservation [9, 38, 75]: the momentum of a system is constant under zero net force. To put it another way, the momentum of a closed system remains constant; but can be changed through the action of forces as described by Newton's laws of motion.

2.1.2 Field Equations

Field equations translate the laws of mass and momentum conservation in smooth parts of the flow (called field in this thesis). Smoothness implies in this case that flow parameters do not present singularities. Under the continuum assumption, a single-phase fluid presents such a smooth behavior. It forms a field. By contrast, a multi-phase flow presents

discontinuities at each interface between phases and does not constitute a field in itself. Hopefully one can sub-divide any multiphase flow into single-phase regions with moving boundaries. Since each sub-region bounded by interface forms a field, the same field equations describe both single and multi-phase flows:

$$\begin{cases} \dfrac{\partial \rho_k}{\partial t} + \nabla.\left(\rho_k \mathbf{v}_k\right) = 0 \\ \dfrac{\partial \rho_k \mathbf{v}_k}{\partial t} + \nabla.\left(\rho_k \mathbf{v}_k \mathbf{v}_k\right) = -\nabla.\mathbf{T}_k + \rho_k \mathbf{F}_k \end{cases} \qquad k = w, g \tag{2.1}$$

where k denotes the phase (k=w for water and k=g for air), ρ_k is the density of the k^{th} phase, $\mathbf{v}_k$ is the velocity of the k^{th} phase, $\mathbf{T}_k$ is the surface stress tensor of the k^{th} phase, and $\mathbf{F}_k$ is the body force acting on the k^{th} phase. The primitive unknowns of the system are the density and velocity. Additional constitutive equations define the surface stresses and body forces. Rigorous demonstration of the field equations is beyond the scope of the thesis. The proof, available in the following books [38, 154, 173], relies on the concept of control volume and the Reynolds transport theorem.

2.1.3 Constitutive Equations

The number of dependent variables in (2.1) exceeds that of the field equations such that it is necessary to close the system by adding relations called constitutive equations. The constitutive laws lean on three different bases [33, 154]. First, the entropy inequality is a restriction on the constitutive laws and must be satisfied regardless of the material response. Second, constitutive axioms idealize in general terms the response and behaviors of all materials included in the theory. In this respect, continuum mechanics frequently employs the principle of determinism and local action. Third, constitutive equations are mathematical models of a particular group of materials. Establishing such equations requires a set of experimental data. Discussion of the entropy inequality and constitutive axioms are beyond the scope of this text and we refer the interested reader to the book of Ishii [154]. In hydrodynamics, the mechanical constitutive equation and the equations of state are sufficient to close the system.

Both air and water are compressible to some extent. It means that the density of the fluid changes with respect to pressure. However, free surface water flows exhibit a sufficiently small compressibility that one can assume water as incompressible. To put it another way, the variation of water density in the range of pressure encountered in free surface flows is so small that one can neglect them. Assuming the incompressibility gives the following equation of state for the water density:

$$\rho_w = C^{st} \tag{2.2}$$

In this case, a thermodynamic relation cannot specify the pressure. Thus, the hydrodynamic pressure is defined as the average of the normal stress:

$$\mathbf{T}_w = \boldsymbol{\tau}_w - p_w \mathrm{I} \tag{2.3}$$

where p_w is the pressure of the water and $\boldsymbol{\tau}_w$ is the viscous stress of the water phase. In pressurized water flows, this assumption no longer holds and the water compressibility plays an important part in transient phenomena like a water hammer. In a similar manner,

the compressibility greatly affects both pure air flows and air-water mixture flows. Assuming them incompressible leads to excessive errors. Additional assumptions are then required to specify the compressibility of the fluid. One possibility is to assume the conservation of both the Energy and the Entropy [38, 152, 255]. Due to the complexity of this theory, applied hydraulics rarely makes use of such assumptions. In this thesis, I assume that equations (2.2) and (2.3) apply for both a pressurized flow and the air phase:

$$\rho_g = C^{st} \quad \text{and} \quad \mathbf{T}_g = \boldsymbol{\tau}_g - p_g \mathrm{I} \tag{2.4}$$

Assumption of incompressibility may seem abusive in this case. For this reason, I will correct models a-posteriori thanks to a pragmatic formulation of the pressure wave celerity. I will prove this method is efficient in accounting for moderate compressibility rates.

Stress tensors $\boldsymbol{\tau}_g$ and $\boldsymbol{\tau}_w$ conventionally describe the effect of viscous forces. For many natural fluids (water, air,…), evidence suggests that the stress state is linearly related to the strain rate (or velocity field). In such a case, the rheological constitutive equation is given by the Newton's Law of Viscosity [255, 280]:

$$\boldsymbol{\tau}_k = \mu_k \left[\left(\nabla \mathbf{v}_k + \left(\nabla \mathbf{v}_k \right)^T \right) - \frac{2}{3} \left(\nabla . \mathbf{v}_k \right) \mathbf{I} \right] \tag{2.5}$$

where μ_k is the dynamic viscosity and $\mathbf{I}$ is the identity matrix. For an incompressible fluid, equation (2.1) reduces to a divergence-free velocity field such that equation (2.5) amounts to shear stresses only:

$$\boldsymbol{\tau}_k = \mu_k \left(\nabla \mathbf{v}_k + \left(\nabla \mathbf{v}_k \right)^T \right) \tag{2.6}$$

2.1.4 Interfacial Balance Equations

Since parameters of the fluids are subject to singular changes at the interfaces, the standard differential balance equations derived in section 2.1.2 hold in each phase up to an interface, but not across it [33, 70, 154, 180]. Accurate description of the fluid behavior across the interface requires additional equations (called jump conditions or interfacial balance equations). Jump conditions simply express the mass and momentum conservation across the interface. Constitutive equations must supplement them to close the system, as in the case of the field equations.

As pointed out by Ishii [154], "various simplified forms of the jump conditions are in frequent use without much notice" even if the choice is not neutral. For this reason, Ishii discusses "in detail the derivation and physical significance of the jump conditions". His proof, available in [154, 174], is based on a control volume defined by a finite thickness interface for which he establishes a general integral balance equation. At the end of the day, he shows that the following jump condition translates the continuity law across the interface:

$$\sum_{k=1}^{2} \rho_k \mathbf{n}_k \left(\mathbf{v}_k - \mathbf{v}_i \right) = \sum_{k=1}^{2} \dot{\mathbf{m}}_k = 0 \tag{2.7}$$

where $\mathbf{n}_k$ are unit vectors normal to the interface, $\mathbf{v}_i$ represents the velocity of the interface and $\dot{m}_k$ is defined as the interfacial mass efflux from the k^{th} phase. Equation (2.7) simply states that phase changes are pure exchanges of mass between the two-phases at the interface. By a similar process, the following jump condition expresses the momentum conservation [154]:

$$\sum_{k=1}^{2}\left[\rho_k \mathbf{n}_k \cdot (\mathbf{v}_k - \mathbf{v}_i)\mathbf{v}_k - \mathbf{n}_k \cdot \mathbf{T}_k\right] + \left(\mathbf{t}_\alpha A^{\alpha\beta}\sigma\right)_{,\beta} = 0 \qquad (2.8)$$

where $\mathbf{T}_k = \tau_k - p_k \mathbf{I}$, σ is the isotropic surface tension, $A^{\alpha\beta}$ is the surface metric tensor and $\mathbf{t}_\alpha$ is the hybrid tensor linking variations of general coordinates $\mathbf{x} = (x_1, x_2, x_3)$ and surface coordinates (u_1, u_2): $\mathbf{t}_\alpha = \partial\mathbf{x}/\partial u_\alpha$. The whole term $(\mathbf{t}_\alpha A^{\alpha\beta}\sigma)_{,\beta}$ accounts for the surface flux contribution due to the surface tension and is described in details in [11, 154]. The summation represents the momentum fluxes from the bulk fluids.

2.1.5 Local Instant Formulation

By assuming that each sub-region bounded by interfaces is a continuum, previous results apply to multiphase flows. This is the Local Instant Formulation (LIF), which governs the evolution of pressure and velocity in three-dimensional two-phase flows. The LIF relies on two types of equations (Figure 24):

- Field equations (2.1) and constitutive equations (2.4) and (2.6) describe each sub-region:

$$\begin{cases} \dfrac{\partial \rho_k}{\partial t} + \nabla.(\rho_k \mathbf{v}_k) = 0 \\ \dfrac{\partial \rho_k \mathbf{v}_k}{\partial t} + \nabla.(\rho_k \mathbf{v}_k \mathbf{v}_k) = \nabla(\tau_k - p_k) + \rho_k \mathbf{F}_k \end{cases} \qquad k = w, g \qquad (2.9)$$

- Jump conditions (2.8) link single-phase region with each other:

$$\begin{cases} \sum_{k=1}^{2} \rho_k \mathbf{n}_k (\mathbf{v}_k - \mathbf{v}_i) = \sum_{k=1}^{2} \dot{m}_k = 0 \\ \sum_{k=1}^{2}\left[\rho_k \mathbf{n}_k \cdot (\mathbf{v}_k - \mathbf{v}_i)\mathbf{v}_k - \mathbf{n}_k \cdot \mathbf{T}_k\right] + \left(\mathbf{t}_\alpha A^{\alpha\beta}\sigma\right)_{,\beta} = 0 \end{cases} \qquad (2.10)$$

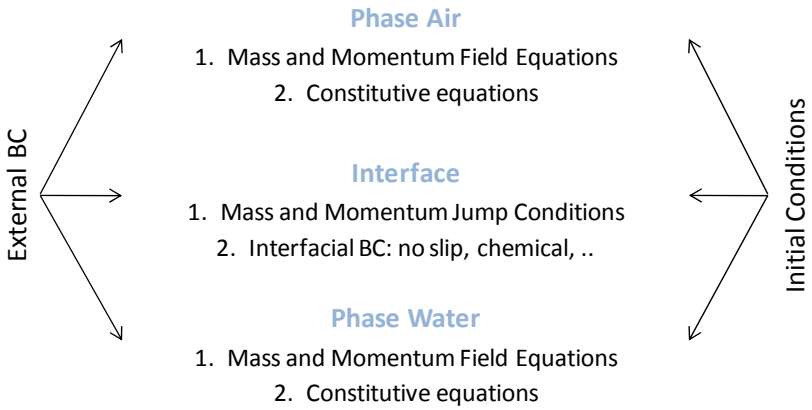

Figure 24 : Local Instant Formulation [154] includes a whole mathematical model for each phase separately and jumps conditions that explicit mass and momentum exchange across the interface.

2.2 SINGLE-PHASE MATHEMATICAL MODELS

By assuming that the fluid is a single-phase pure water flow, the Local Instant Formulation (LIF) reduces to the following governing equations:

$$\begin{cases} \dfrac{\partial \rho_w}{\partial t} + \nabla.\rho_w \mathbf{v}_w = 0 \\ \dfrac{\partial \rho_w \mathbf{v}_w}{\partial t} + \nabla.\left(\rho_w \mathbf{v}_w.\mathbf{v}_w\right) = \nabla\left(-p_w + \boldsymbol{\tau}_w\right) + \rho_w \mathbf{g} \end{cases} \tag{2.11}$$

This is the common form of the Navier-Stokes [75, 93]. Even if the water density is constant, I conserve ρ_w within the derivatives in order to facilitate subsequent demonstration and comparison with multiphase models. System (2.11) constitutes a closed system of 4 equations for 4 primitive unknowns.

In civil and environmental engineering, an advection-diffusion equation for a passive scalar [75, 127, 235] supplements equations (2.11) to account for the dispersed phase:

$$\frac{\partial \rho_d C}{\partial t} + \nabla\left(\rho_d C \mathbf{v}_w\right) = \rho_d \nabla\left(D \nabla C\right) + \rho_d S \tag{2.12}$$

where C is the concentration in passive substance, D is the coefficient of diffusion and S is the source term in passive substance. This equation holds not only for air entrainment [76] but also for pollutant transport [22] and sedimentation [13, 296].

Navier-Stokes equations (NVS) [255] constitute the basis of standard models in hydraulics. An advection-diffusion equation usually complements the pure water models derived from the NVS. This approach aims at describing the evolution of the concentration in dispersed phase. Nevertheless, such models fail in many respects to give an accurate description of transient air-water flows. Indeed, it does not describe rigorously the impact of the dispersed phase on the water flow. It does not characterize correctly the mechanism of dispersion within the water flow. Finally, the definition of the concentration is ambiguous.

Classical one-dimensional models derived from NVS describe either free surface flows (Saint-Venant), pressurized flows (Allievi), or both of them in the case of mixed flows ("mathematical shock-capturing" models like the Preissmann slot). If these methods show good results in some cases, they suffer the same shortcomings as 3D standard models. In addition, mixed flow models remain unable to account for the presence of air in the pressurized flow and present spurious oscillations at the transition bore.

The following five subsections give a detailed review of these affirmations. First, I derive a macroscopic model to account for turbulence without increasing the computational effort. Second, area integrating the model over the flow cross-section further reduces this effort. It results in various models for free surface and pressurized flows. Third, the Saint-Venant equations are extended to pressurized flows for describing mixed flows. Fourth, I review the various friction correlations available to account for internal and external friction. Finally, I discuss the advantages and shortcomings of this approach.

2.2.1 MACROSCOPIC MODEL – 3D RANS

Most flows presented in the introduction chapter display chaotic and stochastic property changes, which ascertain the occurrence of turbulence. Turbulence causes the formation of eddies of many different length scales (Figure 25). Physically, large eddies have the scale of the flow domain. They are intrinsically anisotropic since boundary conditions affect them. On the opposite, viscous forces govern the small eddies, which are then isotropic. Such small structures carry very few energy but are very diffusive. Most of the turbulent kinetic energy is contained in the large scale eddies, which are transported along the flow without much dissipation. Both scales are intimately linked through the "energy cascade of Kolmogorov". The large eddies are indeed unstable and they break up to give birth to smaller eddies. The kinetic energy of the initial large eddy is divided into the smaller eddies that stemmed from it. These smaller eddies undergo the same process, giving rise to even smaller eddies which inherit the energy of their predecessor eddy, and so on. In this way, the energy is passed down from the large scales of the motion to smaller scales. Eventually this process creates structures that are small enough to be subjected to important molecular diffusion and to dissipate energy. The scale at which this happens is the Kolmogorov length scale. In view of the intrinsic coupling between the various scales of the flow, solving the Navier-Stokes equation requires to take into account the whole spectrum of turbulence, from the Kolmogorov eddies to the large-scale structures. Neglecting the local chaotic variations of parameters would cause inacceptable error in the simulation.

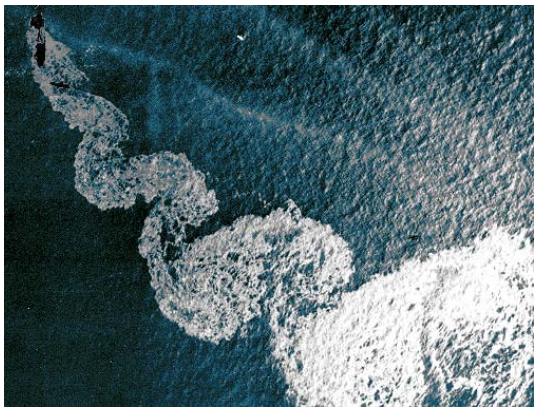

Figure 25: Turbulence in Argo Merchant tank's wake (North Atlantic) [91] causes the formation of eddies

Theoretically, solving the Navier-Stokes under their original form (2.11) is achievable. It is the principle of the Direct Numerical Simulation (DNS). DNS captures all of the relevant scales of turbulence, from the Kolmogorov microscales up to the integral scale associated with the motions containing most of the kinetic energy. However, this approach is extremely expensive, if not intractable, for complex problems on modern computing machines. The cost of DNS prompts researchers to find cheaper alternatives under the form of turbulence models, Large Eddy Simulations (LES), Reynolds-Averaged Navier-Stokes (RANS), and Double-Averaged Navier-Stokes (DANS) equations.

Large Eddy Simulation (LES) consists in calculating explicitly only the large-scale motions of the flow, while the effect of smaller scales (the so-called sub-grid scales) are modeled using a sub-grid scale model [14, 93, 265, 318]. In practical implementations, filtered Navier-Stokes equations are solved with an additional sub-grid scale stress term. The most commonly used sub-grid scale models are the Smagorinsky model and its dynamic variants. They compensate for the unresolved turbulent scales through the addition of an "eddy viscosity" into the governing equations.

Reynolds-averaged Navier-Stokes (RANS) model relies on the observation that knowledge of the local instant fluctuation of the flow parameters is useless in most cases. Introducing the concept of mean state into the Navier-Stokes equations and averaging them over the time gives a new set of equations called Reynolds-averaged Navier-Stokes (RANS).

Just as I am about to write this thesis, a new turbulence model is establishing itself as a standard for simulation in single-phase environmental flows: the Double-averaged Navier-Stokes (DANS). Authors of the method [235, 236] argue that RANS should be supplemented by volume averaging in order to deal with spatial chaotic fluctuations as well. The double averaging procedure gives new momentum and continuity equations that explicitly contain important additional terms such as form-induced stresses as well as form and viscous drag terms. The method is not short of advantages and elegance such that I give additional information about it in Chapter 10. It constitutes a good perspective for further research.

Single-phase models used in this thesis make use of the RANS model. In brief, derivation of the Reynolds-Averaged Navier-Stokes (RANS) equations relies on the decomposition of the variable $\mathbf{F}$ into a mean value $\bar{\mathbf{F}}$ and a fluctuating component $\mathbf{F}'$:

$$\mathbf{F}(\mathbf{x},t)=\bar{\mathbf{F}}(\mathbf{x},t)+\mathbf{F}'(\mathbf{x},t) \tag{2.13}$$

where the mean value is defined as:

$$\bar{\mathbf{F}}(\mathbf{x},t)=\frac{1}{\Delta t}\int_{t-\Delta t/2}^{t+\Delta t/2}\mathbf{F}(\mathbf{x},\tau)d\tau \tag{2.14}$$

Δt designates the characteristic time over which the flow variable is integrated. Its value should be chosen in-between the characteristic time of turbulent fluctuations and the characteristic time of simulated phenomena, assuming separation of time scales.

Next, Reynolds theory states the fundamental hypothesis of smoothness of mean values, which assumes that the averaging does not alter the mean values in macroscopic fields. This hypothesis is propped up by considering a macroscopic process in terms of the mean values. If the characteristic time of the process is sufficiently larger than Δt, we can assume mean values are sufficiently smooth. Any change of mean values is considered infinitesimal except at some isolated singularities. If we further time-average a mean value, we get:

$$\overline{(\bar{\mathbf{F}})}(\mathbf{x},t_0)=\frac{1}{\Delta t}\int_{t_0-\Delta t/2}^{t_0+\Delta t/2}\bar{\mathbf{F}}(\mathbf{x},t)dt \tag{2.15}$$

Since $\bar{\mathbf{F}}$ is continuous, the integral mean value theorem [277] shows:

$$\left(\overline{\bar{\mathbf{F}}}\right)(\mathbf{x},t_0)=\bar{\mathbf{F}}(\mathbf{x},\tau_0) \qquad \text{where} \qquad t_0-\frac{\Delta t}{2}\le\tau_0\le t_0+\frac{\Delta t}{2} \tag{2.16}$$

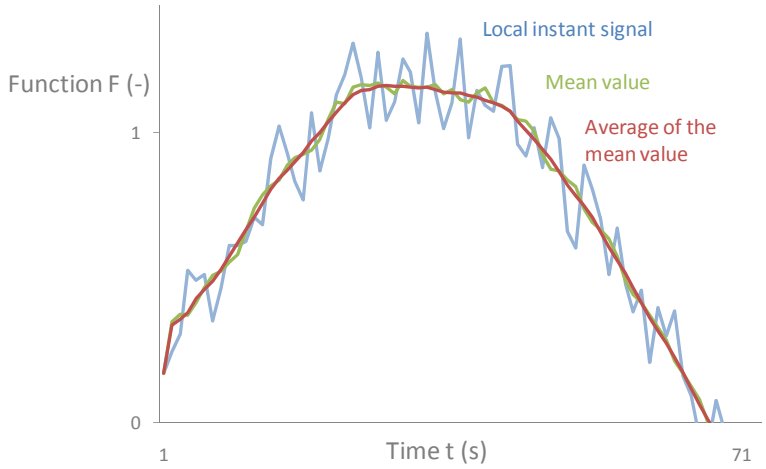

Figure 26 : Fundamental hypothesis of smoothness of the mean value. The time average of a mean value is not exactly identical to the mean value but sufficiently close to make the approximation that time averaging does not alter mean values

Figure 26 exemplifies this result for a given local instant signal (in blue). The green line gives the mean value over 10 seconds of the signal. The red line, which is the mean value over 10 seconds of the mean value, is not identical to the green line but very close. Thus, we make the following approximation:

$$\left(\overline{\bar{\mathbf{F}}}\right)=\bar{\mathbf{F}} \tag{2.17}$$

which is called fundamental hypothesis of smoothness of mean values. The fundamental property of fluctuating components is then derived from the assumption (2.17) as:

$$\bar{\mathbf{F}}'=0 \tag{2.18}$$

Applying the Reynolds averaging methodology onto equation (2.11) gives a set of equations called RANS model [14, 75]:

$$\begin{cases}\dfrac{\partial\bar{\rho}_w}{\partial t}+\nabla.\left(\bar{\rho}_w\bar{\mathbf{v}}_w\right)=0\\ \dfrac{\partial\bar{\rho}_w\bar{\mathbf{v}}_w}{\partial t}+\nabla.\left(\overline{\bar{\rho}_w\mathbf{v}_w}\bar{\mathbf{v}}_w\right)=-\nabla\bar{p}_w+\bar{\rho}_w\upsilon_w\Delta\bar{\mathbf{v}}_w+\nabla\boldsymbol{\tau}^T+\bar{\rho}_w\bar{\mathbf{F}}_w\end{cases} \tag{2.19}$$

where the new Reynolds stresses $\boldsymbol{\tau}^T$ account for the effect of random fluctuations in fluid momentum. Reynolds stresses are formulated as follows:

$$\boldsymbol{\tau}^T\big|_{ij}=\overline{\rho_w\mathbf{v}_w'\big|_i\mathbf{v}_w'\big|_j} \qquad i,j=1,3 \tag{2.20}$$

The same procedure applies onto the transport equation (2.12):

$$\frac{\partial\bar{\rho}_d\bar{C}}{\partial t}+\nabla\left(\overline{\bar{\rho}_d\bar{C}\bar{\mathbf{v}}_w}\right)=\bar{\rho}_d\nabla\left(D\nabla\bar{C}+\mathbf{q}^T\right)+\bar{\rho}_d\bar{S} \tag{2.21}$$

Turbulent fluxes $\mathbf{q}^T$ account for the contribution of the turbulence to the diffusion process.

Evaluating Reynolds stresses (2.20) has been the subject of intense interest for the past century and gave birth to several closure models [44, 48, 93]. In this research, I mainly focus on 1D model in which turbulent stresses are conflated with other head losses into a single term. Friction correlation determines usually the value of these head losses. Reviewing and studying closure models is thus beyond the scope of this thesis such that we refer the interested reader to the vast literature on turbulence modelling. The rest of the section relies on model (2.19) such that the dash over the parameters is dropped from now on.

2.2.2 Cross-sectional integrated Models

Computation of the three-dimensional system of PDE's given by RANS equations (2.19) is in many cases difficult from a mathematical point of view and requires a prohibitive computational effort. The main difficulties arising from solving 3D equations are various:

- 3D meshes are complex to generate and often require millions of cells for actual cases;
- tracking the free surface requires a specific algorithm such as the Level Set method [73, 267, 268], the Volume of Fluid method [183] or Marker and Cell method [137];
- necessary boundary conditions and topographic data are not always available.

Detailed 3D results are usually unnecessary for engineering purpose. Consequently, 1D models can be used if both the flow depth and width are smaller than the flow length. The computation effort is then greatly reduced by cross-sectional integrating the governing equations. It results in a system much easier to solve as it uses 1D meshes and does not require tracking the free surface. In this section, I state the two classical models derived by cross-sectional integration of equations (2.19), namely the Saint-Venant equations for free surface flows and the Allievi equations for pressurized flows. They distinguish themselves in the form of the flow cross-section and the shape of the pressure distribution.

Free surface flows: Saint-Venant equations

Area-integration of 3D RANS equations (2.19) over a general flow cross-section presenting a free surface (Figure 27) gives the so-called Saint-Venant equations [9, 63, 64]:

$$\begin{cases} \dfrac{\partial \rho_w \Omega}{\partial t} + \dfrac{\partial \rho_w u_w \Omega}{\partial x} = q_{w,\perp} \\ \dfrac{\partial \rho_w u_w \Omega}{\partial t} + \dfrac{\partial \beta \rho_w u_w u_w \Omega + g I_1}{\partial x} = \rho_w g \Omega \left(S_0 - S_f \right) + \rho_w g I_2 + \rho_w \theta u_w q_{w,\perp} \end{cases} \tag{2.22}$$

where pressure terms may be written as:

$$I_1(\Omega) = \int_{h_b}^{h_s} (h - \xi) l(x,\xi) d\xi \quad \text{and} \quad I_2(\Omega) = \int_{h_b}^{h_s} (h - \xi) \frac{\partial l(x,\xi)}{\partial x} d\xi \tag{2.23}$$

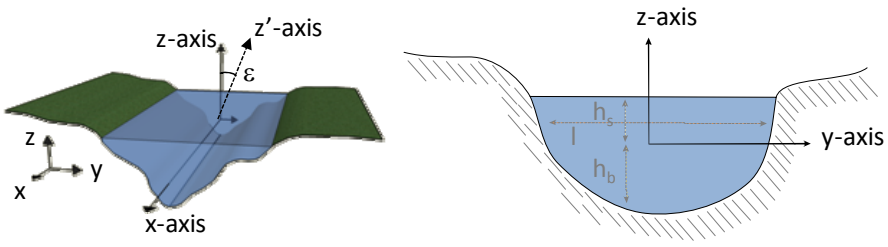

Figure 27: The integration domain consists in a general flow cross-section presenting a free surface

As pointed in Figure 27, equation (2.22) is expressed in a frame of reference for which the x-axis is inclined with respect to the main flow direction and the y-axis is horizontal. Consequently, the z-axis forms with the vertical z' an angle ε. Parameter Ω is the flow area, u_w is the mean flow velocity along the main direction of the flow, g is the gravity, $S_0=\tan\varepsilon$ is the bed slope. S_f is the friction term computed with an empirical resistance law, $q_{w,l}$ is the lateral discharge, and θ is a parameter that accounts for the velocity at which the lateral flows enter the main stream. Finally, h is the water height, l is the free surface width, h_{fs} is the free surface elevation, and h_b is the bottom elevation. The Boussinesq coefficient β [21, 76, 260] accommodates the 1D model with cross-sectional distribution of the velocity.

The term gI_1 represents the hydrostatic pressure. Integral (3.2) depends only on the river geometry and the cross-section Ω such that it can be easily computed under an analytical form or by a numerical integration. It results in a discrete relation between the area Ω and the pressure term gI_1 that is easily implemented in the numerical scheme.

The second pressure term gI_2 accounts for the non-uniformity of the pipe. Even if the treatment of this term remains today a challenge for non-uniform cross-sections, various methods are at hand [29, 125]. In this thesis, I simplify this problem by using a non-conservative formulation [9, 63] equivalent to equations (3.1) :

$$\begin{cases} \dfrac{\partial \rho_w \Omega}{\partial t} + \dfrac{\partial \rho_w u_w \Omega}{\partial x} = q_{w,\perp} \\ \dfrac{\partial \rho_w u_w \Omega}{\partial t} + \dfrac{\partial \beta \rho_w u_w u_w \Omega}{\partial x} = \rho_w g \Omega \left(\dfrac{\partial Z}{\partial x} - S_f \right) + \rho_w \theta u_w q_{w,\perp} \end{cases} \tag{2.24}$$

where Z[m] is the free surface elevation. Validity of the non-conservative Saint-Venant equations is discussed and proven in [93].

As already mentioned, the standard method to account for a dispersed phase consists in supplementing model (3.2) or (3.3) with an equation of transport. Cross-sectional integration of the advection-diffusion equation for the concentration C gives:

$$\frac{\partial \rho_d C \Omega}{\partial t} + \frac{\partial}{\partial x}\left(\rho_d C u_w \Omega\right) = \rho_d \frac{\partial}{\partial x}\left(D \nabla\left(C\Omega\right) + q^T \Omega\right) + \rho_d q_{C,l} \tag{2.25}$$

where $q_{C,l}$ is the lateral inflow in passive substance and q^T is the turbulent flux.

PRESSURIZED FLOWS: ALLIEVI EQUATIONS

Traditionally, computation of pressurized flows relies on the Allievi equations [23, 25, 325]. This model is derived by cross-sectional integrating the RANS equations (2.19) over a closed cross-section (Figure 28). In this process, both the pressure and velocity are assumed uniform over the flow cross-section. At the end of day [31, 131, 132], we have:

$$\begin{cases} \dfrac{\partial \rho_w A}{\partial t} + \dfrac{\partial \rho_w u_w A}{\partial x} = q_{w,\perp} \\ \dfrac{\partial \rho_w u_w A}{\partial t} + A_0 \dfrac{\partial \rho_w u_w u_w + p}{\partial x} = \rho_w g A_0 \left(S_0 - S_f \right) + \theta u_w q_{w,\perp} \end{cases} \tag{2.26}$$

where ρ_w is the water density, A the pipe cross-section area, A_0 the pipe area when no pressure acts on it, and p is the uniform pressure intensity. System (2.26) contains three unknowns, namely the pressure p[N/m²], the area A, and the density ρ_w. The system is closed by establishing an equation of state for the pressure wave celerity a[m/s]:

$$a^2 = A_0 \frac{dp}{d(\rho_w A)} \tag{2.27}$$

In first approximation, its value can be chosen before the computation as a constant. The chosen value depends on the properties of the fluid and the pipe as well as its mean of support [325]. Wave speeds for large steel pipelines may be equal to 1000m/s, whereas speeds in high pressure small pipes may reach 1400m/s.

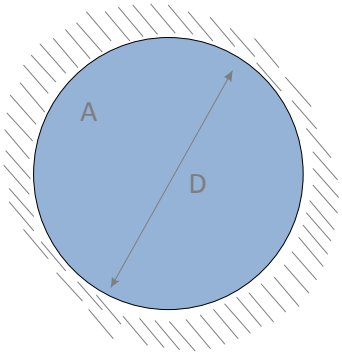

Figure 28: The integration domain consists in closed flow cross-section

To my knowledge, models available in the literature do not use a transport equation to describe the transport of a dispersed phase in a pressurized flow. There is one exception to this. In presence of a small amount of air in the pipe, the pressure wave celerity is no longer constant. Its value drops dramatically [131, 325] and becomes dependant on the pressure. It strongly affects the dynamics of a water hammer. To date, simulation of such an aerated water hammer still relies on the single-phase Allievi equations (2.26). In this case, the value of the celerity in the equation of state takes into account the presence of air and the dependence in pressure. According to Guinot [130-132], the pressure-wave celerity for gas-liquid mixtures can be written as follows:

$$a_m = a_0 \Big/ \sqrt{1 + \alpha_0 \rho_{m,0} a_0^2 p_0^{1/\beta} \Big/ p^{1+\beta/\beta}} \qquad \text{with} \quad \rho_{m,0} = \alpha_0 \rho_d + (1-\alpha_0)\rho_w \tag{2.28}$$

where the subscript 0 designates the reference state characterized by a given pressure. The parameter β is a coefficient equal to 1.0 for isothermal processes and 1.4 for adiabatic conditions. The reference void fraction α_0 is the volume fraction of dispersed air at reference pressure and $\rho_{m,0}$ is the mixture density at reference pressure. Introducing the celerity formulation (2.28) into the equation of state (2.27) gives the following for the pressure p:

$$\rho_w A = \rho_w A_0 + \frac{\rho_w A_0}{a_0^2}\left[p - p_0 + \left(p_0^{-1/\beta} - p^{-1/\beta} \right) \beta \alpha_0 \rho_{m,0} a_0^2 p_0^{1/\beta} \right] \tag{2.29}$$

An iterative Newton-Raphson method enables to solve equation (2.29).

2.2.3 One-dimensional Models for Mixed Flows

In the current research, I aim at describing a wide range of flows likely to appear in civil and environmental engineering (as described in Chapter I). In particular, modelling the simultaneous occurrence of free surface and pressurized flows, designated by "mixed flows", is one of the objectives. Obviously, mixed flows include the following situations:

- free surface and stratified flows;
- pressurized flows which exert a consequent pressure on the roof of a closed pipe;
- pressurized flows which exert a sub-atmospheric pressure on a closed pipe without developing a free surface.

Many researches since the 60's have been aiming at overcoming the discrepancy between pressure gradients appearing in the Saint-Venant (2.22) and the Allievi (2.26) equations for creating a unified mathematical model. In this respect, three families of methods are worth a mention: "mathematical shock-tracking" methods, rigid water column approaches, and "mathematical shock-capturing" models. As I show hereinafter, "mathematical shock-capturing" models constitute the most natural way to simulate mixed flows. Preissmann slot is the most popular of these approaches but fails in accounting for sub-atmospheric pressurized flows. TPA and dual model overcome this shortcoming but present post-transition spurious oscillations that may lead to instabilities (like the Preissmann). Finally, not a single method accounts for the presence of a dispersed phase in the flow.

"Mathematical shock-tracking" approaches consist in solving separately free surface and pressurized flows through different sets of equations. Transitions between free surface and pressurized flows are tracked explicitly and are regarded as internal boundaries across which appropriate jump conditions are imposed. The first application of this approach for computing mixed flows has been proposed by Wiggert [317]. He studied the transient behavior of a combined free surface and pressurized system in a tunnel by using both an experimental apparatus and a numerical model. The experimental results constitute now a traditional benchmark for mixed flow simulation. Subsequent researches by various authors [40, 135, 272] aimed at deriving theoretical model of the flow at the interface and at incorporating it into the general mathematical model as an interfacial boundary condition. Authors assumed in these papers that the pressurized phenomenon is a dynamic shock requiring a special dynamic treatment. In 2003, Fuamba [110] extended the model to predict the surge front location and velocity, the pressure rise in the full flow zone and the water depth change in the free surface zone. In his paper, three one-dimensional models have been applied to both laboratory and field data. Improvement in the method are still today published [192, 248]. The "mathematical shock-tracking" approach has obviously its pros and cons. It enables to simulate complex interactions between the bore and other existing waves. In addition, a true discontinuity represents the transition (infinite resolution). However, the associated algorithms are very complex and become far too complicated or simply impossible to apply for complex wave interactions and multi-dimensional problems. Furthermore, models based on this approach cannot address some features, such as open channel surges, negative interfaces, and interface reversals.

Introduced by the work of Hamam and McCorquodale [218], the Rigid Water Column Approach solves each phase (air/water) separately on the basis of a specific set of equations. These models solve an ordinary differential equation (ODE) expressing the momentum conservation in a rigid column represented by the pressurized portion of the flow. The ODE is solved iteratively and the velocity of the rigid column is updated at each time step. The model of Hamam and McCorquodale assumes a hypothetical stationary bubble that undergoes pseudoadiabatic expansion and compression. The transition from free surface to pressurized flow is classified into six stages, interconnected by 5 internal boundary conditions. Li and McCorquodale [198] extended the model for the motion of the trapped air bubble and its subsequent release. Zhou et al [331, 332] intensively applied the methodology to assess the effect of trapped air in rapidly filling horizontal pipe containing trapped air. If the rigid water column method may be very efficient for very particular situations, it turns out to have severe limitations that prevent its use for practical applications. The approach enables simulating highly complex configurations of the transition, especially when this one is affected by air-water interactions. These models are also conceptually simple, and relatively easy to implement for simple cases. However, utilization for practical application in networks is not possible because of the specificity of the algorithm. What is more, the occurrence of pipe filling bores has to be assumed. It causes problems when an open-channel bore occurs. Oscillations in the rigid column cannot be simulated. Finally, interactions between the pressurized front and other waves present in the system cannot be described in detail [192].

Finally, the so-called “mathematical shock-capturing approach” computes pressurized and free surface flows by using a single set of equations. The main advantage of the method is that there is no need to track explicitly the interface. To my knowledge, only four models fall into this category: the Preissmann slot [249], the two-component pressure approach [304], the dual model [30], and the kinetic model [32].

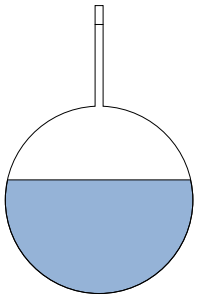

Figure 29: The Preissmann slot model extends the application of free surface flows equations to pressurized flows as well

Historically, “mathematical shock-capturing” model was a byword for the Preissmann slot concept [64, 249]. This model is indeed the most widespread in the scientific and engineering world. In this method, free surface flows and pressurized flows are equally solved through the Saint-Venant equations by adding a narrow slot at the top of the pipe (Figure 29). The slot width is sized to match the celerity of the pressure wave in the pressurized portion. Preissmann slot approach is very popular as this method takes into account the transition between the two kinds of flows in a “natural manner”. Many authors

developed numerical schemes to solve the Saint-Venant equation in conjunction with a Preissmann slot, namely Garcia-Navarro and al. [113], Leon [193], Vasconcelos [299], Trajkovic et al. [287]. Several commercial softwares rely on the Preissmann slot concept: Mouse, HydroWorks, and Canoe for instance. If the method has met with success in all these papers and has been applied for many practical application, two major shortcomings to the method remain unsolved [248]:

- The mathematical formalism does not consider sub-atmospheric pressurized flow that may appear if the closed pipe is not sufficiently supplied in air.
- Spurious numerical post-transition oscillations appear because of the steep change in the wave celerity (from ~10 m/s up to ~1000 m/s) across the transition. These oscillations can compromise the stability of numerical models.

Arora and Roe [12] first and then Vasconcelos [307] proceeded to extensive research on the post-transition oscillations without fixing satisfactorily the problem. Oscillations are usually damped by artificially reducing acoustic wave speeds but it may result in loss of simulation accuracy. Two new techniques to attenuate the oscillation amplitudes have been presented by Vasconcelos [307]. The first is based on the numerical filtering of the oscillations. The second based on a new flux function that judiciously introduces numerical diffusion only in the vicinity of the bore front. Both approaches are effective in decreasing the strength of the numerical oscillations but affect the solution itself. Leon [193] introduced a modified Preissmann slot with a variable width to improve the stability of the scheme. Again, it attenuates oscillations but affects the front velocities.

More recently, Bourdarias and Gerby introduced in [30] a new mathematical model called Dual Model. By revisiting Saint-Venant and Allievi equations, they identified similarities and introduced a common couple of conservative variables:

$$\begin{cases} \dfrac{\partial \Omega_{eq}}{\partial t} + \dfrac{\partial Q_{eq}}{\partial x} = q_{w,\perp} \\ \dfrac{\partial \Omega_{eq}}{\partial t} + \dfrac{\partial Q_{eq} Q_{eq} / \Omega_{eq} + P(x,\Omega,E)}{\partial x} = g\Omega_{eq}\left(S_0 - S_f\right) \end{cases} \tag{2.30}$$

where we define the free surface equivalent wet area $\Omega_{eq}=\rho\Omega_{max}/\ \rho_0$ (Ω_{max} is the cross-sectional area), and the free surface equivalent discharge $Q_{eq}=\rho Q/\ \rho_0$. The parameter E denotes the state of the current point x (free surface or pressurized). The pressure term is given by:

$$p(x,\Omega_{eq},E) = \begin{cases} gI_1\left(\Omega_{eq}\right) & \text{for a free-surface flow} \\ gI_1\left(\Omega_{max}\right) + a^2\left(\Omega_{eq} - \Omega_{max}\right) & \text{for a pressurized flow} \end{cases} \tag{2.31}$$

Formulation (2.31) accounts for sub-atmospheric pressure but does not solve the problem of post-transition oscillations.

In a similar manner, Vasconcelos [302, 304, 305] proposed the two-component pressure approach (TPA) that decouples the hydrostatic pressure in the Saint-Venant equations from surcharged pressures occurring only in pressurized conditions. Vasconcelos designed the method in order to overcome the inability of the Preissmann model to describe sub-atmospheric full pipe flows:

$$\begin{cases} \dfrac{\partial \Omega}{\partial t} + \dfrac{\partial u_w \Omega}{\partial x} = q_{w,\perp} \\ \dfrac{\partial u_w \Omega}{\partial t} + \dfrac{\partial \beta u_w u_w \Omega + g\Omega h_c + g\Omega h_s}{\partial x} = g\Omega\left(S_0 - S_f\right) + gI_2 + \theta u_w q_{w,\perp} \end{cases} \tag{2.32}$$

where h_c refers to the hydrostatic component and h_s to the uniform component of the pressure acting in the pipe. The over-pressure term is given by:

$$h_s = \frac{a^2}{g}\frac{\left(\Omega - \Omega_{max}\right)}{\Omega_{max}} \tag{2.33}$$

Finally, I mention a different "mathematical shock-capturing method" called kinetic formulation, which has been established for the coupling of transient free surface and pressurized flows [32]. The method seems promising but performance does not reach yet the Preissmann slot level and its background differs too much from the know-how of the HACH to be used in this thesis.

It is worth to emphasize here on the nomenclature used in this section. In the literature, the previous methods are simply called "shock-tracking" and "shock-capturing". These names were chosen by analogy with the numerical methods (see section 2.4). Personally, I regret this choice since it induces a confusion between the mathematical model and the numerical scheme. Consequently, I precise here the names by adding "mathematical" in front of them. By analogy, I will refer to the numerical schemes as "numerical shock-capturing" and "numerical shock-tracking" methods. Even if the formulation is quite heavy, it avoids any confusion in the rest of this text.

2.2.4 Internal and External Friction

In both Saint-Venant and Allievi equations, a single parameter S_f conflates all the head losses. It includes the effect of viscous and turbulent stresses as well as the friction on the channel and pipe walls. Since the friction slope S_f is not a primitive unknown, specifying its value requires adding a constitutive equation or a friction correlation. In this respect, both modern and empirical correlations are still of frequent use in civil and environmental engineering. Such closure laws usually rely on a single parameter characterizing the bed structure. None of them accounts for the effect of the dispersed phase.

Modern formulation

Head losses in pressurized and free surface single phase flow can be readily calculated by means of the Darcy-Weisbach equation [9, 63]:

$$S_F = f\frac{u_w^2}{2gD_h} \tag{2.34}$$

where f is the friction factor and D_h the hydraulic diameter that is defined as follows [9, 86]:

$$D_h = 4R_h = 4\frac{\Omega}{\partial\Omega} \tag{2.35}$$

where the hydraulic radius R_h is given by the division of cross-sectional area Ω by the wetted perimeter $\partial\Omega$.

The friction factor f is not a constant and depends on the Reynolds number and the roughness of the pipe, channel,… Various empirical or theoretical relations provide approximations of its value. The Moody-Stanton diagram (Figure 30) gives also indications about its value for practical cases.

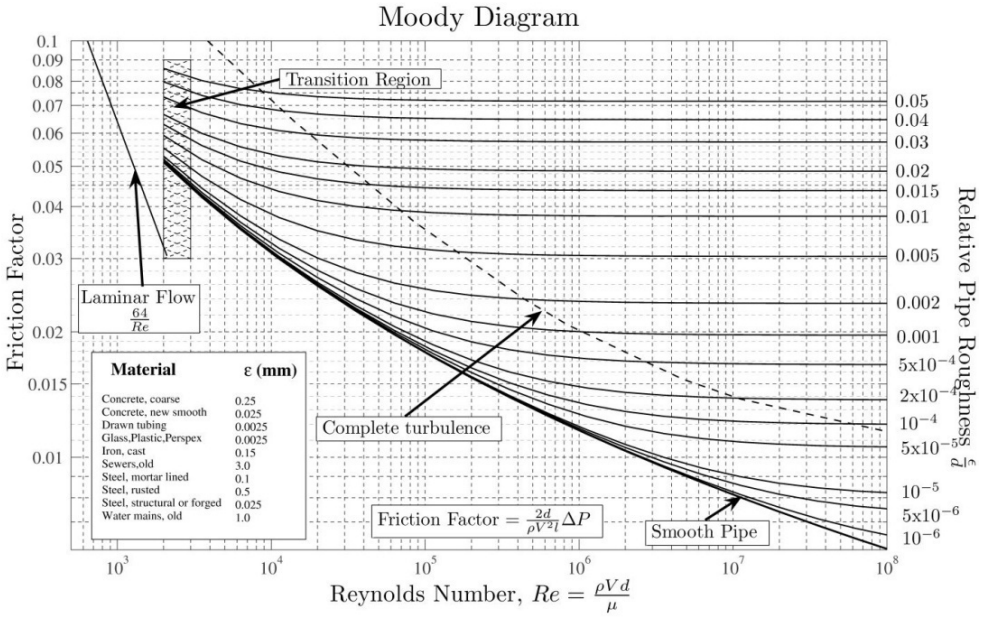

Figure 30 : Moody-Stanton diagram for the prediction of the friction factor [223]

For laminar flows (Reynolds number less than 2300), the friction factor can be computed with the Hagen-Poiseuille law that is written as follows [9, 181]:

$$f = \frac{64}{Re_f} \tag{2.36}$$

The Reynolds number Re_f is given by:

$$Re_f = \frac{\rho_w u_w D_h}{\mu} \tag{2.37}$$

where μ is the dynamic viscosity. Laminar flows are then represented with a straight line in the Moody-Stanton diagram.

For turbulent flows in smooth conduits (Reynolds greater than 4000), the friction factor is usually calculated on the basis of the Prandtl-Von Karman relationship [9]:

$$\sqrt{\frac{1}{f}} = -2\log\frac{2.51}{Re_f\sqrt{f}} \tag{2.38}$$

which is an implicit relation for the friction factor. Blasius linearized this expression to obtain the explicit Blasius law [136] written as:

$$f = C_B Re_f^{-n} \qquad \text{where usually } C_B = 0.3164 \text{ and } n = 0.25 \tag{2.39}$$

For fully turbulent flows in rough conduits, the friction factor remains constant for whatever Reynolds number. Its value only depends on the relative roughness of the cross-section. The friction factor is then given by the Nikuradse formula [86]:

$$\sqrt{\frac{1}{f}} = -2\log\frac{k_d}{3.7D_h} \tag{2.40}$$

where k_d is the roughness height. The Nikuradse formulation is the analogous of the Prandtl-Von Karman law given by (2.38) for rough conduit. It is applicable if the Reynolds number is greater than a limit value given by:

$$Re_f = 560\frac{D_h}{k_d} \tag{2.41}$$

Finally, transition (neither fully laminar nor fully turbulent) flows occur in the range of Reynolds numbers between 2300 and 4000. The value of the friction factor may be subject to large uncertainties in this flow regime. Colebrook and White [57] proposed a compact form of the friction factor suitable not only for the transitional flow, but also for laminar and turbulent flow. The implicit relation is written as [9, 181]:

$$\sqrt{\frac{1}{f}} = -2\log\left(\frac{k_d}{3.7D_h} + \frac{2.51}{Re\sqrt{f}}\right) \tag{2.42}$$

The Colebrook-White equation is clearly the most widespread formula used to compute friction factor in pressurized flow. It can be successfully applied to free surface flows as well.

EMPIRICAL FORMULATION

Hydraulic engineers and hydrologists still use empirical formulations for the determination of the friction slope J instead of the Darcy-Weisbach equation. The most common empirical equation is the Manning-Strickler formulation given under the form [9]:

$$u = K\sqrt{J}\,R_h^{2/3} \tag{2.43}$$

The Bazin correlation is also in frequent use in hydrology and applied hydraulics:

$$u = \frac{87\sqrt{JR_h}}{1+\frac{\gamma}{\sqrt{R_h}}} \tag{2.44}$$

where γ is the Bazin coefficient. Both the Manning-Strickler equation and the Colebrook-White equation will be used in the rest of this thesis.

2.2.5 DISCUSSION

The previous sections review standard models used in civil and environmental engineering to simulate transient mixed flows. As underlined by this analysis, these methods succeed in many respects to describe free surface and pressurized flows. They famously handle two-phase water hammer, air transport in free surface flows, dam breaks, some cases of mixed flows,…

Nevertheless, close scrutiny of these models reveals weaknesses and gaps that may cause inaccuracy or even errors when applied to the kind of flow I am interested in:

1. The definition of the concentration C in the transport equation is wooly, especially its physical meaning at the local level. This lack of rigorous definition causes problems in applying turbulence models.
2. The gas void fraction is a pre-determined constant parameter in the computation of two-phase water hammer. The model is thus unable to account for unsteady transport of air in the pipe.
3. Primitive unknowns of the Saint-Venant equations describe only the water flow and fully neglect the effect of the dispersed phaseon the water phase.
4. The transport equation assumes the velocity of the dispersed phase equals the water velocity and restricts dispersion to the molecular diffusion. Such a limitation does not accord with the physics of multiphase phenomena [154]. Velocities of both phases may indeed be very different.
5. Well-established correlations like Manning-Strickler or Colebrook formulations account for head losses in single-phase flows. However, additional head-losses have to be accounted for in two-phase flows. They originate from the change in turbulence due to the presence of two phases as well as from the stresses produced by the relative velocity between phases. It requires adapting friction correlations more thoroughly than just adjusting the friction factor.
6. Preissmann slot model, which is the most useful and widespread model for mixed flows, is unable to simulate sub-atmospheric pressurized flows like other “mathematical shock-capturing” methods.
7. Mixed flow models cannot account for the presence of air at all.
8. The origin of spurious oscillations at the transition bore is not fully understood. Consequently, no satisfactory solution is available in literature.

These shortcomings of traditional methods motivate the need of further research on the modelling of transient air-water flows in civil and environmental engineering. In particular, it legitimates a fundamental research on the unification of free surface and Saint-Venant equations. It also prompted me to investigate new theoretical paths, in particular two-phase flow models.

2.3 MULTI-PHASE MATHEMATICAL MODELS

To date, the use of multiphase mathematical models in civil and environmental engineering has remained circumscribed to very few attempts. As mentioned in 2008 by Spasojevic and Holly about sedimentation engineering [13], "the two-phase flow approach seems promising" but "the formulation of governing equations in flow-sediment problems are still in their infancy". In this respect, Greimann et al [128] used a two-phase formulation to determine the concentration and velocity profiles of a dilute suspension of particles in a 2D uniform flow. In [324], Wu and Wang reviewed the governing equations of the main two-phase flow models, namely the drift-flux model and the two-fluid models. They present the general basis of the mathematical model without validation. To my knowledge, not a single reference treats of the air entrainment or of the pollutant dispersion in civil engineering by using a multiphase approach. On the contrary, stratified models describing the effect of the air flow above the free surface are relatively widespread. If this kind of model particularly accounts for air-water interactions, the methodology consists more in coupling two single-phase models than establishing a whole multiphase set of equations.

Finding thorough two-phase theories requires investigating results in chemical and mechanical engineering. Various multiphase models are in frequent use in these fields. Most of them rely on the Local Instant Formulation (LIF). In this section, I review the literature about simplified multiphase models in chemical and mechanical engineering. I aim at identifying methods that could successfully be applied in civil and environmental engineering. In this respect, the drift-flux model seems a promising alternative to the Navier-Stokes equations. This model is indeed able to describe in a unified framework the transport of a dispersed phase, its interaction with the water flow, and the notion of concentration naturally arises in the derivation of the diffusion equation. Nevertheless, this model has never been applied in civil and environmental engineering. Furthermore, one-dimensional drift-flux models only describe pressurized flows. Obviously, describing transient air-water flow through this paradigm requires further research.

A review of the macroscopic models frequently used in multiphase engineering is performed in section 2.3.1. In section 2.3.2, I introduce the principle and the equations of the three-dimensional drift-flux model, which seems the most promising multiphase model. I review various simplifications of this model in section 2.3.3, namely the one-dimensional drift-flux model, the homogeneous equilibrium model, and the non-dimensional drift-flux model. The whole review focuses mainly on issues relevant in civil and environmental engineering.

2.3.1 MACROSCOPIC MODELS

In principle, a rigorous multiphase flow solver should solve at the same time the local instant variables in the field equations (2.1) as well as the matching jump conditions given by equations (2.7) and (2.8). Obtaining a solution this way is however mathematically

difficult and beyond the present computational capability for many engineering applications. Overwhelming difficulties encountered in solving LIF stem from [154]:

- the existence of the multiple deformable moving interfaces with their motions being unknown;
- the existence of the fluctuations of variables due to turbulence and to motion of the interfaces;
- significant discontinuities of properties at interfaces.

As presented in section 2.2.1, the same problem arises in single-phase turbulent flow without moving interfaces. It is not always possible to obtain the exact local instant fluctuations. RANS methodology resolves this problem by time averaging the Navier-Stokes equations. Such a simplified model is also required for multiphase problems.

Most simplified mathematical models used in practice result from the LIF (Figure 31). Despite their large number, all have in common a first step of averaging. In this respect, many averaging methods enable to simplify the simulation of two-phase flow systems. Main contributions to the development of averaging methods in relation with two phase flows were proposed by Ishii [154], Yadigarolu and Lahey [326], Mathers and al. [215], Nigmatulin [233], Drew [84], Lahey and Drew [184], and Daniels et al [65]. They can be divided into three main groups [154, 212, 238]: the Eulerian averaging, the Lagrangian averaging, and the Boltzmann statistical averaging. Each of them has its own pros and cons as reviewed in [85]. I provide here a brief description of these methods.

The most widely used group of averaging methods in continuum mechanics is the Eulerian averaging, because it is closely related to human observations and most instrumentations [84, 212, 311]. The basic concept underlying this method is the Eulerian reference frame**.** It is a way of looking at fluid motion that focuses on specific locations in the space through which the fluid flows. Sitting on the bank of a river and watching the water passing the fixed location is a good representation of the frame. This description relies on the spatial coordinates and LFI adapts to this description. Averaging procedure in this case consists in integrating the function F(**x**,t) over time or space coordinates assumed independent. Equation (2.45) gives the Eulerian time average as an example:

$$\text{Time mean value} = \frac{1}{\Delta t}\int_{\Delta t} F(\mathbf{x},t)\,dt \tag{2.45}$$

The second group of averaging, called Lagrangian, directly refers to the Lagrangian reference frame. It is a way of looking at fluid motion where the observer follows individual fluid particles as they move through space and time. Plotting the position of an individual particle through time gives the pathline of the particle. One can envision it like sitting in a boat and drifting down a river. Equation (2.46) gives the Lagrangian time average as an example:

$$\text{Time mean value} = \frac{1}{\Delta t}\int_{\Delta t} F(\mathbf{X},t)\,dt \quad ; \quad \mathbf{X} = \mathbf{X}(\mathbf{x}_0,t) \tag{2.46}$$

Lagrangian methods are popular especially in modeling the dynamics of a single particle or a dilute suspension [90].

Finally, like in the kinetic gas theory, the Boltzmann statistical averaging may be used with the concept of particle density f(x,ξ,t), with ξ the phase velocity of particles. It turns out to be useful when the behavior of a group of many particles exhibits some particular characteristics that differ from a single particle. Field equations derived from the Boltzmann statistical theory have been recently established and used under the name of kinetic theory for 1D free surface flow [5], 2D free surface flow [241], and 1D mixed flow [32]. Equation (2.47) gives an example of transport property based on particle density:

$$\text{Transport properties} = \frac{\int \psi(\xi) f(\mathbf{x},\xi,t)\, d\xi}{\int \psi(\xi) d\xi} \tag{2.47}$$

For my doctoral research, I chose the Eulerian time averaging procedure because it is particularly effective for turbulent and dispersed two-phase flows:

- Eulerian time averaging smoothes out the turbulent fluctuations in a similar manner as for a single-phase flow.
- Eulerian time averaging brings the two phases, which are alternatively occupying a unit volume, into continua simultaneously existing at the same point with a properly defined probability for each phase.
- Constitutive equations for multi-phase models rely usually on experimental data expressed under the form of temporal mean value.
- Experience acquired by the HACH with models of turbulence for single-phase flow supports the development of the time averaged two-phase flow model.
- Coupling Eulerian time averaging with subsidiary space averaging procedures turns out to be simple and effective.

In the time-averaged Eulerian framework, models can be further classified into two separate groups of approach (Figure 31), namely:

1. the Drift-Flux Model (DFM) which can be simplified into the Homogeneous Equilibrium Model (HEM) by assuming both phases are in equilibrium;
2. the Two-Fluid Model (TFM).

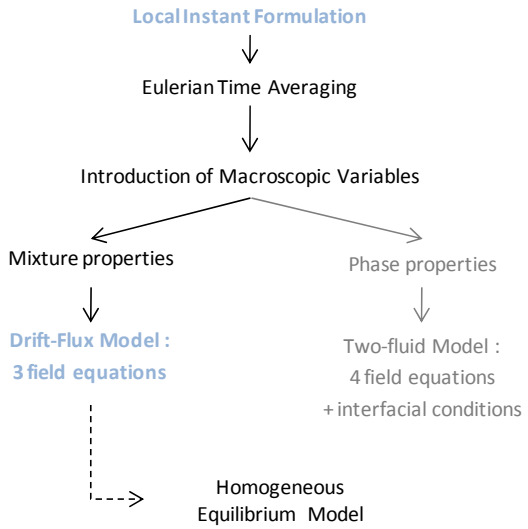

Figure 31 : Derivation of the various two-phase flow models in the Eulerian Framework. Because of the macroscopic variables chosen, we distinguish the drift-flux model from the two-fluid model.

The drift-flux model assumes that the multiphase flow is a single-phase flow of mixture variables, which refer to the motion of the centre of mass of the system. The motion of the dispersed phase is then treated in terms of diffusion through the mixture. The model includes a continuity equation for the mixture, a momentum equation for the mixture, and a continuity equation for the dispersed phase. The two latter equations contain additional terms representing the effect on the mixture flow of the relative velocity between phases. Depending on the exact formulation of the equations and on the personal preference of the author, this model is called drift-flux model [142], mixture model [212], algebraic-slip model [212], suspension approach [311], diffusion model [291], or local-equilibrium model [164]. The momentum equation for the dispersed phase cancels in favor of a constitutive equation for the relative velocity. The form varies in the different models but the relation usually relies on a balance of the forces acting on the dispersed phase and assuming a local equilibrium is established over short spatial length. Governing equations, implementation, and application of the model is available in numerous articles [105, 106, 214, 261].

The homogeneous flow model is a special case of the drift-flux model in which all phases are assumed to have the same velocity and the same pressure [61, 112, 313]. This assumption leans on the belief that differences in pressure and velocity will promote mass and momentum transfer between phases rapidly enough so that thermodynamic equilibrium is reached. Such an assumption is valid in cases where the two-phases are strongly coupled and their relative velocities equalize over short spatial length scales. In any case, Manninen et al [212] advises to always check the validity of the equilibrium assumptions, whenever it is used, by comparing with more accurate theoretical models. Several investigators [157, 224, 269] successfully applied homogeneous equilibrium model to practical applications such as wave propagation in pipelines and magma propagation.

The multiple-fluid model (or two-fluid model) treats each phase or component as a separate fluid with its own set of governing balance equations [43, 154, 238]. Each phase has its own velocity and its own pressure. In this case, the velocity difference does not require introducing a constitutive equation. Computation exploits two different momentum equations, one for each phase. However, difficulties arise in specifying jump conditions at the interface as well as in deriving constitutive equations [155, 156, 289, 290]. In conclusion, the model appropriately takes into account the dynamic interactions between phases but requires numerous constitutive laws for it. It is only useful for applications that require a high level of fidelity in the treatment of the two-phase interactions [66, 67, 129].

In the current project, I decided to investigate the drift-flux model. In many practical applications in civil engineering, the mixture model is indeed a sufficiently accurate approximation, with only a moderate increase in the computational effort compared to a single-phase simulation. In addition, by defining correctly the mixture variables, single-phase algorithm and codes may easily integrate an algorithm for the drift-flux model. Finally, the uncertainties in the closure relations added to the two-fluid model can make it less reliable.

2.3.2 THREE-DIMENSIONAL DRIFT-FLUX MODEL

Originally derived for chemical and mechanical engineering, the three-dimensional drift-flux model is here introduced and discussed in relation with the specific needs of civil and environmental engineering. As pointed in this section, the drift-flux model includes three field equations (2.61) involving suitable mean values of the flow parameters. The model is closed by stating constitutive laws for the drift-velocity, the friction, and the turbulence. This theory directly derives from the classical book of Ishii about thermodynamics of multiphase flows [154].

In a two-phase flow regime, the properties of the flow at a specific point $\mathbf{x}=x_0$ may suffer discontinuous changes at phase interfaces (Figure 32a). If I consider a fixed time interval Δt (and assume it is large enough to smooth out local variations) of the signal at a specific point $\mathbf{x}=x_0$, I can identify three sets of time intervals (Figure 32b):

$$[\Delta t]=[\Delta t]_s+[\Delta t]_w+[\Delta t]_d \tag{2.48}$$

where $[\Delta t]_s ; t\in[t_j-\varepsilon_j ; t_j+\varepsilon_j]$ for j=1,2,....,n is the set of time intervals in which the characteristics of the interface dominate, $[\Delta t]_w$ is the set of time intervals in which the characteristics of the water phase dominate and $[\Delta t]_d$ is the set of time intervals in which the characteristics of the dispersed phase dominate. This decomposition of the time domain enables to define three state density functions M_w, M_d, and M_S:

$$M_k(\mathbf{x},t)=\begin{cases}1 \text{ if } t \in [\Delta t]_k \\ 0 \text{ if } t \notin [\Delta t]_k\end{cases} \quad ; \quad k=S,d,w \tag{2.49}$$

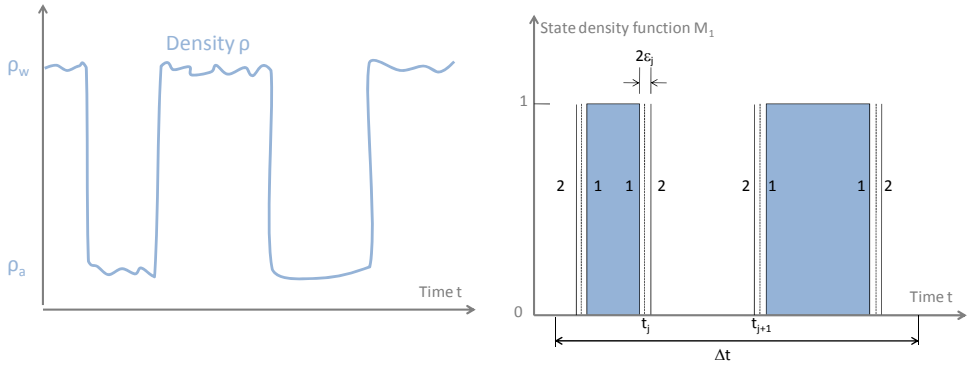

Figure 32: Variation of the fluid properties at a specific point suffers discontinuous changes (Figure a). The state density function separates a given time domain in three parts (Figure b)

State functions facilitate the definition of a general function relative to the k^{th}-phase at a point $\mathbf{x}_0$ as follows:

$$\mathbf{F}_k(\mathbf{x}_0,t)=M_k(\mathbf{x}_0,t)\mathbf{F}=\begin{cases}\mathbf{F}(\mathbf{x}_0,t) & \text{if } t \in [\Delta t]_k \\ 0 & \text{if } t \notin [\Delta t]_k\end{cases} \quad ; \quad k=d,w \tag{2.50}$$

where the general function **F** is associated with two phases and is continuously differentiable everywhere except in the interfacial regions.

Based on the state density functions, I define the void fraction α_k:

$$\alpha_k(\mathbf{x}_0,t_0)=\lim_{\delta\to 0}\frac{1}{\Delta t}\int_{[\Delta t]} M_k(\mathbf{x}_0,t)dt=\frac{[\Delta t]_k}{[\Delta t]} \tag{2.51}$$

where the interfacial thickness δ is assumed arbitrary small. Physically α_k represents a probability of finding the k[th]-phase at a point $\mathbf{x}_0$. By comparison with the single-phase theory, the local void fraction constitutes a rigorously defined concentration. It is not a local value, but an averaged value. This is a key point in the derivation of the drift-flux theory.

I also define the Eulerian time averages (sometimes called Favre averages as in [212]) of the general function **F** and of the k[th]-phase general function $\mathbf{F}_k$ as follows:

$$\bar{\mathbf{F}}(\mathbf{x}_0,t_0)\triangleq\lim_{\delta\to 0}\frac{1}{\Delta t}\int_{[\Delta t]}\mathbf{F}(\mathbf{x}_0,t)dt \quad \text{and} \quad \bar{\mathbf{F}}_k(\mathbf{x}_0,t_0)\triangleq\lim_{\delta\to 0}\frac{1}{\Delta t}\int_{[\Delta t]}\mathbf{F}_k(\mathbf{x}_0,t)dt \tag{2.52}$$

Physically, $\bar{\mathbf{F}}$ is the time mean value in the classical sense. An experimental gauge measures this value at a given point in the flow. The phase mean value $\bar{\mathbf{F}}_k$ is more difficult to represent physically since it gives the mean value of a single phase over the whole time interval [Δt]. Because of these definitions, I may rewrite the local void fraction as:

$$\alpha_k=\overline{M_k} \tag{2.53}$$

I obtain the important relation:

$$\bar{\mathbf{F}}=\bar{\mathbf{F}}_w+\bar{\mathbf{F}}_d \tag{2.54}$$

Considering a non-zero scalar weighting function w, I can further define the weighted mean value of a general function **F**:

$$\bar{\mathbf{F}}^w(\mathbf{x}_0,t_0)\triangleq\frac{\overline{w\mathbf{F}}}{\bar{w}}=\frac{\int_{[\Delta t]} w\mathbf{F}(\mathbf{x}_0,t)dt}{\int_{[\Delta t]} wdt}=\frac{\sum_k \bar{w}_k\bar{\mathbf{F}}^{w_k}}{\sum_k \bar{w}_k} \tag{2.55}$$

By taking the phase density function M_k as a weighting function, the phase average of the k[th]-phase general function $\mathbf{F}_k$ is defined as:

$$\bar{\bar{\mathbf{F}}}_k(\mathbf{x}_0,t_0)\triangleq\frac{\overline{M_k\mathbf{F}_k}}{\bar{M}_k}=\frac{\bar{\mathbf{F}}_k}{\alpha_k}=\frac{1}{\Delta t_k}\int_{[\Delta t]_k}\mathbf{F}_k(\mathbf{x}_0,t)dt \tag{2.56}$$

Physically, $\bar{\bar{\mathbf{F}}}_k$ is more meaningful because it is the mean value in a single phase over the restricted time interval $[\Delta t]_k$. $\bar{\bar{\mathbf{F}}}_k$ is an intrinsic value of the k[th] phase since it does not depend on the other phase. Instead, $\bar{\mathbf{F}}_k$ is dependent on the ratio in which the k[th] phase is present. By considering the fluid density ρ as a weighting function, the mass weighted mean value of the general extensive function $\mathbf{F}=\rho\boldsymbol{\psi}$ is defined as:

$$\hat{\boldsymbol{\psi}}\triangleq\frac{\overline{\rho\boldsymbol{\psi}}}{\bar{\rho}} \tag{2.57}$$

The phase mass weighted mean value of the extensive function **F** = ρ**ψ** is defined as:

$$\widehat{\boldsymbol{\psi}}_k \triangleq \frac{\overline{\rho_k \boldsymbol{\psi}_k}}{\overline{\rho_k}} \tag{2.58}$$

In the same manner in which a turbulent single phase flow is Reynolds averaged in classical fluid mechanics [48], variables of the multiphase flow are broken down into a weighted mean value and a fluctuating component:

$$\mathbf{F}_k = \overline{\mathbf{F}}_k^{w_k} + \mathbf{F}_k' \tag{2.59}$$

In addition, we make the fundamental hypothesis of smoothness of mean values:

$$\overline{\left(\overline{\mathbf{F}}\right)} = \overline{\mathbf{F}} \quad \text{and} \quad \overline{\mathbf{F}_k'}^{w_k} = 0 \tag{2.60}$$

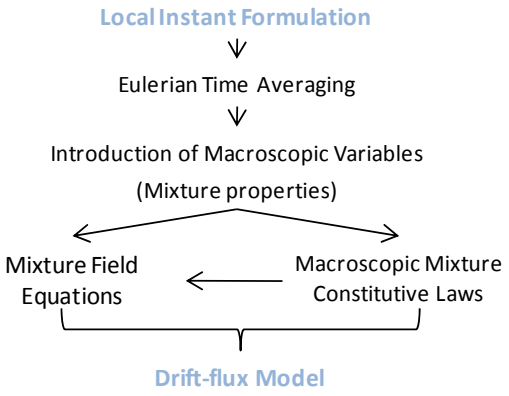

Figure 33 : Process for the derivation of the drift flux model starts from the Local Instant Formulation

Based on these different mean values, I can now apply the Eulerian time averaging process to the local instant formulation in order to derive field equations for the drift-flux model. It requires first to define a domain of integration that is in fact the time interval defined here above. It also requires properly assigning appropriate balance equations to both the bulk fluid and the interface at each time t $\in[\Delta t]$, and integrating them over the whole time domain. During $[\Delta t]_w$, the standard field equation holds for the water phase. During $[\Delta t]_d$, it is then the standard field equation for the dispersed phase that holds. Finally, the jump condition holds in $[\Delta t]_S$. Meanwhile, the introduction of the appropriate mean values defined above enables to simplify the form of the field equations. The whole process of integration (Figure 33) is presented in extenso in [154, 173]. It results in a system of 3 equations, namely the continuity equation for the mixture, the diffusion equation for the dispersed phase and the momentum equation for the mixture:

$$\begin{cases} \dfrac{\partial \rho_m}{\partial t} + \nabla\left(\rho_m \mathbf{v}_m\right) = 0 \\ \dfrac{\partial \alpha_d \overline{\overline{\rho}}_d}{\partial t} + \nabla\left(\alpha_d \overline{\overline{\rho}}_d \mathbf{v}_m\right) + \nabla\left(\alpha_d \overline{\overline{\rho}}_d \mathbf{V}_{dm}\right) = \Gamma_d \\ \dfrac{\partial \rho_m \mathbf{v}_m}{\partial t} + \nabla\left(\rho_m \mathbf{v}_m \mathbf{v}_m\right) = -\nabla p_m + \nabla\left(\tau_m + \tau^T + \tau^D\right) + \rho_m \mathbf{f}_m + \mathbf{M}_m \end{cases} \tag{2.61}$$

where the subscript *d* denotes the dispersed phase and the subscript *m* the mixture made of the phases. Obviously, this model is very similar to the Navier-Stokes equations with a transport equation (section 2.2). This is a direct consequence of the definition of the *mixture velocity* as the velocity of the center of mass (or the mass weighted mean value of the mixture momentum):

$$\mathbf{v}_m \triangleq \frac{\overline{\rho \mathbf{v}}}{\overline{\rho}} = \frac{\sum_{k=w,d} \alpha_k \overline{\overline{\rho}}_k \widehat{\mathbf{v}}_k}{\rho_m} \tag{2.62}$$

The mixture velocity is different from both the dispersed phase velocity $\widehat{\mathbf{v}}_d$ (defined as mass weighted mean value of the dispersed phase momentum) and the water phase velocity $\widehat{\mathbf{v}}_w$ (defined as mass weighted mean value of the water phase momentum):

$$\widehat{\mathbf{v}}_k \triangleq \frac{\overline{\rho_k \mathbf{v}_k}}{\overline{\rho}_k} \tag{2.63}$$

In the drift-flux model, the *mixture density* is defined as:

$$\rho_m \triangleq \overline{\rho} = \sum_k \alpha_k \overline{\overline{\rho}}_k \tag{2.64}$$

Likewise, I define the *phase density* as the phase average of the density of the fluid:

$$\overline{\overline{\rho}}_k \triangleq \frac{\overline{\rho_k}}{\alpha_k} \tag{2.65}$$

Finally, the *diffusion velocity* of each phase $\mathbf{V}_{km}$ appears naturally in the derivation of the drift flux model. The diffusion velocity $\mathbf{V}_{km}$ is in fact the relative velocity with respect to the mass center of the mixture:

$$\mathbf{V}_{km} \triangleq \widehat{\mathbf{v}}_k - \mathbf{v}_m \tag{2.66}$$

To put it in other words, the quantity $\mathbf{V}_{km}$ is sufficient to account for the difference in velocity between both phases.

Physically, the mixture continuity equation (2.61) ensures the conservation of the total mass of the flow (the sum of each phase mass). It has the exact same form as the continuity equation in Navier-Stokes equations. This fortunate form results from the sensitive choice of the mixture mean values. Readers must be aware that the physical significance of both equations is not equivalent. Navier-Stokes continuity describes the water conservation. Drift-flux continuity ensures the mass conservation of the mixture.

Since the mixture continuity equation does not ensure the conservation of each phase taken on their own, the drift-flux model enforces the complete mass conservation by adding a conservation equation for the dispersed phase only. This is the diffusion equation. Physically, the diffusion equation describes the transport of the void fraction α_d of the dispersed phase. The fluxes are broken down into a term of advection of $\nabla\left(\alpha_d \overline{\overline{\rho}}_d \mathbf{v}_m\right)$ and a term of diffusion $\nabla\left(\alpha_d \overline{\overline{\rho}}_d \mathbf{V}_{dm}\right)$ resulting from the difference of velocity between both phases. This term is very general since I have not yet made any phenomenological choice

for the form of the diffusion velocity. Particularly, constitutive equations specify its value. These laws can integrate various phenomena, namely the molecular diffusion, the effect of gravity, of curvature,… Another key point here is the lack of turbulence term in the diffusion equation (by comparison with an advection-diffusion model). This is the direct consequence of the definition of the void fraction as the time-average of the state function in (2.53). It is indeed nonsense to apply Reynolds decomposition on time-averaged values, which are not defined at the turbulence scale. Finally, the source term Γ_d accounts for the exchange of mass between the two phases and is called *mean mass source term*. In large-scale civil engineering applications, it can be stated in terms of correlations originating from empirical observations on scale models:

$$\overline{\Gamma_{d,(i)}} = f\left(\alpha_d, \mathbf{v}_m, ...\right) \tag{2.67}$$

Eventually, the only momentum equation present in the drift-flux model describes the mixture fluid. Its form is similar to the Navier-Stokes momentum equation. However, its physical significance is very different since it ensures the momentum conservation of the mixture as a whole. Drift-flux model does not ensure the momentum conservation in each phase separately. It would require an additional momentum equation for the dispersed phase which is cancelled here in favor of a constitutive equation for the relative velocity. This relation usually relies on a balance of the forces acting on the dispersed phase and on the assumption that a local equilibrium establishes over short spatial length. This approximation may cause small errors in the evaluation of both phase velocities such that the choice of a constitutive equation for the relative velocity is crucial.

Source terms appearing in the mixture momentum equation also differ from the pure water momentum equation. The *mixture pressure* p_m can be considered as a primitive unknown:

$$p_m \triangleq \bar{p} = \sum_k \alpha_k \overline{\overline{p_k}} \tag{2.68}$$

Rigorously, the term of *average mechanical stresses* τ_m is different from the Newtonian laws of viscosity, even if both phases are Newtonian. However, one can formulate it by analogy with the stress tensor for single phase flows expressed in terms of the mixture parameters [33, 180, 313]. If we assume the mixture fluid remains Newtonian, we obtain:

$$\boldsymbol{\tau}_m = \mu_m \left[\left(\nabla \mathbf{v}_m + \left(\nabla \mathbf{v}_m \right)^T \right) - \frac{2}{3} \left(\nabla . \mathbf{v}_m \right) \mathbf{I} \right] \tag{2.69}$$

where μ_m is the dynamic viscosity for the mixture. Several correlations for the mixture viscosity are available in literature [19, 20, 313]. The error remains limited in many cases. The *turbulent stresses* τ^T are caused by the fluctuations of the velocity relative to the mean value. As this term is in general more important in multiphase flows than in single-phase flows, it cannot be neglected in the present study and must be computed as follows:

$$\boldsymbol{\tau}^T = -\sum_k \alpha_k \tau_k^T = -\sum_k \alpha_k \overline{\overline{\rho_k \mathbf{v}_k' \mathbf{v}_k'}} \tag{2.70}$$

which results from the decomposition of the velocities in mean and fluctuating values:

$$\mathbf{v}_k = \hat{\mathbf{v}}_k + \mathbf{v}_k' \tag{2.71}$$

As the development of a turbulence model for τ^T is beyond the scope of this paper, we use a *generalized mixture shear stress*, which lumps viscous and turbulent stresses:

$$\tau_{Gm} = \tau_m + \tau^T \tag{2.72}$$

A third kind of stresses called averaged *diffusion stresses* appear in the drift flux model:

$$\tau^D = -\sum_k \alpha_k \overline{\overline{\rho}}_k \mathbf{V}_{km} \mathbf{V}_{km} \tag{2.73}$$

For experimental reasons, diffusion stresses make preferably use of the *drift-velocity* $\mathbf{V}_{kj}$:

$$\tau^D = -\frac{\alpha_d}{1-\alpha_d} \frac{\overline{\overline{\rho}}_w \overline{\overline{\rho}}_d}{\rho_m} \mathbf{V}_{dj} \mathbf{V}_{dj} \tag{2.74}$$

The *drift-velocity* $\mathbf{V}_{kj}$ is defined as the relative velocity with respect to the center of volume:

$$\mathbf{V}_{kj} \triangleq \hat{\mathbf{v}}_k - \mathbf{j} \tag{2.75}$$

with **j** the mixture volumetric flux, defined as the velocity of the center of volume:

$$\mathbf{j} = \sum_k \mathbf{j}_k = \sum_k \alpha_k \hat{\mathbf{v}}_k \tag{2.76}$$

Drift velocity appears in a natural manner when expressing the equilibrium of forces acting on a particular phase. It explains both its more frequent use and the name of the method. The same simplifications can be introduced in the diffusion terms:

$$\nabla.\left(\alpha_d \rho_d \mathbf{V}_{dm}\right) = \nabla.\left(\alpha_d \rho_d \frac{\rho_w}{\rho_m} \mathbf{V}_{dj}\right) \tag{2.77}$$

It is obvious from equations (2.73) and (2.77) that it is still necessary to state an expression for the drift velocity based on the forces acting on the dispersed phase. Several formulations of the 3D drift velocity are available in literature [153, 154, 238]. Next, the mixture momentum source $\mathbf{M}_m$ accounts for the effects of the surface tension gradient:

$$\mathbf{M}_m = \frac{1}{\Delta t} \sum_j \frac{1}{v_{nj}} \left(\mathbf{t}_\alpha A^{\alpha\beta} \sigma\right)_{,\beta} \tag{2.78}$$

where v_{nj} designates the component of the interface velocity in the direction normal to the interface. Ishii [154] underlines this term is negligible, even for zero interface velocity. The only exception holds for highly dispersed flow in very smooth pipe. In the current work, this term is aggregated in macroscopic friction laws. Finally, the last term appearing in the drift flux model is a term of mixture body force:

$$\mathbf{f}_m = \frac{1}{\rho_m} \sum_k \alpha_k \overline{\overline{\rho}}_k \hat{\mathbf{f}}_k \tag{2.79}$$

which often contains only the gravity **g**.

A thorough study of 3D closure laws is of no interest in this study for two reasons. It may be shown that closure relations for the 2D depth-integrated model are more often specified under the form of experimental correlations than mathematically derived from 3D laws. Furthermore, practical multiphase modeling commonly employs single-phase closure relations extended to multiphase situations [212, 313].

2.3.3 SIMPLIFICATIONS OF THE THREE-DIMENSIONAL DRIFT-FLUX MODEL

Like in single-phase models, computation of 3D multiphase models frequently requires a prohibitive computational effort. Of course, difficulties arise from the complexity of treating three-dimensional problems, but not only. Computation of the drift-flux velocity also becomes sometimes difficult. I present herein three simplifications of the full model: the one-dimensional drift-flux model, the homogeneous flow model, and the non-dimensional model. None of them is sufficient with regard to the simulation of transient air-water flows. The one-dimensional drift-flux model describes only pressurized flows.

CROSS-SECTIONAL INTEGRATED MODEL

In many practical applications in civil and environmental engineering (river, channel, pipe,…), one-dimensional models are sufficient. In this respect, the single existing cross-sectional integrated drift-flux model proposed in literature only describes pressurized flows. It means that it does not meet our objective to describe free surface flows as well.

The one-dimensional drift-flux model is frequently used to predict the gas void fraction in gas-liquid flows. Such flows are in fact crucial in vertical air-lift pumps and nuclear reactors [212]. The classical book of Wallis [313] gives steady analytical solutions for various applications. This theory is based on the comprehensive formulation of volumetric fluxes provided by Zuber and Findlay [333, 334]. In particular, it includes the effect of uneven distributions of parameters across the pipe cross-section. All these results remain limited to pressurized flows in vertical pipes. Brockmeier et al. [34] extended the application of these results to pressurized horizontal pipes and performed a validation in the field of nuclear safety. Several papers proposed an application of the drift-flux theory to two-fluid flow such as air-water mixtures. Steady solutions were applied to co-current gas-liquid flows by Butterworth [35], Mori [224] and Ishii [153]. França and Lahey [108] proposed a validation of steady solutions by comparison with experimental data for horizontal flow of air-water stratified flows. All these applications are still the object of intense research [140, 142, 143, 320, 328]. Particle-fluid mixtures have also been approached with the drift-flux theory, especially for the study of fluidized bed [273]. In conclusion, one-dimensional drift-flux theory succeeds in many different fields of application to address specific multiphase issues. However, its application remains limited to pressurized flows.

Ishii [153, 154] developed a general one-dimensional formulation of the drift-flux model for unsteady pressurized applications. For this purpose, he introduced proper mean values:

- the area-average of a function f(**x**,t) over the cross-sectional area A of the pipe:

$$\langle f \rangle(x,t) \triangleq \frac{1}{A}\int_A f(x,y,z,t)\,dA \tag{2.80}$$

- the void-fraction-weighted mean value of a function f(**x**,t):

$$\langle\langle f_k \rangle\rangle \triangleq \frac{\langle \alpha_k f_k \rangle}{\langle \alpha_k \rangle} \tag{2.81}$$

Physically, the area-average gives the mean value of the parameter f over the flow cross-section. Both phases are considered and the mean value depends on the void fraction value. On the opposite, the void-fraction-weighted mean value accounts for the value of the parameter f in a single phase considered on its own. The two mean values are fundamentally different.

By area-averaging the 3D drift flux model over a given cross-section A, Ishii established the one-dimensional drift-flux model as follows:

$$\begin{cases} \dfrac{\partial \langle \rho_m \rangle}{\partial t} + \dfrac{\partial \langle \rho_m \rangle \tilde{u}_m}{\partial x} = 0 \\ \dfrac{\partial \rho_d \langle \alpha_d \rangle}{\partial t} + \dfrac{\partial}{\partial x}\left(\rho_d \langle \alpha_d \rangle \tilde{u}_m + \langle \alpha_d \rangle \dfrac{\rho_d \rho_w}{\langle \rho_m \rangle} \tilde{U}_{dj} \right) = \langle \Gamma_d \rangle \\ \dfrac{\partial \langle \rho_m \rangle \tilde{u}_m}{\partial t} + \dfrac{\partial \langle \rho_m \rangle \tilde{u}_m \tilde{u}_m + \langle p_m \rangle}{\partial x} + \dfrac{\partial}{\partial x}\left(\dfrac{\langle \alpha_d \rangle}{1 - \langle \alpha_d \rangle} \dfrac{\rho_d \rho_w}{\langle \rho_m \rangle} \tilde{U}_{dj} \tilde{U}_{dj} \right) \\ \qquad = \langle \rho_m \rangle g (S_0 - S_F) - \dfrac{\partial}{\partial x}\left(\sum_k \mathrm{COV}(\alpha_k \rho_k \hat{u}_k \hat{u}_k) \right) \end{cases} \tag{2.82}$$

The proof of equation (2.82) is given in [154]. In the demonstration, the density of both phases ρ_d and ρ_w within any cross-sectional area is considered to be uniform, so that $\rho_k = \langle\langle \rho_k \rangle\rangle$, k=d,w . Under this assumption, the mean mixture density is given by:

$$\langle \rho_m \rangle = \sum_k \alpha_k \rho_k \tag{2.83}$$

The axial component of the weighted mean velocity of k^{th} phase is defined as:

$$\langle\langle u_k \rangle\rangle = \frac{\langle \alpha_k u_k \rangle}{\langle \alpha_k \rangle} \tag{2.84}$$

where the scalar expression of the velocity corresponds to the axial component of the vector. Consequently, the mixture velocity is defined by:

$$\tilde{u}_m = \frac{\langle \rho_m u_m \rangle}{\langle \rho_m \rangle} = \frac{\langle \alpha_d \rangle \rho_d \langle\langle u_d \rangle\rangle + (1 - \langle \alpha_d \rangle) \rho_w \langle\langle u_w \rangle\rangle}{\langle \rho_m \rangle} \tag{2.85}$$

Obviously, the mean mixture velocity is chosen as the mixture density weighted area-average of the mixture velocity. Physically, the mean mixture velocity is the velocity of the center of mass of the mixture. Its value is different from both the mean water velocity $\langle\langle u_w \rangle\rangle$ and the mean dispersed phase velocity $\langle\langle u_d \rangle\rangle$. In order to specify univocally these both velocities, Ishii define the area-averaged drift-velocity:

$$\tilde{U}_{dj} \triangleq \langle\langle u_d \rangle\rangle - \langle j \rangle = (1 - \langle \alpha_d \rangle)(\langle\langle u_d \rangle\rangle - \langle\langle u_w \rangle\rangle) \tag{2.86}$$

where $\langle j \rangle$ is the area-averaged volumetric flux defined as follows:

$$\langle j \rangle = \langle j \rangle_w + \langle j \rangle_d = \langle \alpha_d \rangle_l \langle\langle u_d \rangle\rangle + (1 - \langle \alpha_d \rangle_l) \langle\langle u_w \rangle\rangle \tag{2.87}$$

In the one-dimensional drift-flux formulation, a problem is solved for $\langle p_m \rangle$, $\langle \alpha_d \rangle$, and $\tilde{u}_m$ with a given constitutive equation for the mean drift-velocity $\tilde{U}_{dj}$. Ishii [154] reviewed a large number of this constitutive laws for pressurized flows. The covariance term

represents the difference between the average of a product and the product of the average of two variables (velocities here) such that:

$$\mathrm{COV}\left(\alpha_k\rho_k\hat{u}_k\hat{u}_k\right)=\left\langle\rho_k\alpha_k\hat{u}_k\left(\hat{u}_k-\left\langle\left\langle u_k\right\rangle\right\rangle\right)\right\rangle \tag{2.88}$$

Finally, S_0 designates the topographic slope, and S_F the frictional slope. The first slope is given by the topography of the pipe. The second requires a suitable friction correlation. Due to the utmost importance of this parameter in civil and environmental engineering, I perform a thorough analysis of friction correlations in chapter 7.

Model (2.82) is obviously simpler than the three-dimensional drift-flux model. In particular, there is no need any more to create complex mesh grids or perform heavy computations. Nevertheless, this simplified model has conserved the main qualities of the drift-flux model as regards the transport of a dispersed phase. The model ensures the mass conservation of both phases (taken separately) as well as the momentum conservation of the mixture (both phases taken as a whole). Each set of equations takes into account the effect of the dispersed phase on the main water flow. In particular, the area-averaged void fraction $\langle\alpha_d\rangle$ constitutes an unambiguous definition for the concentration. The single area-averaged drift-velocity accounts for both the dispersion phenomenon and its effect on the momentum of the flow. Finally, the model contains the correct terms of turbulence, covariance and head losses since it is rigorously derived from the LIF.

One-dimensional drift-flux model for pressurized flows is however not sufficient to analyze transient air-water flows as described in the introduction chapter. It is indeed unable to account for free surface and mixed flows. It also lacks of constitutive equations suitable for civil and environmental engineering.

NON DIMENSIONAL FORM OF THE DRIFT-FLUX MODEL

Dimensional analysis is a conceptual tool that is very useful to understand situations involving certain physical quantities and to give insight into the fundamental properties of a system. I apply here this strategy to identify the relevant dimensionless numbers in dispersed two-phase flows. For this purpose, reference parameters are identified for each relevant parameters and are denoted by the subscript o. The characteristic length scale is L_0 and the time scale is taken as the ratio of L_o to the velocity scale. Then we define the following dimensionless parameters:

$$\begin{aligned}
&\rho_m^*=\frac{\rho_m}{\rho_{m0}};\quad \mathbf{v}_m^*=\frac{\mathbf{v}_m}{v_{m0}};\quad t^*=\frac{t}{\tau_0};\quad \nabla^*=L_0\nabla\\
&\rho_d^*=\frac{\rho_d}{\rho_{d0}};\quad \rho_w^*=\frac{\rho_w}{\rho_{w0}};\quad \mathbf{V}_{dj}^*=\frac{\mathbf{V}_{dj}}{\mathbf{V}_{dj0}};\quad \Gamma_d^*=\frac{\Gamma_d}{\Gamma_{d0}^*};\quad p_m^*=\frac{p_m}{\rho_{m0}v_{m0}^2}\\
&\left(\tau_m+\tau^T\right)^*=\frac{\tau_m+\tau^T}{\mu_{m0}v_{m0}/L_0};\quad \mathbf{M}_m^*=\frac{\mathbf{M}_m}{2H_{21o}\sigma_o/L_o};\quad \mathbf{F}_m^*=\frac{\mathbf{F}_m}{\mathbf{F}_{m0}}
\end{aligned} \tag{2.89}$$

Substituting these new parameters into field equations (2.61) gives the non-dimensional drift-flux model:

- for the continuity equation:

$$\frac{\partial \rho_m^*}{\partial t^*} + \nabla^* \left(\rho_m^* \mathbf{v}_m^* \right) = 0 \tag{2.90}$$

- for the diffusion equation:

$$\frac{\partial \overset{=*}{\alpha_d \rho_d}}{\partial t^*} + \nabla^* \left(\overset{=*}{\alpha_d \rho_d} \mathbf{v}_m^* \right) = N_{pch} \Gamma_d^* - N_D \nabla^* \left(\overset{=*=*}{\alpha_d \frac{\rho_d \rho_w}{\rho_m^*}} \mathbf{V}_{dj}^* \right) \tag{2.91}$$

- for the momentum equation:

$$\begin{aligned} \frac{\partial \rho_m^* \mathbf{v}_m^*}{\partial t^*} + \nabla^* \left(\rho_m^* \mathbf{v}_m^* \mathbf{v}_m^* \right) = -\nabla^* p_m^* + \frac{1}{N_{Re}} \nabla^* \left(\tau_m + \tau^T \right)^* + \frac{1}{N_{Fr}} \rho_m^* \mathbf{F}_m^* \\ - N_\rho N_D^2 \nabla^* \left(\frac{\alpha_d}{1-\alpha_d} \frac{\rho_d^* \rho_w^*}{\rho_m^*} \mathbf{V}_{dj}^* \mathbf{V}_{dj}^* \right) + N_\sigma \mathbf{M}_m^* \end{aligned} \tag{2.92}$$

where 6 scaling parameters or non-dimensional numbers give the order of magnitude of the various terms appearing in the field equations for given flow conditions. They are therefore very useful to determine similarities between experimental cases [154]. The classical *Reynolds number* gives a measure of the ratio of inertial forces to viscous forces:

$$N_{Re} = \frac{\rho_{m0} v_{m0} L_0}{\mu_{m0}} \tag{2.93}$$

This number is traditionally used to characterize different flow regimes, namely laminar and turbulent flows. The second dimensionless number that appears is the *Froude number* which compares inertia and body forces (gravitational forces most of the time):

$$N_{Fr} = \frac{v_{m0}^2}{\mathbf{F}_{m0} L_0} \tag{2.94}$$

Numbers specific to two-phase flows and to the drift-flux model appears. The first one, called *phase change number*, compares mass phase change to the mixture momentum:

$$N_{pch} = \frac{\Gamma_{d0} L_0}{\rho_{m0} v_{m0}} \tag{2.95}$$

The *drift number* is a dimensionless number that measure the ratio of drift momentum to mixture momentum:

$$N_D = \frac{\rho_{w0} V_{dj0}}{\rho_{m0} v_{m0}} \tag{2.96}$$

If the phase change number is much larger than the drift number, the system is controlled by the changes of phase. If it is the opposite, the system is controlled by the redistribution of phases. The *density ratio* compares density of both phases:

$$N_\rho = \frac{\rho_{d0}}{\rho_{w0}} \tag{2.97}$$

Finally the *surface number* measures the ratio of forces due interfacial momentum source to inertia forces:

$$N_\sigma = \frac{2 H_{21_0} \sigma_0}{\rho_{m0} v_{m0}^2} \tag{2.98}$$

HOMOGENEOUS FLOW MODEL

The homogeneous flow model is a special case of the drift-flux model in which all phases are assumed to have the same velocity and the same pressure [61, 112, 313]. For justifying this assumption, we believe that differences in pressure and velocity promote mass and momentum transfer between phases rapidly enough so that thermodynamic equilibrium is reached. Using the non-dimensional analysis of the previous section, it corresponds to assume that the drift number is negligible. Equation (2.61) is then written under the following form:

$$\begin{cases} \dfrac{\partial \rho_m}{\partial t} + \nabla\left(\rho_m \mathbf{v}\right) = 0 \\ \dfrac{\partial \alpha_d \overline{\rho}_d}{\partial t} + \nabla\left(\alpha_d \overline{\rho}_d \mathbf{v}\right) = \Gamma_d \\ \dfrac{\partial \rho_m \mathbf{v}_m}{\partial t} + \nabla\left(\rho_m \mathbf{v}\mathbf{v}\right) = -\nabla p_m + \nabla\left(\tau_m + \tau^T\right) + \rho_m \mathbf{F}_m + \mathbf{M}_m \end{cases} \tag{2.99}$$

Homogeneous equilibrium model have been successfully applied to practical applications as wave propagation in pipelines and magma propagation in volcanic conduits [157, 224, 269]. Verloop [311] has discussed the validity of the drift-flux model and argues the model is inaccurate if the terms using the drift-velocity are missing. We can conclude that homogeneous assumption is valid only in cases where the two-phases are strongly coupled and their relative velocities equalize over short spatial length scales. In any case, as it is advised by Manninen et al [212], we should always check the validity of the equilibrium assumptions, whenever it is used, by comparing with more accurate theoretical models.

2.4 NUMERICAL METHODS AND COMPUTATIONAL CODE

When an analytical solution does not exist for a model (except in particular idealized cases), searching an approximate numerical solution constitutes the only alternative to extract information from the set of partial differential equations. This is the subject of the Computational Fluid Dynamics (CFD), which is defined as *the science of computing numerical solutions to Partial Differential or Integral Equations that are models for fluid flow phenomena.*

In its now classical book [285] on fluid mechanics, Toro reports that British scientist L.F. Richardson made the first attempt in to forecast the weather during a single day – 20 May 1910 – by direct computation of partial differential equations. Considering the calculations were done by hand, it is a remarkable achievement. Even if Richardson's forecast failed dramatically, his work marked the beginning of CFD. His work has indeed the four distinguishing characteristics of CFD [285]: A *practical problem* to solve, a *mathematical model* to represent the problem in the form of a set of partial differential equations, a *numerical method* and a *computer* (human beings in Richardson's case).

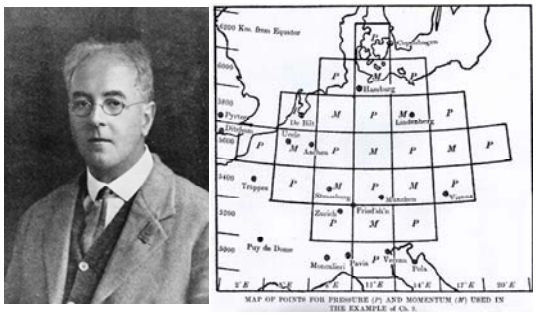

Figure 34 : Lewis Fry Richardson made the first attempt to solve a CFD problem

Since the pioneering works of Richardson, computers have developed to unprecedented levels of power; the accuracy and complexity of mathematical models have increased dramatically; numerical methods have met with success in many areas of modern engineering. CFD provides numerous tools to solve discretised equations. In this section, I propose to review briefly the standard methods in hydraulics. Examination of basic discretisation techniques (subsection 2.4.1) underlines the performance of "numerical shock-capturing" schemes over structured grid, and the ability of the Finite Volume Method to handle discontinuities and to ensure conservation. Subsection 2.4.2 summarizes the bases of the Finite Volume schemes. In particular, Godunov methods and Flux Vector Splitting schemes are compared. Extension of these schemes to higher order of accuracy is considered. This subsection gives a good overview of CFD tools in 2010. Finally, I present the modelling system WOLF (subsection 2.4.3). Entirely developed within the HACH, this software constitutes an application of CFD theory to single-phase free surface hydraulics. It has been a reliable and helpful basis for my work.

2.4.1 BASIC DISCRETIZATION TECHNIQUES

Choosing a discretization method to solve a mathematical problem involves two components, the space discretization, and the equation discretization. For each operation, several different methods exist with their own pros and cons. This section proposes a brief review of the main discretization techniques. In particular, I conclude that the Finite Volume Method is the more suitable technique to solve the problems I am interested in.

SPACE DISCRETIZATION OF THE PHYSICAL DOMAIN

The space discretization consists in replacing the continuum of space (physical domain) by a finite number of points where the values of the variables will have to be determined [144, 145]. A mesh or a grid replaces the physical domain. The accuracy of the numerical solution depends on the size of the mesh. For complex geometry (Figure 35), accuracy also depends on the form of the mesh and its ability to fit geometrical complexities. Since this thesis focuses on one-dimensional models only, mesh-related issues remain very easy to handle with. If necessary, a non-uniform mesh is used to fit geometrical complexities or areas of particular interest. Nevertheless, treating shocks and discontinuities over such discretised domain remains challenging. In this respect, two approaches have been competing: the "numerical shock-tracking" and the "numerical shock-capturing" methods.

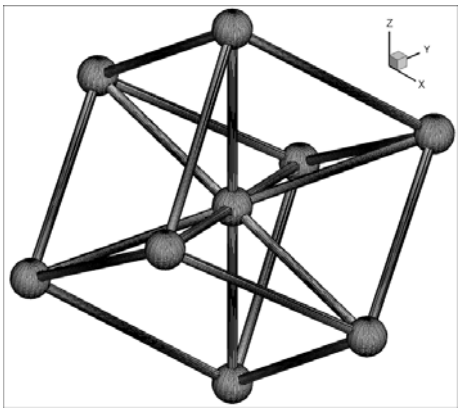

Figure 35: 3D Mesh, like this one representing the Atomium, may become very complex [71]

"Numerical shock-tracking" approach tracks explicitly discontinuities and treats them as internal boundaries across which appropriate jump conditions are imposed. This way, a shock remains a true discontinuity (infinite resolution) located at meshes interface. Consequently, "numerical shock-tracking" methods must use adaptative gridding techniques in which the mesh evolves at each time step to keep the shock at an interface. This school of thought has reported impressive advances [121, 122, 278, 327] but the cost of the algorithms remains important.

In the "numerical shock-capturing" approach, shock-waves and other discontinuities emerge as a part of the complete solution. The shock is smeared or spread over a number of mesh points such that the grid can remain unchanged along the computation. Simplicity and applicability are the main advantages of this method that I have privileged in this

thesis. This choice is based on my strong will to find practical outlets for my research and on the significant know-how that the HACH has about “numerical shock-capturing” schemes. However, a key challenge in this school of thought is to limit the amount of smearing that affects shocks. This requirement may only be achieved by using an adequate discretization for the equations (see section 2.4.2).

DISCRETIZATION OF THE EQUATIONS

Equation discretization consists in transforming the differential equations into discrete algebraic systems involving the values of the unknowns at the mesh points. In this respect, the three most widely used numerical methods to solve PDEs are the finite difference method, the finite element method, and the finite volume method.

The Finite Difference Method (FDM) is based on the properties of Taylor expansions. FDM is the simplest method to discretize equations, particularly on uniform mesh [102, 144]. However, it requires using structured grid such that it does not suit to complex geometries. In addition, discontinuous solutions compromise the strict conservation of the equations because the method relies on local partial derivatives [75]. This inability to capture shocks severely limits the interest of this method in hydraulics.

The Finite Element Method (FEM) is popular for structural analysis of solids, but also in fluids mechanics. Based on a rigorous mathematical background, the method gives a weak solution of the partial differential equations. Generally, stability and robustness of the solution are better in FEM than in any other methods. The Finite Element Method is a good choice for solving partial differential equations over complicated domains (like cars and oil pipelines), when the domain changes (as during a solid state reaction with a moving boundary), when the desired precision varies over the entire domain, or when the solution lacks smoothness. However, it requires a great deal of memory and special care to ensure a conservative solution. Further versions of FEM give partial answers to these problems. It includes the generalized finite element method (GFEM), extended finite element method (XFEM), spectral finite element method (SFEM), mesh-free finite element method, discontinuous Galerkin finite element method (DGFEM),...

The Finite Volume Method (FVM) is the last popular method to solve partial differential equations. It relies on a discretization of the domain in “finite volumes” or small volumes surrounding each node on a mesh. FVM is closely related to FDM. However, FVM is derived based on the integral form of the conservative law. It is the starting point of many advantages. Because the flux entering a given volume is identical to that leaving the adjacent volume, FVM is rigorously conservative. Another advantage of the finite volume method is that it easily allows for unstructured meshes. Finally, the class of admissible solutions of the method includes discontinuous solutions. Shock and rarefaction waves are then naturally captured by FVM. However, the formulation of FVM becomes complicated with evolving domains. Enforcing the stability of FVM is also more difficult. Because of the ability of FVM to treat shocks and ensure conservation, I have chosen FVM in this thesis.

2.4.2 A Brief Introduction to the Finite Volume Method

Spatial and time integrations of the equations give the general formulation of the finite volume method for hyperbolic conservation laws. Stability, consistency, and order of accuracy of the method are linked to the choice of the numerical flux. In this respect, Godunov methods and Flux Vector Splitting schemes compete. What is more, reaching higher order of accuracy requires Total Variation Diminishing Schemes for ensuring the stability of the method.

General formulation for conservations laws

Since most flow equations are the expression of a conservation law, I consider here the following conservation equation in a one-dimensional fixed mesh (Figure 36):

$$\frac{\partial}{\partial t}\int_{x_{i-1/2}}^{x_{i+1/2}} \mathbf{U}(x,t)\,dx + \mathbf{F}\left(\mathbf{U}\left(x_{i+1/2},t\right)\right) - \mathbf{F}\left(\mathbf{U}\left(x_{i-1/2},t\right)\right) = \int_{x_{i-1/2}}^{x_{i+1/2}} \mathbf{S}\left(\mathbf{U}(x,t)\right)dx \qquad (2.100)$$

where i is the spatial index, **U** the conservative unknown, **S** the source term, and **F** the physical flux at the boundaries of the interface. Equation (2.100) expresses that the quantity **U** inside the finite volume increases in time if the physical influx is greater than the physical outflux or if a source S supplies the finite volume.

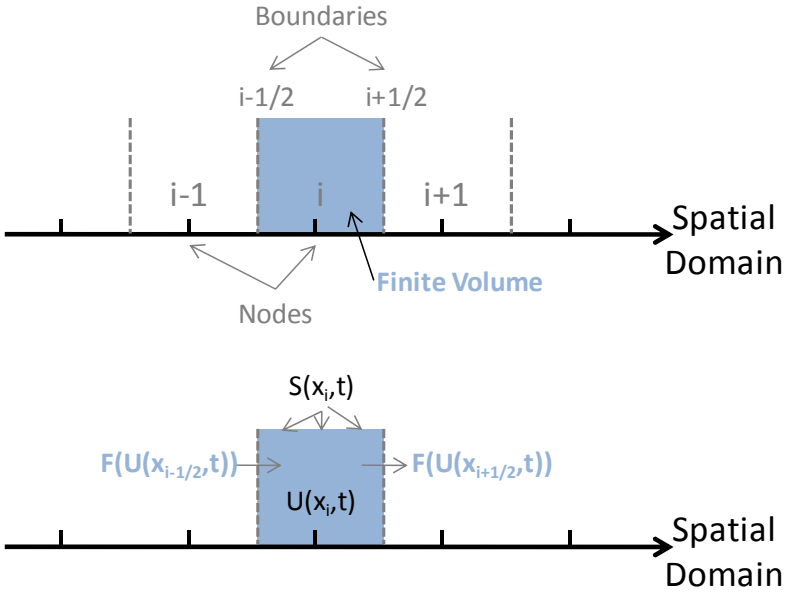

Figure 36: The spatial domain is divided into finite volumes governed by a conservation law

In first approximation, the integrals in equation (2.100) are evaluated with the mean values over the finite volume such that:

$$\int_{x_{i-1/2}}^{x_{i+1/2}} \mathbf{U}(x,t)\,dx = \mathbf{U}_i(t)\times\Delta x_i \quad \text{and} \quad \int_{x_{i-1/2}}^{x_{i+1/2}} \mathbf{S}\left(\mathbf{U}(x,t)\right)dx = \mathbf{S}(\mathbf{U}_i(t))\times\Delta x_i \qquad (2.101)$$

The conservative equation may be rewritten under the integral form I [285]:

$$\frac{\partial}{\partial t}\mathbf{U}_i(t)+\frac{\mathbf{F}\left(\mathbf{U}\left(x_{i+1/2},t\right)\right)-\mathbf{F}\left(\mathbf{U}\left(x_{i-1/2},t\right)\right)}{\Delta x_i}=\mathbf{S}\left(\mathbf{U}_i(t)\right) \qquad (2.102)$$

where U_i (t) is a set of N values that are the unknowns of the method.

In order to be fully discrete, equation (2.102) must be further integrated over the time interval $[t_n,t_{n+1}]$. By this way, I obtain the integral form II of the conservation equation:

$$\int_{t_n}^{t_{n+1}}\left(\frac{\partial}{\partial t}\mathbf{U}_i(t)\right)dt+\frac{1}{\Delta x_i}\left[\int_{t_n}^{t_{n+1}}\left(\mathbf{F}\left(\mathbf{U}\left(x_{i+1/2},t\right)\right)\right)dt-\int_{t_n}^{t_{n+1}}\left(\mathbf{F}\left(\mathbf{U}\left(x_{i-1/2},t\right)\right)\right)dt\right]=\int_{t_n}^{t_{n+1}}\left(\mathbf{S}\left(U_i(t)\right)\right)dt \qquad (2.103)$$

which corresponds in fact to the integration of the conservation law over the control volume $[x_{i+1/2}, x_{i-1/2}]$ x $[t_n,t_{n+1}]$ (Figure 37).

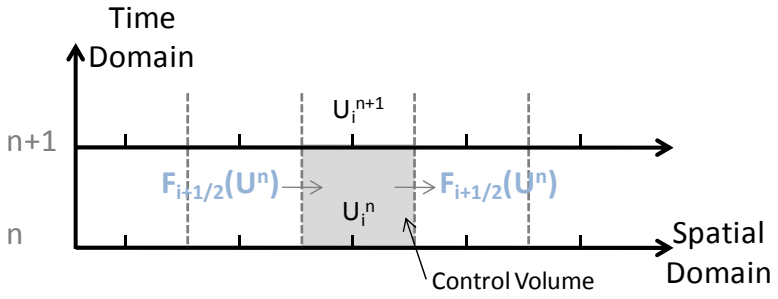

Figure 37: Integral form II relies on a control volume $[x_{i+1/2}, x_{i-1/2}]$ x $[t_n,t_{n+1}]$

Since the value of the **U**(x,t) is not known exactly over the whole control volume, one cannot evaluate rigorously neither the physical flux at the boundary nor the source term. It is then replaced by an approximation of the flux named numerical flux. The numerical flux must depend only on the values of the conservative unknowns **U** at the nodes and at the previous time step (in explicit method), or at the new time level (in implicit methods). I have chosen here to use only explicit methods:

$$\int_{t_n}^{t_{n+1}}\left(\mathbf{F}\left(\mathbf{U}\left(x_{i+1/2},t\right)\right)\right)dt=\mathbf{F}_{i+1/2}\left(\mathbf{U}_{i-1}^n,\mathbf{U}_i^n,\mathbf{U}_{i+1}^n,\ldots\right)*\Delta t \qquad (2.104)$$

The time integral of the source term is also approximated by means of the values of the conservative unknowns **U** at the nodes and at the previous time step:

$$\int_{t_n}^{t_{n+1}}\left(\mathbf{S}\left(\mathbf{U}_i(t)\right)\right)dt=\mathbf{S}\left(\mathbf{U}_{i-1}^n,\mathbf{U}_i^n,\mathbf{U}_{i+1}^n,\ldots\right)*\Delta t \qquad (2.105)$$

It results in the canonic form of the Finite Volume Method:

$$\mathbf{U}_i^{n+1}=\mathbf{U}_i^n-\frac{\Delta t}{\Delta x_i}\left[\mathbf{F}_{i+1/2}\left(\mathbf{U}_i^n,\ldots\right)-\mathbf{F}_{i-1/2}\left(\mathbf{U}_i^n,\ldots\right)\right]+\mathbf{S}\left(\mathbf{U}_i^n,\ldots\right)*\Delta t \qquad (2.106)$$

According to the definition of Toro [285], this numerical scheme is conservative. However, stability, consistency, and order of accuracy of the methods are still not ensured. These features are linked to the choice of the numerical flux, which is then the core of the finite volume method. The following sections give a brief overview of the various methods available to construct an efficient numerical flux. I make a distinction between the Godunov Method, and the Flux Vector Splitting approach.

GODUNOV METHOD

In order to overcome the errors made in the computation of shocks by the methods available at that time, Godunov [123, 124] sought a conservative formulation for solving linear and non-linear problems. The method resulting from his work is maybe the most popular result in CFD and is treated in numerous books [132, 144, 145, 197, 285, 286].

The Godunov method states that the intercell numerical flux given by the physical flux of the solution of the Riemann problem arising at the interface:

$$\mathbf{F}_{i+1/2} = \mathbf{F}\left(\mathbf{U}_{i+1/2}(0)\right) \tag{2.107}$$

ensures stability, consistency, and 1st order accuracy if the time step satisfies the CFL condition:

$$\Delta t \leq \frac{\Delta x}{S^n_{max}} \tag{2.108}$$

where S^n_{max} denotes the maximum wave velocity present throughout the domain at time t^n.

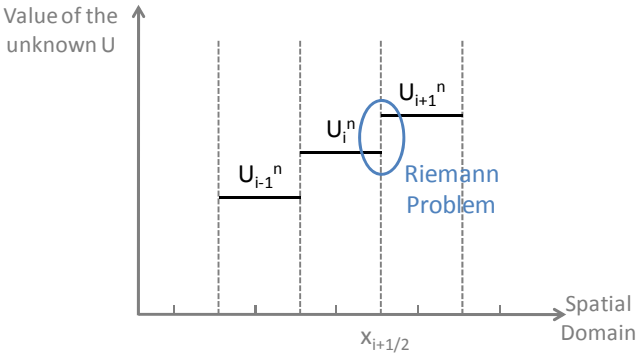

Figure 38: A Riemann problem arises at each boundary interface due to the FVM discretisation

In order to understand the Godunov method, one must start from the finite volume discretization. At a given time step t_n, data of the problem are given by a piecewise constant (first order method) distribution of the unknowns U_i (Figure 38). Formally, it results from averaging the unknown over the finite volume. The evolution of this distribution is governed by the hyperbolic equation. If we consider locally the boundary $x_{i+1/2}$, the problem reduces to a conservation law with initial data that consist of two constant states separated by a discontinuity:

$$\frac{\partial \mathbf{U}}{\partial t} + \frac{\partial \mathbf{F}}{\partial x} = 0$$
$$\mathbf{U}\left(x, t^n\right) = \begin{cases} \mathbf{U}_i^n & \text{if} \quad x < x_{i+1/2} \\ \mathbf{U}_{i+1}^n & \text{if} \quad x \geq x_{i+1/2} \end{cases} \tag{2.109}$$

This is a local Riemann Problem with data $\mathbf{U}_i^n$ (left side) and $\mathbf{U}_{i+1}^n$ (right side), centered at the cell boundary $x_{i+1/2}$. The source term cancels because it is assumed locally negligible. The Godunov flux $\mathbf{F}_{i+1/2}$ is defined as the physical flux function **F** evaluated with the solution $\mathbf{U}_{i+1/2}(x,t)$ of the Local Riemann Problem (2.109). Because of the definition of the numerical

flux (2.104), the solution $\mathbf{U}_{i+1/2}$ used in the flux computation is evaluated along the t-axis (or the cell boundary). This solution is noted $\mathbf{U}_{i+1/2}(0)$ because it follows the axis x/t=0 in the local coordinates. Consequently, two items are needed to evaluate the Godunov flux:

- the solution $\mathbf{U}_{i+1/2}(x,t)$ of the Riemann problem with data $\mathbf{U}_i^n$ and $\mathbf{U}_{i+1}^n$;
- a sampling procedure to correctly identify the required value along the t-axis.

Both steps constitute a Riemann solver.

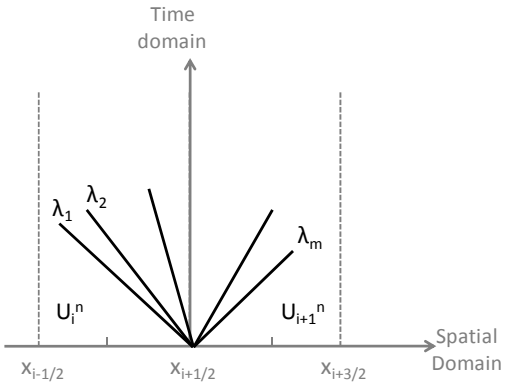

Figure 39: The structure of the solution of the Riemann problem for a linear hyperbolic problem consists in m waves emanating from the origin

For linear hyperbolic problems, the local Riemann problem has an analytical solution that gives birth to the exact Godunov numerical flux. A linear problem is a special conservation law for which the physical flux is linearly related to the primitive unknowns **F=AU** (A is a matrix of constant coefficients). What is more, the problem is said hyperbolic if the matrix **A** of size m has m real eigenvalues $\lambda_1,\ldots,\lambda_m$ and a corresponding set of m linearly independent right eigenvectors. The structure of the solution for such a problem is depicted in Figure 39. It consists in m waves emanating from the local origin and propagating at a given velocity λ_i. Each wave carries a jump discontinuity in **U**. Naturally, the solution to the left of the first wave is simply the initial data $\mathbf{U}_i^n$, and the solution the right of the last wave is $\mathbf{U}_{i+1}^n$. Since the information propagates at a finite speed in hyperbolic problems, these areas are not affected by the initial discontinuity. The proof of this result, and of the following theorems, can be found in [132, 144, 145, 197, 285, 286]. The task is now to find the solution in the wedge between the two extreme waves. Since the eigenvectors $\mathbf{K}^{(1)},..,\mathbf{K}^{(m)}$ are linearly independent, the final solution can be written in terms of the original variables as:

$$\mathbf{U}(x,t)=\sum_{i=I+1}^{m}\alpha_i K^{(i)}+\sum_{i=1}^{I}\beta_i K^{(i)} \tag{2.110}$$

where the integer I is the maximum value of the sub-index I for which $x-\lambda_i t>0$. The constant coefficients α_i and β_i (i=1,m) are the coefficients of the linear expansion of the initial data $\mathbf{U}_i^n$ and $\mathbf{U}_{i+1}^n$ in the basis of the right eigenvectors:

$$\mathbf{U}_i^n=\sum_{i=1}^{m}\alpha_i K^{(i)} \quad \text{and} \quad \mathbf{U}_{i+1}^n=\sum_{i=1}^{m}\beta_i K^{(i)} \tag{2.111}$$

Simple arithmetic computations show then that the corresponding Godunov numerical flux is given by [197, 285]:

$$\mathbf{F}_{i+1/2} = \frac{1}{2}\left[\mathbf{F}\left(\mathbf{U}_i^n\right) + \mathbf{F}\left(\mathbf{U}_{i+1}^n\right)\right] - \frac{1}{2}\sum_{i=1}^{m} \alpha_i \left|\lambda_i\right| \mathbf{K}^{(i)} \tag{2.112}$$

In conclusion, computing an exact Godunov numerical flux for a linear hyperbolic problem requires expressions for the wave strength α_i, eigenvalues λ_i, and the right eigenvectors $\mathbf{K}^{(i)}$.

The Riemann solver of Roe extends the applicability of the formulation (2.112) to non-linear hyperbolic problems by freezing the value of its Jacobian Matrix. The Roe solver is the most famous approximate Riemann solver. It was first published in 1981 [257]. Since then, researchers have been refining the methods [139, 258, 259] and extending its application to a large variety of physical problems [125, 261, 262, 304]. The idea of the method is to solve approximately the non-linear local Riemann problem (2.109) by introducing the Jacobian matrix:

$$\frac{\partial \mathbf{U}}{\partial t} + \mathbf{A}(\mathbf{U})\frac{\partial \mathbf{U}}{\partial x} = 0 \qquad \text{where} \quad \mathbf{A}(\mathbf{U}) = \frac{\partial \mathbf{F}}{\partial \mathbf{U}} \tag{2.113}$$

and by freezing the value of the Jacobian matrix, i.e. replacing $\mathbf{A}(\mathbf{U})$ by a constant Jacobian matrix $\tilde{\mathbf{A}}$. An approximate Riemann problem replaces the local Riemann problem (2.109):

$$\begin{aligned} &\frac{\partial \mathbf{U}}{\partial t} + \tilde{\mathbf{A}}\frac{\partial \mathbf{U}}{\partial x} = 0 \\ &\mathbf{U}\left(x, t^n\right) = \begin{cases} \mathbf{U}_i^n & \text{if} \quad x < x_{i+1/2} \\ \mathbf{U}_{i+1}^n & \text{if} \quad x \geq x_{i+1/2} \end{cases} \end{aligned} \tag{2.114}$$

This problem may be solved exactly and gives the following Godunov numerical flux:

$$\mathbf{F}_{i+1/2} = \frac{1}{2}\left[\mathbf{F}\left(\mathbf{U}_i^n\right) + \mathbf{F}\left(\mathbf{U}_{i+1}^n\right)\right] - \frac{1}{2}\sum_{i=1}^{m} \tilde{\alpha}_i \left|\tilde{\lambda}_i\right| \tilde{\mathbf{K}}^{(i)} \tag{2.115}$$

where the wave strength $\tilde{\alpha}_i$, the eigenvalues $\left|\tilde{\lambda}_i\right|$, and the right eigenvectors $\tilde{\mathbf{K}}^{(i)}$ refer to the freezed Jacobian matrix. Complexity of the method arises when choosing the best freezed Jacobian matrix in function of the right and left states:

$$\tilde{\mathbf{A}} = \tilde{\mathbf{A}}\left(\mathbf{U}_i^n, \mathbf{U}_{i+1}^n\right) \tag{2.116}$$

This choice must ensure that the hyperbolicity, the consistency, and the conservation across discontinuities are conserved in the approximate Riemann solver. Since this choice varies in function of the model, I refer the interested to the large literature about freezing methods [132, 144, 145, 197, 285, 286].

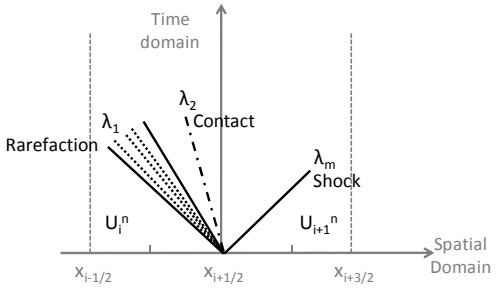

Figure 40: For a non-linear hyperbolic problem, the solution of the local Riemann problem consists of m+1 constant states separated by m waves that can be either rarefaction, shock, or contact waves

For non-linear hyperbolic problems, the local Riemann problem has also an analytical solution but the associated Godunov numerical flux is very complex and computationally time-consuming. The structure of the solution is indeed self-similar [186], i.e. the solution depends only on the x/t. In other words, information propagates along straight lines in the phase space (the xt-plane). The similarity solution **U**(x/t) consists of m+1 constant states separated by m waves, as depicted in Figure 40. The possible types of waves depend on the nature of the physical flux **F**, and on the left and right states. A *rarefaction wave* appears when the characteristics of the problem (i.e. the λ_i-wave) diverge due to the non-linearity of the conservation law (Figure 41). They let an undetermined area in the phase space across which the unknown **U** smoothly links the adjacent states $\mathbf{U_L}$ and $\mathbf{U_R}$. A rarefaction wave meets the following conditions:

- The consistency of the generalized Riemann invariant:

$$\frac{dU_1}{K_1^{(i)}} = \frac{dU_2}{K_2^{(i)}} = \ldots = \frac{dU_m}{K_m^{(i)}} \tag{2.117}$$

- The divergence of characteristics:

$$\lambda_i\left(\mathbf{U_L}\right) = S_{i,tail} < S_{i,head} = \lambda_i\left(\mathbf{U_R}\right) \tag{2.118}$$

A *shock wave* occurs when the characteristics of the problem converge due to the non-linearity of the conservation law (Figure 41). The adjacent states $\mathbf{U_L}$ and $\mathbf{U_R}$ are connected through a single jump discontinuity of speed S_i and the following conditions apply:

- The Rankine-Hugoniot Conditions:

$$\mathbf{F}\left(\mathbf{U_L}\right) + \mathbf{F}\left(\mathbf{U_R}\right) = S_i\left(\mathbf{U_R} - \mathbf{U_L}\right) \tag{2.119}$$

- The entropy conditions:

$$\lambda_i\left(\mathbf{U_L}\right) > S_i > \lambda_i\left(\mathbf{U_R}\right) \tag{2.120}$$

Finally, a *contact wave* arises when the characteristics of the problem never converge or diverge but remain parallel in the phase space (Figure 41). The contact wave is a single jump discontinuity of speed S_i across which the unknown U jumps from $\mathbf{U_L}$ to $\mathbf{U_R}$. The following conditions apply:

- The Rankine-Hugoniot Conditions:

$$\mathbf{F}\left(\mathbf{U_L}\right) + \mathbf{F}\left(\mathbf{U_R}\right) = S_i\left(\mathbf{U_R} - \mathbf{U_L}\right) \tag{2.121}$$

- The consistency of the generalized Riemann invariant:

$$\frac{dU_1}{K_1^{(i)}} = \frac{dU_2}{K_2^{(i)}} = \ldots = \frac{dU_m}{K_m^{(i)}} \tag{2.122}$$

- The entropy condition:

$$\lambda_i\left(\mathbf{U_L}\right) = S_i = \lambda_i\left(\mathbf{U_R}\right) \tag{2.123}$$

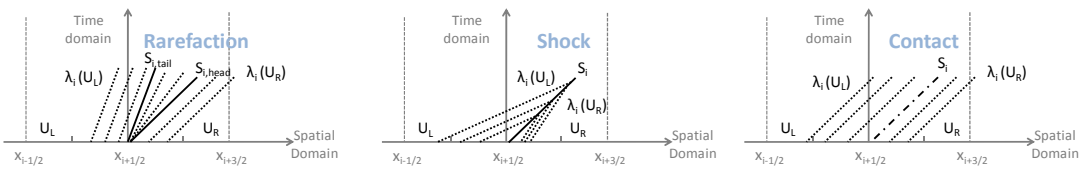

Figure 41: Elementary wave solution of a non-linear problem may contain rarefaction, shock, or contact waves

In order to solve the local Riemann problem, any exact solver must discriminate the particular type of wave in presence, and then enforce the previous conditions. This process is highly iterative and becomes very complex for large systems, if not intractable. To my knowledge, the only exact Riemann solver for a non-linear problem that is sufficiently efficient to be used in practice has been proposed by Toro for the shallow water equations [284, 286]. It consists in an algebraic equation for the water height that is solved iteratively by a Newton-Raphson scheme. I refer the interested reader to the previous references for more details about this solver, as well as to chapter 4 of this thesis.

FLUX VECTOR SPLITTING

The Flux Vector Splitting (FVS) approach proposes to develop numerical fluxes that rely on the direction of propagation of the information on that mesh. Contrary to the Godunov method, FVS does not solve a Riemann problem but identifies the propagation of information thanks to the celerities of the model. Resulting numerical fluxes are simpler and somewhat more efficient, which explains their popularity.

Flux Vector Splitting (FVS) approach splits the flux vector **F** into two components $\mathbf{F}^-$ and $\mathbf{F}^+$ such that:

$$\mathbf{F}(\mathbf{U}) = \mathbf{F}^+(\mathbf{U}) + \mathbf{F}^-(\mathbf{U}) \tag{2.124}$$

under the restriction that eigenvalues λ_i^+ and λ_i^- of the Jacobian matrices:

$$\mathbf{A}^+ = \frac{\partial \mathbf{F}^+}{\partial \mathbf{U}} \quad ; \quad \mathbf{A}^- = \frac{\partial \mathbf{F}^-}{\partial \mathbf{U}} \tag{2.125}$$

satisfy the condition:

$$\lambda_i^+ \geq 0 \quad ; \quad \lambda_i^- \leq 0 \tag{2.126}$$

In addition, a good splitting must meet the following conditions:

- It must reproduce regular upwinding when all eigenvalues λ_i of the Jacobian matrix A are one-sided, that is, all positive or zero, or all negative or zero:

$$\begin{aligned} \mathbf{F}^+(\mathbf{U}) &= \mathbf{F}(\mathbf{U}) \quad \text{if } \lambda_i \geq 0 \quad \text{for } i = 1,\ldots,m \\ \mathbf{F}^-(\mathbf{U}) &= \mathbf{F}(\mathbf{U}) \quad \text{if } \lambda_i \leq 0 \quad \text{for } i = 1,\ldots,m \end{aligned} \tag{2.127}$$

- It must satisfy at the homogeneity property:

$$\begin{aligned} \mathbf{F}(\mathbf{U}) &= \mathbf{F}^+(\mathbf{U}) + \mathbf{F}^-(\mathbf{U}) \\ \lambda_i &= \lambda_i^+ + \lambda_i^- \\ \mathbf{A} &= \mathbf{A}^+ + \mathbf{A}^- \end{aligned} \tag{2.128}$$

This approach gave birth to several kinds of implementations, evolutions,... The pioneering work of Sanders and Prendergast [266], Steger and Warming [276], Van Leer [294, 295] has been followed by numerous applications in the 80's. I refer the interested reader to the following books [144, 145, 197, 285] for further information. Despite numerous successes, the FVS approach as defined previously has rapidly shown limitations in its evolution, in particular in comparison with Godunov schemes. The diffusive nature of flux-vector

splitting has indeed caused dissatisfaction in various cases [295]. Consequently, the 90's were a second period of intense research about FVS schemes. Most new schemes were intermediate between classical FVS and Godunov schemes. They aimed at combining the advantages of both methods. In the following, I give the bases of two worthwhile methods that I will use in this thesis: the AUSM scheme and the Wolf splitting.

The AUSM scheme, which stands for Advection Upstream Splitting Method, is a numerical flux function that distinguishes two parts in any model in fluid mechanics: a convective and a pressure contribution. Originally proposed by Liou and Steffen [206], the scheme combines the advantages of both FVS and Godunov methods. Like FVS, the numerical flux remains simple because it does not require identifying the Jacobian matrix. What is more, the number of operations to compute the flux vectors is proportional to n (n is the number of equations). On the opposite, Roe solver requires n^2 operations. This feature may save an enormous amount of computation time. On the other hand, performance of AUSM schemes remains analogous, and even surpasses in some cases, the performance of Godunov schemes. Performance is here assessed in terms of accuracy and numerical diffusion. This conclusion is particularly true for the improved AUSM schemes that appeared in the late 90's [101, 201-203, 205, 312].

For the general conservative model given by equation (2.100), the AUSM numerical flux is written as:

$$\mathbf{F}_{i+1/2}(\mathbf{U}) = \underbrace{\frac{1}{2}M_{i+1/2}\left[\mathbf{U}_L + \mathbf{U}_R\right] - \frac{1}{2}\left|M_{i+1/2}\right|\left[\mathbf{U}_R + \mathbf{U}_L\right]}_{\mathbf{F}^{conv}_{i+1/2}(\mathbf{U})} + \mathbf{F}^{pressur}_{i+1/2}\left(\mathbf{U}_L, \mathbf{U}_R\right) \tag{2.129}$$

where the convective flux is upwinded $\mathbf{F}^{conv}_{i+1/2}$ to the left L or to the right R as a function of the Mach (or Froude) number $M_{i+1/2} = u_{i+1/2} / c_{i+1/2}$ at the cell interface. The pressure is a weighted value of the left and right pressures. Clearly, AUSM scheme is neither a full upwind method nor a simple average of L and R states with a diffusion term. It is rather a celerity-weighted-average of the right and left states. Full definition of the method still requires defining the inter-cell celerity and the pressure flux. In this respect, a successful approach consists in combining the contributions from both the 'left' and 'right' states:

$$M_{i+1/2} = M_L^+ + M_R^- \tag{2.130}$$

for which various ways of defining the split Mach number $M^{\pm}$ exist. The most common is the Van Leer splitting [294]:

$$M^{\pm} = \begin{cases} \pm\frac{1}{4}(M \pm 1)^2 & \text{if } |M| \le 1 \\ \frac{1}{2}(M \pm |M|) & \text{if } |M| > 1 \end{cases} \tag{2.131}$$

In a similar way, the pressure flux combines the contributions from both the 'left' and 'right' states:

$$\mathbf{F}^{pressur}_{i+1/2} = P_L^+ + P_R^- \tag{2.132}$$

The split pressure $P^{\pm}$ is evaluated by means of:

$$P^{\pm} = \begin{cases} \frac{1}{2} P\left(1 \pm M\right) & \text{if } |M| \le 1 \\ \frac{1}{2} P \frac{\left(M \pm |M|\right)}{M} & \text{if } |M| > 1 \end{cases} \tag{2.133}$$

or

$$P^{\pm} = \begin{cases} \frac{1}{4} P\left(M \pm 1\right)^2 \left(2 \mp M\right) & \text{if } |M| \le 1 \\ \frac{1}{2} P \frac{\left(M \pm |M|\right)}{M} & \text{if } |M| > 1 \end{cases} \tag{2.134}$$

On the other hand, the Wolf splitting is a very simple splitting developed within the HACH for Saint-Venant equations [9, 10] and shallow-water equations [75, 93, 95]. This splitting distinguishes also two parts in the equations: a convective and a pressure contribution. The numerical flux consists in always upwinding the convective terms upstream and the pressure terms downstream (according to the sign of the water velocity u):

$$\mathbf{F}_{i+\frac{1}{2}}\left(\mathbf{U}\right) = F^{conv}\left(\mathbf{U}_{L/R}\right) + \mathbf{F}^{pressur}\left(\mathbf{U}_{R/L}\right)$$

$$\text{where} \quad \mathbf{U}_{L/R} = \begin{cases} \mathbf{U}_L & \text{if } u_{i+\frac{1}{2}} > 0 \\ \mathbf{U}_R & \text{if } u_{i+\frac{1}{2}} < 0 \end{cases} \quad \text{and} \quad \mathbf{U}_{R/L} = \begin{cases} \mathbf{U}_R & \text{if } u_{i+\frac{1}{2}} > 0 \\ \mathbf{U}_L & \text{if } u_{i+\frac{1}{2}} < 0 \end{cases} \tag{2.135}$$

Stability analysis and evaluation of the order of accuracy show the reliability of the method. In particular, the method present three major advantages over solvers that are more complex. First, only a minimal amount of numerical diffusion affects the Wolf splitting. Second, the splitting enables to solve non-conservative forms of the equations (such as the Saint-Venant equations in terms of free surface slope). Finally, it enables to treat source terms in an easier way than other schemes. As I will show in the following chapters, these features will be crucial in the choice of the splitting for multiphase models.

HIGHER ORDER METHODS

Previous methods ensure a first-order accurate solution to the hyperbolic problems. The error of the solution has the same scale as the time step and the spatial step. If sufficient in many applications, these methods fail to provide reliable solutions in particular cases. Non-uniform grid is one of them. 1st order methods give indeed an overall 0th order of accuracy on non-uniform meshes. What is more, some cases require a minimum numerical diffusion that can only be reached by using higher order methods.

The most famous time discretization that reaches a higher order of accuracy is the Runge-Kutta method. A Runge-Kutta scheme RKMN involves M-1 predictor steps and one corrector step. N designates the linear order of accuracy of the method that is never greater than M. Let us consider the following equation for the conservative unknown **U** and the spatial operator **L**:

$$\frac{d\mathbf{U}}{dt} + \mathbf{L}\left(\mathbf{U}\right) = 0 \tag{2.136}$$

M-1 predictor steps give the first part of the general formulation of RKMN:

$$\mathbf{U}^{(k)} = \mathbf{U}^{0} + \alpha_k \Delta t \mathbf{L}\left(\mathbf{U}^{(k-1)}\right) \qquad k = 1, M-1 \tag{2.137}$$

The corrector step closes the formulation:

$$\mathbf{U}^{n+1} = \mathbf{U}^{n} + \Delta t \sum_{k=0}^{M-1} a_k \mathbf{L}\left(\mathbf{U}^{(k)}\right) \tag{2.138}$$

where the coefficients a_k and α_k are characteristic parameters of the scheme. In the rest of the thesis, only Runge-Kutta schemes are used. For further information about them, we refer the interested reader to the thesis of B.J. Dewals [75].

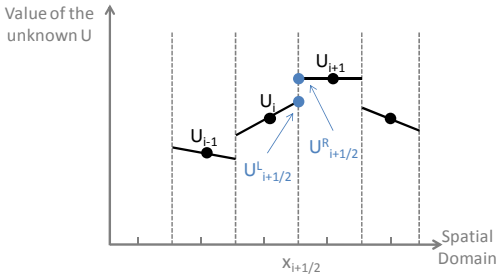

Figure 42: Second order accuracy may be reached by linearly reconstructing the values of the primitive unknowns at the boundaries of the finite volume.

Higher order methods for the spatial discretization are intimately linked with the MUSCL scheme (Monotone Upstream-centered Schemes for Conservation Laws) introduced by Van Leer in 1979 [293]. In this paper, Van Leer constructed the first second order spatial accuracy scheme that remains stable and does not exhibit spurious oscillations. For this purpose, the primitive unknowns at the center of the finite volume were linearly extrapolated up to the boundaries of the grid (Figure 42). This linear reconstruction (in opposition with the constant reconstruction) required estimating the gradient of the primitive unknown in the finite volume:

$$\mathbf{U}^{n}(x) = \mathbf{U}_i^{n} + (x - x_i)\left.\widetilde{\frac{\partial \mathbf{U}}{\partial x}}\right|_i^{n} \tag{2.139}$$

and defined two values at each boundaries (Figure 42):

$$\mathbf{U}^{L}_{i+1/2} = \mathbf{U}_i^{n} + \left(x_{i+1/2} - x_i\right)\left.\widetilde{\frac{\partial \mathbf{U}}{\partial x}}\right|_i \qquad \text{and} \qquad \mathbf{U}^{R}_{i+1/2} = \mathbf{U}_{i+1}^{n} + \left(x_{i+1/2} - x_{i+1}\right)\left.\widetilde{\frac{\partial \mathbf{U}}{\partial x}}\right|_{i+1} \tag{2.140}$$

Several methods exist for estimating the gradient of the primitive unknown. In this thesis, I restrict myself to the centered slope (Fromm) that is proven efficient [75]:

$$\left.\widetilde{\frac{\partial \mathbf{U}}{\partial x}}\right|_i^{n} = \frac{\mathbf{U}_{i+1}^{n} - \mathbf{U}_{i-1}^{n}}{x_{i+1} - x_{i-1}} \tag{2.141}$$

Although the previous second-order scheme provides greater accuracy for smooth solutions, it introduces spurious oscillations into the solution where discontinuities or shocks are present. It can be easily understood by noting that linear reconstructions may create an overshoot or numerical extremum at the discontinuity (Figure 43). Such extrema are likely to create spurious oscillations. This fact is summarized in the Godunov theorem

[124]: "Any numerical scheme of order of accuracy greater than one is non-monotone (creates spurious oscillations)". Consequently, the slope must be limited in the neighborhood of a discontinuity. It means the scheme is no more second order at the discontinuity. Methods based on this idea are known as slope-limiter methods (or Total Variation Diminishing TVD Methods). They are extensively presented in the following texts [9, 75, 144, 145, 197, 285, 286]. The minmod slope gives second-order accuracy for smooth solutions while still satisfying the TVD property:

$$\left.\frac{\widetilde{\partial \mathbf{U}}}{\partial x}\right|_i^n = \text{minmod}\left(\frac{\mathbf{U}_i^n - \mathbf{U}_{i-1}^n}{x_i - x_{i-1}}; \frac{\mathbf{U}_{i+1}^n - \mathbf{U}_i^n}{x_{i+1} - x_i}\right) \tag{2.142}$$

where the minmod function of two arguments is defined by:

$$\text{minmod}(a;b) = \begin{cases} a & \text{if } |a| < |b| \quad \text{and} \quad ab > 0 \\ b & \text{if } |b| < |a| \quad \text{and} \quad ab > 0 \\ 0 & \text{if } ab \le 0 \end{cases} \tag{2.143}$$

If a and b have the same sign, then this selects the one that is smaller in modulus, else it returns to zero.

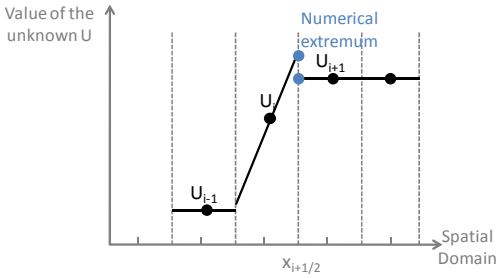

Figure 43: Linear reconstruction creates a local extremum at the discontinuity.

2.4.3 MODELLING SYSTEM WOLF

Two decades of research within the HACH gave birth to the modelling system WOLF. WOLF is an integrated package of various computational schemes for pure water flows and sediment flows. The software offers several levels of simulation (Figure 44), including physically-based hydrological flows (WOLF HYDRO), free surface river flows (WOLF 1D) and shallow-water flows (WOLF2D), and 3D flows (WOLF2DV-WOLF3D). What is more, a genetic algorithm (WOLF AG) enables to optimize the parameterization in any of these modules. All modules are integrated in a user-friendly interface. It is worth noting here that the modeling system WOLF uses the Wolf flux vector splitting. In the rest of the text, I make a clear distinction when I use the software (denoted WOLF in capital letters), and when I use the splitting (Wolf) in another computational code.

WOLFHydro simulates the inception of hydrological flows based on rainfalls and its propagation up to rivers [179]. The current version of the software solves the conservative form of the two-dimensional diffusion wave over three layers: runoffs, hypodermic flows, and deep infiltration. Unsteady coupling terms describe the vertical exchanges between each layer. Various friction correlations describe the effect of macro-roughness elements.

WOLF1D accounts for the propagation of waves and floods within a river or a channel network [166, 167]. Its current version solves the non-conservative Saint-Venant equations over a main riverbed and floodplains. Unsteady coupling terms describe the exchanges between these beds. A coupling with WOLFhydro also enables to simulate the propagation of water from the rain to the ocean. Due to its simplicity, WOLF1D enables indeed to simulate events at the scale of the basin.

WOLF2D offers a refined description of the propagation of waves and floods within a river or a channel [78-80, 94, 95]. WOLF2D solves the shallow-water equations over a fixed or a mobile bed. Moment equations complement these equations to enhance the description of vertical structure of the flow.

The whole modelling system is under continuous development and enhancements such that 2DV and 3D modules are currently developed.

In my work, I have made the most of the various skills and of the know-how available in the unit in order to reach more rapidly valuable results from both a scientific and organizational point of view. Consequently, the module WOLF 1D constitutes a reliable basis for my work on single-phase flows

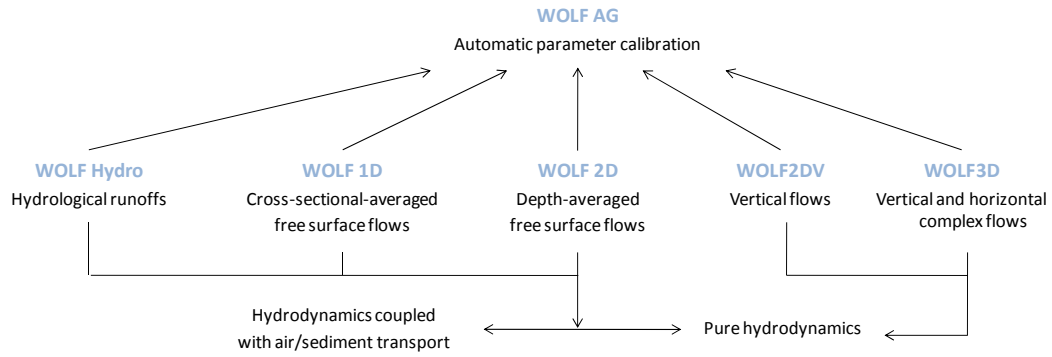

Figure 44: Description of the modelling system WOLF developed within the HACH – Integration of 5 modules: Hydro, 1D, 2D, 2DV, 3D

Summary and conclusions

As pointed in this section, Computational Fluid Dynamics has been becoming a reliable basis to design hydraulic structures and describe environmental flows. Four elements form a method in CFD: a practical problem, a mathematical model, its discretization, and its implementation in a computational code. For each element, specialized literature provides more or less thorough results and methods. This chapter proposes a brief reminder of state-of-the-art results in CFD with regard to environmental and civil engineering.

The continuum assumption and the laws of mass and momentum conservation constitute a reputable paradigm to develop mathematical models in fluid mechanics. In this respect, I have introduced the Local Instant Formulation, which describes both single- and multi-phase flows. This model is however impossible to solve in most the practical cases. Consequently, simplified models must be established.

In civil and environmental engineering, simulations usually make use of a single-phase model (RANS or Saint-Venant equations) coupled with an advection-diffusion equation for a passive scalar. These models fail to define rigorously the concentration, to describe accurately the diffusion of the dispersed phase, and to account for the effect of the dispersed phase on the water stream. What is more, simulation of mixed flows by means of "mathematical shock-capturing" methods is difficult in presence of air and sub-atmospheric pressurized problems, if not impossible.

Application of two-phase flow theories is still very limited in civil and environmental engineering. On the opposite, various multiphase models are in frequent use in chemical and mechanical engineering. In this respect, the drift-flux model seems a promising alternative to Navier-Stokes equations. This model is indeed able to describe in a unified framework the transport of a dispersed phase, its interaction with the water flow, and the notion of concentration naturally arises in the derivation of a diffusion equation. Nevertheless, this model has never been applied in civil and environmental engineering. What is more, one-dimensional drift-flux models only describe pressurized flows. Obviously, describing transient air-water flow through this paradigm is not a foregone conclusion.

For the discretization of mathematical models, the Finite Volume method seems the most promising technique. This choice results from its ability to treat discontinuities and ensures conservativity. In this respect, both Godunov method and Flux Vector splitting have their own advantages and shortcomings. The modelling system WOLF gives a reliable and helpful basis for my work.

In conclusion, literature gives various results to base my research on transient air-water flows. However, I identified numerous knowledge gaps that need to be filled in order to reach my objective: creating a one-dimensional computational code for single and multiphase flows in pipes and rivers. This is the purpose of the following chapters.

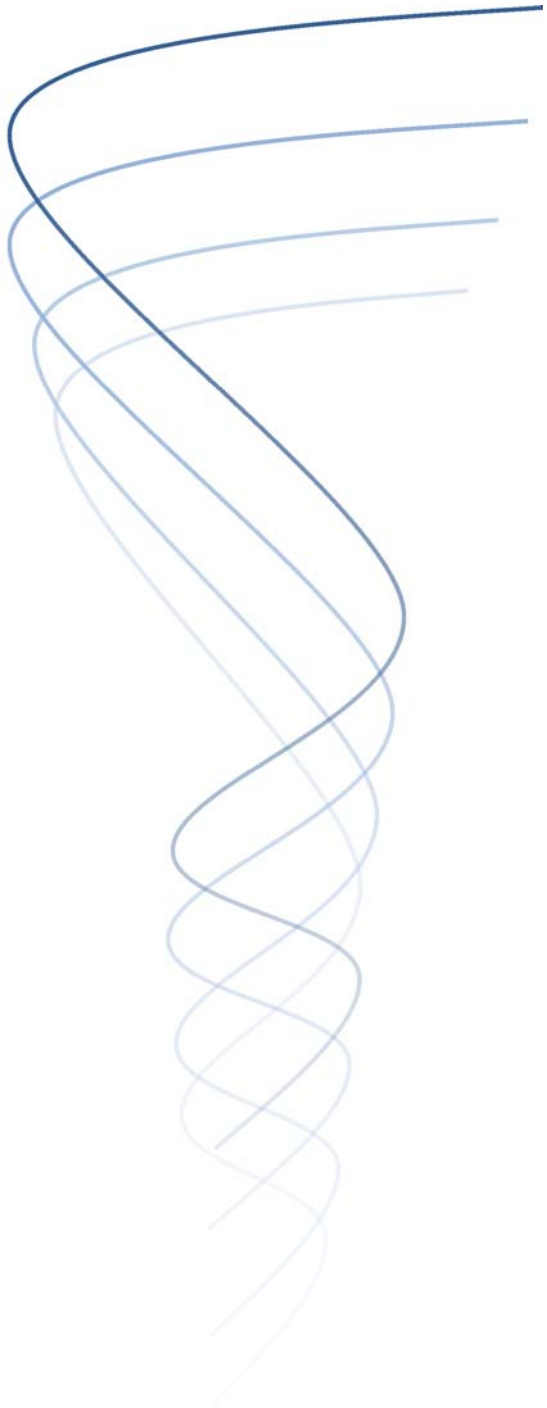

Modelling Transient Air-water Flows in Civil and Environmental Engineering

Part I: Pure Water Flows

Chapter 3 Pure Water Flows: Mathematical Model

This chapter aims at:

- ✓ extending the applicability of Saint-Venant equations to pressurized flows;
- ✓ including the description of sub-atmospheric pressurized flows.

In a first step to meet the objectives of my thesis, I neglect the air-water interactions that are likely to appear in the cases I am considering. That is to say, reaching a correct description of pure water transient mixed flows is the first goal of this thesis. The rationale behind this decision is manifold. First, the range of applications in which air-water interactions may be disregarded in first approximation is very wide. Second, the modelling system WOLF gives a reliable basis to reach quick results for pure water flows. Finally, this partial objective already requires important research since new concepts must be developed.

Standard methods in hydraulic engineering are insufficient to form an efficient mathematical model for free surface, pressurized, and mixed flows in rivers and pipes. As pointed in Chapter 2, ”mathematical shock-capturing” methods give a very natural framework to simulate mixed flows. Nevertheless, various shortcomings appear already in these mathematical models. The main weaknesses appear when considering sub-atmospheric pressure.

Consequently, I dedicate this chapter to the establishment of an improved “mathematical shock-capturing model” for pure water mixed flows. For this purpose, I remind the form of the Saint-Venant equations, which describe one-dimensional free surface flows (section 3.1). In section 3.2, I investigate the mathematical foundations of the Preissmann slot. In particular, the development of an original negative Preissmann slot makes possible to simulate sub-atmospheric pressurized flows without losing the simplicity of the Preissmann framework (section 3.3). This result has been published in a peer-reviewed journal [167]. In addition, I discuss the differences and similarities between the Preissmann, TPA, and Dual models (section 3.4) in order to derive a state-of-the-art mathematical model for the Preissmann slot.

3.1 THE SAINT-VENANT EQUATIONS

Named after Adhémar Jean Claude Barré de Saint-Venant [64], the Saint-Venant equations describe the dynamics of free surface flows in rivers and channels. The model relies on the following series of assumptions [44, 63]:

1. The flow is one-dimensional, i.e the velocity is uniform over the cross-section, and the transverse free surface profile is horizontal.
2. The streamline curvature is small, and vertical accelerations are negligible. Consequently, the pressure is hydrostatic as proven in [9, 75, 242].
3. The effects of boundary friction and turbulence can be accounted for through resistance formulae established for a steady uniform equilibrium flow.
4. The average channel bed slope is small enough to consider that $\cos \varepsilon \cong 1$ and $\tan \varepsilon \cong \sin \varepsilon \cong \theta$. Parameter ε is the angle that the bed slope makes with the horizontal. In the following, it is denoted S_0 to avoid confusion with other parameters.
5. The water density is constant.
6. The bed is assumed constant over the time, i.e sediment motion is neglected.

Under these basic assumptions, the integration of the Reynolds-Averaged Navier-Stokes equations over a general cross-section (Figure 27) gives the conservative form of the Saint-Venant equations [9, 63, 64]:

$$\begin{cases} \dfrac{\partial \rho_w \Omega}{\partial t} + \dfrac{\partial \rho_w u_w \Omega}{\partial x} = q_{w,\perp} \\ \dfrac{\partial \rho_w u_w \Omega}{\partial t} + \dfrac{\partial \beta \rho_w u_w u_w \Omega + g I_1}{\partial x} = \rho_w g \Omega \left(S_0 - S_f \right) + \rho_w g I_2 + \rho_w \theta u_w q_{w,\perp} \end{cases} \tag{3.1}$$

where pressure terms may be written as:

$$I_1(\Omega) = \int_{h_b}^{h_s} (h_s - \xi) l(x,\xi) d\xi \quad \text{and} \quad I_2(\Omega) = \int_{h_b}^{h_s} (h_s - \xi) \frac{\partial l(x,\xi)}{\partial x} d\xi \tag{3.2}$$

Ω is the flow area, u_w is the flow velocity along the main direction of the flow, g is the gravity, S_0 is the bed slope. S_f is the friction term computed with empirical resistance law, $q_{w,l}$ is the lateral discharge, and θ is a computational parameter which accounts for the velocity at which the lateral flows enter the main stream. As pointed in Figure 27, h is the water height, l is the free surface width, h_s is the free surface elevation, and h_b is the bottom elevation. Finally, the Boussinesq coefficient β [21, 76, 260] accommodates the area-averaged model with cross-sectional distribution of the velocity.

As already discussed in section 2.2.2, the term gI_1 represents the hydrostatic pressure, which is easily implemented in the numerical scheme as a discrete relation. The second pressure term gI_2 accounts for the non-uniformity of the pipe. In this thesis, this term is simplified by using a non-conservative formulation [9, 63] equivalent to equations (3.1):

$$\begin{cases} \dfrac{\partial \rho_w \Omega}{\partial t} + \dfrac{\partial \rho_w u_w \Omega}{\partial x} = q_{w,\perp} \\ \dfrac{\partial \rho_w u_w \Omega}{\partial t} + \dfrac{\partial \beta \rho_w u_w u_w \Omega}{\partial x} = \rho_w g \Omega \left(\dfrac{\partial Z}{\partial x} - S_f \right) + \rho_w \theta u_w q_{w,\perp} \end{cases} \tag{3.3}$$

where Z[m] is the free surface elevation. Validity of the non-conservative Saint-Venant equations is discussed and proven in [93].

As pointed in the previous chapter, “mathematical shock-capturing” models constitute the most natural way to extend the applicability of the Saint-Venant equations to pressurized flows as well. It results in a unified framework for simulating mixed flows. In this respect, the most popular method is the Preissmann slot. Since this approach only requires modifying the geometry of the flow cross-section in any free surface software, Preissmann slot is very popular in hydraulic engineering. However, this mathematical approach is known to suffer one major shortcoming in single-phase flow: its inability to simulate sub-atmospheric pressurized flows. In order to overcome this flaw, the Two-Pressure Approach (TPA) [304] and Dual Model [30, 31] have been developed. They use a modified pressure gradient.

3.2 The Preissmann Slot Model

The Preissmann slot model makes the most of an analogy between the quasi-linear form of the Saint-Venant equations (free surface flows) and the Allievi equations (pressurized flows) expressed in their primitive variables, namely the section Ω and the discharge $Q_w=u_w\Omega$:

$$\begin{cases} \dfrac{\partial \rho_w \Omega}{\partial t} + \dfrac{\partial \rho_w Q_w}{\partial x} = q_{w,\perp} \\ \dfrac{\partial \rho_w Q_w}{\partial t} + \left(cel^2 - u^2\right)\dfrac{\partial \rho_w \Omega}{\partial x} = \rho_w g \Omega \left(S_0 - S_f\right) + \rho_w g I_2 + \rho_w \theta u_w q_{w,\perp} \end{cases} \tag{3.4}$$

where the pressure I_2 cancels in the Allievi equations. Only the celerity of the pressure wave differs in both models:

$$cel^2 = \begin{cases} a^2 = A_0 \dfrac{\partial p}{\partial(\rho A)} & \text{for a pressurized flow} \\ c^2 = \dfrac{g\Omega}{\partial\Omega / \partial Z\big|_{x\ cst}} & \text{for a free-surface flow} \end{cases} \tag{3.5}$$

This difference of pressure wave celerity originates from dissimilarity in the dynamics of both flows. In a free surface flow, the pressure propagates as a surface wave that creates an elevation of the free surface. In first approximation, the celerity in shallow water is given by the Lagrange equation $c^2=gh$. Its value usually oscillates between 0.1m/s and 10m/s. In pressurized flows, the pressure propagates as a dilatation of the pipe and the contraction of the fluid. The pressure wave celerity depends on the fluid properties, and the stiffness of both the pipe and its mean of support. Its value may reach 1400 m/s.

The Preissmann method consists in adding a slot of width T_s at the top of the pipe (Figure 45). In such a case, pressurized flows artificially appear as free surface flows whose celerity is given by:

$$c = \sqrt{\frac{g\Omega}{T_s}} \tag{3.6}$$

Consequently, the celerity c of the artificial free surface flow is equal to celerity a of the pressurized flow as long as the slot width is given by:

$$T_s = \frac{g\Omega}{a^2} \tag{3.7}$$

where the celerity a is computed thanks to relations of the material mechanics [25, 280, 325]. Physically, the storage capacity of the slot accounts for the fluid compressibility and/or the pipe dilatation resulting from an increase in pressure in the pipe. Clearly, Preissmann slot extends the applicability of Saint-Venant equations to pressurized flows by adding such a slot at the top of the pipe. Since a single mathematical model describes both free surface and pressurized flows, this method enables to simulate mixed flows in a "natural manner".

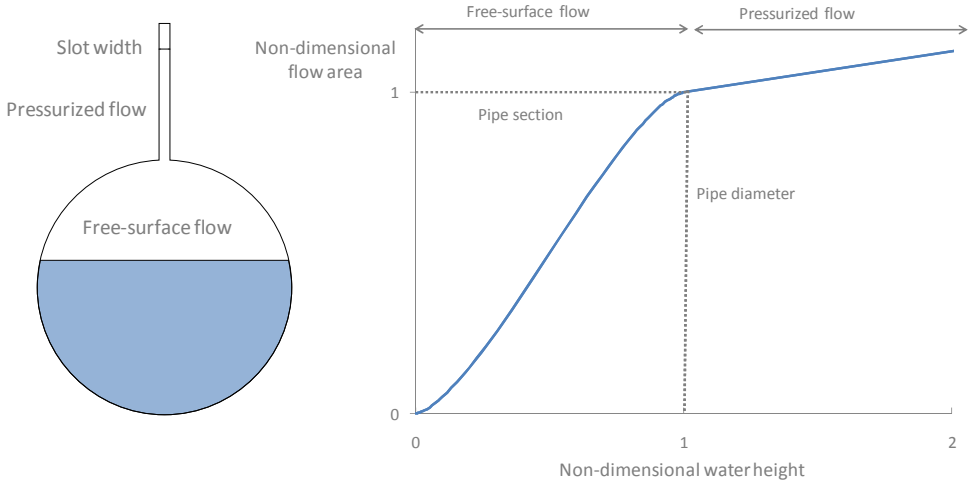

Figure 45: The Preissmann slot extends the applicability of Saint-Venant equations to pressurized flows by adding a slot at the top of the pipe. It is equivalent to pursuing the relation water height/area with a straight line whose slope is given by the slot width.

From a hydraulic point of view, a single relation contains all the relevant information specifying the geometry. For the non-conservative Saint-Venant equations (3.3), this is the relation linking the water height H to the flow area Ω (Figure 45). For the conservative Saint-Venant equations (3.1), this is the relation linking the flow area Ω to the hydrostatic pressure gI_1. In the non-conservative case, the Preissmann slot method is thus equivalent to pursuing the relation water height/area above the pipe crown with a straight line whose slope is given by the slot width (Figure 45). A similar conclusion holds for the conservative equations.

3.3 The Original Negative Preissmann Slot

The classical method of Preissmann assumes that the flow is correctly aerated everywhere. If the pressure drops below the atmospheric pressure, a free surface appears above which the air is at atmospheric pressure. However, a lack of aeration devices in the pipe (like air vents, tanks,…) prevents the apparition of the free surface. A negative (or sub-atmospheric) pressure thus appears and creates a sub-atmospheric pressurized flow. Classical Preissmann slot fails to account for this kind of flows. For many authors [198, 248], this is its

main shortcoming. In order to overcome this difficulty, I developed an innovative method called negative Preissmann slot based on an original idea of P. Archambeau [9] .

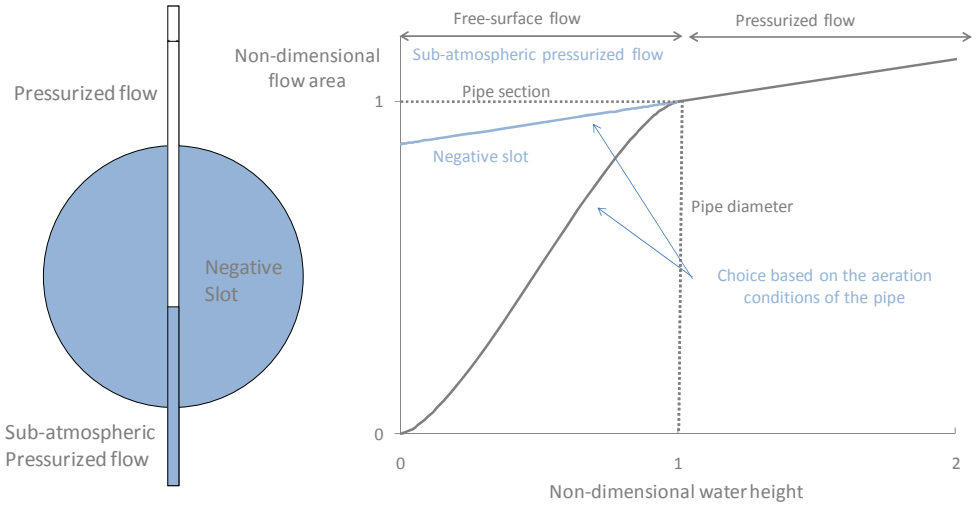

Figure 46: The original negative slot extends the applicability of the Preissmann method to sub-atmospheric pressurized flows as well.

In the absence of efficient aeration devices in the closed pipe, any decrease in pressure below the atmospheric pressure causes the fluid dilatation and/or the pipe contraction. According to the linear theory of the mechanics of continuum material [38, 152], the dilatation/contraction rate is exactly the same as for pressurized flow. To put it in other words, the celerity of a pressurized flow remains constant even for sub-atmospheric pressure. Because of this conclusion, extending the "Preissmann straight line" in the relation H-Ω for water heights below the pipe crown corresponds to a sub-atmospheric pressurized flow (Figure 46). According to the relation H-Ω , the section Ω in the negative slot is smaller than the maximal section of the pipe (at atmospheric pressure). It explains the name "Negative slot" I gave to this method (Figure 46). Physically, the storage capacity of the slot accounts for the fluid dilatation and/or the pipe contraction resulting from an decrease in pressure in the pipe.

As pointed in Figure 46, any water height H below the pipe crown corresponds to two flow areas Ω. The first one describes the free surface flow and the second accounts for the sub-atmospheric pressurized flow. Aeration conditions guide the choice between these two curves. For airtight closed pipes like water supply networks, lack of air prevents the apparition of free surface such that the negative slot curve describes the flow. On the other hand, sewer-systems equipped with sufficient manholes and air vents are in full accordance with the free surface curve. For all the intermediate cases with ill-designed air vents, air-water interactions appear. Specific two-phase codes are thus required. However, these two curves bound the real flow.

3.4 UNIFICATION OF "MATHEMATICAL SHOCK-CAPTURING" MODELS

As mentioned in Chapter 2, alternative "mathematical shock-capturing" models for mixed flows has been proposed in the literature. They do not greatly differ from the Preissmann slot model (now that it describes negative pressure). Nevertheless, these models introduce some interesting concept worth to explore here.

Bourdarias and Gerby derived a new shock capturing model called Dual Model [30, 31]. It relies on both a modified pressure term and the exploitation of the similarity between Saint-Venant and Allievi equations. In their approach, they make explicit a tacit hypothesis of the Preissmann approach: compressibility of the water is accounted for by the pipe dilatation (i.e the variation of Ω). For this purpose, they rewrite the Saint-Venant equations in terms of free surface equivalent wet area $\Omega_{eq}=\rho\Omega_{max}/\rho_0$ and free surface equivalent discharge $Q_{eq}=\rho Q_w/\rho_0$, where ρ_0 is the water density at atmospheric pressure:

$$\begin{cases} \dfrac{\partial \Omega_{eq}}{\partial t}+\dfrac{\partial Q_{eq}}{\partial x}=q_{w,\perp} \\ \dfrac{\partial Q_{eq}}{\partial t}+\dfrac{\partial \beta Q_{eq}Q_{eq}/\Omega_{eq}+gI_1}{\partial x}=g\Omega_{eq}\left(S_0-S_f\right)+\rho_w g I_2+\rho_w \theta u_w q_{w,\perp} \end{cases} \tag{3.8}$$

In equation (3.8), the modified pressure term is given by:

$$gI_1\left(x,\Omega_{eq},E\right)=\begin{cases} gI_1\left(\Omega_{eq}\right) & \text{for a free-surface flow} \\ gI_1\left(\Omega_{max}\right)+a^2\left(\Omega_{eq}-\Omega_{max}\right) & \text{for a pressurized flow} \end{cases} \tag{3.9}$$

where free surface equivalent wet area is given by $\Omega_{eq}=\rho\Omega_{max}/\rho_0$. The great merit of this approach is its mathematical rigor.

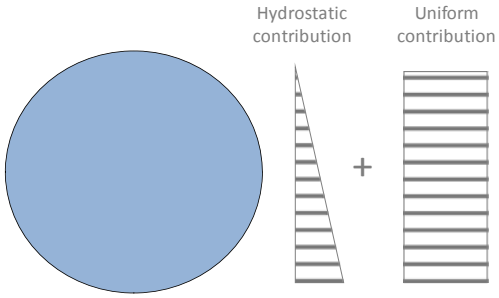

Figure 47: TPA model decouples the pressure into two contributions: an inform part and a hydrostatic one.

The second alternative "mathematical shock-capturing" model for mixed flows presented in literature is the Two Pressures Approach of Vasconcelos [298, 302, 304, 305, 307]. TPA model is based on the identification of two contributions to the total pressure in the cross-section: the hydrostatic contribution and the uniform contribution (Figure 47). Consequently, the pressure term is modified in the Saint-Venant equations as follows:

$$gI_1\left(x,\Omega\right)=\begin{cases} g\Omega h_c & \text{for a free-surface flow} \\ g\Omega_{max}h_c+a^2\left(\Omega_{eq}-\Omega_{max}\right) & \text{for a pressurized flow} \end{cases} \tag{3.10}$$

This pressure term is thus identical to the pressure term of the dual model, even if the thought process leading to both methods is fully different. The great advantage of this method is to decoupling the pressure in two terms: and hydrostatic and a uniform one.

Fundamentally, the Preissmann slot model may integrate the two advantages of the previous methods. First, the slot may be used with the rigorous Saint-Venant equations (3.8) in terms of free surface equivalent parameters. Second, Preissmann slot is a geometrical trick to modify the pressure term gI_1 such that it describes pressurized flows as well. By analogy with the two previous methods, one can give a mathematical formulation to the Preissmann method. In the case of a general closed section surmounted by a slot of width T_s, the hydrostatic pressure term is given by:

$$gI_1\left(\Omega_{eq}\right) = g\int_{h_b}^{h_s} I_w(z)(h_s - z)dz \tag{3.11}$$

If the free surface is located in the slot, equation (3.11) can be rewritten as:

$$gI_1\left(\Omega_{eq}\right) = g\int_{h_b}^{h_{max}} I_w(z)(h_{max} - z)dz + g\int_{h_b}^{h_{max}} I_w(z)(h_s - h_{max})dz + gT_s\int_{h_{max}}^{h_s}(h_s - z)dz \tag{3.12}$$

which gives after integration of each term:

$$gI_1\left(\Omega_{Pr}\right) = gI_1\left(\Omega_{max}\right) + g(h_s - h_{max})\Omega_{eq} + g\frac{T_s}{2}\left(h_s - h_{max}\right)^2 \tag{3.13}$$

Finally, rearranging all the terms and introducing the value of the slot width given in equation (3.7) lead to the following mathematical formulation for the Preissmann pressure term:

$$gI_1\left(\Omega_{eq}\right) = \begin{cases} gI_1\left(\Omega_{eq}\right) & \text{if the flow is free-surface} \\ \underbrace{gI_1\left(\Omega_{max}\right)}_{\text{hydrostatic}} + \underbrace{a^2(\Omega_{eq} - \Omega_{max})}_{\text{1st order uniform}} + \underbrace{a^2\frac{(\Omega_{eq} - \Omega_{max})^2}{2\Omega_{max}}}_{\text{2nd order uniform}} & \text{if the flow is pressurized} \end{cases} \tag{3.14}$$

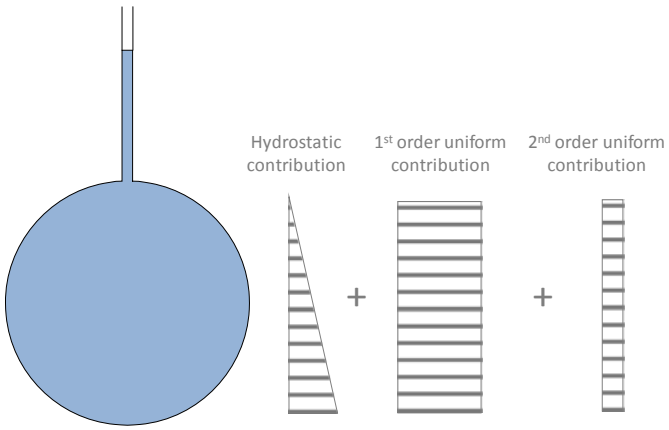

Figure 48: The pressure according to Preissmann includes three components

Equation (3.14) makes appear three contributions to the global pressure, whose graphical representations are provided in Figure 48. First, a hydrostatic term accounts for the contribution of the gravity on the global pressure. It has the standard form of a free surface flow pressure. Second, a uniform contribution results from the dilatation of the pipe (and implicitly the contraction of the fluid). It has the classical form of a pressurized flow pressure. Finally, a second order uniform contribution appears in the Preissmann formulation. This term is said second order because it accounts for the increase in overall pressure due to the increase of the pipe area on which the first order uniform pressure

acts. To put it in other words, the first order uniform pressure increases the section of the pipe. Consequently, the first order uniform pressure acts on a bigger area and its resultant is higher.

The apparition of the second order term in equation (3.14) holds in the definition of the pressure wave celerity. Indeed, the Allievi equations define the pressure wave celerity as:

$$a^2 = A_{max}\frac{\partial p}{\partial(\rho A)} \tag{3.15}$$

By integration, the pressure term p is given as follows:

$$p = a^2\frac{(\rho A - \rho A_{max})}{A_{max}} \tag{3.16}$$

and the term gI_1 takes the form:

$$gI_1 = \frac{pA_{max}}{\rho} = a^2(A - A_{max}) \tag{3.17}$$

which accords with the TPA and Dual models. In the Preissmann model, we modify the section on which p is applied to take into account the pipe dilatation:

$$\begin{aligned} gI_1 &= \frac{p}{\rho}\frac{A_{max}+A}{2} = a^2(A-A_{max})\left(1+\frac{(A-A_{max})}{2}\right) \\ &= a^2(A-A_{max}) + a^2\frac{(A-A_{max})^2}{2} \end{aligned} \tag{3.18}$$

This last equation accords with the Preissmann model. Hopefully, the three methods give quasi-identical numerical results since the pipe dilatation is very feeble in most applications.

In conclusion, TPA, Dual, and Preissmann model each improve in their manner the description of mixed flows. A state-of-the-art model for Preissmann slot is thus obtained by combining the pressure formulation (3.14) with the rigorous definition of the free surface equivalent wet area $\Omega_{eq}=\rho\Omega_{max}/\rho_0$. TPA model gives a physical significance to this approach. The new model writes as:

$$\begin{cases} \dfrac{\partial \Omega_{eq}}{\partial t} + \dfrac{\partial Q_{eq}}{\partial x} = q_{w,\perp} \\ \dfrac{\partial Q_{eq}}{\partial t} + \dfrac{\partial \beta Q_{eq}Q_{eq}/\Omega_{eq} + gI_1}{\partial x} = g\Omega_{eq}(S_0 - S_f) + \rho_w gI_2 + \rho_w \theta u_w q_{w,\perp} \end{cases} \tag{3.19}$$

where the pressure term is given by

$$gI_1(\Omega_{eq}) = \begin{cases} gI_1(\Omega_{eq}) & \text{if the flow is at free-surface} \\ \underbrace{gI_1(\Omega_{max})}_{\text{hydrostatic}} + \underbrace{a^2(\Omega_{eq}-\Omega_{max})}_{\text{1st order uniform}} + \underbrace{a^2\frac{(\Omega_{eq}-\Omega_{max})^2}{2\Omega_{max}}}_{\text{2nd order uniform}} & \text{if the flow is pressurized} \end{cases} \tag{3.20}$$

What is more, this formulation paves the way to the integration of air effects in the pressure term (chapter 6). The subscript “eq” is dropped in the following for the sake of readability. This is however always the equivalent values that I refer to.

Summary and conclusion

The current chapter concerns the simulation of pure water transient mixed flows. Air-water interactions are neglected in a first time. In this respect, standard methods in hydraulic engineering form a reliable basis but remain insufficient to constitute an efficient mathematical model. Consequently, a part of my research was dedicated to the establishment of an improved “mathematical shock-capturing” model for pure water mixed flows.

In this chapter, I have developed a new “mathematical shock-capturing” model for free surface, pressurized, and mixed flows. First, an original negative Preissmann slot has been devised in order to simulate sub-atmospheric pressurized flows with Saint-Venant equations. Then I compared the new Preissmann slot model with other “mathematical shock-capturing” approaches (TPA and Dual models). Their unification leads to a new state-of-the-art model for the simulation of mixed flows.

Since no analytical solution exists for the new model, discretizing the equations is the only way to exploit the model on real cases. In this respect, Computational Fluid Mechanics (CFD) gives a reliable basis of results and methods. The next step is thus to analyze the properties of the new model and to derive an adapted numerical scheme.

Chapter 4 Pure Water Flows: Numerical Model

This chapter aims at:

- ✓ establishing the mathematical properties of the new model;
- ✓ developing numerical schemes adapted to the new equations;
- ✓ understanding and diminishing spurious oscillations at the transition bore.

Based on original investigations about "mathematical shock-capturing" approaches, a state-of-the-art unified mathematical model has been established in the previous chapter. It combines the advantages of the Preissmann, TPA, and Dual models:

$$\begin{cases} \dfrac{\partial \Omega_{eq}}{\partial t} + \dfrac{\partial Q_{eq}}{\partial x} = q_{w,\perp} \\ \dfrac{\partial Q_{eq}}{\partial t} + \dfrac{\partial \beta \, Q_{eq} Q_{eq} / \Omega_{eq} + gI_1}{\partial x} = g\Omega_{eq}\left(S_0 - S_f\right) + \rho_w g I_2 + \rho_w \theta u_w q_{w,\perp} \end{cases} \tag{4.1}$$

where the pressure term is given by:

$$gI_1\left(\Omega_{eq}\right) = \begin{cases} gI_1\left(\Omega_{eq}\right) & \text{if the flow is at free-surface} \\ \underbrace{gI_1\left(\Omega_{max}\right)}_{\text{hydrostatic}} + \underbrace{a^2\left(\Omega_{eq} - \Omega_{max}\right)}_{\text{1st order uniform}} + \underbrace{a^2 \dfrac{\left(\Omega_{eq} - \Omega_{max}\right)^2}{2\Omega_{max}}}_{\text{2nd order uniform}} & \text{if the flow is pressurized} \end{cases} \tag{4.2}$$

Since no analytical solution exists for the new model, discretizing the equations is the only way to exploit the model on real cases. In this respect, Computational Fluid Mechanics (CFD) gives a reliable basis of results and methods. The objective of this chapter is to present the results of the discretization and implementation of equations (4.1). For this purpose, I analyze the properties of the new model (section 4.1). The linear analysis gives insight into the information propagation properties and the required boundary conditions. The non-linear analysis provides a solution to the associated Riemann problem. Consequently, I derive an adapted numerical scheme analogous to the FVS Wolf. In order to reach rapidly results, the model is implemented into the computational code WOLF (section 4.2). In particular, a pseudo-unsteady strategy drastically reduces the computation time for steady flows. Von Neumann analysis proves the stability of both models. Nevertheless, oscillations appear at the transition bore. In section 4.3, I give a new insight into the cause of numerical oscillations. I also introduce alternative numerical schemes likely to reduce instabilities: The Roe solver, the AUSM scheme, an original Exact Riemann solver, and the Lax-Friedrichs scheme. Even if the amplitude of oscillations, they do not disappear as long as a "numerical shock-capturing scheme" is used.

4.1 MATHEMATICAL PROPERTIES OF THE MIXED FLOW MODEL

Investigating the fundamental mathematical properties of a system of PDE's is a prerequisite prior to numerically integrating the model. In particular, the determination of the characteristics of the model gives useful insight into the propagation of information and into the boundary conditions to prescribe. In this section, model (4.1)-(4.2) is first analyzed under its quasi-linear form. The two waves define two flow regimes: super-critical flow and sub-critical flow. At each flow regime correspond specific boundary conditions. Finally, the non-linear analysis shows the apparition of shocks and rarefactions in the solution of the Riemann Problem. Reader is here presumed to be familiar with the linear and non-linear theory of PDE's as exposed in classical handbooks [144, 158, 159, 197, 285, 286].

4.1.1 LINEAR ANALYSIS

Identifying the wave propagation in the model requires deriving its Jacobian matrix **A**, which is defined as the derivative of the physical fluxes with respect to the conservative unknowns Q and Ω:

$$\mathbf{A} = \frac{\partial \mathbf{F}}{\partial \mathbf{U}} = \begin{bmatrix} 0 & 1 \\ c^2 - \beta u_w^2 & 2\beta u_w \end{bmatrix} \tag{4.3}$$

where β is assumed constant and the celerity of the pressure wave is by definition given as:

$$c^2 = \frac{\partial g I_1(\Omega)}{\partial \Omega} \tag{4.4}$$

For the free-surface flow, I showed in Chapter 2 that pressure terms can be expressed in terms of free surface elevation Z:

$$g \frac{\partial I_1(\Omega)}{\partial x} - g I_2(\Omega) = g\Omega \frac{\partial Z(\Omega)}{\partial x} \tag{4.5}$$

Consequently, the celerity c is given by:

$$c = g\Omega \frac{\partial Z(\Omega)}{\partial \Omega} = \frac{g\Omega}{l} \tag{4.6}$$

where l is by definition the free surface width. For the pressurized flow, the derivation is even simpler and gives:

$$c^2 = c^2(\Omega_{max}) + a^2 + a^2 \frac{(\Omega - \Omega_{max})}{\Omega_{max}} = c^2(\Omega_{max}) + a^2 \frac{\Omega_{eq}}{\Omega_{max}} \tag{4.7}$$

In conclusion, the celerity in equation (4.3) is defined as follows:

$$c^2 = \frac{\partial g I_1(\Omega)}{\partial \Omega} \begin{cases} \dfrac{g\Omega}{l} & \text{if the flow is free-surface} \\ c^2(\Omega_{max}) + a^2 \dfrac{\Omega}{\Omega_{max}} & \text{if the flow is pressurized} \end{cases} \tag{4.8}$$

The eigenvalues of the Jacobian matrix give the slopes of the characteristics (i.e. velocities of the waves):

$$\lambda_1 = c\left(\beta Fr - \sqrt{\beta Fr^2(\beta - 1) + 1}\right) \quad \text{and} \quad \lambda_2 = c\left(\beta Fr + \sqrt{\beta Fr(\beta - 1) + 1}\right) \tag{4.9}$$

where the Froude number Fr is the non-dimensional number that compares inertia and gravitational forces:

$$Fr = \frac{u_w}{c} \tag{4.10}$$

The eigenvalues are real as long as the radicand is non-negative (which is never the case since β is always bigger than one [75]). Consequently, the model is hyperbolic [8, 144, 145]. Hyperbolic problems are known to accept wave-like solutions which are the superposition of several simple waves propagating at a finite speed [197]. The sign of the celerity defines the direction of propagation of the information. As pointed in Figure 49, λ_2 is always positive whatever is the value of the Froude number (for a positive water velocity of course). On the opposite, the sign of λ_1 changes at the critical Froude number defined as $Fr^2_{cr} = 1/\beta$. The eigenvalue λ_1 is negative for Froude number lower than the critical value, and positive for Froude number greater than the critical value. This change of sign marks the limit between two flow regimes (Figure 49). In the sub-critical regime, the information propagates partly upstream and partly downstream because the celerities have opposite signs. In the super-critical regime, celerities have the same sign such that all information propagates downstream. The transition between the two regimes is called critical flow. This coexistence of two regimes plays a key role in the interpretation of studied flow as well as in the development of a numerical scheme.

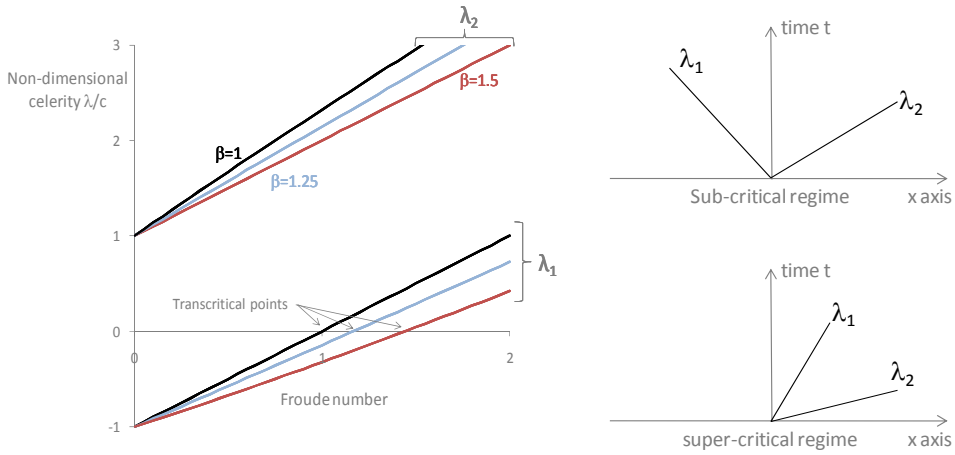

Figure 49: Values of the celerities define two flow regimes according to the value of the Froude number: a sub-critical regime (Fr<1) and a super-critical regime (Fr>1)

4.1.2 Boundary Conditions.

The imposition of Boundary Conditions (BC) is a crucial step in any differential problem. A system of partial differential equations may only be solved if it is supplemented by an adequate set of BC and Initial conditions (IC). In the case of hyperbolic systems, boundary conditions must be prescribed in the same number as the number of characteristics entering the computational domain at the considered boundary [144]. This number is easily determined by examining the sign of the eigenvalues at the boundary. In this respect, two types of boundaries may be distinguished: solid and liquid ones. At a solid or impermeable boundary, the specific discharge rate normal to the boundary cancels.

Table 1 summarizes the number and type of BC prescribed at a liquid boundary. The suggested nature of BC corresponds to the most usual choice. At the inflow boundary, the equivalent discharge Q is naturally always imposed. Depending on the regime, the equivalent section Ω is required as well. At the outflow boundary, only the sub-critical regime requires a boundary condition. Usually the equivalent section Ω is imposed.

Table 1: Number and nature of the boundary conditions to impose at the boundaries of the domain

Type of boundary and regime		Number of BC	Nature of BC
Inflow	$u_w < c$	1	Q
($u_w > 0$)	$u_w > c$	2	Q, Ω
Outflow	$u_w < c$	1	Ω
($u_w < 0$)	$u_w > c$	0	-

4.1.3 NON-LINEAR ANALYSIS: SOLUTION TO THE RIEMANN PROBLEM

The Riemann problem for the homogeneous Saint-Venant equations, whose applicability has been extended to pressurized flows, is the following system of PDE's:

$$\frac{\partial}{\partial t}\begin{bmatrix}\Omega\\ Q\end{bmatrix}+\frac{\partial}{\partial x}\begin{bmatrix}Q\\ QQ/\Omega+gI_1\end{bmatrix}=\begin{bmatrix}0\\ 0\end{bmatrix} \tag{4.11}$$

with piecewise constant initial data given by:

$$\mathbf{U}(x)=\begin{cases}\mathbf{U}_L & \text{if } x<0\\ \mathbf{U}_R & \text{if } x>0\end{cases} \qquad \text{where } \mathbf{U}=\begin{bmatrix}\Omega & Q\end{bmatrix}^T \tag{4.12}$$

The subscripts L and R denote the left and right states respectively.

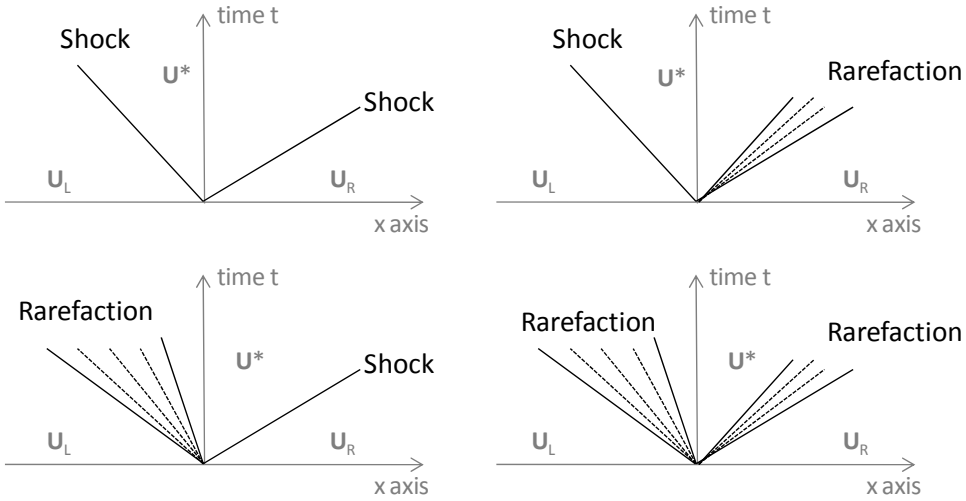

Figure 50: The solution of the Riemann problem has four different possible wave patterns in the phase plane

The Riemann problem can be solved exactly and the solution represented in the phase plane x-t (Figure 50). This solution consists in two waves that can be either shocks or rarefactions. It results in four possible wave patterns: shock-shock, shock-rarefaction, rarefaction-shock, and rarefaction-rarefaction. These waves may propagate both downstream, or one may propagate upstream and one downstream. They separate three

states in the phase plane: the left state $\mathbf{U}_L$, the right state $\mathbf{U}_R$, and the star state $\mathbf{U}^*$. The value of the star state can be determined by using the properties of the shocks and rarefactions (see chapter 2). In this respect, Toro proposed an elegant method for the shallow water equations [286]. In the following, I apply the same approach to the Saint-Venant equations.

SHOCK WAVES

This original demonstration is performed for the left wave. The approach is exactly the same for a right shock. Left wave is thus a shock travelling with velocity S_L. In a steady frame of reference moving with the shock speed, the conservation laws (4.11) re-write:

$$\begin{cases} \hat{u}^* \triangleq u^* - S_L \\ \hat{u}_L \triangleq u_L - S_L \end{cases} \Rightarrow \begin{cases} \Omega^* \hat{u}^* = \Omega_L \hat{u}_L \triangleq M_L \\ \Omega^* \hat{u}^{*2} + gI_1(\Omega^*) = \Omega_L \hat{u}_L^{\,2} + gI_1(\Omega_L) \end{cases} \tag{4.13}$$

where the velocity $u=Q/\Omega$. Inserting M_L in the momentum equation gives:

$$M_L(\hat{u}^* - \hat{u}_L) = gI_1(\Omega_L) - gI_1(\Omega^*) \tag{4.14}$$

From the continuity in equation (4.13), we have $\hat{u}^* = M_L/\Omega^*$ and $\hat{u}_L = M_L/\Omega_L$. After some algebraic manipulations, relation (4.14) becomes:

$$M_L = \sqrt{\frac{\left[gI_1(\Omega_L) - gI_1(\Omega^*)\right]\Omega^*\Omega_L}{\Omega_L - \Omega^*}} \tag{4.15}$$

From equation (4.13) we have $S_L = u^* - \hat{u}^* = u_L - \hat{u}_L$. We may relate the speed u^* to the parameter M_L and find the following relation for the star velocity:

$$u^* = u_L - f_L(\Omega^*, \Omega_L) \quad \text{with} \quad f_L(\Omega^*, \Omega_L) = \sqrt{\frac{\left[gI_1(\Omega_L) - gI_1(\Omega^*)\right]\left[\Omega_L - \Omega^*\right]}{\Omega^*\Omega_L}} \tag{4.16}$$

The speed S_L can now be calculated as a function of Ω^*. From (4.13), we have:.

$$S_L = u_L - M_L/\Omega_L \tag{4.17}$$

The velocity of the left shock is then:

$$S_L = u_L - \sqrt{\frac{\left[gI_1(\Omega_L) - gI_1(\Omega^*)\right]\Omega^*}{(\Omega_L - \Omega^*)\Omega_L}} \tag{4.18}$$

The relation for a right shock is derived in an analogous way. We find the following relations for the star section:

$$u^* = u_R + f_R(\Omega^*, \Omega_R) \quad \text{with} \quad f_R(\Omega^*, \Omega_R) = \sqrt{\frac{\left[gI_1(\Omega_R) - gI_1(\Omega^*)\right]\left[\Omega_R - \Omega^*\right]}{\Omega^*\Omega_R}} \tag{4.19}$$

and the speed of the right shock is then:

$$S_R = u_R + \sqrt{\frac{\left[gI_1(\Omega_R) - gI_1(\Omega^*)\right]\Omega^*}{(\Omega_R - \Omega^*)\Omega_R}} \tag{4.20}$$

For given initial conditions, relations (4.16) and (4.19) are sufficient to determine the star state $U^*=[\Omega^* \quad Q^*]^T$ as long as the structure of the solution is two shocks. This assumption may be assessed a posteriori by comparing the solution Ω^* with the initial data. If $\Omega^*>\Omega_R$, the right wave is actually a shock. In a similar manner, the left wave is a shock if $\Omega^*>\Omega_L$. Otherwise, the wave is a rarefaction and the star state is computed differently.

RAREFACTION WAVES

The case of rarefaction waves is more difficult since there is no analytical expression of the Generalised Riemann Invariants (GRI) for the Saint-Venant equations. As introduced in chapter 2, expressing the constancy of the GRI's across the rarefaction wave links the left and right states:

$$\frac{dU_1}{r_1^{(L)}}=\frac{dU_2}{r_2^{(L)}} \quad \text{across the left rarefaction} \tag{4.21}$$

$$\frac{dU_1}{r_1^{(R)}}=\frac{dU_2}{r_2^{(R)}} \quad \text{across the right rarefaction} \tag{4.22}$$

where $\mathbf{r}^{(L)}$ and $\mathbf{r}^{(R)}$ are the right eigenvector of the Jacobian matrix expressed in terms of left and right states respectively. They correspond to a left and a right rarefaction respectively. In the case of the Saint-Venant equations, expressing the consistency of the GRI's leads to the following differential equations that hold across the rarefaction waves:

$$du+\sqrt{\frac{g}{\Omega * l}}d\Omega=0 \quad \text{across the left rarefaction} \tag{4.23}$$

$$du-\sqrt{\frac{g}{\Omega * l}}d\Omega=0 \quad \text{across the right rarefaction} \tag{4.24}$$

where l is the width of free surface. In order to derive relations (4.23) and (4.24), the system of PDE's has been expressed in its primitive variables: the flow cross-section Ω and the fluid velocity u. This approach remains rigorous since rarefactions are smooth waves that are correctly captured by non-conservatives equations.

Let us consider relation (4.23) holding for a left rarefaction. We can connect the left state to the star state across the left wave by integrating (4.23) between Ω_L and Ω^*, and using the additivity of integration on intervals:

$$\left(u^*-u_L\right)+\underbrace{\int_0^{\Omega^*}\sqrt{g/\Omega l}\,d\Omega}_{\phi^*}-\underbrace{\int_0^{\Omega_L}\sqrt{g/\Omega l}\,d\Omega}_{\phi_L}=0 \tag{4.25}$$

Consequently, we have for the left rarefaction:

$$u^*=u_L-f_L\left(\Omega^*,\Omega_L\right) \quad \text{with} \quad f_L\left(\Omega^*,\Omega_L\right)=\phi^*-\phi_L \tag{4.26}$$

and for the right rarefaction:

$$u^*=u_R+f_R\left(\Omega^*,\Omega_R\right) \quad \text{with} \quad f_R\left(\Omega^*,\Omega_R\right)=\phi^*-\phi_R \tag{4.27}$$

where the value of function ϕ depends on the geometry of the section. Its value must be computed on a case-by-case basis.

The speed of the head S_{HL} and the tail S_{TL} of a left rarefaction can also be calculated once Ω^* is known. It is trivial to show that:

$$S_{HL} = u_L - c_L \text{ and } S_{TL} = u^* - c^* \tag{4.28}$$

To find the solution inside the rarefaction, we consider a point $P = (\hat{x}, \hat{t})$ inside the wave and a characteristic joining the origin 0 and P. The speed of the characteristic is

$$u - c = \frac{dx}{dt} = \frac{\hat{x}}{\hat{t}} \tag{4.29}$$

The simultaneous solution of (4.25) and (4.29) gives a single non-linear algebraic equation for the flow area Ω that can be solved iteratively:

$$c(\Omega) + \phi(\Omega) - u_L - \phi_L = 0 \tag{4.30}$$

For given initial conditions, relations (4.26) and (4.27) are sufficient to determine the star state $\mathbf{U}^* = [\Omega^* \quad Q^*]^T$ as long as the structure of the solution is two rarefactions. This assumption may be assessed a posteriori by comparing the solution Ω^* with the initial data. If $\Omega^* < \Omega_R$, the right wave is actually a rarefaction. In a similar manner, the left wave is a rarefaction if $\Omega^* < \Omega_L$. Otherwise, the wave is a shock. Relations (4.16) and (4.19) are valid in these cases. Nevertheless, relations (4.26) and (4.27) depends on the geometry of the section through the function ϕ. This function must be determined analytically or numerically before solving the Riemann problem.

4.2 Discretization of the Mixed Flow Model: Wolf FVS

Originally developed for free surface flows [9, 75, 93], the Wolf flux vector splitting distinguishes two parts in the equations: a convective and a pressure contribution. According to the sign of the fluid velocity, convective terms are always up-winded and the pressure terms down-winded.

For the conservative Saint-Venant equations (4.1) whose pressure term (4.2) is modified to account for pressurized flows as well, the Wolf splitting gives the following equation for the continuity:

$$\Omega_i^{n+1} = \Omega_i^n - \frac{\Delta t}{\Delta x}\left[Q_{i+1/2}^n - Q_{i-1/2}^n \right] + \Delta t q_{w,\perp}\Big|_i^n \tag{4.31}$$

and the following expression for the momentum equation:

$$\begin{aligned} Q_i^{n+1} = Q_i^n &- \frac{\Delta t}{\Delta x}\left[\left(QQ/\Omega + g I_1(\Omega) \right)\Big|_{i+1/2}^n - \left(QQ/\Omega + g I_1(\Omega) \right)\Big|_{i-1/2}^n \right] \\ &+ \Delta t g \left(\frac{\Omega_{i+1/2}^n + \Omega_{i-1/2}^n}{2} \right)\left(\frac{z_b\big|_{i+1/2}^n - z_b\big|_{i-1/2}^n}{\Delta x} - S_f\left(Q_i^n, \Omega_i^n \right) \right) + \Delta t\left(\rho_w I_2 + \rho_w \theta u_w q_{w,\perp} \right)\Big|_i^n \end{aligned} \tag{4.32}$$

As usual, n is the time index and i the spatial index.

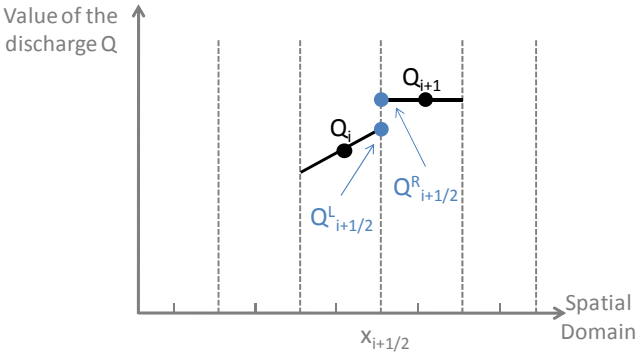

Figure 51: Wolf Flux vector splitting uses the left or the right reconstructed value to compute the numerical flux.

Since the discharge Q is a convective term, its value at the boundary i+1/2 is given by the following splitting:

$$Q_{i+1/2}^n = \begin{cases} Q_L^n & \text{if} \quad u_L > 0 \quad \text{and} \quad u_R > 0 \\ Q_R^n & \text{if} \quad u_L < 0 \quad \text{and} \quad u_R < 0 \\ \left(Q_L^n + Q_R^n \right)/2 & \text{otherwise} \end{cases} \tag{4.33}$$

where L and R designate the left and right reconstructed values. Reconstruction can be either constant, linear,… For the fluid momentum, the splitting gives:

$$\left(\frac{QQ}{\Omega} \right)_{i+1/2}^n = \begin{cases} Q_L^n Q_L^n / \Omega_L^n & \text{if} \quad u_L > 0 \quad \text{and} \quad u_R > 0 \\ Q_R^n Q_R^n / \Omega_R^n & \text{if} \quad u_L < 0 \quad \text{and} \quad u_R < 0 \\ \left(Q_L^n Q_L^n / \Omega_L^n + Q_R^n Q_R^n / \Omega_R^n \right)/2 & \text{otherwise} \end{cases} \tag{4.34}$$

For the hydrostatic pressure, the value at the boundary is down-winded such that:

$$gI_1\left(\Omega^n_{i+\frac{1}{2}}\right)=\begin{cases} gI_1\left(\Omega^n_R\right) & \text{if} \quad u_L>0 \quad \text{and} \quad u_R>0 \\ gI_1\left(\Omega^n_L\right) & \text{if} \quad u_L<0 \quad \text{and} \quad u_R<0 \\ \left(gI_1\left(\Omega^n_R\right)+gI_1\left(\Omega^n_L\right)\right)/2 & \text{otherwise} \end{cases} \tag{4.35}$$

The requirement of adequacy between the pressure gradient and the bottom slope prompts us to split the topographic gradient in the same direction as the pressure. For the flow cross-section, we consequently have:

$$\Omega^n_{i+\frac{1}{2}}=\begin{cases} \Omega^n_R & \text{if} \quad u_L>0 \quad \text{and} \quad u_R>0 \\ \Omega^n_L & \text{if} \quad u_L<0 \quad \text{and} \quad u_R<0 \\ \left(\Omega^n_R+\Omega^n_L\right)/2 & \text{otherwise} \end{cases} \tag{4.36}$$

The topography at the boundary is given by:

$$z_b\big|^n_{i+\frac{1}{2}}=\begin{cases} z_b\big|^n_R & \text{if} \quad u_L>0 \quad \text{and} \quad u_R>0 \\ z_b\big|^n_L & \text{if} \quad u_L<0 \quad \text{and} \quad u_R<0 \\ \left(z_b\big|^n_R+z_b\big|^n_L\right)/2 & \text{otherwise} \end{cases} \tag{4.37}$$

In uniform pipes, the second pressure term gI_2 cancels and the previous equations can be solved. For non-uniform pipes, computing gI_2 is difficult. For this reason, I use the non-conservative form of the Saint-Venant equations, which are expressed in terms of free surface slope instead of pressure gradient. The continuity equation remains unchanged. However, the Wolf splitting gives for the momentum equation:

$$\begin{aligned} Q^{n+1}_i=Q^n_i-\frac{\Delta t}{\Delta x}\left[QQ/\Omega\big|^n_{i+\frac{1}{2}}-QQ/\Omega\big|^n_{i-\frac{1}{2}}\right] \\ +\Delta t g\left(\frac{\Omega^n_{i+\frac{1}{2}}+\Omega^n_{i-\frac{1}{2}}}{2}\right)\left(\frac{Z\big|^n_{i+\frac{1}{2}}-Z^n_{i-\frac{1}{2}}}{\Delta x}-S_f\left(Q^n_i,\Omega^n_i\right)\right)+\Delta t\rho_w\theta u_w q_{w,\perp}\big|^n_i \end{aligned} \tag{4.38}$$

Since the free surface elevation term conflates the effects of both the pressure and the topographic gradients, its value at the boundary is down-winded as follows:

$$Z\big|^n_{i+\frac{1}{2}}=\begin{cases} Z\big|^n_R & \text{if} \quad u_L>0 \quad \text{and} \quad u_R>0 \\ Z\big|^n_L & \text{if} \quad u_L<0 \quad \text{and} \quad u_R<0 \\ \left(Z\big|^n_R+Z^n_L\right)/2 & \text{otherwise} \end{cases} \tag{4.39}$$

Even if the model is non-conservative, Erpicum [93] showed the error in the computation of shocks remains very limited. For free surface flows, a discretised relation gives the link between the free surface elevation Z and the flow cross-section Ω (according to the geometry). For pressurized flows, the free surface elevation can be linked to the pressure term. Consequently, we have:

$$Z(\Omega)=\begin{cases} H_{disc}(\Omega)+z_b & \text{if the flow is free-surface} \\ \dfrac{I_1(\Omega)}{\Omega_{max}}+\dfrac{H_{disc}(\Omega_{max})}{2}+z_b & \text{if the flow is pressurized} \end{cases} \tag{4.40}$$

I do not dispose of a rigorous demonstration for this last relation. However, its accuracy is verified for all analytical profiles I had to face during my doctoral research. What is more, it accords with the physical signification of the Preissmann slot.

The scheme presents various advantages and drawbacks that I briefly mention here. Its application on validation benchmarks and practical cases in the next chapter provides a more thorough analysis of the performance of the model. First, the scheme presents the major advantage of treating continuously regime transitions. The splitting remains indeed unchanged in the neighborhood of the critical Froude. In a similar manner, inversion of the flow direction is continuously managed in the convective terms. Since the velocity is zero at the transition, convective fluxes cancel when the splitting is reverting. On the opposite, the splitting produces a discontinuity in the evaluation of the pressure term when the velocity is zero. This feature makes the scheme inappropriate for implicit temporal integration [75]. Fourth, the splitting eases drastically the evaluation of source terms (by comparison with other FVS and Godunov schemes). In particular, discretization of the non-conservative form of the Saint-Venant equations (4.38) is straightforward. What is more, computing steady states with the Wolf splitting renders a continuous solution without jump in the discharge profile or in the water height profile in spite of the source term. This is rarely the case with Godunov schemes, which require balancing the source terms [51, 195, 196, 308]. Finally, very little numerical diffusion affects the splitting and its "numerical shock-capturing" nature is obvious. However, many questions remain with respects to its behavior in presence of water hammer phenomena.

4.2.1 STABILITY ANALYSIS

Von Neumann method [47, 62, 75, 144, 145] is used here to demonstrate the stability of the Wolf FVS applied to the new model. Rigorously, this approach only applies to linear problems. Nevertheless, its results are a necessary condition for the stability of non-linear problems and provide good indications on the restrictions to apply on the time step used in the scheme. For this purpose, the Jacobian Matrix of the discretised equation is applied to a Fourier series of the solution. Since the numerical error does not increase with the time, the Wolf splitting is shown unconditionally stable.

As I just mentioned, Von Neumann method relies on the discretised quasi-linear form of the model, which can be written as:

$$\frac{\partial \mathbf{U}_i}{\partial t} = -\left[\mathbf{A}^+ \frac{\partial \mathbf{U}_i^n}{\partial x}\bigg|^+ + \mathbf{A}^- \frac{\partial \mathbf{U}_i^n}{\partial x}\bigg|^- \right] \tag{4.41}$$

where the super-script $|^+$ and $|^-$ designates the respectively down-winded and up-winded gradients. Consequently, the splitted Jacobian matrixes are given by:

$$\mathbf{A}^- = \begin{bmatrix} 0 & 0 \\ c^2 & 0 \end{bmatrix} \quad \text{and} \quad \mathbf{A}^+ = \begin{bmatrix} 0 & 1 \\ -\beta u^2 & 2\beta u \end{bmatrix} \tag{4.42}$$

The solution **U** of the equations is hence developed in a Fourier series:

$$\mathbf{U}_k^n = \sum_{m=-N}^{+N} \tilde{\mathbf{U}}_m^n e^{\left[\mathbf{i} l_m (k\Delta x - c_m(l_m)t)\right]} \tag{4.43}$$

where N is the number of mesh intervals, k the mesh index, $\mathbf{i}=\sqrt{-1}$, $\tilde{\mathbf{U}}_m^n$ the amplitude of the m^{th} harmonic, l_m[rad/m] the wave number and c_m[m/s] has real and imaginary parts : $c_m = c_{rm}(l_m) + \mathbf{i} c_{im}(l_m)$. By using this last decomposition, equation (4.43) is rewritten as:

$$\mathbf{U}_k^n = \sum_{m=-N}^{+N} \tilde{\mathbf{U}}_m^n e^{l_m c_{im}(l_m) t} e^{\left[\mathbf{i} l_m (k\Delta x - c_{rm}(l_m)t)\right]} \tag{4.44}$$

In this equation, the amplification rate of the wave is identified as the imaginary part c_{im} of the velocity multiplied by the wave number l_m. Obviously, this amplification rate is negative if the following condition is respected:

$$l_m c_{im}(l_m) \le 0 \tag{4.45}$$

This is the stability criterion.

Introducing any of these Fourier modes into the discretised quasi-linear form (4.42) gives:

$$-\mathbf{i} l_m c_m(l_m) \tilde{\mathbf{U}}_m^n e^{\left[\mathbf{i} l_m (k\Delta x - c_m(l_m)t)\right]} = -\underbrace{\left[\begin{bmatrix} 0 & 0 \\ c^2 & 0 \end{bmatrix} \frac{e^{\mathbf{i} l_m \Delta x} - 1}{\Delta x} + \begin{bmatrix} 0 & 1 \\ -\beta u^2 & 2\beta u \end{bmatrix} \frac{1 - e^{-\mathbf{i} l_m \Delta x}}{\Delta x}\right]}_{\mathbf{A}^{discretised}} \tilde{\mathbf{U}}_m^n e^{\left[\mathbf{i} l_m (k\Delta x - c_m(l_m)t)\right]} \tag{4.46}$$

In particular, the criterion (4.45) is verified only if the real part of the discretised operator is positive. Positivity of the eigenvalues real part of the discretised operator is thus a necessary and sufficient condition:

$$\mathrm{Re}\left[\lambda_i^{discretised}\right] \ge 0 \tag{4.47}$$

The eigenvalues of this discretised Jacobian matrix are:

$$\lambda_{1/2} = -\frac{c}{\Delta x}\left(1 - e^{-\mathbf{i} l_m \Delta x}\right)\left[\beta \mathrm{Fr} \pm \sqrt{\left(\frac{e^{\mathbf{i} l_m \Delta x} - 1}{1 - e^{-\mathbf{i} l_m \Delta x}}\right) + \beta(\beta - 1)\mathrm{Fr}^2}\right] \tag{4.48}$$

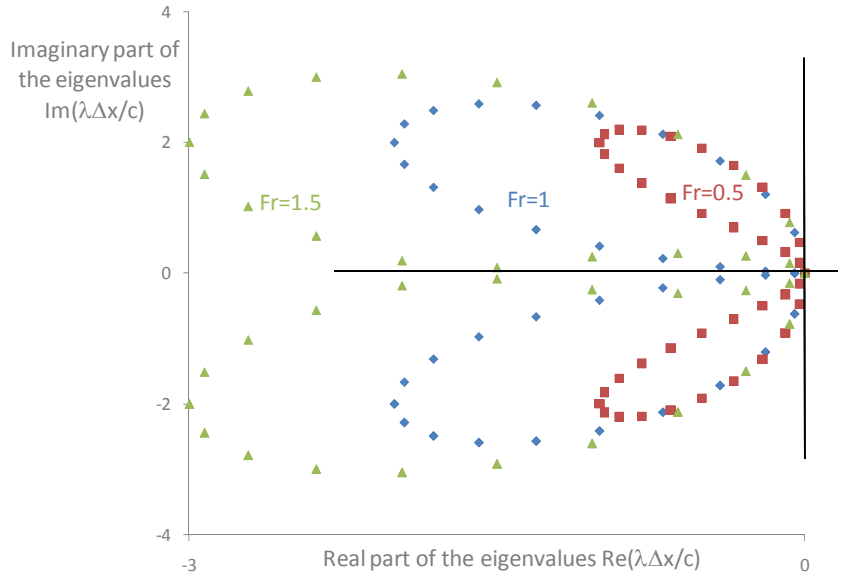

Figure 52: Non-dimensional eigenvalues of the discretised Jacobian matrix are complex numbers whose real part is always negative

By introducing the trigonometric functions $e^{ix} = \cos x + i \sin x$ and assuming the coefficient of Boussinesq equals to one, we simply obtain:

$$\lambda_{1/2} = -\frac{2c}{\Delta x}\left[Fr \ \sin^2\left(\frac{l_m \Delta x}{2}\right) + i \sin\left(\frac{l_m \Delta x}{2}\right)\left(\pm 1 - Fr \cos\left(\frac{l_m \Delta x}{2}\right)\right)\right] \quad (4.49)$$

These eigenvalues are complex numbers. As pointed in Figure 52, their real part is negative whatever are the values of both the Froude number and the coefficient of Boussinesq. The Von Neumann stability criterion $Re(\lambda) \leq 0$ is thus verified and the scheme is unconditionally stable. What is more, discretised eigenvalues (4.48) tend to the mathematical eigenvalues (4.9) for correct Fourier modes ($k \ll 1$).

4.2.2 Simplification for Steady Flows

Steady states are of great interest in civil and environmental engineering. Design guidelines for many hydraulic structures specify indeed that specific critical steady states have to be addressed. Practitioners should then rely on robust and efficient 1D solvers suitable for each flow pattern (free surface, pressurized, and mixed) as well as each flow regime (sub-, trans-, and super-critical). Traditionally, computation of such steady states is performed with standard methods for solving ordinary differential equations [16]. They require setting apart supercritical and subcritical flows and treating regime transitions in a particular way. These two features are their major drawback. Another method consists in computing the unsteady scheme proposed in the previous section over a sufficient number of time steps in order to converge onto the steady state solution. Since a system of Partial Differential Equations (PDE's) is solved instead of an ordinary differential equation, this method requires a pointless computational effort.

In this thesis, I set up and assess a fast universal solver for one-dimensional continuous and discontinuous steady flows in rivers and pipes. The idea originates from the pseudo-unsteady strategy presented by Archambeau [9] for free surface flows. The model I am presenting here is suitable to handle steady free surface, pressurized, and mixed single-phase flows. It has been published in the International Journal for Numerical Methods in Fluids [166]. The model relies on a reformulation of the steady form of the Saint-Venant equations into a pseudo-unsteady equation for the flow area. The derived pseudo-unsteady formulation aims at keeping the hyperbolic feature of the complete set of equations. Using the new scheme considerably reduces the computation time.

As mentioned above, an ordinary differential equation rigorously describes steady states. This ODE may be obtained from the system of PDE's given by equation (4.1). By assuming that each time derivative is equal to zero ($\partial A/\partial t = \partial Q/\partial t = 0$), equation (4.1) is re-written as follows:

$$\begin{cases} Q = Cst + \sum q_{w,\perp} \\ \dfrac{\partial \beta Q Q / \Omega + g I_1}{\partial x} = g\Omega\left(S_0 - S_f\right) + \rho_w g I_2 + \rho_w \theta u_w q_{w,\perp} \end{cases} \quad (4.50)$$

First equation is trivial since the discharge is imposed by boundary conditions upstream the computational domain. In order to solve the unique unknown Ω, several numerical techniques can be applied. As mentioned in the introduction, equation (4.50) is usually simplified by using standard properties of the derivatives. It results in a non conservative ordinary differential equation (ODE):

$$\frac{d\Omega}{dx} = \frac{g\Omega\left(S_0 - S_f\right) + \rho_w l_2 + \rho_w \theta u_w q_{w,\perp}}{c^2 - \beta\left(Q/\Omega\right)^2} \tag{4.51}$$

where the celerity is given by equation (4.8). In principle, standard methods could solve this ODE but the presence of a singularity for trans-critical flows in which $Q/\Omega \cong c$ makes these methods fail. Specific methods derived for solving equation (4.51) require to set apart super- and sub-critical flows, and to treat the singularity (regime transitions) with caution.

The original method presented in this thesis consists in deriving a pseudo-unsteady equation instead of using the actual unsteady system or the simplified ODE. The pseudo-unsteady strategy consists in adding a pseudo-temporal term into the ordinary differential equation (4.50). This false time is denoted τ to avoid confusion with the full unsteady model. The introduction of the new term provides however an additional degree of freedom (parameter ω) that must be determined subsequently:

$$\omega\frac{\partial\Omega}{\partial\tau} + \frac{\partial\beta Q^2/\Omega + g l_1}{\partial x} = g\Omega\left(S_0 - S_f\right) + \rho_w l_2 + \rho_w \theta u_w q_{w,\perp} \tag{4.52}$$

In this model, the flow discharge is now a given parameter of the problem. The characteristic velocity λ is given by:

$$\lambda = \frac{c^2 - u^2}{\omega} = \frac{c^2\left(1 - Fr^2\right)}{\omega} \tag{4.53}$$

Table 2: Sign of the celerity of the pseudo-steady hydrodynamic model

	Fr < 1	Fr > 1
$\omega < 0$	$\lambda < 0$	$\lambda > 0$
$\omega > 0$	$\lambda > 0$	$\lambda < 0$

The sign of the real characteristic velocity only depends on the value of the degree of freedom ω and the flow regime. Table 2 shows that a supercritical flow ($|Fr| > 1$) requires only an upstream boundary condition if ω is negative, and only a downstream boundary condition if β is positive. The exact opposite conclusion holds for a subcritical flow ($|Fr| < 1$). Comparing the sign of λ with the sign of the characteristics velocities λ_1 and λ_2 of the full model gives an insight into the value of ω to select. Indeed, it has been shown that the system for unsteady flows requires two upstream boundary conditions for a supercritical flow (Table 1). As the discharge is assumed constant, the pseudo-unsteady model (4.52) would require only one upstream boundary condition for a supercritical flow if ω is chosen as negative. In conclusion, ω is imposed as negative in order to keep the new model consistent with the full unsteady model. What is more, the value of ω does not affect the rate of convergence of the scheme such that it can be simply set to ω=-sign(Q).

NUMERICAL MODEL: THE WOLF FLUX VECTOR SPLITTING

Because of its hyperbolic nature, I may successfully apply the Wolf FVS onto the pseudo-unsteady equation (4.52). The philosophy of the splitting is still to distinguish two parts in the equation. The convective terms are up-winded while the pressure terms are down-winded. The resulting numerical scheme can be written as follows:

$$\Omega_i^{n+1} = \Omega_i^n + \frac{\Delta\tau}{\Delta x}\left[\left(\beta QQ/\Omega + gI_1(\Omega)\right)\Big|_{i+1/2}^n - \left(\beta QQ/\Omega + gI_1(\Omega)\right)\Big|_{i-1/2}^n\right] - \Delta\tau g\left(\frac{\Omega_{i+1/2}^n + \Omega_{i-1/2}^n}{2}\right)\left(\frac{z_b\big|_{i+1/2}^n - z_b\big|_{i-1/2}^n}{\Delta x} - S_f\left(\Omega_i^n\right)\right) - \Delta\tau\left(\rho_w I_2 + \rho_w \theta u_w q_{w,\perp}\right)\Big|_i^n \tag{4.54}$$

Since the flow cross-section appears in both pressure and convective terms, its up-winding depends on the nature of the term in which it appears. The momentum of the fluid is a convective term such that we have:

$$\left(\beta\frac{QQ}{\Omega}\right)_{i+1/2}^n = \begin{cases} \beta QQ/\Omega_L^n & \text{if } u_L > 0 \text{ and } u_R > 0 \\ \beta QQ/\Omega_R^n & \text{if } u_L < 0 \text{ and } u_R < 0 \\ \left(\beta QQ/\Omega_L^n + \beta QQ/\Omega_R^n\right)/2 & \text{otherwise} \end{cases} \tag{4.55}$$

On the opposite, its value is down-winded in the pressure gradient:

$$gI_1\left(\Omega_{i+1/2}^n\right) = \begin{cases} gI_1\left(\Omega_R^n\right) & \text{if } u_L > 0 \text{ and } u_R > 0 \\ gI_1\left(\Omega_L^n\right) & \text{if } u_L < 0 \text{ and } u_R < 0 \\ \left(gI_1\left(\Omega_R^n\right) + gI_1\left(\Omega_L^n\right)\right)/2 & \text{otherwise} \end{cases} \tag{4.56}$$

The requirement of adequacy between the pressure term and the topographic slope gives:

$$\Omega_{i+1/2}^n = \begin{cases} \Omega_R^n & \text{if } u_L > 0 \text{ and } u_R > 0 \\ \Omega_L^n & \text{if } u_L < 0 \text{ and } u_R < 0 \\ \left(\Omega_R^n + \Omega_L^n\right)/2 & \text{otherwise} \end{cases} \tag{4.57}$$

and

$$z_b\big|_{i+1/2}^n = \begin{cases} z_b\big|_R^n & \text{if } u_L > 0 \text{ and } u_R > 0 \\ z_b\big|_L^n & \text{if } u_L < 0 \text{ and } u_R < 0 \\ \left(z_b\big|_R^n + z_b\big|_L^n\right)/2 & \text{otherwise} \end{cases} \tag{4.58}$$

STABILITY ANALYSIS

The Von Neumann stability shows that the scheme (4.54) is unconditionally stable if the parameter ω is negative. Indeed, the solution of equation (4.54) may be developed in a Fourier series that is written as:

$$\Omega_k^n = \sum_{m=-N}^{+N} \tilde{\Omega}_m^n e^{\left[i I_m\left(k\Delta x - c_m(I_m)\tau\right)\right]} \tag{4.59}$$

where N is the number of mesh intervals, k the mesh index, $i = \sqrt{-1}$, $\tilde{\Omega}_m^n$ the amplitude of the m^{th} harmonic, I_m[rad/m] the wave number, and c_m[m/s] has real and imaginary parts : $c_m = c_{rm}(I_m) + i c_{im}(I_m)$. The real part c_{rm} is the wave velocity. Physical significance of the

imaginary part is exposed below. In a one dimensional domain of length L, the fundamental frequency corresponds to the maximum wavelength of $\lambda_{max}=2L$, associated to the minimum value of wave number $l_{min}=\pi/L$. On the other hand, the maximum value of the wave number is given by $l_{min}=\pi/\Delta x$ associated with the shortest resolvable wavelength $\lambda_{min}=2\Delta x$ on the mesh grid chosen. All the harmonics represented on the finite mesh are given by:

$$l_m = k l_{min} = k\frac{\pi}{N\Delta x} \tag{4.60}$$

The solution (4.59) can be rewritten as follows:

$$\Omega_k^n = \sum_{m=-N}^{N} \widetilde{\Omega}_m^n e^{l_m c_{im}(l_m)\tau} e^{\left[i l_m\left(k\Delta x - c_{rm}(l_m)\tau\right)\right]} \tag{4.61}$$

The amplification rate of the wave in equation (4.61) is identified as the imaginary part c_{im} multiplied by l_m. The Von Neumann stability criteria imposes then that $k_m=l_m\ c_{im}(l_m) \le 0$ to ensure stability.

We now aim at determining the expression of the amplification rate k_m for the particular flux vector splitting introduced in (4.54). For a positive velocity, its discretised quasi-linear form is written as:

$$\omega\left(\frac{\partial\Omega}{\partial\tau}\right)_i + c^2\frac{\left(\Omega_{i+1}^n - \Omega_i^n\right)}{\Delta x} - u^2\frac{\left(\Omega_i^n - \Omega_{i-1}^n\right)}{\Delta x} = S_i^n \tag{4.62}$$

where S conflates all the source terms that does not affect the stability of the scheme. Inserting the Fourier series given by equation (4.59) into this quasi-linear scheme leads to:

$$-\omega i l_m c_m + c^2\frac{\left(e^{i l_m \Delta x} - 1\right)}{\Delta x} - u^2\frac{\left(1 - e^{-i l_m \Delta x}\right)}{\Delta x} = 0 \tag{4.63}$$

By introducing the trigonometric functions $e^{ix} = \cos x + i\sin x$, we simply obtain:

$$-l_m c_m = \frac{\left(u^2 - c^2\right)\sin\left(l_m\Delta x\right) + i\left(u^2 + c^2\right)\left[\cos\left(l_m\Delta x\right) - 1\right]}{\omega\Delta x} \tag{4.64}$$

The Von Neumann stability criteria established above states that the scheme is stable only if:

$$k_m = l_m c_{im} = \frac{-\left(u^2 + c^2\right)\left[\cos\left(l_m\Delta x\right) - 1\right]}{\omega\Delta x} \le 0 \tag{4.65}$$

which is unconditionally assured if the parameter ω is negative.

4.3 Reducing Oscillations: Alternative Numerical Schemes

Establishing an adequate mathematical model and developing a stable, efficient, and consistent numerical scheme is a necessary but not sufficient condition to meet success in CFD. Indeed, spurious oscillations have been reported at transition bores between free surface and pressurized flows. On top of reducing the accuracy of the results, these oscillations may compromise the stability of the computation. In this respect, the literature does offer neither a thorough explanation of their origin nor an efficient palliative to the problem.

This section provides a brief physical interpretation of the spurious oscillations as well as some elements of resolution. In particular, I show that spurious oscillations are due to an incorrect evaluation by the numerical scheme of the celerity in the transition finite volume. Consequently, I propose four other splittings that could reduce the intensity of these oscillations: Roe, AUSM, Lax-Friedrich and exact Riemann solver. The last one is an original result of this thesis.

4.3.1 Investigation into the Numerical Oscillations

Oscillations appearing in the solution of an unsteady computation may result from particular conditions of the problem. In such a case, variations correspond to a physical reality. The most common example in this respect is the water hammer resulting from the closure of a valve in a full pipe. Nevertheless, non-physical (i.e. numerical) oscillations are also frequently observed in steady and unsteady computations. Their presence contaminates the solution, reduce its reliability, and even compromises the stability in some cases. Sorting out numerical oscillations from transient variations is the daily work of CFD engineers. Their objective is to diminish the first category while strengthening the second.

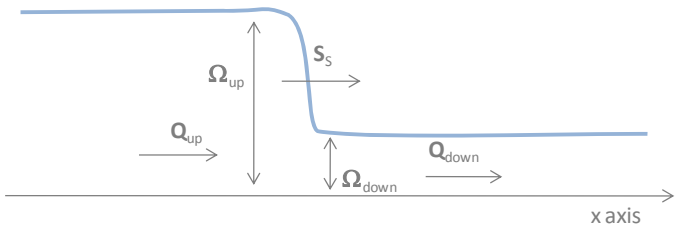

Figure 53: Rankine-Hugoniot conditions give the upstream pressure and shock velocity

The numerical oscillations that I am interested in accompany the computation of transition bores with “mathematical shock-capturing” methods for mixed flows. Many authors report such oscillations that can become very severe [12, 83, 110, 193, 248, 287, 307], and compromise the stability of the scheme. I present herein a concrete example of such oscillations (Figure 54). This case consists in a square pipe of 0.5m width. The conduit is assumed frictionless and horizontal. Initially, the water is at rest at 0.4m height (free surface flow). The celerity of the pressurized flow is equal to 10m/s. This value is chosen

artificially low in order to make appear small oscillations. A realistic value like 1200m/s would have instantaneously compromise the stability of the computation. A sudden inflow of 0.303m³/s at the upstream end of the pipe creates a moving transition bore. The transition propagates from the upstream to the downstream end of the pipe. Rankine-Hugoniot condition gives then the pressure upstream the transition (pressurized flow) and the shock velocity S_s (Figure 53):

$$\begin{cases} S_s = \dfrac{gI_1(\Omega_{down}) - gI_1(\Omega_{up})}{Q_{down} - Q_{up}} \\ S_s = \dfrac{Q_{down} - Q_{up}}{\Omega_{down} - \Omega_{up}} \end{cases} \tag{4.66}$$

which can be easily solved. Consequently, the shock propagates at 5.1m/s and the water height after the transition is 0.89m. Figure 54 compares the analytical water profile with the computed solution, 2 seconds after the inflow starts. Post-transition oscillations clearly appear in the graph. In this case, computation was performed with a Runge-Kutta RK22. The time step was 0.005s and the mesh size 0.1m.

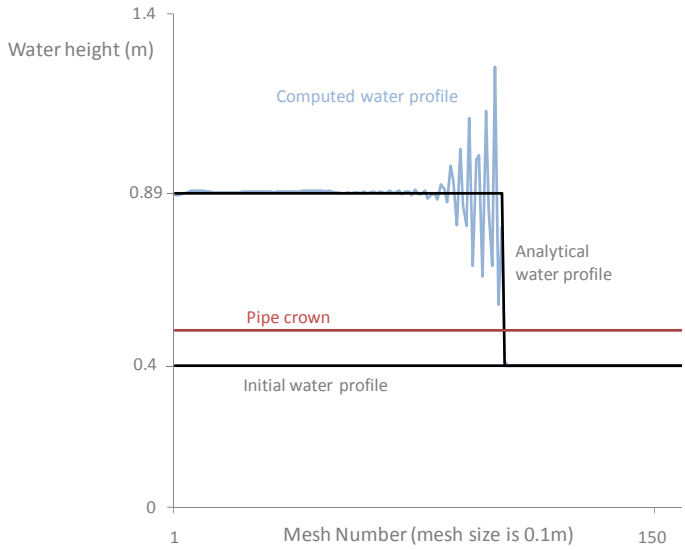

Figure 54: The numerical water profile after 2 seconds exhibits spurious oscillations at the transition bore

Systematic investigation of post-transition oscillations is very rare in literature. Regarding such study, Vasconcelos [298, 307] made a remarkable work of characterization and investigation of the spurious oscillations. He based his method on the mathematical approach of Arora and Roe [12]. In particular, he showed that the "strength of the numerical oscillations is associated with the sharp discontinuities in the flow parameters across the jump, particularly the wave celerity". What is more, he performed an extensive numerical investigation onto the characteristics of numerical oscillations generated with a numerical scheme employing the Roe solver [257]. The general conclusions were:

- Strong numerical oscillations occur only when a transition from free surface to pressurized flows goes with the shock.
- The strength of the oscillations increases with the pressure wave celerity.

- The period T and the wavelength W of the numerical oscillations comply with the predictions of Woodward and Colella [321]: The period is $T=\Delta x/S_s$ and the wavelength is $W=a\Delta x/S_s$ (a is the pressure wave celerity).
- The grid size has no direct relationship to the amplitude of the numerical oscillations. It affects only the oscillation period.
- Friction and diffusion tend to decrease the extent of the oscillations.

In this thesis, I do not intend to make such a large-scale research on the source and characteristics of the post-transition oscillations. My work only aims at validating briefly the conclusion of Vasconcelos and drawing some avenue worth exploring in this respect. By an original physical reasoning, I simply show that a discrepancy between the physical and numerical celerity causes the apparition of the oscillations. To my opinion, developing an oscillation-free numerical scheme requires to use an evolving grid. Such development is beyond the scope of this thesis.

The first step of my argument relies on the identification of the physical celerity in a transition mesh (upstream finite volumes are pressurized and downstream FV are at free surface). In this mesh, the transition propagates at a velocity S_s, which is the velocity of the shock formed by the discontinuity (Figure 55). In a very simple case like the one that I have proposed in the previous section, the transition forms a Riemann problem and the velocity S_s is constant all along the length of the finite volume. Consequently, the Rankine-Hugoniot relations (4.66) determine the shock-velocity.

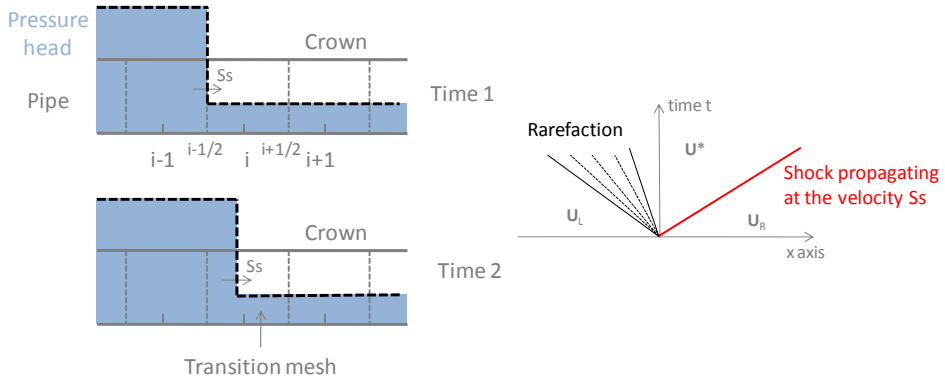

Figure 55: The transition propagates at a velocity given by the Rankine-Hugoniot conditions. This shock speed S_s is the celerity in the transition mesh.

The second step of the argument consists in identifying the approximate celerity given by the numerical scheme to the transition mesh. In particular, I show that two kinds of error affect this approximate celerity.

The first error is linked to the choice of the numerical flux. Indeed, the celerity actually captured within a computational mesh by a discretised conservative equation depends on the fluxes at the boundaries. By application of the definition of the celerity in the Saint-Venant equations, we have

$$c = \sqrt{\frac{\partial(gI_1)}{\partial\Omega}} \quad \rightarrow \quad c_i = \sqrt{\frac{gI_1\big|_{i+\frac{1}{2}} - gI_1\big|_{i-\frac{1}{2}}}{\Omega_{i+\frac{1}{2}} - \Omega_{i-\frac{1}{2}}}} \tag{4.67}$$

which is directly determined by the type of reconstruction and splitting adopted. In the case of WOLF splitting, the pressure splitting is always downstream. In the case of the rapid filling of the pipe from the upstream end, celerity remains thus low a very long time (Figure 58). On the opposite, the celerity remains high in case of rapid filling from the downstream end. Clearly, the splitting affects the computed celerity. The same remark applies for the shock velocity captured by the numerical scheme. Application of Rankine-Hugoniot relations (4.66) to discretised conservative equations gives

$$\begin{cases} S_S^i = \dfrac{gI_1\big|_{i+\frac{1}{2}} - gI_1\big|_{i-\frac{1}{2}}}{Q_{i+\frac{1}{2}} - Q_{i-\frac{1}{2}}} & \text{in the momentum equation} \\ S_S^i = \dfrac{Q\big|_{i+\frac{1}{2}} - Q\big|_{i-\frac{1}{2}}}{\Omega_{i+\frac{1}{2}} - \Omega_{i-\frac{1}{2}}} & \text{in the continuity equation} \end{cases} \tag{4.68}$$

which directly depends on the numerical scheme chosen. In fact, the evaluated velocity differs even between the momentum and continuity equations. This is clearly a source of error in the computation that became unacceptable if celerities vary rapidly within a single mesh.

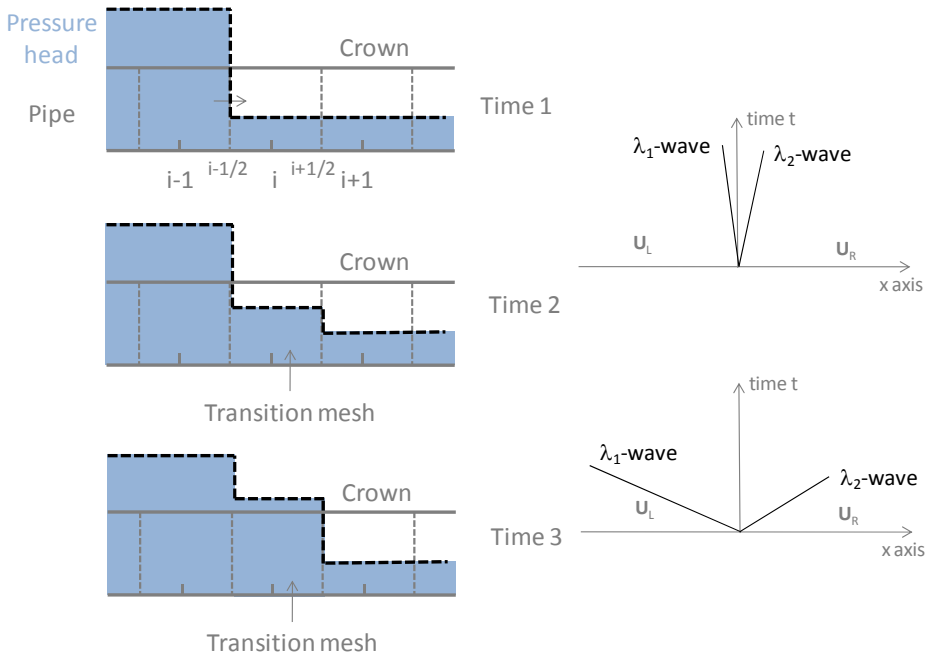

Figure 56: In a discretised domain, averaging the water section over the finite volume affects the structure of the solution in the transition mesh.

The previous argument suggests that an adequate numerical flux should fix the problem of post-transition oscillations. However, another source of error aggravates the previous error. It originates from the discretisation of the computational domain. In any finite volume scheme, a single value determines the water cross-section (or pressure head) in each mesh. Consequently, propagation of a transition translates into a slow elevation of the

free surface in the transition mesh (Figure 56). The celerity in such a mesh remains very low because it is still the celerity of a free surface flow. The structure of the waves differs notably from the one identified in Figure 55. Their velocity is indeed very close from the celerities given by the eigenvalues of the Jacobian matrix (Figure 56). When finally the free surface reaches the pipe crown, the celerity changes abruptly. Its value jumps in one time step from a free surface flow celerity (±10m/s) to a pressurized flow celerity (±1000m/s). The structure of the wave remains however analogous: celerities are very close to the eigenvalues of the Jacobian matrix. This error in the evaluation of the celerity is intimately linked to the discretised nature of the domain.

Consequently, comparison between the physical and numerical celerities in a transition mesh makes appear large discrepancies. Figure 57 compares the physical value with both the value due to the discretization of the domain and the value approximated by the WOLF FVS. The celerity computed with Wolf is clearly very different from the physical value. In particular, its value remains low so much time that the transition mesh plays the role of a boundary condition for the pressurized flows. When high velocity pressure waves reach the transition mesh, they found a very slowly changing mesh. They reflect on this mesh like a water hammer on an impermeable end of a pipe. This causes the oscillations observed

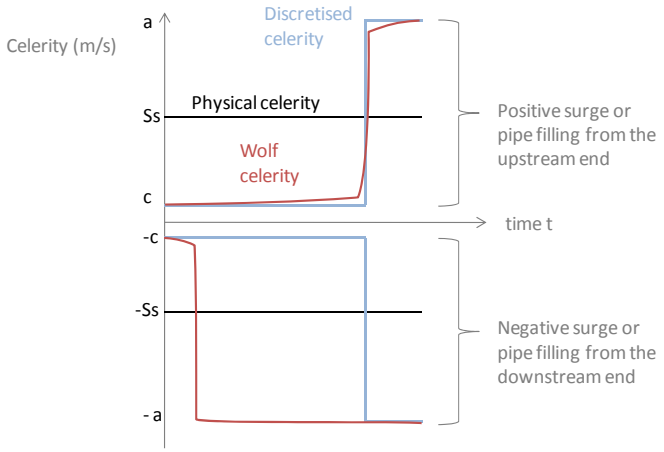

Figure 57: Comparison between the physical and numerical celerities makes appear discrepancies

Various remedies to the problem of numerical oscillations are available in literature. None of them gives full satisfaction, mainly because they introduce other undesirable effects into the solution [307].

1. The first approach consists in doing nothing and interpreting the results by the yardstick of their average value. This approach gives sufficiently good solution as long as numerical oscillations do not compromise the stability of the scheme.
2. The second and most frequent trick involves decreasing the pressure wave celerity to artificially low values such that the amplitude of the oscillations drastically declines. For steady and slowly-varying flows, this method gives excellent results as I will show in the following chapter. Nevertheless, it causes intolerable errors when applied to a transient flow like a water hammer. One can sometimes find a happy medium by increasing more

smoothly the celerity when the free surface reaches the pipe-crown. This is the basis of the modified Preissmann slot [192].

3. The third approach consists in using diffusive schemes like the Lax-Friedrichs method that damps numerical oscillations. Recent research even aims at localizing this diffusivity only in the neighborhood of the transition [307].
4. Filtering the numerical solution at each time step is the fourth method. This approach is highly critic since the filter must differentiate physical and numerical oscillations. Since both oscillations may have the same frequency, this distinction is often intractable.
5. The fifth approach is composed of various shock-tracking numerical schemes applied to a single mathematical model. Such moving-mesh methods always locate the transition at a boundary [110, 120-122, 135, 138, 150, 278].
6. The last approach makes use of efficient shock-capturing numerical schemes that give a good approximation of the celerity in transition meshes. In the following, we compare four different schemes in respect with their ability to provide a reliable celerity.

4.3.2 GODUNOV SCHEME COUPLED WITH THE ROE SOLVER

The Roe scheme is a very popular way to discretize hyperbolic systems of non-linear PDE's. It consists in a Godunov scheme coupled with an approximate Riemann solver. This last one gives in fact the exact solution to an approximate Riemann problem in which the equation is linear. Consequently, the Roe solver relies on the following linearization of the Saint-Venant equations whose applicability has been extended to pressurized flows:

$$\frac{\partial \mathbf{U}}{\partial t} + \underbrace{\begin{pmatrix} 0 & 1 \\ \tilde{c}_{i+1/2}^2 - \left(\tilde{Q}_{i+1/2} / \tilde{\Omega}_{i+1/2}\right)^2 & 2\tilde{Q}_{i+1/2} / \tilde{\Omega}_{i+1/2} \end{pmatrix}}_{\tilde{A}_{i+1/2}} \frac{\partial \mathbf{U}}{\partial x} = \mathbf{S} \tag{4.69}$$

where $\tilde{A}_{i+1/2}$ is called the "freezed" Jacobian matrix. This matrix is defined as the classical Jacobian matrix in which the values of the primitive unknowns are set to a given value. Obviously, this linearization only holds in the neighborhood of the boundary i+1/2. A different "freezing" is then required at each boundary. For the freezed values, several kinds of mean values are available in literature [30, 125, 257, 304]. I tested most of them. In accordance with [304, 307], I chose to approximate the flow cross-section with:

$$\tilde{\Omega}_{i+1/2} = \sqrt{\Omega_L * \Omega_R} \tag{4.70}$$

For the discharge, I chose:

$$\tilde{Q}_{i+1/2} = \frac{\sqrt{\Omega_L} * Q_L + \sqrt{\Omega_R} * Q_R}{\sqrt{\Omega_L} + \sqrt{\Omega_R}} \tag{4.71}$$

Finally, the most convenient average for the pressure wave celerity is given by [119]:

$$\tilde{c}_{i+1/2} = \begin{cases} \sqrt{\dfrac{g I_1(\Omega_R) - g I_1(\Omega_L)}{\Omega_R - \Omega_L}} & \text{if} \quad \Omega_R \neq \Omega_L \\ \dfrac{c(\Omega_R) + c(\Omega_L)}{2} & \text{if} \quad \Omega_R = \Omega_L \end{cases} \tag{4.72}$$

Expression (4.72) directly derives from the definition of the celerity (4.4).

Clearly, equation (4.69) is a linear system with constant coefficients that one can easily solve by decoupling the problem in the space of right eigenvectors. The resulting Roe numerical flux function is expressed as [257]:

$$F_{i+\frac{1}{2}} = \frac{1}{2}\left[F(\mathbf{U}_L) + F(\mathbf{U}_R)\right] - \frac{1}{2}\sum_{k=1}^{2} \tilde{\alpha}_k \tilde{\lambda}_k \tilde{\mathbf{R}}_k \tag{4.73}$$

where the physical fluxes are given by:

$$F = \begin{bmatrix} Q \\ Q^2/\Omega + g I_1(\Omega) \end{bmatrix} \tag{4.74}$$

The eigenvalues are written as follows:

$$\tilde{\lambda}_{1-2} = \tilde{Q}_{i+\frac{1}{2}} / \tilde{\Omega}^R_{i+\frac{1}{2}} \pm \tilde{c}_{i+\frac{1}{2}} \tag{4.75}$$

and the wave strengths are given by:

$$\begin{aligned} \tilde{\alpha}_1 &= \left[-\tilde{\lambda}_2\left(\Omega_R - \Omega_L\right) + \left(Q_R + Q_L\right)\right] / 2\tilde{c}_{i+\frac{1}{2}} \\ \tilde{\alpha}_2 &= \left[\tilde{\lambda}_1\left(\Omega_R - \Omega_L\right) - \left(Q_R + Q_L\right)\right] / 2\tilde{c}_{i+\frac{1}{2}} \end{aligned} \tag{4.76}$$

For the right eigenvectors, we have:

$$\tilde{\mathbf{R}}_1 = \begin{bmatrix} 1 & \tilde{\lambda}_1 \end{bmatrix}^T \quad \text{and} \quad \tilde{\mathbf{R}}_2 = \begin{bmatrix} 1 & \tilde{\lambda}_2 \end{bmatrix}^T \tag{4.77}$$

When using a linearized Riemann solver, the resulting approximate Riemann solution consists only of discontinuities, with no rarefaction waves. This is known to lead to a violation of the entropy condition [197, 258, 285, 321]. Such entropy-violating solutions cause difficulties in the case of a trans-critical rarefaction wave. In this case, it is necessary to modify the Roe solver in order to obtain entropy-satisfying solutions. For this purpose, I use the Harten-Hyman Entropy Fix [139] which defines new wave speeds:

$$\bar{\lambda}_i = \lambda_i^R \left(\left(\tilde{\lambda}_i - \lambda_i^L\right) / \left(\lambda_i^R - \lambda_i^L\right) \right) \tag{4.78}$$

One major problem of the Roe solver is its inability to discretize a non-conservative model like the Saint-Venant equations in terms of free surface slope. For this model, I tried to find an efficient formulation but all my attempts failed. From a more general point of view, discretizing any source term with the Roe scheme turns out to be difficult. In this respect, two families of methods try to make source and flux terms compatible: using well-balanced schemes [196, 308, 309] and adding complementary PDE's for the evolution of source terms [30, 111, 195]. This issue is beyond the scope of this thesis such that I limit my research to uniform pipes.

In 2009, Vasconcelos [307] modified the classical Roe scheme in order to attenuate post-transition oscillations. The proposed approach gradually increases the eigenvalues of a computational cell by adding a term to this wave speed that depends on the proximity of the flow discontinuity and $\Delta x/\Delta t$:

$$\lambda_{1-2} = \min\left[\frac{\Delta x}{\Delta t}, \left|\tilde{Q}_{i+\frac{1}{2}} \Big/ \tilde{\Omega}_{i+\frac{1}{2}} \pm \tilde{c}_{i+\frac{1}{2}}\right| + (1-L)\left(\Delta c_{i+\frac{1}{2}}\right)^{L} \frac{\Delta x}{\Delta t}\right] \tag{4.79}$$

where the parameter L ranges from 1 to 0. The proximity of the flow discontinuity is determined by a nonlinear, dimensionless function of the spatial variation of the flow celerity:

$$\Delta c_{i+\frac{1}{2}} = \frac{\left|\tilde{c}_{i+1} - \tilde{c}_i\right|}{\max\left(\left|\tilde{c}_{i+1} - \tilde{c}_i\right|\right)} \tag{4.80}$$

My tests show that the modified method gives good results in many cases but increases instability in specific cases with slowly moving transitions. This explains that we prefer to use the classical scheme.

4.3.3 AUSM SCHEME

Introduced by Liou in [101, 201-206], the AUSM scheme is an intermediate method between the Godunov approach and a flux vector splitting. It distinguishes itself by its simplicity. It is known to compete and even to surpasse Roe's solver in some cases. The numerical flux function consists in separating the convective component of the flux from the pressure component:

$$F_{i+\frac{1}{2}} = Fr_{i+\frac{1}{2}} \begin{pmatrix} c\Omega \\ cQ \end{pmatrix}_{L/R} + \begin{pmatrix} 0 \\ P_{1u}\big|_{i+\frac{1}{2}} \end{pmatrix} \tag{4.81}$$

AUSM method gives birth to a whole family of schemes differing by the choice of the interfacial Froude and pressure. I use the following functions [286] for the pressure:

$$gI_1\big|_{i+\frac{1}{2}} = \left(gI_1\big|(\Omega_L)\right)^{+} + \left(gI_1\big|(\Omega_R)\right)^{-} \tag{4.82}$$

where the split functions for the pressure are chosen as:

$$p^{\pm} = \begin{cases} 1/4\, p(Fr \pm 1)^2 (2 \mp Fr) & \text{if } |Fr| \le 1 \\ p\left(Fr \pm |Fr|\right)/2Fr & \text{if } |Fr| > 1 \end{cases} \tag{4.83}$$

For the boundary Froude number, we have:

$$Fr_{i+\frac{1}{2}} = \left(Fr^{R}\right)^{+} + \left(Fr^{L}\right)^{-} \tag{4.84}$$

where the split functions for the Froude are given by:

$$Fr^{\pm} = \begin{cases} \pm 1/4 (Fr \pm 1)^2 & \text{si } |Fr| \le 1 \\ \left(Fr \pm |Fr|\right)/2 & \text{si } |Fr| > 1 \end{cases} \tag{4.85}$$

Finally, we have for the convective flux a simple splitting:

$$(\bullet)_{L/R} = \begin{cases} (\bullet)_L & \text{if } Fr_{i+\frac{1}{2}} \ge 0 \\ (\bullet)_R & \text{if } Fr_{i+\frac{1}{2}} < 0 \end{cases} \tag{4.86}$$

4.3.4 GODUNOV SCHEME COUPLED WITH AN EXACT RIEMANN SOLVER

Godunov method consists in considering conservative variables as piecewise constant over the mesh cells at each time step. The time evolution is determined by the solution of the Riemann Problem (RP) arising at each mesh boundary. I propose here an efficient exact

Riemann solver for the Saint-Venant equations whose applicability is extended to pressurized flows as well. The solver is developed by analogy with the work of Toro on shallow water equations [286]. The demonstration relies on the non-linear analysis performed in section 4.1. I have submitted these results to the International Journal for Computational and Applied Mathematics [168].

In this method, the root of an algebraic equation gives the solution to the Riemann problem:

$$f\left(\Omega^*\right) \equiv f_L\left(\Omega^*, \Omega_L\right) + f_R\left(\Omega^*, \Omega_R\right) + u_R - u_L = 0 \tag{4.87}$$

According to section 4.1, the function f_L for the left wave is given by:

$$f_L\left(\Omega^*, \Omega_L\right) = \begin{cases} \phi\left(\Omega_L\right) - \phi\left(\Omega^*\right) & \text{if } \Omega^* \le \Omega_L \quad \text{(left wave is a rarefaction)} \\ \sqrt{\frac{\left[gI_1\left(\Omega_L\right) - gI_1\left(\Omega^*\right)\right]\left(\Omega_L - \Omega^*\right)}{\Omega_L \Omega^*}} & \text{if } \Omega^* > \Omega_L \quad \text{(left wave is a shock)} \end{cases} \tag{4.88}$$

and for the right wave, we have:

$$f_R\left(\Omega^*, \Omega_R\right) = \begin{cases} \phi\left(\Omega_R\right) - \phi\left(\Omega^*\right) & \text{if } \Omega^* \le \Omega_R \quad \text{(right wave is a rarefaction)} \\ \sqrt{\frac{\left[gI_1\left(\Omega_R\right) - gI_1\left(\Omega^*\right)\right]\left(\Omega_R - \Omega^*\right)}{\Omega_R \Omega^*}} & \text{if } \Omega^* > \Omega_R \quad \text{(right wave is a shock)} \end{cases} \tag{4.89}$$

The solution for the discharge Q^* is consequently written:

$$Q^* = \frac{\Omega^*}{2}\left(u_R + u_L\right) + \frac{\Omega^*}{2}\left[f_L\left(\Omega^*, \Omega_L\right) + f_L\left(\Omega^*, \Omega_R\right)\right] \tag{4.90}$$

A Newton-Raphson scheme solves equation (4.87) at each time step and at each boundary. The results Ω^* and Q^* fully determine the solution of the Riemann problem.

The function ϕ results from the expression of the consistency of generalized Riemann invariant. As I previously mentioned, computing the generalized Riemann invariant is difficult since it depends on the shape of the closed section. There is no general analytical solution. It explains the introduction of a generic function ϕ that needs to be determined prior any computation:

- For a rectangular section, the function ϕ is given by:

$$\phi\left(\Omega\right) = \begin{cases} 2c\left(\Omega\right) & \text{if the flow is free-surface} \\ \phi_{SL}\left(\Omega_{max}\right) + 2a\left(\sqrt{\Omega / \Omega_{max}} - 1\right) & \text{if the flow is pressurized} \end{cases} \tag{4.91}$$

- For a circular section, the function results from a Taylor expansion [192]:

$$\phi\left(\Omega\right) = \begin{cases} \sqrt{\frac{gR}{4}}\left[\sqrt{3}\,\theta - \frac{\sqrt{3}}{80}\theta^3 + \frac{19\sqrt{3}}{448000}\theta^5 + \frac{\sqrt{3}}{10035200}\theta^7 + \frac{491\sqrt{3}}{27\times 7064780800}\theta^9\right] & \\ & \text{if the flow is free-surface} \\ \phi_{SL}\left(\Omega_{max}\right) + 2a\left(\sqrt{\Omega / \Omega_{max}} - 1\right) & \text{if the flow is pressurized} \end{cases} \tag{4.92}$$

Cunge proposes that the formula for rectangular cross-section should be used in most cases [63]. I found that the proposition holds for most prismatic channel but may cause inaccuracy in some cases.

Once Ω^* and Q^* are known, the speed of both shock and rarefaction is easy to compute thanks to equations (4.18) and (4.20) for shocks and equations (4.28) for rarefactions. Consequently, it is easy to compute Godunov fluxes by evaluating the physical flux with the solution of the Riemann problem along the axis x/t=0. Depending on the sign of the wave velocities, the value $\mathbf{U}(x/t=0)$ may be the left state $\mathbf{U_L}$, the right state $\mathbf{U_R}$ or the star state $\mathbf{U}^*$. If the axis x/t=0 is inside a rarefaction, one may additionally solve equation (4.30) to find the exact value $\mathbf{U}(x/t=0)$.

4.3.5 LAX-FRIEDRICH SOLVER

The Lax-Friedrich (LxF) method relies on the following numerical flux function:

$$F_{i+1/2} = \frac{1}{2}\left[F\left(\mathbf{U}^L_{i+1/2}\right) + F\left(\mathbf{U}^R_{i+1/2}\right)\right] - \frac{\Delta x}{2\Delta t}\left(\mathbf{U}^R_{i+1/2} - \mathbf{U}^L_{i+1/2}\right) \tag{4.93}$$

where F is the physical flux. It is known to introduce a consequent amount of numerical diffusion in the system [197]. Actually, the scheme adds much more diffusion than required to stabilize the solution and tends to smear out discontinuities. This feature has proved valuable in order to attenuate post-transition oscillations.

Summary and conclusion

Since no analytical solution exists for the new model, discretizing the equations is the only way to apply it on real cases. Consequently, a part of my research was dedicated to the establishment and implementation of discretised equations for pure water mixed flows.

First, investigations into the fundamental mathematical properties of a system of PDE's have given useful insight into the properties of information propagation and into the boundary conditions to prescribe (section 4.1). The linear analysis has identified two flow regimes: super-critical flow and sub-critical flow. At each flow regime correspond specific boundary conditions. Finally, the non-linear analysis has shown the apparition of shocks and rarefactions in the solution of the Riemann Problem.

Implementation of the new equations into the computational code WOLF has been presented in section 4.2. For this purpose, the system of PDE's has been discretised with the WOLF splitting. In addition, a fast universal solver for steady flows has enabled to reduce the computation time. This original scheme relies on a pseudo-unsteady strategy and a reformulation of the equations in order to keep the hyperbolic nature of the problem.

Finally, I have given an original insight into the problem of post-transition numerical oscillations (section 4.3). As physical reasoning highlights, oscillations originate from an incorrect evaluation of the pressure wave celerity in transition meshes. The inaccuracy results from the discretization of both the computational domain and the fluxes equations. The first source of error cannot be tackled without abandoning "numerical shock-capturing" schemes. Nevertheless, using alternative numerical schemes should diminish the second source of error. In this respect, I have introduced four alternative solvers: the Roe solver, the Lax-Friedrich scheme, the AUSM splitting and an exact Riemann solver. This last one is original.

In conclusion, the current chapter gives a theoretical background for the numerical simulation of single-phase mixed flows. Implementation of these models into the modelling system Wolf paves the way to validation and application of the research. Extending the applicability of WOLF1D to pressurized flows opens indeed a new horizons for application: sewer systems, water networks, galleries,… Notably, I present in the next chapter its application on two cases: the design of a city low-pressure network, and the design of a sewer system.

Chapter 5 Pure Water Flows: Validation and Application

Chapter aims at:

- ✓ validating the new model on published benchmarks;
- ✓ comparing the performance of various numerical schemes;
- ✓ preparing the development of a multiphase computational code;
- ✓ applying the modified module WOLF1D on practical cases.

In chapter 3, combining the TPA, Dual, and Preissmann models has given an original state-of-the-art model for pure water mixed flows. This model relied on the Saint-Venant equations. A modified pressure term extended their applicability to pressurized flows. Such a mathematical model would be useless if the solution cannot be found. In this respect, numerical schemes introduced in chapter 4 provided approximate solutions for most of the practical cases. Linear and non-linear analysis already gave insight into the performance of the models. Nevertheless, such theoretical analysis does not replace a thorough validation by comparison with analytical, numerical, and experimental data.

This chapter is dedicated to the validation of the modified module WOLF1D (whose applicability has been extended to pressurized flows) on published benchmarks and to its application on actual cases. In particular, comparing the performance of the various schemes enables a coherent choice for the best-suited numerical flux for the applications. This argued comparison is especially valuable for developing a multiphase computational code in the next chapters.

In the course of this doctoral research, more than 50 validation benchmarks have been considered. It amounts to hundreds of simulations that validate the mathematical model, its discretization, as well as its implementation. As pointed in section 5.1, this campaign of validation confirmed the ability of the new model to simulate consistently pure water mixed flows (i.e both free surface and mixed flows), including sub-atmospheric pressurized flows. The comparison between the six solvers (Wolf, Wolf pseudo-unsteady, Roe, Exact Riemann, AUSM, and Lax-Friedrich) underlines advantages and backwards of each method. For different reasons commented in the next section, I choose to use exclusively the Wolf splitting (unsteady and pseudo-unsteady) in the following.

Once validated, the modified module WOLF1D has served for assessing the hydraulic design of two different sewer systems: the storm water gravity drainage system of an airport (section 5.2), and a city low-pressure sewer network (section 5.3). In the first case, frequent inundations of the airport's parking facilities prompted authorities to assess the design of the gravity sewer network. Based on the performance criteria prescribed by the norm

prEN752-4:1997, WOLF1D is shown to be an efficient tool to make the hydraulic design. Thanks to steady and unsteady simulations, the model enables indeed to identify four causes for the inundations. It also paves the way for adapting the deficient network. In the second case, the sewer system is very different since it involves low-pressure pipes. Pumping stations intercept waters from the old drainage system and inject them into a pressurized pipe. Consequently, both steady and transient phenomena are critical in the assessment of its hydraulic design. In this respect, the use of WOLF1D enables to identify various defects in the first design of the low-pressure pipe. They originate from the apparition of negative pressure in transient phenomena, from a wrong choice for certain pumps, and from insufficient velocity for flushing out some pipes.

In conclusion, the new module WOLF1D whose applicability has been extended to pressurized flows is a useful and efficient tool for simulating pure water flows. It constitutes a reliable basis for many practical problems arising in civil and environmental engineering. However, it still suffers two major shortcomings that prevent its application in some problems: post-transition oscillations may cause the instability of the computation, and the code neglects air-water interactions in the pipe. The cause of the first shortcoming has been identified in chapter 4. Solving this problem requires using self-adapting mesh grid which is out of the scope of this thesis. On the other hand, Part II proposes a method for integrating the effect of the air phase.

5.1 Validation on Benchmarks and Choice of Scheme

For a hydraulic software, validating the mathematical model, its discretization, and its implementation is a prerequisite to any industrial application. For this purpose, I have considered more than 50 validation benchmarks in the course of my doctoral research. It amounts to hundreds of simulations that consider successively free surface (including sub-, trans-, and super-critical regimes), pressurized, and mixed flows. Benchmarks include both steady and transient cases. The current section summarizes the result of this campaign. First, the validity of the mathematical model is assessed. Next, performances of the various solvers are compared.

For the sake of simplicity, I do not present here the results of each benchmark (in any case, it would be materially impossible). Instead, Table 3 gives a qualitative summary of the conclusions drawn from the whole validation campaign. Considering fifteen criteria, each solver is attributed an appreciation for its performance. The grade '++' designates an excellent behavior with respect to the criterion considered. On the opposite, the grade '--' accounts for a poor performance. In-between, grades '-' and '+' denote a rather bad performance and a rather good behavior.

Table 3: The qualitative comparison of the performances of each solver underlines their respective advantages and backwards. Evidence suggests that the Wolf splitting constitutes a satisfactory choice.

Property	Wolf Unsteady	Wolf Pseudo-unsteady	Roe	Exact Riemann	AUSM	Lax-Friedrich
Consistency for						
- Pressurized flow	++	++	++	++	++	++
- Free surface flow	++	++	++	++	++	++
- Mixed flow	++	++	++	++	++	++
Sub-atmospheric Pressure	++	++	++	++	++	++
Capture of shock	-		++	++	-	-
Capture of rarefaction	+		++	++	+	-
Capture of dry bed	++	++	+	+	+	+
Imposition of BC	-	-	++	++	++	++
Regime transition	++	++	-	++	++	+
Steady Discharge profile	++	++	-	-	-	-
Source terms treatment	++	++	-	-	-	-
Non uniform pipes	++	++	-	-	-	-
Computation Time	+	++	-	--	+	+
Transition Free surface/pressurized	-	-	+	+	-	--
Robustness of the scheme	+	+	++	-	-	+

First, validation campaign aims at assessing the ability of the new mathematical model to simulate with consistency pure water mixed flows, including sub-atmospheric pressurized flows. In other words, simulations check the consistency of the mathematical model whatever discretization scheme used. Simulations underlined this consistency for pressurized flows, free surface flows (including sub-, super-, and trans-critical regimes), and mixed flows (three first criteria of Table 3). It confirms the theoretical results of the previous section.

Subsequent criteria of Table 3 assess the performances of each solver, namely the Godunov method with both the Roe solver and the original exact Riemann solver, the Lax-Friedrich scheme, the AUSM splitting, and the Wolf flux vector splitting. Successively, I evaluate their ability to handle with shocks, rarefactions, dry beds, regime transitions, source terms, and transition bores.

In this respect, Godunov methods with the exact Riemann solver and the Roe solver offer analogous results. They present an excellent ability to capture shocks and rarefactions in pressurized flows. In free surface flows, both solvers adequately capture fixed and mobile hydraulic jumps. They also present the better results with respect to the transition free surface/pressurized flows. Nevertheless, spurious oscillations still appear for important pressure wave celerities. What is more, the Roe solver has some difficulties to handle with critical points, even with an entropy fix. Both solvers require complicated discretization of the source terms. In other words, no formulation exists for the non-conservative form of the Saint-Venant equations and the discretization of the second pressure terms gI_2 turns out to be difficult. Finally, simple discretizations of source terms create discontinuities in the discharge profile of a steady flow. In conclusion, the exact Riemann solver causes an increase in computation time but does not improve substantially the performance of the Godunov method (in comparison with the Roe approximate solver). What is more, complexities arising in the discretisation of the source term make them difficult to apply on actual applications.

The Lax-Friedrich splitting provides the poorest results in most of the cases. Especially, inacceptable diffusion is created by the disparities in the eigenvalues of the Jacobian matrix. It causes error in both the propagation velocity and the amplitude of shocks. Trans-critical points are also affected by the diffusion. Even if the diffusion reduces the amplitude of spurious oscillations at the transition bore, they may become sufficiently important to compromise the stability (even for low celerities). In conclusion, all these shortcomings make the Lax-Friedrich inadequate for an industrial computational code. Nevertheless, it shows that important diffusion may reduce the amplitude of post-transition oscillations.

The AUSM scheme also presents insufficient performances to be used in practical applications. Granted, it shows a certain ability to treat regime transitions. Nevertheless, the splitting captures shocks and rarefactions with difficulty. What is more, important oscillations appear at the transition bore. Their intensity is sufficient to compromise the stability, even with low pressure wave celerity. Finally, the complexity of the splitting makes difficult a consistent discretization of the source terms. For steady cases, it creates discontinuities in the discharge profile. For non-uniform pipes, it prevents from using the non-conservative form of the Saint-Venant equations (in terms of free surface elevation).

Finally, the home-made Wolf splitting turns out to be an adequate compromise between simplicity, robustness, and accuracy for the treatment of convective, pressure, and source terms. It makes the scheme particularly suited for developing industrial softwares. This choice relies on a conjunction of favorable results. First, the Wolf splitting gives valuable results in presence of dry bed and rarefactions. Next, it easily captures regime transitions in free surface flows. In addition, the treatment of source terms is easy. This conclusion is particularly true for the non-conservative form of the Saint-Venant equations. The computation time remains moderated. In case of steady flows, this effort decreases drastically by using the pseudo-unsteady strategy. Finally, the scheme seems particularly robust. Nevertheless, the splitting still suffers a number of shortcomings. The capture of shock appears difficult when using first order time integration. This flaw is addressed by using diffusive three-step Runge-Kutta schemes. What is more, the imposition of Boundary conditions is restrictive. The splitting has indeed no tolerance for BC differing from the physically required one. Finally, spurious oscillations affect the transition free surface/pressurized flows. This flaw may be slightly reduced by using a three-step Runge-Kutta time integration and reducing the pressure wave celerity. Finally, HACH unit disposes of a solid knowledge in the use of this splitting.

In conclusion, the campaign of validation of the new model has proven its consistency for simulating pure water free surface, pressurized, and mixed flows. In particular, the equations account adequately for sub-atmospheric pressure. The comparison between the six solvers (Wolf, Wolf pseudo-unsteady, Roe, Exact Riemann, AUSM, and Lax-Friedrich) underlines advantages and backwards of each method. Results suggest that the Wolf splitting proposes the best compromise between simplicity, robustness, and accuracy for the treatment of convective, pressure, and source terms. The key argument here is the easy treatment of source terms. In order to explicit a little bit more the previous comparison and give a scientific basis to the grades given in Table 3, I present here the results of six validation benchmarks. They consider pressurized, free surface, and mixed flows.

5.1.1 WATER HAMMER

A water hammer is a pressure surge resulting from a rapid change in fluid velocity. It occurs only in pressurized flows and constitutes the most transient phenomenon that may affect pipe flows. Consequently, it is a first-choice case to assess the validity of the model in presence of transient pressurized flows, including the apparition of sub-atmospheric pressures. As shown by the two following benchmarks, the new mathematical model successfully describes the main features of a water hammer, namely its amplitude and its propagation velocity. The comparison between the five numerical solvers introduced in Chapter 4 underlines the particular ability of the Godunov schemes to treat discontinuities. On the other hand, FVS schemes are shown not sufficiently diffusive to remain stable in case of water hammer. Using a diffusive time integration method fixes this problem. Finally, Wolf splitting exhibits an important sensitivity to the incorrect imposition of boundary conditions.

ANALYTICAL CASE: VALVE CLOSURE AT THE UPSTREAM END OF A PIPE

This analytical benchmark consists in a water hammer due to the instantaneous closure of a valve at the downstream end of a pipe. It considers a 600m long circular pipe (1m diameter). The pipe is horizontal and frictionless. The pressure wave celerity is 1200m/s. The initial condition is a steady pressurized state with a discharge of 0.477m³/s and a constant pressure head of 45m. Along the computation, the downstream pressure head is kept constant at 45m. At the upstream extremity, the discharge is instantaneously decreased from 0.477m³/s down to 0.077m³/s in order to produce a transience that propagates along the pipe.

Joukowsky equation [325] provides an analytical solution for the water hammer pulse induced by the diminution of the inflow rate:

$$\Delta H = \frac{a\Delta v}{g} = a\frac{\Delta Q}{g\Omega} = \frac{1200 * 0.4}{9.81 * 0.7854} = 62.3\text{m} \tag{5.1}$$

In conclusion, the reduction of the inflow rate at the upstream end creates a decrease of the pressure down to -17.3m. This negative wave propagates from the upstream end up to the reservoir at a velocity of 1200m/s. At the downstream end, the wave reflects after 1s and creates a pressure surge up to 107.9m. This wave propagates from the downstream up the upstream at 1200m/s. In this manner, the wave propagates back and forth until the numerical diffusion cancels its amplitude.

For all the numerical schemes, the comparison between the analytical and the numerical time evolution of the pressure head at the valve shows an overall good agreement (Figure 58). In particular, the model accounts adequately for sub-atmospheric pressurized flows. It proves that the modified pressure term (3.20) correctly extends the applicability of Saint-Venant equations to pressurized flows. This computation is performed on 600 meshes and using a constant reconstruction for all schemes. The Roe solver, the Exact Riemann solver, and Lax-Friedrich scheme make use of one-step time integration with a CFL number of NbC=0.9. On the opposite, the Wolf scheme (with conservative and non-conservative equations) as well as the AUSM scheme make use of a three-step Runge-Kutta scheme RK31C (a_1=0.291 and a_2=0.215), which is known to be relatively diffusive. The CFL number is NbC= 0.5. Single- and two-step Runge-Kutta schemes are indeed unstable with the WOLF and AUSM solvers. These instabilities originate from the very feeble diffusion that affects the pressure gradient. This feature is characteristic of FVS schemes.

A more detailed analysis of Figure 58 gives further insight into the performance of the numerical schemes. In the first graph, the Wolf scheme provides the exact same solution for the conservative and non-conservative forms of the equations. This is a first validation of our expression of the Saint-Venant equations in terms of free surface elevation. In the five first graphs, comparison of the numerical solution with the analytical solution gives an idea of the amount of numerical diffusion that affects the solution. In most of the cases, this amount remains limited. In the sixth graph that gives a focus onto the water hammer shock, one can observe that Roe solver and Exact Riemann solver give an analogous

solution, while Lax-Friedrich, Wolf and AUSM provide much diffusive solutions. This is a first proof of the particular ability of Godunov schemes to treat shocks.

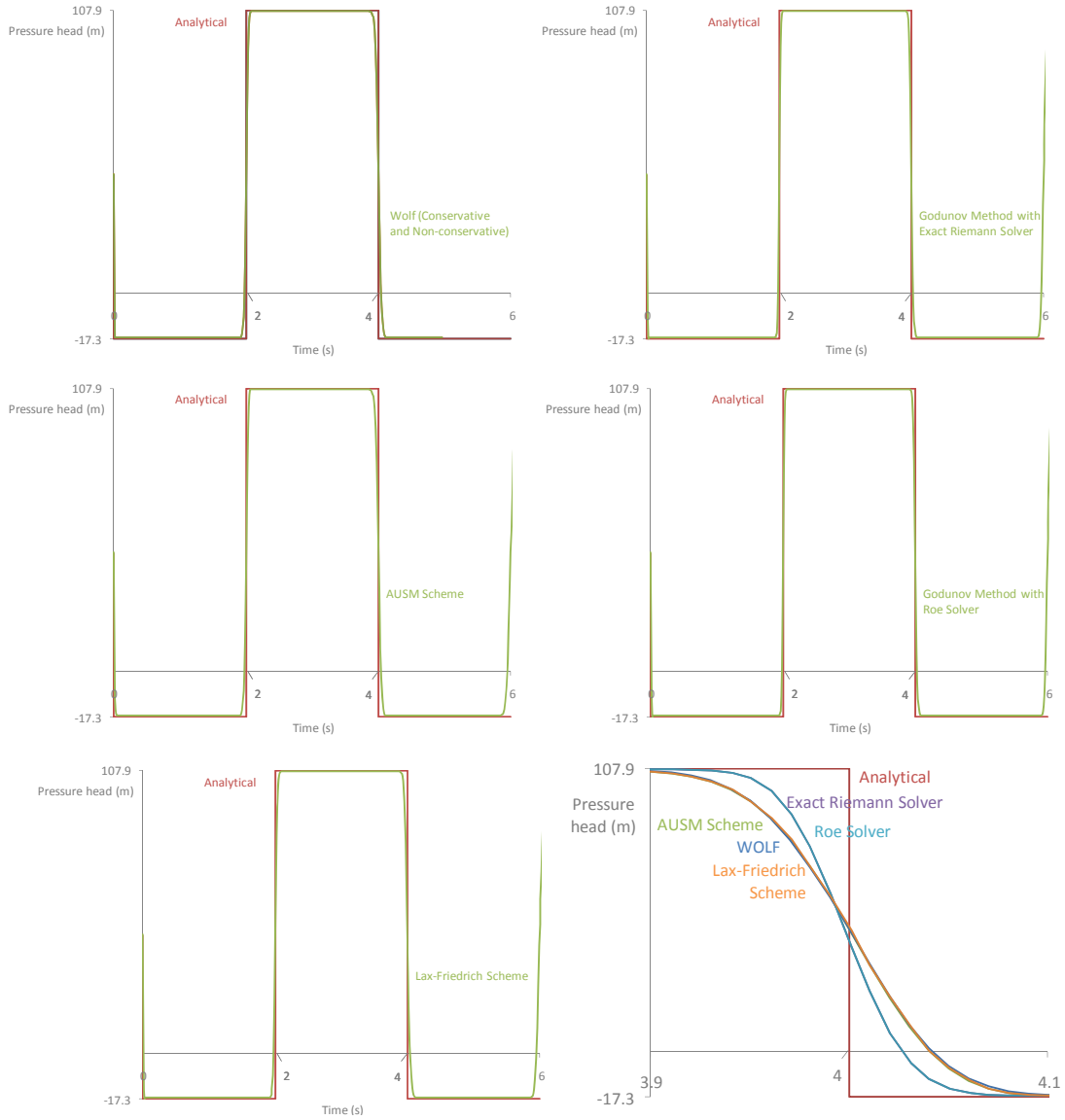

Figure 58: The comparison between the analytical and numerical solutions exhibits the ability of the model to simulate transient pressurized flows, including sub-atmospheric pressures.

NUMERICAL CASE: WYLIE&STREETER VALVE CLOSURE

Originally proposed by Wylie&Streeter in [325], this classical benchmark consists in a water hammer due to the progressive closing of a downstream valve. The case includes a 600m long pipeline having a horizontal slope. The pipe is circular and has a diameter of 0.5m. The friction factor of the conduit is constant at f=0.012. The celerity is 1200m/s. The pipe connects upstream to a reservoir at constant level (150m) and downstream to a valve that closes according to the following equation:

$$Q\left[m^3/s\right] = 0.477 * \left(1 - \left(\frac{t[s]}{2.1}\right)^{0.75}\right) \tag{5.2}$$

The closure of the pipe creates a pressure surge that propagates from the downstream end up to the reservoir at 1200m/s. This wave reaches the reservoir after 1s and reflects on this boundary. It results in an increase of the pressure that propagates from the reservoir up to the valve. Contrary to the case of the instantaneous closure, the wave presents here a smooth front.

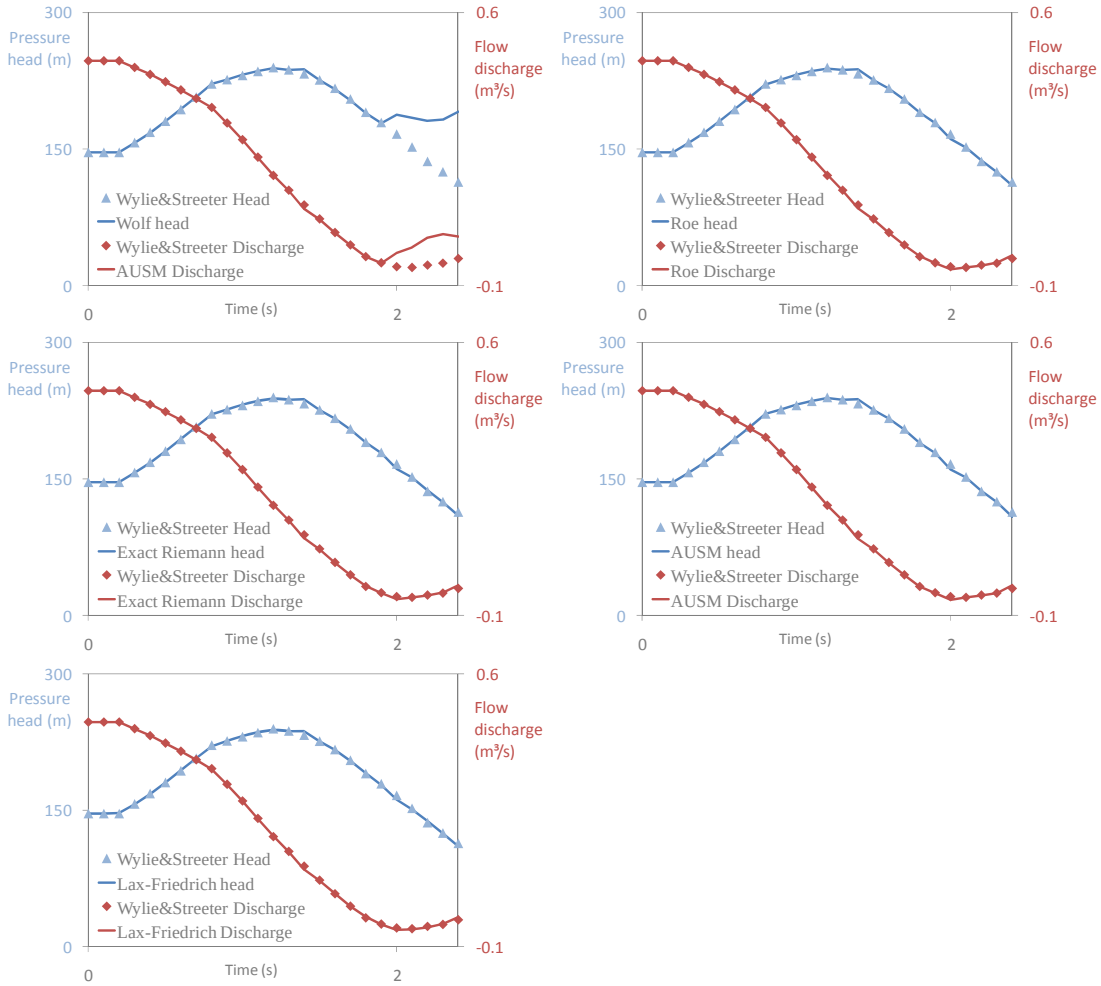

Figure 59: Computed time evolutions of the pressure head and the discharge at 360m from the reservoir show good agreement with the numerical data from Wylie and Streeter [325]

As pointed on Figure 59, computed time evolutions of the pressure head and the discharge at 360m from the reservoir show good agreement with the data from Wylie and Streeter [325]. It proves again the validity of the new equations. These reference data were computed with a classical Method Of Characteristics (MOC) scheme. They have been widely validated in literature. Computation is here performed on a 600 cells uniform grid. For the Roe solver, the Exact Riemann solver, and the Lax-Friedrich scheme, I use a one-step time integration with a CFL Number of NbC=0.5. On the opposite, AUSM and Wolf schemes are unstable for single- and two-step Runge-Kutta methods. Consequently, I use a three-step Runge-Kutta scheme RK31C (a_1=0.291 and a_2=0.215) with a CFL number of NbC=0.25. This issue reinforces the conclusion of the previous benchmark about the feeble numerical diffusion in FVS schemes. In addition, the first graph in Figure 59 makes appear a

divergence between reference data and values computed with the Wolf splitting after 1.9s of simulation. This is a direct consequence of an improper imposition of Boundary Conditions (BC). The Wylie and Streeter benchmark imposes indeed the upstream pressure head and the downstream discharge. The Wolf splitting requires the exact opposite: the discharge upstream and the pressure downstream. These BCs are in adequacy with the physical propagation of information in the pipe. Contrary to other splittings that have a certain tolerance against an improper imposition of BC, the Wolf splitting requires a physical imposition of BC and otherwise causes errors.

5.1.2 Free surface Flows

On top of the treatment of transient phenomena, other difficulties arise when simulating free surface flows: the capture of regime transitions and the evaluation of source terms. Since regime transitions may affect steady and unsteady flows indistinctly, I present herein the case of a trans-critical flow over a bump (steady) and the famous case of the dam break (unsteady).

As shown by the two following benchmarks, the Wolf splitting provides a valuable solution to simulate free surface flows. For steady state, this splitting gives a constant discharge contrary to the other solvers. In addition, the pseudo-unsteady strategy reduces the computational time by a factor ten and reaches the same solution than the Wolf unsteady splitting. In the other solvers, troubles in the discharge profile arise if source terms are not treated with well-balanced schemes. For steady and unsteady states, all solvers are able to handle with the propagation of shocks (hydraulic jump) and rarefactions (dam break). Nevertheless, simplicity of the Wolf splitting enables a rigorous treatment of dry beds.

Analytical case: Steady transcritical flow over a bump

Originally presented by Caleffi et al. [36], this analytical benchmark consists in a steady hydraulic jump over a bump. The spatial domain is represented by a 25mx1m channel that is supposed frictionless. Its cross-section is rectangular. The following function gives the bottom elevation z_b:

$$z_b(x) = \begin{cases} 0 & \text{if x<8m or x>12m} \\ 0.2 - 0.05(x-10)^2 & \text{if 8m<x<12m} \end{cases} \quad (5.3)$$

The flow discharge is imposed to 0.18m³/s. The downstream boundary condition is set equal to 0.33m for the water height. The initial water level is set to 0.33m. Bernouilli's theorem provides an analytical solution to the problem. It consists in two constant states: the total head is 0.33m downstream the bump and 0.4233m upstream. A hydraulic jump above the bump links these two states.

Comparison of the computation time needed to reach convergence argues in favor of the pseudo-unsteady strategy used with the wolf splitting. Table 4 shows that this original solver takes 1302 computational steps to converge, instead of the 25000 required by other solvers (RK31C with NbC=0.5). The Riemann solver does not even converge at all (with the

criterion used) because it relies on iterative solvers that introduce very small oscillations at each computational step. Nevertheless, it provides a valuable solution (Figure 60).

Table 4: Results of the computation prove the performance of the pseudo-unsteady strategy coupled with the Wolf splitting

Scheme	Upstream total head (m)	Error	Crest elevation (m)	Error	Number of steps	Computation time (s)
Analytic	0.4233		0.3491			
Wolf Unsteady	0.4214	0.4%	0.3499	0.2%	25854	29.92
Pseudo-Unsteady	0.4215	0.4%	0.3499	0.2%	1302	1.45
Roe	0.4247	0.3%	0.3418	2.1%	NC	NC
Exact Riemann	0.4235	0.0%	0.3552	1.7%	22085	36
Lax-Friedrich	0.4175	1.4%	0.3525	1.0%	27023	9.57
AUSM	0.4236	0.1%	0.3514	0.7%	26499	35.73

All solvers capture the hydraulic jump with sufficient fidelity for the purpose of this thesis. Figure 60 gives the height profile only for the pseudo-unsteady solver and the Exact Riemann solver. Other solvers give similar profiles.

Finally, the analyses of the discharge profile underlines the necessity to adapt the discretization of the source term to the numerical scheme used. Wolf splitting converges indeed towards a constant discharge of Q=0.18m³/s all along the channel (Figure 60). On the opposite, other solvers converge towards variable discharge profiles. For the exact Riemann solver notably, strong discontinuities appear in the discharge (Figure 60). This is due to an inadequacy between the discretization of the source terms and the fluxes. Correction of this flaw is currently the object of intense research [51, 195, 196, 308] that goes beyond the scope of this thesis.

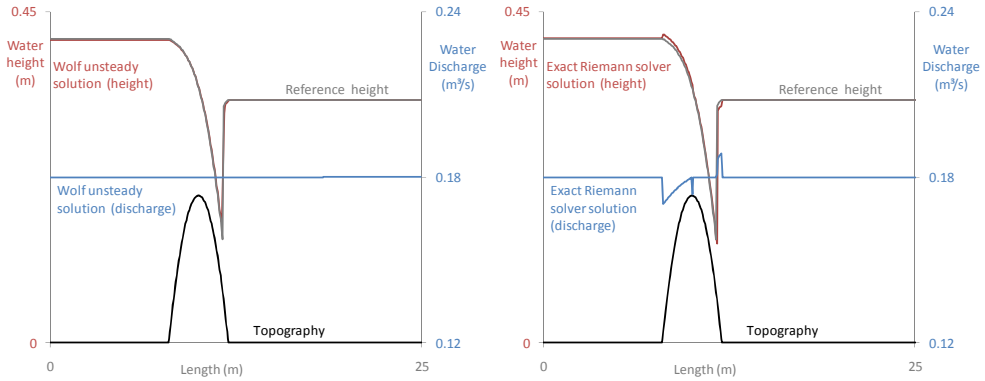

Figure 60: Computed profile in pressure and discharge exhibits flaws in the convergence of most of the solver except Wolf

Analytical case: Dam break flow

The dam break problem is of utmost importance in free surface hydraulic engineering. The reason is not only that important casualties may go with dam failures. It constitutes also a traditional benchmark to assess the ability of a free surface solver to handle with strong discontinuities and dry beds. The case considers a horizontal channel of uniform,

rectangular cross-section. The water level in the reservoir is initially at 0.5m. Downstream the wall (dam), the bed is dry (h=0m). The collapse of the wall containing the water induces a flow. Formally, this flow is the solution of a particular Riemann problem:

$$\frac{\partial \mathbf{U}}{\partial t}+\frac{\partial \mathbf{F}(\mathbf{U})}{\partial x}=\mathbf{0}$$
$$\mathbf{U}(x,0)=\begin{bmatrix}\Omega & Q\end{bmatrix}^T(x,0)=\begin{cases}\begin{bmatrix}0 & \Omega_{res}\end{bmatrix}^T & \text{if } x<0\\ \begin{bmatrix}0 & 0\end{bmatrix}^T & \text{if } x>0\end{cases} \tag{5.4}$$

The structure of the solution of this problem is different from a classical dam break over a wet bed. As pointed by Toro [286], a shock wave cannot be adjacent to a region of dry bed. Instead, the solution contains a contact discontinuity of speed S^{*L} as well as a left rarefaction wave associated with the eigenvalues λ=u-c (Figure 61).

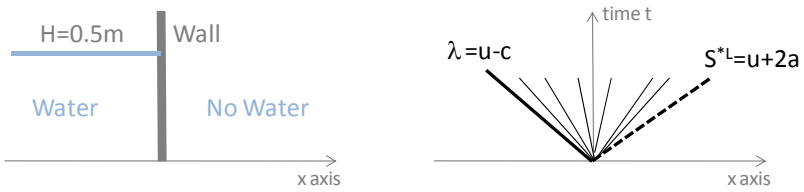

Figure 61: The structure of the solution of the dam break problem over a dry bed contains a left rarefaction and a contact discontinuity

Ritter (1892) derived first the analytic solution of the dam break over the dry bed (cited in [46, 93]). The bore propagates at a celerity $S^{*L}=2+\sqrt{gH_{res}}$. The tail velocity of the rarefaction is given by $S^{L}=-\sqrt{gH_{res}}$. Between these two waves, the instantaneous profile for the water height follows a parabolic law:

$$\frac{x}{t^*\sqrt{gH_{res}}}=2-3\sqrt{\frac{h}{H_{res}}} \tag{5.5}$$

and the profile of the velocity is given by:

$$u=\frac{2}{3}\sqrt{gH_{res}}\left(1+\frac{x}{\sqrt{gH_{res}}t}\right) \tag{5.6}$$

Since the new mathematical model only describes wet beds, handling dry beds is complicated from a computational point of view. A classical method [226] consists in filling any computational mesh with a minimal water section. Consequently, the whole domain contains water such that the new mathematical model applies everywhere. In the case of the Wolf splitting, another method exists and is more accurate. First introduced by Erpicum [93], this approach consists in considering the water section as a positive value. Its cancellation translates drying of the mesh. This mesh is not anymore in the computation domain. The idea is to compute these meshes but ensure that performed operations do not include a division by zero. The simplicity of the Wolf splitting enables to implement such conditions.

As pointed by Figure 62, the Wolf splitting gives a profile of height after 1s, 2s, and 3s very close to the analytical solution of Ritter. Computations are performed on 500 meshes of 0.1m and a three-step Runge-Kutta RH31C with a CFL number of NbC=0.5. In each case, the curves moves around the fixed point called critical height. For the contact discontinuity, the rigorous treatment of the dry bed gives better results than the artificial bed-wetting. This last method creates indeed a right shock instead of a contact wave. What is more, artificial bed-wetting causes error in the conservation of water. This proves the ability of the Wolf splitting to treat shocks, rarefactions, and contact discontinuities in free surface flows. What is more, the simplicity of the splitting enables a rigorous treatment of dry beds.

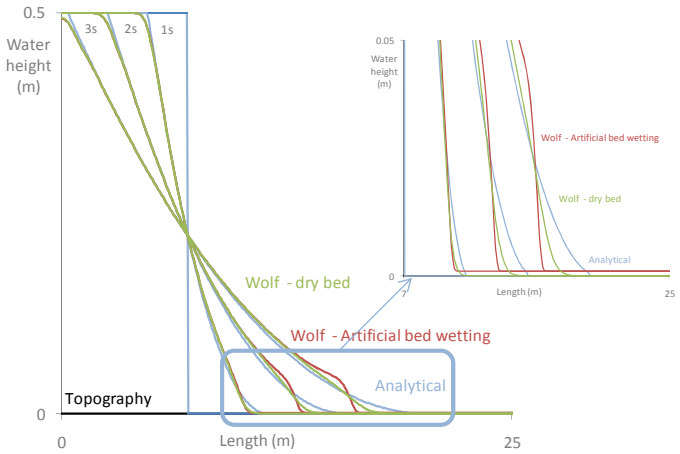

Figure 62: A correct treatment of the dry bed enables to improve the solution given by the Wolf splitting

The profiles computed with the four other solvers (Roe, exact Riemann, Lax-Friedrichs, and AUSM) present various discrepancies with the analytical solution (Figure 63). First, all these solvers require using the artificial bed-wetting method to treat the dry bed. Only fundamental modifications of the solvers equations enable a rigorous capture of the contact discontinuity. I do not implement these features and refer the interested reader to the specialized literature. Even with artificial bed-wetting, the Roe solver cannot provide a valuable solution (Figure 63). Problems appear at the bore and at the critical points. These errors originate from the incorrect evaluation of the celerity at the bore. It is a limitation of the entropy fix used here. On the opposite, the Exact Riemann solver treats correctly the critical point. However, it presents a high sensitivity to the CFL number and slight difficulties arise at the bore. The solution may however be considered as good. With the Lax-Friedrich scheme, critical point and bore are correctly evaluated. Nevertheless, the scheme exhibits difficulties to handle with the rarefaction. Finally, AUSM scheme provides a correct solution except at the bore, where a spurious wave is created. Only a diffusive scheme may solve this problem.

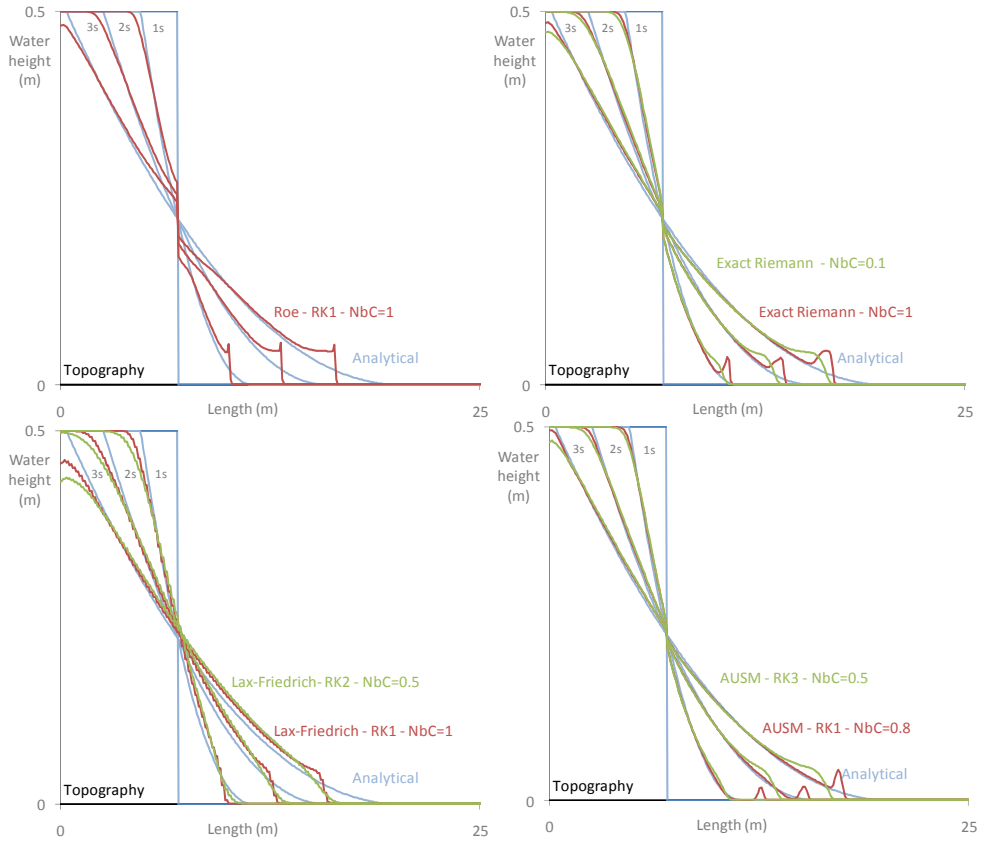

Figure 63: Other solvers present various discrepancies with the analytical solutions

5.1.3 Mixed Flows

Solving a mixed flow, characterized by the simultaneous occurrence of free surface and pressurized flows, is still today challenging. As I already evocated in Chapter 3, the main difficulty consists in reducing the amplitude of the spurious oscillations arising at the transition bore. Due to the strong variation of celerity at the transition bore, they indeed compromise the stability of the computation. The incorrect evaluation of the celerity explains this problem. In this respect, several avenues worth exploring have been introduced previously. In particular, performance of the various schemes and fixes proposed in Chapter 3 are herein assessed on two benchmarks: the analytical case of a pipe filling and the experimental case of a fast closing gate.

Presented in the rest of this sub-section, the results of the computation suggest that Godunov schemes provide the best results with respect to the amplitude of the oscillations. In this respect, the Roe approximate solver and the exact Riemann solver seem to have similar performances. Nevertheless, the amplitude of residual oscillations remains too important to be acceptable. In addition, the Lax-Friedrich scheme does not reach stability without creating inacceptable diffusion in the solution. The AUSM scheme creates also important oscillations and does not compete with Godunov schemes. Finally, the WOLF splitting has a better ability to treat transition than Lax-Friedrich and AUSM schemes. However, it does not compete with Godunov schemes. Finally, reducing the celerity and increasing the diffusion seems the two best ways to reduce oscillations.

ANALYTICAL CASE: PIPE FILLING BY BOTH ENDS

This analytical benchmark considers two moving transitions that cross each other and creates a water hammer. The test includes a square pipe of 0.5m width. The length of the pipe is 50m and the conduit is frictionless. The initial condition is a constant height profile at 0.4m and no discharge. At both extremities of the pipe, the discharge is instantaneously increased from 0.0m³/s up to 0.3026m³/s. It results in a pressurization of the pipe from both ends. Pressure below the transition and velocity of the bore are given by the Rankine-Hugoniot conditions. The transition propagates at 5.95m/s and the pressure below it is 1m. All the following computations are performed on 500 meshes of 0.1m length.

The exact Riemann solver computes the case with fidelity for celerity of 50 m/s (Figure 64). This computation is performed with a one-step time integration and a constant time step of 0.0018s. Clearly, the model handles correctly with crossing transitions, which is a difficult situation. In particular, the velocity of the transition is correctly captured. Nevertheless, spurious oscillations already appear behind the transition bore. For celerity above 100m/s, the amplitude of these oscillations compromises the stability of the scheme. What is more, a moderate diffusion appears and smoothes out the water hammer. This originates from the low value of CFL number. Godunov schemes become indeed very diffusive when the CFL number decreases.

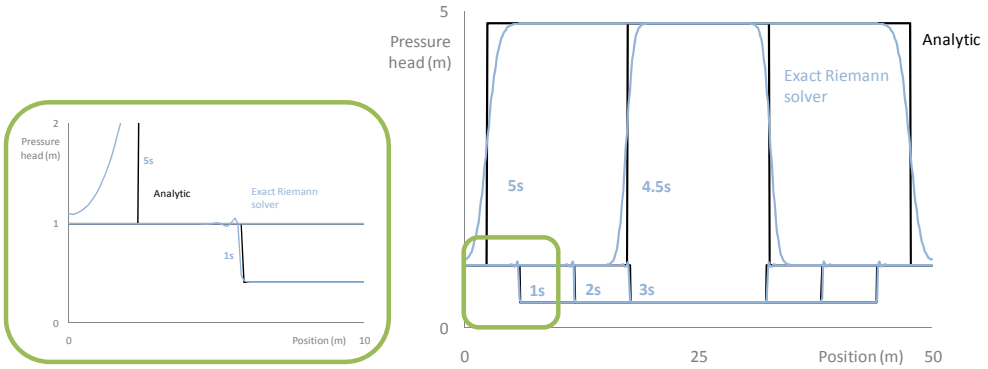

Figure 64: Exact Riemann solver computes with fidelity the crossing of transition but creates moderate spurious oscillations in the pressure profile

For a celerity of 50m/s, the Roe solver reaches the same results than the exact Riemann solver (Figure 65). This computation is performed with a one-step time integration and a constant time step of 0.0018s. Again, pressure head profiles accord with the analytical solution but spurious oscillations appear. These oscillations have the same amplitude as the ones obtained with the previous solver. It proves that the Roe and the Exact Riemann solvers provide analogous approximations of the celerity in the transition mesh. For celerity above 100m/s, the amplitude of these oscillations compromises the stability of the scheme.

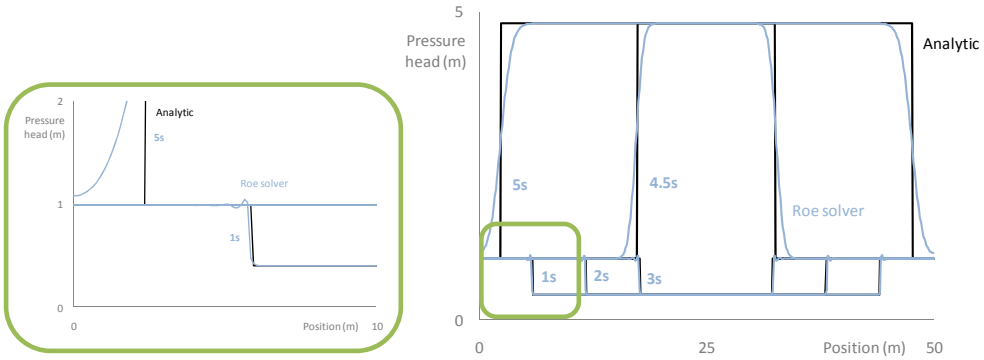

Figure 65: Water head profiles at given time computed with the Roe solver are analogous to the ones computed with the Exact Riemann solver

Other solvers create oscillations of great amplitude such that their stability is compromised for a celerity of 50m/s. The pressure wave celerity is thus decreased to 5m/s. The analytical solution is again given by the Rankine-Hugoniot conditions. The pressure behind the transition is 0.77m and the shock velocity is 4.01m/s. The time integration is also changed for a three-step Runge Kutta scheme RK31C with a time step of 0.0018s. In these conditions, the WOLF splitting gives a decent solution even if oscillations are still present (Figure 69). In a similar manner, oscillations affect also the AUSM splitting (Figure 69). Finally, the Lax-Friedrich scheme does not reach stability in these conditions.

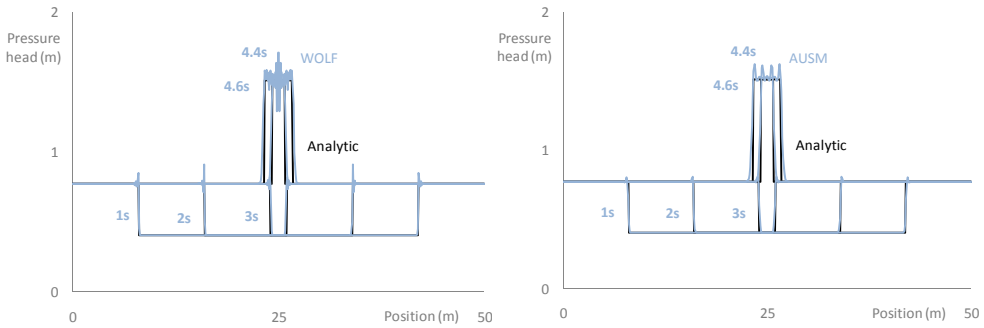

Figure 66: The Wolf and AUSM profiles are affected by important oscillations such that the celerity is decreased to 5m/s. Water head profiles for this celerity differs notably from previous solutions.

Experimental case: Fast closing gate (Trajkovic)

First published by Trajkovic et al [287] in 1999, this experimental case consists in the physical modeling of a transition from a free surface to a pressurized flow due to the fast closing of a gate at the downstream end of the pipe. Originally, investigation aimed at producing the conditions of the filling of sewers during storm events. Data of this research are now a classical benchmark for mixed flows. The experimental apparatus consists in a 10m long circular pipe. The inner diameter of the pipe is 0.1m. Its Manning coefficient is 0.008 and the celerity has been measured to 9m/s. In order to avoid air-water interactions within the pipe, air vents are distributed along the pipe. Two pressure transducers record the height variation. P5 is placed 7.2m downstream the entrance and P7 is 9.9m downstream the entrance. Experiments of type A, considered for this validation, are carried out with a slope of 2.7%. The water level at the entrance is maintained at H=0.0014m and

the discharge at 0.0013m³/s. Initially, the downstream gate is open and a steady supercritical free surface flow is observed. At some point in the experiment, the downstream gate is suddenly closed. As pointed by the experimental data, a pipe-filling bore appears and moves from the downstream gate up to the upstream gate of facilities. The transition bore is a moving trans-critical hydraulic jump. The bore is detected at P7 after 3s and at P5 after 15s. Thirty seconds after the closure, the downstream gate is partially reopened (e=0.015m). Trajkovic et al [287] indicates that the outflow is thus given by:

$$Q = C_Q \Omega \sqrt{2g(H - C_c e)} \tag{5.7}$$

where the discharge coefficient is C_Q=0.78, the contraction coefficient is C_c=0.83 and H is the head just upstream to the gate. After this reopening, the pressure head tends to level off and small oscillations observed. All the following numerical computations are performed on a 100 cells uniform grid.

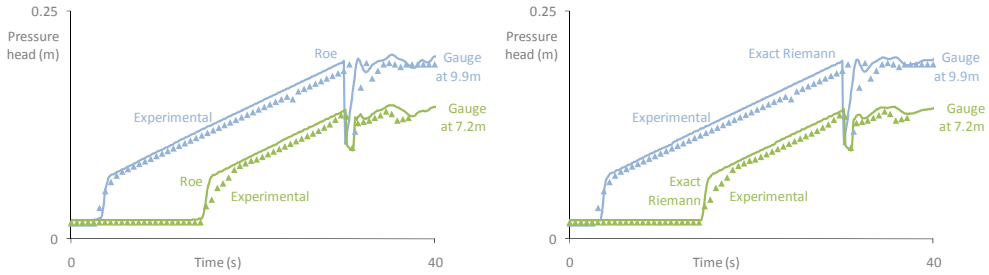

Figure 67: Godunov schemes with both the Roe solver and the exact Riemann solver give accurate solutions for the time evolution of the pressure head at P5 and P7

In this case, Godunov schemes with both the Roe solver and the exact Riemann solver give accurate solutions for the pipe filling bore (Figure 67). For the computation, a first order explicit time integration is used with a CFL number of NbC=0.4. The computed values accord remarkably well with the time evolution of the pressure head at P7 and P5. In particular, the decrease in pressure due to the valve reopening is correctly captured. Finally, no oscillations appear in the computation. It is a direct consequence of the choice of an artificially low value for the pressure wave celerity.

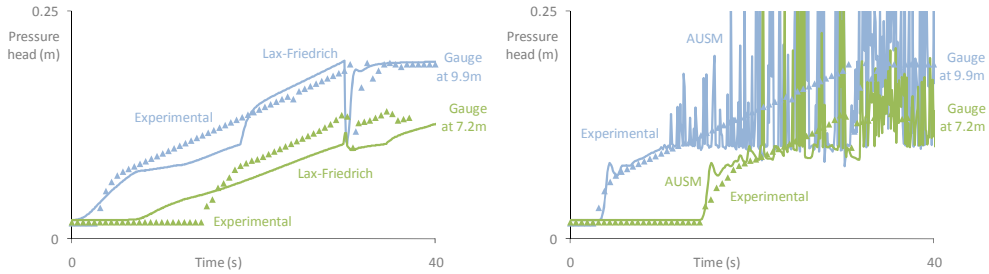

Figure 68: Lax-Friedrich scheme and AUSM splitting present important inaccuracies in the time evolution of the pressure head at P5 and P7.

On the opposite, Lax-Friedrichs scheme and AUSM splitting present important discrepancies with the experimental data (Figure 68). For the computation, a first order explicit time integration is used with a CFL number of NbC=0.4. The Lax-Friedrichs scheme is

way too much diffusive, especially in the free surface part of the flow. The lowest the CFL number is, the greater is the diffusion. Interestingly, the diffusion also smoothes out the spurious oscillations. On the other hand, the AUSM scheme creates important oscillations such that the solution looses accuracy.

Finally, the solution given by the WOLF splitting accords remarkably well with the experimental data. For the computation, a three-step Runge-Kutta scheme RK31C with a CFL number of NbC=0.1 is required to stabilize the solution. This time integration scheme is indeed a little diffusive. The computed values accord remarkably well with the time evolution of the pressure head at 9.9m and 7.2m downstream the entrance. In particular, the decrease in pressure due to the valve reopening is correctly captured. Finally, no oscillations appear in the computation.

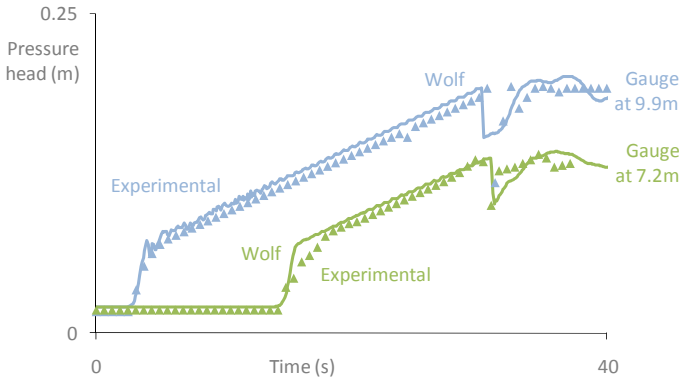

Figure 69: The Wolf splitting gives an accurate solution with limited oscillations for the evolution of the pressure head at P5 and at P7.

5.2 Design of an Airport Gravity Drainage System

Sewer systems are a crucial substructure of any city or inhabited area. Their purpose is to collect and transport both sanitary sewages and storm water runoffs up to treatment stations and/or natural rivers. Sanitary engineering distinguishes:

- sanitary sewer, which transports only human wastewater;
- storm drain, which conveys only rainfalls;
- combined sewer, ensuring the function of both a sanitary sewer and a storm drain.

Usually, such sewers are designed to remain at free surface under normal circumstances. In the case of a storm water drainage system, the size of the network depends then directly on the intensity of the maximum rain events in the region. Inaccurate design would lead to important inundations and major damages to the sub- and super-structures.

The norm prEN 752-4:1997 (which is applicable in Belgium) prescribes performance criteria for the design of storm water drainage systems. Completely preventing the risk of inundation is indeed inconceivable. A compromise must be found between the cost and the level of protection. Therefore, the norm indicates frequencies for the pressurization and for the overflow of the network. As pointed in Table 5, this frequency depends on the nature of the site. On the other hand, the norm prEN 752-4:1997 leaves the choice of the design method to the appreciation of the contracting authority or the project managers.

Table 5: The norm prEN 752-4:1997 prescribes performance criteria designing storm water drainage systems

Nature of the location	Frequency of pressurization	Frequency of inundation
Rural area	1 every year	1 every 10 years
Residential area	1 every 2 years	1 every 20 years
City centers, industrial or commercial areas		
• with inundation control system	1 every 2 years	1 every 30 years
• without inundation control system	1 every 5 years	1 every 30 years
Metro and underground passage	1 every 10 years	1 every 50 years

The storm water drainage system of the parking facilities of the South-Brussels airport is an example of deficient sewer network. Several inundations have indeed occurred due to the heavy rain events observed in the springtime 2008. These inundations have made the level -1 unusable for cars. The University of Liège investigated the cause of these dysfunctions.

As I will point out in the following, the modified module WOLF 1D constitutes an efficient tool for investigating the hydraulic design of such sewer systems. The model computes indeed the pressure head profile in the network in function of the inflow discharge. It enables to identify four causes for the inundations: the connection of an unplanned drained area to the network, the presence of a downsized hydrocarbon separator, the presence of obstructions in the pipe, and the use of a too small intensity for the rain event. These conclusions result from steady state simulations (subsection 5.2.2) and unsteady state simulations (subsection 5.2.3). This section just briefly summarizes the result of this study. I refer the interested reader to the three reports [243-245] written at this occasion.

5.2.1 Description of the Situation

The drainage system of the South-Brussels airport includes three parking facilities (Figure 70). The parking C1 is a 4-floor building with one underground level. The level of the underground slab is 171.1m and the drained area is 21956m². The inundations that I am interested in occurred in this area. The parking C2 is an open air concrete area of 17985m². Its level varies around 180m. The parking C3 is made of draining asphalt (21012m²). Its level is 174m. In situ investigations underlined a certain storage capacity for this area [59].

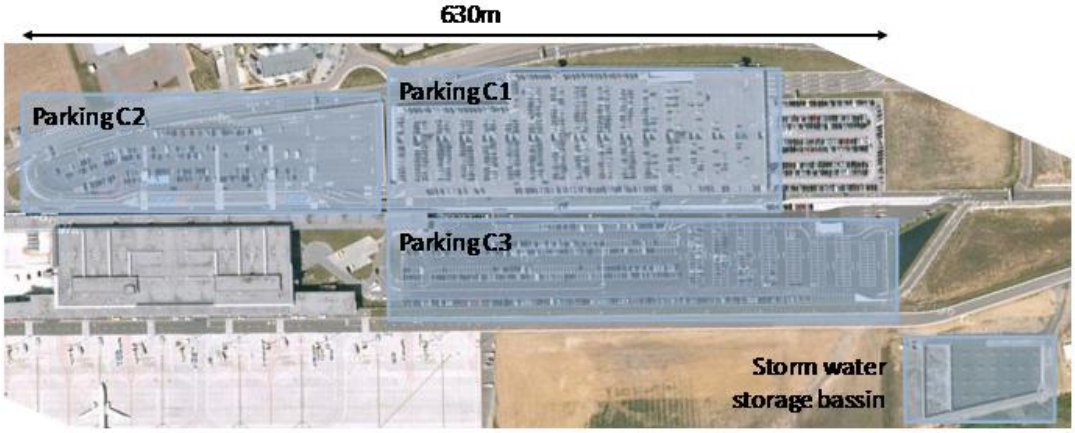

Figure 70: The storm water drainage system covers three parking and an area of 60 000m²

The whole network conveys the rainfalls up to a storm water storage basin that collects all the water from the parking facilities (Figure 71). Two concrete pipes drain water from C2 to C1. From a hydraulic point of view, the flow in C2 is independent from the flow in C1. The link pipe between the two parking has indeed a slope of 7%, which means that a local critical flow appears. C1 is drained by three pipes that are collected in a single transversal pipe. A porous drain circumscribes the whole area. For the parking C3, a single concrete pipe collects all the water conveyed by the porous drains distributed below the draining asphalt. The water from both parking C3 and C1 (and consequently C2) are conflated into a hydrocarbon separator. This device aims at diminishing the ecological impact of the parking. The capacity of this drain is 0.5m³/s. At the initial design, the parking C3 was not supposed to connect to the separator. Finally, a 0.7m diameter pipe conveys water from the separator up to the storage basin, where a critical section is imposed.

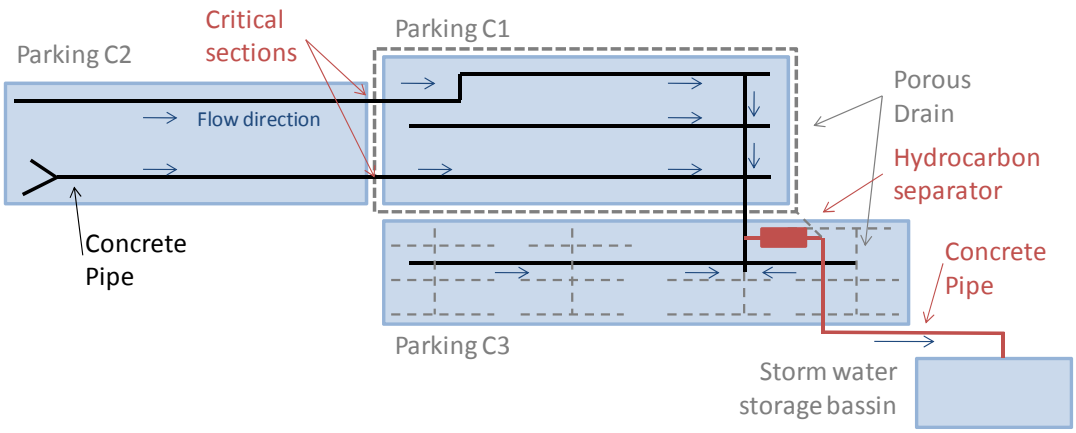

Figure 71: The storm water drainage system includes porous drains and concrete pipes

According to the norm prEN 752-4:1997, the inflow at each manhole is evaluated by:

$$Q_{inflow} = \Psi * i * A \tag{5.8}$$

where A[m²] is the catchment area. The runoff coefficient Ψ[-] is equal to 1 for small impermeable areas (catchment area less than 100m²). Finally, the rainfall intensity i[l/s/ha] depends on the location of the sewer, the rainfall design frequency, and the rainfall characteristic time. In this respect, the initial design considered a fixed intensity of 165l/s/ha. A more rigorous approach makes use of the Intensity-Duration-Frequency curves computed by the Belgian administration. An IDF curve indicates indeed the rainfall intensity that will occur for a given duration and a return period. In the current case, evidence suggests that the characteristic time of the design rainfall must be 10 minutes (see [243] for the whole demonstration). As pointed by Table 5, the rainfall design frequency is 5 years for the pressurization and 30 years for the flood risk. For the city of Charleroi, IDF curve given in [254] shows that:

- A rainfall event of 240l/s/ha must be considered for the risk of pressurization (5 years).
- A rainfall event of 340l/s/ha must be considered for the risk of inundation (30 years).

5.2.2 Steady States

The norm prEN 752-4:1997 does not impose any method for designing the pipe based on the performance criteria presented above. A simple empirical method consists in computing the uniform height and limiting its value to the pipe diameter. The computational code WOLF1D (extended to pressurized flows) constitutes a more efficient and reliable method. The model enables to compute the steady states for a rainfall intensity of both 240l/s/ha and 340l/s/ha. Simulation results indicate the occurrence of pressurization and/or inundation.

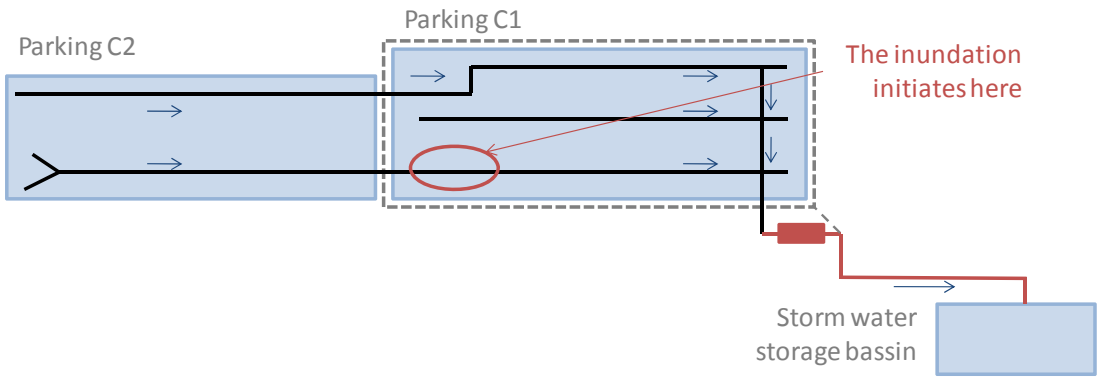

Figure 72: The network "as initially designed" consists in the parking C1+C2

In this respect, the first case considered is the network C1+C2 "as originally designed" (Figure 72). Simulations show that the network is locally pressurized for a rainfall of 165l/s/ha, but does not cause inundations. The total outflow is 0.659m³/s such that the hydrocarbon separator is already not sufficient. What is more, the network C1+C2 does not satisfy the performance criteria of the norm prEN 752-4:1997. The network is indeed pressurized for rainfall intensities lower than 240l/s/ha, and causes inundations for

intensities lower than 340l/s/ha. In conclusion, the combination of an inaccurate design rainfall and a downsized separator explains partly the inundations that motivated the study. Additional reasons make the situation worse. In particular, the network “as built” differs notably from the one originally designed.

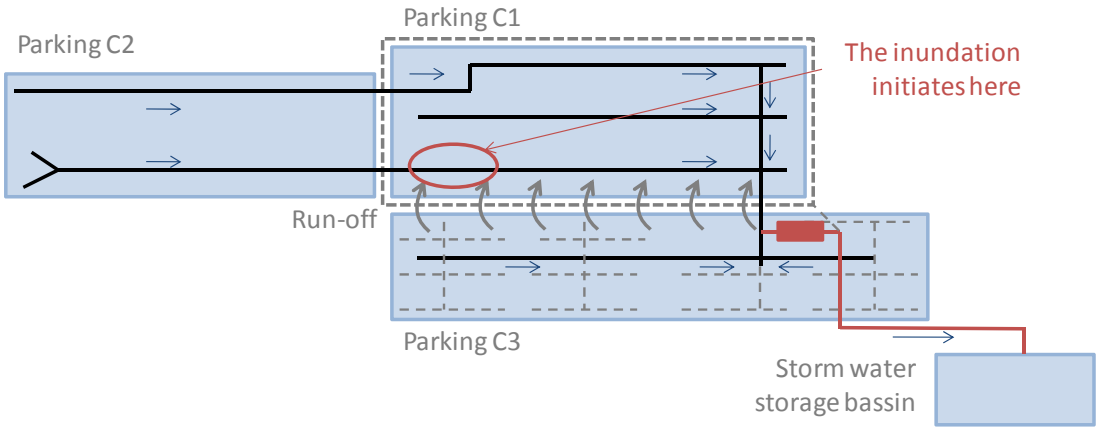

Figure 73: The model predicts the occurrence of an inundation for a rainfall frequency between 6.9 and 8.1 months at a location that accords with in-situ observations.

The second case considers the network “as build” (C1+C2+C3+obstructions). The parking C3 has indeed been connected after the initial design of the system (Figure 73). What is more, an endoscopy of the network has revealed the presence of several obstructions (Figure 74). In this case, simulations show that the inundation is initiating for intensities between 125l/s/ha and 132.5l/s/ha. It corresponds to a rainfall frequency between 6.9 and 8.1 months. As a rough guide, Figure 75 shows the profile of pressure head within the network. The graphs contain also the profile of the pipe crown and the level of the manhole covers. When the pressure head is greater than the pipe crown, the flow is pressurized. When the pressure head is also greater than the manhole covers level, it causes an inundation. As shown on the graph, WOLF1D predicts the flood inception in section 5. This location accords with in-situ observations (Figure 73). A conjunction of four phenomena causes this inundation. First, the adjunction of C3 to network C1+C2 increases the undersizing of the hydrocarbon separator and the discharge pipe in the storage basin. Second, the porous drains of C3 are saturated such that a part of rainfall over C3 streams onto parking C1. The porous drain circumscribing C1 collects this runoff and conveys it downstream the hydrocarbon separator. Third, C1+C2 are more undersized than before. Finally, the obstructions considerably reduce the water-conveyance capacity of the network.

Figure 74: The endoscopy has revealed the presence of several obstructions

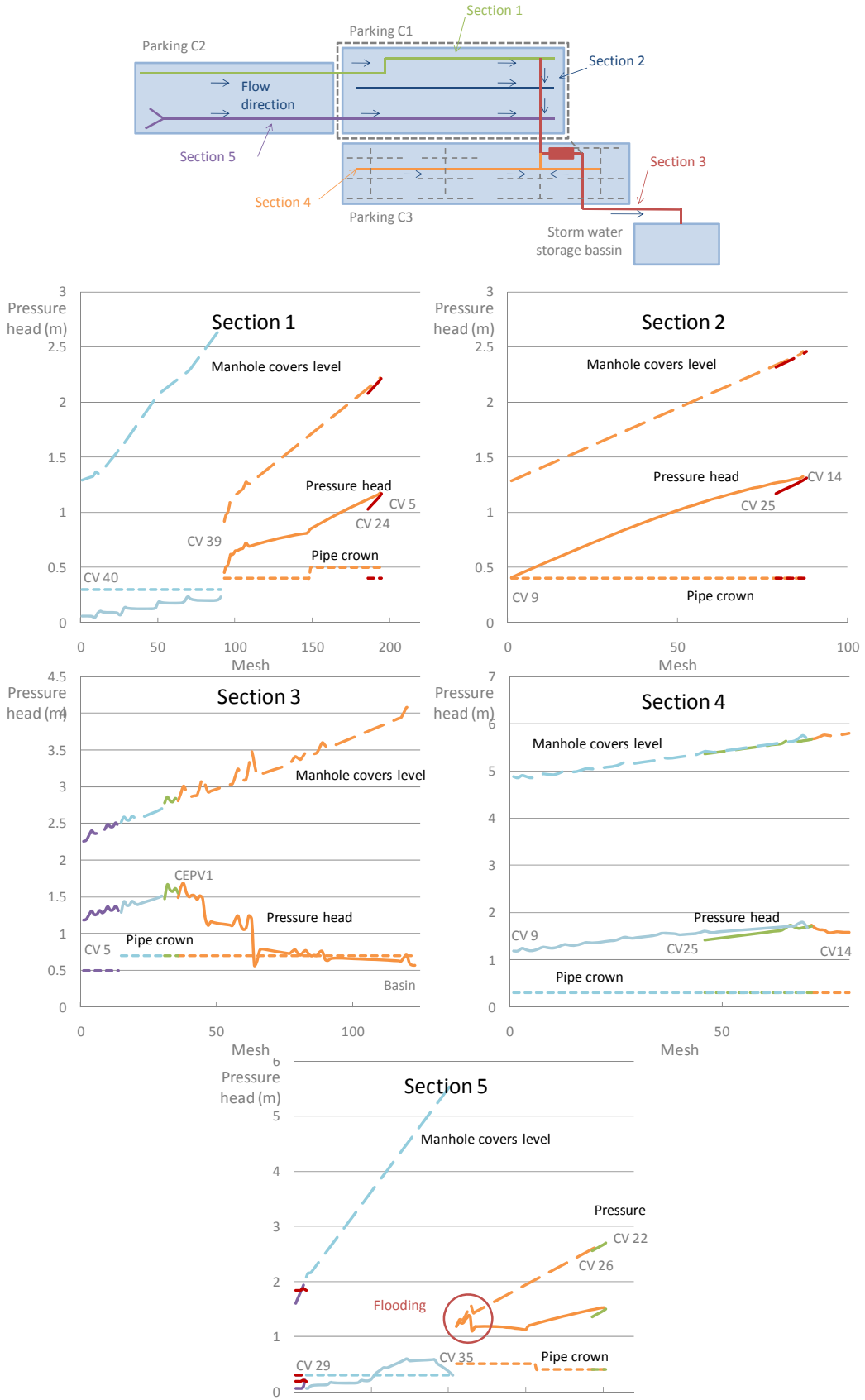

Figure 75: Wolf 1D gives the pressure head profile within the whole network. The inundation arises when the pressure head is greater than the manhole covers level

Steady design enables also to provide various solutions in order to decrease the intensity and the frequency of inundations in parking C1. The first requirement is to increase the capacity of the hydrocarbon separator from 0.5m³/s up to 2m³/s. This may be achieved by replacing the current separator or placing three others in parallel. The second necessity is to collect water at the exit of the parking C2 and to by-pass the parking C1. Finally, the capacity of the outflow pipe between the separator and the storage basin should be greatly augmented. Doubling this pipe could be a good idea.

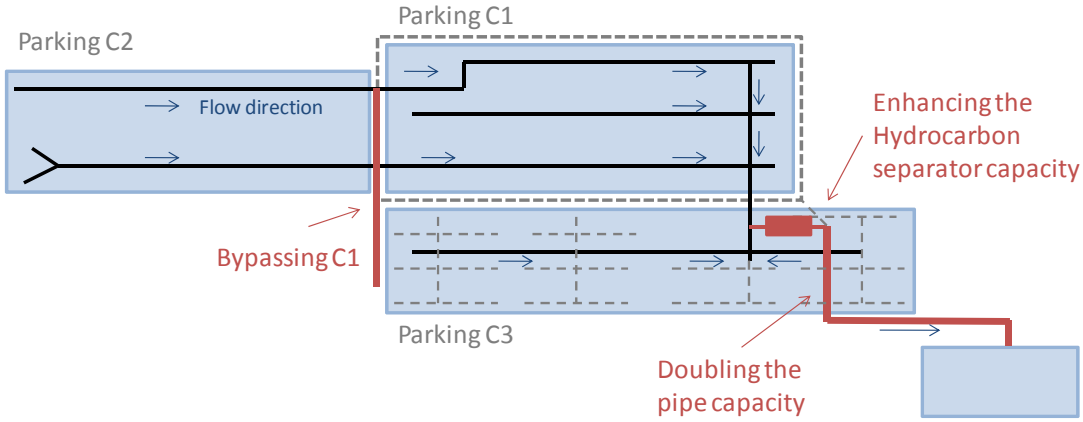

Figure 76: WOLF1D gives solutions worth exploring

5.2.3 Unsteady States

Based on the previous results, the contracting authority has decided to clean out the whole network and to remove the hydrocarbon separator. These two first measures aimed at diminishing the frequency of the inundations while a final solution was searched for. In parallel, the company Belgocontrol that runs the air space control in Belgium has recorded a rainfall event of intensity 175 l/s/ha (10 minutes) on July, 5th 2009 (Figure 77). This event does not cause the network to overflow. The University of Liège was again appointed to study this event and check the validity of the model on a real case.

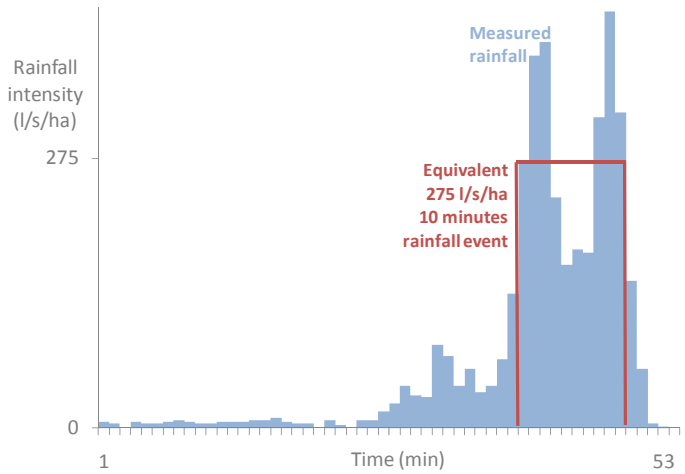

Figure 77: Belgocontrol recorded a rainfall event of 275l/s/ha during 10 minutes that does not cause the network to overflow

Unsteady simulations performed with WOLF1D and the measured rainfall event show that the network gets pressurized, but that the overflow remains limited in terms of time and extension (less than 2 minutes at a single manhole). Comparison of the outflow discharge curve at the entrance of storage basin with the intensity of the rainfall event shows a similarity in their behavior. Two pikes of rain intensity are observed in both curves. The very small overflow occurs at the second pike.

The conjunction of three factors explains that the network does not overflow for this rainfall event of 275l/s/ha (which may seem contradictory with steady design conclusions). First, all the rainfall water of C3 is stored in the porous drain and cannot reach sufficiently rapidly the concrete network. The absence of hydrocarbon separator has greatly diminished the localized head loss in the main pipe. Finally, the cleaning out of the whole network has induced a decrease in the overall head loss of the network.

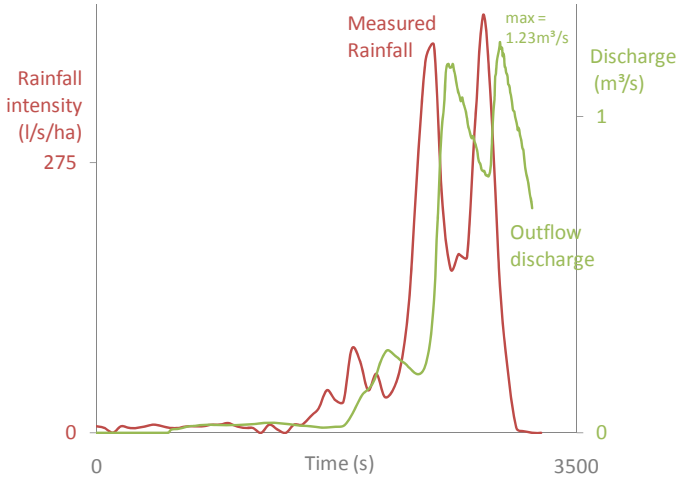

Figure 78: The outflow discharge is mainly governed by the intensity of the rainfall event

5.3 Design of a City Low-pressure Sewer Network

Namur is a city of 105000 inhabitants located at the confluence of three watercourses, namely the Meuse, the Sambre, and the Hoyoux. The collective sewage system of the city collects the water from 95000 people. It is a combined sewage system. At the beginning of the 90's, the network was still a more or less integrated juxtaposition of small systems resulting from the historical development of the city. It collects the sewage water from the inhabitants, the storm water of the city, and a small number of natural streams having their source in the drained area. Polluted water was directly discharged into the watercourses. In 1991, a European directive imposed to collect and treat wastewaters. The directive imposed performance criteria for the concentration in pollutants that may be discharged in natural flows. What is more, the management of the Meuse had become a major economical, political, and environmental issue. The necessity to modernize the sewer system was then acute [188-191].

Technical studies and dialogues lead the authorities to choose a collecting system composed of three separated networks. The principal network, called "Namur-Brumagne" (Figure 79), has a capacity of 90 000 EH (Equivalent Habitant). As pointed in Figure 79, the network includes five branches, namely Right Sambre, Left Sambre, Upstream Meuse, Hoyoux, and Downstream Meuse. Since the separation of sewage, storm water, and natural stream is too expensive, the new system collects all kinds of water and conveys them up to the new treatment plant of Brumagne.

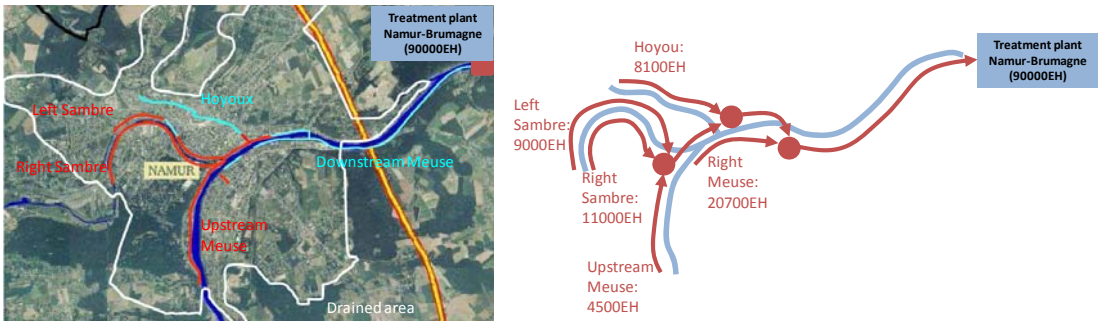

Figure 79: A collector network conveys sewage, storm water and natural streams up to a treatment plant [188].

From a technical point of view, the collecting network Namur-Brumagne consists mainly in a system of low-pressure pipes. As pointed in Figure 80, 38 compact pumping stations intercept water conveyed by the historical sewer pipes just upstream its discharge into the Meuse/Sambre. The pumps inject the water in a pressurized pipe that is very close to the ground level. When the discharge in the pumping station exceeds its capacity, overflow is discharged directly into the watercourses. Four reasons explain this technical choice. First, the required section for low-pressure pipes is smaller than for gravity pipes. Second, pipes are only superficially buried (<2m). The energy supplied to this kind of system is lower than standard gravity sewers. Finally, it requires limited modifications to the existing networks. All these reasons are source of economy.

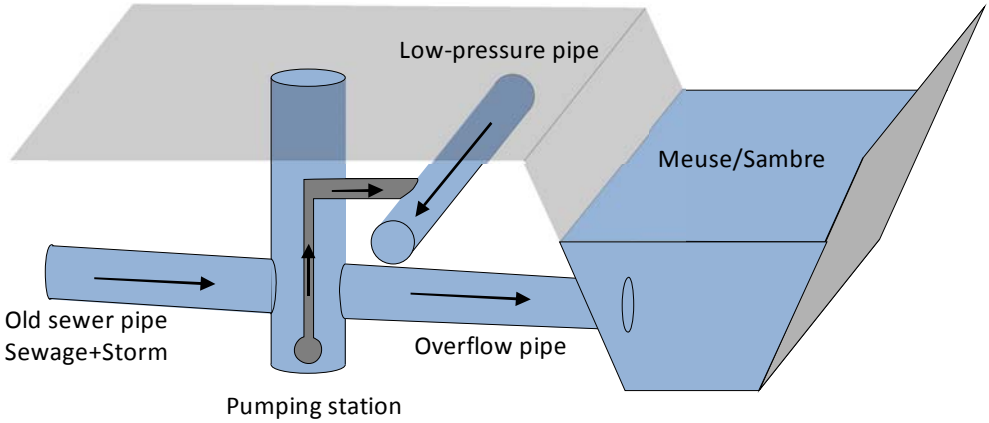

Figure 80: The low-pressure collecting network is above the level of the exits of the historical sewer system [191].

The treatment of overflow storm water is ensured through a dynamic process in a vortex separator placed within some pumping stations. Indeed, the quantity of sewage and storm water that a pumping station may inject in the low-pressure pipe is limited to a maximal value. On the other hand, the inflow in the station varies with time as a function of the water consumption and the occurrence of rain events. Consequently, overflow must be discharged into the natural watercourse. Direct evacuation would cause an important decrease in water quality. A partial treatment of the overflow is thus necessary before its is discharged in the environment. In this respect, vortex cells ensure a dynamic separation of sediments and pollutants. Their functioning principle is represented in Figure 80 [1]. The sewage water flow is introduced into the vortex via a tangentially positioned inlet causing a rotational flow path around the dip plate. The flow spirals along the wall of the chamber as solids settle out by gravitational and rotational forces. The bottom grit collects solid particles that are evacuated for further treatment.

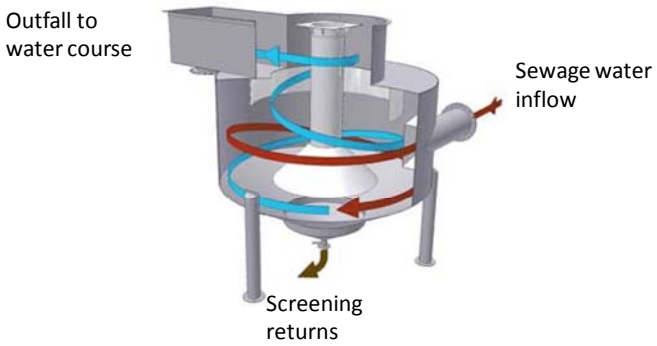

Figure 81: Vortex cell is an advanced hydrodynamic separator that augments gravitational forces to separate grit from water [1]

The verification of the hydraulic design of the network Namur-Brumagne is taken on by the HACH. In particular, the HACH is in charge of validating the hypothesis made for the design, assessing the properties of steady flows in the network, and evaluating the intensity of unsteady and transient phenomena.

The purpose of this section is to show the results provided by WOLF1D for the behavior of the network. This summary is clearly partial since this work is still in progress. In particular, I only present results related to the Right Sambre Branch. First, I present the main hydraulic features of this part of the network (sub-section 5.3.1). A key issue here is the presence of a high point that separates a pressurized part and a free surface part (with trans-critical regimes). The low-pressure pipe is alimented by seven pumping stations. ARAA vessels and air vents prevent the apparition of inadequate pressures. Next, I evocate the design criteria and critical cases that need to be verified for the design of the pipe (sub-section 5.3.2). In particular, I show how five design criteria (imposed by the contracting authority) must be verified in 16 critical situations. A first phase of verification consists in performing steady simulations (sub-section 5.3.3) that underline defects in one of the pumping station and the pipe that connects this station with the low-pressure gallery. Unsteady simulations (sub-section 5.3.4) complete this analysis. They mainly consist in verifying the intensity pressure surges created by the starting/stopping of the pumps as well as by check valve slams. Again, defects are identified in one pumping station. What is more, I observe a inadequate aeration of the ARAA vessels in functioning conditions.

5.3.1 Presentation of the Right Sambre Pipe

The branch “Right Sambre “ of the collecting network “Namur-Brumagne” is a 4112m long pipe supplied in sewage water by seven pumping stations (six of them include a vortex cell). The topography of the pipe has a high point at 3435m of the upstream end (Figure 82). This high point separates a low-pressure part of the pipe (left) from a gravity part (right). When no pump supplies the pipe, the left part remains under pressure. The pipe diameter varies from 150mm up to 450mm as pointed in Figure 82. A corollary small pipe of 125mm connects on the pipe. Since all the pipes are in cast-iron, the pressure wave celerity is approximately 1200m/s.

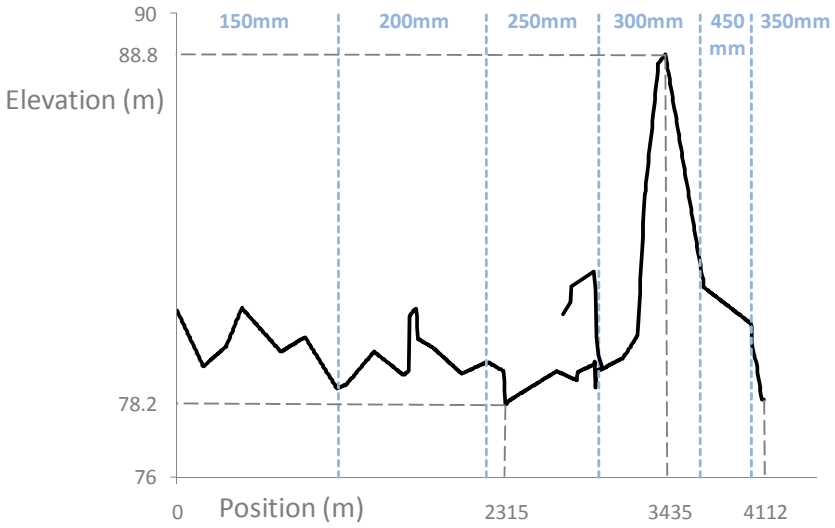

Figure 82: Topography of the pipe has a high point delimiting a low-pressure and a gravity part

Six pumping stations equipped with a vortex cell supply the pipe in sewage water. They are designated by the following codes: SD6/A, SD7/A, SD/8, SD10/B, SD11/D, SD12/A. Additionally, a smaller pumping station SD10/A (without vortex separator) is connected to the pipe. The location of all the stations is pointed out in Figure 83. For each station, maximum and minimum levels of the water in the temporary storage tanks complete the graph. The manufacturers graphically describe the behavior of each pump with characteristics curves of performance. The pump curve describes the relation between flow rate and head for the actual pump. Other important information for proper pump selection are also included, such as the efficiency curve, the NPSH curve, the power consumption, the velocity,… Implemented by P. Archambeau, WOLF1D includes a module to simulate the behavior of the pumps according to these curves. Finally, check valves equip the seven pumping stations. They prevent the apparition of negative discharge in the pumping system.

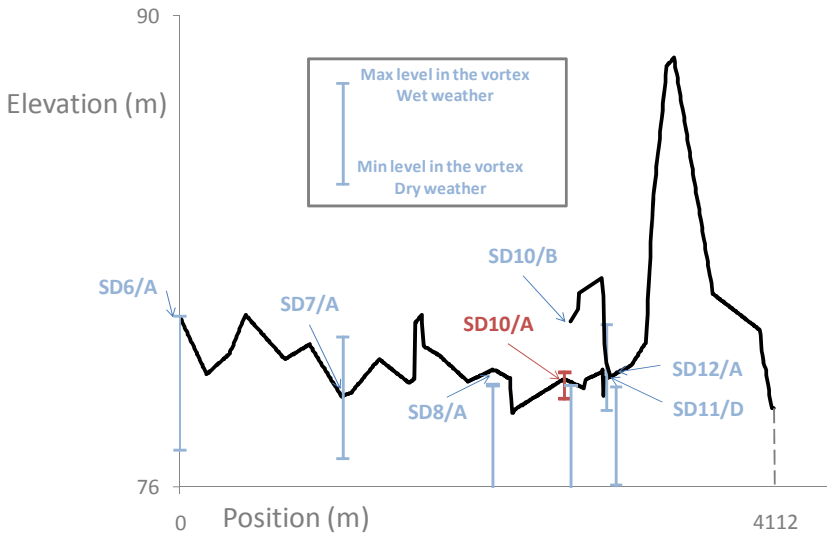

Figure 83: 6 vortex cells +1 pumping station supply the pipe in sewage water

In order to reduce the intensities of water hammer induced by the starting/stopping of the pumps, ARAA surge vessels equip the pumping stations (except SD10/A) and air vents are placed at each high points of the pipe. Araa vessel is a vertical tank connected to the pipework by a large connection at the bottom (Figure 84). The top of this vessel has a compression chamber limited by the ventilation tube with a shut off float valve. When the pump starts, the pressure arises in the pipe. Since the vessel is at atmospheric pressure, water discharges into it. As the level of the water rises in the level, it expels air. The liquid level increases until it reaches the bottom of a ventilation tube. The air volume situated above the water level is then trapped and compressed. As the system pressure increases, the trapped air is compressed more and more until the system is balanced. Finally, air vents are placed at each high points of the pipe in order to prevent sub-atmospheric pressure to appear. It would indeed cause cavitation.

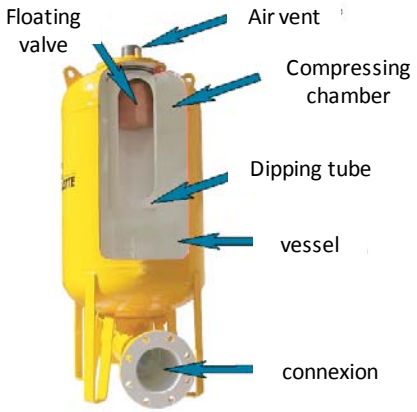

Figure 84: ARAA vessel prevent too intense water hammer

For the evaluation of head losses, the mission statement distinguishes steady cases from unsteady flows. For steady states, the friction is computed by the Colebrook-White correlation with a global roughness height of 1.5mm. This value is greater than the actual roughness height in order to take into account the local head losses. For transient cases, the roughness height is set to 0.2mm, which is a more realistic value for iron-cast pipes. However, a local head-loss coefficient is affected at each pumping stations. Based on the guidelines for such coefficient [151], I confirmed the values given by the mission statement (detailed in Table 6).

Table 6: A local head-loss coefficient is affected at each pumping station for unsteady cases

Pump	SD6/A	SD7/A	SD8/A	SD10/B	SD11/D	SD12/A
Coefficient k	5	5.6	5	6.7	4.7	5

5.3.2 Design Criteria and Critical Cases

The hydraulic design consists in assessing a number of criteria in all the situations likely to occur in the low-pressure network. For this purpose, it is necessary to identify the criteria to meet and the most critical cases of functioning that may occur.

The mission statement, imposed by the contracting authorities, imposes five main design criteria. First, the pumps must operate with a hydraulic efficiency superior to minimal values (35% in extreme cases and 50% in optimal cases). Second, the NPSH must remain greater than the required NPSH in all operating cases. Third, the maximum pressure head in the pipes is set at 100m, and the minimum pressure head is set at -3m. Fourth, the velocity of the pipe must reach several times a day the minimum value necessary to ensure the flushing out of the pipe. This value is evaluated around 1.2m/s. Finally, the ARAA vessel must be aerated (put at atmospheric pressure) at least two times a day.

Determined by the HACH, the critical cases consist in both the dry weather and the wet weather. Dry weather designates the minimum level of water inside the pumping stations. Wet weather corresponds to its maximum level. We also distinguish the cases where all pumps run simultaneously from the cases where a single pump is functioning.

5.3.3 Results of Steady Simulations

The first verification considers the steady states, for which the whole system (low-pressure pipe and pumping stations) has reached equilibrium. It requires performing 16 simulations:

- all pumps discharge in the pipe in dry and wet weather conditions (2 cases);
- each pump discharges on its own in dry and wet conditions (7x2 cases).

This subsection presents the results of theses simulations. In particular, I underline that the current situation does not meet all the design criteria. Some modifications of the low-pressure pipe are necessary.

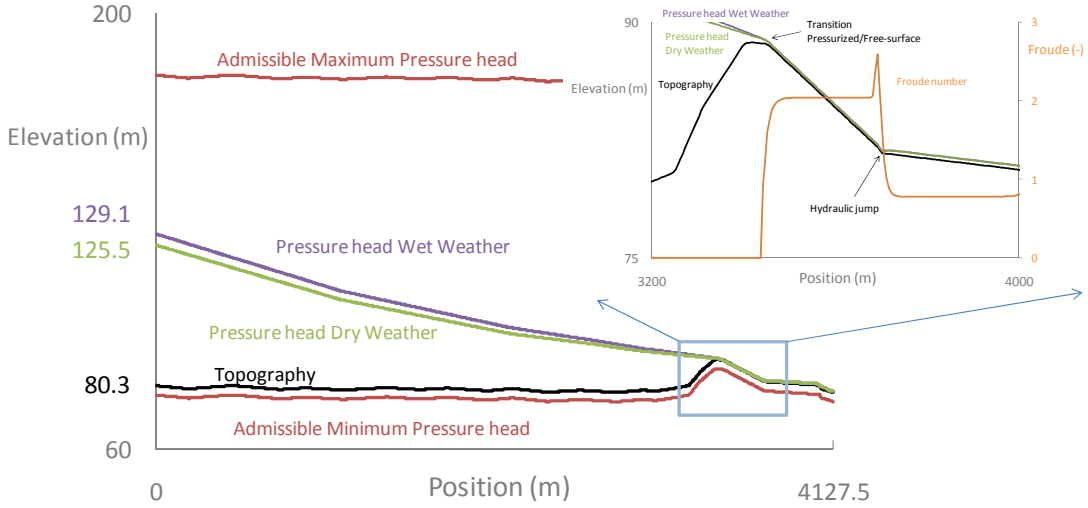

Figure 85: The pressure profiles along the low-pressure pipe show a pressurized part and a free surface part. A hydraulic jump connects the super- and sub-critical parts of the gravity flow.

In both dry and wet weather conditions, the flow is pressurized upstream the high point and free surface downstream (Figure 85). It is an obvious example of mixed flow. The transition at the high point also corresponds to a trans-critical point. The first part of the gravity flow is indeed super-critical (see the Froude profile given in Figure 85). A hydraulic jump connects the super- and sub-critical parts of the gravity flow. According to the mission statement, admissible pressure heads range between -3m and 100m. In steady states, the pressure head remains within these limits. Design criteria in terms of pressure are then clearly met.

When all pumps discharge in the low-pressure pipe in dry weather conditions, the total discharge is 78.8l/s (Table 7). For each pump, the water elevation corresponding to the equilibrium of the dynamic characteristic is given. The pump efficiency is greater than 30% for the first four pumps (SD6/A, SD7/A, SD8/A, and SD10/A), but not for the last three. The efficiency design criteria are then not met for these cases. The computed NPSH for each pump is lower than the required 9.9m. Finally, the analysis of both the velocity along the pipe and the velocities in the junction pipes between the pumping stations and the low-pressure pipes shows that the minimum velocity is not reached in the pipe linking the last three stations with the gallery. This may cause sedimentation.

Table 7: Functioning parameters of the pumping stations - all pumps discharge in dry weather conditions

Pumping Station	Water level in the vortex cell	Water elevation	Discharge	Added discharge	Pipe Area	Velocity	Pump Efficiency	NPSH	Connection pipe area	Velocity in the connection
	[m]	[m]	[l/s]	[l/s]	[m²]	m/s	%	[m]	[m²]	[m/s]
SD6/A	77.08	125.5	21.9	21.9	0.019	1.13	54	3.3	0.014	1.60
SD7/A	76.84	108.0	16.8	38.6	0.034	1.13	48	2.9	0.010	1.76
SD8/A	74.44	97.0	16.0	54.6	0.053	1.03	48	2.9	0.015	1.10
SD10/A	79.41	93.6	3.9	58.5	0.053	1.10	39	0.0	0.002	2.00
SD10/B	76.78	94.1	10.7	10.7	0.014	0.78	15	3.9	0.015	0.74
SD11/D	78.27	91.3	3.3	72.6	0.076	0.95	30	4.0	0.015	0.23
SD12/A	76.03	91.1	6.2	78.8	0.076	1.03	22	3.8	0.010	0.65

In wet weather conditions, the total discharge in the gallery is 92.1l/s (Table 8). The water elevation corresponding to the equilibrium state of each pump is naturally higher than for dry weather conditions, but remains within the admissible range. In terms of pump efficiency, stations SD10/B and SD11/D still not reach the design criteria. The computed NPSH for each pump is lower than the required 9.9m. Finally, the minimum velocity is reached in each pipe except in connections of the pumping stations SD10/B and SD11/D.

Table 8: Functioning parameters of the pumping stations - all pumps discharge in wet weather conditions

Pumping Station	Water level in the vortex cell	Water elevation	Discharge	Added discharge	Pipe Area	Velocity	Pump Efficiency	NPSH	Connection pipe area	Velocity in the connection
	[m]	[m]	[l/s]	[l/s]	[m²]	m/s	%	[m]	[m²]	[m/s]
SD6/A	81.08	129.1	22.3	22.3	0.019	1.15	54	3.5	0.014	1.63
SD7/A	80.46	110.8	17.8	40.2	0.034	1.17	52	3.0	0.010	1.88
SD8/A	79.02	98.9	20.0	60.2	0.053	1.13	52	3.2	0.015	1.38
SD10/A	79.71	94.7	2.8	63.0	0.053	1.19	33	0.0	0.002	1.43
SD10/B	78.60	96.1	12.7	12.7	0.014	0.93	35	3.7	0.015	0.87
SD11/D	80.82	79.2	4.8	80.4	0.076	1.05	26	5.0	0.015	0.33
SD12/A	78.97	91.9	11.6	92.1	0.076	1.20	41	2.8	0.010	1.22

Eventually, Table 9 gives the functioning parameters of each pumping station discharging alone in the low-pressure pipe. Naturally, each pump supplies the gallery with a greater discharge than in the previous scenario. However, it is still not sufficient to reach the minimum velocity in the junction pipe with SD10/B.

Table 9: Functioning parameters of the pumping stations – a single pump discharges in wet weather conditions

Pumping Station	Water level in the vortex cell	Water elevation	Discharge	Added discharge	Pipe Area	Velocity	n pipe area	the connection
	[m]	[m]	[l/s]	[l/s]	[m²]	m/s	[m²]	[m/s]
SD6/A	81.08	121.4	26.5	26.5	0.019	1.37	0.014	1.94
SD7/A	80.46	97.6	30.2	30.2	0.034	0.88	0.010	3.17
SD8/A	79.02	90.3	25.7	25.7	0.053	0.48	0.015	1.77
SD10/A	79.71			0.0	0.053	0.00	0.002	0.00
SD10/B	78.60	92.9	13.0	13.0	0.014	0.95	0.015	0.89
SD11/D	80.82	89.0	18.1	18.1	0.076	0.24	0.015	1.25
SD12/A	78.97	88.9	11.8	11.8	0.076	0.15	0.010	1.24

In conclusion, there is clearly a problem in the design of the station SD10/B. The efficiency of the pump is lower than the requirement of the contracting authority. Its discharge is not important enough to reach a velocity of 1.2m/s and to prevent the sedimentation.

5.3.4 Results of Unsteady Simulations

Once the steady states verified, it is necessary to define the situations likely to produce water hammers and other transient phenomena. Principally, either the starting/stopping of one or several pumps, the closure/opening of one or several gates, or the apparition of a check valve slam may induce a water hammer. Consequently, unsteady verifications require here performing 28 simulations:

- simultaneous starting of all pumps in dry and wet weather conditions (2 cases);
- starting of a single pump in dry and wet weather conditions (7x2 cases);
- simultaneous stopping of all pumps in dry and wet weather conditions (2 cases);
- starting of a single pump in dry and wet weather conditions (7x2 cases).

In each of these simulations, the extreme pressure heads must be compared with admissible values. In particular, specific verifications aim at assessing the impact of the check valve slam. Finally, the aeration of ARAA vessels is checked in the case of pump's stopping. This subsection presents the results of these simulations. To be more precise, I show that pressure heads remain within the admissible range, except at the pumping station SD10/B. What is more, the presence of the high point prevents the aeration of ARAA vessels.

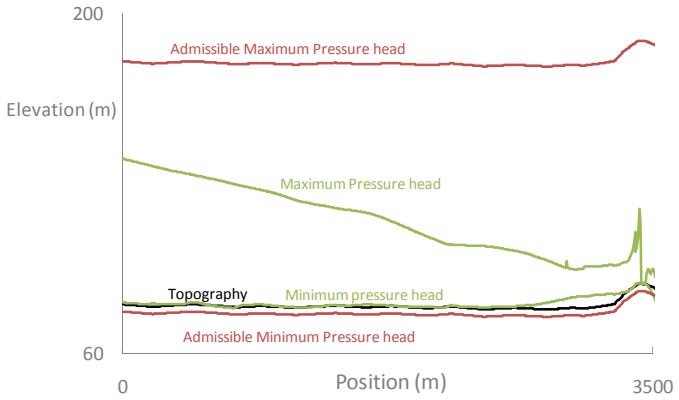

Figure 86: Extreme pressure heads induced by the simultaneous starting/stopping of all pumps remain within the admissible range in dry weather conditions

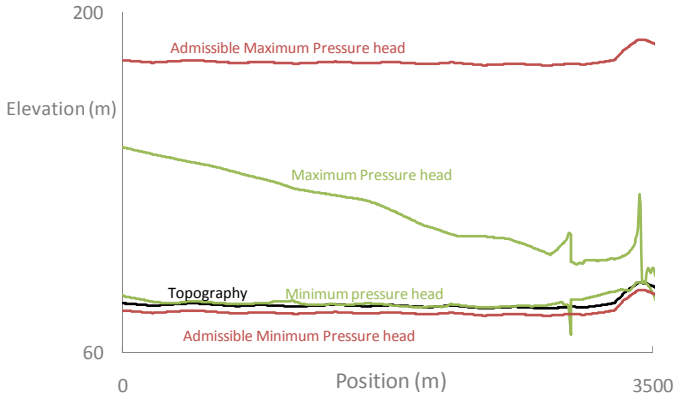

Figure 87: Extreme pressure heads induced by the simultaneous starting/stopping of all pumps remain within the admissible range in wet weather conditions

Extreme pressure heads induced by the simultaneous starting/stopping of all pumps are given in Figure 86 for dry weather conditions and in Figure 87 for wet weather conditions. Their values remain clearly within the admissible range such that the design criterion is met. Nevertheless, the profiles underline the apparition of oscillations. A part of them is due to the water hammer, other results from numerical instabilities. This problem has been widely investigated in Chapter 5. The same results apply for the starting/stopping of each pump on its own.

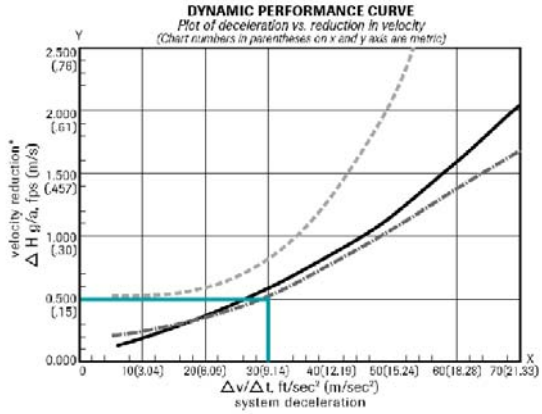

Figure 88: The dynamic performance curve predicts the maximum reverse velocity

Check valve slam occurs after pump stoppage when the system flow reverses back towards the pump before the check valve is fully closed [292]. The reverse flow causes the check valve to close rapidly through the remaining portion of its travel. The closed valve stops the reverse flow instantaneously. It causes a water hammer in the pipe. In order to evaluate the intensity of the reverse flow (and the associated pressure surge), the valve manufacturer provides the dynamic characteristics of the valve (Figure 88). It gives the relationship between the deceleration of the liquid column and the maximum reverse velocity. The reverse velocity can be converted directly into a water hammer pressure using the Joukowsky equation[325]. As pointed in Table 10, this water hammer pressure is compared with the available pressure in order to check the adequacy of the check valve for the pumping situation. By available pressure, I mean maximum pressure variation that can occur without creating pressure heads out of the admissible range. In the case of “Sambre Droite”, all required heads are lower than available heads, except for the pumping station SD10/B. This station does not meet the design criteria.

Table 10: Required and available pressure heads are compared to check the adequacy of the check valve.

		SD6/A	SD7/A	SD8/A	SD11/D	SD12/A	SD10/B
All pumps Dry weather	Velocity variation	-7.89	-7.35	-3.99	-2.64	-2.78	-5.88
	Required head	20.68	20.68	11.339	7.337	8.04	16
	Available head	37.25	27.36	17.2	13.6	12.53	11.34
All pumps Wet weather	Velocity variation	-7.94	-7.56	-4.42	-2.91	-3.41	-5.84
	Required head	18	18	8.67	6	6	12.673
	Available head	40.12	29.6	18.86	14.1	12.76	12.46
Single pump wet weather	Velocity variation	-8.10	-8.07	-3.05	-2.50	-2.54	-8.47
	Required head	18	18	6.67	6	6	20
	Available head	39.67	19	9.89	10.86	7.81	13.9

Finally, verification of the water level in the ARAA vessel shows that the air remains in all cases under pressure. After a certain time, the entrapped air dissolves within the water. It causes malfunction in the ARAA vessel. Modifications must be brought to the ARAA vessels in order to ensure their aeration twice a day.

Summary and conclusion

Based on the new mathematical model for pure water flows (Chapter 3) and its discretization (Chapter 4), I have extended the applicability of the module WOLF1D to pressurized flows as well. As pointed in section 5.1, a large campaign of validation confirmed the ability of the modified computational code to simulate pure water mixed flows, including sub-atmospheric pressurized flows. In addition, comparison between the six solvers (Wolf, Wolf pseudo-unsteady, Roe, Exact Riemann, AUSM, and Lax-Friedrich) argued in favor of the Wolf splitting (unsteady and pseudo-unsteady).

Once validated, the modified module WOLF1D has served for assessing the hydraulic design of two different sewer systems: the storm water gravity drainage system of an airport (section 5.2), and a city low-pressure sewer network (section 5.3). In the first case, frequent inundations of the airport's parking facilities prompted authorities to assess the design of the gravity sewer network. Based on the performance criteria prescribed by the norm prEN752-4:1997, WOLF1D has been proven an efficient tool for investigating the hydraulic design. In the second cases, the sewer system involved low-pressure pipes. The assignment consisted in validating the hydraulic design. Both steady and transient phenomena were critical. In this respect, WOLF1D was again proven very useful and enabled to identify various defects in the first design of the low-pressure pipe.

In conclusion, the new module WOLF1D is a useful and efficient tool for simulating pure water flows. It extended the applicability of WOLF to new practical problems arising in civil and environmental engineering. This is a major competitive advantage for consultancy firms.

However, the model still suffers two shortcomings that prevent its application in some cases. First, post-transition oscillations may cause the instability of the computation. The cause of the first shortcoming has been identified in chapter 4. Solving this problem requires using self-adapting mesh grid that is out of the scope of this thesis. Second, the code neglects air-water interactions in the pipe. However, the presence of air may strongly affect the dynamics of the flow. Clearly, further work is required to extend the approach presented in chapter 3-5 to air-water flows. This is the topic of the next chapters.

Modelling Transient Air-water Flows in Civil and Environmental Engineering

Part II: Multiphase Flows

Chapter 6 Multiphase Flows: Free Surface Model

Chapter aims at:

- ✓ establishing the conditions of validity of the one-dimensional approximation;
- ✓ introducing suitable definitions for area-averaged parameters;
- ✓ deriving a one-dimensional free surface drift-flux model;
- ✓ accommodating the model with a vertical distribution of the parameters.

Presented in Chapter 2, the literature review has shown that both standard single- and multiphase models are not fully suitable for describing transient air-water flows. On the one hand, single-phase computational codes make use of an advection-diffusion equation that describes the transport of air. This approach reveals five weaknesses that may cause inaccuracy and even errors in some cases. First, the definition of the concentration in dispersed phase is wooly. Second, the model does not account for the adverse impact of the dispersed phase on the water flow. Third, velocity of the dispersed phase may differ largely from the water velocity. It does not accord with the definition of diffusion usually used in the advection-diffusion equation. Fourth, friction correlations simply neglect the effect of the dispersed phase. Finally, mixed flow models cannot account for the presence of air at all. On the other hand, multiphase models are based on the Local Instant Formulation such that they describe accurately interactions between phases. In this respect, I showed in Chapter 2 that the drift-flux model seems a promising alternative to the Reynolds-Averaged Navier Stokes equations (RANS) for simulating environmental flows. This model is indeed able to describe in a unified framework the transport of a dispersed phase, its interaction with the water flow, and the notion of concentration naturally arises in the derivation of a diffusion equation. Theoretically, it is a good candidate to create a solver for transient air-water flows. However, its use in civil and environmental engineering has remained circumscribe to a very few attempts. In particular, 1D drift-flux models available in the literature only describe pressurized flows.

Obviously, further research is needed for establishing a 1D mathematical formulation based on the drift-flux model. It requires integrating the 3D drift-flux model, discretizing the result, implementing it into a computational code, and validating it by comparison with experimental, numerical, and analytical data.

In this respect, the present chapter proposes an original demonstration of the cross-sectional integration of the 3D drift-flux model over a very general cross section. As pointed in Figure 89, the domain of integration presents a free surface. In order to accommodate

the model with a vertical distribution of the flow parameters, the cross-section is divided into N-1 layers. The subscript l denotes an arbitrary layer. The depth of the l^{th} layer is defined as h_l. In this framework, the free surface and bottom ground can be considered as peculiar interfaces. Finally, a Cartesian coordinate system Oxyz is set in such a way that x-axis is parallel to the predominating flow direction of the computational domain. The inclination of the z-axis with the vertical is given by the angle θ.

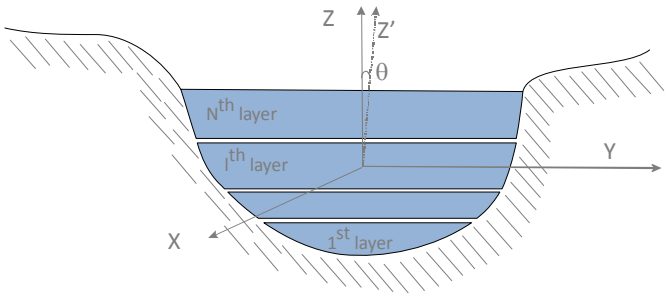

Figure 89: The domain of integration presents a free surface and includes l layers

The whole development results in a general mathematical model for free surface stratified two-phase flows. Completely original, the model includes three partial differential equations for each layer. The simplicity of the original model results from suitable definitions of the area average $\langle\ \rangle_l$, and of the mixture velocity $\tilde{u}_{m,l}$. The first equation expresses the mixture continuity:

$$\frac{\partial \langle \rho_m \rangle_l \Omega_l}{\partial t} + \frac{\partial \langle \rho_m \rangle_l \tilde{u}_{m,l} \Omega_l}{\partial x} = q_{m,\perp,l} \tag{6.1}$$

It ensures the mass conservation of both the water and the dispersed phase as a whole; but not separately. In order to enforce the mass conservation of both phases taken on their own, a diffusion equation complements the model:

$$\frac{\partial \langle \alpha_d \rangle_l \Omega_l}{\partial t} + \frac{\partial}{\partial x}\left(\langle \alpha_d \rangle_l \tilde{u}_{m,l} \Omega_l + \langle \alpha_d \rangle_l \frac{\rho_w}{\langle \rho_m \rangle_l} \tilde{U}_{dj,l} \Omega_l \right) = \left\langle \Gamma_d / \rho_d \right\rangle_l \Omega_l + q_{\alpha,\perp,l} \tag{6.2}$$

where the area-averaged drift velocity $\tilde{U}_{dj,l}$ accounts for the relative velocity between both phases. Finally, a single equation accounts for the momentum conservation of the mixture (water and dispersed phase) taken as a whole:

$$\begin{aligned} &\frac{\partial \langle \rho_m \rangle_l \tilde{u}_{m,l} \Omega_l}{\partial t} + \frac{\partial \beta_l \langle \rho_m \rangle_l \tilde{u}_{m,l} \tilde{u}_{m,l} \Omega_l}{\partial x} + \frac{\partial}{\partial x}\left(\beta_l \frac{\langle \alpha_d \rangle_l}{1 - \langle \alpha_d \rangle_l} \frac{\rho_d \rho_w}{\langle \rho_m \rangle_l} \tilde{U}_{dj,l} \tilde{U}_{dj,l} \Omega_l \right) \\ &= \langle \rho_m \rangle_l F_{m,x} \Omega_l - \frac{\partial p_{l/l+1}}{\partial x} \Omega_l - F_{m,z} \frac{\partial P_{\Omega_l}}{\partial x} + F_{m,z} P_{G,\partial\Omega_l} - F_{m,z} \langle \rho_m \rangle \Big|_z^{h_{l/l+1}} h_l(x,t) l_w\left(h_{l-1/l}\right) \frac{\partial h_{l-1/l}}{\partial x} \\ &+ \frac{\partial \langle \tau_{Gm,xx} \rangle_l \Omega_l}{\partial x} + \langle M_x \rangle_l \Omega_l + F_{\partial\Omega,l} - E_{\partial\Omega,l} \end{aligned} \tag{6.3}$$

where the area-averaged drift velocity $\tilde{U}_{dj,l}$ has the same value than in the diffusion equation. Its value is defined by a constitutive equation that replaces the momentum equation of the dispersed phase. Finally, the form of the hydrostatic pressure term $P_{\Omega l}$ results from the simplification of the momentum equations along the y- and z-axis.

The following sections provide a complete demonstration of equations (6.1)-(6.3). First, a dimensional analysis underlines the validity of the one-dimensional assumption (section 6.1). Next, I introduce properly-defined mean values such that the formulation of the new model remains simple (section 6.2). In section 6.3, physical boundary conditions are defined at the boundaries of the integration domain. At this point, I can begin the cross-sectional integration of the 3D drift-flux model over the cross-section (Figure 90). Consecutively, I integrate the mixture continuity equation (sub-section 6.4.1), the diffusion equation (sub-section 6.4.2), and the mixture momentum equation along the x-axis (sub-section 6.4.3). This last expression is further simplified by introducing a particular formulation for the convective term (sub-section 6.4.4) and for the pressure gradient (sub-section 6.4.5).

6.1 DIMENSIONAL ANALYSIS AND SIMPLIFICATION

In order to integrate the 3D drift-flux model over the flow cross-section, we need to decouple the various equations from each other. The following dimensional analysis underlines the validity of the decoupling conditions. In particular, it shows that the approximation remains valid only if transversal velocities are small by comparison with the longitudinal velocity. It also shows that the momentum equations along both the y-axis and the z-axis simplify into a hydrostatic distribution of the pressure over the flow cross-section.

Dimensional analysis relies on the definition of the following non-dimensional variables:

- l_0 is a characteristic dimension of the section, like the river width for instance;
- ρ_0 is the characteristic density of the mixture;
- u_0, v_0, w_0 are the characteristic velocities of the mixture fluid.

We can compare the velocities along the three axes to the characteristic velocity along the predominating flow direction (x-axis) by defining:

$$\varepsilon_x \triangleq \frac{u_0}{u_0} \quad ; \quad \varepsilon_y \triangleq \frac{v_0}{u_0} \quad ; \quad \varepsilon_z \triangleq \frac{w_0}{u_0} \tag{6.4}$$

The ratio of the characteristic velocities gives the characteristic lengths:

$$\lambda_x \triangleq l_0 \frac{\varepsilon_x}{\varepsilon_y} \quad ; \quad \lambda_y \triangleq l_0 \quad ; \quad \lambda_z \triangleq l_0 \frac{\varepsilon_z}{\varepsilon_y} \tag{6.5}$$

Let us choose the characteristic time as:

$$t_0 \triangleq \frac{\lambda_x}{u_0} \triangleq \frac{\lambda_y}{v_0} \triangleq \frac{\lambda_z}{w_0} = \frac{l_0}{v_0} \tag{6.6}$$

We can logically make non-dimensional both the coordinates and the time:

$$x' \triangleq \frac{x}{\lambda_x} \quad ; \quad y' \triangleq \frac{y}{\lambda_y} \quad ; \quad z' \triangleq \frac{z}{h_0} \quad ; \quad t' \triangleq \frac{t}{t_0} = \frac{v_0}{l_0} t \tag{6.7}$$

and deduce from them non-dimensional velocities:

$$u'_m \triangleq \frac{dx'}{dt'} = \frac{1}{u_0}\frac{dx}{dt} = \frac{u_m}{u_0}; \qquad v'_m \triangleq \frac{dy'}{dt'} = \frac{1}{v_0}\frac{dy}{dt} = \frac{v_m}{v_0}; \qquad w'_m \triangleq \frac{dz'}{dt'} = \frac{1}{w_0}\frac{dz}{dt} = \frac{w_m}{w_0} \tag{6.8}$$

By analogy, the diffusion velocities can be made non-dimensional as follows:

$$U'_{dm} \triangleq \frac{U_{dm}}{u_0} \quad ; \quad V'_{dm} \triangleq \frac{V_{dm}}{v_0} \quad ; \quad W'_{dm} \triangleq \frac{W_{dm}}{w_0} \tag{6.9}$$

If we assume pressure gradient occurs essentially along the predominating flow direction, the non-dimensional pressure can be defined as:

$$p'_m \triangleq \frac{p_m}{\rho_0 u_0^2} \tag{6.10}$$

In a similar manner, the non-dimensional density and body forces are legitimately given by:

$$\rho'_m \triangleq \frac{\rho_m}{\rho_0} \qquad ; \qquad \mathbf{F}'_m \triangleq \frac{\mathbf{F}_m \lambda_z l_0}{u_0^2} = \mathbf{F}_m l_0 \frac{w_0}{u_0^2 v_0} \tag{6.11}$$

Non-dimensional form of the viscous, turbulent, and diffusion stresses are given by:

$$\tau'_{ij} \triangleq \frac{\tau_{m,ij}}{\rho_0 u_0^i u_0^j} \quad ; \quad \tau'^{T}_{ij} \triangleq \frac{\tau^T_{ij}}{\rho_0 u_0^i u_0^j} \quad \text{and} \quad \tau'^{D}_{ij} \triangleq \frac{\tau^D_{ij}}{\rho_0 u_0^i u_0^j} \tag{6.12}$$

Similarly, the mixture momentum source has the following non-dimensional form:

$$M'_i \triangleq t_0 \frac{M_{m,i}}{\rho_0 u_0^i} \tag{6.13}$$

Finally, the non-dimensional phase change mass generation is defined as:

$$\Gamma'_d \triangleq t_0 \frac{\Gamma_d}{\rho_0} \tag{6.14}$$

By introducing definition (6.4) to (6.14) into the 3D drift-flux model, we obtain the non-dimensional equations for an essentially one-dimensional flow:

- for the mixture continuity equation:

$$\frac{\partial \rho'_m}{\partial t'} + \frac{\partial \rho'_m u'_m}{\partial x'} + \frac{\partial \rho'_m v'_m}{\partial y'} + \frac{\partial \rho'_m w'_m}{\partial z'} = 0 \tag{6.15}$$

- for the diffusion equation:

$$\frac{\partial \alpha_d}{\partial t'} + \frac{\partial \alpha_d u'_m}{\partial x'} + \frac{\partial \alpha_d v'_m}{\partial y'} + \frac{\partial \alpha_d w'_m}{\partial z'} + \frac{\partial \alpha_d U'_{dm}}{\partial x'} + \frac{\partial \alpha_d V'_{dm}}{\partial y'} + \frac{\partial \alpha_d W'_{dm}}{\partial z'} = \Gamma'_d \tag{6.16}$$

- for the mixture momentum equation along the x-axis:

$$\begin{aligned} &\varepsilon_x \varepsilon_y \left(\frac{\partial \rho'_m u'_m}{\partial t'} + \frac{\partial \rho'_m u'_m u'_m}{\partial x'} + \frac{\partial \rho'_m u'_m v'_m}{\partial y'} + \frac{\partial \rho'_m u'_m w'_m}{\partial z'} \right) - \frac{\varepsilon_y}{\varepsilon_z} \rho'_m F'_{m,x} + \frac{\varepsilon_y}{\varepsilon_x} \frac{\partial p'_m}{\partial x'} \\ &= \\ &+\varepsilon_x \varepsilon_y \left(\frac{\partial \tau'_{xx}}{\partial x'} + \frac{\partial \tau'_{yx}}{\partial y'} + \frac{\partial \tau'_{zx}}{\partial z'} + \frac{\partial \tau'^{T}_{xx}}{\partial x'} + \frac{\partial \tau'^{T}_{yx}}{\partial y'} + \frac{\partial \tau'^{T}_{zx}}{\partial z'} + \frac{\partial \tau'^{D}_{xx}}{\partial x'} + \frac{\partial \tau'^{D}_{yx}}{\partial y'} + \frac{\partial \tau'^{D}_{zx}}{\partial z'} + M'_{m,x} \right) \end{aligned} \tag{6.17}$$

- for the mixture momentum equation along the y-axis:

$$\begin{aligned} &\varepsilon_y^2 \left(\frac{\partial \rho'_m v'_m}{\partial t'} + \frac{\partial \rho'_m v'_m u'_m}{\partial x'} + \frac{\partial \rho'_m v'_m v'_m}{\partial y'} + \frac{\partial \rho'_m w'_m v'_m}{\partial z'} \right) - \frac{\varepsilon_y}{\varepsilon_z} \rho'_m F'_{m,y} + \frac{\partial p'_m}{\partial y'} \\ &= \\ &+\varepsilon_y^2 \left(\frac{\partial \tau'_{xy}}{\partial x'} + \frac{\partial \tau'_{yy}}{\partial y'} + \frac{\partial \tau'_{zy}}{\partial z'} + \frac{\partial \tau'^{T}_{xy}}{\partial x'} + \frac{\partial \tau'^{T}_{yy}}{\partial y'} + \frac{\partial \tau'^{T}_{zy}}{\partial z'} + \frac{\partial \tau'^{D}_{xy}}{\partial x'} + \frac{\partial \tau'^{D}_{yy}}{\partial y'} + \frac{\partial \tau'^{D}_{zy}}{\partial z'} + M'_{m,y} \right) \end{aligned} \tag{6.18}$$

- for the mixture momentum equation along the z-axis:

$$\begin{aligned} &\varepsilon_z \varepsilon_y \left(\frac{\partial \rho'_m w'_m}{\partial t'} + \frac{\partial \rho'_m w'_m u'_m}{\partial x'} + \frac{\partial \rho'_m w'_m v'_m}{\partial y'} + \frac{\partial \rho'_m w'_m w'_m}{\partial z'} \right) - \frac{\varepsilon_y}{\varepsilon_z} \rho'_m F'_{m,z} + \frac{\varepsilon_y}{\varepsilon_z} \frac{\partial p'_m}{\partial z'} \\ &= \\ &+\varepsilon_z \varepsilon_y \left(\frac{\partial \tau'_{xz}}{\partial x'} + \frac{\partial \tau'_{yz}}{\partial y'} + \frac{\partial \tau'_{zz}}{\partial z'} + \frac{\partial \tau'^{T}_{xz}}{\partial x'} + \frac{\partial \tau'^{T}_{yz}}{\partial y'} + \frac{\partial \tau'^{T}_{zz}}{\partial z'} + \frac{\partial \tau'^{D}_{xz}}{\partial x'} + \frac{\partial \tau'^{D}_{yz}}{\partial y'} + \frac{\partial \tau'^{D}_{zz}}{\partial z'} + M'_{m,z} \right) \end{aligned} \tag{6.19}$$

The cross-sectional scale of the computational domain has been assumed way smaller than the predominating flow direction scale. Consequently, transversal velocities are way smaller than velocities along the x-axis such that ε_z and ε_y are relatively small. On account of this, ε_z^2, ε_y^2, and $\varepsilon_z * \varepsilon_y$ are negligible in comparison to the unit. Except at localized singularities, most of the flows accord with such an assumption. It includes cases for which feeble cross-sectional flow appears due to gradual variation of the flow cross-section, large scale meanders, and smooth variation of the predominating flow direction. By this way, the momentum equations along both the y-axis and the z-axis are simplified in a very useful

form that makes think of a hydrostatic distribution of the pressure over the flow cross-section:

- The mixture pressure is constant over the flow width:

$$\frac{\partial p_m}{\partial y} = 0 \tag{6.20}$$

- The mixture pressure is hydrostatic over the flow depth:

$$\frac{\partial p_m}{\partial z} = -\rho_m F'_{m,z} \tag{6.21}$$

The system of PDE's does not go through other simplifications. However, these simple relations virtually cancel the momentum equations along the y-axis and z-axis, and provide instead a constitutive equation for the pressure that may be introduced in the cross-sectional integrated form of the remaining equations.

6.2 Definitions of Area-Averaged Values

Like in the case of the 3D drift-flux model, properly defining the mean values greatly simplifies the formulation of the one-dimensional model. For this purpose, I successively introduce herein the area-average $\langle f \rangle_l(x,t)$ of a function $f(\mathbf{x},t)$ over the l^{th} layer; the void-fraction weighted area-average $\langle\langle f_k \rangle\rangle_l(x,t)$ of a phase function $f_k(\mathbf{x},t)$; the mixture velocity $\tilde{u}_{m,l}(x,t)$, and the area-averaged diffusion velocity $\tilde{U}_{dm,l}$, and the area-averaged drift velocity $\tilde{U}_{dj,l}$. Subsequently, important relations between these values are mathematically derived.

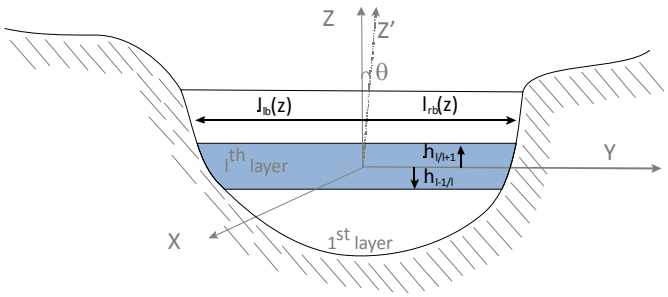

Figure 90: The domain of integration is divided in layers over which mean values are defined

As pointed out in Figure 90, the domain over which mean values are defined consists in a single layer of the whole domain of integration (Figure 89). The water depth h_l of the layer is defined as:

$$h_l \triangleq h_{l/l+1} - h_{l-1/l} \tag{6.22}$$

For any given elevation z, the flow width is defined as (Figure 90):

$$l(z) \triangleq l_{rb}(z) - l_{lb}(z) \tag{6.23}$$

Consequently, the flow cross-section Ω_l of the l^{th} layer is defined as:

$$\Omega_l \triangleq \int_{h_{l-1/l}}^{h_{l/l+1}} \int_{l_{lb}}^{l_{rb}} dydz \tag{6.24}$$

Naturally, the *area-average* of a general function $f(\mathbf{x},t)$ over this layer is defined as follows:

$$\langle f \rangle_l(x,t) \triangleq \frac{1}{\Omega_l} \int_{\Omega_l} f(\mathbf{x},t) dA = \frac{1}{\Omega_l} \int_{h_{l-1/l}}^{h_{l/l+1}} \int_{l_{lb}}^{l_{rb}} f(\mathbf{x},t) dydz \tag{6.25}$$

I also introduce the *void fraction weighted area-average* of a general function $f_k(\mathbf{x},t)$:

$$\langle\langle f_k \rangle\rangle_l(x,t) \triangleq \frac{\langle \alpha_k f_k \rangle_l}{\langle \alpha_k \rangle_l} = \frac{\int_{h_{l-1/l}}^{h_{l/l+1}} \int_{l_{lb}}^{l_{rb}} (\alpha_k f_k) dydz}{\int_{h_{l-1/l}}^{h_{l/l+1}} \int_{l_{lb}}^{l_{rb}} (\alpha_k) dydz} \tag{6.26}$$

Based on definitions (6.25) and (6.26), I may define adequate mean values for flow variables appearing in the 3D drift-flux model. Since both fluids are assumed incompressible, the area-averaged *mixture density* in the l^{th} layer is given by:

$$\langle \rho_m \rangle_l = \langle \alpha_d \rangle_l \rho_d + \left(1 - \langle \alpha_d \rangle_l\right) \rho_w \tag{6.27}$$

The void fraction weighted area-averaged *phase velocity* is given as:

$$\langle\langle u_k \rangle\rangle_l \triangleq \frac{\langle \alpha_k u_k \rangle_l}{\langle \alpha_k \rangle_l} \tag{6.28}$$

Physically, this value would be the mean velocity in the l^{th} layer if the fluid in it was only the phase k. It is an intrinsic value to the k^{th} phase. In addition, the *mixture velocity* is defined as the mixture density weighted area-average of the mixture velocity:

$$\tilde{u}_{m,l} \triangleq \frac{\langle \rho_m u_m \rangle_l}{\langle \rho_m \rangle_l} = \frac{\langle \alpha_d \rangle_l \rho_d \langle\langle u_d \rangle\rangle_l + \left(1 - \langle \alpha_d \rangle_l\right) \rho_w \langle\langle u_w \rangle\rangle_l}{\langle \rho_m \rangle_l} \tag{6.29}$$

From a physical point of view, this value is the velocity of the centre of mass of the mixture composed of the water and the dispersed phase. This new definition is worthwhile in many respects. First, it greatly simplifies the formulation of equations. Second, it is intimately related to mixture discharge, which is an experimental value:

$$Q_{m,l} = \int_{h_{l-1/l}}^{h_{l/l+1}} \int_{l_b} \rho_m u_m \, dy dz = \left(\langle \alpha_d \rangle_l \rho_d \langle\langle u_d \rangle\rangle_l + \left(1 - \langle \alpha_d \rangle_l\right) \rho_w \langle\langle u_w \rangle\rangle_l \right) \Omega_l = \langle \rho_m \rangle_l \tilde{u}_{m,l} \, \Omega_l \tag{6.30}$$

Obviously, the area-averaged volumetric flux can be written as:

$$\langle j \rangle_l = \langle j_g \rangle_l + \langle j_w \rangle_l = \langle \alpha_d \rangle_l \langle\langle u_d \rangle\rangle_l + \left(1 - \langle \alpha_d \rangle_l\right) \langle\langle u_w \rangle\rangle_l \tag{6.31}$$

The area-averaged *diffusion velocity* and *drift velocity* are naturally defined as:

$$\tilde{U}_{dm,l} \triangleq \langle\langle u_d \rangle\rangle_l - \tilde{u}_m \quad \text{and} \quad \tilde{U}_{dj,l} \triangleq \langle\langle u_d \rangle\rangle_l - \langle j \rangle_l \tag{6.32}$$

Under these new definitions of velocity fields in multiphase flows, basic algebra gives important equations relating the flow parameters. It is thus easy to demonstrate the fundamental relation for the area-averaged diffusion velocity:

$$\rho_g \langle \alpha_g \rangle_l \tilde{U}_{gm,l} + \rho_w \langle \alpha_w \rangle_l \tilde{U}_{wm,l} = 0 \tag{6.33}$$

The relationship between the diffusion velocity and the drift velocity is derived as:

$$\tilde{U}_{dm,l} = \frac{\rho_w}{\langle \rho_m \rangle_l} \tilde{U}_{dj,l} \tag{6.34}$$

Combining equation (6.33) with relation (6.34) gives also:

$$\tilde{U}_{wm,l} = -\frac{\rho_g \langle \alpha_d \rangle_l}{\langle \rho_m \rangle_l \langle \alpha_w \rangle_l} \tilde{U}_{dj,l} \tag{6.35}$$

Combining the definition of the diffusion velocity given by equation (6.32) with the important relations (6.34) and (6.35) gives:

$$\langle\langle u_d \rangle\rangle = \tilde{u}_m + \frac{\rho_w}{\langle \rho_m \rangle} \tilde{U}_{dj} \qquad \text{and} \qquad \langle\langle u_w \rangle\rangle = \tilde{u}_m - \frac{\langle \alpha_d \rangle}{1 - \langle \alpha_d \rangle} \frac{\rho_d}{\langle \rho_m \rangle} \tilde{U}_{dj} \tag{6.36}$$

In the drift-flux model, a problem is solved in terms of averaged void fraction and averaged mixture velocity with a constitutive relation for the drift velocity. Thus, equations (6.36) can be used to recover a solution for the velocity of each phase after a problem is solved.

6.3 BOUNDARY CONDITIONS

When integrating a mathematical formulation, specifying conditions at the boundaries of the integration domain enables to obtain a single result, without any ambiguity. Since the current domain is a cross-section divided in several layers (Figure 89), I must establish boundary conditions at the free surface, at the bottom ground, at the left/right river banks, and at each interfaces between layers. For this purpose, I express impermeability of the interfaces and dynamic equilibrium of the fluid. It results in kinematic boundary conditions, for the mixture fluid and for both phases, as well as dynamic boundary conditions for the mixture.

6.3.1 GENERAL FORMULATION FOR A KINEMATIC BOUNDARY CONDITION

Obviously, one can assume that the free surface, the bottom, the lateral banks, or the layer interfaces circumscribe completely the flow in any given layer. All these interfaces can be described by a mathematical function of the form:

$$f(\mathbf{x},t)=0 \tag{6.37}$$

In addition, I assume that all boundaries are characterized by the property of impermeability [75, 316]. Therefore, the fluid velocity component normal to the interface must be equal to the velocity of the interface in the same direction.

From a geometrical point of view, the component of the velocity of an interface f(**x**,t)=0 normal to itself is given by:

$$\frac{u_I\frac{\partial f}{\partial x}+v_I\frac{\partial f}{\partial y}+w_I\frac{\partial f}{\partial z}}{\sqrt{\left(\frac{\partial f}{\partial x}\right)^2+\left(\frac{\partial f}{\partial y}\right)^2+\left(\frac{\partial f}{\partial z}\right)^2}} \tag{6.38}$$

where u_I, v_I et w_I, are the Cartesian components of the velocity of one interfacial point. Since the identity f(**x**,t)=0 is verified at any given time, its total derivative verifies:

$$\frac{Df}{Dt}=\frac{\partial f}{\partial t}+u_I\frac{\partial f}{\partial x}+v_I\frac{\partial f}{\partial y}+w_I\frac{\partial f}{\partial z}=0 \tag{6.39}$$

This relation can be used to reformulate expression (6.38) as follows:

$$\frac{-\frac{\partial f}{\partial t}}{\sqrt{\left(\frac{\partial f}{\partial x}\right)^2+\left(\frac{\partial f}{\partial y}\right)^2+\left(\frac{\partial f}{\partial z}\right)^2}} \tag{6.40}$$

On the other hand, the fluid velocity normal to the interface is written as:

$$\frac{u_m\frac{\partial f}{\partial x}+v_m\frac{\partial f}{\partial y}+w_m\frac{\partial f}{\partial z}}{\sqrt{\left(\frac{\partial f}{\partial x}\right)^2+\left(\frac{\partial f}{\partial y}\right)^2+\left(\frac{\partial f}{\partial z}\right)^2}} \tag{6.41}$$

Eventually, expressing the equality between equations (6.40) and (6.41) gives the following relation for the total derivative of the function f(**x**,t):

$$\frac{\partial f}{\partial t} + u_m \frac{\partial f}{\partial x} + v_m \frac{\partial f}{\partial y} + w_m \frac{\partial f}{\partial z} = 0 \tag{6.42}$$

It proves that all superficial particles remain at the interface. This result is applied below to derive various boundary conditions [9, 75].

6.3.2 KINEMATIC BOUNDARY CONDITIONS

Kinematic boundary conditions describe the motion of the mixture fluid or of the different phases alone at the boundaries of the integration domain. Consequently, I must establish three different kinematic conditions at each boundary, one for the mixture and one for each phase (water and dispersed phases).

For establishing mixture kinematic conditions, I consider a very general interface between the l^{th} and l^{th+1} layer. Its position is given by the following function:

$$f(\mathbf{x},t) \equiv z = h_{l/l+1}(x,y,t) \qquad l = 1,\ldots,N-1 \tag{6.43}$$

The mixture kinematic condition at the interface between the two layers is derived by application of equation (6.42):

$$\frac{\partial h_{l/l+1}}{\partial t} + u_m\big|_{z=h_{l/l+1}} \frac{\partial h_{l/l+1}}{\partial x} + v_m\big|_{z=h_{l/l+1}} \frac{\partial h_{l/l+1}}{\partial y} - w_m\big|_{z=h_{l/l+1}} \triangleq e_{m,l/l+1} \tag{6.44}$$

where $e_{m,l/l+1}$ [ms^{-1}] accounts for the exchange of mixture fluid through the interface ($e_{m,l/l+1}$ is positive for fluid losses in $l+1^{th}$ layer). In the case of the bottom ground or the free surface, particularization of equation (6.44) gives:

$$\frac{\partial h_b}{\partial t} + u_m\big|_{z=h_b} \frac{\partial h_b}{\partial x} + v_m\big|_{z=h_b} \frac{\partial h_b}{\partial y} - w_m\big|_{z=h_b} \triangleq r_b \tag{6.45}$$

$$\frac{\partial h_s}{\partial t} + u_m\big|_{z=h_s} \frac{\partial h_s}{\partial x} + v_m\big|_{z=h_s} \frac{\partial h_s}{\partial y} - w_m\big|_{z=h_s} \triangleq r_s \tag{6.46}$$

where r_b [ms^{-1}] accounts for the infiltration of fluid into the bottom (r_b is positive for fluid losses) and r_s [ms^{-1}] for the precipitation and evaporation (r_s is positive for fluid injection). At the bank sides, the same approach based on the impermeability of the wall applies. For this purpose, I consider a very general cross section whose width depends on the time and which is defined by the following function:

$$y = l_{rb}(x,z,t) \qquad \text{and} \qquad y = l_{lb}(x,z,t) \tag{6.47}$$

The kinematic condition at the right and left bank of the cross-section is derived as:

$$\frac{\partial l_{rb}}{\partial t} + u_m\big|_{y=l_{rb}} \frac{\partial l_{rb}}{\partial x} - v_m\big|_{y=l_{rb}} + w_m\big|_{y=l_{rb}} \frac{\partial l_{rb}}{\partial z} \triangleq i_l\big|_{y=l_{rb}} \tag{6.48}$$

$$\frac{\partial l_{lb}}{\partial t} + u_m\big|_{y=l_{lb}} \frac{\partial l_{lb}}{\partial x} - v_m\big|_{y=l_{lb}} + w_m\big|_{y=l_{lb}} \frac{\partial l_{lb}}{\partial z} \triangleq i_l\big|_{y=l_{lb}} \tag{6.49}$$

where i_l [ms^{-1}] accounts for the lateral exchange of fluid (i_l is positive for fluid losses).

By analogy with the previous paragraph, the kinematic boundary conditions for the dispersed phase result from equation (6.42). For a very general interface between the l^{th} and l^{th+1} layer whose position is given by equation (6.43), we have:

$$\frac{\partial h_{l/l+1}}{\partial t} + \hat{u}_d\Big|_{z=h_{l/l+1}} \frac{\partial h_{l/l+1}}{\partial x} + \hat{v}_d\Big|_{z=h_{l/l+1}} \frac{\partial h_{l/l+1}}{\partial y} - \hat{w}_d\Big|_{z=h_{l/l+1}} \triangleq e_{d,l/l+1} \tag{6.50}$$

where $e_{d,l/l+1}$ [ms^{-1}] accounts for the exchange of dispersed phase through the interface ($e_{d,l/l+1}$ is positive for fluid losses in $l+1^{th}$ layer). For the bottom ground or the free surface, particularization of equation (6.50) gives:

$$\frac{\partial h_b}{\partial t} + \hat{u}_d\Big|_{z=h_b} \frac{\partial h_b}{\partial x} + \hat{v}_d\Big|_{z=h_b} \frac{\partial h_b}{\partial y} - \hat{w}_d\Big|_{z=h_b} \triangleq r_{bd} \tag{6.51}$$

$$\frac{\partial h_s}{\partial t} + \hat{u}_d\Big|_{z=h_s} \frac{\partial h_s}{\partial x} + \hat{v}_d\Big|_{z=h_s} \frac{\partial h_s}{\partial y} - \hat{w}_d\Big|_{z=h_s} \triangleq r_{sd} \tag{6.52}$$

where r_{sd} [ms^{-1}] and r_{bd} [ms^{-1}] account for infiltration or precipitation/evaporation of dispersed phase. At the river banks, the kinematic condition is given by:

$$\frac{\partial l_{rb}}{\partial t} + \hat{u}_d\Big|_{y=-l_{rb}} \frac{\partial l_{rb}}{\partial x} - \hat{v}_d\Big|_{y=-l_{rb}} + \hat{w}_d\Big|_{y=-l_{rb}} \frac{\partial l_{rb}}{\partial z} \triangleq i_{l,d}\Big|_{y=-l_{rb}} \tag{6.53}$$

$$\frac{\partial l_{lb}}{\partial t} + \hat{u}_d\Big|_{y=l_{lb}} \frac{\partial l_{lb}}{\partial x} - \hat{v}_d\Big|_{y=l_{lb}} + \hat{w}_d\Big|_{y=l_{lb}} \frac{\partial l_{lb}}{\partial z} \triangleq i_{l,d}\Big|_{y=l_{lb}} \tag{6.54}$$

where i_l [ms^{-1}] accounts for the lateral exchange of fluid (i_l is positive for fluid losses).

For the water phase, the exact same relations hold. All you have to do is to replace the subscript “d” by the subscript “w”. The proof is left to the reader.

6.3.3 Dynamic Boundary Conditions

Dynamic boundary conditions describe the dynamic of the fluid flow at the boundaries of the integration domain. More precisely, they describe the forces acting on the fluid and express their equilibrium. Since the cross-sectional integrated drift-flux model considers only one momentum equation for the mixture, I must establish dynamic boundary conditions for the mixture fluid at each boundary.

The dynamic boundary condition at the bottom is derived herein by expressing the equilibrium of a fluid volume in contact with the bed. The stress state of the mixture fluid is characterized by the tensor $\boldsymbol{\tau}^G$ which is defined as the sum of the viscous and turbulent stress tensors:

$$\boldsymbol{\tau}^G = \boldsymbol{\tau}_m + \boldsymbol{\tau}^T \tag{6.55}$$

Consequently, the product of $\boldsymbol{\tau}^G$ with the unit vector $\mathbf{n}_b$ locally normal to the bottom gives the force vector $\boldsymbol{\tau}_f$ applied by the fluid flow on an elementary surface of the bottom:

$$\boldsymbol{\tau}_f = \boldsymbol{\tau}^G \cdot \mathbf{n}_b. \tag{6.56}$$

Components of the normal to the bottom are given by:

$$\mathbf{n}_b = \left(\frac{\partial z_b}{\partial x} \quad \frac{\partial z_b}{\partial y} \quad -1 \right)^T \Bigg/ \sqrt{1 + \left(\frac{\partial z_b}{\partial x} \right)^2 + \left(\frac{\partial z_b}{\partial y} \right)^2} \tag{6.57}$$

The action-reaction principle enables to deduce the force vector $\boldsymbol{\tau}_b$ applied by the bottom on the fluid, which is the actual drag force. By specifying relation (6.55) we obtain the dynamic boundary conditions suitable for the bottom:

$$\begin{aligned}
&\left(\tau_{Gm,xx}\frac{\partial h_b}{\partial x}+\tau_{Gm,xy}\frac{\partial h_b}{\partial y}-\tau_{Gm,xz}\right)\Bigg|_{z=h_b} \triangleq -\tau_{b,x}\Delta\Sigma_b \\
&\left(\tau_{Gm,yx}\frac{\partial h_b}{\partial x}+\tau_{Gm,yy}\frac{\partial h_b}{\partial y}-\tau_{Gm,yz}\right)\Bigg|_{z=h_b} \triangleq -\tau_{b,y}\Delta\Sigma_b \\
&\left(\tau_{Gm,zx}\frac{\partial h_b}{\partial x}+\tau_{Gm,zy}\frac{\partial h_b}{\partial y}-\tau_{Gm,zz}\right)\Bigg|_{z=h_b} \triangleq -\tau_{b,z}\Delta\Sigma_b
\end{aligned} \tag{6.58}$$

where the section $\Delta\Sigma=\sqrt{1+\left(\frac{\partial z_b}{\partial x}\right)^2+\left(\frac{\partial z_b}{\partial y}\right)^2}$. Estimating the stress vector $\boldsymbol{\tau}_b$ is made by means of friction laws which are specified later in this text. The parameter $\Delta\Sigma$ accounts for the increase of surface on which the shear stress applies whenever the bottom is not in the (x, y) plane. In a similar manner, the dynamic boundary condition at the free surface is identical to equation (6.58). All you need is to replace the subscript 'b' by the subscript 's'. In this case, $\boldsymbol{\tau}_s$ is the stress vector applied, for instance, by the air flowing above the free surface or the roof of a pipe. Finally, the dynamic boundary condition at the interface between the l^{th} and l^{th+1} layer is also derived by expressing the equilibrium of a fluid volume in contact with the interface. The resulting equation is analogous to equation (6.58) All you need is to replace the subscript 'b' by the subscript 'l/l+1'. Estimating the force vector $\boldsymbol{\tau}_{l/l+1}$ is made by means of friction laws which are specified later in this text. The stress tensors $\boldsymbol{\tau}_b$, $\boldsymbol{\tau}_s$, $\boldsymbol{\tau}_{l/l+1}$ include the effects of both viscous and turbulent stresses.

Similarly, the dynamic boundary condition at the left banks may be written as:

$$\begin{aligned}
&\left(\tau_{Gm,xx}\frac{\partial l_{lb}}{\partial x}-\tau_{Gm,xy}+\tau_{Gm,xz}\frac{\partial l_{lb}}{\partial z}\right)\Bigg|_{y=l_{lb}} \triangleq -\tau_{lb,x}\Delta\Sigma_{lb} \\
&\left(\tau_{Gm,yx}\frac{\partial l_{lb}}{\partial x}-\tau_{Gm,yy}-\tau_{Gm,yz}\frac{\partial l_{lb}}{\partial z}\right)\Bigg|_{y=l_{lb}} \triangleq -\tau_{lb,y}\Delta\Sigma_{lb} \\
&\left(\tau_{Gm,zx}\frac{\partial l_{lb}}{\partial x}-\tau_{Gm,zy}-\tau_{Gm,zz}\frac{\partial l_{lb}}{\partial z}\right)\Bigg|_{y=l_{lb}} \triangleq -\tau_{lb,z}\Delta\Sigma_{lb}
\end{aligned} \tag{6.59}$$

where τ_{lb} accounts for the friction of left bank. The exact same relation holds for the right bank. All you need is replacing the subscript 'lb' by the subscript 'rb'. The proof of these relations is identical to the demonstration for the bottom dynamic boundary condition (see above).

6.4 CROSS-SECTIONAL INTEGRATION OF THE 3D DRIFT-FLUX MODEL

Based on the mean values defined in section 6.2 and the boundary conditions established in section 6.3, I can perform the integration of the 3D drift-flux model over the l^{th} layer of the flow cross-section (Figure 90). This is the topic of this section. First, I integrate the mixture continuity equation (sub-section 6.4.1), then the diffusion equation (sub-section 6.4.2), and finally the mixture momentum equation along the x-axis (sub-section 6.4.3). In this last equation, I pay a particular attention to the formulation of the convection flux. I introduce indeed two methods to accommodate this equation with non-uniform profiles of the flow parameters over the cross-section: the coefficient of Boussinesq and the covariance correction term.

The one-dimensional model obtained through this cross-sectional integration is an original result of this thesis. To my knowledge, it is indeed the first fully multiphase model that describes free surface flows in a one-dimensional framework. This model meets most of the objectives of this thesis (see chapter 1). First, it accounts for the multiphase character of the flows. Second, it may handle with unsteady and transient phenomena. Third, it accounts for scale heterogeneities thanks to a rigorous time- and space-integration. Finally, the model is sufficiently simple to be applicable by consulting firms and experts.

These original equations present several advantages over a single-phase formulation like the Saint-Venant equations. First, the notion of concentration appears naturally and relies on a rigorous mathematical definition. Second, the adverse impact of the dispersed phase over the water is taken into account in the mathematical description. Finally, the notion of drift velocity $\tilde{U}_{dj,l}$ accounts for all the diffusive mechanisms that can be encountered in civil and environmental engineering. It enhances the coherence of the model.

6.4.1 CROSS-SECTIONAL INTEGRATION OF THE CONTINUITY EQUATION

Integration over the l^{th} layer (Figure 90) of the continuity equation of the 3D drift-flux model can be written under the following general formulation:

$$\int_{h_{l-1/l}}^{h_{l/l+1}} \int_{l_{lb}}^{l_{rb}} \left[\frac{\partial \rho_m}{\partial t} + \frac{\partial \rho_m u_m}{\partial x} + \frac{\partial \rho_m v_m}{\partial y} + \frac{\partial \rho_m w_m}{\partial z} \right] dydz = 0 \tag{6.60}$$

INTEGRATION OVER THE LOCAL WIDTH

If we choose to perform first the integration over the local width and then over the flow depth, integration of each addend independently using the Leibniz integral rule gives:

$$\begin{aligned} &\frac{\partial}{\partial t}\int_{l_{lb}}^{l_{rb}} \rho_m dy + \frac{\partial}{\partial x}\int_{l_{lb}}^{l_{rb}} \rho_m u_m dy + \frac{\partial}{\partial z}\int_{l_{lb}}^{l_{rb}} \rho_m w_m dy \\ &= \\ &\rho_m\big|_{y=l_{rb}} \left(\frac{\partial l_{rb}}{\partial t} + u_m \frac{\partial l_{rb}}{\partial x} - v_m + w_m \frac{\partial l_{rb}}{\partial z} \right)\Bigg|_{y=l_{rb}} - \rho_m\big|_{y=l_{lb}} \left(\frac{\partial l_{lb}}{\partial t} + u_m \frac{\partial l_{lb}}{\partial x} - v_m + w_m \frac{\partial l_{lb}}{\partial z} \right)\Bigg|_{y=l_{lb}} \end{aligned} \tag{6.61}$$

The kinematic boundary conditions for the mixture fluid, given by equations (6.48) and (6.49), appears naturally in equation (6.61) so that we can write:

$$\frac{\partial}{\partial t}\int_{l_{lb}}^{l_{rb}}\rho_m dy+\frac{\partial}{\partial x}\int_{l_{lb}}^{l_{rb}}\rho_m u_m dy+\frac{\partial}{\partial z}\int_{l_{lb}}^{l_{rb}}\rho_m w_m dy=\rho_m i_l\Big|_{y=l_{rb}}-\rho_m i_l\Big|_{y=l_{lb}} \tag{6.62}$$

INTEGRATION OVER THE FLOW DEPTH

Integration over the flow depth of equation (6.62) can be written as:

$$\int_{h_{l-1/l}}^{h_{l/l+1}}\left[\frac{\partial}{\partial t}\int_{l_{lb}}^{l_{rb}}\rho_m dy+\frac{\partial}{\partial x}\int_{l_{lb}}^{l_{rb}}\rho_m u_m dy+\frac{\partial}{\partial z}\int_{l_{lb}}^{l_{rb}}\rho_m w_m dy\right]dz=\int_{h_{l-1/l}}^{h_{l/l+1}}\left[\rho_m i_l\Big|_{y=l_{rb}}-\rho_m i_l\Big|_{y=l_{lb}}\right]dz \tag{6.63}$$

The integration of each addend independently using the Leibniz integral rule gives:

$$\begin{aligned}&\frac{\partial}{\partial t}\int_{h_{l-1/l}}^{h_{l/l+1}}\int_{l_{lb}}^{l_{rb}}\rho_m dy dz+\frac{\partial}{\partial x}\int_{h_{l-1/l}}^{h_{l/l+1}}\int_{l_{lb}}^{l_{rb}}\rho_m u_m dy dz-\int_{h_{l-1/l}}^{h_{l/l+1}}\left[\rho_m i_l\Big|_{y=l_{rb}}-\rho_m i_l\Big|_{y=l_{lb}}\right]dz\\ &=\\ &\int_{l_{lb}}^{l_{rb}}\rho_m\Big|_{z=h_{l/l+1}}dy\frac{\partial h_{l/l+1}}{\partial t}+\int_{l_{lb}}^{l_{rb}}\rho_m u_m\Big|_{z=h_{l/l+1}}dy\frac{\partial h_{l/l+1}}{\partial x}-\int_{l_{lb}}^{l_{rb}}\rho_m w_m\Big|_{z=h_{l/l+1}}dy\\ &-\int_{l_{lb}}^{l_{rb}}\rho_m\Big|_{z=h_{l-1/l}}dy\frac{\partial h_{l-1/l}}{\partial t}-\int_{l_{lb}}^{l_{rb}}\rho_m u_m\Big|_{z=h_{l-1/l}}dy\frac{\partial h_{l-1/l}}{\partial x}+\int_{l_{lb}}^{l_{rb}}\rho_m w_m\Big|_{z=h_{l-1/l}}dy\end{aligned} \tag{6.64}$$

The kinematic boundary condition for the fluid mixture at the interface between layers, given by equation (6.44), does not appear directly here. However, integration of the formulation (6.44) over the flow width gives the following relation:

$$\begin{aligned}&\int_{l_{lb}}^{l_{rb}}\rho_m\Big|_{z=h_{l/l+1}}\frac{\partial h_{l/l+1}}{\partial t}dy+\int_{l_{lb}}^{l_{rb}}\rho_m u_m\Big|_{z=h_{l/l+1}}\frac{\partial h_{l/l+1}}{\partial x}dy-\int_{l_{lb}}^{l_{rb}}\rho_m w_m\Big|_{z=h_{l/l+1}}dy\\ &+\rho_m v_m h_{l/l+1}\Big|_{\substack{z=h_{l/l+1}\\ y=l_{rb}}}-\rho_m v_m h_{l/l+1}\Big|_{\substack{z=h_{l/l+1}\\ y=l_{lb}}}=\int_{l_{lb}}^{l_{rb}}\rho_m e_m\Big|_{z=h_{l/l+1}}dy\end{aligned} \tag{6.65}$$

If we assume the time and spatial derivatives of the interface elevation do not depend on y-abscissa, we obtain from equation (6.65):

$$\begin{aligned}&\int_{l_{lb}}^{l_{rb}}\rho_m\Big|_{z=h_{l/l+1}}dy\frac{\partial h_{l/l+1}}{\partial t}+\int_{l_{lb}}^{l_{rb}}\rho_m u_m\Big|_{z=h_{l/l+1}}dy\frac{\partial h_{l/l+1}}{\partial x}-\int_{l_{lb}}^{l_{rb}}\rho_m w_m\Big|_{z=h_{l/l+1}}dy\\ &=\int_{l_{lb}}^{l_{rb}}\rho_m e_m\Big|_{z=h_{l/l+1}}dy-\rho_m v_m h_{l/l+1}\Big|_{\substack{z=h_{l/l+1}\\ y=l_{rb}}}+\rho_m v_m h_{l/l+1}\Big|_{\substack{z=h_{l/l+1}\\ y=l_{lb}}}\end{aligned} \tag{6.66}$$

By analogy, we obtain an identical formulation for the lower interface:

$$\begin{aligned}&\int_{l_{lb}}^{l_{rb}}\rho_m\Big|_{z=h_{l-1/l}}dy\frac{\partial h_{l-1/l}}{\partial t}+\int_{l_{lb}}^{l_{rb}}\rho_m u_m\Big|_{z=h_{l-1/l}}dy\frac{\partial h_{l-1/l}}{\partial x}-\int_{l_{lb}}^{l_{rb}}\rho_m w_m\Big|_{z=h_{l-1/l}}dy\\ &=\int_{l_{lb}}^{l_{rb}}\rho_m e_m\Big|_{z=h_{l-1/l}}dy-\rho_m v_m h_{l-1/l}\Big|_{\substack{z=h_{l-1/l}\\ y=l_{rb}}}+\rho_m v_m h_{l-1/l}\Big|_{\substack{z=h_{l-1/l}\\ y=l_{lb}}}\end{aligned} \tag{6.67}$$

Obviously, the lower interface of the first layer corresponds to the bottom ground and kinematic condition (6.45) applies. The same consideration holds for the upper interface of the upper layer. It corresponds to the free surface and kinematic condition (6.46) applies. In view of the similarity of all these boundary conditions, I treat these two particular cases under the previous general formulation for a given layer l.

Combining equation (6.64) with equations (6.66) and (6.67) gives:

$$\frac{\partial}{\partial t}\int_{h_{l-1/l}}^{h_{l/l+1}}\int_{l_{lb}}^{l_{rb}}\rho_m dydz+\frac{\partial}{\partial x}\int_{h_{l-1/l}}^{h_{l/l+1}}\int_{l_{lb}}^{l_{rb}}\rho_m u_m dydz-\int_{h_{l-1/l}}^{h_{l/l+1}}\left[\rho_m i_l\big|_{y=l_{rb}}-\rho_m i_l\big|_{y=l_{lb}}\right]dz$$

$$=$$

$$\left[\int_{l_{lb}}^{l_{rb}}(\rho_m e_m)dy-\rho_m v_m h_{l/l+1}\big|_{y=l_{rb}}+\rho_m v_m h_{l/l+1}\big|_{y=l_{lb}}\right]_{z=h_{l/l+1}} \tag{6.68}$$

$$-\left[\int_{l_{lb}}^{l_{rb}}(\rho_m e_m)dy-\rho_m v_m h_{l-1/l}\big|_{y=l_{rb}}+\rho_m v_m h_{l-1/l}\big|_{y=l_{lb}}\right]_{z=h_{l-1/l}}$$

By introducing the area-averaged mixture velocity defined by equation (6.29) and the area-averaged density, the relation can be further simplified:

$$\frac{\partial\langle\rho_m\rangle_l\Omega_l}{\partial t}+\underbrace{\frac{\partial\langle\rho_m\rangle_l\tilde{u}_{m,l}\Omega_l}{\partial x}}_{\text{Convective term}}=\underbrace{q_{m,L,l}}_{\substack{\text{Lateral}\\ \text{transfert term}}} \tag{6.69}$$

where the symbol $\langle\ \rangle_l$ indicates the area-average over the l_{th} layer. The mixture lateral discharge accounts for the exchange of fluid between the l_{th} layer and the adjacent layers as well as the external environment:

$$q_{m,L,l}=\underbrace{\int_{h_{l-1/l}}^{h_{l/l+1}}\left[\rho_m i_l\big|_{y=l_{rb}}-\rho_m i_l\big|_{y=l_{lb}}\right]dz}_{\text{Balance of fluid flow through the right and left bank}}$$

$$+\underbrace{\left[\int_{l_{lb}}^{l_{rb}}(\rho_m e_m)dy-\rho_m v_m h_{l/l+1}\big|_{y=l_{rb}}+\rho_m v_m h_{l/l+1}\big|_{y=l_{lb}}\right]_{z=h_{l/l+1}}}_{\text{Balance of fluid flow through upper interlayer}} \tag{6.70}$$

$$-\underbrace{\left[\int_{l_{lb}}^{l_{rb}}(\rho_m e_m)dy-\rho_m v_m h_{l-1/l}\big|_{y=l_{rb}}+\rho_m v_m h_{l-1/l}\big|_{y=l_{lb}}\right]_{z=h_{l-1/l}}}_{\text{Balance of fluid flow through the lower interlayer}}$$

In conclusion, cross-sectional integration of the 3D drift-flux continuity equation over a multi-layer cross-section presenting a free surface gives the following simple equation for each layer:

$$\frac{\partial\langle\rho_m\rangle_l\Omega_l}{\partial t}+\frac{\partial\langle\rho_m\rangle_l\tilde{u}_{m,l}\Omega_l}{\partial x}=q_{m,L,l} \tag{6.71}$$

The form of this equation is similar to the continuity equation of the Saint-Venant equations. However, its physical significance is completely different. While the single-phase model ensures the mass conservation of pure water between two cross-sections, equation (6.71) expresses the mass conservation of both phases taken as a whole. Nevertheless, computational techniques developed for Saint-Venant equations should be easily applied to the new model. The mixture density is here rigorously defined and linked with the void fraction. It enhances the coherence of the model.

6.4.2 Cross-sectional Integration of the Diffusion Equation

In view of the 3D drift-flux model, integration of the diffusion equation over the flow cross-section of the l^{th} layer can be written as:

$$\int_{h_{l-1/l}}^{h_{l/l+1}}\int_{l_{lb}}^{l_{rb}}\left[\frac{\partial\alpha_d}{\partial t}+\frac{\partial\alpha_d\hat{u}_d}{\partial x}+\frac{\partial\alpha_d\hat{v}_d}{\partial y}+\frac{\partial\alpha_d\hat{w}_d}{\partial z}\right]dydz=\int_{h_{l-1/l}}^{h_{l/l+1}}\int_{l_{lb}}^{l_{rb}}\left[\Gamma_d\Big/\rho_d\right]dydz \tag{6.72}$$

Equation (6.72) is expressed in terms of phase velocity because the integration is much easier by this way. However, I will express the resulting equation in terms of mixture and drift-velocity. This is indeed the philosophy of the drift-flux theory.

Integration over the local width

First, I choose to perform the integration over the flow width. Integration of each addend independently using the Leibniz integral rule gives:

$$\begin{gathered}\frac{\partial}{\partial t}\int_{l_{lb}}^{l_{rb}}\alpha_d dy+\frac{\partial}{\partial x}\int_{l_{lb}}^{l_{rb}}\alpha_d\hat{u}_d dy+\frac{\partial}{\partial z}\int_{l_{lb}}^{l_{rb}}\alpha_d\hat{w}_d dy-\int_{l_{lb}}^{l_{rb}}\left[\Gamma_d\Big/\rho_d\right]dy\\ =\\ \alpha_d\Big|_{y=l_{rb}}\left(\frac{\partial l_{rb}}{\partial t}+\hat{u}_d\frac{\partial l_{rb}}{\partial x}-\hat{v}_d+\hat{w}_d\frac{\partial l_{rb}}{\partial z}\right)\Bigg|_{y=l_{rb}}-\alpha_d\Big|_{y=l_{lb}}\left(\frac{\partial l_{lb}}{\partial t}+\hat{u}_d\frac{\partial l_{lb}}{\partial x}-\hat{v}_d+\hat{w}_d\frac{\partial l_{lb}}{\partial z}\right)\Bigg|_{y=l_{lb}}\end{gathered} \tag{6.73}$$

Obviously, the terms in the right-hand side of equation (6.73) corresponds to the kinematic boundary condition for the dispersed phase. Introducing equations (6.53) and (6.54) into the previous equation gives:

$$\frac{\partial}{\partial t}\int_{l_{lb}}^{l_{rb}}\alpha_d dy+\frac{\partial}{\partial x}\int_{l_{lb}}^{l_{rb}}\alpha_d\hat{u}_d dy+\frac{\partial}{\partial z}\int_{l_{lb}}^{l_{rb}}\alpha_d\hat{w}_d dy=\int_{l_{lb}}^{l_{rb}}\left[\Gamma_d\Big/\rho_d\right]dy+\alpha_d i_{l,d}\Big|_{y=l_{rb}}-\alpha_d i_{l,d}\Big|_{y=l_{lb}} \tag{6.74}$$

Integration over the flow depth

The subsequent integration over the flow depth of the l^{th} layer of equation (6.74) gives:

$$\begin{gathered}\int_{h_{l-1/l}}^{h_{l/l+1}}\left[\frac{\partial}{\partial t}\int_{l_{lb}}^{l_{rb}}\alpha_d dy+\frac{\partial}{\partial x}\int_{l_{lb}}^{l_{rb}}\alpha_d\hat{u}_d dy+\frac{\partial}{\partial z}\int_{l_{lb}}^{l_{rb}}\alpha_d\hat{w}_d dy\right]dz\\ =\int_{h_{l-1/l}}^{h_{l/l+1}}\int_{l_{lb}}^{l_{rb}}\left[\Gamma_d\Big/\rho_d\right]dydz+\int_{h_{l-1/l}}^{h_{l/l+1}}\left[\alpha_d i_{l,d}\Big|_{y=l_{rb}}-\alpha_d i_{l,d}\Big|_{y=l_{lb}}\right]dz\end{gathered} \tag{6.75}$$

By integrating each addend independently using the Leibniz integral rule, we obtain:

$$\begin{gathered}\frac{\partial}{\partial t}\int_{h_{l-1/l}}^{h_{l/l+1}}\int_{l_{lb}}^{l_{rb}}\alpha_d dydz+\frac{\partial}{\partial x}\int_{h_{l-1/l}}^{h_{l/l+1}}\int_{l_{lb}}^{l_{rb}}\alpha_d\hat{u}_d dydz-\int_{h_{l-1/l}}^{h_{l/l+1}}\int_{l_{lb}}^{l_{rb}}\left[\Gamma_d\Big/\rho_d\right]dydz-\int_{h_{l-1/l}}^{h_{l/l+1}}\left[\alpha_d i_{l,d}\Big|_{y=l_{rb}}-\alpha_d i_{l,d}\Big|_{y=l_{lb}}\right]dz\\ =\\ \int_{l_{lb}}^{l_{rb}}\alpha_d\Big|_{z=h_{l/l+1}}dy\frac{\partial h_{l/l+1}}{\partial t}+\int_{l_{lb}}^{l_{rb}}\alpha_d\hat{u}_d\Big|_{z=h_{l/l+1}}dy\frac{\partial h_{l/l+1}}{\partial x}-\int_{l_{lb}}^{l_{rb}}\alpha_d\hat{w}_d\Big|_{z=h_{l/l+1}}dy\\ -\int_{l_{lb}}^{l_{rb}}\alpha_d\Big|_{z=h_{l-1/l}}dy\frac{\partial h_{l-1/l}}{\partial t}-\int_{l_{lb}}^{l_{rb}}\alpha_d\hat{u}_d\Big|_{z=h_{l-1/l}}dy\frac{\partial h_{l-1/l}}{\partial x}+\int_{l_{lb}}^{l_{rb}}\alpha_d\hat{w}_d\Big|_{z=h_{l-1/l}}dy\end{gathered} \tag{6.76}$$

The kinematic boundary conditions do not appear directly here. However, integration of equation (6.50) over the width of the upper interface gives:

$$\int_{l_{id}}^{l_{rd}} \alpha_d\big|_{z=h_{l/l+1}} dy \frac{\partial h_{l/l+1}}{\partial t} + \int_{l_{id}}^{l_{rd}} \alpha_d \hat{u}_d\big|_{z=h_{l/l+1}} dy \frac{\partial h_{l/l+1}}{\partial x} + \alpha_d \hat{v}_d h_{l/l+1}\Big|_{\substack{z=h_{l/l+1}\\ y=l_{rb}}} - \alpha_d \hat{v}_d h_{l/l+1}\Big|_{\substack{z=h_{l/l+1}\\ y=l_{lb}}} \triangleq \int_{l_{id}}^{l_{rd}} \alpha_d e_d\big|_{z=h_{l/l+1}} dy \qquad (6.77)$$

where I have assumed the spatial derivative of the interface elevation does not depend on y-abscissa. The exact same formulation applies for the lower interface of the l^{th} layer. Consequently, equation (6.76) may be rewritten as:

$$\begin{aligned} &\frac{\partial}{\partial t}\int_{h_{l-1/l}}^{h_{l/l+1}}\int_{l_{lb}}^{l_{rb}} \alpha_d dy dz + \frac{\partial}{\partial x}\int_{h_{l-1/l}}^{h_{l/l+1}}\int_{l_{lb}}^{l_{rb}} \alpha_d \hat{u}_d dy dz - \int_{h_{l-1/l}}^{h_{l/l+1}}\int_{l_{lb}}^{l_{rb}} \left[\Gamma_d \big/ \rho_d\right] dy dz - \int_{h_{l-1/l}}^{h_{l/l+1}} \left[\alpha_d i_{l,d}\big|_{y=l_{rb}} - \alpha_d i_{l,d}\big|_{y=l_{lb}}\right] dz \\ &= \\ &\int_{l_{id}}^{l_{rd}} \alpha_d e_d\big|_{z=h_{l/l+1}} dy - \alpha_d \hat{v}_d h_{l/l+1}\Big|_{\substack{z=h_{l/l+1}\\ y=l_{rb}}} + \alpha_d \hat{v}_d h_{l/l+1}\Big|_{\substack{z=h_{l/l+1}\\ y=l_{lb}}} \\ &- \int_{l_{id}}^{l_{rd}} \alpha_d e_d\big|_{z=h_{l-1/l}} dy + \alpha_d \hat{v}_d h_{l-1/l}\Big|_{\substack{z=h_{l-1/l}\\ y=l_{rb}}} - \alpha_d \hat{v}_d h_{l-1/l}\Big|_{\substack{z=h_{l-1/l}\\ y=l_{lb}}} \end{aligned} \qquad (6.78)$$

Finally, I introduce the definition of the averaged void fraction and the averaged mixture velocity. Thanks to equation (6.36), I also split the averaged dispersed phase velocity in terms of mixture and drift velocity. At the end of the day, I obtain the following equation.

$$\frac{\partial \langle \alpha_d \rangle_l \Omega_l}{\partial t} + \underbrace{\frac{\partial \langle \alpha_d \rangle_l \tilde{u}_{m,l} \Omega_l}{\partial x}}_{\text{convection term}} + \underbrace{\frac{\partial}{\partial x}\left(\langle \alpha_d \rangle_l \frac{\rho_w}{\langle \rho_m \rangle_l} \tilde{U}_{dj,l} \Omega_l \right)}_{\text{diffusion term}} = \underbrace{\left\langle \Gamma_d \big/ \rho_d \right\rangle_l \Omega_l}_{\substack{\text{dispersed phase}\\ \text{volume generation}}} + \underbrace{q_{\alpha,\perp,l}}_{\substack{\text{dispersed phase}\\ \text{lateral transfer term}}} \qquad (6.79)$$

where the dispersed phase lateral discharge in the l^{th} layer is defined as:

$$\begin{aligned} q_{\alpha,\perp,l} = &-\int_{h_{l-1/l}}^{h_{l/l+1}} \left[\alpha_d i_{l,d}\big|_{y=l_{rb}} - \alpha_d i_{l,d}\big|_{y=l_{lb}}\right] dz + \left[\int_{l_{id}}^{l_{rd}} \alpha_d e_d dy - \alpha_d \hat{v}_d h_{l/l+1}\Big|_{y=l_{rb}} + \alpha_d \hat{v}_d h_{l/l+1}\Big|_{y=l_{lb}}\right]_{z=h_{l/l+1}} \\ &- \left[\int_{l_{id}}^{l_{rd}} \alpha_d e_d dy - \alpha_d \hat{v}_d h_{l-1/l}\Big|_{y=l_{rb}} + \alpha_d \hat{v}_d h_{l-1/l}\Big|_{y=l_{lb}}\right]_{z=h_{l-1/l}} \end{aligned} \qquad (6.80)$$

In conclusion, cross-sectional integration of the 3D diffusion equation over a multi-layer cross-section presenting a free surface gives the following equation for the l^{th} layer:

$$\frac{\partial \langle \alpha_d \rangle_l \Omega_l}{\partial t} + \frac{\partial \langle \alpha_d \rangle_l \tilde{u}_{m,l} \Omega_l}{\partial x} + \frac{\partial}{\partial x}\left(\langle \alpha_d \rangle_l \frac{\rho_w}{\langle \rho_m \rangle_l} \tilde{U}_{dj,l} \Omega_l \right) = \left\langle \Gamma_d \big/ \rho_d \right\rangle_l \Omega_l + q_{\alpha,\perp,l} \qquad (6.81)$$

From a physical point of view, this equation expresses the mass conservation of the dispersed phase. Coupled with the mixture continuity equation (6.71), mass conservation of each phase on its own is ensured. The motion of the dispersed phase results from two mechanisms: the entrainment of the phase with the center of mass of the mixture, and the diffusion of the phase with respect to the center of mass. The drift velocity $\tilde{U}_{dj,l}$ accounts for all the diffusive mechanisms. An additional constitutive equation expresses its value, which depends from the considered situation. The concentration is rigorously defined as the averaged void fraction of the dispersed phase. This global value is not affected by turbulence.

6.4.3 Cross-sectional Integration of the Momentum Equation

Integration over the l[th] layer of the momentum equation along the x-axis is written as:

$$\int_{h_{l-1/l}}^{h_{l/l+1}}\int_{l_{lb}}^{l_{rb}}\left[\frac{\partial \rho_m u_m}{\partial t}+\frac{\partial}{\partial x}\left(\sum_k \alpha_k\rho_k\hat{u}_k u_k\right)+\frac{\partial}{\partial y}\left(\sum_k \alpha_k\rho_k\hat{u}_k\hat{v}_k\right)+\frac{\partial}{\partial z}\left(\sum_k \alpha_k\rho_k\hat{u}_k\hat{w}_k\right)\right]dydz = \int_{h_{l-1/l}}^{h_{l/l+1}}\int_{l_{lb}}^{l_{rb}}\left[\rho_m F_{m,x}-\frac{\partial p_m}{\partial x}+M_{m,x}\right]dydz+\int_{h_{l-1/l}}^{h_{l/l+1}}\int_{l_{lb}}^{l_{rb}}\left[\frac{\partial \tau_{Gm,xx}}{\partial x}+\frac{\partial \tau_{Gm,yx}}{\partial y}+\frac{\partial \tau_{Gm,zx}}{\partial z}\right]dydz \tag{6.82}$$

It is only worthwhile integrating the momentum equation along the x-axis seeing that other momentum equations have been simplified by the dimensional analysis performed in section 6.1. A restriction on the pressure distribution over the flow cross-section replaces momentum equations along the y- and z-axis. Again, equation (6.82) is expressed in terms of phase velocities because the integration is easier this way. At the end of day, I will however express everything in terms of mixture and drift-velocity, according to the philosophy of the drift-flux theory.

Integration over the local width

If we choose to first perform the integration over the local width and then integrate over the flow depth, integration of each addend of the left-hand side independently gives:

$$\begin{aligned}&\frac{\partial}{\partial t}\int_{l_{lb}}^{l_{rb}}\rho_m u_m dy+\frac{\partial}{\partial x}\int_{l_{lb}}^{l_{rb}}\left(\sum_k \alpha_k\rho_k\hat{u}_k\hat{u}_k\right)dy+\frac{\partial}{\partial z}\int_{l_{lb}}^{l_{rb}}\left(\sum_k \alpha_k\rho_k\hat{u}_k\hat{w}_k\right)dy\\ &-\left(\sum_k \alpha_k\rho_k\hat{u}_k\right)\Big|_{y=l_{rb}}\frac{\partial l_{rb}}{\partial t}-\left(\sum_k \alpha_k\rho_k\hat{u}_k\hat{u}_k\right)\Big|_{y=l_{rb}}\frac{\partial l_{rb}}{\partial x}+\left(\sum_k \alpha_k\rho_k\hat{u}_k\hat{v}_k\right)\Big|_{y=l_{rb}}-\left(\sum_k \alpha_k\rho_k\hat{u}_k\hat{w}_k\right)\Big|_{y=l_{rb}}\frac{\partial l_{rb}}{\partial z}\\ &+\left(\sum_k \alpha_k\rho_k\hat{u}_k\right)\Big|_{y=l_{lb}}\frac{\partial l_{lb}}{\partial t}+\left(\sum_k \alpha_k\rho_k\hat{u}_k\hat{u}_k\right)\Big|_{y=l_{lb}}\frac{\partial l_{lb}}{\partial x}-\left(\sum_k \alpha_k\rho_k\hat{u}_k\hat{v}_k\right)\Big|_{y=l_{lb}}+\left(\sum_k \alpha_k\rho_k\hat{u}_k\hat{w}_k\right)\Big|_{y=l_{lb}}\frac{\partial l_{lb}}{\partial z}\end{aligned} \tag{6.83}$$

where I have used the definition of the mixture velocity (chapter 2). Kinematic boundary conditions do not appear naturally in this relation such that we need to perform some calculations before introducing them. It mainly consists in separating the contribution of both phases. By this way, we obtain for the new terms at the right bank:

$$\begin{aligned}&-\left(\sum_k \alpha_k\rho_k\hat{u}_k\right)\Big|_{y=l_{rb}}\frac{\partial l_{rb}}{\partial t}-\left(\sum_k \alpha_k\rho_k\hat{u}_k\hat{u}_k\right)\Big|_{y=l_{rb}}\frac{\partial l_{rb}}{\partial x}+\left(\sum_k \alpha_k\rho_k\hat{u}_k\hat{v}_k\right)\Big|_{y=l_{rb}}-\left(\sum_k \alpha_k\rho_k\hat{u}_k\hat{w}_k\right)\Big|_{y=l_{rb}}\frac{\partial l_{rb}}{\partial z}\\ &=-\alpha_d\rho_d\hat{u}_d\Big|_{y=l_{rb}}\left[\frac{\partial l_{rb}}{\partial t}+\hat{u}_d\Big|_{y=l_{rb}}\frac{\partial l_{rb}}{\partial x}-\hat{w}_d\Big|_{y=l_{rb}}+\hat{u}_d\Big|_{y=l_{rb}}\frac{\partial l_{rb}}{\partial z}\right]\\ &-\alpha_w\rho_w\hat{u}_w\Big|_{y=l_{rb}}\left[\frac{\partial l_{rb}}{\partial t}+\hat{u}_w\Big|_{y=l_{rb}}\frac{\partial l_{rb}}{\partial x}-\hat{w}_w\Big|_{y=l_{rb}}+\hat{u}_w\Big|_{y=l_{rb}}\frac{\partial l_{rb}}{\partial z}\right]\end{aligned} \tag{6.84}$$

Obviously, kinematic boundary conditions for the water and dispersed phases appear now. Introducing equation (6.53) and its equivalent for the water phase in equation (6.84) gives:

$$\begin{aligned}&-\left(\sum_k \alpha_k\rho_k\hat{u}_k\right)\Big|_{y=l_{rb}}\frac{\partial l_{rb}}{\partial t}-\left(\sum_k \alpha_k\rho_k\hat{u}_k\hat{u}_k\right)\Big|_{y=l_{rb}}\frac{\partial l_{rb}}{\partial x}+\left(\sum_k \alpha_k\rho_k\hat{u}_k\hat{v}_k\right)\Big|_{y=l_{rb}}-\left(\sum_k \alpha_k\rho_k\hat{u}_k\hat{w}_k\right)\Big|_{y=l_{rb}}\frac{\partial l_{rb}}{\partial z}\\ &=-\alpha_d\rho_d\hat{u}_d i_{l,d}\Big|_{y=l_{rb}}-\alpha_w\rho_w\hat{u}_w i_{l,w}\Big|_{y=l_{rb}}\end{aligned} \tag{6.85}$$

By applying the same strategy to the left bank, equation (6.83) may be rewritten as:

$$\begin{aligned}&\frac{\partial}{\partial t}\int_{l_{lb}}^{l_{rb}}\rho_m u_m dy+\frac{\partial}{\partial x}\int_{l_{lb}}^{l_{rb}}\left(\sum_k \alpha_k\rho_k\hat{u}_k\hat{u}_k\right)dy+\frac{\partial}{\partial z}\int_{l_{lb}}^{l_{rb}}\left(\sum_k \alpha_k\rho_k\hat{u}_k\hat{w}_k\right)dy\\&-\alpha_d\rho_d\hat{u}_d i_{l,d}\Big|_{y=l_{rb}}-\alpha_w\rho_w\hat{u}_w i_{l,w}\Big|_{y=l_{rb}}+\alpha_d\rho_d\hat{u}_d i_{l,d}\Big|_{y=l_{lb}}+\alpha_w\rho_w\hat{u}_w i_{l,w}\Big|_{y=l_{lb}}\end{aligned} \tag{6.86}$$

For the generalized stresses (viscous and turbulent), we have:

$$\begin{cases}\displaystyle\int_{l_{lb}}^{l_{rb}}\frac{\partial\tau_{Gm,xx}}{\partial x}dy=\frac{\partial}{\partial x}\int_{l_{lb}}^{l_{rb}}\tau_{Gm,xx}dy-\tau_{Gm,xx}\Big|_{y=l_{rb}}\frac{\partial l_{rb}}{\partial x}+\tau_{Gm,xx}\Big|_{y=l_{lb}}\frac{\partial l_{lb}}{\partial x}\\\displaystyle\int_{l_{lb}}^{l_{rb}}\frac{\partial\tau_{Gm,yx}}{\partial y}dy=\tau_{Gm,yx}\Big|_{y=l_{rb}}-\tau_{Gm,yx}\Big|_{y=l_{lb}}\\\displaystyle\int_{l_{lb}}^{l_{rb}}\frac{\partial\tau_{Gm,zx}}{\partial z}dz=\frac{\partial}{\partial z}\int_{l_{lb}}^{l_{rb}}\tau_{Gm,zx}dy-\tau_{Gm,zx}\Big|_{y=l_{rb}}\frac{\partial l_{rb}}{\partial z}+\tau_{Gm,zx}\Big|_{y=l_{lb}}\frac{\partial l_{lb}}{\partial z}\end{cases} \tag{6.87}$$

By using the dynamic boundary conditions (6.59) for the bank sides, equation (6.87) is rewritten as:

$$\frac{\partial}{\partial x}\int_{l_{lb}}^{l_{rb}}\tau_{Gm,xx}dy+\frac{\partial}{\partial z}\int_{l_{lb}}^{l_{rb}}\tau_{Gm,zx}dy+\left(\tau_{rd}\Delta\Sigma_{rd}-\tau_{ld}\Delta\Sigma_{ld}\right) \tag{6.88}$$

INTEGRATION OVER THE FLOW DEPTH

Integration over the flow depth of convective terms (6.86) may be written as:

$$\begin{aligned}&\int_{h_{l-1/l}}^{h_{l/l+1}}\left[\frac{\partial}{\partial t}\int_{l_{lb}}^{l_{rb}}\rho_m u_m dy+\frac{\partial}{\partial x}\int_{l_{lb}}^{l_{rb}}\left(\sum_k \alpha_k\rho_k\hat{u}_k\hat{u}_k\right)dy+\frac{\partial}{\partial z}\int_{l_{lb}}^{l_{rb}}\left(\sum_k \alpha_k\rho_k\hat{u}_k\hat{w}_k\right)dy\right]dz\\&+\int_{h_{l-1/l}}^{h_{l/l+1}}\left[-\alpha_d\rho_d\hat{u}_d i_{l,d}\Big|_{y=l_{rb}}-\alpha_w\rho_w\hat{u}_w i_{l,w}\Big|_{y=l_{rb}}+\alpha_d\rho_d\hat{u}_d i_{l,d}\Big|_{y=l_{lb}}+\alpha_w\rho_w\hat{u}_w i_{l,w}\Big|_{y=l_{lb}}\right]dz\end{aligned} \tag{6.89}$$

Integration of each addend independently using the Leibniz integral rule gives:

$$\begin{aligned}&\frac{\partial}{\partial t}\int_{h_{l-1/l}}^{h_{l/l+1}}\int_{l_{lb}}^{l_{rb}}\rho_m u_m dydz+\frac{\partial}{\partial x}\int_{h_{l-1/l}}^{h_{l/l+1}}\int_{l_{lb}}^{l_{rb}}\left(\sum_k \alpha_k\rho_k\hat{u}_k\hat{u}_k\right)dydz\\&-\left[\int_{l_{lb}}^{l_{rb}}\rho_m u_m dy\right]\Big|_{z=h_{l/l+1}}\frac{\partial h_{l/l+1}}{\partial t}-\left[\int_{l_{lb}}^{l_{rb}}\left(\sum_k \alpha_k\rho_k\hat{u}_k\hat{u}_k\right)dy\right]\Big|_{z=h_{l/l+1}}\frac{\partial h_{l/l+1}}{\partial x}+\left[\int_{l_{lb}}^{l_{rb}}\left(\sum_k \alpha_k\rho_k\hat{u}_k w_k\right)dy\right]\Big|_{z=h_{l/l+1}}\\&+\left[\int_{l_{lb}}^{l_{rb}}\rho_m u_m dy\right]\Big|_{z=h_{l-1/l}}\frac{\partial h_{l-1/l}}{\partial t}+\left[\int_{l_{lb}}^{l_{rb}}\left(\sum_k \alpha_k\rho_k\hat{u}_k\hat{u}_k\right)dy\right]\Big|_{z=h_{l-1/l}}\frac{\partial h_{l-1/l}}{\partial x}-\left[\int_{l_{lb}}^{l_{rb}}\left(\sum_k \alpha_k\rho_k\hat{u}_k\hat{w}_k\right)dy\right]\Big|_{z=h_{l-1/l}}\end{aligned} \tag{6.90}$$

By analogy with the previous sub-section, I separate the contribution of both phases to the new terms at the layers interfaces. Sadly, the kinematic boundary conditions (6.50) for the dispersed phase and its equivalent for the water phase do not appear. It is still necessary to integrate these conditions in order to make appear the boundary terms. At the end of the day, equation (6.90) may be rewritten as:

$$\frac{\partial\left\langle\rho_m\right\rangle_l\tilde{u}_{m,l}\Omega_l}{\partial t}+\frac{\partial}{\partial x}\left(\left\langle\sum_k\alpha_k\rho_k\hat{u}_k\hat{u}_k\right\rangle_l\Omega_l\right)$$
$$-\left[\int_{l_{lb}}^{l_{rb}}\alpha_d\rho_d u_d dy\right]_{z=h_{l/l+1}}\left[\int_{l_{lb}}^{l_{rb}}e_{d,l/l+1}dy-\hat{v}_d h\Big|_{\substack{y=l_{rd}\\z=h_{l/l+1}}}+\hat{v}_d h\Big|_{\substack{y=l_{ld}\\z=h_{l/l+1}}}\right]$$
$$-\left[\int_{l_{lb}}^{l_{rb}}\alpha_w\rho_w u_w dy\right]_{z=h_{l/l+1}}\left[\int_{l_{lb}}^{l_{rb}}e_{w,l/l+1}dy-\hat{v}_w h\Big|_{\substack{y=l_{rd}\\z=h_{l/l+1}}}+\hat{v}_w h\Big|_{\substack{y=l_{ld}\\z=h_{l/l+1}}}\right] \tag{6.91}$$
$$+\left[\int_{l_{lb}}^{l_{rb}}\alpha_d\rho_d u_d dy\right]_{z=h_{l-1/l}}\left[\int_{l_{lb}}^{l_{rb}}e_{w,l-1/l}dy-\hat{v}_d h\Big|_{\substack{y=l_{rd}\\z=h_{l-1/l}}}+\hat{v}_d h\Big|_{\substack{y=l_{ld}\\z=h_{l-1/l}}}\right]$$
$$+\left[\int_{l_{lb}}^{l_{rb}}\alpha_w\rho_w u_w dy\right]_{z=h_{l-1/l}}\left[\int_{l_{lb}}^{l_{rb}}e_{w,l-1/l}dy-\hat{v}_w h\Big|_{\substack{y=l_{rd}\\z=h_{l-1/l}}}+\hat{v}_w h\Big|_{\substack{y=l_{ld}\\z=h_{l-1/l}}}\right]$$

The integration of the topographic term gives:

$$\int_{h_{l-1/l}}^{h_{l/l+1}}\int_{l_{lb}}^{l_{rb}}\rho_m F_{m,x}dydz=\left\langle\rho_m\right\rangle_l F_{m,x}\Omega_l \tag{6.92}$$

Integration of the mixture momentum source term gives:

$$\int_{h_{l-1/l}}^{h_{l/l+1}}\int_{l_{lb}}^{l_{rb}}M_{m,x}dydz=\left\langle M_{m,x}\right\rangle_l\Omega_l \tag{6.93}$$

For the generalized viscous stresses, we have:

$$\begin{cases}\displaystyle\int_{h_{l-1/l}}^{h_{l/l+1}}\left[\frac{\partial}{\partial x}\int_{-l_{rb}}^{l_{rb}}\tau_{Gm,xx}dy\right]dz=\frac{\partial}{\partial x}\int_{h_{l-1/l}}^{h_{l/l+1}}\int_{l_{lb}}^{l_{rb}}\tau_{Gm,xx}dz-\left[\int_{l_{lb}}^{l_{rb}}\tau_{Gm,xx}dy\right]_{z=h_{l/l+1}}\frac{\partial h_{l/l+1}}{\partial x}+\left[\int_{l_{lb}}^{l_{rb}}\tau_{Gm,xx}dy\right]_{z=h_{l-1/l}}\frac{\partial h_{l-1/l}}{\partial x}\\ \displaystyle\int_{h_{l-1/l}}^{h_{l/l+1}}\left[\frac{\partial}{\partial z}\int_{l_{lb}}^{l_{rb}}\tau_{Gm,zx}dy\right]dz=+\left[\int_{l_{lb}}^{l_{rb}}\tau_{Gm,zx}dy\right]_{z=h_{l/l+1}}-\left[\int_{l_{lb}}^{l_{rb}}\tau_{Gm,zx}dy\right]_{z=h_{l-1/l}}\end{cases} \tag{6.94}$$

Dynamic boundary conditions do not appear directly here. However, the integration over the flow width of the dynamic boundary condition layers interface gives:

$$\left[\int_{l_{lb}}^{l_{rb}}\tau_{Gm,xx}\frac{\partial h_{l/l+1}}{\partial x}dy\right]_{z=h_{l/l+1}}-\left[\int_{l_{lb}}^{l_{rb}}\tau_{Gm,xz}dy\right]_{z=h_{l/l+1}}=\left[\int_{l_{lb}}^{l_{rb}}-\tau_s dy\right]_{z=h_{l/l+1}}$$
$$-\left[\tau_{Gm,xy}h_{l/l+1}\Big|_{y=l_{rb}}-\tau_{Gm,xy}h_{l/l+1}\Big|_{y=l_{lb}}\right]_{z=h_{l/l+1}} \tag{6.95}$$

where I have assumed that the spatial derivative of the interface does not depend on the y-abscissa. By analogy, we find the dynamic condition for the lower interface. It has the exact same form than equation (6.95). Consequently, the generalized viscous term is written as:

$$\frac{\partial\left\langle\tau_{Gm,xx}\right\rangle_l\Omega_l}{\partial x}+\int_{h_{l-1/l}}^{h_{l/l+1}}\left[\left(\tau_{ld}-\tau_d\right)\right]dz-\left[\int_{l_{lb}}^{l_{rb}}-\tau_s dy\right]_{z=h_{l/l+1}}+\left[\int_{l_{lb}}^{l_{rb}}-\tau_b dy\right]_{z=h_{l-1/l}}$$
$$+\left[\tau_{Gm,xy}h_{l/l+1}\Big|_{y=l_{rb}}-\tau_{Gm,xy}h_{l/l+1}\Big|_{y=l_{lb}}\right]_{z=h_{l/l+1}}-\left[\tau_{Gm,xy}h_{l-1/l}\Big|_{y=l_{rb}}-\tau_{Gm,xy}h_{l-1/l}\Big|_{y=l_{lb}}\right]_{z=h_{l-1/l}} \tag{6.96}$$

In conclusion, I obtain the cross-sectional integrated momentum equation by combining equations (6.91), (6.92), (6.93), (6.96). It has the following form:

$$\frac{\partial \left\langle \rho_m \right\rangle_l \tilde{u}_{m,l} \Omega_l}{\partial t} + \frac{\partial}{\partial x}\left(\left\langle \sum_k \alpha_k \rho_k \hat{u}_k \hat{u}_k \right\rangle_l \Omega_l \right) = \left\langle \rho_m \right\rangle_l F_{m,x} \Omega_l - \left\langle \frac{\partial p_m}{\partial x} \right\rangle_l \Omega_l + \frac{\partial \left\langle \tau_{Gm,xx} \right\rangle_l \Omega_l}{\partial x} + \left\langle M_x \right\rangle_l \Omega_l + F_{\partial\Omega,l} - E_{\partial\Omega,l} \tag{6.97}$$

where the external friction factor accounts for the friction of cross-section outline on the flow and is defined as follows:

$$\begin{aligned} F_{\partial\Omega,l} = & \left.\int_{h_{l-1/l}}^{h_{l/l+1}} \left[\left(\tau_{ld} - \tau_d \right) \right] dz \right\} \text{Balance of the friction of the right and left lateral banks} \\ & - \left[\int_{l_{lb}}^{l_{rb}} -\tau_{l/l+1} dy \right]_{z=h_{l/l+1}} + \left[\tau_{Gm,xy} h_{l/l+1} \Big|_{y=l_{rb}} - \tau_{Gm,xy} h_{l/l+1} \Big|_{y=l_{lb}} \right]_{z=h_{l/l+1}} \Bigg\} \text{Balance of the friction at the upper interlayer} \\ & + \left[\int_{l_{lb}}^{l_{rb}} -\tau_{l-1/l} dy \right]_{z=h_{l-1/l}} - \left[\tau_{Gm,xy} h_{l-1/l} \Big|_{y=l_{rb}} - \tau_{Gm,xy} h_{l-1/l} \Big|_{y=l_{lb}} \right]_{z=h_{l-1/l}} \Bigg\} \text{Balance of the friction at the lower interlayer} \end{aligned} \tag{6.98}$$

and the external momentum body source accounts for the balance of momentum transported with the mixture flow through boundaries of the cross-section and is defined as

$$E_{\partial\Omega,l} = \left\{ \begin{aligned} & - \left[\int_{l_{lb}}^{l_{rb}} \alpha_d \rho_d u_d dy \right]_{z=h_{l/l+1}} \left[\int_{l_{lb}}^{l_{rb}} e_{d,l/l+1} dy - \hat{v}_d h \Big|_{\substack{y=l_{rd} \\ z=h_{l/l+1}}} + \hat{v}_d h \Big|_{\substack{y=l_{ld} \\ z=h_{l/l+1}}} \right] \Bigg\} \text{Balance of momentum transported by the dispersed phase} \\ & + \left[\int_{l_{lb}}^{l_{rb}} \alpha_d \rho_d u_d dy \right]_{z=h_{l-1/l}} \left[\int_{l_{lb}}^{l_{rb}} e_{w,l-1/l} dy - \hat{v}_d h \Big|_{\substack{y=l_{rd} \\ z=h_{l-1/l}}} + \hat{v}_d h \Big|_{\substack{y=l_{ld} \\ z=h_{l-1/l}}} \right] \Bigg\} \text{through the layers interfaces, and the lateral banks} \\ & - \left[\int_{l_{lb}}^{l_{rb}} \alpha_w \rho_w u_w dy \right]_{z=h_{l/l+1}} \left[\int_{l_{lb}}^{l_{rb}} e_{w,l/l+1} dy - \hat{v}_w h \Big|_{\substack{y=l_{rd} \\ z=h_{l/l+1}}} + \hat{v}_w h \Big|_{\substack{y=l_{ld} \\ z=h_{l/l+1}}} \right] \Bigg\} \text{Balance of momentum transported by the water phase} \\ & + \left[\int_{l_{lb}}^{l_{rb}} \alpha_w \rho_w u_w dy \right]_{z=h_{l-1/l}} \left[\int_{l_{lb}}^{l_{rb}} e_{w,l-1/l} dy - \hat{v}_w h \Big|_{\substack{y=l_{rd} \\ z=h_{l-1/l}}} + \hat{v}_w h \Big|_{\substack{y=l_{ld} \\ z=h_{l-1/l}}} \right] \Bigg\} \text{through the layers interfaces, and the lateral banks} \end{aligned} \right. \tag{6.99}$$

6.4.4 Convective Flux

The philosophy of the drift-flux model incites to express equations in terms of mixture and drift parameters. Consequently, I want to replace the phase parameters that appear in the convective flux of equation (6.97) by primitive unknowns, namely the area-averaged mixture, the area-averaged drift velocity, the area-averaged void fraction, and the flow area. For this purpose, we need to specify the cross-sectional distribution of the phase velocities and the void fraction. In this section, convective flux is rewritten by assuming each profile depends on only one unsteady parameter, which is chosen as its mean value. Correction terms need to be introduced to accommodate the depth-integration of the convective fluxes with an uneven distribution of flow unknowns. In this respect, two types of coefficient are useful: the coefficient of uneven distribution and the covariance correction term.

In the process of simplifying convective fluxes, I do not perform a second Reynolds decomposition, which would be necessary for integrating additional turbulent stresses. Indeed, the first Reynolds decomposition in the derivation of the 3D drift-flux model made appear isotropic turbulent stresses (Chapter 2). The generalized stress tensor $\boldsymbol{\tau}_{Gm}$ conflates this turbulent contribution with the viscous stresses. Consequently, the effect of isotropic turbulence is taken into account in the cross-sectional integration. Nevertheless, a correct account of turbulent fluctuations requires making a second decomposition during the subsequent cross-sectional integration. This decomposition would make appear secondary turbulent terms that accounts for the fluctuations of the scale of the flow width. I choose to neglect this second decomposition in the following because it makes the formulation more complex without affecting the final model. Since turbulent closure relations lost their sense in the one-dimensional framework, the turbulent term would be eventually conflated with other head losses in a friction slope term (chapter 7). An empirical friction correlation gives an approximation of this term. It seems then reasonable to lighten the formulation by assuming here that the secondary turbulent terms are negligible.

COVARIANCE CORRECTION TERM

In order to accommodate area-averaged models with cross-sectional distributions of the parameters, a very popular method, especially in fluid-fluid flow, consists in introducing a covariance term $\mathrm{COV}(\alpha_k\rho_k u_k u_k)$, which represents the difference between the average of a product and the product of the average of two-variables:

$$\frac{\partial}{\partial x}\left(\sum_k \left\langle \alpha_k\rho_k\hat{u}_k\hat{u}_k\right\rangle_l\Omega_l\right)=\frac{\partial}{\partial x}\left(\sum_k \rho_k\left\langle\alpha_k\right\rangle_l\left\langle\left\langle u_k\right\rangle\right\rangle_l\left\langle\left\langle u_k\right\rangle\right\rangle_l\Omega_l\right)+\frac{\partial}{\partial x}\left(\sum_k \underbrace{\left\langle \rho_k\alpha_k\hat{u}_k\left(\hat{u}_k-\left\langle\left\langle u_k\right\rangle\right\rangle_l\right)\right\rangle_l}_{\mathrm{COV}_l\left(\alpha_k\rho_k\hat{u}_k\hat{u}_k\right)}\Omega_l\right) \quad (6.100)$$

If the profile of velocity is flat, then the covariance term reduces to zero. In terms of mixture and drift parameters, the convective flux along the x-axis is given by:

$$\begin{aligned}\frac{\partial}{\partial x}\left(\sum_k \left\langle \alpha_k\rho_k\hat{u}_k\hat{u}_k\right\rangle_l\Omega_l\right)=&\frac{\partial\left\langle\rho_m\right\rangle_l\tilde{u}_{m,l}\tilde{u}_{m,l}\Omega_l}{\partial x}+\frac{\partial}{\partial x}\left(\frac{\left\langle\alpha_g\right\rangle_l}{\left(1-\left\langle\alpha_g\right\rangle_l\right)}\frac{\rho_g\rho_w}{\left\langle\rho_m\right\rangle_l}\tilde{U}_{dj,l}\tilde{U}_{dj,l}\Omega_l\right)\\&+\frac{\partial}{\partial x}\left(\sum_k \mathrm{COV}_l\left(\alpha_k\rho_k\hat{u}_k\hat{u}_k\right)\Omega_l\right)\end{aligned} \quad (6.101)$$

To close the set of governing equations, one must specify analytical functions for the covariance term. This can be only done by assuming a cross-sectional distribution for both the void fraction and the phase velocity.

COEFFICIENT OF UNEVEN DISTRIBUTION

Popular in hydraulic engineering, this approach consists in introducing a coefficient of uneven distribution or Boussinesq coefficient [21, 76, 260]. Accordingly, the convective flux can be written as follows:

$$\frac{\partial}{\partial x}\left(\sum_k \left\langle \alpha_k\rho_k\hat{u}_k\hat{u}_k\right\rangle_l\Omega_l\right)=\frac{\partial}{\partial x}\left(\beta_l\sum_k \left\langle\alpha_k\right\rangle_l\rho_k\left\langle\left\langle u_k\right\rangle\right\rangle_l\left\langle\left\langle u_k\right\rangle\right\rangle_l\Omega_l\right) \quad (6.102)$$

where the coefficient of uneven distribution β_l is simply defined as:

$$\beta_l \triangleq \frac{\sum_k \langle \alpha_k \rho_k \hat{u}_k \hat{u}_k \rangle_l \Omega_l}{\sum_k \langle \alpha_k \rangle_l \rho_k \langle\langle u_k \rangle\rangle_l \langle\langle u_k \rangle\rangle_l \Omega_l} \tag{6.103}$$

β_l must be given by a functional relation depending only on the primitive unknowns. This relation is computed based on vertical distributions assumed a priori and defined by the mean values. By introducing the mixture velocity and the drift velocity, the convective flux can be rewritten as:

$$\frac{\partial}{\partial x}\left(\sum_k \langle \alpha_k \rho_k \hat{u}_k \hat{u}_k \rangle_l \Omega_l\right) = \frac{\partial \beta_l \langle \rho_m \rangle_l \tilde{u}_{m,l} \tilde{u}_{m,l} \Omega_l}{\partial x} + \frac{\partial}{\partial x}\left(\beta_l \frac{\langle \alpha_d \rangle_l}{1-\langle \alpha_d \rangle_l} \frac{\rho_d \rho_w}{\langle \rho_m \rangle_l} \tilde{U}_{dj,l} \tilde{U}_{dj,l} \Omega_l\right) \tag{6.104}$$

In view of this relation, the convective flux has been broken down into a mixture convective flux and a diffusion flux due to the relative velocity between both phases. This last term can also be viewed as a diffusion stress along the x-axis. In order to compute this additional stress, constitutive equation for the drift-velocity is introduced on a case-by-case basis (see chapter 7).

6.4.5 Constitutive Equation for the Pressure Gradient

In the derivation of the cross-sectional integrated drift-flux model, I put aside the pressure gradient. Nevertheless, stating an additional constitutive equation for the pressure is required in order to close the system of PDE's. The choice of this constitutive equation must be in accordance with the two conditions obtained at the end of the dimensional analysis (section 6.1). This results in a hydrostatic distribution over the flow cross-section.

Pressure distribution over the flow cross-section

The distribution of the mixture pressure over the whole cross-section is derived from the conditions (6.20) and (6.21). Indeed, I assume the pressure at the free surface is given by a function $p_s(x,t)$, which depends on the time and the position along the x-axis. Since the body force vector **F** does not depend on the spatial coordinates, the pressure distribution in the fluid is derived by solving the partial differential equation (6.21) in a recursive way:

$$\begin{cases} p_{N-1/N} = p_s \\ p(x,y,z,t) = p_{l/l+1} + F_{m,z} \langle \rho_m \rangle \Big|_z^{h_{l/l+1}} \left(h_{l/l+1}(x,t) - z\right) \qquad l = 1,\ldots,N-1 \end{cases} \tag{6.105}$$

where the mean value of the mixture density over the limited depth $[z;h_{l/l+1}]$ is given by:

$$\langle \rho_m \rangle \Big|_z^{h_{l/l+1}} = \frac{1}{h_{l/l+1} - z} \int_z^{h_{l/l+1}} \rho_m(x,z,t)\,dz \tag{6.106}$$

Distribution (6.105) accounts for all kinds of free surface flows with transport of a dispersed phase. In free surface flows, the pressure p_s is obviously zero. In a stratified flow, the pressure over the free surface is not anymore zero.

INTEGRATION OVER THE FLOW CROSS-SECTION

According to the area-averaged drift-flux momentum equation (6.97), the pressure gradient is given as follows:

$$-\left\langle \frac{\partial p_m}{\partial x} \right\rangle_l \Omega_l = \int_{h_{l-1/l}}^{h_{l/l+1}} \int_{l_{lb}}^{l_{rb}} \frac{\partial p_m}{\partial x} dydz \tag{6.107}$$

By introducing the pressure distribution (6.105) in this formulation, I have:

$$-\left\langle \frac{\partial p_m}{\partial x} \right\rangle_l \Omega_l = -\frac{\partial p_{l/l+1}}{\partial x}\Omega_l - \int_{h_{l-1/l}}^{h_{l/l+1}} \int_{l_{lb}}^{l_{rb}} \frac{\partial}{\partial x}\left(F_{m,z} \left\langle \rho_m \right\rangle \Big|_z^{h_{l/l+1}} \left(h_{l/l+1}(x,t) - z \right) \right) dydz \tag{6.108}$$

I choose to integrate the second term in right-hand side of equation (6.108) over the local width first. Application of the Leibniz integral rule gives:

$$\int_{h_{l-1/l}}^{h_{l/l+1}} \int_{l_{lb}}^{l_{rb}} \frac{\partial}{\partial x} \underbrace{\left(F_{m,z} \left\langle \rho_m \right\rangle \Big|_z^{h_{l/l+1}} \left(h_{l/l+1}(x,t) - z \right) \right)}_{p_{mh}} dydz = \int_{h_{l-1/l}}^{h_{l/l+1}} \left[\frac{\partial p_{mh} l_w}{\partial x} - p_{mh} \frac{\partial l_w}{\partial x} \right] dz \tag{6.109}$$

In a similar manner, integration over the flow depth gives:

$$\begin{aligned} \int_{h_{l-1/l}}^{h_{l/l+1}} \int_{l_{lb}}^{l_{rb}} \frac{\partial}{\partial x} \underbrace{\left(F_{m,z} \left\langle \rho_m \right\rangle \Big|_z^{h_{l/l+1}} \left(h_{l/l+1}(x,t) - z \right) \right)}_{p_{mh}} dydz &= \frac{\partial}{\partial x} \int_{h_{l-1/l}}^{h_{l/l+1}} \left(F_{m,z} \left\langle \rho_m \right\rangle \Big|_z^{h_{l/l+1}} \left(h_{l/l+1}(x,t) - z \right) l_w(z) \right) dz \\ &- \int_{h_{l-1/l}}^{h_{l/l+1}} \left(F_{m,z} \left\langle \rho_m \right\rangle \Big|_z^{h_{l/l+1}} \left(h_{l/l+1}(x,t) - z \right) \frac{\partial l_w(z)}{\partial x} \right) dz \\ &+ F_{m,z} \left\langle \rho_m \right\rangle_l h_l(x,t) l_w\left(h_{l-1/l} \right) \frac{\partial h_{l-1/l}}{\partial x} \end{aligned} \tag{6.110}$$

By combining equation (6.108) with equation (6.110), the area integrated pressure gradient may be rewritten as follows:

$$-\left\langle \frac{\partial p_m}{\partial x} \right\rangle \Omega = -\frac{\partial p_{l/l+1}}{\partial x}\Omega_l - F_{m,z} \frac{\partial P_{\Omega_l}}{\partial x} + F_{m,z} P_{G,\partial\Omega_l} - F_{m,z} \left\langle \rho_m \right\rangle_l h_l(x,t) l_w\left(h_{l-1/l} \right) \frac{\partial h_{l-1/l}}{\partial x} \tag{6.111}$$

with the following definitions:

$$\begin{aligned} P_{\Omega_l} &= \int_{h_{l-1/l}}^{h_{l/l+1}} \left(\left\langle \rho_m \right\rangle \Big|_z^{h_{l/l+1}} \left(h_{l/l+1}(x,t) - z \right) l_w(z) \right) dz \\ P_{G,\partial\Omega_l} &= \int_{h_{l-1/l}}^{h_{l/l+1}} \left(\left\langle \rho_m \right\rangle \Big|_z^{h_{l/l+1}} \left(h_{l/l+1}(x,t) - z \right) \frac{\partial l_w(z)}{\partial x} \right) dz \end{aligned} \tag{6.112}$$

One can recognize 4 terms in formulation (6.111). The first term accounts for the uniform contribution due to the pressure acting at the upper interface. The second term is the hydrostatic contribution over the layer. The third one is the reaction of the banks onto the fluid flow. Finally, the last terms take into account the reaction of the lower interface. All these terms are analogous to the formulation obtained in a single-phase flow. Equation (6.111) is called conservative formulation of the 1D mixture pressure gradient. The formulation cannot go through other simplifications without further assumption.

In conclusion, cross-sectional integration of the 3D drift-flux momentum equation over a multi-layer cross-section presenting a free surface gives the following equation for the l^{th} layer:

$$\frac{\partial \langle \rho_m \rangle_l \tilde{u}_{m,l} \Omega_l}{\partial t} + \frac{\partial \beta_l \langle \rho_m \rangle_l \tilde{u}_{m,l} \tilde{u}_{m,l} \Omega_l}{\partial x} + \frac{\partial}{\partial x}\left(\beta_l \frac{\langle \alpha_d \rangle_l}{1 - \langle \alpha_d \rangle_l} \frac{\rho_d \rho_w}{\langle \rho_m \rangle_l} \tilde{U}_{dj,l} \tilde{U}_{dj,l} \Omega_l \right)$$
$$= \langle \rho_m \rangle_l F_{m,x} \Omega_l - \frac{\partial p_{l/l+1}}{\partial x} \Omega_l - F_{m,z} \frac{\partial P_{\Omega_l}}{\partial x} + F_{m,z} P_{G,\partial\Omega_l} - F_{m,z} \langle \rho_m \rangle_l h_l(x,t) l_w\left(h_{l-1/l}\right) \frac{\partial h_{l-1/l}}{\partial x} \qquad (6.113)$$
$$+ \frac{\partial \langle \tau_{Gm,xx} \rangle_l \Omega_l}{\partial x} + \langle M_x \rangle_l \Omega_l + F_{\partial\Omega,l} - E_{\partial\Omega,l}$$

From a physical point of view, this equation expresses the momentum conservation along the x-axis of both phases taken as a whole. Momentum conservation of each phase on its own is not ensured. Instead, I introduce the notion of drift-velocity, which accounts for the relative velocity between both phases. The constitutive equation that defines this velocity replaces the second momentum equation. Equation (6.113) presents several advantages over a single-phase model like the Saint-Venant equations. First, the formulation accounts for the adverse impact of the dispersed phase on the water flow. Since the drift-velocity appearing in both the diffusion and momentum equation is the same, the model accounts coherently for the diffusion of the dispersed phase in terms of mass and momentum conservation. Third, by combining a coefficient of Boussinesq and a multi-layer structure, the approach accommodates with vertical distribution of the flow parameters.

Summary and conclusion

The previous sections provide a thorough demonstration of the cross-sectional integrated drift-flux model (6.1)-(6.3) for the free surface flows. First, a dimensional analysis underlines the validity of the one-dimensional assumption (section 6.1). Next, I introduce properly-defined mean values such that the formulation of the new model remains simple (section 6.2). In section 6.3, physical boundary conditions are defined at the boundaries of the integration domain. At this point, I can begin the cross-sectional integration of the 3D drift-flux model over the l^{th} layer of the cross-section (section 6.4).

The model obtained at the end of the integration is an original, rigorous, and useful result for describing free surface flows with entrainment of a dispersed phase. To my knowledge, it is indeed the first fully multiphase model that describes free surface flow in a one-dimensional framework. It can be viewed as the multiphase equivalent of the Saint-Venant equations, except that it presents several advantages over the single-phase model. First, the concentration is rigorously defined as the probability of presence of the dispersed phase in a given section. Second, the model takes into account the adverse impact of the dispersed phase on the water flow. Third, the diffusion equation is rigorous and broader in scope than a single-phase model. Finally, introduction of a multi-layer domain of integration and of the Boussinesq coefficient enables to accommodate the one-dimensional framework with a vertical distribution of the flow parameters. The one-dimensional free surface drift-flux model is a powerful tool to design hydraulic structures, assess natural flows, and forecast transport phenomena. In particular, the equations meet most of the objectives of the thesis: the model is rigorously multiphase, it accounts for scale heterogeneities, the computation time will remain limited since the computational domain is 1D, and the model is adapted to civil and environmental engineering problems.

This result paves the way for the development of a particularized mathematical model for transient air-water flows. The model may indeed be simplified for air-entrainment. In addition, its applicability must be extended to pressurized flows. What is more, the model needs to be completed with suitable constitutive equations for the drift-velocity and the friction. All these issues are tackled in the following chapter.

Chapter 7 Multiphase Flows: Air-water Model

This chapter aims at:

1. particularizing the multi-layer free surface drift-flux model to air-water flows;
2. extending it applicability to pressurized flows;
3. introducing suitable constitutive equations for the drift-velocity and the friction.

All the air-water flows introduced in chapter 1 as topics of my thesis present one of the three following cross-sections (Figure 91): a free surface air-water flow, a stratified flow with a free surface separating a pure airflow and a water flow with air entrainment, or a pressurized cross-section with dispersed air in the water. In all these cases, air-water interactions appear between the water flow, the dispersed air within the water, and/or the pure air flowing above the free surface.

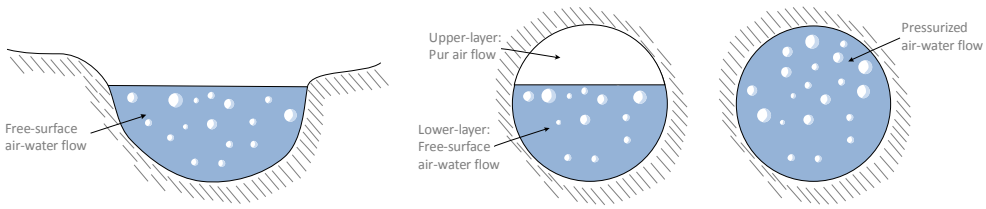

Figure 91: Air-water flows in civil and environmental engineering present three different types of cross-section

In an original way, I unify the three cases in a single conceptual model describing air-water mixed flows (Figure 92). The stratified part of the mixed flow is broken down into two layers. The upper layer is a pure airflow, while the lower layer is a mixture of water and dispersed air. The flow includes then three phases: a water phase, a dispersed air phase, and a pure air phase above the free surface. In an open channel, the upper layer naturally does not exist. Only the lower layer with two phases remains. In a pipe, the upper layer disappears also when the free surface reaches the pipe crown. It results in a pressurized two-phase flow.

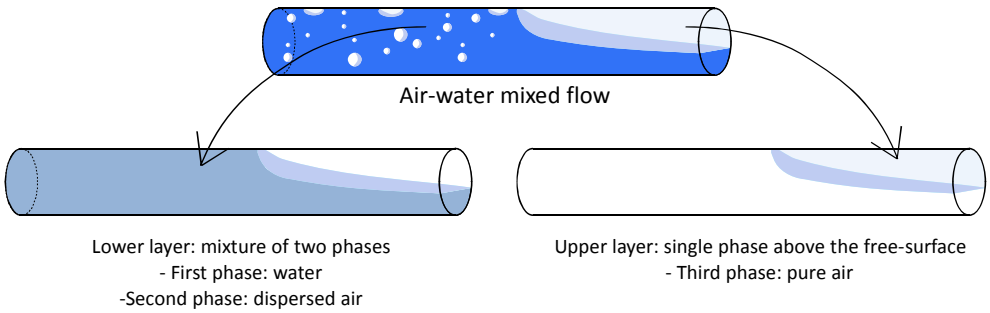

Figure 92: An original conceptual model describes all cases of air-water flows

In this chapter, I intend to particularize/reformulate the original one-dimensional drift-flux model established in the previous chapter to this original conceptual model (Figure 92). For this purpose, I rewrite the equations for two layers and extend the formulation of the pressure terms for pressurized flows as well (sections 7.1 and 7.2). Finally, suitable constitutive equations for both the drift-velocity and the friction close the system of PDE's (sections 7.3 and 7.4).

Particularization of the multi-layer drift-flux model to air-water mixed flows results in five partial differential equations. They describe a three-phase two-layer flow as proposed in the conceptual model.

In the lower layer, simplifications give the following equations:

$$\begin{cases} \dfrac{\partial \langle \rho_m \rangle \Omega}{\partial t} + \dfrac{\partial \langle \rho_m \rangle \tilde{u}_m \Omega}{\partial x} = q_{m,\perp} \\ \dfrac{\partial \langle \alpha_d \rangle \Omega}{\partial t} + \dfrac{\partial}{\partial x}\left(\langle \alpha_d \rangle \tilde{u}_m \Omega + \langle \alpha_d \rangle \dfrac{\rho_w}{\langle \rho_m \rangle} \tilde{U}_{dj} \Omega \right) = \left\langle \Gamma_d \middle/ \rho_d \right\rangle \Omega + q_{\alpha,\perp} \\ \dfrac{\partial \langle \rho_m \rangle \tilde{u}_m \Omega}{\partial t} + \dfrac{\partial \langle \rho_m \rangle \tilde{u}_m \tilde{u}_m \Omega}{\partial x} + \dfrac{\partial}{\partial x}\left(\dfrac{\langle \alpha_d \rangle}{1 - \langle \alpha_d \rangle} \dfrac{\rho_d \rho_w}{\langle \rho_m \rangle} \tilde{U}_{dj} \tilde{U}_{dj} \Omega \right) + g \dfrac{\partial P_\Omega}{\partial x} \\ \qquad = -\langle \rho_m \rangle g \Omega \left(S_F + S_0 \right) - \dfrac{\partial p_\Gamma}{\partial x} \Omega + g P_{G,\partial\Omega} - S_\Gamma + \theta \langle \rho_m \rangle \dfrac{q_{m,\perp}^2}{\Omega} \end{cases} \tag{7.1}$$

which ensure the mass and momentum conservation of the mixture as well as the mass conservation of each phase on its own. In the momentum equation, the friction slope S_F conflates all the head losses affecting the flow, except the interfacial term S_Γ that expresses the friction at the free surface. As shown by a critical analysis of the friction correlation available in the literature, the best formulation for evaluating the friction slope S_F is the homogeneous assumption. Under this assumption, suitable mixture parameters are introduced into the Darcy-Weisbach equation coupled with the Colebrook correlation. In particular, the MacAdam formulation seems to give the best results for evaluating the mixture viscosity. On the other hand, a simple relation based on the slip velocity gives the interfacial term S_Γ. By analogy with the single-phase mixed flow model, the pressure term integrates both hydrostatic and uniform contributions in order to extend the applicability of the free surface model to pressurized flows:

$$P_\Omega = \begin{cases} \displaystyle\int_{h_b}^{h_s} \left(\langle \rho_m \rangle \Big|_z^{h_s} \left(h_s(x,t) - z \right) I_w(z) \right) dz & \text{if free surface} \\ P_\Omega\left(\Omega_{max}, FS \right) + p\Omega & \text{if pressurized} \end{cases} \tag{7.2}$$

The uniform contribution is computed by solving the following equation:

$$a_0^2 \frac{\Omega - \Omega_{max}}{\Omega_{max}} = p - p_0 + \left(p_0^{-1/\beta} - p^{-1/\beta} \right) \beta \alpha_0 \rho_{m,0} a_0^2 p_0^{1/\beta} \tag{7.3}$$

Finally, two constitutive equations give accurate approximation of the drift-velocity. First, the homogeneous assumption set the drift-velocity to zero. It corresponds to a situation of equilibrium between both phases. Second, the Dix correlation provides acceptable results for horizontal and upward inclined pipes regardless of the flow regime.

For the upper layer, particularization of the drift-flux model gives the following set of equations:

$$\begin{cases} \dfrac{\partial \rho_g \Omega_g}{\partial t} + \dfrac{\partial \rho_g \langle\langle u_g \rangle\rangle \Omega_g}{\partial x} = q_{g,l} \\ \dfrac{\partial \rho_g \langle\langle u_g \rangle\rangle \Omega_g}{\partial t} + \dfrac{\partial \rho_g \langle\langle u_g \rangle\rangle \langle\langle u_g \rangle\rangle \Omega_g}{\partial x} + a_a^2 \Omega_g \dfrac{\partial \rho_g}{\partial x} = -\rho_g g \Omega_g S_g + S_\Gamma + \theta \rho_g \dfrac{q_{g,l}^2}{\Omega_g} \end{cases} \tag{7.4}$$

These equations ensure the mass and momentum conservation of the air phase. The air sound celerity is chosen constant at 330m/s. The friction slope S_g includes all the head losses except the interfacial friction S_Γ. The Colebrook equation is sufficient to set the value of S_g. The pressure p_Γ is uniform and related to the density through an equation of state.

7.1 MATHEMATICAL MODEL FOR THE AERATED LOWER LAYER

In this section, I establish a set of three equations that describe the air-water flow in the lower layer of the original conceptual model. Particular attention is paid to the description, in a unified framework, of both free surface and pressurized flows. For this purpose, I particularize the equations of the one-dimensional drift-flux model derived in the previous chapter. What is more, I complement the hydrostatic pressure with a uniform contribution in order to extend the applicability of the model to pressurized flows. The original formulation proposed for this contribution takes into account the presence of air. Finally, I derive a non-conservative formulation of the model that is easier to solve in non-uniform sections.

7.1.1 FREE SURFACE MODEL

As depicted in Figure 92, the lower layer of the conceptual model includes two phases, namely water and dispersed air. This layer accords perfectly with the assumptions made in the previous chapter for deriving the one-dimensional drift-flux model. Consequently, the three following partial differential equations describe the flow motion in the lower layer:

$$\begin{cases} \dfrac{\partial\langle\rho_m\rangle\Omega}{\partial t}+\dfrac{\partial\langle\rho_m\rangle\tilde{u}_m\Omega}{\partial x}=q_{m,L} \\ \dfrac{\partial\langle\alpha_d\rangle\Omega}{\partial t}+\dfrac{\partial}{\partial x}\left(\langle\alpha_d\rangle\tilde{u}_m\Omega+\langle\alpha_d\rangle\dfrac{\rho_w}{\langle\rho_m\rangle}\tilde{U}_{dj}\Omega\right)=\left\langle\Gamma_d/\rho_d\right\rangle\Omega+q_{\alpha,L} \\ \dfrac{\partial\langle\rho_m\rangle\tilde{u}_m\Omega}{\partial t}+\dfrac{\partial\langle\rho_m\rangle\tilde{u}_m\tilde{u}_m\Omega}{\partial x}+\dfrac{\partial}{\partial x}\left(\dfrac{\langle\alpha_d\rangle}{1-\langle\alpha_d\rangle}\dfrac{\rho_d\rho_w}{\langle\rho_m\rangle}\tilde{U}_{dj}\tilde{U}_{dj}\Omega\right)+g\dfrac{\partial P_\Omega}{\partial x} \\ \qquad =-\langle\rho_m\rangle g\Omega\left(S_F+S_0\right)-\dfrac{\partial\Omega}{\partial x}p_\Gamma+gP_{G,\partial\Omega}-S_\Gamma+\theta\langle\rho_m\rangle\dfrac{q_{m,L}^2}{\Omega} \end{cases} \tag{7.5}$$

where the subscript "l" has been dropped since this layer is considered as the main layer. Several simplifications have been introduced to make the equations usable in practice. In the following paragraphs, I discuss the validity and the interest of the resulting equations.

The first equation (7.5) accounts for the mass conservation of both the water and the dispersed air. The equation is expressed in terms of mixture density and velocity. These parameters have been defined in Chapter 6. In addition, the area Ω designates the section of the lower layer flow. Lateral discharge $q_{m,L}$ is given as boundary conditions in each mesh depending on the local conditions. For instance, the mesh can be connected to a pump, to another pipe, to a lateral spillway, to an erodible levee….Obviously, it would be useless to attempt to foresee all the situations likely to appear. Consequently, I propose to specify the lateral discharge on a case-by-case basis.

Formulation of this equation is very similar to the continuity in the Saint-Venant model. However, its physical significance differs completely. While Saint-Venant equation describes a pure water flow, the multiphase equation of continuity translates the conservation of the air-water mixture. Nevertheless, it is worthwhile noting that the mixture continuity

equation in (7.5) simplifies into the Saint-Venant continuity equation when the dispersed phase is neglected.

Mass conservation of both phases taken separately is ensured by adding a diffusion equation for the concentration in air $\langle \alpha_d \rangle$. This concentration is rigorously defined from a mathematical point of view. Physically, it corresponds to the probability of presence of the dispersed air within a given cross-section of the lower layer. The air motion is expressed in terms of mixture and drift-velocities. Accounting for the relative velocity between each phases, this last one is given by a constitutive equation (section 7.4). Other constitutive equations are needed to specify the lateral air discharge $q_{\alpha,l}$, and the mean air volume source term $\langle \Gamma_d / \rho_d \rangle \Omega$. This last term accounts for the dissolution/gasification of air within the water. To put it another words, it accounts for the exchange between both phases. From a practical point of view, the phase-change constitutive equation should be written in a functional form to close the set of equations:

$$\langle \Gamma_d \rangle = \langle \Gamma_d \rangle \left(\langle \alpha_d \rangle, \langle p_m \rangle, \tilde{u}_m, \partial \langle p_m \rangle / \partial t, \ldots \right) \tag{7.6}$$

Again it is useless to attempt to foresee all the situations likely to appear. Consequently, I propose to specify its formulation on a case-by-case basis.

By comparing the multiphase diffusion equation with a simple-advection diffusion equation, either similarities and discrepancies appear. Regarding the similarities, the structure of both equations is analogous. A temporal term, a convective term, and a dispersive term govern the variations of concentration in air. Sometimes, source terms complement the equation. However, the physical significance of the parameters appearing in these terms differs notably. In the new model, the convection is expressed in terms of mixture velocity, while the diffusion makes use of a single parameter, the drift-velocity. Finally, the diffusion equation relies on a rigorous theory about multiphase flows.

Finally, the last equation (7.5) accounts for the momentum conservation of the mixture (water and dispersed air) along the main direction of the flow. For deriving this equation, I have made basic assumptions that simplify the model. First, I assumed that the lower interface of the layer was the bottom ground given by its slope S_0. Next, the friction slope S_F conflates all head-losses affecting the lower layer, except the friction at the interface given by the interfacial friction S_Γ. Their value is specified by constitutive equations (section 7.3). Third, the width at the bottom of the cross-section is assumed negligible. Fourth, gravity is the only body force considered such that:

$$\begin{cases} F_{m,x} = g \tan \varepsilon \approx g\varepsilon \approx g S_0 \\ F_{m,z} = g \cos \varepsilon \approx g \end{cases} \tag{7.7}$$

Fifth, all the flow parameters are assumed constant over the layer such that the Boussineq coefficient β=1. Nevertheless, equation (7.5) includes most of the features of the multi-layer drift-flux model. All terms are indeed expressed in terms of the mixture parameters that were defined in the previous chapter. Totally, the pressure terms are given by:

$$P_{\Omega} = \int_{h_b}^{h_s} \left(\langle \rho_m \rangle \Big|_z^{h_s} \left(h_s(x,t) - z \right) l_w(z) \right) dz$$
$$P_{G,\partial\Omega} = \int_{h_b}^{h_s} \left(\langle \rho_m \rangle \Big|_z^{h_{l/l+1}} \left(h_s(x,t) - z \right) \frac{\partial l_w(z)}{\partial x} \right) dz \tag{7.8}$$

Using proper mean values keeps the formulation very simple and close to the Saint-Venant momentum equation. Most of the terms appearing in the single-phase model are still present in the multiphase model. Nevertheless, the physical significance of equation (7.5) differs from the Saint-Venant model. While the last one describes the water flow, the new equation ensures the momentum conservation of the air-water mixture. In particular, using mixture parameters enables to account for the adverse impact of the air over the water flow. What is more, the single parameter called drift-velocity describes the relative velocity between phases in both diffusion and momentum equations. It ensures coherence within the model.

7.1.2 Modification of the Pressure Term

When the free surface level reaches the pipe crown, the flow gets pressurized. Equations (7.5) do not hold anymore. Nevertheless, I derived in Chapter 3 a state-of-the-art model that extends the applicability of the single-phase free surface model to pressurized flows as well. For this purpose, I added a uniform contribution to the hydrostatic pressure. Its value depends on the pipe section and the pressure wave celerity. I propose to apply in this section a similar approach for the multiphase model. The key issue here is to account adequately for the presence of air within the water flow.

By analogy with the single-phase model for mixed flows, I can extend the applicability of the pressure term P_{Ω} to pressurized flows and express it as a function of the pressure wave celerity a. Indeed, the pressure may be assumed uniformly distributed over the flow cross-section in a multiphase pressurized flow. By definition, the value of this uniform component "p" depends directly on the pressure wave celerity a through the following relation:

$$a^2 = \Omega_{max} \frac{\partial p}{\partial \left(\langle \rho_m \rangle \Omega \right)} \tag{7.9}$$

where the value of the pressure wave celerity is given by the continuum mechanics. By integration of equation (7.9), we obtain an expression of the uniform contribution to the general term P_{Ω}. Consequently, I derive a unified pressure term for mixed flow by combining the hydrostatic pressure (6.112) with the uniform contribution (7.9):

$$P_{\Omega} = \begin{cases} \int_{h_b}^{h_s} \left(\langle \rho_m \rangle \Big|_z^{h_s} \left(h_s(x,t) - z \right) l_w(z) \right) dz & \text{if FS} \\ P_{\Omega}(\Omega_{max}, FS) + \Omega \int_{\langle \rho_m \rangle \Omega_{max}}^{\langle \rho_m \rangle \Omega} \frac{a^2}{\langle \rho_m \rangle \Omega} d\left(\langle \rho_m \rangle \Omega \right) & \text{if PP} \end{cases} \tag{7.10}$$

where Ω_{max} is the value of Ω at the pipe crown, the State FS indicates that the flow is at free surface and the State PP that the flow is pressurized. If $\Omega > \Omega_{max,}$ the flow is obviously

pressurized PP. If $\Omega \leq \Omega_{max}$, the flow is chosen either pressurized PP or free surface FS according to the aeration rate. Lack of aeration devices prevents indeed that a free surface appears when the pressure drops below the atmospheric pressure. Instead, a sub-atmospheric pressurized flow is observed.

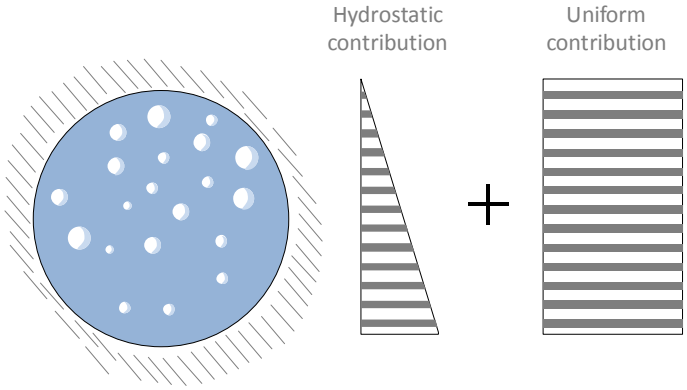

Figure 93: The original pressure term contains an hydrostatic and a uniform component

In order to simplify expression (7.10), it is necessary to give an expression or a value to the pressure wave celerity. As already mentioned in Chapter 2, the value of celerity may be a constant value in a pure water flow. Computed prior the simulation, this value depends on the pipe strength, on the fluid compressibility, and on the strength of the support means. It ranges between 1400m/s for a rigid pipe to about 100m/s for very flexible conduits. In presence of air, the value of the pressure wave velocity depends also on the air concentration. Even in presence of a very small amount of air, the celerity may drop drastically. According to Guinot [1-4], the celerity of such a gas-liquid mixture is given by the following formulation:

$$a_m = a_0 \Big/ \sqrt{1+\alpha_0 \rho_{m,0} a_0^2 \, p_0^{1/\beta} \Big/ p^{1+\beta/\beta}} \qquad \rho_{m,0} = \alpha_0 \rho_d + (1-\alpha_0)\rho_w \tag{7.11}$$

where the subscript 0 designates the reference state characterized by a pressure p=101325Pa (atmospheric pressure). β is a coefficient equal to 1.0 for isothermal processes and 1.4 for adiabatic conditions. The reference void fraction α_0 is the volume fraction of dispersed air at reference pressure, and the $\rho_{m,0}$ is the mixture density at reference pressure.

The formulation (7.11) for the celerity in mixture fluid enables to simplify the integral appearing in equation (7.10). Indeed, introducing (7.11) within integral (7.10) gives the following unified pressure term:

$$P_\Omega = \begin{cases} \int_{h_b}^{h_s} \left(\langle \rho_m \rangle \Big|_z^{h_s} \left(h_s(x,t) - z \right) l_w(z) \right) dz & \text{if FS} \\ P_\Omega\left(\Omega_{max}, FS\right) + \Omega p & \text{if PP} \end{cases} \tag{7.12}$$

where p is obtained by solving iteratively the following equation (Guinot [130-133]):

$$a_0^2 \frac{\Omega - \Omega_{max}}{\Omega_{max}} = p - p_0 + \left(p_0^{-1/\beta} - p^{-1/\beta} \right) \beta \alpha_0 \rho_{m,0} a_0^2 p_0^{1/\beta} \tag{7.13}$$

A Newton-Raphson scheme provides an efficient scheme to solve it.

7.1.3 NON-CONSERVATIVE FORMULATION

Like for the Saint-Venant equations, computing the pressure term $P_{\partial\Omega}$ turns out to be difficult. A simple manner to get round this difficulty consists in expressing the pressure term in terms of free surface elevation. This is the non-conservative form of the equations.

FREE SURFACE FLOW

For a free surface flow, expressing the model (7.5) in terms of free surface elevation requires manipulating three terms, namely the hydrostatic pressure term, the lateral reaction pressure term, and the bottom slope:

$$-g\frac{\partial P_\Omega}{\partial x}-\langle\rho_m\rangle g\Omega S_0+gP_{G,\partial\Omega} \tag{7.14}$$

Indeed, these three terms may be simplified by assuming the distribution of the concentration in air is uniform over the cross-section. Application of the Leibnitz integral rule to equations (6.112) and (7.14) gives:

$$-g\left[\int_{h_b}^{h_s}\left(l_w(z)\frac{\partial}{\partial x}\left[\langle\rho_m\rangle\left(h_s(x,t)-z\right)\right]\right)dz\right]-\langle\rho_m\rangle g\Omega S_0 \tag{7.15}$$

Since the free surface height h_s and the z-axis does not depend on the variable x, we have

$$-g\langle\rho_m\rangle\Omega\frac{\partial h_s}{\partial x}-\langle\rho_m\rangle g\Omega S_0-g\Omega\frac{h^2}{2}\frac{\partial\langle\rho_m\rangle}{\partial x} \tag{7.16}$$

By definition, the topographic slope S_0 is given by:

$$S_0=\frac{\partial h_b}{\partial x} \tag{7.17}$$

and the free surface elevation $Z=h_s+h_b$. Then, equation (7.16) is rewritten as:

$$-g\langle\rho_m\rangle\Omega\frac{\partial Z}{\partial x}-g\Omega\frac{h^2}{2}\frac{\partial\langle\rho_m\rangle}{\partial x} \tag{7.18}$$

In conclusion, the mixture momentum equation for the free surface air-water lower layer may be rewritten as:

$$\begin{aligned}&\frac{\partial\langle\rho_m\rangle\tilde{u}_m\Omega}{\partial t}+\frac{\partial\langle\rho_m\rangle\tilde{u}_m\tilde{u}_m\Omega}{\partial x}+\frac{\partial}{\partial x}\left(\frac{\langle\alpha_d\rangle}{1-\langle\alpha_d\rangle}\frac{\rho_d\rho_w}{\langle\rho_m\rangle}\tilde{U}_{dj}\tilde{U}_{dj}\Omega\right)\\&\quad=-\langle\rho_m\rangle g\Omega\left(S_F+\frac{\partial Z}{\partial x}\right)-g\Omega\frac{h^2}{2}\frac{\partial\langle\rho_m\rangle}{\partial x}-\frac{\partial p_\Gamma}{\partial x}\Omega-S_\Gamma\end{aligned} \tag{7.19}$$

PRESSURIZED FLOW

In the case of a pressurized flow, the notion of free surface elevation looses most of its sense. However, one can note that the notions of free surface elevation and pressure head are analogous. That being so, applicability of equation (7.19) may be extended to pressurized flow by redefining the free surface elevation as follows:

$$Z=\begin{cases}h_s+h_b & \text{if FS}\\ Z(\Omega_{max},FS)+\dfrac{P_\Omega-P_\Omega(\Omega_{max},FS)}{\langle\rho_m\rangle\Omega_{max}} & \text{if PP}\end{cases} \tag{7.20}$$

7.2 Mathematical Model for the Pure Air Upper Layer

In this section, I derive a set of equations describing the motion of pure air in the upper layer. It complements the equations that describe the lower layer. First, I simplify the one-dimensional drift-flux model obtained in the previous chapter under the assumption that a single air phase is present. Next, I particularize the pressure gradient with respect to the peculiar features of pure air. It results in two partial differential equations for the pressure and the velocity in the upper layer.

If present, the upper layer of the flow contains pure air and constitutes a particular case of the free surface multi-layer drift-flux model derived in the previous chapter. In fact, proper equations may be derived by assuming the mixture is pure air. Since the diffusion equation becomes trivial, simplifications give the two following partial differential equations:

$$\begin{cases} \dfrac{\partial \rho_g \Omega_g}{\partial t} + \dfrac{\partial \rho_g \left\langle\!\left\langle u_g \right\rangle\!\right\rangle \Omega_g}{\partial x} = q_{g,l} \\ \dfrac{\partial \rho_g \Omega_g}{\partial t} + \dfrac{\partial \rho_g \left\langle\!\left\langle u_g \right\rangle\!\right\rangle \left\langle\!\left\langle u_g \right\rangle\!\right\rangle \Omega_g}{\partial x} + \dfrac{\partial p_\Gamma}{\partial x}\Omega_g = -\rho_g g \Omega_g S_g + S_\Gamma + \theta \rho_g \dfrac{q_{g,l}^2}{\Omega_g} \end{cases} \tag{7.21}$$

where the subscript "g" accounts for the third phase (pure air). In this formulation, the mixture velocity reduced to the air velocity, while the drift-velocity cancelled. The area Ω_g designates the air cross-section. The friction slope S_g conflates all the head-losses, except the friction at the interface that is given by S_Γ. Both terms are specified by a friction correlation (section 7.3). The density is assumed sufficiently small to neglect the effect of the gravity. Consequently, the pressure p_Γ is constant over the cross-section.

Model (7.21) provides two equations for three primitive unknowns: the density, the velocity, and the pressure. The cross-section area Ω_g is indeed not a unknown since it may be correlated with the lower layer area as follows:

$$\Omega_g = \Omega_{max} - \Omega \tag{7.22}$$

In order to close this model, an additional equation is necessary. For this purpose, I use an equation of state defining the speed of sound in pure air denoted a_a:

$$a_a^2 = \frac{dp_\Gamma}{d\left(\rho_g\right)} \tag{7.23}$$

In some approximation, the air sound speed can be assumed constant at 330m/s. Consequently, the momentum equation may be rewritten in a non-conservative form:

$$\frac{\partial \rho_g \Omega_g}{\partial t} + \frac{\partial \rho_g \left\langle\!\left\langle u_g \right\rangle\!\right\rangle \left\langle\!\left\langle u_g \right\rangle\!\right\rangle \Omega_g}{\partial x} + a_a^2 \Omega_g \frac{\partial \rho_g}{\partial x} = -\rho_g g \Omega_g S_g + S_\Gamma \tag{7.24}$$

which does make appear the density and the velocity only.

7.3 CONSTITUTIVE EQUATIONS FOR THE FRICTION

In the one-dimensional equations established in the previous sections, various head-losses appear in the momentum equations. Rigorously computing these terms is delicate if not intractable. Consequently, the usual approach consists in conflating all the head-losses in a limited number of parameters, called friction slopes or pressure drops.

In the lower layer model, three head-loss terms appear in the mixture momentum equation. The first term accounts for the contribution of the viscous and turbulent terms (conflated in the generalized stresses) in the direction of the predominating flow. The second term is the external friction factor. Finally, the area-averaged mixture momentum source is the third term of friction. It accounts for the head losses induced by the surface tension at bubbles' and pocket's interfaces. In general two-phase flow theory, these three terms are aggregated into a unique parameter called Frictional Pressure Drop [33, 181, 313]. In this thesis, the frictional pressure drop is broken down into two terms: a friction term S_Γ that develops between the free surface and the air flowing above the free surface, and the friction slope, denoted S_F, for all the other contributions. Thus, we can write the following relationship:

$$-\left(\frac{dp}{dx}\right)_{Fm} = \frac{\partial\left\langle\tau_{Gm,xx}\right\rangle\Omega}{\partial x} + \left\langle M_x\right\rangle\Omega + F_{\partial\Omega} = \left\langle\rho_m\right\rangle g\Omega S_F + S_\Gamma \tag{7.25}$$

In the upper layer model, only two head-loss terms remain at the end of the simplification. The first term is the spatial derivative of the viscous and turbulent stresses. The second is the external friction factor. For the sake of simplicity, I express all these terms in a single parameter S_g called the air friction slope. Nevertheless, I keep apart the interfacial friction term denoted S_Γ in order to ensure the coherency between both layers. At the end of the day, the frictional pressure drop within the upper layer is given by:

$$-\left(\frac{dp}{dx}\right)_{Fm} = \frac{\partial\left\langle\tau_{Gg,xx}\right\rangle\Omega}{\partial x} + F_{\partial\Omega} = \rho_g g\Omega_g S_g - S_\Gamma \tag{7.26}$$

Next, the value of these friction slopes is determined by means of empirical friction correlations. The purpose of this section is to identify the most suitable friction correlations for the two-layer three-phase drift-flux model. Clearly, this chapter does not aim at establishing a thorough theory over frictional pressure drop in air-water flows. Instead, it provides an overview of the most widespread methods with a critical analysis of their performance (with respect to the objective of this thesis). In particular, I review the most usual single-phase correlations (sub-section 7.3.1), and extend their applicability to two-phase flows by means of the homogeneous assumption (sub-section 7.3.2). Next, I introduce two typical two-phase correlations: the Lockhart-Martinelli correlation (sub-section 7.3.3), and the Muller-Steinhagen and Heck correlation (sub-section 0). Finally, a suitable law determines the interfacial friction (sub-section 7.3.5).

The critical review enables to identify the most suitable correlations in single and two-phase flows. On the one hand, literature proposes a large number of single-phase formulations widely validated and applied in civil and environmental engineering. In this respect, both the Manning-Strickler and the Colebrook correlations seem the best choices. On the other hand, various two-phase correlations are frequently used in chemical and mechanical engineering. The homogenous assumption, the Lockhart-Martinelli correlation, and the Muller-Steinhagen and Heck formulation are the most popular of them. If the two last equations account precisely for the two-phase interactions, they completely neglect the influence of the pipe roughness. Since this effect is of utmost importance in civil and environmental engineering, the two correlations are useless in this thesis. Hopefully, using the Colebrook correlations with the mixture parameters (homogenous assumption) gives sufficiently accurate results to be used in practice. This assumption enables indeed to take into account the effects of both the multiphase interactions and the pipe roughness. What is more, this formulation simplifies into the single-phase Colebrook correlation if the dispersed phase is neglected. Finally, a simple correlation based on the slip velocity gives a good approximation of the friction at the interface.

7.3.1 SINGLE-PHASE FRICTION LAWS

As pointed in section 2.2.4 page 48, head loss in pressurized and free surface single phase flow can be readily calculated by means of the Darcy-Weisbach. The friction factor f is evaluated for given conditions by the use of various empirical or theoretical relations, or it may be obtained from the Moody-Stanton diagram (Figure 30). In the modern formulations, the Colebrook-White equation is clearly the most widespread formula. However, hydraulic engineers and hydrologists still use empirical formulations like Manning-Strickler formulation. Both the Manning-Strickler equation and the Colebrook-White equation give reliable assessment of single-phase head losses. For further detail, I refer the interested reader to section 2.2.4 page 48.

7.3.2 TWO-PHASE FRICTION LAWS: HOMOGENEOUS ASSUMPTION

When the mixture is thoroughly mixed, both air and water can be assumed to move at the same velocity. The frictional pressure drop can be approximated by the friction coefficient for a single phase flow which is calculated on the basis of suitable mixture parameters. This model is called homogeneous [33, 313] or no-slip [19] model. Brennen [33] has exemplified the applicability of the method by using slurry pipeline data. It shows good agreement for low void fraction. The most thorough discussion of the model is given by Wallis [313]. The frictional pressure gradient is then calculated by means of the Darcy-Weisbach equation:

$$-\left(\frac{dp}{dx}\right)_F = \langle \rho_m \rangle g \Omega S = \langle \rho_m \rangle f \frac{\tilde{u}_m^2}{2gD_h} \tag{7.27}$$

The friction coefficient f is a complex function of the Reynolds Number, the relative roughness and, in the case of the homogeneous flow assumption, of the void fraction. In parallel with the traditional Moody-Stanton diagram for single-phase flow, these friction

coefficients are usually presented as functions of a Reynolds number for various mixture ratios characterized by the void fraction α_g or the quality x_g. Commonly used Reynolds numbers are defined as follows:

$$Re_{f,m} = \frac{\langle \rho_m \rangle \tilde{u}_m D_h}{\langle \mu_m \rangle} \qquad \text{or} \qquad Re_{f,w} = \frac{\rho_w \langle\langle u_w \rangle\rangle D_h}{\mu_w} \tag{7.28}$$

FRICTION FACTOR FOR LAMINAR FLOWS

Scientists proposed many methods for evaluating the two-phase homogeneous friction factor. Wallis [313] provides a very simple technique that consists in using the mixture density as the effective density of an equivalent single-phase flow. Based on this mixture viscosity μ_m, equation (7.28) gives the mixture Reynolds number. This Reynolds number is introduced in classical single-phase flow friction laws, namely the Blasius law, or the Colebrook correlation.

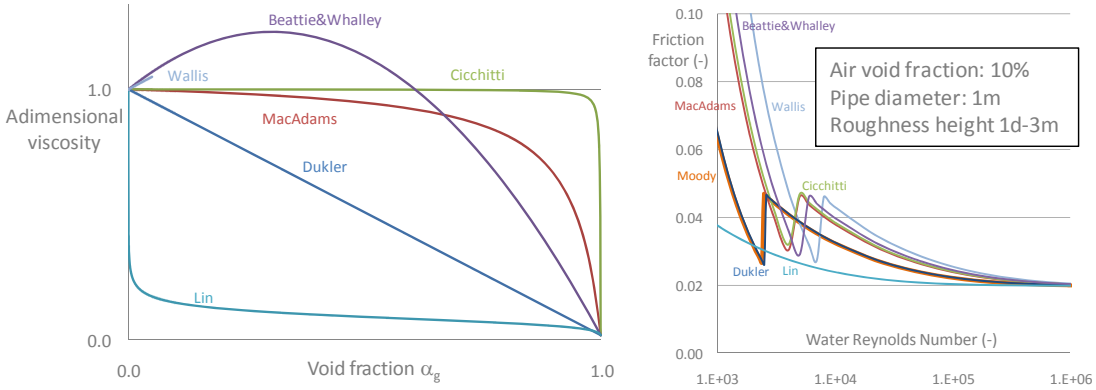

Figure 94: Various correlations give very different mixture viscosities in function of the void fraction (left). Moody diagram is also affected by the correlation chosen.

The mixture viscosity is approximated with rheological models that take into account the void fraction. Many workers have chosen averages that fit the limiting cases in which either phase is not present. The most common expressions for gas liquid flow are the Wallis correlation [313], McAdams et al. formulation [217], the Cicchitti et al. formulation [53], the Dukler et al. formulation [89], the Beattie and Whalley formulation, and the Lin et al formulation [200]. By analyzing these functions, strong dissimilarities appear qualitatively and quantitatively (Figure 94). On the left graph, the mixture viscosity given by these six correlations is represented as a function of the gas void fraction α_g. Discrepancy arises in both value and shape. On the right graph, the friction factor is given as a function of the water Reynolds number for these various correlations (by analogy with the Moody-Stanton diagram for single-phase flows). Since the gas void fraction affects the friction factor, this graph is not anymore general. The present graph is computed for a gas void fraction of 50%, a pipe diameter of 1m and a roughness height of 10^{-3}m. Large discrepancies appear between the various correlations. Since the Dukler correlation is shown to have no impact on the friction factor, it is avoided. The Wallis correlation gives the greatest values of friction factor but its validity is restrained for void fraction below 5%. Finally, McAdams et al, Cicchiti et al, and Beattie&Whalley correlation exhibit consistent results.

Even if literature mentions that results seem in accordance with experimental data [217, 239], the method obviously suffers from a lack of consistency. In the realm of two-phase flow viscosity models, Collier and Thome [58] mention that the definition of the mixture viscosity proposed by McAdams et al is the most common:

$$\frac{1}{\langle \mu_m \rangle} = \frac{\langle x_g \rangle}{\mu_g} + \frac{1-\langle x_g \rangle}{\mu_w} \tag{7.29}$$

It is usually argued that this formulation gives a sufficiently accurate approximation for the whole range of quality x (or void fraction α). Coupled with the Colebrook correlation, this approach seems to be the best choice for application in civil and environmental engineering. Contrary to other two-phase correlations, the approach enables indeed to take into account the pipe roughness. What is more, assuming a 0% void fraction renders a classical single-phase correlation. Finally, my personal investigations and comparisons with published experimental data confirmed the fidelity of the results. For all these advantages, this approach will be used in the following.

7.3.3 Two-phase Friction Laws: Lockhart-Martinelli Correlation

In chemical and mechanical engineering, two-phase friction pressure drops are still nowadays modeled on the basis of the classical theory established by Lockhart and Martinelli [207] and by Martinelli and Nelson [213]. In this method, two-phase flow is considered to be divided into liquid and gas streams. The correlations are constructed with the results for the frictional pressure gradient in single-phase pipe flows of each of the two fluids. These are calculated on the basis of the Darcy-Weisbach equation applied to each single-phase stream:

$$\begin{cases} -\left(\frac{dp}{dx}\right)_{F,w} = \rho_w f_{f,w} \frac{\left(\tilde{u}_m \left(1-\langle \alpha_g \rangle\right)\right)^2}{2D_h} \Omega & \text{for the water flow} \\ -\left(\frac{dp}{dx}\right)_{F,g} = \rho_g f_{f,g} \frac{\left(\tilde{u}_m \langle \alpha_g \rangle\right)^2}{2D_h} \Omega & \text{for the air flow} \end{cases} \tag{7.30}$$

Friction factors are calculated by means of the modified Blasius-like equation:

$$f_f = C_B \, Re_f^{-n} \tag{7.31}$$

For the parameter C_B, it is usually recommended to use C_B=0.3164 (Blasius) for laminar flow and C_B=64 for turbulent flow (Hagen-Poiseuille). In the original paper of Lockhart and Martinelli [207] they found that using the exact Blasius equation does not fit adequately when compared with experimental data. They achieve agreement when setting n=0.2 and C_B =0.184 for turbulent flow. These values are still used nowadays in chemical engineering. They also have been validated on a scale model for civil engineering applications in [165].

The pressure drops computed this way are then correlated with the Lockhart-Martinelli parameter X^2. This parameter gives a measure of the degree to which the two-phase mixture behaves as the water rather than as the gas:

$$X^2 \triangleq \left(\frac{dp}{dx}\right)_{F,w} \Big/ \left(\frac{dp}{dx}\right)_{F,g} \tag{7.32}$$

In addition, the two-phase frictional pressure drop is expressed in terms of two-phase multipliers defined as:

$$\Phi_{f,w}^2 \triangleq \left(\frac{dp}{dx}\right)_F \Big/ \left(\frac{dp}{dx}\right)_{F,w} \quad \text{and} \quad \Phi_{f,g}^2 \triangleq \left(\frac{dp}{dx}\right)_F \Big/ \left(\frac{dp}{dx}\right)_{F,g} \tag{7.33}$$

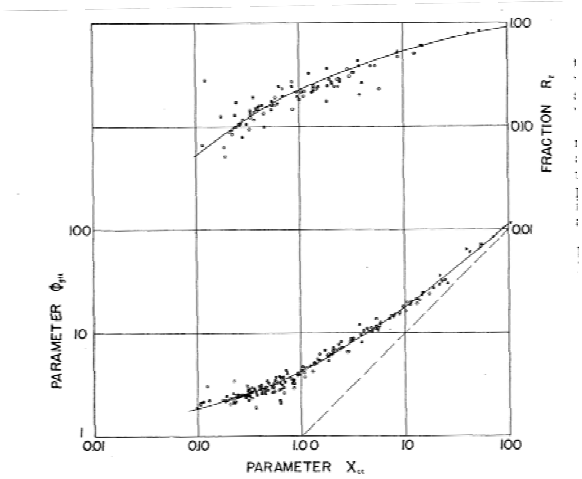

Fig. 1. Relation between R_f, ϕ_{ft}, and parameter X for mechanism 1, turbulent-turbulent flow. Experimental groups 3, 5, 8, 10, 13-17 are included. A few points from experimental groups 4, 7, and 9 for flow mechanism 3, turbulent-viscous flow are also plotted

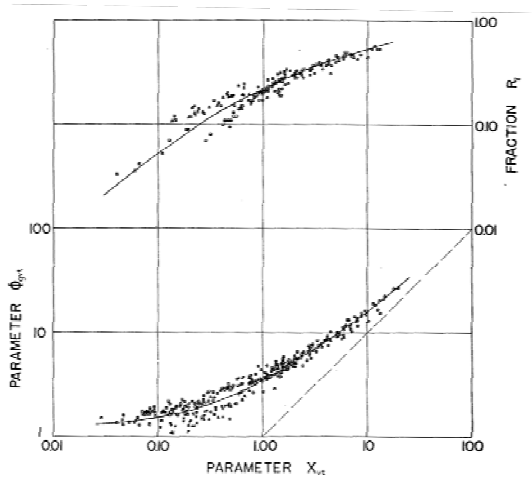

Fig. 2. Relation between R_f, ϕ_{gv}, and parameter X for mechanism 2, viscous-turbulent flow. Experimental groups 1, 2, 3, 5, 6, 11-21 are included

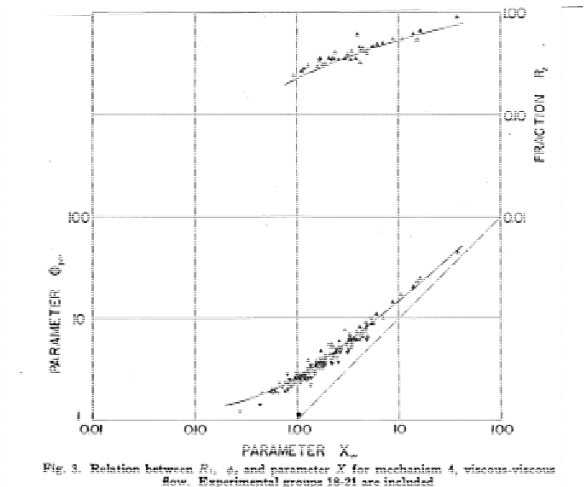

Fig. 3. Relation between R_f, ϕ_f, and parameter X for mechanism 4, viscous-viscous flow. Experimental groups 18-21 are included

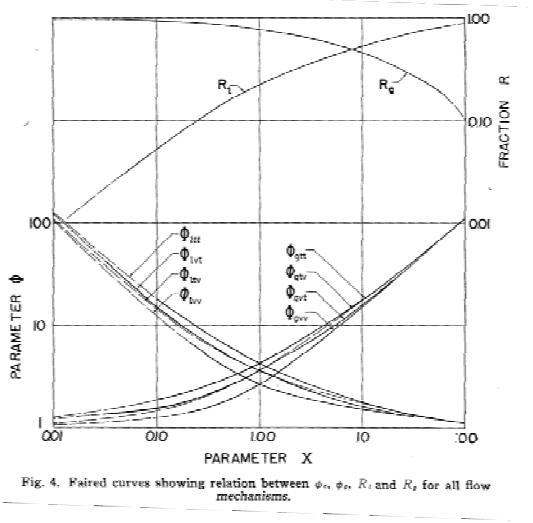

Fig. 4. Faired curves showing relation between ϕ_{tt}, ϕ_{vv}, R_f and R_g for all flow mechanisms.

Figure 95 : Graphical relations for the two-phase multipliers as given in [207]

In the initial paper of Martinelli and Lockhart [207], the relations of two-phase frictional pressure drops as a function of X^2 were presented in graphical forms for the 4 flow regimes (Figure 95): turbulent-turbulent, viscous-turbulent, turbulent-viscous and viscous-viscous. For sake of easier numerical application, Chisholm [52] develop simplified equations:

$$\Phi_{f,w}^2 = 1 + \frac{N}{X} + \frac{1}{X^2} \qquad \text{and} \qquad \Phi_{f,g}^2 = 1 + N.X + X^2 \tag{7.34}$$

The coefficient N can thereby be set according to Table 11.

If very successful in chemical and mechanical engineering, the Lockhart-Martinelli approach suffers major shortcomings in civil and environmental engineering. The complete neglect of the pipe roughness effect is the most important of them. This parameter is indeed way

much important than multiphase interactions in most of the practical applications. Consequently, Lockhart-Martinelli approach is not used in this thesis. Nevertheless, further research would be useful in order to integrate the pipe roughness effect in this multiphase approach.

Table 11: Coefficient N according to [52]

Liquid	Gas	Value of N
Turbulent	Turbulent	20
Viscous	Turbulent	12
Turbulent	Laminar	10
Viscous	Laminar	5

7.3.4 Two-phase Friction Laws: Muller-Steinhagen and Heck Correlation

Müller-Steinhagen and Heck [227] suggested a new correlation for the prediction of the frictional pressure gradient in two-phase flow in pipes. Their approach explicitly aims at developing a method that is simpler in application but still reliable in terms of accuracy. Their development is based on the observation that the frictional head-loss of a gas-liquid two-phase flow for a quality of 0.5 is nearly always identical to the single-phase gas pressure drop for a unit quality. The pressure drops of the respective single-phase flows are calculated as:

$$\left(\frac{dp}{dx}\right)_{F,w0} = f_{f,w0}\frac{G^2}{2\rho_w D_h} = A_{MSH} \qquad \text{and} \qquad \left(\frac{dp}{dx}\right)_{F,g0} = f_{f,g0}\frac{G^2}{2\rho_g D_h} = B_{MSH} \tag{7.35}$$

where the total mass flux is given by

$$G = \langle \rho_m \rangle \tilde{u}_m \tag{7.36}$$

In this method, the friction factors are given by a Blasius-like correlation:

$$f_{f,k0} = \begin{cases} 64\,Re_{f,k0}^{-1} & \text{if} \quad Re_{f,k0}^{-1} \le 1187 \\ 0.3164\,Re_{f,k0}^{-0.25} & \text{if} \quad Re_{f,k0}^{-1} > 1187 \end{cases} \tag{7.37}$$

where the Reynolds numbers are given by:

$$Re_{f,g0} = \frac{GD_h}{\mu_g} \quad \text{and} \quad Re_{f,w0} = \frac{GD_h}{\mu_w} \tag{7.38}$$

For quality below 0.7, the frictional pressure drop of Muller-Steinhagen and Heck is given by the following linear equation:

$$G_{MSH} = A_{MSH} + 2\left(B_{MSH} - A_{MSH}\right)x \tag{7.39}$$

To cover the full range of flow quality $0 \le x \le 1$, a superimposition of equations (7.35) and (7.39) is used:

$$\left(\frac{dp}{dx}\right)_F = G_{MSH}\left(1-x\right)^{1/C} + B_{MSH}x^C \tag{7.40}$$

A value of C=3 was found by curve fitting measured data.

To determine the reliability of the method, Müller-Steinhagen and Heck [227] assessed their correlation and 14 other correlations from literature against a data bank containing 9313 measurements of pressure gradient for different fluids, different pipe diameters, and different flow conditions. They reported accuracy similar to the more complicated methods.

For engineering applications, Keller [165] shows this method does not reach the same degree of accuracy than the Lockhart-Martinelli correlation when compared to measurement on scale model. Nevertheless, the approach is again useless with respect to the objective of this thesis. Neglecting the pipe roughness causes indeed important errors. Further research is required to integrate this effect within the Muller-Steinhager and Heck approach. In particular, an experimental research is clearly necessary.

7.3.5 INTERFACIAL FRICTION LAW

Among the different forces acting on the flow, the interfacial drag between both layers has a key role in the modeling of momentum transfer in a stratified flow. This term is usually written in the following form [165, 220]:

$$S_\Gamma = \rho_g f_\Gamma \frac{\left(u_g - \tilde{u}_m\right)^2}{2gD} \tag{7.41}$$

where f_Γ is the interfacial friction coefficient and D is the length characteristic of the two-phase flow. For further information about the methods to determine the values of these two parameters, I refer the interested reader to the specialized literature [154, 220].

7.4 CONSTITUTIVE EQUATIONS FOR THE DRIFT-VELOCITY

In the drift-flux framework, the area-averaged drift-velocity expresses the effects of the relative velocity between phases. It replaces the momentum equation for the dispersed phase. Appearing in both the diffusion and the momentum equations, its value still needs to be expressed under a functional form as follows:

$$\tilde{U}_{g,j} = \tilde{U}_{g,j}\left(\langle\alpha_g\rangle, \langle p_m\rangle, g_z, \tilde{u}_m, \ldots\right) \tag{7.42}$$

For this purpose, I analyze herein experimental data found in the literature and investigate constitutive equations proposed by other authors. At the end of this critical review, I choose to use two different constitutive equations for the drift-velocity. First, the homogenous assumption set the velocity to zero. It corresponds to a situation of equilibrium between both phases. Second, the Dix correlation provides acceptable results for horizontal and upward inclined pipes regardless of the flow regime.

By definition of the area-averaged drift velocity, I may relate it with mean values of the drift velocity and of the volumetric flux:

$$\tilde{U}_{gj} \triangleq \left\langle\left\langle u_g\right\rangle\right\rangle - \langle j\rangle = \left\langle \frac{\alpha_g\left(j + U_{gj}\right)}{\langle\alpha_g\rangle} - j \right\rangle = \left\langle\left\langle U_{gj}\right\rangle\right\rangle + \left(C_0 - 1\right)\langle j\rangle \tag{7.43}$$

where

$$\left\langle\left\langle U_{gj}\right\rangle\right\rangle = \frac{\left\langle\alpha_g U_{gj}\right\rangle}{\langle\alpha_g\rangle} \quad \text{and} \quad C_0 = \frac{\left\langle\alpha_g j\right\rangle}{\langle\alpha_g\rangle\langle j\rangle} = \mathrm{COV}\left(\frac{\left\langle\alpha_g j\right\rangle}{\langle\alpha_g\rangle}\right) \tag{7.44}$$

The factor C_0 is known as the distribution parameter [333, 334]. It is defined as the covariance between the concentration profile and the volumetric flux profile. Physically, it accounts for the non-uniformity of the velocity and void fraction profiles. This effect arises from the fact that the dispersed phase is locally transported with the drift velocity U_{gj} with respect to the local volumetric flux and not its area-averaged value $\langle j\rangle$.

To evaluate the area-averaged drift velocity, one must specify the distribution parameter C_0 and the area-average of the drift-velocity $\left\langle\left\langle U_{gj}\right\rangle\right\rangle$ by means of constitutive equations. Basic methodologies used to determine these parameters are described herein. A short review of correlations available in the literature is also given. Finally, I choose useful correlations for the rest of this thesis.

7.4.1 CORRELATION FOR THE DISTRIBUTION PARAMETER

Review of literature shows that C_0 depends on the pressure, the channel geometry, and perhaps the flow rate. It also shows that two different methods have been used to correlate the distribution parameter with other flow parameters: phenomenological models and completely empirical approaches.

The value of C_0 can be determined from phenomenological models such as the profiles of the void fraction α_g and the total volumetric flux j [153, 154, 333]. For instance, we may assume power-law profiles in a circular pipe for both α_g and j:

$$\frac{j}{j_0} = 1 - \left(\frac{r}{R_w}\right)^m \quad \text{and} \quad \frac{\alpha_g - \alpha_{gW}}{\alpha_{g0} - \alpha_{gW}} = 1 - \left(\frac{r}{R_w}\right)^n \tag{7.45}$$

where j_0, α_{g0}, α_{gW}, r and R_W are, respectively, the value of j and α at the center, the void fraction at the wall, radial distance, and the radius of the pipe. By introducing these profiles into equation (7.44) we obtain for the distribution parameter:

$$C_0 = 1 + \frac{2}{m+n+2}\left(1 - \frac{\alpha_{gw}}{\langle\alpha_g\rangle}\right) \tag{7.46}$$

This distribution parameter is further discussed in [334]. In this study, this method is used only if sufficient information on the flow behavior is available. Sadly, it is rarely the case.

Another method to specify the drift velocity is to develop an empirical correlation. Empirical methods are based on the plot of experimental data in a [phase gas velocity-volumetric flux] plane from which a functional correlation is derived. Equation (7.43) may indeed be transformed to:

$$\langle\langle u_g \rangle\rangle = \langle\langle U_{gj} \rangle\rangle + C_0 \langle j \rangle \tag{7.47}$$

This equation exhibits two important characteristics [61]. First, when C_0 and the area-averaged drift-velocity are constant, a linear relation exists between the phase gas velocity and the volumetric flux. The slope of the drawn line gives the value of the distribution parameter whereas the intercept of the curve with the y-axis gives the phase averaged drift-velocity. As a result, these two parameters can be easily determined from experiments even when the measured profiles required for the direct calculation are not available. The second important characteristic pertains to any abrupt measured changes in the value of the distribution parameter and the drift-velocity. These indicate a change of flow pattern in the conduct of the experiment.

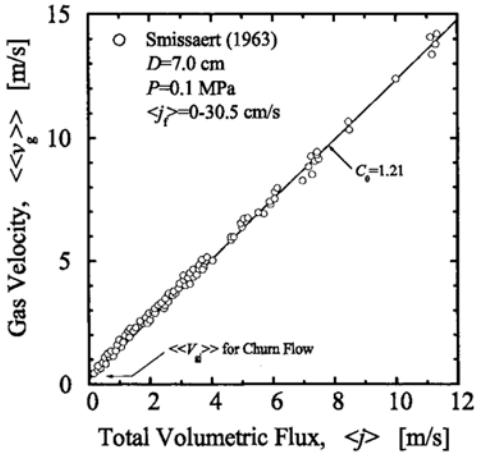

Figure 96: Example of fully developed air-water flow data [153] – data cluster around a straight line whose slope is the value of the distribution parameter C_0.

Specifying and commenting all the correlations for the distribution parameter available in the literature is way beyond the scope of this study. I have counted more than 30 equations. Accuracy of most of them has been compared in a plethora of comparative papers [82, 88, 320]. As a rough guide, most widespread correlations are given in Table 12. Correlations we have chosen to use in this study are summed up in section 7.4.3.

7.4.2 Phase Averaged Drift-velocity

The calculation of the phase averaged drift-velocity requires establishing the equilibrium of the forces acting on the gas phases and weighting the result by the void fraction distribution. For horizontal and near-horizontal flows, the drift-velocity is then usually related to the phase distribution and the local slip resulting from the lateral and axial pressure gradients. Since forces acting on the gas phase are not known precisely in many cases, the exact determination of the drift velocity is beyond our grasp. However, simplified models can be established by idealizing all the parameters. Correction factor are then added to accord with experimental data. For instance, Hibiki and Ishii [141] developed a correlation based on the equilibrium of a modified drag force and the gravity field.

The second methodology to establish the drift velocity is the empirical correlation of experimental data as exposed in the previous section for the distribution parameter. Again, more than 30 correlations are available and summarized in Table 11. Correlations we have chosen to use in this study are summed up in section 7.4.3.

7.4.3 Homogeneous and Dix Correlations

In the current work, we only use a few correlations and we choose between them according to the information available and/or the strength of the interaction between air and water. As long as sufficient information on the flow behavior is available, a phenomenological model can be established as proposed in the previous section. If we do not dispose of so much information, two empirical correlations can be used. The most simple correlation corresponds to the homogeneous assumption in which all phases are assumed to be in equilibrium in terms of velocity and pressure. It results in the following equalities:

$$\tilde{U}_{gj} = 0 \quad \leftrightarrow \quad \left\langle\left\langle U_{gj} \right\rangle\right\rangle = 0 \quad \text{and} \quad C_0 = 1 \tag{7.48}$$

The second correlation used is the Dix correlation [56]. As pointed in [320], this correlation is proven to give acceptable results for horizontal and upward inclined pipes regardless of the flow regime:

$$\left\langle\left\langle U_{gj} \right\rangle\right\rangle = 2.9\left(\frac{g\sigma\left(\rho_w - \rho_g\right)}{\rho_w^2} \right)^{1/4} \quad \text{and} \quad C_0 = \frac{j_g}{j}\left(1 + \left(\frac{j}{j_g} - 1 \right)^{\left(\frac{\rho_g}{\rho_w}\right)^{0.1}} \right) \tag{7.49}$$

where σ is the surface tension of the fluid against air (75 10^{-4} N/m).

Table 12: Expressions of the most widespread correlations for the distribution parameter and the drift velocity

Authors	Distribution parameter Correlation	Drift velocity correlation	Comments
Zuber and Findlay [333]	$C_0 = 1.2$	$\langle\langle U_{gj}\rangle\rangle = 1.53\left(\frac{g\sigma\Delta\rho}{\rho_w^2}\right)^{1/4}$	Adiabatic liquid-gas vertical flow for various two-phase flow regimes over a wide pressure range
Ishii [153]	$C_0 = \begin{cases} 1.2 - 0.2\sqrt{\rho_g/\rho_w}\left(1 - e^{-18\langle\alpha_g\rangle}\right); \text{ round tube} \\ 1.35 - 0.35\sqrt{\rho_g/\rho_w}\left(1 - e^{-18\langle\alpha_g\rangle}\right); \text{ rectangular channel} \end{cases}$	$\langle\langle U_{gj}\rangle\rangle = (C_0 - 1)\langle j\rangle + \sqrt{2}\left(\frac{g\sigma\Delta\rho}{\rho_w^2}\right)^{1/4}\frac{\rho_w - \rho_g}{\Delta\rho}$	Bubbly and Churn turbulent vertical flow
Ishii [153]	$C_0 = \frac{\left(1 - \langle\alpha_g\rangle\right)}{\langle\alpha_g\rangle + \sqrt{\left(\frac{1.75\left(1 - \langle\alpha_g\rangle\right)}{\sqrt{\langle\alpha_g\rangle}}\right)\left(\frac{\rho_g}{\rho_w}\right)}}$	$\langle\langle U_{gj}\rangle\rangle = (C_0 - 1)\left[\langle j\rangle + \sqrt{2\frac{gd_h\Delta\rho\left(1 - \langle\alpha_g\rangle\right)}{\rho_w}}\right]$	Annular vertical flow where the relative motions between phases are governed by the interfacial geometry, the body force field, and the interfacial momentum transfer
Sonnenburg [56]	$C_0 = 1\left(0.32 - 0.32\sqrt{\rho_g/\rho_w}\right)$	$\langle\langle U_{gj}\rangle\rangle = \frac{C_0(1 - C_0\alpha)}{C_0\alpha/\sqrt{gd_h\Delta\rho/\rho_g} + 1 - C_0\alpha/\sqrt{gd_h\Delta\rho/\rho_w}}$	Combination of flooding correlation [313] and Ishii correlation [153]
Toshiba [225]	$C_0 = 1.08$	$\langle\langle U_{gj}\rangle\rangle = 0.45$	Constant coefficient from BWR
Bestion [24]	$C_0 = 1$	$\langle\langle U_{gj}\rangle\rangle = 0.188\left(\frac{gd_h\Delta\rho}{\rho_g}\right)^{1/2}$	Developed for Cathare and includes a geometry dependent parameter
Chexal et al [56]	$C_0 = \frac{\left(1 - e^{-C_1\alpha}\right)/\left(1 - e^{-C_1}\right)}{K_0 + (1 - K_0)\alpha^{\frac{1 + 1.57\rho_g/\rho_w}{1 - B_1}}}$	$\langle\langle U_{gj}\rangle\rangle = 1.41\left(\frac{g\sigma\Delta\rho}{\rho_w^2}\right)^{1/4} C_2C_3C_4C_9$	Based on Zuber-Findlay, cover full range of pressures, mass fluxes and void fraction
Inoue et al [56]	$C_0 = 6.76\,10^{-3}p + 1.026$	$\langle\langle U_{gj}\rangle\rangle = \left(5.1\,10^{-3}W - 6.91\,10^{-2}\right) * \left(9.42\,10^{-2}p^2 - 1.99p + 12.6\right)$	Based on Zuber-Findlay correlation
Maier and Coddington [56]	$C_0 = 2.57\,10^{-3}p + 1.0062$	$\langle\langle U_{gj}\rangle\rangle = \left(6.73\,10^{-7}p^2 - 8.81\,10^{-5}p + 1.05\,10^{-3}\right)G + \left(5.63\,10^{-3}p^2 - 1.23\,10^{-1}p + 0.8\right)$	Statistical correlation based on main databases available in 1997

Summary and conclusion

In this chapter, the general free surface drift flux model has been particularized for describing air-water mixed flows. The model includes two layers and three phases: a water phase, an air phase dispersed within water, and pure air above the free surface. On the one hand, three partial differential equations describe the motion in the lower layer. By complementing the hydrostatic pressure term with an original uniform contribution that takes into account the presence of air, applicability of these three equations has been extended to pressurized flows. On the other hand, two partial differential equations account for the pure air flow in the upper layer. In particular, the pressure is linked to the density by an equation of state. In order to close the model, I reviewed and chose various constitutive equations for the drift-velocity and the friction within each flow.

In conclusion, I proposed in this chapter an original and useful mathematical model for describing transient air-water flows in pipes. The model is original because it relies on a multiphase theory that has never been applied in civil and environmental engineering. It is also said useful because it meets the objective of this thesis in many respects. First, it accounts for the multiphase character of the flow. Second, it handles with transient features. Third, it accounts for scale heterogeneities in time and space by using state-of-the-art methods in averaging. Fourth, it unifies the description of pressurized and free surface flows. Applying this model in civil and environmental engineering would provide many benefits. Notably, high fidelity prediction would decrease the cost of hydraulic structures and improve their security. Because of the one-dimensional approach, the additional cost in computation effort remains very limited.

Since an analytical solution of this model is not available without important simplifications, application on real cases must make use of a discretised form of the equations. This is the topic of the next chapter. In this respect, particular attention is paid to let the computation affordable for classical computers.

Chapter 8 Multiphase Flows: Numerical Model

This chapter aims at:

- ✓ analyzing the mathematical properties of the model for air-water mixed flows;
- ✓ deriving a suitable discretization of the equations;
- ✓ proving the stability of the discretised equations;
- ✓ implementing the scheme into a computational code (called WOLF IMPack).

By application of the theory of multiphase flows, I derived in this thesis a general multi-layer drift-flux model for free surface flows (Chapter 6). Afterwards, I particularized this model for air-water flows in channels and closed conduits (Chapter 7). This simplification gave the following system of five PDE's:

$$\begin{cases} \dfrac{\partial \langle \rho_m \rangle \Omega}{\partial t} + \dfrac{\partial \langle \rho_m \rangle \tilde{u}_m \Omega}{\partial x} = q_{m,\perp} \\ \dfrac{\partial \langle \alpha_d \rangle \Omega}{\partial t} + \dfrac{\partial}{\partial x}\left(\langle \alpha_d \rangle \tilde{u}_m \Omega + \langle \alpha_d \rangle \dfrac{\rho_w}{\langle \rho_m \rangle} \tilde{U}_{dj} \Omega \right) = \left\langle \Gamma_d \middle/ \rho_d \right\rangle \Omega + q_{\alpha,\perp} \\ \dfrac{\partial \langle \rho_m \rangle \tilde{u}_m \Omega}{\partial t} + \dfrac{\partial \langle \rho_m \rangle \tilde{u}_m \tilde{u}_m \Omega}{\partial x} + \dfrac{\partial}{\partial x}\left(\dfrac{\langle \alpha_d \rangle}{1 - \langle \alpha_d \rangle} \dfrac{\rho_d \rho_w}{\langle \rho_m \rangle} \tilde{U}_{dj} \tilde{U}_{dj} \Omega \right) + g \dfrac{\partial P_\Omega}{\partial x} \\ \qquad = -\langle \rho_m \rangle g \Omega \left(S_F + \dfrac{\partial z_b}{\partial x} \right) - \dfrac{\partial p_\Gamma}{\partial x} \Omega + g P_{G,\partial\Omega} - S_\Gamma + \theta \langle \rho_m \rangle \dfrac{q_{m,\perp}^2}{\Omega} \\ \dfrac{\partial \rho_g \Omega_g}{\partial t} + \dfrac{\partial \rho_g \langle\langle u_g \rangle\rangle \Omega_g}{\partial x} = q_{g,\perp} \\ \dfrac{\partial \rho_g \langle\langle u_g \rangle\rangle \Omega_g}{\partial t} + \dfrac{\partial \rho_g \langle\langle u_g \rangle\rangle \langle\langle u_g \rangle\rangle \Omega_g}{\partial x} + a_a^2 \Omega_g \dfrac{\partial \rho_g}{\partial x} = -\rho_g g \Omega_g S_g + S_\Gamma + \theta \rho_g \dfrac{q_{g,\perp}^2}{\Omega_g} \end{cases} \tag{8.1}$$

In order to make this model suitable for numerical evaluation, it is necessary to discretize the equations and to implement them under the form of algorithms. Coupling these solvers with discretised data gives birth to a computational code. Since the discretization and implementation of equations are crucial in many respects, I devote this chapter to the creation of an efficient algorithm for solving model (8.1). First, I identify the mathematical properties of the system by means of both linear and non-linear analyses (section 8.1). Second, the form of the wave structure enables to apply the WOLF strategy and to prove its stability (section 8.2). Third, I implement discretised equations in a new academic code called WOLF IMPack, which stands for Integrated Multi-Phase Pack (section 8.3). Written in Fortran, this algorithm constitutes an efficient computational code for designing hydraulic structures and making impact studies.

8.1 MATHEMATICAL PROPERTIES

Investigating the fundamental mathematical properties of a system of PDE's is a prerequisite prior any numerical discretization. Numerical methods are indeed strongly linked to both the physical and mathematical properties of the equations. It is therefore justified to devote some efforts to identify the various aspects of the equations that seem essential to keep in their numerical solution.

For this purpose, I perform herein both linear and non-linear analyses of the original model (8.1) describing transient air-water flows. The eigenstructure of the problem gives insight into the propagation of information within the flow. In particular, it makes appear two flow regimes in both layers: sub- and super-sonic (upper layer); sub- and super-critical (lower layer). I also show that non-conservative terms make the model non-hyperbolic. Hyperbolicity is found back only by neglecting the lateral pressure terms. Next, boundary conditions are identified in accordance with the results of the linear analysis. Finally, non-linear analysis gives the structure of the solution in terms of shocks, rarefactions, and contact discontinuities.

8.1.1 LINEAR ANALYSIS

The linear analysis of a system of partial differential equations requires transforming the problem in its quasi-linear form as well as identifying the eigenvalues and the eigenvectors of the quasi-linear matrix. By definition, the quasi-linear form of a system is given under the following generic formulation:

$$\frac{\partial \mathbf{U}}{\partial t} + \mathbf{A}(\mathbf{U})\frac{\partial \mathbf{U}}{\partial x} = \mathbf{RHS} \tag{8.2}$$

where **U** is the vector of the conserved variables, **A(U)** is the Jacobian matrix of the flux function, and **RHS** conflates all the source terms. The elements of the Jacobian matrix are the derivatives of the flux vector **F(U)** with respect to the conserved variables.

In view of these notations, the following vector gives the conservative unknowns of the model (8.1) describing air-water mixed flows:

$$\mathbf{U} = \begin{pmatrix} u_1 \\ u_2 \\ u_3 \\ u_4 \\ u_5 \end{pmatrix} = \begin{pmatrix} \langle \rho_m \rangle \Omega \\ \langle \alpha_d \rangle \Omega \\ \langle \rho_m \rangle \tilde{u}_m \Omega \\ p_\Gamma (\Omega_{max} - \Omega) / a_a^2 \\ p_\Gamma \langle \langle u_g \rangle \rangle (\Omega_{max} - \Omega) / a_a^2 \end{pmatrix} \tag{8.3}$$

where the pure air density ρ_g is replaced by the pressure p_Γ thanks to the equation of state for pure air. The drift velocity is approximated by the Homogeneous or Dix correlations, which do not depend on primitive unknowns. Consequently, diffusion terms can be considered as source terms. Source terms also include all the terms linked to the lateral discharge, to the friction, and to the topographic slope. Since it does not affect the celerity

of the model, lateral pressure term $gP_{\partial\Omega}$ is also included in the source term. All other terms are part of the fluxes. A preliminary step to the derivation of the Jacobian matrix consists in expressing all the flux terms under the form of functions of the conservative unknowns. For this purpose, I use the following relations for the section and the pressure:

$$\begin{cases} \Omega = \dfrac{u_1 + u_2\left(\rho_w - \rho_d\right)}{\rho_w} \\ \Omega_g = \dfrac{\rho_w \Omega_{max} - u_1 - u_2\left(\rho_w - \rho_d\right)}{\rho_w} \\ p_\Gamma = \dfrac{a_a^2 u_4}{\Omega_g} = \dfrac{\rho_w a_a^2 u_4}{\rho_w \Omega_{max} - u_1 - u_2\left(\rho_w - \rho_d\right)} \\ p_\Gamma \Omega = \dfrac{a_a^2 u_4 \left(u_1 + u_2\left(\rho_w - \rho_d\right)\right)}{\rho_w \Omega_{max} - u_1 - u_2\left(\rho_w - \rho_d\right)} \end{cases} \tag{8.4}$$

These relations result from simple algebraic manipulations. At the end of the day, the Jacobian matrix of model (8.1) has the following form:

$$\mathbf{A}(\mathbf{U}) = \begin{bmatrix} 0 & 0 & 1 & 0 & 0 \\ -\dfrac{u_2 u_3}{(u_1)^2} & \dfrac{u_3}{u_1} & \dfrac{u_2}{u_1} & 0 & 0 \\ c^2 - \left(\dfrac{u_3}{u_1}\right)^2 + \dfrac{a_a^2 u_4 \Omega}{\rho_w \Omega_g^2} & \dfrac{\left(\rho_w - \rho_d\right) a_a^2 u_4 \Omega}{\rho_w \Omega_g^2} & \dfrac{2u_3}{u_1} & a_a^2 \dfrac{\Omega}{\Omega_g} & 0 \\ 0 & 0 & 0 & 0 & 1 \\ \dfrac{a^2 u_4}{\rho_w \Omega_g} & \dfrac{\left(\rho_w - \rho_d\right) a_a^2 u_4}{\rho_w \Omega_g} & 0 & a_a^2 - \left(\dfrac{u_5}{u_4}\right)^2 & \dfrac{2u_5}{u_4} \end{bmatrix} \tag{8.5}$$

where c is the celerity, and a_a is the sound celerity in pure air.

A system of partial differential equations like (8.1) is said hyperbolic as long as the Jacobian matrix admits real eigenvalues and a corresponding set of linearly independent right eigenvectors [286]. Hyperbolic problems admit wave-like solutions. In the linear theory, the eigenvalues λ_i of the matrix **A** are the velocities of the waves propagating within the flow. These waves transport physical quantities along the domain. Both the domain of dependence and zone of influence of a given point are limited to its close neighborhood. It enables determining asymmetric physical boundary conditions. When one or more of the eigenvalues are equal (and does not correspond to linearly independent eigenvectors), the system is said parabolic. It means that several waves have the same velocity. The problem admits damped waves as solutions. For a strictly parabolic problem, the region of dependence reduces to a segment in the phase space, while the zone of influence is the whole region limited by the characteristic. Finally, the problem is elliptic when eigenvalues become complex (negative radicand). In this case, the problem does not admit wave-like solutions. The behavior of the flow is dominated by diffusion phenomena. The region of dependence and the zone of influence consist in the whole computational domain. The nature of the problem (hyperbolic, parabolic, or elliptic) has a significant impact on the type of boundary conditions required and on the choice of the numerical scheme.

The eigenvalues of the Jacobian matrix are solutions of the characteristic polynomial:

$$\left|\mathbf{A}-\lambda\mathbf{I}\right|=0 \tag{8.6}$$

Expanding this determinant for the Jacobian matrix (8.5) gives the following 5th order algebraic equation:

$$\begin{cases}\lambda-\tilde{u}_m=0\\ \left[\lambda^2-2\tilde{u}_m\lambda-\left(c^2-\tilde{u}_m^2+a_a^2\frac{\rho_g}{\rho_w}\frac{\Omega}{\Omega_g}\right)\right]*\left[\lambda^2-2\left\langle\left\langle u_g\right\rangle\right\rangle\lambda-\left(a_a^2-\left\langle\left\langle u_g\right\rangle\right\rangle^2\right)\right]=a_a^4\frac{\rho_g}{\rho_w}\frac{\Omega}{\Omega_g}\end{cases} \tag{8.7}$$

Obviously, the first eigenvalue is the area-averaged mixture velocity. It means that the wave associated to this eigenvalue propagates at the velocity of the mixture fluid in the lower layer. It is a standard result of transport phenomena. The quantity transported by this wave is the concentration in dispersed phase. It is easily demonstrated by setting the model (8.2) under its characteristic form. Nevertheless, the second equation does not have any analytical solution such that we cannot identify the four other eigenvalues. It prevents us from identifying the direction of propagation of the information. I bypass this problem by searching approximate formulations for the eigenvalues. This tactic gives indeed some insight into the wave-like solution.

APPROXIMATE SOLUTION: EQUAL VELOCITIES IN BOTH LAYERS

When the fluid velocities in each layer are equal or even close $\tilde{u}_m=\left\langle u_g\right\rangle=u$, the solution of the polynomial (8.7) gives the four distinct eigenvalues:

$$\lambda=u\pm\sqrt{\frac{1}{2}\underbrace{\left(c^2+a_a^2(1-\varepsilon)\right)}_{+}\pm\sqrt{\underbrace{\left(c^2-2u+a_a^2(1-\varepsilon)\right)^2}_{+}-4\left(a_a^2-u^2\right)\left(c^2-u^2+a_a^2\varepsilon\right)+4a_a^4\varepsilon}_{+/-}} \tag{8.8}$$

with $\varepsilon=\frac{\rho_g}{\rho_m}\frac{\Omega}{\Omega_g}<1$

Depending on the value of the velocity u, the radicands of equation (8.8) can be either positive or negative. In the first case, the Jacobian matrix has five real eigenvalues and a corresponding set of five linearly independent right eigenvectors. By definition [286], the system is hyperbolic and admits wave-like solutions. Sadly, it is difficult to retrieve more information about the structure of the solution in such a complex formulation. In the second case, eigenvalues are complex since the radicand is negative. This makes the system (8.5) non-hyperbolic (elliptic and/or parabolic). From a physical point of view, the homogeneous part of the model does not admit anymore wave-like solutions [144, 145]. This lost of hyperbolicity is a classical problem in multi-layer models [15-18, 28].

Theoretically, classical explicit numerical schemes are unable to solve such non-hyperbolic models for two reasons. First, information propagates at non-finite velocity in the domain. It makes explicit time integration schemes unfit for solving unsteady flows. Second, the system cannot be decoupled in independent advection equations. Schemes based on such decomposition fails, like the Roe solver.

From a practical point of view, numerical schemes initially developed for hyperbolic problems have however reached some success when applied to non-hyperbolic problems. Indeed, many elliptic problems include both a hyperbolic part and an elliptic part. To put in other words, the ellipticity of the problem comes from a very small number of terms in the equations (one or two). When neglecting these terms, the problem is hyperbolic and admits a wave-like solution. A numerical scheme can be established for this simplified model. Next, its applicability is extended to the full elliptic problem. Practice shows that this method works in some cases. This success results from the fact that non-hyperbolic terms are diffusive terms. If their celerity is infinite, their intensity diminishes rapidly with time until it can be neglected. If this time is sufficiently small, the behavior of the solution is analogous to a hyperbolic solution. For this reason, I identify and analyze in the next section the hyperbolic part of model (8.1) in order to have sufficient information for applying the Wolf splitting.

APPROXIMATE SOLUTION: LATERAL PRESSURE TERM NEGLECTED

Several authors describe the lost of hyperbolicity in multi-layer models [15-18, 28, 92]. They also underline that expressing the upper layer equations in their conservative form makes the problem hyperbolic again. In the drift-flux model (8.1) for air-water mixed flows, the only non-conservative term that causes problems is the pressure term in the upper layer. For setting the model in its conservative form, I apply the product rule of derivation and neglect the lateral pressure term in the derivation of the Jacobian matrix:

$$\frac{\partial p_\Gamma}{\partial x}\Omega_g = \frac{\partial p_\Gamma \Omega_g}{\partial x} - \cancel{p_\Gamma \frac{\partial \Omega_g}{\partial x}} \tag{8.9}$$

Physically, this assumption consists in neglecting the effect of cross-section variations on the pressure gradient within the fluid, at least in the derivation of the Jacobian matrix. Under this hypothesis, the Jacobian matrix becomes:

$$\mathbf{A}(\mathbf{U}) = \begin{bmatrix} 0 & 0 & 1 & 0 & 0 \\ -\frac{u_2 u_3}{(u_1)^2} & \frac{u_3}{u_1} & \frac{u_2}{u_1} & 0 & 0 \\ c^2 - \left(\frac{u_3}{u_1}\right)^2 + \frac{a_a^2 u_4 \Omega}{\rho_w \Omega_g^2} & \frac{(\rho_w - \rho_d) a_a^2 u_4 \Omega}{\rho_w \Omega_g^2} & \frac{2u_3}{u_1} & a_a^2 \frac{\Omega}{\Omega_g} & 0 \\ 0 & 0 & 0 & 0 & 1 \\ 0 & 0 & 0 & a_a^2 - \left(\frac{u_5}{u_4}\right)^2 & \frac{2u_5}{u_4} \end{bmatrix} \tag{8.10}$$

Determinant of this matrix gives the same result than equation (8.7), except that the term on the right-hand side cancels. Obviously, the first eigenvalue is still the mixture velocity, while other eigenvalues are determined by solving the following polynomials:

$$\begin{cases} \lambda - \tilde{u}_m = 0 \\ \lambda^2 - 2\tilde{u}_m \lambda - \left(c^2 - \tilde{u}_m^2 + a_a^2 \varepsilon\right) = 0 \\ \lambda^2 - 2\langle\langle u_g \rangle\rangle \lambda - \left(a_a^2 - \langle\langle u_g \rangle\rangle^2\right) = 0 \end{cases} \tag{8.11}$$

These simplified polynomials are easy to solve. It defines five real celerities:

$$\begin{cases} \lambda_1 = \tilde{u}_m \\ \lambda_2 = \tilde{u}_m - \sqrt{c^2 + a_a^2 \varepsilon} \\ \lambda_3 = \tilde{u}_m + \sqrt{c^2 + a_a^2 \varepsilon} \\ \lambda_4 = \left\langle \left\langle u_g \right\rangle \right\rangle + a_a \\ \lambda_5 = \left\langle \left\langle u_g \right\rangle \right\rangle - a_a \end{cases} \tag{8.12}$$

Since five linearly independent right eigenvectors correspond to these eigenvalues, the system is clearly hyperbolic. The information propagates at a finite speed within the computational domain. Each of these waves transports a certain amount of information.

The values of the eigenvalues give interesting insight into the model. The first eigenvalue is the mixture velocity. As already underlined, this celerity is linked with the propagation of the concentration in dispersed air. The fourth and fifth eigenvalues have a classical form of single-phase flow. It is the velocity plus or minus the sound speed. They are related with the propagation of aerodynamic information in the upper layer. Finally, the second and third eigenvalues seem similar to the ones of the Saint-Venant equations (chapter 4). Nevertheless, this similarity is only apparent. First, the velocity in (8.12) refers to the mixture fluid, not the water. Second, the pressure wave celerity "c" is corrected by a portion ε of the sound speed "a_a". From a physical point of view, it means that the pressurization of the upper layer has an impact on the velocity of the pressure wave within the mixture flow. In other words, information of pressure in the lower-layer propagates faster than in absence of upper-layer. This result accords with empirical observation: pressurization of entrapped air creates small waves at the free surface of a water flow. Third, eigenvalues λ_2 and λ_3 tends to the infinity when the upper-layer is vanishing (its section Ω_g tends to zero). It is a classical case of dry bed, for which a special numerical treatment is required.

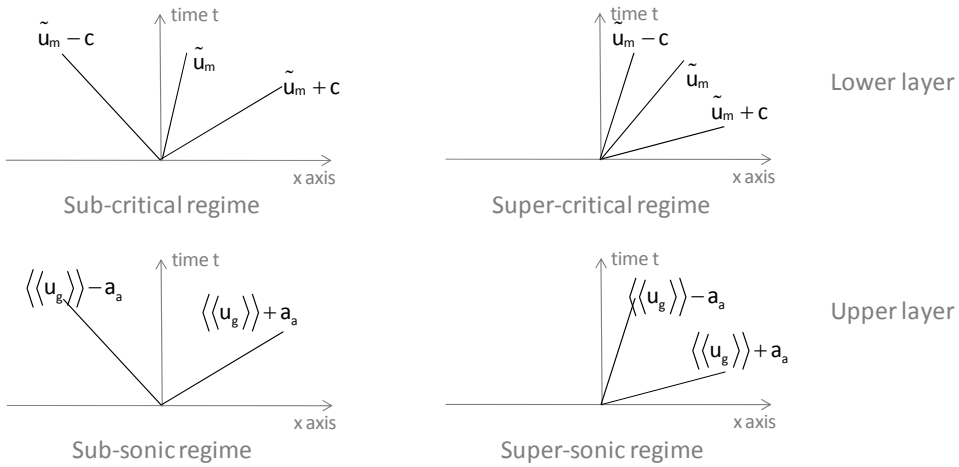

Figure 97: The signs of the eigenvalues define four flow regimes: sub- and super-critical (lower layer); sub- and super-sonic (upper layer)

The signs of the eigenvalues determine four flow regimes (Figure 97). In the lower layer, a super-critical flow regime occurs when eigenvalues λ_1, λ_2, and λ_3 have the same sign (the sign of the mixture velocity). The information propagates only downstream. On the opposite, the information propagates both upstream and downstream when the second eigenvalue has a sign opposite to the mixture velocity:

$$\left|\tilde{u}_m\right| \le \sqrt{c^2 + a_a^2 \frac{\rho_g}{\rho_m} \frac{\Omega}{\Omega_g}} \tag{8.13}$$

This is the sub-critical regime. In the upper layer, a super-sonic regime arises if both eigenvalues have the same sign (the sign of the air velocity). The information in the pure air propagates only downstream. On the opposite, a sub-sonic regime is observed when the fifth eigenvalue has a sign opposite to the air velocity:

$$\left|\left\langle\left\langle u_g \right\rangle\right\rangle\right| \le \left|a_a\right| \tag{8.14}$$

Like in single-phase flows, I use two non-dimensional numbers for distinguishing the flow regimes, namely the Froude number Fr and the Mach number M:

$$Fr = \frac{\tilde{u}_m}{\sqrt{c^2 + a_a^2 \frac{\rho_g}{\rho_m} \frac{\Omega}{\Omega_g}}} \qquad \text{and} \qquad M = \frac{\left\langle\left\langle u_g \right\rangle\right\rangle}{a_a^2} \tag{8.15}$$

On the one hand, sub-critical regimes correspond to a Froude number below one, while the super-critical regime arises for Froude number greater than one. On the other hand, sub-sonic regimes correspond to a Mach number below one.

APPROXIMATE SOLUTION: PRESSURIZED FLOW

In a pressurized flow, the upper-layer cancels. Only three equations describing the mixture flow remains in the model. This case is important since it will appear frequently in the simulations. The Jacobian matrix for this reduced model is:

$$\mathbf{A}(\mathbf{U}) = \begin{bmatrix} 0 & 0 & 1 \\ -\dfrac{u_2 u_3}{(u_1)^2} & \dfrac{u_3}{u_1} & \dfrac{u_2}{u_1} \\ c^2 - (u_3/u_1)^2 & 0 & 2u_3/u_1 \end{bmatrix} \tag{8.16}$$

Solving the determinant of the Jacobian matrix gives the three distinct eigenvalues:

$$\lambda_1 = \tilde{u}_m, \quad \lambda_2 = \tilde{u}_m - c, \quad \text{and} \quad \lambda_3 = \tilde{u}_m + c \tag{8.17}$$

Since all eigenvalues are different and real, the system is hyperbolic. The celerity c is the pressure wave velocity in a pipe. Its value depends on the fluid compressibility, on the pipe strength, and on the concentration in dispersed air. In any case, its value is always greater than the velocity. Consequently, only sub-critical regimes occur in pressurized flows. Waves propagate both upstream and downstream. The first eigenvalue is still linked to the transport of the dispersed phase, while the second and third velocity are linked with the mixture flow.

8.1.2 BOUNDARY CONDITIONS

As already mentioned in Chapter 4, the imposition of boundary conditions is a crucial step in any differential problem. A system of partial differential equations may only be solved if it is supplemented by an adequate set of boundary and initial conditions. In the case of hyperbolic systems, boundary conditions must be prescribed in the same number as the number of characteristics entering the computational domain at the considered boundary [144]. In order to determine this number, I use the eigenvalues (8.12) obtained for the conservative form of the two-layer air-water model.

Table 1 summarizes the number and type of BC prescribed at a liquid boundary. The suggested nature of BC corresponds to the most usual choice. Depending on the flow regime, I impose the mixture discharge, the concentration in dispersed air, and the flow section at either the upstream or the downstream boundary of the lower layer. In an analogous way, I impose the pure air discharge and the pressure at the boundaries of the upper layer.

Table 13: Number and nature of the boundary conditions to impose at the boundaries of the domain

	Type of boundary and regime		Number of BC	Nature of BC
Lower layer	Inflow ($\tilde{u}_m < 0$)	$\tilde{u}_m \le \sqrt{c^2 + a_a^2 \rho_g \Omega / (\rho_m \Omega_g)}$	2	$Q_m ; \langle \alpha_d \rangle$
		$\tilde{u}_m > \sqrt{c^2 + a_a^2 \rho_g \Omega / (\rho_m \Omega_g)}$	3	$Q_m ; \langle \alpha_d \rangle ; \Omega$
	Outflow ($\tilde{u}_m > 0$)	$\tilde{u}_m \le \sqrt{c^2 + a_a^2 \rho_g \Omega / (\rho_m \Omega_g)}$	1	Ω
		$\tilde{u}_m > \sqrt{c^2 + a_a^2 \rho_g \Omega / (\rho_m \Omega_g)}$	0	-
Upper layer	Inflow ($\langle u_g \rangle < 0$)	$\langle \langle u_g \rangle \rangle > a_a^2$	2	$Q_g ; p_\Gamma$
		$\langle \langle u_g \rangle \rangle \le a_a^2$	1	Q_g
	Outflow ($\langle u_g \rangle > 0$)	$\langle \langle u_g \rangle \rangle > a_a^2$	0	-
		$\langle \langle u_g \rangle \rangle \le a_a^2$	1	p_Γ

8.1.3 NON LINEAR ANALYSIS: SOLUTION TO THE RIEMANN PROBLEM

Contrary to what the linear theory states, the solution of a non-linear hyperbolic system like the two-layer air-water model does not simply include waves translating uniformly. Instead, conservative laws are known to develop discontinuous solutions even with smooth initial conditions [197]. In particular, it gives birth to shock waves across which the solution is discontinuous. In order to include such discontinuous solutions into the class of admissible solution of the problem, using the integral form of PDE's is necessary. Hopefully, the finite volume method makes uses of these integral equations (see Chapter 2).

Determining the structure of the non-linear problem is equivalent to solving the associated Riemann problem. For the homogeneous two-layer air-water model, this problem is given by the following system of PDE's (where the source terms have been set to zero):

$$\frac{\partial}{\partial t}\begin{bmatrix} \langle \rho_m \rangle \Omega \\ \langle \alpha_d \rangle \Omega \\ \langle \rho_m \rangle \tilde{u}_m \Omega \\ \rho_g \Omega_g \\ \rho_g \langle\langle u_g \rangle\rangle \Omega_g \end{bmatrix} + \frac{\partial}{\partial x}\begin{bmatrix} \langle \rho_m \rangle \tilde{u}_m \Omega \\ \langle \alpha_d \rangle \tilde{u}_m \Omega \\ \langle \rho_m \rangle \tilde{u}_m \tilde{u}_m \Omega + g P_\Omega + p_I \Omega \\ \rho_g \langle\langle u_g \rangle\rangle \Omega_g \\ \rho_g \langle\langle u_g \rangle\rangle \langle\langle u_g \rangle\rangle \Omega_g + p_I \Omega_g \end{bmatrix} = \begin{bmatrix} 0 \\ 0 \\ 0 \\ 0 \\ 0 \end{bmatrix} \tag{8.18}$$

Piecewise constant initial data complement the model:

$$\mathbf{U}(x) = \begin{cases} \mathbf{U}_L & \text{if } x<0 \\ \mathbf{U}_R & \text{if } x>0 \end{cases} \tag{8.19}$$

The subscripts L and R denote the left and right states.

The Riemann problem can be solved exactly and the solution is represented in the phase plane x-t. In the lower layer, this solution consists in three waves that can be either shocks, rarefactions, and contact discontinuities. It results in four possible wave patterns (Figure 98): shock-contact-shock, shock-contact-rarefaction, rarefaction-contact-rarefaction, and rarefaction-contact-shock. In the upper layer, the solution has also four different possible wave patterns (Figure 99): shock-shock, shock-rarefaction, rarefaction-rarefaction, and rarefaction-shock.

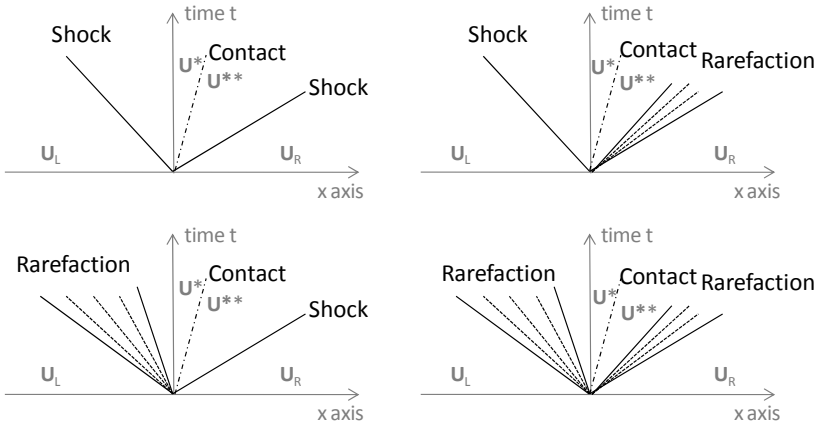

Figure 98: In the lower layer, the solution of the Riemann problem has four different possible wave patterns

Velocity of a shock differs from the associated eigenvalue. Indeed, the velocity of a shock is the solution of the Rankine-Hugoniot relations (Chapter 2). These relations also give the value of the unknown **U*** as a function of the left and right states. For a rarefaction, the velocity of both tails is given by the associated eigenvalue computed with the value of the primitive unknowns at each side of the rarefaction. The unknown **U*** is computed by means of the generalized Riemann invariants. Finally, the velocity of the contact discontinuity is the associated eigenvalue. The unknown **U*** is solution of both the Rankine-Hugoniot relations and the generalized Riemann invariant.

Since I do not intend to create an exact Riemann solver here, I do not present the solutions of both the Rankine-Hugoniot relations and the Generalized Riemann Invariants. Indeed, it does not provide any further information that is necessary to apply the Wolf splitting to the original model.

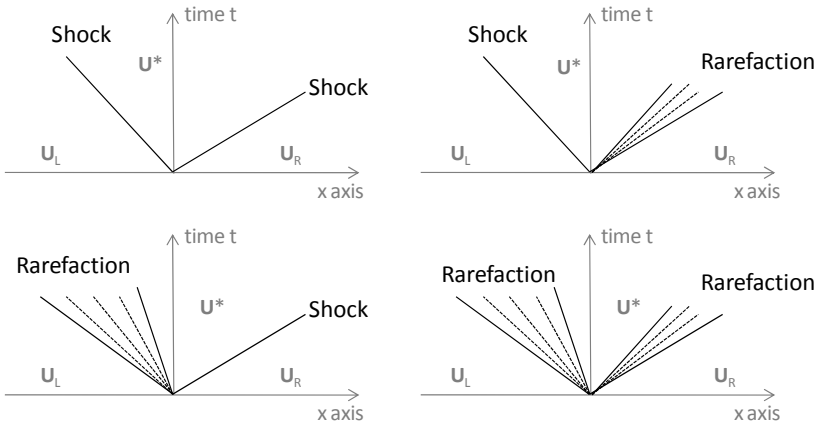

Figure 99: In the lower layer, the solution of the Riemann problem has four different possible wave patterns

8.2 DISCRETISED FORM OF THE EQUATIONS

The linear and non-linear analyses of the mathematical model (8.1) underline a specific structure for the propagation of the waves in the flow. In the lower layer, the information in concentration propagates at the mixture velocity $\tilde{u}_m$, and the hydrodynamic information propagates at two different velocities $\lambda_2 = \tilde{u}_m - \sqrt{c^2 + a_a^2 \varepsilon}$ and $\lambda_3 = \tilde{u}_m + \sqrt{c^2 + a_a^2 \varepsilon}$. According to the sign of these celerities, a sub- or a super-critical regime appears. In the upper layer, the aerodynamic information propagates at two different velocities $\lambda_4 = \langle\langle u_g \rangle\rangle + a_a$ and $\lambda_5 = \langle\langle u_g \rangle\rangle - a_a$. According to the sign of these celerities, we observe a sub- or a super-sonic regime. In both layers, the analogy with the structure of waves in free surface pure water flows is obvious.

Based on these results, the discretization with the Wolf splitting is possible. Indeed, this splitting was deemed the best choice for single-phase mixed flows (Chapter 4). What is more, the discretization relies on a simple upwinding whose application is straightforward in a model presenting the same typical wave structure as model (8.1). Discretization results in five algebraic equations that are time-integrated with a Runge-Kutta scheme. What is more, a Von Neumann stability analysis proves the stability of the scheme.

8.2.1 DISCRETIZATION: WOLF FLUX VECTOR SPLITTING

As shown in Chapter 4, the Wolf flux vector splitting was originally developed for free surface flows [9, 75, 93]. It distinguishes two parts in the equations: the convective and the pressure contributions. According to the sign of the fluid velocity, convective terms are always up-winded and the pressure terms down-winded. The scheme presents various advantages and drawbacks that I mentioned in Chapter 4. By comparison with four other solvers, I showed that this solver was the best compromise between a good treatment of the convective part (necessary to treat shocks and discontinuities) and a correct integration of source terms (which are of utmost importance in civil and environmental engineering). Its simplicity is clearly a major advantage, especially in a system of five PDE's like here.

For the mixture continuity equation in the lower-layer, the discretization gives:

$$\mu_i^{n+1} = \mu_i^n - \frac{\Delta t}{\Delta x}\left[Q^n_{i+1/2} - Q^n_{i-1/2} \right] + \Delta t\, q_{m,\perp}\Big|_i^n \tag{8.20}$$

where n is the time index, i the spatial index, the conservative parameters μ and Q are given by:

$$\mu = \langle \rho_m \rangle \Omega \quad \text{and} \quad Q = \langle \rho_m \rangle \tilde{u}_m \Omega \tag{8.21}$$

Since the discharge Q is a convective term, its value at the boundary i+1/2 is given by the following splitting:

$$Q^n_{i+1/2} = \begin{cases} Q^n_L & \text{if} \quad \tilde{u}_{mL} > 0 \quad \text{and} \quad \tilde{u}_{mR} > 0 \\ Q^n_R & \text{if} \quad \tilde{u}_{mL} < 0 \quad \text{and} \quad \tilde{u}_{mR} < 0 \\ \left(Q^n_L + Q^n_R\right)/2 & \text{otherwise} \end{cases} \tag{8.22}$$

The subscripts L and R designate the left and right reconstructed values (Figure 100). Reconstruction can be either constant, linear,…

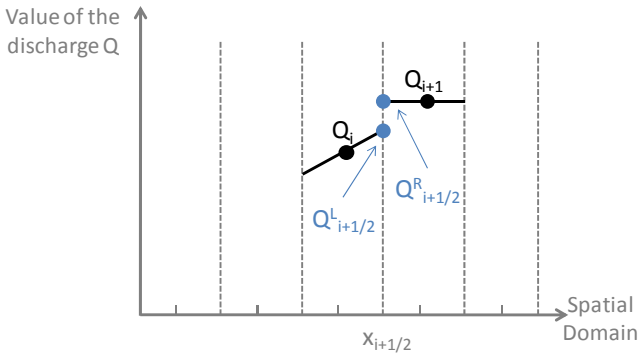

Figure 100: Wolf Flux vector splitting uses the left or the right reconstructed value to compute the numerical flux.

The diffusion equation is also a continuity equation, but for the dispersed phase. Its discretised form can be written as:

$$\Psi_i^{n+1} = \Psi_i^n - \frac{\Delta t}{\Delta x}\left[Q_{\alpha_{i+1/2}}^{\ n} - Q_{\alpha_{i-1/2}}^{\ n} \right] + \Delta t \left(q_{\alpha,L} - \langle \alpha_d \rangle \frac{\rho_w}{\langle \rho_m \rangle} \tilde{U}_{dj} \Omega \right)\Bigg|_i^n \tag{8.23}$$

where the parameters Ψ and Q_α are given by:

$$\Psi = \langle \alpha_d \rangle \Omega \quad \text{and} \quad Q_\alpha = \langle \alpha_d \rangle \tilde{u}_m \Omega \tag{8.24}$$

The flux in concentration is a convective term. Its value is consequently up-winded:

$$Q_{\alpha_{i+1/2}}^{\ n} = \begin{cases} Q_{\alpha L}^{\ n} & \text{if} \quad \tilde{u}_{mL} > 0 \quad \text{and} \quad \tilde{u}_{mR} > 0 \\ Q_{\alpha R}^{\ n} & \text{if} \quad \tilde{u}_{mL} < 0 \quad \text{and} \quad \tilde{u}_{mR} < 0 \\ \left(Q_{\alpha L}^{\ n} + Q_{\alpha R}^{\ n}\right)/2 & \text{otherwise} \end{cases} \tag{8.25}$$

For the momentum equation in the lower layer, the discretised equation is written as

$$\begin{aligned} Q_i^{n+1} = Q_i^n - \frac{\Delta t}{\Delta x}\left[\left(QQ/\mu + g P_\Omega(\mu) \right)\Big|_{i+1/2}^n - \left(QQ/\mu + g P_\Omega(\mu) \right)\Big|_{i-1/2}^n \right] \\ - \Delta t \left(\frac{\mu^n_{i+1/2} + \mu^n_{i-1/2}}{2} \right) \left(g \frac{z_b\big|_{i+1/2}^n - z_b\big|_{i-1/2}^n}{\Delta x} + g \frac{\left(p_\Gamma / \langle \rho_m \rangle\right)\Big|_{i+1/2}^n - \left(p_\Gamma / \langle \rho_m \rangle\right)\Big|_{i-1/2}^n}{\Delta x} + S_f\left(Q_i^n, \mu_i^n\right) \right) \\ + \Delta t \left(g P_{G,\partial\Omega} - S_\Gamma + \theta \langle \rho_m \rangle \frac{q^2_{m,L}}{\Omega} - \frac{\langle \alpha_d \rangle}{1 - \langle \alpha_d \rangle} \frac{\rho_d \rho_w}{\langle \rho_m \rangle} \tilde{U}_{dj} \tilde{U}_{dj} \Omega \right)\Bigg|_i^n \end{aligned} \tag{8.26}$$

where I perform a special treatment for the source terms involving a gradient. As pointed in Chapter 4 for pure water flows, this treatment is necessary in order to keep the adequacy between the pressure and the topographic discretizations. For the mixture fluid momentum term, the Wolf splitting gives:

$$\left(\frac{QQ}{\mu}\right)^n_{i+\frac{1}{2}} = \begin{cases} Q_L^n Q_L^n / \mu_L^n & \text{if} \quad \tilde{u}_{mL} > 0 \quad \text{and} \quad \tilde{u}_{mR} > 0 \\ Q_R^n Q_R^n / \mu_R^n & \text{if} \quad \tilde{u}_{mL} < 0 \quad \text{and} \quad \tilde{u}_{mR} < 0 \\ \left(Q_L^n Q_L^n / \mu_L^n + Q_R^n Q_R^n / \mu_R^n\right)/2 & \text{otherwise} \end{cases} \tag{8.27}$$

For the hydrostatic pressure, the value at the boundary is down-winded such that:

$$gP_\Omega\left(\mu^n_{i+\frac{1}{2}}\right) = \begin{cases} gP_\Omega\left(\mu_R^n\right) & \text{if} \quad \tilde{u}_{mL} > 0 \quad \text{and} \quad \tilde{u}_{mR} > 0 \\ gP_\Omega\left(\mu_L^n\right) & \text{if} \quad \tilde{u}_{mL} < 0 \quad \text{and} \quad \tilde{u}_{mR} < 0 \\ \left(gP_\Omega\left(\mu_R^n\right) + gP_\Omega\left(\mu_L^n\right)\right)/2 & \text{otherwise} \end{cases} \tag{8.28}$$

The requirement of adequacy between the pressure gradient and the bottom slope prompts us to split the topographic gradient in the same direction than the pressure. For the flow cross-section, we consequently have:

$$\mu^n_{i+\frac{1}{2}} = \begin{cases} \mu_R^n & \text{if} \quad \tilde{u}_{mL} > 0 \quad \text{and} \quad \tilde{u}_{mR} > 0 \\ \mu_L^n & \text{if} \quad \tilde{u}_{mL} < 0 \quad \text{and} \quad \tilde{u}_{mR} < 0 \\ \left(\mu_R^n + \mu_L^n\right)/2 & \text{otherwise} \end{cases} \tag{8.29}$$

For the same reason, the topography at the finite volume boundary is given by:

$$z_b\big|^n_{i+\frac{1}{2}} = \begin{cases} z_b\big|^n_R & \text{if} \quad \tilde{u}_{mL} > 0 \quad \text{and} \quad \tilde{u}_{mR} > 0 \\ z_b\big|^n_L & \text{if} \quad \tilde{u}_{mL} < 0 \quad \text{and} \quad \tilde{u}_{mR} < 0 \\ \left(z_b\big|^n_R + z_b\big|^n_L\right)/2 & \text{otherwise} \end{cases} \tag{8.30}$$

Since the pressure in the upstream layer acts as a uniform pressure term within the lower layer, its value is down-winded as follows:

$$\left(p_\Gamma / \langle\rho_m\rangle\right)^n_{i+\frac{1}{2}} = \begin{cases} p_\Gamma\big|^n_R / \langle\rho_m\rangle^n_R & \text{if} \quad \tilde{u}_{mL} > 0 \quad \text{and} \quad \tilde{u}_{mR} > 0 \\ p_\Gamma\big|^n_L / \langle\rho_m\rangle^n_L & \text{if} \quad \tilde{u}_{mL} < 0 \quad \text{and} \quad \tilde{u}_{mR} < 0 \\ \left(p_\Gamma\big|^n_L / \langle\rho_m\rangle^n_L + p_\Gamma\big|^n_R / \langle\rho_m\rangle^n_R\right)/2 & \text{otherwise} \end{cases} \tag{8.31}$$

The non-conservative momentum equation in the lower layer makes use of the free surface elevation (or pressure head) instead of the pressure. It enables to cancel the lateral pressure term in non-uniform sections. Its discretised form is written as:

$$\begin{aligned} Q_i^{n+1} = Q_i^n - \frac{\Delta t}{\Delta x}\left[\left(QQ/\mu\right)\Big|^n_{i+\frac{1}{2}} - \left(QQ/\mu\right)\Big|^n_{i-\frac{1}{2}}\right] + \Delta t\left(-S_\Gamma + \theta\langle\rho_m\rangle\frac{q^2_{m,L}}{\Omega} - \frac{\langle\alpha_d\rangle}{1-\langle\alpha_d\rangle}\frac{\rho_d\rho_w}{\langle\rho_m\rangle}\tilde{U}_{dj}\tilde{U}_{dj}\Omega\right)\Bigg|^n_i \\ - \Delta t\left(\frac{\mu^n_{i+\frac{1}{2}} + \mu^n_{i-\frac{1}{2}}}{2}\right)\left(g\frac{Z\big|^n_{i+\frac{1}{2}} - Z\big|^n_{i-\frac{1}{2}}}{\Delta x} + g\frac{\left(p_\Gamma/\langle\rho_m\rangle\right)\Big|^n_{i+\frac{1}{2}} - \left(p_\Gamma/\langle\rho_m\rangle\right)\Big|^n_{i-\frac{1}{2}}}{\Delta x} + S_f\left(Q_i^n, \mu_i^n\right)\right) \end{aligned} \tag{8.32}$$

where the elevation Z is down-winded like the other pressure terms:

$$Z\big|^n_{i+\frac{1}{2}} = \begin{cases} Z\big|^n_R & \text{if} \quad \tilde{u}_{mL} > 0 \quad \text{and} \quad \tilde{u}_{mR} > 0 \\ Z\big|^n_L & \text{if} \quad \tilde{u}_{mL} < 0 \quad \text{and} \quad \tilde{u}_{mR} < 0 \\ \left(Z\big|^n_R + Z\big|^n_L\right)/2 & \text{otherwise} \end{cases} \tag{8.33}$$

In the upstream layer, the discretised continuity equation may be written by analogy with the mixture continuity equation:

$$\mu_g\Big|_i^{n+1} = \mu_g\Big|_i^n - \frac{\Delta t}{\Delta x}\left[Q_g\Big|_{i+1/2}^n - Q_g\Big|_{i-1/2}^n \right] + \Delta t q_{g,\perp}\Big|_i^n \tag{8.34}$$

where the parameters μ_g and Q_g are defined as:

$$\mu_g = \rho_g \Omega_g \quad \text{and} \quad Q_g = \rho_g \left\langle\left\langle u_g \right\rangle\right\rangle \Omega_g \tag{8.35}$$

Since the air discharge is a convective term, its value is up-winded:

$$Q_g\Big|_{i+1/2}^n = \begin{cases} Q_g\Big|_L^n & \text{if} \quad \left\langle\left\langle u_g \right\rangle\right\rangle_L > 0 \quad \text{and} \quad \left\langle\left\langle u_g \right\rangle\right\rangle_R > 0 \\ Q_g\Big|_R^n & \text{if} \quad \left\langle\left\langle u_g \right\rangle\right\rangle_L < 0 \quad \text{and} \quad \left\langle\left\langle u_g \right\rangle\right\rangle_R < 0 \\ \left(Q_g\Big|_L^n + Q_g\Big|_R^n \right)/2 & \text{otherwise} \end{cases} \tag{8.36}$$

In a similar manner, the air momentum equation is discretised as follows:

$$\begin{aligned} Q_{gi}^{n+1} = Q_{gi}^{\,n} &- \frac{\Delta t}{\Delta x}\left[\left(Q_g Q_g / \mu_g \right)\Big|_{i+1/2}^n - \left(Q_g Q_g / \mu_g \right)\Big|_{i-1/2}^n \right] \\ &- \Delta t g \left(\left(\mu_{g_{i+1/2}}^n + \mu_{g_{i-1/2}}^n \right)/2 \right) \left(\left(\left(p_\Gamma/\rho_g \right)\Big|_{i+1/2}^n - \left(p_\Gamma/\rho_g \right)\Big|_{i-1/2}^n \right) \Big/ \Delta x + S_g\left(Q_i^n, \mu_i^n \right) \right) \\ &+ \Delta t \left(\rho_g \theta q_{g,\perp}^2 + S_\Gamma \right)\Big|_i^n \end{aligned} \tag{8.37}$$

where the parameters μ_g and Q_g have been defined above. Source terms involving a gradient go through a special discretization for keeping coherence with the lower layer. Since the air momentum term is a convective flux, it is up-winded as follows:

$$\left(\frac{Q_g Q_g}{\mu_g} \right)_{i+1/2}^n = \begin{cases} Q_g\Big|_L^n Q_g\Big|_L^n / \mu_g\Big|_L^n & \text{if} \quad \left\langle\left\langle u_g \right\rangle\right\rangle_L > 0 \quad \text{and} \quad \left\langle\left\langle u_g \right\rangle\right\rangle_R > 0 \\ Q_g\Big|_R^n Q_g\Big|_R^n / \mu_g\Big|_R^n & \text{if} \quad \left\langle\left\langle u_g \right\rangle\right\rangle_L < 0 \quad \text{and} \quad \left\langle\left\langle u_g \right\rangle\right\rangle_R < 0 \\ \left(Q_g\Big|_L^n Q_g\Big|_L^n / \mu_g\Big|_L^n + Q_g\Big|_R^n Q_g\Big|_R^n / \mu_g\Big|_R^n \right)/2 & \text{otherwise} \end{cases} \tag{8.38}$$

On the other hand, the pressure term is down-winded:

$$\left(p_\Gamma/\rho_g \right)_{i+1/2}^n = \begin{cases} p_\Gamma\Big|_R^n / \rho_g & \text{if} \quad \left\langle\left\langle u_g \right\rangle\right\rangle_L > 0 \quad \text{and} \quad \left\langle\left\langle u_g \right\rangle\right\rangle_R > 0 \\ p_\Gamma\Big|_L^n / \rho_g & \text{if} \quad \left\langle\left\langle u_g \right\rangle\right\rangle_L < 0 \quad \text{and} \quad \left\langle\left\langle u_g \right\rangle\right\rangle_R < 0 \\ \left(p_\Gamma\Big|_L^n / \rho_g + p_\Gamma\Big|_R^n / \rho_g \right)/2 & \text{otherwise} \end{cases} \tag{8.39}$$

By analogy, the air cross-section is down-winded:

$$\mu_{g_{i+1/2}}^n = \begin{cases} \mu_g\Big|_R^n & \text{if} \quad \left\langle\left\langle u_g \right\rangle\right\rangle_L > 0 \quad \text{and} \quad \left\langle\left\langle u_g \right\rangle\right\rangle_R > 0 \\ \mu_g\Big|_L^n & \text{if} \quad \left\langle\left\langle u_g \right\rangle\right\rangle_L < 0 \quad \text{and} \quad \left\langle\left\langle u_g \right\rangle\right\rangle_R < 0 \\ \left(\mu_g\Big|_R^n + \mu_g\Big|_L^n \right)/2 & \text{otherwise} \end{cases} \tag{8.40}$$

8.2.2 STABILITY ANALYSIS

The Von Neumann stability analysis proves that the previous numerical scheme is stable. Indeed, the solution of the discretised model may be developed in Fourier series as follows:

$$\mathbf{U}_k^n = \sum_{m=-N}^{+N} \tilde{\mathbf{U}}_m^n e^{\left[\mathbf{i} l_m (k\Delta x - c_m(l_m)t)\right]} \tag{8.41}$$

where N is the number of mesh intervals, k the mesh index, $\mathbf{i}=\sqrt{-1}$, $\tilde{\mathbf{U}}_m^n$ the amplitude of the m^{th} harmonic, l_m[rad/m] the wave number, and c_m[m/s] has real and imaginary parts : $c_m = c_{rm}(l_m) + \mathbf{i} c_{im}(l_m)$. By using this last decomposition, equation (8.41) is rewritten as:

$$\mathbf{U}_k^n = \sum_{m=-N}^{+N} \tilde{\mathbf{U}}_m^n e^{l_m c_{im}(l_m)t} e^{\left[\mathbf{i} l_m (k\Delta x - c_{rm}(l_m)t)\right]} \tag{8.42}$$

In this equation, the amplification rate of the wave is identified as the imaginary part c_{im} of the velocity multiplied by the wave number l_m. Obviously, this amplification rate is negative if the following condition is respected:

$$l_m c_{im}(l_m) \le 0 \tag{8.43}$$

This is the Von Neumann stability criterion.

At this point, I introduce these Fourier series into the quasi-linear form of the discretised model. By definition of the Wolf splitting, this equation may be written as:

$$\frac{\partial \mathbf{U}_i}{\partial t} = -\left[\mathbf{A}^+ \frac{\partial \mathbf{U}_i^n}{\partial x}\bigg|^+ + \mathbf{A}^- \frac{\partial \mathbf{U}_i^n}{\partial x}\bigg|^- \right] \tag{8.44}$$

where the super-script $|^+$ and $|^-$ designates the respectively down-winded and up-winded gradients. Consequently, the splitted Jacobian matrixes for the conservative model are given by:

$$\mathbf{A}^+ = \begin{bmatrix} 0 & 0 & 0 & 0 & 0 \\ 0 & 0 & 0 & 0 & 0 \\ c^2 + a_a^2\left(\rho_g\Omega/\rho_w\Omega_g\right) & \left(\rho_w - \rho_d\right)a_a^2\left(\rho_g\Omega/\rho_w\Omega_g\right) & 0 & a_a^2\Omega/\Omega_g & 0 \\ 0 & 0 & 0 & 0 & 0 \\ 0 & 0 & 0 & a_a^2 & 0 \end{bmatrix}$$

$$\mathbf{A}^- = \begin{bmatrix} 0 & 0 & 1 & 0 & 0 \\ -\langle\alpha_d\rangle\tilde{u}_m/\langle\rho_m\rangle & \tilde{u}_m & \langle\alpha_d\rangle/\langle\rho_m\rangle & 0 & 0 \\ -\tilde{u}_m^2 & 0 & 2\tilde{u}_m & 0 & 0 \\ 0 & 0 & 0 & 0 & 1 \\ 0 & 0 & 0 & -\langle\langle u_g\rangle\rangle^2 & 2\langle\langle u_g\rangle\rangle \end{bmatrix} \tag{8.45}$$

Thanks to this particularized Jacobian matrixes and the Fourier series (8.41), equations (8.44) are rewritten as:

$$-\mathbf{i} l_m c_m(l_m)\mathbf{U}_i = -\left[\mathbf{A}^+ \frac{e^{\mathbf{i} l_m \Delta x} - 1}{\Delta x} + \mathbf{A}^- \frac{1 - e^{-\mathbf{i} l_m \Delta x}}{\Delta x} \right] \mathbf{U}_i \tag{8.46}$$

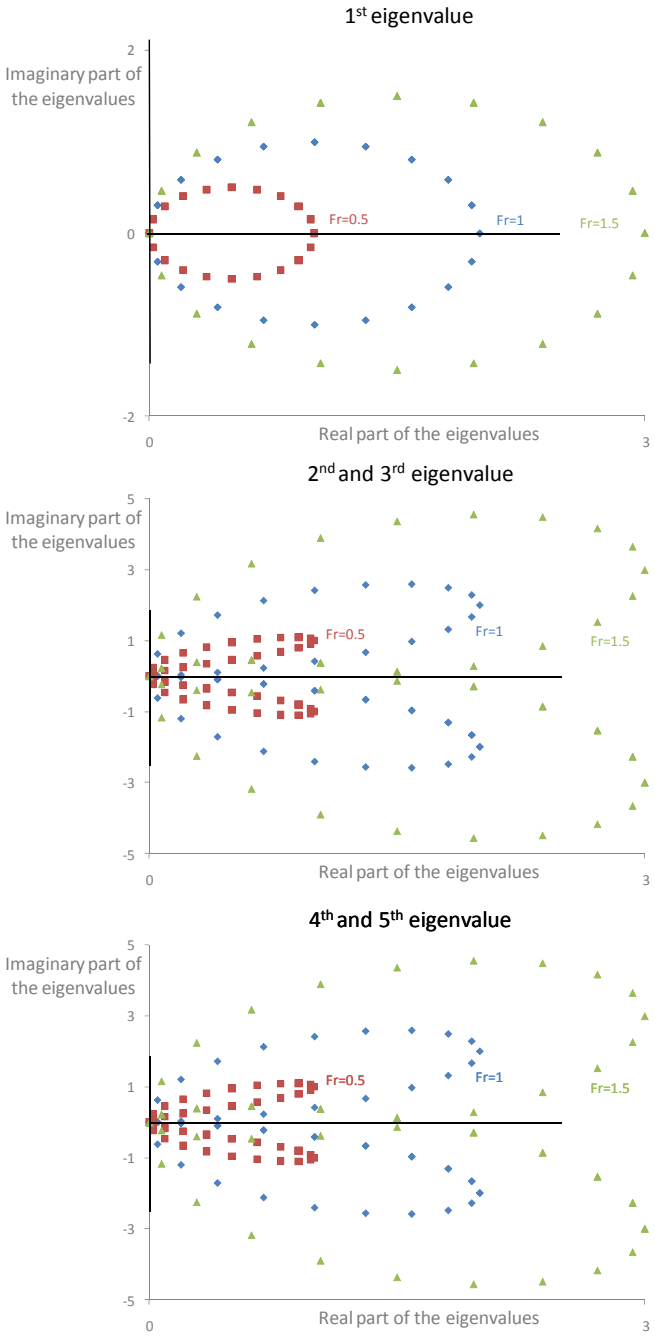

Figure 101: Non-dimensional eigenvalues of the discretised Jacobian matrixes are complex numbers whose real part is always positive

By identification in this equation, criterion (8.43) can be written in terms of the Jacobian matrixes of the discretised operator.

$$l_m c_{im}(l_m) = \mathrm{Re}\left[-i l_m c_m(l_m)\right] = -\mathrm{Re}\left[\mathbf{A}^+ \frac{e^{i l_m \Delta x} - 1}{\Delta x} + \mathbf{A}^- \frac{1 - e^{-i l_m \Delta x}}{\Delta x}\right] \tag{8.47}$$

In particular, the criterion (8.43) is verified only if the real part of the discretised operator is positive. Positivity of the real part of the eigenvalues of the discretised operator is thus a necessary and sufficient condition for stability:

$$\mathrm{Re}\left[\lambda_i^{\text{discretised}}\right] \geq 0 \tag{8.48}$$

By using the values of the Jacobian matrixes (8.45), the eigenvalues are given by:

$$\begin{aligned}
\lambda_1^{discr} &= \tilde{u}_m\left(\frac{1-e^{-il_m\Delta x}}{\Delta x}\right)\\
\lambda_{2-3}^{discr} &= \left(\frac{1-e^{-il_m\Delta x}}{\Delta x}\right)\left[\tilde{u}_m \pm \sqrt{\left(c^2+a_a^2\varepsilon\right)e^{il_m\Delta x}}\right]\\
\lambda_{4-5}^{discr} &= \left(\frac{1-e^{-il_m\Delta x}}{\Delta x}\right)\left[\left\langle\left\langle u_g\right\rangle\right\rangle \pm a\sqrt{e^{il_m\Delta x}}\right]
\end{aligned} \tag{8.49}$$

By introducing the trigonometric functions $e^{ix}=\cos x+i\sin x$ and by introducing the Froude and the Mach numbers defined as (8.15), we simply obtain:

$$\begin{aligned}
\lambda_1^{discr} &= Fr\frac{2}{\Delta x}\sin\left(\frac{l_m\Delta x}{2}\right)\left[\sin\left(\frac{l_m\Delta x}{2}\right)+i\cos\left(\frac{l_m\Delta x}{2}\right)\right]\\
\lambda_{2-3}^{discr} &= \frac{2}{\Delta x}Fr\sin^2\left(\frac{l_m\Delta x}{2}\right)+\frac{2}{\Delta x}i\sin\left(\frac{l_m\Delta x}{2}\right)\left[Fr\cos\left(\frac{l_m\Delta x}{2}\right)\pm 1\right]\\
\lambda_{4-5}^{discr} &= \frac{2}{\Delta x}M\sin^2\left(\frac{l_m\Delta x}{2}\right)+\frac{2}{\Delta x}i\sin\left(\frac{l_m\Delta x}{2}\right)\left[M\cos\left(\frac{l_m\Delta x}{2}\right)\pm 1\right]
\end{aligned} \tag{8.50}$$

As shown on Figure 101, the real parts of eigenvalues (8.50) are positive whatever the value of the Froude and Mach numbers. This observation accords with the stability criterion (8.48). Consequently, the Wolf splitting as proposed in this chapter is unconditionally stable.

8.3 IMPLEMENTATION: WOLF IMPACK

For practical application, the mathematical model (8.1) and its discretization (8.20)-(8.40) are always implemented under the form of an algorithm. Computers are indeed imperative for performing such a large number of operations. In this respect, computer science offers a large spectrum of different methods with specific advantages and drawbacks [297].

In the normal course of events, researchers from the HACH rely on the modelling system WOLF for implementing innovations and improvements. Two reasons justify this strategy. First, it enables to reach results faster by using, as a reliable basis, all the algorithms already implemented by other members of the team. It spares the implementation of many common parts like pre- and post-processing algorithms. Second, industrial application of the innovations is straightforward when the associated algorithm is implemented in a professional platform like WOLF. In this thesis, I followed this approach for the single-phase model (Chapter 4).

Nevertheless, I decided to implement the multiphase model in its own computational code, called WOLF IMPack. Standing for Integrated Multi-phase Pack, WOLF IMPack constitutes an original algorithm for computing air-water flows with the drift-flux model. Two reasons explain this choice of not using WOLF here. First, the multiphase equations strongly differ in number, nature, and necessary algebraic operations from the pure water model. Implementing the new model in WOLF requires major modifications in the code. Second, model (8.1) is an original and quite bold proposition of this thesis. At the time of the implementation, a large program of corrections and validations was necessary before any industrial application. I preferred making these adjustments in a light algorithm like WOLF IMPack, instead of professional software like WOLF. In view of the success of the validation (Chapter 9), the next step of the project would surely consist in implementing the new model into WOLF.

WOLF IMPack provides all the results presented in the end of this thesis. Clearly, WOLF IMPack is an academic computational code that aims at validating an approach and gaining insight into complex phenomena. I did not create user interfaces for the pre- and post-processing. Instead, I use commercial software's for visualizing the results (Excel, Matlab,…). I favored a computational efficiency by using Fortran as programming language. Indeed, it is especially suited for scientific and engineering applications.

Summary and conclusion

From a general point of view, this chapter was dedicated to the discretization and implementation of the original model (8.1) describing air-water mixed flows. For this purpose, I first established the wave structure of the solution by performing both a linear and non-linear analysis of the system of equations. The five waves forming the solution defined two flow regimes in each layer: a sub- and super-critical regime in the lower layer, and a sub- and super-sonic regime in the upper layer. Based on this mathematical analysis, the Wolf flux vector splitting was applied to the equations. The Von Neumann stability analysis proved the unconditional stability of the scheme. Finally, discretised equations were implemented in a new academic code called WOLF IMPack (Integrated Multi-Phase Pack).

In conclusion, I created in this chapter an original computational code for the purpose of validating the new mathematical model and making fundamental research on air-water flows. WOLF IMPack constitutes an efficient computational code for designing hydraulic structures and making impact studies. It meets most of the objectives of this research.

Up to now, only theoretical considerations proved the validity and originality of the approach. Further assessment of WOLF IMPack requires comparing numerical data with published benchmarks and experimental data. This is the purpose of the next chapter.

Chapter 9 Multiphase Flows: Validation and Application

This chapter aims at

- ✓ validating the new model on published benchmarks;
- ✓ applying WOLF IMPack on practical cases.

In the previous chapters, I detailed the theoretical developments underlying the creation of a new computational code called WOLF IMPack. Standing for Integrated Multi-Phase pack, WOLF IMPack simulates one-dimensional air-water flows. The algorithm relies on an original two-layer three-phase mathematical model. In addition, equations are discretised thanks to the finite volume method coupled with the Wolf flux vector splitting. Theoretically, WOLF IMPack should provide an efficient tool for many practical situations likely to appear in civil and environmental engineering. In practice, that remains to be proved.

In order to assess the actual fidelity and the usefulness of WOLF IMPack, I dedicate this chapter to its validation and its application on a real case. In section 9.1, I provide some of the results of the validation campaign. For all the situations in the scope of applicability of WOLF IMPack, the numerical results are compared with experimental, numerical, and analytical data published in literature. This validation results prove that WOLF IMPack is an efficient and useful tool for investigating air-water flows in open channels and closed conduits, except for the cases involving a moving transition, which are affected by numerical oscillations. Consequently, the code is applied for the design of a real case, namely the bottom outlet of a large dam. Used in conjunction with a physical model built in the of Engineering Hydraulics (ULG-HACH), these investigations underline the apparition of strong air-water interactions that affects the flow dynamics. The use of WOLF IMPack gives insight into the measured data and enables to predict accurately the effect of design modification on the discharge capacity of the gallery and the pressure profile along the structure.

9.1 VALIDATION

By comparing the numerical results with experimental, numerical, and theoretical data found in literature, I prove herein the fidelity of the computational code WOLF IMPack and identify the limits of its applicability. This validation campaign covers a wide spectrum of situations likely to raise a problem in civil and environmental engineering. Only the most interesting results are presented here. In particular, I successively consider:

- pure water free-surface, pressurized, and mixed flows;
- two-phase water hammer phenomena;
- the air entrainment affecting the free surface flow over a stepped spillway;
- the air entrapment within closed pipes.

As proven in the following pages, WOLF IMPack is an efficient and useful tool for investigating air-water flows in open channels and closed conduits. Indeed, application of WOLF IMPack on pure water flows in sub-section 9.1.1 gives the exact same results as WOLF1D (which was expected). Consequently, it demonstrates the same advantages: it simulates in a single framework both free surface and pressurized flows (including sub-atmospheric pressure) and it integrates easily the effects of source terms. However, it suffers from the same shortcoming. Post-transition oscillations compromise the fidelity and stability of the simulations. When used for simulating a two-phase water hammer (sub-section 9.1.2), WOLF IMPack succeeds in capturing shock and rarefaction waves, as well as non-linear behaviors due to the variability of the pressure wave celerity. By analogy with the work of B.J.Dewals [75], WOLF IMPack is used for simulating the flow over a stepped spillway (sub-section 9.1.3). The dynamics of such streams is strongly affected by air entrainment and non-uniform distribution of the flow velocity over the cross-section. Thanks to adequate laws for the air entrainment and for the Boussinesq coefficient, numerical data accords remarkably well with the experimental data gained at the LCH-EPFL by S.André [6]. Finally, the computation of the upper layer dynamics partly enables to account for air entrapment in closed conduits (sub-section 9.1.4). WOLF IMPack gives indeed accurate behavior for a stratified flow as well as the behavior of a fixed bubble within a pressurized flow. In particular, it gives interesting insight into the behavior of surge vessels. Nevertheless, post-transition oscillations appear in the lower layer, propagate to the upper layer, and compromise very rapidly the stability of the code (even when using the fixes proposed in Chapter 4 and 5). This behavior is similar to the one observed when solving pure water mixed flows with WOLF1D. The observation proves again that “numerical shock-capturing” methods are partly inefficient in presence of highly variable celerities. Except this restriction, WOLF IMPack may be considered as a success with respect to the objectives of this thesis (Chapter 1).

9.1.1 Pure Water Flows: Free surface, Pressurized, and Mixed Cases

Theoretically, the multiphase model for air-water flows simplifies into the single-phase model proposed in Chapter 3 if air-water interactions are neglected. Consequently, WOLF IMPack has to give accurate results for pure water flows as well. In Chapter 5, WOLF1D was assessed on more than 50 validations benchmarks. These successively considered free-surface (including sub-, trans-, and super-critical regimes), pressurized, and mixed flows without air-water interactions. Obviously, WOLF IMPack must give the same results than WOLF1D for these benchmarks. This assessment constitutes the first step of validation.

By analogy with Chapter 5, the validation campaign of WOLF IMPack on pure water flows contains more than 50 cases. First, benchmarks consider steady pressurized flows and classical water hammer phenomena [1-6]. Second, the code is assessed on free surface cases with fixed and moving discontinuities (including transitions of regime) [9, 36, 93, 286]. Finally, data given by WOLF IMPack are compared with experimental, analytical, and numerical data in cases involving mixed patterns [30, 40, 41, 192, 193, 287, 298, 300, 317].

For all these cases, WOLF IMPack gives the same results (at the truncation error level) than WOLF1D. This proves that single-phase equations are a particularized case of the original multiphase model proposed in this thesis. Consequently, WOLF IMPack has the same advantages than WOLF. First, it consistently simulates mixed flows, including sub-atmospheric pressurized flows. Second, it handles naturally with regime transitions in free-surface flows. Third, it gives accurate pressure profiles for shocks and rarefactions, especially in pressurized flows. Finally, the treatment of roughness and non-uniform cross-sections is straightforward. Nevertheless, WOLF IMPack suffers the same drawbacks than WOLF1D. First, spurious oscillations appear at the transition bore and may compromise the stability of the scheme. Second, it requires a diffusive time integration scheme for smoothing oscillations appearing in the neighborhood of shocks.

9.1.2 Air-water Flows: Water Hammer

These standard benchmarks consist in the simulation of water hammers in air-water mixture. These cases assess the capacity of WOLF IMPack to describe correctly the propagation of shock and rarefaction waves. The evaluations of both a correct celerity and an adequate pressure intensity are crucial here. The first case is the instantaneous closure of a valve downstream a pipe (originally presented by Leon [194]). The second standard case considers a sudden pressure decrease upstream a pipe. This benchmark was originally presented by Guinot [131].

Instantaneous valve closure by Leon

As pointed out in [194], this test considers a horizontal frictionless pipe connected to an upstream reservoir and a downstream valve. The duct is 10000m long and has a diameter of 1m. The upstream head (in the reservoir) is kept constant at 200m while the initial steady-state discharge is 2.0m³/s. The fluid is a mixture of air and water. At the reference

pressure (101325Pa), the concentration in air is 0.2%. The pressure wave celerity of reference is 1000m/s. A sharp transience is created in the pipe by closing instantaneously the downstream valve. The discontinuity propagates from the downstream end to the upstream end of the pipe. It reflects at the reservoir. Since the celerity depends on the pressure head, the water hammer takes the form of either a rarefaction or a shock wave according of the direction of propagation.

Numerical computation is performed with WOLF IMPack on a uniform grid of 1000-cells of 10m length. Time integration is performed with a three-step Runge-Kutta scheme (RK31). The Courant number is kept constant at 0.5. The reconstruction is constant such that the scheme is 1st order accurate.

Reference data comes from [194]. It consists in the near-exact solution of a two-phase water hammer model (two equations) computed using a Method Of Characteristic (MOC) scheme for a very fine grid.

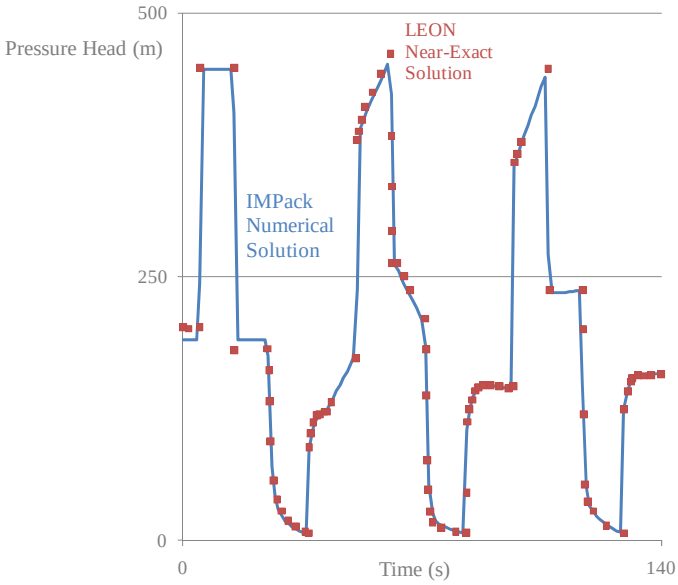

Figure 102: The time evolution of the pressure head at the middle of the pipe computed with WOLF IMPack shows a good accordance with the Near-Exact Solution of Leon [194]

The time evolution of the pressure head at the middle of the pipe computed with WOLF IMPack shows a good accordance with the Near-Exact Solution (Figure 102). In particular, the rarefaction wave clearly appears for the propagation of the depression. On the opposite, the creation of a shock wave is clear when the pressure arises. Diffusion appears and dissipates the waves along the time. Since no physical friction is considered in the case, it means the numerical scheme is affected by numerical diffusion. Comparison of the profiles of the pressure head after 140s computed with WOLF IMPack and the Near-Exact Solution shows that numerical solution is partly smeared out (Figure 103). This is still a consequence of the numerical diffusion that affects WOLF IMPack. However, the graph clearly underlines the ability of the code to propagate shock and rarefaction waves at a correct velocity.

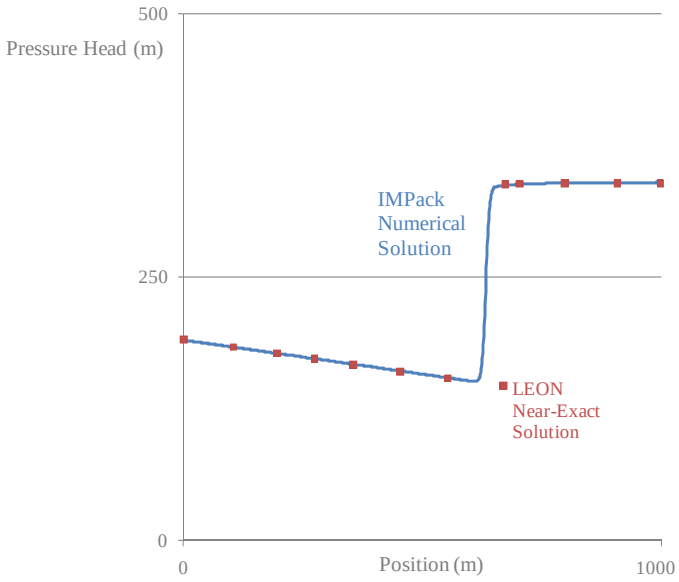

Figure 103: Comparison of the profiles of the pressure head after 140s computed with WOLF IMPack and the Near-Exact Solution of [194] shows that numerical solution is partly smeared out.

TWO-PHASE WATER HAMMER BY GUINOT

This case is a standard benchmark presented in [131]. It consists in a 3000m long circular pipe of area Ω_{max}=0.29m². The reference celerity is a_0=981m/s while the reference density is 992kg/m³. The void fraction is assumed constant at α_0=0.2%. The fluid is initially at rest, at a pressure of 5x10^{5}Pa. At time t=0, the pressure at the left-hand boundary is lowered down to 10^{5}Pa. It causes a rarefaction wave to travel to the right. When it bounces back at the end of the pipe, a shock wave appears.

Numerical computation is performed on a uniform grid of 300 cells of 10m length. Time integration is performed with a three-step Runge-Kutta scheme (RK31) and the Courant number is kept constant at 0.6.

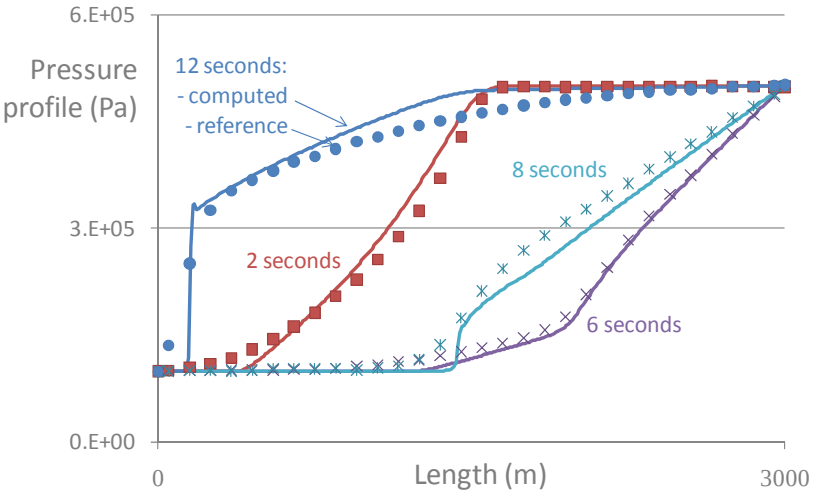

Figure 104: Comparison between the results of Guinot [131] (computed with a 1st order Godunov scheme for two- phase water hammer) and the data given by WOLF IMPack

In Figure 104, numerical data computed with WOLF IMPack are compared with the results of Guinot [131]. These data result from a two phase water hammer code. Computed pressure profiles are given at 7 given times. Figure 104 gives four of them (2s, 6s, 8s, and 12s after the pressure decrease). Contrary to a single phase water hammer which is characterized by a sharp shock wave translating at constant velocity, we observe here a rarefaction wave due to the dependence between the pressure and the celerity. The wave reflects at the right-hand side of the pipe and the resulting wave is steepening when travelling to the left hand-side. This water hammer is thus strongly non-linear. The lower the pressure is, the lower the celerity is. Results from WOLF IMPack are in good accordance with the data of Guinot. In fact, discontinuities remain sharper with the FVS scheme such that we can deduce that WOLF IMPack is less diffusive than Guinot's Godunov scheme. At the shock front, small oscillations appear. They are characteristic of the Wolf FVS. These oscillations are sufficiently feeble to not compromise the stability of the computation.

9.1.3 Air-water Flows: Stepped Spillway

In the introduction chapter, I listed all the applications of interest in civil and environmental engineering where air-water interactions affect the flow dynamics. In particular, it was shown that flows over stepped spillways appear as "white water", which is characteristic of air-water interactions. Since stepped spillways present an important industrial interest (as a promising solution to enhance the discharge capacity of large dams), I simulate herein these flows with WOLF IMPack and compare the numerical results with experimental data.

All the validation data used in this section come from the experiments led by S. André at LCH-EPFL [6, 76, 77] over a 30° stepped flume. In addition, I make use of the calibration data proposed by B.J.Dewals [6, 75-77] for the air entrainment capacity and the Boussinesq coefficient. Thanks to these important results, WOLF IMPack gives interesting insight into the flow dynamics and provides accurate profiles for the free surface elevation. Of course, this validation does not seek after obtaining the same level of accuracy than 2D vertical and 3D models [49, 50]. Instead, WOLF IMPack constitutes a good compromise between level of accuracy and computation time.

Dynamics of the flow over a stepped spillway

Because of the high turbulence, the self-aeration process, and the irregular wavy free surface, the mechanisms acting within the flow over stepped spillways are very complex and difficult to apprehend. Consequently, such flows have been essentially investigated with physical models. These research campaigns gave many elements to understand the flow dynamics and provided a panel of case-specific empirical relations. As largely described in [6, 75, 76], the main characteristics of the flow are the self-aeration of the fluid and the macro-turbulent structures due to the form effects of the steps.

For a given structure, the flow discharge determines two different flow regimes. For low discharge, a nappe flow arises. It is characterized by a plunging jet impacting on the downstream portion of the horizontal step. An air cavity is trapped under the jet. For higher discharge rates, a skimming flow appears when the air cavities are filled. The upper layer of the flow seems to skim over a pseudo-bottom determined by the edges of the steps. Under the pseudo-bottom, recirculation cells develop and spread over almost the whole step length and height (Figure 105). Near the step edge, an internal jet ensures the exchange between the upper layer and the recirculation cell. The transition stage between both regimes combines parts of the flow in nappe regime and parts of the flow in skimming regime.

Similarly to smooth spillways (see chapter 1), three distinct regions are identifiable along the slope (Figure 105). Upstream, we observe a non-aerated area characterized by a developing shear layer. When the shear layer reaches the free surface at the so-called inception point, the air-entrainment developing region begins. Finally, the flow becomes quasi-uniform if the spillway is sufficiently long. In this case, the structure of macro-turbulence, the concentration of air, and the velocity profile are uniform between each step.

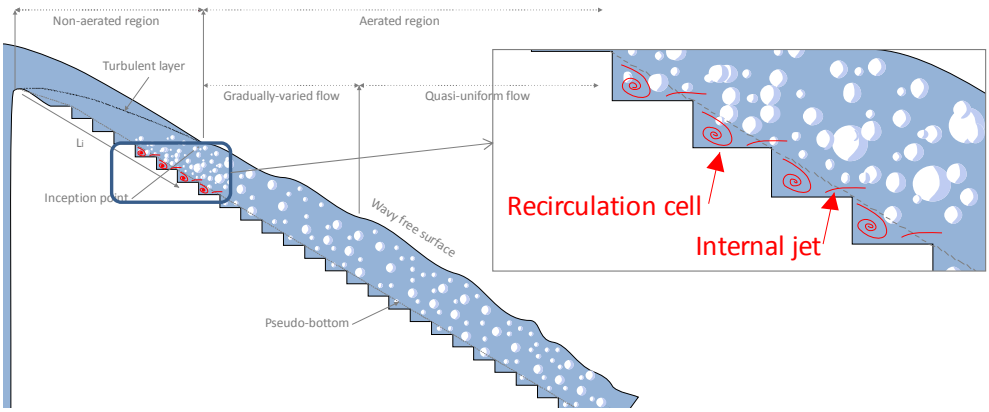

Figure 105: Schematic view of the flow over a stepped spillway

Experimental data used here for validating WOLF IMPack have been published by S. André for a 30° stepped spillway. The flume is 0.5m wide and 8m long. The height of the installation is 3.85m. The spillway is constituted of 64 steps, whose height is 0.06m and length is 0.104m. The alimentation system and the measurement apparatus are described thoroughly in [6].

Numerical model

Even if the flow dynamics presented above exhibits strong transversal phenomena (in particular a non-uniform vertical distribution of the flow parameters), WOLF IMPack may provide accurate results at a very low cost-time. The approach eludes indeed two classical difficulties in 2DV and 3D models, namely the free surface tracking and the turbulence modelling.

For the purpose of applying WOLF IMPack to the stepped spillway, we define a particular frame of reference. The x-axis is inclined along the main flow direction, which is parallel to the pseudo-bottom (Figure 106). The topography is then given by the step elevation k and the water height is given by h. Since the angle ε between the x-axis and the horizontal is not negligible here, approximations made in chapter 7 for developing the original model are no more licit. However, it is very simple to show that the following set of equation describes the dynamics of the lower layer in an inclined frame of reference:

$$\begin{cases} \dfrac{\partial \langle \rho_m \rangle \Omega}{\partial t} + \dfrac{\partial \langle \rho_m \rangle \tilde{u}_m \Omega}{\partial x} = q_{m,\perp} \\ \dfrac{\partial \langle \alpha_d \rangle \Omega}{\partial t} + \dfrac{\partial}{\partial x}\left(\langle \alpha_d \rangle \tilde{u}_m \Omega + \langle \alpha_d \rangle \dfrac{\rho_w}{\langle \rho_m \rangle} \tilde{U}_{dj} \Omega \right) = \left\langle \Gamma_d \middle/ \rho_d \right\rangle \Omega + q_{\alpha,\perp} \\ \dfrac{\partial \langle \rho_m \rangle \tilde{u}_m \Omega}{\partial t} + \dfrac{\partial \beta_{xx} \langle \rho_m \rangle \tilde{u}_m \tilde{u}_m \Omega}{\partial x} + \dfrac{\partial}{\partial x}\left(\beta_{xx} \dfrac{\langle \alpha_d \rangle}{1 - \langle \alpha_d \rangle} \dfrac{\rho_d \rho_w}{\langle \rho_m \rangle} \tilde{U}_{dj} \tilde{U}_{dj} \Omega \right) + g \cos\theta \dfrac{\partial P_\Omega}{\partial x} \\ \qquad = -\langle \rho_m \rangle g \Omega \left(\sin\theta + S_F + \dfrac{\partial z_b}{\partial x} \right) - \dfrac{\partial p_\Gamma}{\partial x} \Omega + g \cos\theta P_{G,\partial\Omega} - S_\Gamma + \theta \langle \rho_m \rangle \dfrac{q_{m,\perp}^2}{\Omega} \end{cases} \tag{9.1}$$

This correction was implemented in WOLF IMPack.

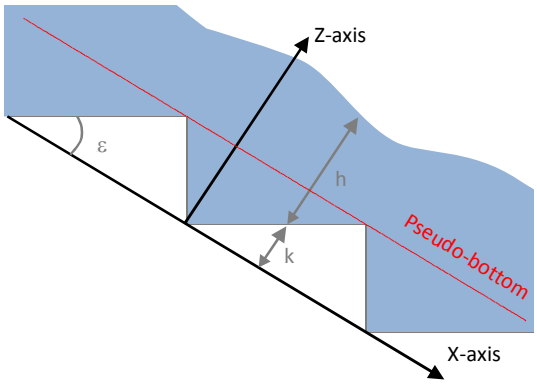

Figure 106: Stepped spillway in the inclined frame of reference

Numerically, the spatial discretisation relies on a regular grid of 0.01m-long meshes. The temporal integration is performed with a three-step Ruge-Kutta RK31B method and a constant Courant number equal to 0.5. It offers the optimal performance for the convergence.

Upstream the computational domain (in the filling tank), the flow is sub-critical. Consequently, the necessary boundary conditions are both the air and water discharges. For the simulation, the water discharge is set at Q=0.06m³/s and the air discharge is kept to zero. Downstream the stepped spillway, the flow is super-critical such that no boundary conditions are required.

As mentioned above, the process of air entrainment initiates at a given distance from the spillway crest. The localization of this inception point is determined by means of empirical relations available in the literature [6]. In any case, it does not really affect the flow in the quasi-uniform region.

In order to simulate the air entrainment, the air source term $\left\langle \Gamma_d/\rho_d \right\rangle \Omega$ must be given by a constitutive law adapted to the situation. This law must account for air entrainment and detrainment as a function of the flow conditions. It must also accord with experimental observations. As shown by Dewals et al. [75, 76], the optimal representation of the self-aeration process is given by the following formulation:

$$\left\langle \Gamma_d \middle/ \rho_d \right\rangle = -0.25 * m * \left(\left\langle \alpha_d \right\rangle - \left\langle \alpha_d \right\rangle_{sat} \right) \tag{1.2}$$

The parameter m is equal to zero upstream the inception point and equal one downstream. The saturation concentration $\left\langle \alpha_d \right\rangle_{sat}$ is the maximum value of the air void fraction. Its value is a function of the slope. For a 30° slope, experimental observation sets its value to 0.46%.

Since the vertical profile of the flow velocity is not constant, integration of the advective terms in the momentum equation makes appear a Boussinesq coefficient β_{xx}. Indirectly, this coefficient accounts for the macro-turbulent structures of the flow. Its value must be determined a priori thanks to the following formulation:

$$\beta_{xx} = \frac{\left\langle \rho_m u_m u_m \right\rangle}{\left\langle \rho_m \right\rangle \tilde{u}_m \tilde{u}_m} \tag{1.3}$$

It requires assuming a given vertical profile for the flow velocity. Based on a idealized profile (triangular within the recirculation cell and uniform above), Dewals [75] proposed a first formulation for the coefficient of Boussinesq:

$$\beta_{xx} = \frac{h\left(h - \frac{2}{3}k \right)}{\left(h-k \right)^2} \tag{1.4}$$

which must be always above the unity. By means of a 2DV numerical simulation, this formulation is further refined as follows:

$$\beta_{xx} = \frac{1}{3}\frac{hk}{\left(h-k \right)^2}\left(\frac{u_b}{\bar{u}} \right) + \frac{h}{\left(h-k \right)}\beta_{edge} \tag{1.5}$$

where the parameter u_b designates the velocity at the pseudo bottom and $\bar{u}$ the mean velocity along the flow depth. Experimentations [6] set the value of their quotient to 1.28. The parameter β_{edge} is also given for the 30°stepped spillway as a function of the step Froude number:

$$\beta_{edge} = 0.0067 * Fr^* + 1.0574 \qquad \text{with} \qquad Fr^* = Q_w \Big/ L\sqrt{g \sin\theta k^3} \tag{1.6}$$

with L the flume width.

Finally, the Manning-Strickler correlation provides an estimation of the friction slope J along the flow. According to [6, 76], the Strickler coefficient is set to K=30. According to Dewals [75], the correlation is further adapted to take into account the uneven vertical distribution of the velocity:

$$J = \frac{\beta_{xx} \tilde{u}_m^2}{K^2 R_h^{4/3}} \tag{9.7}$$

where R_h is the hydraulic radius as defined previously.

RESULTS

Numerical data computed with WOLF IMPack are herein compared with the experimental data published in [6, 75, 76]. They consist in the profile of the free surface elevation (in the inclined frame of reference) along a portion of quasi-uniform flow.

The first computation case considers a pure water flow with a Boussinesq coefficient equal to one (in red on Figure 107). Comparison between numerical and experimental data shows a large discrepancy between the profiles. The computed elevation is systematically lower than the measured one. In addition, the profile given by WOLF IMPack suffers large oscillations in phase with the topography. Instead, the actual profile exhibits small oscillations that are in opposition of phase with the topography. This result is clearly unsatisfactory.

The second case integrates the phenomenon of air entrainment thanks to the law given by equation (1.2). As observed in green on Figure 107, the computed flow depth get thicker than the previous one, but the free surface keeps the same form. The profile given by WOLF IMPack still exhibits oscillations in phase with the topography, which contrasts with the measured profile. Additional elements must be introduced in the computation to reach sufficient agreement.

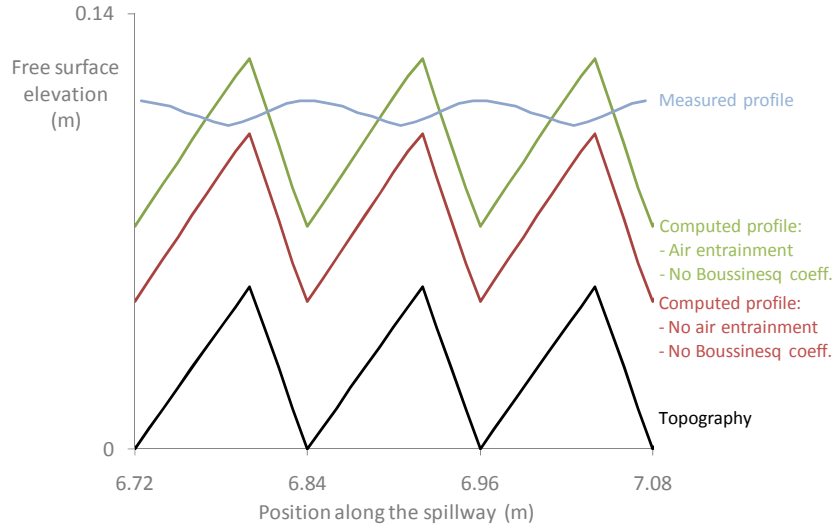

Figure 107: Free surface profiles computed without taking into account the non-uniform distribution of velocity differ from the measured profile

In the third case, equation (1.4) is used to compute an approximation of the Boussinesq coefficient. As shown in red on Figure 108, introducing this coefficient strongly affects the form of the free surface elevation. The profile exhibits large oscillations, but in opposition of phase with the topography. This shape is similar to the measured profile. Nevertheless, the amplitude of the oscillations is still largely over-estimated in the computation.

Finally, the last profile is computed by assuming that the Boussinesq coefficient is given by equations (1.5) and (1.6). This more precise formulation damps the oscillations down (in

green on Figure 108). This profile clearly accords more rigorously with the measured data, even if WOLF IMPack does not accounts totally for the small oscillations. Since coefficient (1.5) has been initially developed for a single-phase model with a transport equation, one can conclude that this validation is a success. Of course, developing a Boussinesq coefficient more adapted to the drift-flux model should provide a better agreement. However, this is beyond the scope of this thesis.

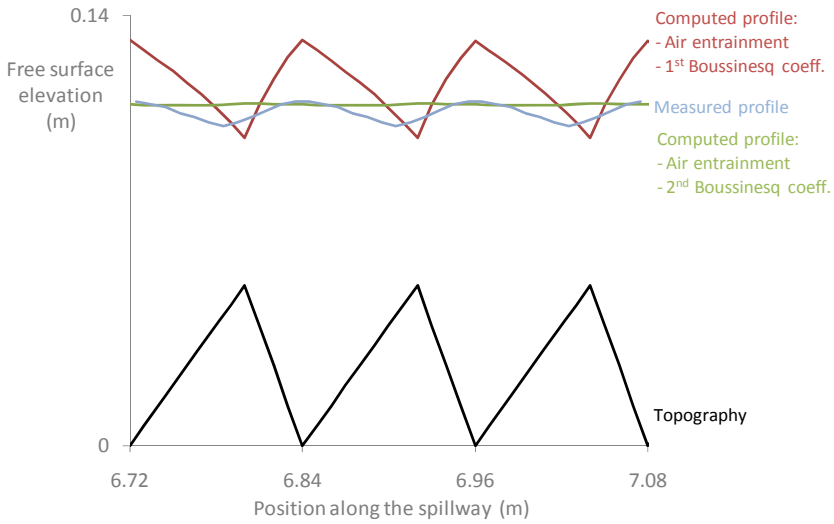

Figure 108: Free surface profiles computed with Boussinesq coefficients accord better with the measured profile

9.1.4 AIR-WATER FLOWS: AIR ENTRAPMENT

Due to the coupling between the upper and lower layers, any variation of the free surface in a closed pipe induces a variation of pressure in the air above, and reciprocally. The benchmarks presented in this sub-section exemplify and assess the ability of WOLF IMPack to handle with this inter-layer coupling. The first case consists in the illustration of a stratified flow in a circular closed pipe. The second case depicts the effect of the expansion of a bubble within a pressurized flow. The third case shows how a vessel tank damps a water hammer in a pipe. These last two cases involve mixed flows with a fixed transition. On the opposite, the fourth case includes attempts to capture a moving transition. In fact, I consider two situations, the bubble entrapment at high points [98] and the air entrapment in stormwater storage tunnels [306]. Due to the post-transition oscillations, the stability of the scheme is compromised in such cases.

STRATIFIED FLOW

A movement of the free-surface in a closed pipe flow should lead to a reaction of the air in the upper layer in terms of pressure and discharge. Since experimental data for such flows are not available, I simply illustrate here such a situation. The circular pipe is 100m long and its diameter is 2m. The pipe is assumed frictionless and with no slope. The initial pure water discharge in the lower layer is $0.01m^3/s$ and the initial water height is H=1.703m. The void fraction in the lower layer is set to zero. In the upper layer, the initial pressure is 140861 Pa because the air density is assumed equal to 1.29349 kg/m^3 and the celerity equal to

330m/s. The air is initially still. At the left boundary, we impose an impermeable boundary for the air (u_g=0m/s) and water discharge is linearly increased from 0.01m³/s to 0.5m³/s during 25s. From then the discharge is maintained constant. At the right boundary, the pressure is fixed at 140861Pa and the water height is assumed constant at 1.703m. Numerical computation is performed on a 100-cells uniform grid of 1m. Time integration is performed with a three-step Runge-Kutta scheme (RK31) and the Courant number is kept constant at 0.6. Figure 109 illustrates the time evolution of the pressure and the discharge in the lower layer at the middle of the pipe. We clearly observe, in a first time, a surge in height and discharge due to the injection of water at the upstream boundary. This stage is followed by a decrease in both height and discharge after reflection on the right boundary. In the upper layer (Figure 110), time evolution shows an increase in pressure up to 1.4atm followed by a decrease up to 0.8 atm. This pressure variation entrains an oscillatory motion of air between both impermeable ends. This is a consequence of the air entrapment.

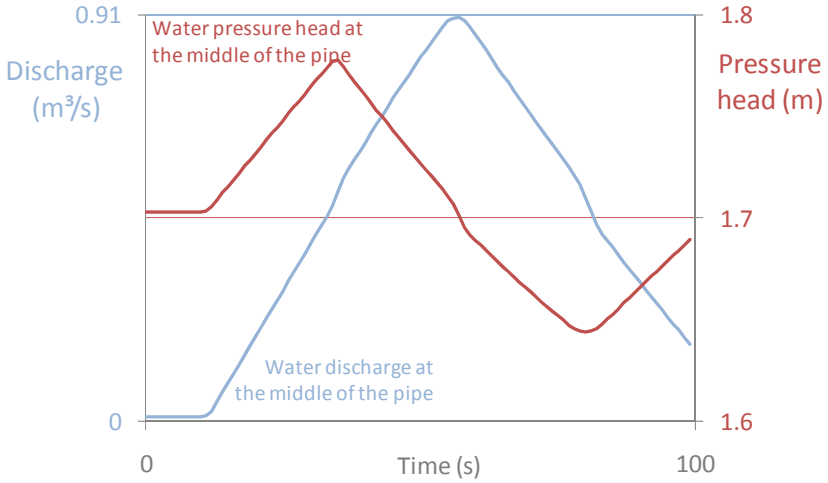

Figure 109: Time evolution of the pressure head and the velocity in the lower layer shows the motion of the free surface due to the injection of water at the upstream boundary.

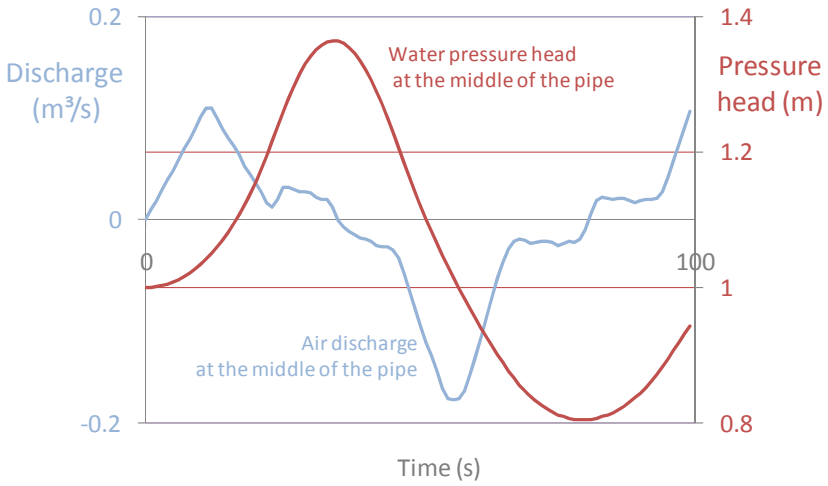

Figure 110: Time evolution of the pressure head and the velocity in the upper layer shows the motion induced in the upper layer due to the motion of the free surface.

MOTION INDUCED BY A BUBBLE EXPANSION

The present benchmark exemplifies the ability of WOLF IMPack to compute the effect of entrapped air on a pure water mixed flow. The case considers a closed tank located upstream a 14.05m long circular pipe (Figure 111). The pipe has a 0.094m diameter. Upstream, the conduit is connected to a 0.25m large, 1.25m long, and 1m high closed tank. Downstream, the water height is assumed constant at 0.1825m. Initially, the pressure head along the pipe and the tank is constant at 0.1825m, the discharge is negligible and the pressure in the air tank is equal to zero. The air celerity is set to 330m/s and the pressure wave celerity to 10m/s. Computation are performed on a uniform grid of 0.025m-long meshes. A three-step Runge-Kutta scheme ensures the time integration.

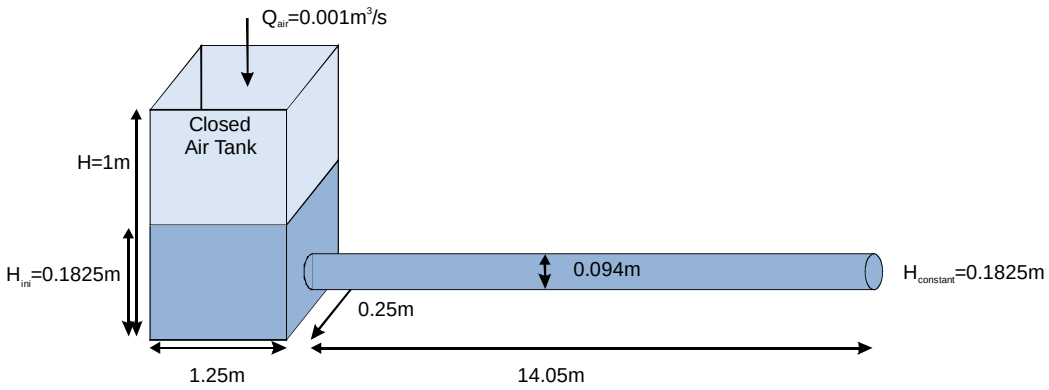

Figure 111: The injection of air within the closed tank creates a motion of water within the pipe

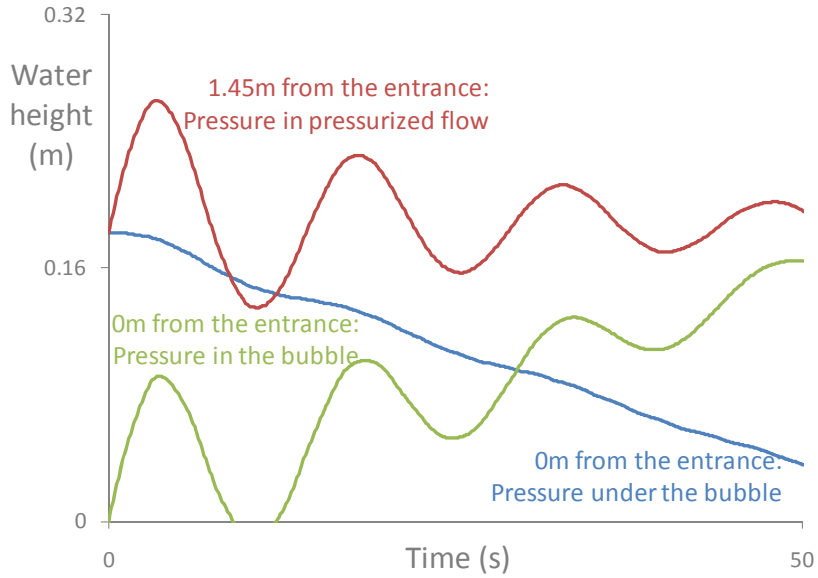

Figure 112: Injection of air within the tank increases the air pressure and decreases the water level in the tank. In addition, the pressure information propagates in the pipe as a water hammer.

At a given time, a constant discharge of 0.001m³/s of air is injected within the closed air tank. This air injection increases the pressure in the air tank, as shown in green on Figure 112. This pressure increase induces a diminution of the water level in the tank (in blue on Figure 112). Consequently, a pressure wave propagates along the pipe. Due to the

transience of the injection, this wave takes the form of a water hammer that reflects on the downstream BC (in red on Figure 112). It explains the apparition of oscillations in all time evolutions. For the pressure in the pipe, the value oscillates around the constant value imposed by the downstream BC. This value is obviously equal to the sum of the pressure within the air tank and the pressure head of the free surface flow.

As shown on Figure 113, the water height profiles at different given times show the same behavior. The more air is injected within the closed tank, the more the free surface level decreases. This variation induces a water hammer within the pipe around the constant value imposed by the downstream BC. These results qualitatively prove the ability of WOLF IMPack to treat mixed stratified flows with a fixed transition.

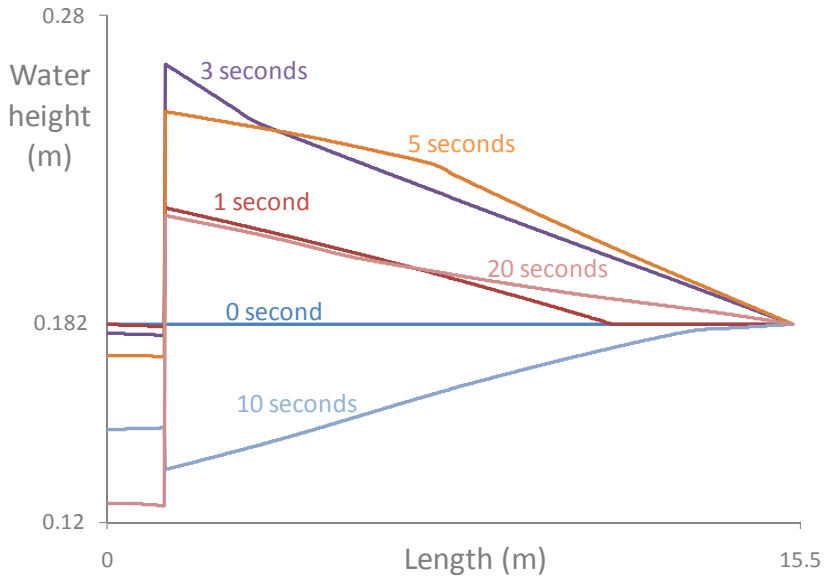

Figure 113: Water height profile at given times show the discontinuity between the water tank and the pipe

SURGE TANK DYNAMICS

Closed surge tanks constitute another interesting benchmark for WOLF IMPack. Indeed, the code may give important insight into the functioning principles of surge tanks and vessels, which are widely used in pipe networks to prevent over-pressure.

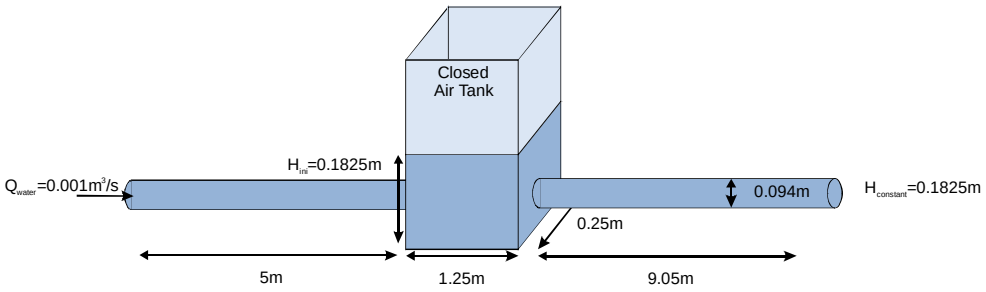

Figure 114: The benchmark exemplifies the functioning principle of a closed surge tank located in the middle of a circular pipe.

The benchmark considers a circular pipe of 0.094m diameter. A closed surge tank is placed 5m downstream the pipe entrance. The tank is 1.25m long, 0.25m large, and 1m high. Downstream the tank, a 9.05m long pipe is connected to a device keeping the pressure at 0.1825m. Initially, the water is at rest with a pressure head of 0.1825m. The discharge upstream the conduit is suddenly increased to 0.001m³/s such that a water hammer appears in the conduit.

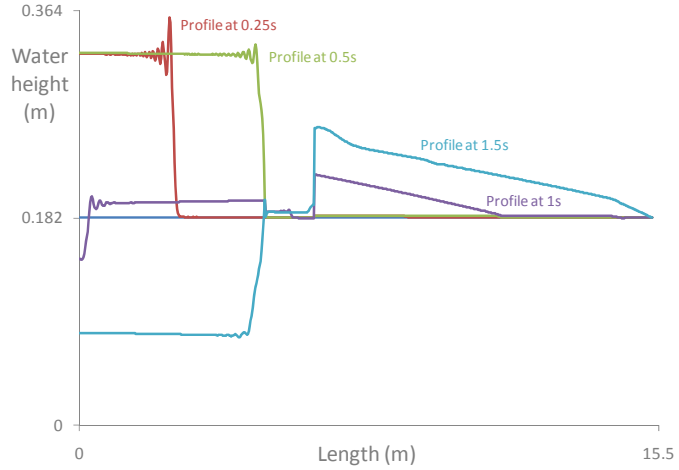

Figure 115: The pressure head profiles at different given times underlines the effect of the water tank

As shown on Figure 115, the sudden increase of discharge creates a pressure surge that propagates at the pressure wave celerity within the pipe. After 0.5s, the water hammer hits the surge tank (green curve). The level of the free surface in the tank slowly increases. As shown by the purple curve, the elevation of the free surface levels induces an increase of pressure in the pipe downstream the tank. Nevertheless, the pressure surge downstream the tank is much smaller than the increase upstream. While a high-intensity water hammer propagates between the upstream end and the tank, a smaller wave translates between the tank and the downstream end.

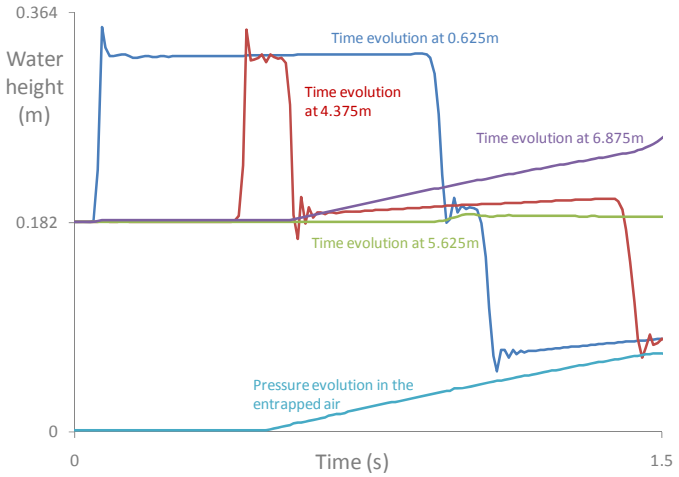

Figure 116: Time evolutions of the pressure head in the water and the air bubble give insight into the dynamics of the flow.

The time evolutions of the pressure head at 0.625m, 4.375m, 5.625m and 6.875m of the upstream end confirm this flow dynamics (Figure 116). What is more, the time evolution of the pressure head in the air bubble shows an increase of pressure due to the elevation of the free surface in the tank. Efficiency of the tank is explained by both the small celerity characteristic of free surface flows and the cushion effect of the entrapped air. In any case, WOLF IMPack proves useful to describe this behavior.

MOVING MIXED FLOWS

One of the objectives of this thesis, largely discussed in the introduction chapter, was to describe air-water interactions in transient mixed flows. For this purpose, the "mathematical shock-capturing" approach was chosen. It resulted in state-of-the-art mathematical models for both pure water (Chapter 3) and air-water flows (Chapter 7).

In Chapter 4 and 5, the discretization of the single-phase mathematical model was largely discussed and assessed. In particular, I showed that post-transition oscillations affect the numerical solution and may even compromise the stability of the computation. This shortcoming was linked to the discretization of both the equations and the computational domain. In particular, it was shown that any "numerical shock-capturing" solver was affected by this flaw. Consequently, I advised to make use of "numerical shock-tracking" solvers for computing the "mathematical shock-capturing" model.

Since the same numerical solver was used to compute the three-phase two-layer mathematical model, the same problem was expected to appear in the solution of transient mixed flows. Nevertheless, I applied WOLF IMPack on two different benchmarks involving mobile transitions:

- The entrapment of air bubbles at high point in pipelines as exposed in [98]
- The rapid filling of storm water storage pipes as described in [298, 307].

Results of this computation may be seen as a failure. Indeed, post-transition oscillations appear in the lower layer and contaminate the upper layer. Since the pressure celerity in the upper layer is large, it compromise very rapidly the stability of the computation. This observation proves again that numerical shock-capturing methods are partly inefficient in presence of highly variable celerities.

9.2 Design of a Bottom Outlet

Designing a dam requires important studies in various fields of engineering. An adequate hydraulic design contributes significantly to the security and efficiency of the structure. I exemplify this affirmation herein for a particular case: the hydraulic design of a bottom outlet placed in a dam in construction in the south of France. The study was realized in 2009 such that the gallery is partially constructed at the time I am writing this thesis.

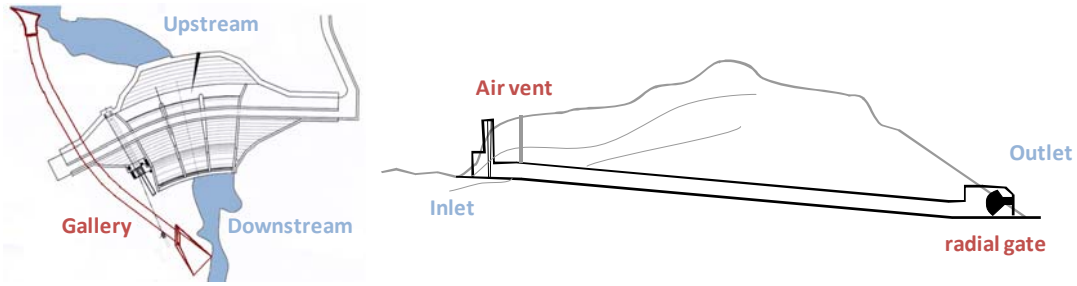

Figure 117: The gallery aims at bypassing the building site at the construction stage and at serving of bottom outlet at the exploitation stage.

As pointed in Figure 117, the gallery is a 150m long circular pipe of 4.2m diameter. At the construction stage, the gallery bypasses the river in order to keep the building site dry. At the exploitation stage, the gallery serves as a bottom outlet for emptying reservoir (and flushing the sediments). The inlet consists in a concrete structure that ensures an adequate water intake (Figure 118). The gallery inlet is designed to decrease head losses. It includes a transition square/circular that ensures the correct links between the intake and the pipe. The outlet structure in concrete is equipped with a radial gate (3.6mx3.6m) that controls the outflow in the river. The outlet also includes a transition circular/square. The level difference between the entrance and the exit of the conduit is 9.3m. The conduit slope is 6.96%.

Figure 118: Actual inlet structure has been build according to the result of the design (left). The exit of the tunnel where the outlet still need to be constructed (right)

The University of Liège was tasked to design and assess the hydraulic behavior of the gallery. It consisted mainly in determining the expected flow discharge through the gallery as a function of the water head in the reservoir. A second important point concerned the influence of the aeration rate on the flow discharge capacity. Finally, the study aimed at identifying the characteristics of the flows appearing in the gallery. For this purpose, experimental investigations have been carried out on a scale model in the Laboratory of Engineering Hydraulics (ULG-HACH). Numerical simulations performed with both WOLF1D and WOLF IMPack complemented experimental data. Since the design only considers steady cases, computations make use of the pseudo-unsteady strategy. The results of this study have been summarized in a journal paper accepted for publication in Advance in Engineering Software [176].

As shown in sub-section 9.2.2, experimental investigations on the scale model gives interesting insight into the flow dynamics. In particular, either free surface, pressurized, and mixed flows occur in the gallery. Depending on the flow discharge, strong air-water interactions appear. The six classical two-phase patterns are observed and a vortex crops up at the water intake. In absence of adequate aeration systems, air-water interactions induce a periodic instability. Addition of air vents prevents from the apparition of this instability, but it reduces the water carrying capacity of the gallery.

The first campaign of numerical simulations neglects the air-water interactions and relies on WOLF1D (sub-section 9.2.3). It enables to assess rapidly the impact of modifications onto the gallery design and to give further insight into the signification of experimental results. In particular, WOLF1D simulations accord remarkably well for free-surface and pressurized flows (for which air-water interactions are mild), but not for mixed flows with intense air-water interactions.

The incapacity of WOLF1D to take into account air-water interactions suggest to use WOLF IMPack for performing a multi-phase computation.

9.2.1 DESCRIPTION OF THE SCALE MODEL

The experimental facilities are made of two tanks (an upstream and a downstream one) linked by a 5m long circular gallery with a 0.14m diameter. The scale model corresponds to the actual gallery at a 1/30 Froude scale. The natural topography of a mountain river bed is represented in both tanks. The gallery inlet and outlet are located in the right bank of the river, at the level of the river bottom. The constant gallery slope is 6.96 percents. A radial gate is placed at the outlet to control the discharge. The flow is there critical. The tanks are made of steel. The tanks topography has been build with concrete blocks and mortar painted with latex (Figure 120). The gallery is in transparent Plexiglas, and the inlet and outlet are made of aluminum and PVC. The roughness height of the gallery has been estimated to be 2.10^{-5}m.

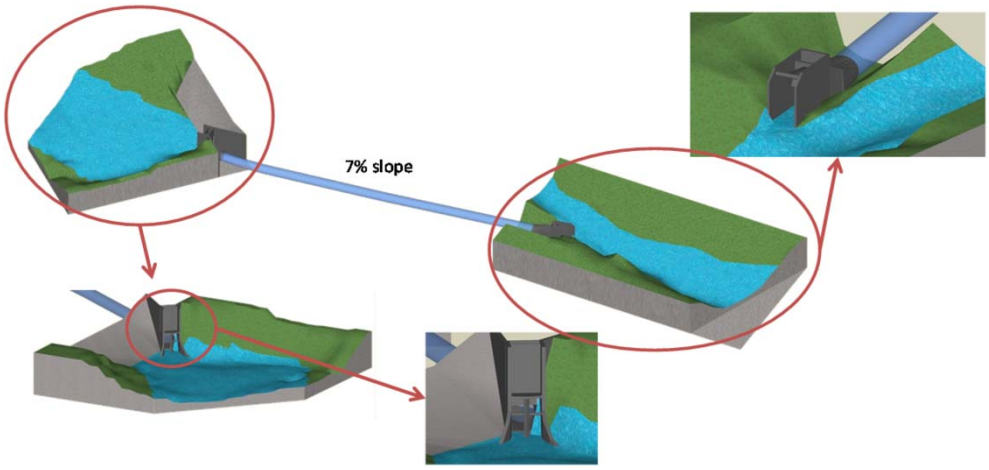

Figure 119 : Sketch of the experimental device

The water feeding system is a closed circuit that injects water in the upstream tank and collects water flowing from the downstream tank. The discharge in the upstream tank is the upstream boundary condition. The head level upstream of the gallery regulates naturally regarding the gate-opening rate and the system release capacity. Downstream of the physical model, the natural topography is very steep so no specific boundary condition is needed (trans-critical flow).

The model is equipped with the following measurement system. The upstream discharge is measured with an electromagnetic dischargemeter (accuracy of ± 1l/s) on the pumping system. The water level in the upstream tank is measured using a limnimeter (accuracy of 0.1mm), a Pitot tube (accuracy of ± 0.1mm), and an electronic piezo-resistive transducer (accuracy of ± 0.1 mm, sampling rate of $100s^{-1}$). 9 Pitot tubes and 5 electronic piezo-resistive transducers (accuracy of ± 0.1mm, sampling rate of $100s^{-1}$) are regularly distributed along the gallery to measure the pressure head in the gallery (accuracy of ± 0.1mm). 14 graduated scales are fixed on the gallery perimeter to measure the water level for non-pressurized flows.

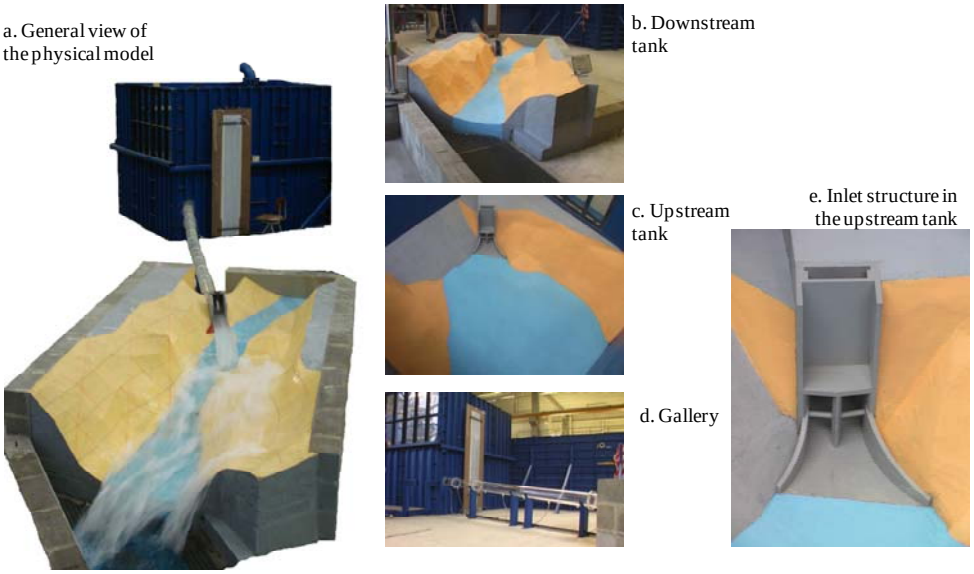

Figure 120 : Details of the physical model

9.2.2 EXPERIMENTAL RESULTS

Investigations consider only stationary flows. We mostly aim at determining the flow discharge through the gallery as a function of the upstream pressure head. As pointed in Figure 121, the flow discharge in the gallery depends directly on the value of the upstream pressure head (zero level is set at the upstream reservoir bottom level). The bigger the head in the reservoir is, the bigger the discharge in the gallery is. In free-surface flows (lower discharge), a small increase in the pressure head entrains an important increase of the discharge. To put it another way, the slope of the curve is relatively horizontal. In pressurized flows (higher discharge), an increase of pressure head induces a lower increase in the discharge. This is a standard result from single-phase fluid mechanics.

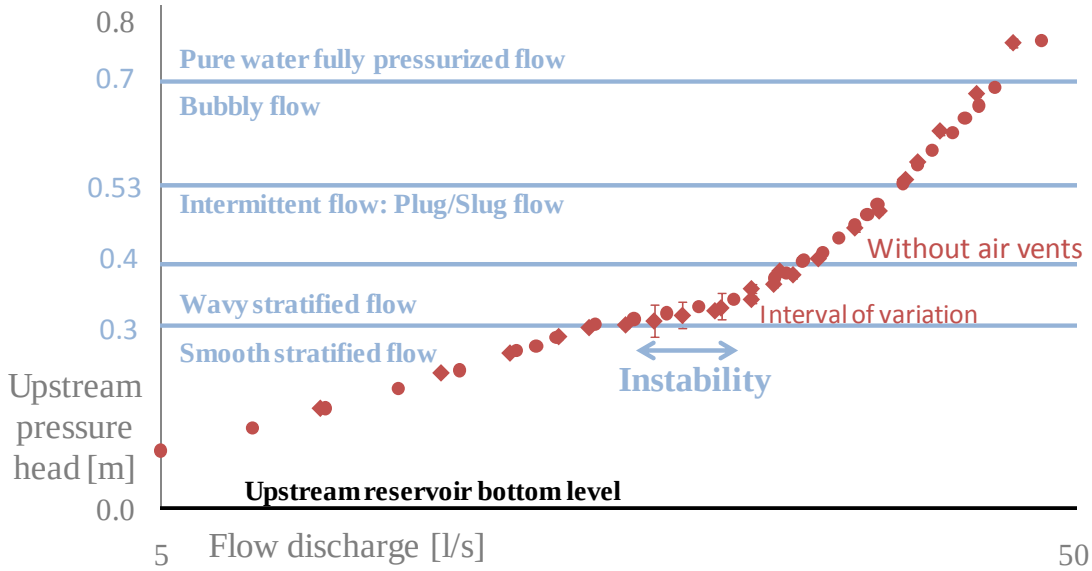

Figure 121: Experimental discharge curves (pressure head-flow discharge) are affected by air-water interactions

AIR-WATER INTERACTIONS AFFECTS THE FLOW IN THE GALLERY

Various air-water interactions considerably affect the discharge curve and the flow behavior. Indeed, the 6 flow patterns (Figure 121) traditionally mentioned in the literature [313] are experienced in the gallery:

- Smooth stratified flow is observed for pressure head below 0.3m (Figure 121). It is characterized by two phases, air and water, flowing separately by gravity. A smooth interface between phases appears only if both phases flow with almost the same velocity.
- Wavy stratified flow is observed for pressure head between 0.3m and 0.4m. This flow does not differ that much from smooth stratified flow in terms of hydro-mechanic characteristics. Surface ripples and waves appear and create a rather rough interface.
- Slug and plug flows are observed for pressure head between 0.4m and 0.53m. Slug flow appears when the waves touch the top of the tube and form a liquid slug which passes rapidly along the gallery. In plug flow, large bubbles flow near the top of the tube. As the transition from plug to slug is gradual and not very sharp, plus and slug flows are often simply referred to as intermittent flow patterns with no further specifications. This flow pattern is not strictly speaking a steady flow as it is characterized by a time periodic oscillation between a free surface flow and a slug flow, according to the aeration rate and the amplitude of the waves. This leads to significant fluctuations in the measured data.
- Bubbly flow, characterized by the entrainment of small bubbles dispersed in the liquid continuum, is observed for pressure head between 0.53m and 0.7m. The larger bubbles (but smaller than the resulting pockets during plug flow) propagate below the conduit ceiling due to buoyancy. Smaller bubbles, primarily transported by liquid turbulence, may be detected dispersedly over the whole cross-section. Bubbles appear where the pressure of the liquid falls below the atmospheric pressure.
- Pure water pressurized flow is observed for pressure head above 0.7m. This is the most classical flow pattern in fluid mechanics.

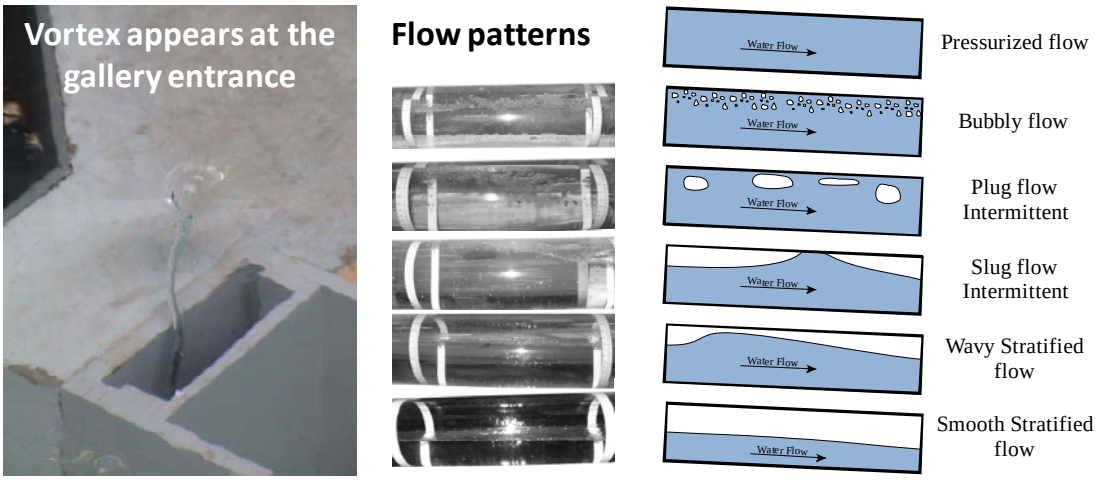

Figure 122: Various two-phase flow phenomena appears according the pressure head in the reservoir

In absence of air vents, a vertical vortex appears at the gallery entrance for pressure heads between 0.3m and 0.53m. This vortex entrains water to supply the phase flowing above the free surface as well as the dispersed phase within the water flow. The dissolved air in water (2% at atmospheric pressure) also aliments bubbles appearing in the flow.

The absence of air-supply system induces a periodic instability originating from the variations in the aeration rate. This instability seems to be first evocated in [216]. It appears under the form of large period oscillations of the water level in the upstream reservoir (10 to 60 seconds). The amplitude of the oscillation reaches 0.02m. In addition, pressure oscillations all along the gallery may reach amplitude of 0.04m. The inception of the instability is intimately linked with the aeration rate of the gallery, and in particular the amount of air entrained through the vertical vortex appearing at the water intake. Indeed, the minimum of the oscillation corresponds to a highly stratified flow below an air phase at sub-atmospheric pressure. This flow pattern gives the minimum water carrying capacity for a given upstream head. If the upstream reservoir is supplied with a constant flow discharge, the water level in the reservoir increases. As the water level arises in the reservoir, the amount of air entrained through the vortex decreases [250]. Decrease of the air void fraction in the flow generates the formation of Kelvin-Helmholtz instabilities characteristic of intermittent flows (pressurized flow pattern). The maximum of the oscillations corresponds to this poorly aerated intermittent flow. This flow pattern corresponds to the maximum water carrying capacity for a given upstream head. Consequently, the water level decreases because the flow discharge in the gallery is higher than the flow discharge supplying the reservoir. The cycle of the instability may then start again.

As pointed in Figure 123, the measured pressure profile for a discharge of 38.4 l/s exhibits large oscillations due to intermittent character of the flow and the instability described above. What is more, the pressure in the pipe becomes lower than the atmospheric pressure in some parts of the flow. Distributions of two values are plotted on Figure 123, the water head and the total head along the gallery. Data measured with the pressure transducers includes an interval that delimits the maxima recorded during the trial. These intervals give a good idea of the importance of variations in these flows.

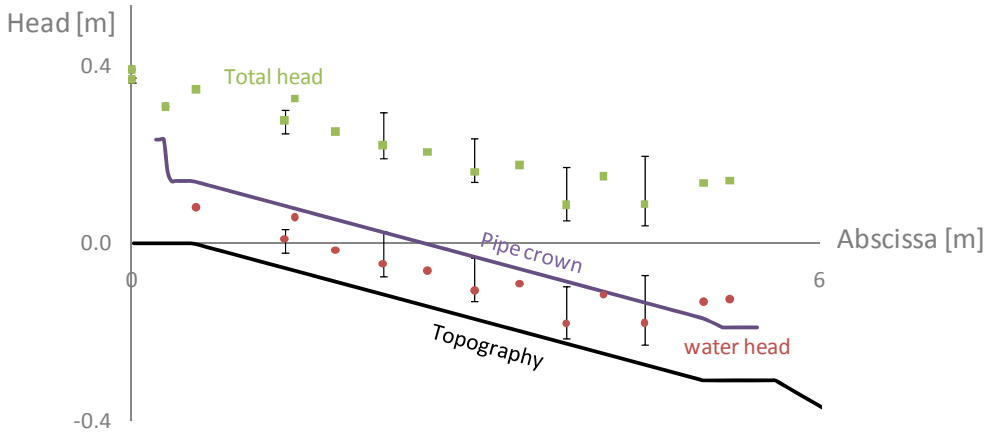

Figure 123: For a discharge of 38.4l/s, the pressure profile exhibits large oscillations and negative pressures

In order to decrease the amplitude of the instability, three air vents with a 0.02m diameter are added just downstream the gallery inlet, on the top of the circular cross-section. The purpose of these vents is to ensure an adequate aeration rate to the gallery. It prevents the apparition of both sub-atmospheric pressurized flows and the instable cycle. As pointed on Figure 124, addition of air vents does not affect the discharge capacity of the gallery for pure water free-surface and pressurized flows. On the opposite, the water-carrying capacity of the gallery diminishes when two-phase interactions arise. The area of observation of each flow pattern is also affected. The ranges of discharge corresponding to both bubbly and intermittent flow are narrowed to the benefit of the wavy stratified flow. This result is logical since it was the purpose of adding air vents.

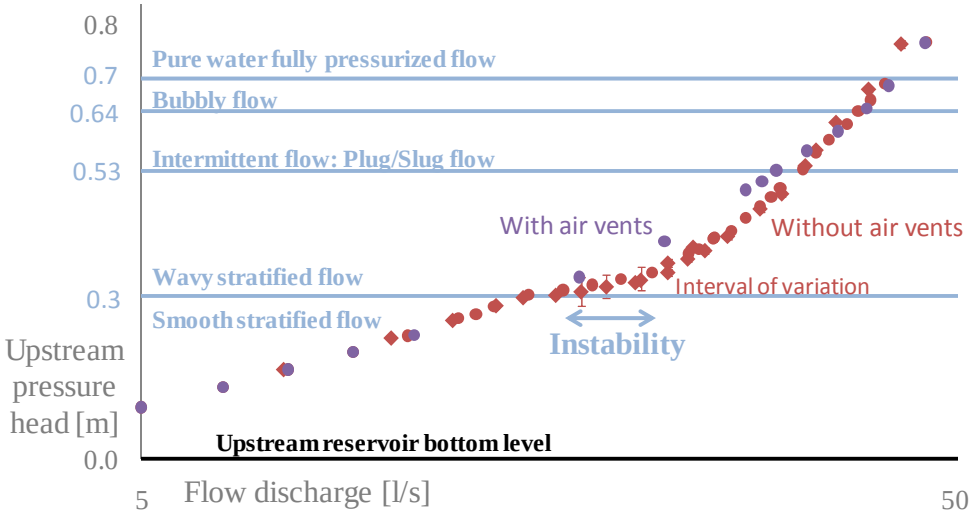

Figure 124: Adding air vents reduces the amplitude of the instability, but also the water carrying capacity

PARTIAL CLOSE THE RADIAL GATE REDUCES THE FLOW DISCHARGE

When the radial gate at the downstream end is closed, the water discharge capacity of the gallery considerably decreases and the pressure profile drastically changes. For a given upstream total head, the most the gate is closed, the smaller the discharge capacity of the pipe is. Logically, a pressurized flow occurs faster, and the transition area is thus smaller. Air-water interactions are also less intense. A stationary hydraulic jump characterizes the transition area. In fact, the downstream part of the pipe is pressurized while the upper part is a super-critical free-surface flow. The hydraulic jump entrains a certain amount of air. It forms a mixed flows with air-water interactions.

Figure 125: When the gate is partially closed (80% here), a stationary hydraulic jump occurs in the transition area

The discharge capacity of the gallery is measured for a closure rate of 20%, 40%, 60% and 80%. In all these cases, three air-vents supply the gallery in air. Summarized in Figure 126, experimental data defines 5 different curves. The transition between the free-surface and the pressurized flow pattern appears clearly on the graph.

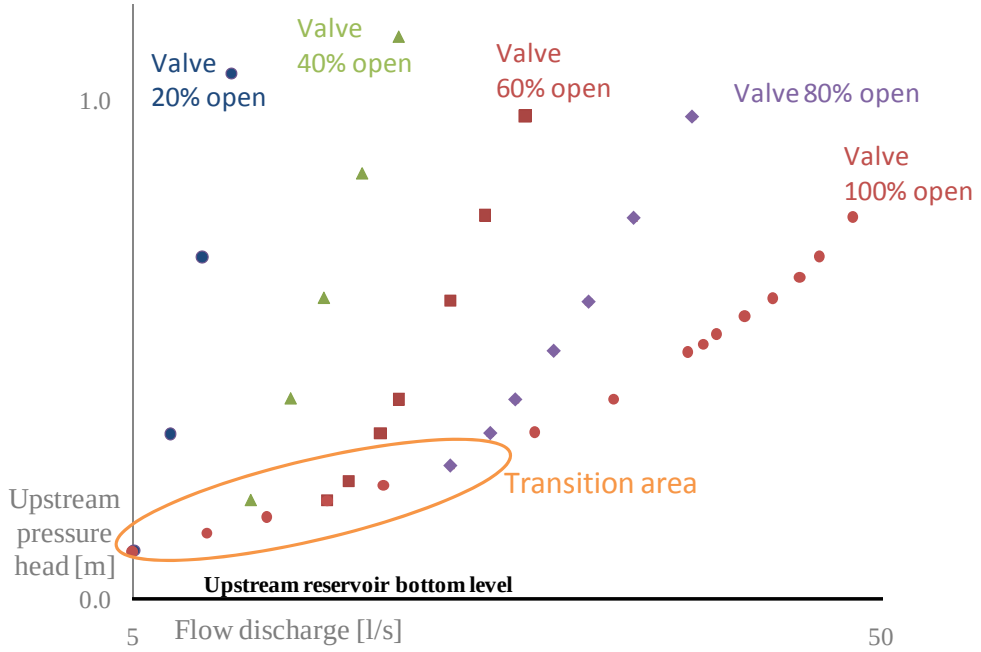

Figure 126: Partial close of the radial gate decrease drastically the discharge capacity of the pipe

9.2.3 Comparison with Single-Phase Numerical Result

Simulations performed with WOLF1D constitute a first complement to experimental data. As presented in chapter 4, WOLF only considers pure water flows. However, comparing numerical and experimental data enables to assess rapidly the impact of modifications onto the gallery design. It also gives further insight into the experimental results. Consequently, this section presents the results of the computation performed on the gallery with a single-phase code. Since the design only considers steady cases, computations make use of the pseudo-unsteady strategy. Presented in chapter 3, the state-of-the-art model is shown reliable for depicting free-surface, pressurized, and mixed flows. The correct capture of negative pressure is also underlined by the comparison. As expected, the model fails to account for situations where air-water interactions arise. Finally, the pseudo-unsteady strategy proves very efficient in terms of computation effort.

Simulations are performed under the assumption of a pure water flow (void fraction is equal to zero), with a spatial discretization step Δx=3.33cm. Since a three step Runge-Kutta scheme is used, the CFL number must be limited to 0.5 for stability reasons (this limitation results from non-linear stability analysis proposed in [144]). Simulation considers non uniform sections as measured on the scale model. For distributed head losses, the Colebrook-White correlation is used with a roughness height $k_D = 2.10^{-5}$m (corresponding to the properties of PVC). For local head losses, the computation integrates two contributions.

A first one results from the reaction of the banks on the flow and is taken into account naturally by the computational code (because it relies on the non-conservative Saint-Venant equations). Here and there, a second head loss coefficient accounts for the additional contribution due to elements non explicitly described, like the flow disturbance.

GATE OPEN AT 100%

These first results do not consider the effect of the downstream radial gate. As pointed in Figure 127, WOLF1D gives two discharge capacity relations for a flow discharge ranging between 5l/s and 55l/s. A first head/discharge relation is computed by assuming that a free surface appears in each mesh if the water height is below the pipe crown (air phase above the free surface is at atmospheric pressure). The second head/discharge relation is computed by activating the negative Preissmann slot (sub-atmospheric pressurized flow). Numerical results are in good accordance with experimental data for smooth stratified and fully pressurized flows. This is not the case anymore for other air-water flow patterns.

In presence of air vents, experimental data stay closer to the free-surface curve (green) for all discharge value. However, the matching is not perfect, especially when observing wavy stratified and intermittent flows. One may draw the conclusion that air-water interactions arise even if air vents supply the gallery. What is more, computations clearly show that aerating the gallery diminishes its discharge capacity.

Without air vents, bubbly and intermittent flows show important discrepancies with the numerical data. In these areas, the flow exhibits a similar behavior to the sub-atmospheric pressurized flows (purple), but the presence of air reduces the discharge capacity. What is more, the transition from pressurized to free-surface is subjected to a flow instability [96, 216]. As clearly showed by numerical results, the instability oscillates between a free-surface flow and a sub-atmospheric pressurized state. It confirms my first conclusion presented in the previous section.

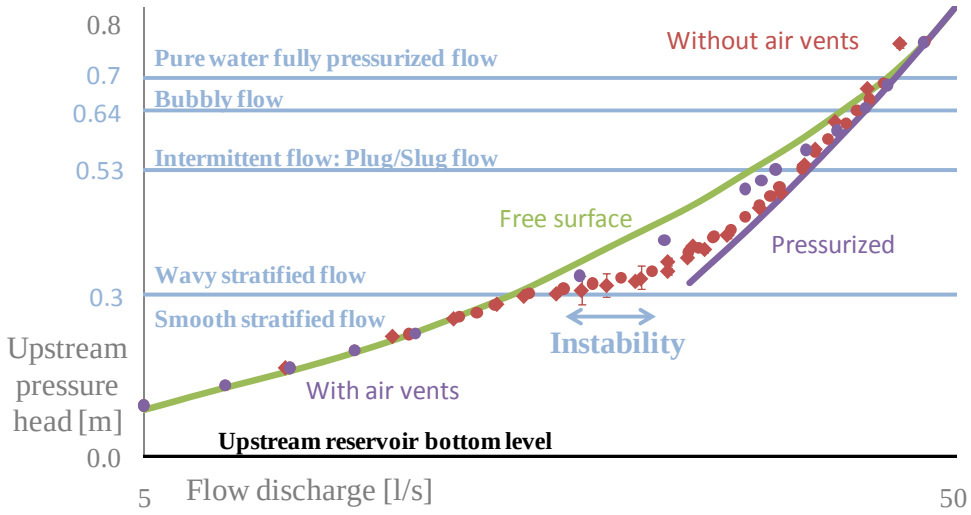

Figure 127: WOLF1D enables to draw two curves: the green one if the gallery is adequately aerated such that a free surface may appear; the mauve one that the gallery is not supplied in air (sub-atmospheric pressurized flow)

The analysis of the pressure and total head profiles along the gallery proves the ability of WOLF1D to simulate pure water mixed flows. For a pressurized flow of 51 l/s, both the computed pressure and total heads accord with the experimental data measured with the pressure transducers and the Pitot tube (Figure 128). It underlines the ability of the modified WOLF1D module to simulate pressurized flows as well. For a free-surface flow, the accordance between experimental and numerical results is also obvious. As pointed in Figure 129, profiles for a discharge of 9.5l/s correspond.

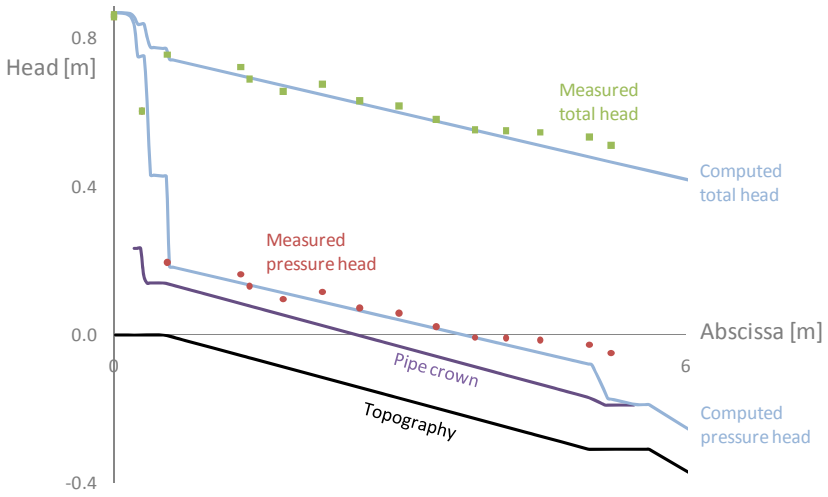

Figure 128: For a pressurized flow of 51l/s, the profiles of pressure and total heads computed with WOLF 1D accord with experimental data.

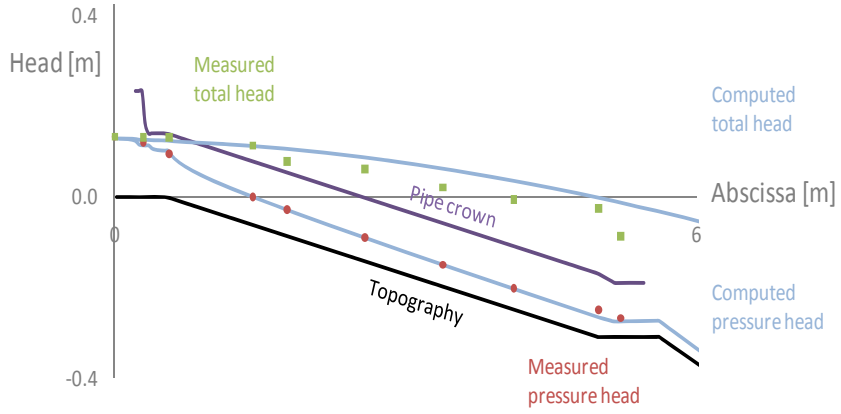

Figure 129: For a free-surface flow of 9.5l/s, the profiles of pressure and total heads computed with WOLF 1D accord with experimental data

As expected, numerical and experimental data for the profiles diverge as soon as air-water interactions arise and affect the flow behavior. This result is logical since the model is only single-phase. For a free surface flow of 18l/s, WOLF1D gives a good evaluation of the required upstream pressure head (0.23m). However, other measured data within the gallery diverges from the computed data (Figure 130). It suggests that the air layer above the free-surface is not anymore at atmospheric pressure. Consequently, the negative pressure above the free-surface alter the water flow. A similar conclusion holds for intermittent and wavy stratified flow, with the aggravating circumstance that air may now be entrained within the water flow. For a flow discharge of 32.5l/s, the flow is wavy

stratified. WOLF1D provides two profiles (Figure 131). The first assumes that the gallery is airtight such that a free-surface cannot appear. The profile makes thus appear sub-atmospheric pressure at the entrance of the pipe. The second profile assumes that the pipe is adequately supplied in air through air vents. The resulting flow exhibit a clear free surface. Both profiles differ from the experimental data. Computation suggests however that the actual flow is a pressurized flow partially aerated.

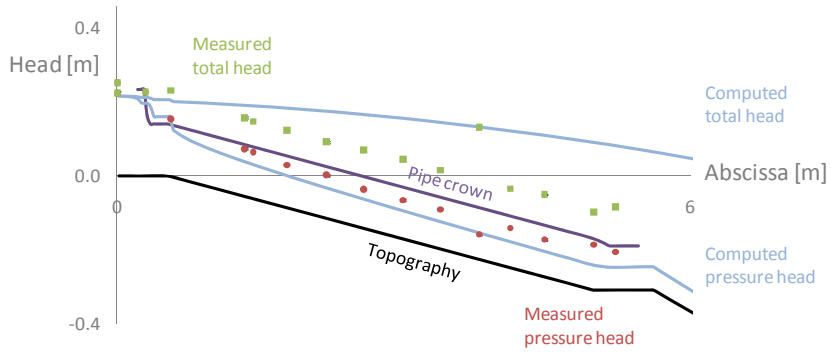

Figure 130: For a free-surface flow of 18l/s, the profiles of pressure and total heads computed with WOLF 1D do not accord with experimental data, even if the upstream head is correct.

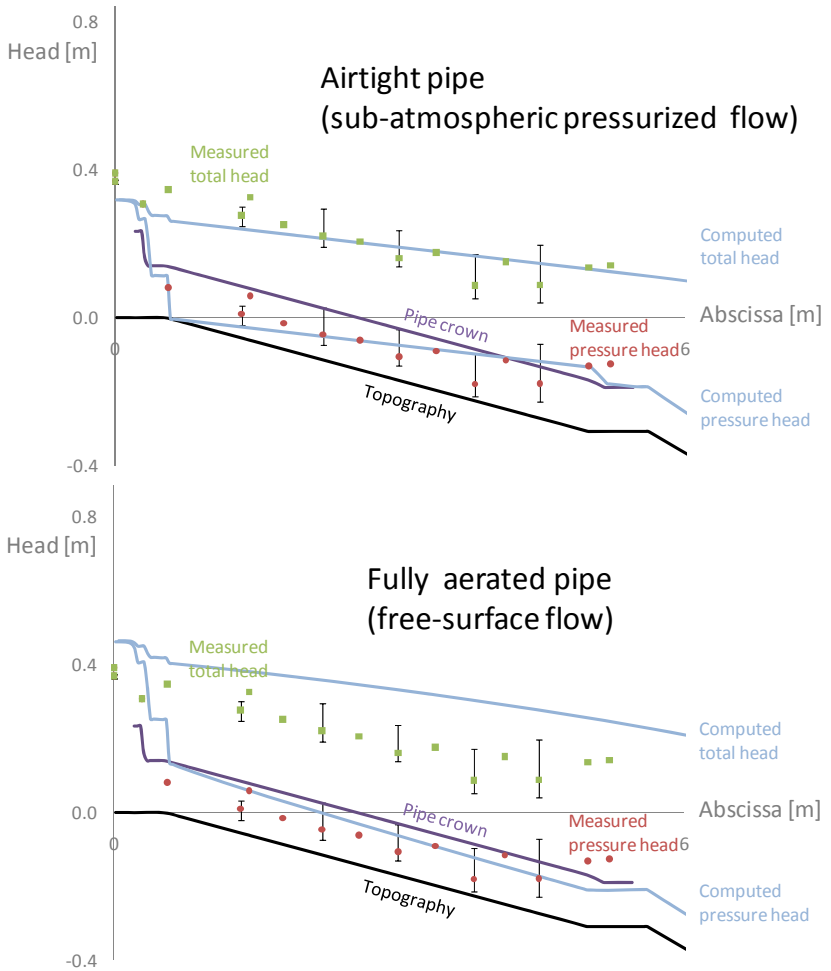

Figure 131: For a free-surface flow of 35.2l/s, WOLF1D gives two profiles of pressure and total heads according to the assumption made on the aeration rate

INFLUENCE OF THE PARTIALLY CLOSED GATE

Adjusting the height of the rectangular section in one mesh enables to account for downstream valve closure in the computation. The height of the cross-section at the gate position is given by the following function [151]:

$$H_{Gate} = C_{open} * C_{contraction} * H_{max} \quad (1.8)$$

where C_{open} is the coefficient of opening in percent, $C_{contraction}$ is the coefficient of contraction, and H_{max} is the maximum height of the pipe (gate opened at 100%). The coefficient of contraction is defined as the ratio between the normal wetted cross-section over the nominal area of the cross-section. The variation of $C_{contraction}$ in function of C_{open} has been determined from experimental data (Figure 132). It results in a polynomial of order 4.

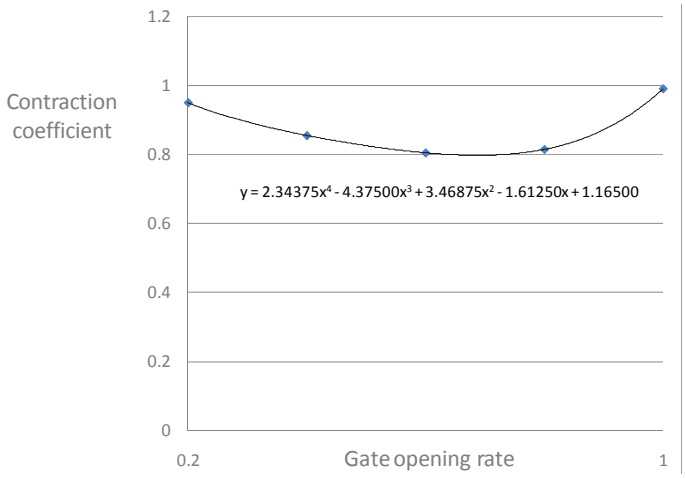

Figure 132: The law for the coefficient of contraction is given by a polynomial of order 4.

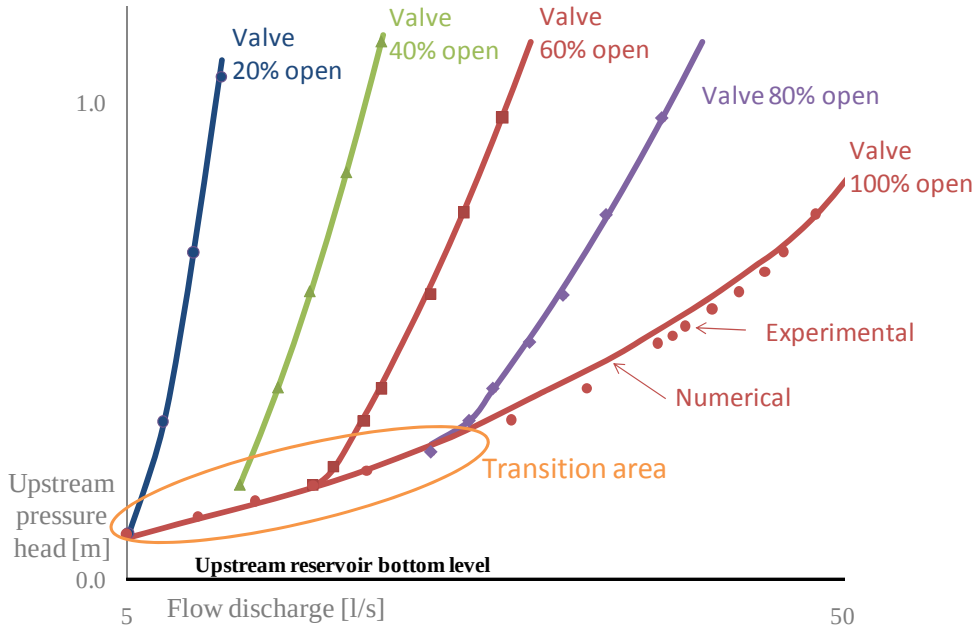

Figure 133: When the radial gate is partially closed, the measured discharge capacity of the gallery accords with the curves computed with WOLF1D

When the radial gate is partially closed, the measured discharge capacity of the gallery accords with the curves computed with WOLF1D (Figure 133). For lower upstream pressure head, the rate of closure does not affect the discharge since the stream is free-surface and flows below the gate. The discharge curve is thus identical to the one calculated for an open gate in presence of air vents. When the free surface reaches the lower part of the gate, it creates a concentrated head loss that limits the discharge capacity of the gallery. As pointed in Figure 133, the slope of the curve becomes steeper. The more the gate is closed, the steeper the curve is. This obstruction of the stream induces a very fast pressurization of the gallery. Air water interactions are very limited in such cases. Consequently, computed curves accords with the measured data. It proves again the reliability of our approach.

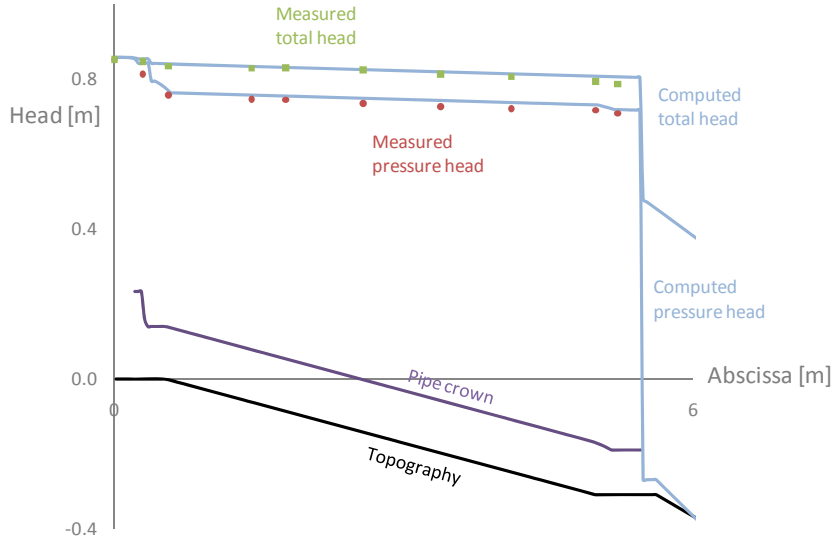

Figure 134: When the gate is only 40% open, a discharge of 18.9l/s corresponds to a fully pressurized flow

Accordance between experimental and numerical data is also obvious in the profiles of pressure and total heads. In Figure 134, the profiles computed for a discharge of 18.9l/s with a gate at 40% open accords with experimental data. The concentrated head loss at the gate is obvious on this curve. For a discharge of 24.1l/s and a gate open at 80%, a stationary mixed flow pattern appears in the gallery. The free-surface/pressurized flow transition corresponds to a hydraulic jump. The compute profiles accord quite well with the experimental data, except for the location of the transition. Its position is indeed extremely sensitive to the flow condition. Because of this, the result is considered extremely accurate.

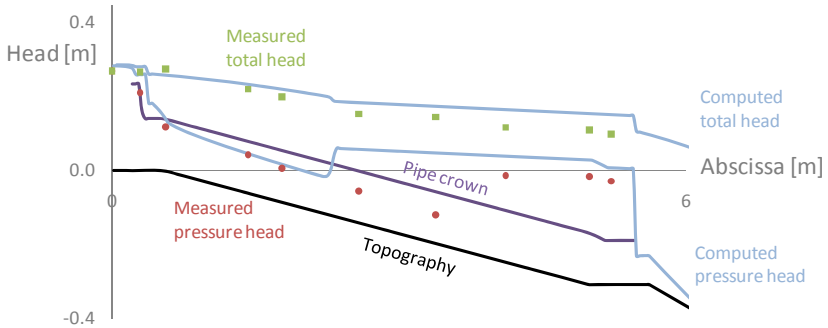

Figure 135: When the gate is only 80% open, a 24.1l/s flow discharge corresponds to a stationary mixed flow

9.2.4 Comparison with Multi-phase Results

Since WOLF1D gives inaccurate results when air-water interactions arise in the pipe, The multiphase code WOLF IMPack is used to enhance the accuracy of the computation. Fo this purpose, we consider the exact same simulations than previously, except that the air phase is taken into account. The spatial discretization step Δx=3.33cm. A three step Runge-Kutta scheme is used for the time integration. The CFL number is limited to 0.5.

To close the diffusion equation, I use the same fundamental relation for the phase change volume generation as for the stepped spillway (sub-section 9.1.3):

$$\left\langle \Gamma_g / \rho_g \right\rangle \Omega = -m\Gamma\left(\alpha_g - \alpha_{g,eq}\right) \tag{9.9}$$

where Γ and $\alpha_{g,eq}$ are constants calibrated with experimental results (this last one is the equilibrium air concentration reached when the flow is fully developed). The onset of air entrainment is controlled by the parameter m=1 or m=0.

Single-layer computation

In a first time, I neglect the effect of the upper layer and compute a single-layer pressurized flow with air-entrainment. The effect of the entrained air on the water flow is accurately computed by using equation (9.9) for the phase change volume generation Γ_g. The parameter Γ is set at 25 and α_g is calibrated according to the flow pattern observed. For bubbly flows, as bubbles arise from the air dissolved in water, equilibrium void fraction is chosen between 0.5% and 2%. For intermittent flows, an additional air supply is provided through a vertical vortex appearing at the water intake. Equilibrium void fraction is then chosen between 2% and 4.5%.

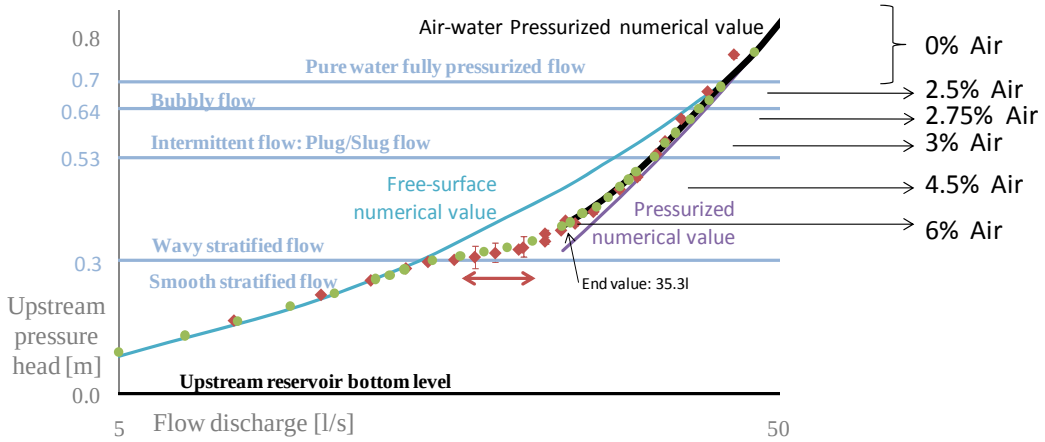

Figure 136: Results in terms of upstream pressure head and void fraction of the air-water mixture simulation

As shown on Figure 138, the discharge curve computed by assuming such a variation of the equilibrium void fraction accords better with the experimental curve (without air-pressure). By assuming an aeration rate between 0% and 6%, WOLF IMPack provides a correct curve for discharges above 35.3l/s. This is a clear improvement by comparison with the single-phase WOLF1D. The pressure head and water head profiles computed with WOLF IMPack

accords also better with experimental results (Figure 137). This last figure was computed for a pressurized flow of 35.2l/s and an equilibrium void fraction of 6%.

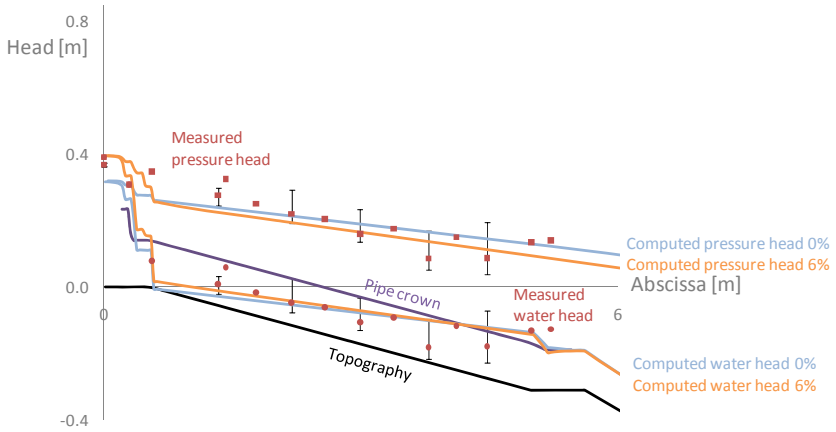

Figure 137: For a pressurized flow of 35.2l/s, WOLF IMPack provides both a pressure head and a water head profile in better accordance with experimental results.

The influence of the friction correlation on the simulation results is an important issue worth to investigate. For this purpose, a computation is performed for a bubbly flow of 36.5 l/s, a void fraction of 4.5%, and four friction correlations: the Homogeneous Colebrook-White (k_D = 2.10^{-5}m), Homogeneous Blasius, Lockhart-Martinelli, and Müller-Steinhagen and Heck. Results in terms of the upstream total head, which is the parameter the most affected by the friction, are given in Table 14. Obviously, accuracy of the results is only slightly affected by the choice of the friction correlation. It results from the feeble roughness and air void fraction observed. However, simulation on large scale prototype exhibits important discrepancies. Further research is thus required to integrate both the effect of the pipe roughness and of the multiple phases.

Table 14: Comparison between the various friction correlations

	Upstream Total Head [cm]	Error [%]
Experimental	40.53	
Homogeneous Colebrook	39.5036	2.5%
Homogeneous Blasius	39.5027	2.5%
Lockhart-Martinelli	39.5004	2.5%
Müller-Steinhagen and Heck	39.5018	2.5%

Summary and conclusion

The validation campaign presented in section 9.1 proves the efficiency and usefulness of WOLF IMPack with respect to the simulation of transient air-water flows in open channels and closed conduits. Applied to pure water flows, WOLF IMPack gave the exact same results as WOLF1D (Chapter 5). It also accounted adequately for air entrainment in pressurized flows (two-phase water hammer) and free surface streams (stepped spillway). To some extent, computation of the upper layer dynamics enabled to account for air entrainment in closed conduits. Indeed, WOLF IMPack gave good results for mixed flows with a fixed transition. However, post-transition oscillations appeared in the solution like for WOLF1D. They contaminated the upper layer and compromise very rapidly the stability of the computation. Except this restriction, WOLF IMPack may be considered as a success with respect to the objectives of this thesis.

In section 9.2, WOLF IMPack was applied to the hydraulic design of a real case, namely the bottom of a large dam. Experimental investigations on a physical model underlined the apparition of strong air-water interactions that affects the flow dynamics. Application of the single-phase code made appear discrepancies in the results. By using WOLF IMPack, part of problem was overcome. WOLF IMPack gave insight into the measured data. In addition, it enabled to predict accurately the effect of design modification on the discharge capacity of the gallery and the pressure profile along the structure.

In conclusion, this chapter showed that the new multiphase mathematical model developed in this thesis enhance the fidelity of hydraulic software's and constitute a useful tool for civil and environmental engineer. Based on these results, further work is needed or wished. I present some of the perspectives of this research in the following chapter.

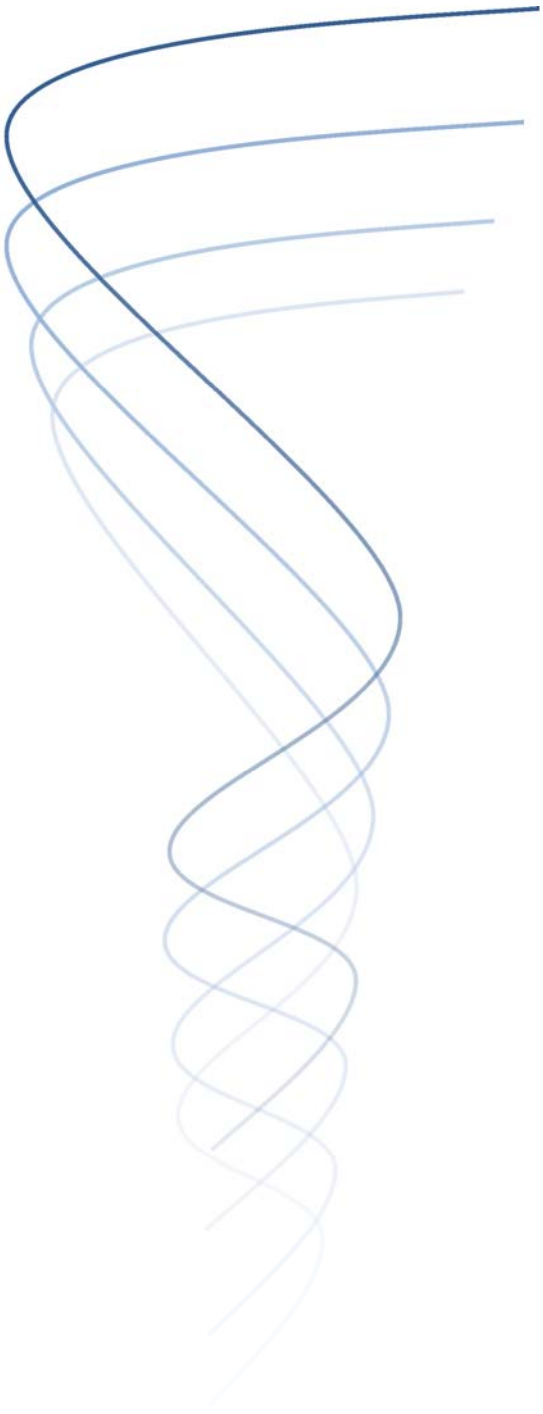

Modelling Transient Air-water Flows in Civil and Environmental Engineering

Part III: Generalization

Chapter 10 Generalization to Environmental Flows

This chapter aims at:

- ✓ generalizing the drift-flux theory to other transport phenomena;
- ✓ developing a 2D shallow-water-like drift-flux model;
- ✓ extending applicability of 2D free surface models to mixed flows;
- ✓ introducing the notion of double-averaged models.

Initially, the identification of shortcomings and knowledge gaps in classical models for one-dimensional air-water flows has initiated the investigations whose results are presented in this thesis. In this respect, my work led to two scientific propositions. First, I showed that both single- and multi-phase one-dimensional models describing free surface flows could be extended to pressurized and mixed flows. Second, I proved that the drift-flux model provided an improved description of free-surface flows affected by air-water interactions. All these results successfully meet the different objectives of my doctoral research.

Nevertheless, I have every reason to believe that these two propositions provide a fruitful theory for investigating not only 1D air-water flows, but also many other phenomena of interest in civil and environmental engineering. Indeed, there exist many hydraulic phenomena whose understanding and description requires additional works. They constitute as many challenges for researchers and engineers. In this chapter, I identify three fundamental problems into which the drift-flux theory should provide more insight.

As mentioned in chapter 2, the application of multiphase theories has remained circumscribed to a very limited number of attempts in civil and environmental engineering. The success of the drift-flux theory for air-water flows prompts me to investigate if the approach could give interesting results when applied to other transport phenomena. Indeed, similar shortcomings affect classical models describing water flow with transport of sediments or pollutants.

In a similar manner, transversal velocities arise in many flows such that the one-dimensional approach is not anymore valid. It is still possible to solve the 3D model but it requires sophisticated algorithms and resources beyond the present computational capability. Tracking the interface and generating 3D meshes requires indeed a very large number of operations. Accordingly, an intermediate model is necessary between the one-dimensional approach and the three-dimensional model.

Finally, interactions between the flow and the boundaries of its domain may affect considerably the fluid motion. In particular, vegetation and macro-roughness constitute mobile boundaries that strongly affect the hydrodynamic of the flow and the properties of dispersion. The correct capture of these features is still challenging in both mathematical models and subsequent computational codes.

All these limitations and knowledge gaps pave the way for further research in relation with the results of this thesis. Accordingly, I already anticipate here the next steps of research by widening my results to other environmental flows. To be more precise, I provide preliminary results and avenues worth exploring with respect to the shortcomings identified above. First, I extend the applicability of the original multi-layer one-dimensional drift-flux model to the main transport phenomena in free surface flows (section 10.1). The multiphase approach enhances the fidelity of the description of sediment and pollutants transport. Second, I develop an original shallow-water-like drift-flux model that is an intermediate model between 1D and 3D models (section 10.2). The model is able to simulate 2D free surface flows and even 3D intricate streams when using methods to accommodate the depth-integration with the vertical distribution of the flow parameters. Third, applicability of both the shallow-water model for pure water flows and the shallow-water-like model for two-phase flows is extended to pressurized flows as well. For this purpose, I develop an original Preissmann tube that is placed at the top of the computational model. Finally, time-integrated models are shown inadequate when applied to streams affected by scale heterogeneities like turbulent flows over rough-beds and canopies (section 10.4). For overcoming this flaw of classical approaches, the use of Double-Averaged Models (DAM) is growing. DAM has been successfully used for developing numerical models, designing experiments, data analysis and interpretation, and guiding conceptual developments and parameterizations [237]. Since the current research trend suggests that DAM may soon become a standard tool, I investigate in section 10.4 the main features of the approach and their implications with respect to the objectives of the research. Most of the preliminary original results presented in this chapter have been presented in a book [173], a chapter book [172], a journal paper [171], and a conference paper [170].

10.1 Unified Description of Transport Phenomena in Environmental Flows

From a general point of view, hydraulic engineering treats of the conveyance of fluids in natural or anthropogenic environments, which I called environmental flows in this thesis. In first approximation, such situations are treated by analyzing the flow as pure water flowing in an immutable external environment. However, this approach neglects the various interactions that may arise between the flow and the global system in which it is inserted.

Mechanisms of interaction that could alter the flow behavior are multiple. The first kind, air-water interaction, has been widely investigated in this thesis. Nevertheless, it is not the only type of transport phenomenon that may affect the flow dynamics. Indeed, sedimentation and erosion also result from the transport of a dispersed phase within the water flow [13]. In this second case, the interaction is highly reciprocal since sedimentation alters the bed topography as well as suspended sediments alter the water flow behavior [13, 80]. Sedimentation analysis is largely used for the design of storm-water storage reservoirs and dam reservoirs [87], for fluvial geomorphology analysis [323], for streambank and coastal erosion assessment (Figure 138), for bridge scour evaluation, for gravity current analysis [42],… Third, a most sensitive interaction arises between pollutants and shallow water flows such as rivers, lagoons, and coastal regions. In many situations, this pollution has detrimental impact on the environment and may cause potential risk on the human health and local economy. Efficient and reliable estimates of damages are impossible without knowledge of acting processes [22].

Figure 138: Examples of pollutant release in a river (left) and of erosion, deposition, and sediment transport (right)

In this section, I show that standard mathematical models describing sediment and pollutant transport suffer shortcomings analogous to their counterparts for air-water flows. Consequently, I assess the applicability of the drift-flux theory for all types of transport phenomena. Even if both the sediment dynamics and the pollutant dispersion differ from the behavior of air bubbles, the multiphase approach rigorously gives a set of equations that enhance the fidelity and enable the unification of the description of these processes. Originally presented in a book I published with colleagues of the HACH [173, 174], this result paves the way to the creation of a unified multiphase computational code for all transport phenomena in civil and environmental engineering.

10.1.1 FUNDAMENTALS OF SEDIMENTS TRANSPORT

In sedimentation engineering [13], two transport modes are traditionally distinguished, namely bed load transport and suspended load transport (Figure 139). Bed load consists in the coarser particles that are transported along the bed intermittently by rolling, sliding, or saltating. Suspended load consists of the finer sediments maintained in suspension by turbulence. Although the distinction is a little arbitrary, models based on one or another type of transport have given accurate results to date.

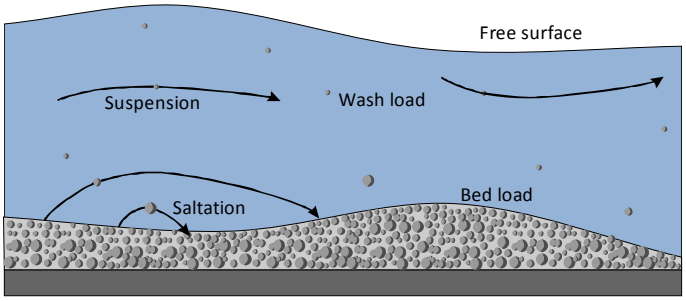

Figure 139: Two different modes of sediment transport: bed load and suspended load

In view of the capital importance of erosion and sedimentation, a lot of researches have been dedicated to the development of an accurate description of both bed and suspended loads transport. It resulted in a large number of models that differ in many respects. Each one has its advantages and drawbacks that make it suitable for specific applications. Reviewing this large literature is beyond the scope of this thesis. Nevertheless, I briefly present here the main categories of models for sedimentation engineering in order to precise my contribution to the field.

According to their dimensionality, flow and sediment transport models are classified as 1D, 2D Horizontal, 2D vertical, and 3D [323]. This classification is perfectly analogous to the one for pure water (see Chapter 1 and 2). For intricate flows, 3D models gives a precise velocity field for the water and concentration field for the sediments [13, 104]. Since such computation is often time-consuming, 3D models are further integrated to reduce the number of equations and the size of the computational grid. It results in 2D vertical models [73, 163], 2D horizontal models [3, 75, 80], or even 1D models [9, 160, 240].

Sedimentation models can be also classified as uniform or non-uniform [323]. Uniform models represent the entire sediment mixture using a single-sized class [75], while non-uniform models divide the sediment mixture into a number of size classes and study the behavior of each size class [13, 323].

By analogy with the two sediment transport modes identified above, sediment transport models are often group as bed-load, suspended-load, and total-load. As pointed by Dewals [75], the intrinsic coupling between both modes argues in favor of a total-load model or “continuous transition” model.

A fundamental distinction in sedimentation engineering is made between equilibrium (or saturated) models and non-equilibrium (or unsaturated models). In a equilibrium model, the actual sediment transport rate is equal to the capacity of the flow carrying sediment at equilibrium conditions. The actual sediment transport is thus assumed to reach, without any delay, the local capacity. Most of the classical models relies on the saturated approach [75], which is only coupled with the Exner equation for describing the bed motion [187, 323]. On the opposite, non-equilibrium model assume that the actual sediment transport rate does not reach instantaneously the sediment transport capacity. In some one-dimensional models [240], a specific differential equations enables to evaluate the actual rate. In most of the cases however, an empirical constitutive law imposes the entrainment/deposition rate such that a time-lag appears between the actual rate and the capacity [109, 134].

Depending on how to conceptualize sediment, sediment transport models can be discerned as particulate and continuous-medium models. Particulate models treat sediment as a group of particulate entities and describe the movement of single particles, whereas continuous-medium models assume sediment as a kind of pseudo-continuous medium.

Depending on the calculation procedure, flow and sediment transport models can be classified as fully decoupled, semi-coupled, or fully coupled [323]. Fully decoupled models ignore the influence of sediment transport and bed change on the flow field by assuming a low sediment concentration and a small bed change. They calculate the flow and sediment transport separately at each time step. Standard uncoupled mathematical models make use of single-phase models coupled with various forms of continuity equations for the sediments [13]. In the one-dimensional framework, standard models rely thus on the Saint-Venant equations for a pure water free-surface flow (Chapter 2):

$$\begin{cases} \dfrac{\partial \Omega}{\partial t} + \dfrac{\partial u_w \Omega}{\partial x} = q_{w,L} \\ \dfrac{\partial u_w \Omega}{\partial t} + \dfrac{\partial u_w u_w \Omega + g I_1}{\partial x} = -g\Omega\left(\dfrac{\partial z_b(\Omega_s)}{\partial x} + S_f \right) + g I_2 + \theta u_w q_{w,L} \end{cases} \tag{10.1}$$

Pressure terms are defined as usual:

$$I_1(\Omega) = \int_{h_b}^{h_s} (h-\xi) I(x,\xi) d\xi \qquad I_2(\Omega) = \int_{h_b}^{h_s} (h-\xi) \frac{\partial I(x,\xi)}{\partial x} d\xi \tag{10.2}$$

Complementing the Saint-Venant equations, the one-dimensional advection-diffusion equation for passive scalars describes the transport of the concentration C in suspended load [7-9]:

$$\frac{\partial C\Omega}{\partial t} + \frac{\partial}{\partial x}(C u_w \Omega) = \frac{\partial}{\partial x}\left(D \frac{\partial}{\partial x}(C\Omega) + q^T \Omega \right) + q_{c,L} \tag{10.3}$$

where D is the diffusion coefficient, q^T is the turbulent contribution to the flux. Additional constitutive equations close the system by specifying D and q^T.

In most of the cases in hydraulics, this approach is largely justified and gives accurate results. Nevertheless, in transient flows, concentrations may reach considerable values such that we cannot neglect anymore the bed variations and the flow density modification [74, 107]. In such cases, equations (10.1)-(10.3) can be refined by integrating the variation of the density in the equations [75, 323] and the Exner equation [127, 210] that accounts for the mobility of the bed caused by deposition and erosion:

$$(1-p)\frac{\partial \Omega_s}{\partial t}+\frac{\partial Q_s}{\partial x}=-e_s \tag{10.4}$$

where p is the grain porosity of the mobile bed, z_b is the bed elevation, q_s is the sediment flux, and e_s is the net erosion rate. Additional constitutive equations specify the value of the last two terms.

The previous coupled model still suffers various shortcoming. In particular, the definition of the concentration C is wooly, especially its physical meaning at the local level. This lack of definition causes problems in applying turbulence models. Indeed, a turbulent term is applied on the concentration, which is not a local variable. Second, primitive unknowns of the Navier-Stokes equations describe only the water flow and fully neglect the velocity of the dispersed phase (which may be different from the water velocity). In order to overcome these shortcomings, Capart [39] proposed a two-layer approach with different velocities between the water layer and the sediment layer. Another approached proposed by Wu [324] consisted in considering the water and the sediments as two different fluid phases. He proposed some equations without validation nor applications. This multiphase approach was next applied by Hsu et al. [147, 148], Bombardelli and Jha [26, 27, 160, 161] to sheet flows. Their approach made use of equations similar to the two-fluid models.

10.1.2 Drift-flux Model For Sediments Transport

To some extent, the dynamics of both sediments and air transport are similar. Therefore, the solution developed in this thesis for air-water flows should be applicable to sediments transport as well. In other words, the drift flux theory presented in chapter 6 should account naturally for the transport of bed and suspended loads.

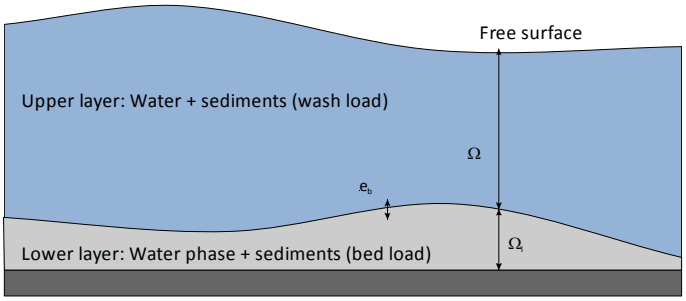

Figure 140: Conceptual model consists in two layers and two phases

For this purpose, I consider a two-layer cross-section and two phases, namely the sediment phase and the water phase (Figure 140). The upper layer consists in a mixture flow of water

and suspended load. The lower layer contains a mixture of water and bed load. In both layers, the sediment phase is considered as a granular flow. What is more, the fluid mixture is assumed to be an incompressible Newtonian flow. This hypothesis remains valid as long as the concentration of sediment is moderate. Based on the following remarks, applying the 1D free-surface drift-flux model (established in Chapter 6) to sediments transport seems legitimate.

For the upper layer (aka main layer), I conflate all head losses in a single term S_F called friction slope. Based on the results of Chapter 6, the drift-flux model can be written as:

$$\begin{aligned}
&\frac{\partial\langle\rho_m\rangle\Omega}{\partial t}+\frac{\partial\langle\rho_m\rangle\tilde{u}_m\Omega}{\partial x}=q_{m,\perp}+\rho_d e_d\\
&\frac{\partial\langle\alpha_d\rangle\Omega}{\partial t}+\frac{\partial}{\partial x}\left(\langle\alpha_d\rangle\tilde{u}_m\Omega+\langle\alpha_d\rangle\frac{\rho_w}{\langle\rho_m\rangle}\tilde{U}_{dj}\Omega\right)=q_{\alpha,\perp}+e_d\\
&\frac{\partial\langle\rho_m\rangle\tilde{u}_m\Omega}{\partial t}+\frac{\partial}{\partial x}\left(\beta\langle\rho_m\rangle\tilde{u}_m\tilde{u}_m\Omega+\beta\frac{\langle\alpha_d\rangle}{1-\langle\alpha_d\rangle}\frac{\rho_d\rho_w}{\langle\rho_m\rangle}\tilde{U}_{dj}\tilde{U}_{dj}\Omega+gP_\Omega\right)\\
&=-\langle\rho_m\rangle g\Omega\left(S_F+\frac{\partial h_{int}}{\partial x}\right)+gP_{G,\partial\Omega_i}-g\langle\rho_m\rangle\Big|_z^{h_s}h(x,t)l_w(h_{int})\frac{\partial h_{int}}{\partial x}+\langle\rho_m\rangle\theta\tilde{u}_m q_{m,\perp}+\rho_d\theta\tilde{u}_m e_d
\end{aligned}\tag{10.5}$$

where the pressure terms are classically given by

$$\begin{aligned}
P_\Omega&=\int_{h_{int}}^{h_s}\left(\langle\rho_m\rangle\Big|_z^{h_s}(h_s(x,t)-z)l_w(z)\right)dz\\
P_{G,\partial\Omega_i}&=\int_{h_{int}}^{h_s}\left(\langle\rho_m\rangle\Big|_z^{h_s}(h_s(x,t)-z)\frac{\partial l_w(z)}{\partial x}\right)dz
\end{aligned}\tag{10.6}$$

The parameter e_d designates the volumetric flux of sediment exchanged between both layers. It is a particular type of lateral discharge.

For the lower layer, we obtain in a similar manner the three following PDE's:

$$\begin{aligned}
&\frac{\partial\langle\rho_m\rangle_s\Omega_s}{\partial t}+\frac{\partial\langle\rho_m\rangle_s\tilde{u}_{m,s}\Omega_s}{\partial x}=q_{m,\perp,s}-\rho_d e_d\\
&\frac{\partial\langle\alpha_d\rangle_s\Omega_s}{\partial t}+\frac{\partial}{\partial x}\left(\langle\alpha_d\rangle_s\tilde{u}_{m,s}\Omega_s+\langle\alpha_d\rangle_s\frac{\rho_w}{\langle\rho_m\rangle_s}\tilde{U}_{dj,s}\Omega_s\right)=q_{\alpha,\perp,s}-e_d\\
&\frac{\partial\langle\rho_m\rangle_s\tilde{u}_{m,s}\Omega_s}{\partial t}+\frac{\partial}{\partial x}\left(\beta_s\langle\rho_m\rangle_s\tilde{u}_{m,s}\tilde{u}_{m,s}\Omega_s+\beta_s\frac{\langle\alpha_d\rangle_s}{1-\langle\alpha_d\rangle_s}\frac{\rho_d\rho_w}{\langle\rho_m\rangle_s}\tilde{U}_{dj,s}\tilde{U}_{dj,s}\Omega_s+gP_{\Omega_s}\right)\\
&=-\langle\rho_m\rangle_s g\Omega_s\left(\frac{\partial h_b}{\partial x}-S_F\right)-\frac{\partial p_{int}}{\partial x}\Omega_s+gP_{G,\partial\Omega_s}+\langle\rho_m\rangle_s\theta\tilde{u}_{m,s}q_{m,\perp,s}-\rho_d\theta\tilde{u}_{m,s}e_d
\end{aligned}\tag{10.7}$$

Pressure terms are given by formulations similar to equations (6.112).

Physically, the multiphase model ensures the mass and momentum conservation of the mixture as well as the mass conservation of each phase separately. Since the flow is highly stratified, the separation in two layers is legitimate. Therefore, two values of the void fraction characterize the concentration in sediment (one in the upper layer, and one in the lower layer). This model differs notably from standard models. In the upper layer, equations are indeed expressed in terms of parameters linked to the mixture, and not the

water phase. It enables to account for the adverse impact of the sediments on the water flow. What is more, the introduction of the drift-velocity makes the model more coherent and broader in scope. Finally, the void fraction appears naturally in the derivation of the model. It constitutes a rigorously-defined concentration. In particular, it results in the disappearance of turbulent terms in the diffusion equation. In the lower layer, discrepancies are even greater. The motion of the bed load is described by three PDE's instead of one (the Exner equation). It enables to ensure a strict mass conservation of both water and sediment, as well as a momentum conservation for the mixture.

Under a series of assumptions, equations (10.7) simplify into the Exner equation (10.4) for the mobile bed. Indeed, imposing a given porosity comes down to impose the void fraction:

$$\left\langle \alpha_d \right\rangle_s = 1 - p \tag{10.8}$$

What is more, an empirical constitutive equation imposes the flux of sediment. For instance, Meyer-Peter and Muller [221] proposed a simple relation for the sediment discharge:

$$Q_s = \begin{cases} 0 & \text{if } \tau_{sf}^* < \tau_{cr}^* \\ 8L\sqrt{(s-1)gd_{50}^3}\left(\tau_{sf}^* - \tau_{cr}^*\right)^{3/2} & \text{if } \tau_{sf}^* \geq \tau_{cr}^* \end{cases} \tag{10.9}$$

where L is the width of the exchange area between both layers, τ_{sf}^* is the non-dimensional skin-friction shear stress, and τ_{cr}^* is the threshold value of the shear stress for initiation of the saltation. The parameter d_{50} is a statistical value that specifies the diameter of the sediments. The parameter s is the relative density of the sediment. For further information about constitutive equations for the flux of sediment, I refer the interested reader to the specialized literature [1, 4, 11]. In any case, these two simplifications make trivial both the continuity and momentum equations for the mixture. Consequently, the remaining diffusion equation identifies to the Exner Equation:

$$(1-p)\frac{\partial \Omega_s}{\partial t} + \frac{\partial Q_s}{\partial x} = -e_s \tag{10.10}$$

This equation only ensures the mass conservation in sediment.

10.1.3 Pollutant Transport: Fundamentals and Drift-flux Model

In a global context, water pollution is a crucial issue. This problem concerns both developed and developing countries, and does not distinguish national borders. Recent news has again underlined the acuteness of this problem. At the time I am writing this thesis, a massive oil spill is indeed affecting the Gulf of Mexico. This pollution results directly from the explosion of the Deepwater Horizon drilling rig (Figure 141). It is already considered as one of the largest oil spill in the world's history. It will result in an environmental disaster with a dramatic impact on marine and wildlife habitats.

The sources of surface water pollution, like the previous drilling rig, are generally grouped in two categories. First, point source pollution refers to contaminants that enter the natural environment through a localized point, such as a pipe or ditch. It includes discharges from a

sewage treatment plant, a factory, or a city storm drain. Second, non-point source pollution refers to a diffuse contamination that does not originate from a single discrete source. It usually results from the cumulative effect of small amounts of contaminants gathered from a large area. Pollution by fertilizers is a typical example.

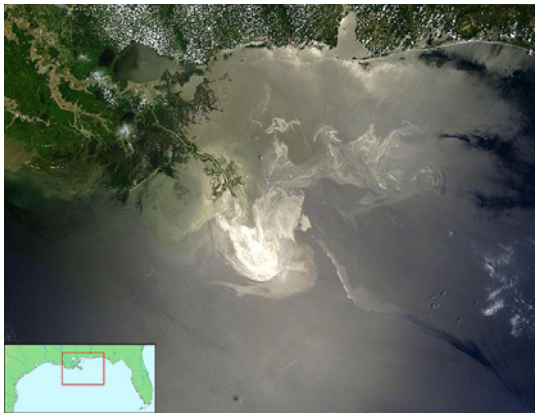

Figure 141: The oil slick as seen from space by NASA's Terra satellite on May 24, 2010

In both cases, it is necessary to prevent the pollution and monitor its source, its intensity, and its motion. This can be done a posteriori, when a pollution is detected, or a priori, when anthropogenic transformations of the landscape are in preparation. In the first case, in-situ measurement are most of the time privileged. The water pollution is then analyzed through physical, chemical, and biological tests. In the second case, experimental methods are difficult to apply, if not impossible. Theoretical models are then the best way to predict the evolution of the concentration in pollutants.

In this respect, transport models are very useful. Based on the description of the point-source and non point-source pollution distribution, such models predict the evolution of the concentration in pollutant in the free surface waters. Like for sediments and air transport phenomena, standard transport models for pollutants rely on a single-phase model coupled with an advection-diffusion equation. I have shown this model suffers various shortcomings that a multiphase model may overcome. Consequently, the multi-layer drift-flux model established for air-water flow in Chapter 6 may be applied to pollutant transport as well. In the case of a dispersed pollutant, like fertilizers, the single-layer model given by equation (10.5) is sufficient. For pollutants of lower density like oil, the two layer system (10.5)-(10.7) gives a high-fidelity description of the flow.

When handling with pollutant transport, a key issue is the creation/destruction of the pollutant phase. Indeed, most of the pollutants are active phases, which means that they react with other components. This feature strongly alters the evolution of the concentration in pollutant. The volumetric phase generation term appearing in the drift-flux theory is crucial in order to simulate this characteristic of reactive flows. A constitutive equation provides its value.

10.2 SHALLOW-WATER-LIKE DRIFT-FLUX MODEL

Solving 3D mathematical models by using the numerical methods developed in Computational Fluid Dynamics [63, 144, 145, 197, 285] is frequent in order to analyze intricate flows in hydraulic structures. It provides a precise description of the flow motion. However, it remains expensive from a computational point of view. It requires sophisticated algorithms and resources beyond the present computational capability.

On the other hand, 1D mathematical models are affordable from a computational point of view and enable to make simulations over a large domain of computation (city, region,…). However, the validity of the 1D assumption relies on the fact that cross-sectional velocities remain much smaller than the main velocity. Many situations of practical interest do not verify this hypothesis such that one-dimensional models cannot be applied.

Two-dimensional shallow-water-like models offer an intermediate step between both 1D and 3D models. Such models are derived from 3D models by integrating the partial differential equations over the flow depth. Their validity relies on the assumption that the vertical velocity is negligible in comparison with the horizontal velocities. The computation effort is greatly reduced since 2D models make use of planar meshes and do not require tracking explicitly the free surface [119, 286]. In many practical applications including single-phase flows, the approach succeeds in providing accurate results. For instance, one can cite flood prediction [72], channel flow analysis [97], dam break flow prediction [95], …

There is no reason that this strategy could not be successfully applied to the drift-flux theory. In fact, an easy extension to multidimensional problems has always been an objective of my doctoral research. Consequently, I present in this section a shallow-water-like drift-flux model for the simulation of free surface environmental flows. This includes the entrainment of air, sediments, pollutants, or any dispersed phase. By analogy with single-phase models, this original set of equations is derived by integrating the 3D drift-flux model over the flow depth. For this purpose, a dimensional analysis decouples momentum equations and simplifies the pressure distribution (section 10.2.1). What is more, I introduce suitable depth-averaged values and boundary conditions (sections 10.2.2 and 10.2.3). Based on these results, I obtain the depth-integrated drift-flux model (section 10.2.4). In all this process, I assume a uniform vertical distribution of the flow parameters. Since this assumption may cause errors in some cases, I introduce in section 10.2.5 three different methods to accommodate depth-averaged model with non-uniform vertical distributions of the velocity and the concentration in dispersed phase.

These original results have been extensively presented in a book [173], a chapter book [172], a journal paper [171], and a conference paper [170]. Since this approach is beyond the scope of this thesis, I do not present here a thorough demonstration and analysis of the equations. Instead, I present the most interesting results and I refer the interested reader to the previous publications for further information.

10.2.1 Dimensional Analysis and Simplification

In order to integrate the drift-flux model over the flow depth, a Cartesian coordinate system Oxyz is set in such a way that both the x-axis and y-axis follow the mean plane of the topography (Figure 142). The angles θ_x, θ_y, and θ_z used in the equations are the angles between the z'-axis (absolute vertical direction) and the x-, y-, and z-axis respectively.

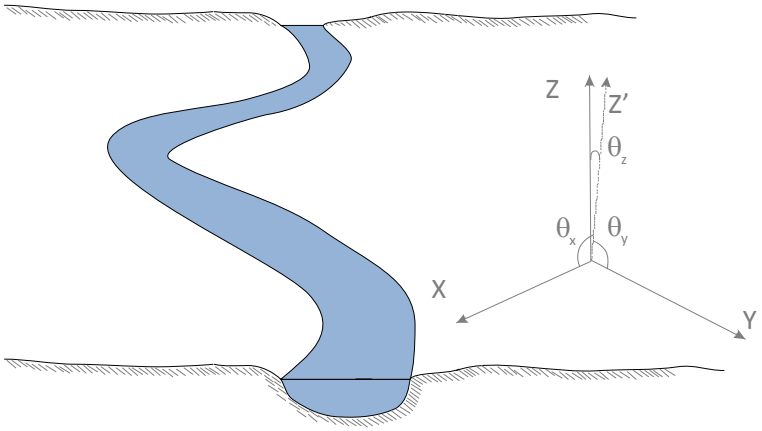

Figure 142: Axis of reference in the simplified two-dimensional computational domain

Expressing the drift-flux model in its non-dimensional form enables to decouple and simplify the momentum equations [173, 174]. For this purpose, I assume that the vertical velocity is way smaller than the horizontal velocities. Under this assumption, the momentum equation along the z-axis simplifies into the following form:

$$\frac{\partial p_m}{\partial z} = -\rho_m g \sin\theta_z \tag{10.11}$$

The system of PDE's does not go through other simplifications. However, this simple relation virtually cancels the momentum equation along the z-axis and provides a restriction for the pressure distribution in the flow. Indeed, the distribution has to be hydrostatic to meet the assumption of negligible vertical velocities.

10.2.2 Definitions of Depth-Integrated Values

As in the case of the one-dimensional drift-flux model, introducing suitable definitions for mean values greatly simplifies the formulation of the depth-averaged drift-flux model. For this purpose, I define the depth-average of a general function f(**x**,t) as follows:

$$\langle f \rangle(x,y,t) \triangleq \frac{1}{h}\int_{h_b}^{h_s} f(x,y,z,t)\,dz \tag{10.12}$$

where the flow depth h is defined by the bottom height h_b and the free surface height h_s as:

$$h \triangleq h_s + h_b \tag{10.13}$$

I also introduce the void fraction weighted depth-average of a general function $f_k(x,y,z,t)$ related to the k^{th} phase (water or dispersed phase):

$$\langle\langle f_k \rangle\rangle \triangleq \frac{\langle \alpha_k f_k \rangle}{\langle \alpha_k \rangle} = \int_{h_b}^{h_s} \alpha_k f_k\,dz \Big/ \int_{h_b}^{h_s} \alpha_k\,dz \tag{10.14}$$

By applying definitions (10.12) and (10.14) to the flow variables appearing in the drift-flux model, we obtain the depth-averaged flow parameters. Since both fluids are incompressible, the depth-averaged mixture density is given by:

$$\langle \rho_m \rangle = \langle \alpha_d \rangle \rho_d + \left(1 - \langle \alpha_d \rangle\right) \rho_w \tag{10.15}$$

The phase velocities are defined as the void fraction weighted depth-averaged velocities:

$$\langle\langle u_k \rangle\rangle \triangleq \frac{\langle \alpha_k \hat{u}_k \rangle}{\langle \alpha_k \rangle} \quad \text{and} \quad \langle\langle v_k \rangle\rangle \triangleq \frac{\langle \alpha_k \hat{v}_k \rangle}{\langle \alpha_k \rangle} \tag{10.16}$$

where the hat symbol is dropped for the simplicity of the notation. I also define the mean mixture velocity as the mixture density weighted depth-average of the mixture velocity:

$$\begin{aligned} \tilde{u}_m &\triangleq \frac{\langle \rho_m u_m \rangle}{\langle \rho_m \rangle} = \frac{\langle \alpha_d \rangle \rho_d \langle\langle u_d \rangle\rangle + \left(1 - \langle \alpha_d \rangle\right) \rho_w \langle\langle u_w \rangle\rangle}{\langle \rho_m \rangle} \\ \tilde{v}_m &\triangleq \frac{\langle \rho_m v_m \rangle}{\langle \rho_m \rangle} = \frac{\langle \alpha_d \rangle \rho_d \langle\langle v_d \rangle\rangle + \left(1 - \langle \alpha_d \rangle\right) \rho_w \langle\langle v_w \rangle\rangle}{\langle \rho_m \rangle} \end{aligned} \tag{10.17}$$

This new definition is related to the experimental value of depth-averaged mixture discharge:

$$\begin{aligned} q_{m,x} &= \int_{h_b}^{h_s} \rho_m u_m dz = \int_{h_b}^{h_s} \left[\alpha_d \rho_d \hat{u}_d + \left(1 - \alpha_d\right) \rho_w \hat{u}_w \right] dz \\ &= \left(\langle \alpha_d \rangle \rho_d \langle\langle u_d \rangle\rangle + \left(1 - \langle \alpha_d \rangle\right) \rho_w \langle\langle u_w \rangle\rangle \right) h \\ &= \langle \rho_m \rangle \tilde{u}_m \, h \end{aligned} \tag{10.18}$$

In an analogous way, the depth-averaged volumetric fluxes can be written as:

$$\begin{aligned} \langle j_x \rangle &= \langle j_{d,x} \rangle + \langle j_{w,x} \rangle = \langle \alpha_d \rangle \langle\langle u_d \rangle\rangle + \left(1 - \langle \alpha_d \rangle\right) \langle\langle u_w \rangle\rangle \\ \langle j_y \rangle &= \langle j_{d,y} \rangle + \langle j_{w,y} \rangle = \langle \alpha_d \rangle \langle\langle v_d \rangle\rangle + \left(1 - \langle \alpha_d \rangle\right) \langle\langle v_w \rangle\rangle \end{aligned} \tag{10.19}$$

and the depth-averaged diffusion velocity and drift-velocity are naturally defined as:

$$\tilde{U}_{dm} \triangleq \langle\langle u_d \rangle\rangle - \tilde{u}_m \quad \text{and} \quad \tilde{V}_{dm} \triangleq \langle\langle v_d \rangle\rangle - \tilde{v}_m \tag{10.20}$$

$$\tilde{U}_{dj} \triangleq \langle\langle u_d \rangle\rangle - \langle j_x \rangle \quad \text{and} \quad \tilde{V}_{dj} \triangleq \langle\langle v_d \rangle\rangle - \langle j_y \rangle \tag{10.21}$$

Several important equations relate the various velocity parameters with each other. The depth-averaged fundamental relation for the diffusion velocities [154, 173] can be written as:

$$\rho_d \langle \alpha_d \rangle \tilde{U}_{dm} + \rho_w \langle \alpha_w \rangle \tilde{U}_{wm} = 0 \quad \text{and} \quad \rho_d \langle \alpha_d \rangle \tilde{V}_{dm} + \rho_w \langle \alpha_w \rangle \tilde{V}_{wm} = 0 \tag{10.22}$$

The relation between the diffusion velocity and the drift velocity is derived as:

$$\tilde{U}_{dm} = \frac{\rho_w}{\langle \rho_m \rangle} \tilde{U}_{dj} \quad \text{and} \quad \tilde{V}_{dm} = \frac{\rho_w}{\langle \rho_m \rangle} \tilde{V}_{dj} \tag{10.23}$$

Combining equations (10.22) with (10.23) also gives:

$$\begin{aligned} \tilde{U}_{wm} &= -\frac{\rho_d \langle \alpha_d \rangle}{\rho_w \langle \alpha_w \rangle} \tilde{U}_{dm} = -\frac{\rho_d \langle \alpha_d \rangle}{\langle \rho_m \rangle \langle \alpha_w \rangle} \tilde{U}_{dj} \\ \tilde{V}_{wm} &= -\frac{\rho_d \langle \alpha_d \rangle}{\rho_w \langle \alpha_w \rangle} \tilde{V}_{dm} = -\frac{\rho_d \langle \alpha_d \rangle}{\langle \rho_m \rangle \langle \alpha_w \rangle} \tilde{V}_{dj} \end{aligned} \tag{10.24}$$

Combining the definition of the diffusion velocity given by equation (10.20) with the important relations (10.23) and (10.24) gives for the dispersed phase:

$$\left\langle\left\langle u_d\right\rangle\right\rangle = \tilde{u}_m + \frac{\rho_w}{\left\langle\rho_m\right\rangle}\tilde{U}_{dj} \quad \text{and} \quad \left\langle\left\langle v_d\right\rangle\right\rangle = \tilde{v}_m + \frac{\rho_w}{\left\langle\rho_m\right\rangle}\tilde{V}_{dj} \tag{10.25}$$

and for the water phase:

$$\left\langle\left\langle u_w\right\rangle\right\rangle = \tilde{u}_m - \frac{\left\langle\alpha_d\right\rangle}{1-\left\langle\alpha_d\right\rangle}\frac{\rho_d}{\left\langle\rho_m\right\rangle}\tilde{U}_{dj} \quad \text{and} \quad \left\langle\left\langle v_w\right\rangle\right\rangle = \tilde{v}_m - \frac{\left\langle\alpha_d\right\rangle}{1-\left\langle\alpha_d\right\rangle}\frac{\rho_d}{\left\langle\rho_m\right\rangle}\tilde{V}_{dj} \tag{10.26}$$

In the drift flux model, a problem is solved in terms of averaged void fraction and averaged mixture velocities with a constitutive relation for the drift velocities. Thus, equations (10.25) and (10.26) can be used to recover a solution for the velocity of each phase after a problem is solved.

10.2.3 Boundary Conditions

As already mentioned, specifying conditions at the boundaries of the integration domain enables to obtain a single result at the end of the integration, without any ambiguity. Since the current domain is a thin layer, I must establish boundary conditions at the free surface and at the bottom ground. According to the philosophy of the drift-flux theory, kinematic boundary conditions must express the mass conservation of the mixture and of each phase taken on its own. In addition, the momentum conservation of the mixture flow must be forced by means of dynamic boundary conditions.

Kinematic boundary conditions translate the property of impermeability of the interfaces. It means that the component of the fluid velocity normal to the interface is equal to the velocity of this interface in the same direction. Three kinematic conditions are defined at each boundary: one for the mixture and two for each phase.

Dynamic boundary conditions express the dynamic equilibrium of the fluid mixture at the interfaces. In other words, the forces acting on an infinitesimal element of fluid at the interfaces are the direct cause of its motion. The drift-flux model includes only one momentum equation, describing the mixture fluid. Consequently, I establish only two dynamic boundary conditions, one for the free surface and one for the bottom.

10.2.4 Depth-integrated Drift-flux Model

Based on both the mean values defined in section 10.2.2 and the boundary conditions established in section 10.2.3, I can perform the integration of the 3D drift-flux model over the flow depth (Figure 142). In particular, I successively integrate the mixture continuity equation, the diffusion equation, and the mixture momentum equations along both the x-axis and y-axis. In these last equations, I pay a particular attention to the formulation of the convection fluxes in terms of mixture and drift velocities. Thoroughly demonstrated in [174], equations of this original model are only briefly introduced here.

At the end of the integration, the depth-averaged continuity equation is written as:

$$\frac{\partial \langle \rho_m \rangle h}{\partial t} + \frac{\partial \langle \rho_m \rangle \tilde{u}_m h}{\partial x} + \frac{\partial \langle \rho_m \rangle \tilde{v}_m h}{\partial y} = i_{m,s}\rho_{m,s} - i_{m,b}\rho_{m,b} \tag{10.27}$$

where $i_{m,b}$ accounts for the infiltration into the bottom ($i_{m,b}$ is positive for fluid losses), and $i_{m,s}$ for the precipitations or evaporation ($i_{m,s}$ is positive for fluid injection). Equation (10.27) ensures the mass conservation of the mixture (water+dispersed phase).

The depth-averaged diffusion equation complements equation (10.27) in order to ensure the mass conservation of each phase on its own:

$$\begin{aligned}\frac{\partial \langle \alpha_d \rangle h}{\partial t} + \frac{\partial \langle \alpha_d \rangle \tilde{u}_m h}{\partial x} + \frac{\partial \langle \alpha_d \rangle \tilde{v}_m h}{\partial y} + \frac{\partial}{\partial x}\left(\langle \alpha_d \rangle \frac{\rho_w}{\langle \rho_m \rangle} \tilde{U}_{dj} h \right) + \frac{\partial}{\partial y}\left(\langle \alpha_d \rangle \frac{\rho_w}{\langle \rho_m \rangle} \tilde{V}_{dj} h \right) \\ = \frac{1}{\rho_d}\langle \Gamma_d \rangle h + \alpha_{d,s} i_{d,s} - \alpha_{d,b} i_{d,b}\end{aligned} \tag{10.28}$$

where $i_{d,b}$ accounts for the infiltration of dispersed phase into the bottom ($i_{d,b}$ is positive for fluid losses), and $i_{d,s}$ for the precipitations or evaporation of dispersed phase ($i_{d,s}$ is positive for fluid injection). The drift-velocity along the x- and y-axis accounts for the relative velocity between both phases. Constitutive equations like the Dix correlation set their value. Finally, the phase generation term accounts for the volumetric exchange between both phases.

For the momentum equation, two depth-averaged equations ensure the momentum conservation of the mixture along the x- and y-axis:

$$\begin{aligned}&\frac{\partial \langle \rho_m \rangle \tilde{u}_m h}{\partial t} + \frac{\partial}{\partial x}\left(\langle \rho_m \rangle \tilde{u}_m \tilde{u}_m h + \frac{\langle \alpha_d \rangle}{1 - \langle \alpha_d \rangle} \frac{\rho_d \rho_w}{\langle \rho_m \rangle} \tilde{U}_{dj} \tilde{U}_{dj} h + g P_h \right) \\ &+ \frac{\partial}{\partial y}\left(\langle \rho_m \rangle \tilde{u}_m \tilde{v}_m h + \frac{\langle \alpha_d \rangle}{1 - \langle \alpha_d \rangle} \frac{\rho_d \rho_w}{\langle \rho_m \rangle} \tilde{U}_{dj} \tilde{V}_{dj} h \right) \\ &= \rho_w u_w i_w + \rho_d u_d i_d\big|_{z=h_s} - \rho_w u_w i_w + \rho_d u_d i_d\big|_{z=-h_b} - \langle \rho_m \rangle g h \frac{\partial z_b}{\partial x} \\ &+ \frac{\partial \langle \tau_{Gm,xx} \rangle h}{\partial x} + \frac{\partial \langle \tau_{Gm,yx} \rangle h}{\partial y} + (\tau_{b,x} - \tau_{s,x})\Delta\Sigma + \langle M_{m,x} \rangle h\end{aligned} \tag{10.29}$$

and

$$\begin{aligned}&\frac{\partial \langle \rho_m \rangle \tilde{v}_m h}{\partial t} + \frac{\partial}{\partial x}\left(\langle \rho_m \rangle \tilde{u}_m \tilde{v}_m h + \frac{\langle \alpha_d \rangle}{1 - \langle \alpha_d \rangle} \frac{\rho_d \rho_w}{\langle \rho_m \rangle} \tilde{U}_{dj} \tilde{V}_{dj} h \right) \\ &+ \frac{\partial}{\partial y}\left(\langle \rho_m \rangle \tilde{v}_m \tilde{v}_m h + \frac{\langle \alpha_d \rangle}{1 - \langle \alpha_d \rangle} \frac{\rho_d \rho_w}{\langle \rho_m \rangle} \tilde{V}_{dj} \tilde{V}_{dj} h + g P_h \right) \\ &= \rho_w v_w i_w + \rho_d v_d i_d\big|_{z=h_s} - \rho_w v_w i_w + \rho_d v_d i_d\big|_{z=-h_b} - \langle \rho_m \rangle g h \frac{\partial z_b}{\partial y} \\ &+ \frac{\partial \langle \tau_{Gm,xy} \rangle h}{\partial x} + \frac{\partial \langle \tau_{Gm,yy} \rangle h}{\partial y} + (\tau_{b,y} - \tau_{s,y})\Delta\Sigma + \langle M_{m,y} \rangle h\end{aligned} \tag{10.30}$$

Drift velocities appearing in equations (10.29) and (10.30) are the same than the one present in the diffusion equation. The topographic slope is specified by the bottom elevation z_b. Head-loss terms include the gradient of the generalized stress tensor, the

effect of the friction at the external boundaries (bottom and free surface), as well as the effect of the surface tension at the surface of the bubbles. Pressure term is given by:

$$P_h = \int_{h_b}^{h_s} \left(\langle \rho_m \rangle \Big|_z^{h_s} \left(h_s(x,t) - z \right) \right) dz \tag{10.31}$$

These original equations present several advantages over a single-phase formulation like the Saint-Venant equations. First, the notion of concentration appears naturally and relies on a rigorous mathematical definition. Second, the adverse impact of the dispersed phase over the water is taken into account in the mathematical description. Finally, the notion of drift velocity $\tilde{U}_{dj,l}$ accounts for all the diffusive mechanisms that can be encountered in civil and environmental. It enhances the coherence of the model.

10.2.5 Non-uniform Vertical Distribution of Flow Parameters

When integrating over the flow depth, I assume the vertical uniformity of all flow parameters. It causes most of the flow features along the integration direction to be lost. In many applications, the loss of details over the vertical dimension has no significant impact on the simulation. In contrast, the assumption of vertical uniformity may cause considerable errors in other cases. It is especially true in curved channels [114] or meandering rivers, for flows over spillways [79, 182], as well as for processes associated with sediment transport [323] and air transport [76]. Therefore, the range of validity of the system may become too limited for practical applications.

Various methods have been developed to accommodate depth-averaged models with the vertical distribution of the parameters. In our book [174], we refer to three methods that have been proven useful in this respect. The first one solves the same number of equations than model (10.27)-(10.30). However, equations include correction coefficients that depend on a single parameter and on a pre-determined distribution of the flow parameters. The second makes use of additional moment equations. The third is based on a multi-layer integration domain. All methods make the two-dimensional model a reliable alternative to three-dimensional models, even in presence of feeble vertical phenomena. I briefly present here the principle of these three methods.

In the first method, vertical profiles are described prior to the computation by a function depending on a single unsteady parameter for each profile. This parameter is traditionally chosen as the depth mean value, which is also the primitive unknown of depth-integrated model. Introduction of one-parameter distributions does not require additional differential equations to be solved but leads to either Boussinesq coefficients [21, 76, 260] or a covariance term [153, 154, 330]. Boussinesq coefficients are frequent in free-surface hydraulics, while covariance terms appear more often in multiphase applications. Nevertheless, they rely on the exact same theory and partly correct the equations without increasing the computational effort.

Steffler and Jin [275] proposed the second method to refine the description of the vertical distribution of flow parameters. Their model, although still depth-averaged, assumes that the functional profile depends on more than one parameter. To solve the additional parameters, moment equations are generated by depth-integrating the 3D model equations pre-multiplied by a weighting function [75, 114, 115, 162, 177, 178, 182, 228].

Finally, the third method is based on multi-layer models. This approach is useful to compute situations in which a finite number of layers exhibit specific behavior [42, 263, 281]. A set of shallow-water-like equations is derived for each layer and the profile of each flow parameter is assumed constant over a single layer. It results in N coupled sub-systems for the N layers. By applying these methods, 2D horizontal model remains a valuable alternative to 3D models even in presence of vertical phenomena.

10.3 TWO-DIMENSIONAL MIXED FLOW MODEL

As shown in the previous section, shallow-water-like models constitute a good compromise between a reduction in the computational effort and a good fidelity in the description. Since the approach makes use of two-dimensional grids and does not require tracking explicitly the free surface, computation is possible on personal computers. What is more, this method simulates two-dimensional and even three-dimensional flow patterns (as far as correction methods are used like the multi-layer approach, the Boussinesq coefficients, or the moment equations). It provides more accurate results than the one-dimensional approach.

The classical shallow-water model for pure water flows [9, 286], as well as the original shallow-water-like drift-flux model for two-phase flows (previous section), describe only free surface flows. However, mixed flow patterns arise in many situations of practical interest involving 2D or 3D flows. When computing flood events or dam break accidents, parts of the flow get pressurized in tunnels and openings within dikes. In a similar manner, many hydraulic structures are surrounded by complex flows including free surface and pressurized flows. Shallow-water-like models are useless in such situations.

The purpose of this section is to extend the applicability of the shallow-water models for single- and two-phase flows to pressurized flows as well. For this purpose, I rely on the original strategy that I have used for one-dimensional models. In other words, I make the most of the analogy between the equations describing pressurized and free-surface flows. In the free surface models, I complement the hydrostatic pressure term with a uniform contribution. This original pressure term overcomes the discrepancy arising in pressure gradients of free surface and pressurized flows models. It results in a unified model for mixed flows.

In this section, I present two original models. The first one is a depth-integrated mathematical model for pure water free surface flows in which I modify the pressure term for modelling pressurized flows (section 10.3.1). The second original model is a depth-integrated set of equations for two-phase flows (water + dispersed phase). It relies on the drift-flux model and a unified two-phase pressure term (section 10.3.2). Only the mathematical models are presented here. Their discretization and implementation are scheduled in my post-doctoral research.

10.3.1 SINGLE-PHASE MODEL: MIXED FLOWS

The shallow-water model for pure water flows is a classical model in free-surface hydraulics [75, 286]. It is a two-dimensional system of PDE's of hyperbolic type. Equations are derived by depth integrating the Reynolds-averaged Navier-Stokes equations with the key assumption of hydrostatic distribution of the pressure:

$$p(z) = \rho_w g(h - z) \tag{10.32}$$

This hypothesis results from a dimensional analysis that prescribes conditions for neglecting the momentum equation along the z-axis. At the end of the day, we obtain the following set of equations:

$$\begin{aligned}
&\frac{\partial h}{\partial t}+\frac{\partial hu_w}{\partial x}+\frac{\partial hv_w}{\partial y}=s_1\\
&\frac{\partial hu_w}{\partial t}+\frac{\partial}{\partial x}\left(hu_w u_w+P_h\right)+\frac{\partial hu_w v_w}{\partial y}=s_2\\
&\frac{\partial hv_w}{\partial t}+\frac{\partial hv_w u_w}{\partial x}+\frac{\partial}{\partial y}\left(hv_w v_w+P_h\right)=s_3
\end{aligned} \tag{10.33}$$

where s_1, s_2, and s_3 conflates all the source terms. The parameter h is the water depth and the pressure term is simply given by:

$$P_h=\frac{1}{2}gh^2 \tag{10.34}$$

By virtue of the chain rule, equations (10.33) may be written in its quasi-linear form as:

$$\frac{\partial \mathbf{U}}{\partial t}+\mathbf{A}(\mathbf{U})\frac{\partial \mathbf{U}}{\partial x}+\mathbf{B}(\mathbf{U})\frac{\partial \mathbf{U}}{\partial y}=\mathbf{S} \tag{10.35}$$

where **A** and **B** are the Jacobian matrixes of the shallow-water equations, **U** is the conservative unknown matrix:

$$\mathbf{U}=\begin{bmatrix} h & hu_w & hv_w \end{bmatrix}^T \tag{10.36}$$

The matrix **S** conflates all the source terms. The entries of these matrixes are the partial derivative of the flux components with respect to the conservative unknowns. The Jacobian matrixes are given by:

$$\mathbf{A(U)}=\begin{bmatrix} 0 & 1 & 0\\ c^2-u_w^2 & 2u_w & 0\\ -u_w v_w & v_w & u_w \end{bmatrix} \quad ; \quad \mathbf{B(U)}=\begin{bmatrix} 0 & 1 & 0\\ -u_w v_w & v_w & u_w\\ c^2-v_w^2 & 0 & 2v_w \end{bmatrix} \tag{10.37}$$

Since the density is assumed constant, the free surface celerity is given by:

$$c^2=\frac{\partial P_h}{\partial(h)}=gh \tag{10.38}$$

Result (10.38) corresponds to the velocity of a wave at the free surface. The relation is analogous to the definition of the pressure wave celerity in the Saint-Venant equations (Chapter 2), except that the width of the section is constant.

By analogy, one may depth-integrate the Reynolds-averaged Navier-Stokes equations under two different assumptions. First, the pressure distribution is chosen uniform over the flow depth. Second, the water density is variable. These assumptions correspond to the classical hypotheses of pressurized flows. At the end of the day, we obtain:

$$\begin{aligned}
&\frac{\partial \rho_w h}{\partial t}+\frac{\partial \rho_w hu_w}{\partial x}+\frac{\partial \rho_w hv_w}{\partial y}=s_1\\
&\frac{\partial \rho_w hu_w}{\partial t}+\frac{\partial}{\partial x}\left(\rho_w hu_w u_w+ph\right)+\frac{\partial \rho_w hu_w v_w}{\partial y}=s_2\\
&\frac{\partial \rho_w hv_w}{\partial t}+\frac{\partial \rho_w hv_w u_w}{\partial x}+\frac{\partial}{\partial y}\left(\rho_w hv_w v_w+ph\right)=s_3
\end{aligned} \tag{10.39}$$

where the parameter p designates the uniform distribution of the pressure (i.e p(z)=p). This model has the same eigenstructure than its free surface counterpart except that the pressure wave celerity a replaces free surface celerity c. By definition, the celerity a is given by the following equation:

$$a^2 = \frac{\partial ph}{\partial \rho_w h} \tag{10.40}$$

where p is the uniform contribution to the pressure in the mesh and the water density is assumed variable. The value a depends on the compressibility rate of the water, and on the strength of both the walls of the mesh and its mean of support. In pure water flows, this parameter may be chosen as a constant. Its value is computed by means of continuum mechanics relations [325]. By integration of equation (10.40), I express the uniform pressure contribution as a function of the celerity and the water height h:

$$p = a^2 \left(\rho_w h - \rho_{w,0} h_{max,0} \right) / h \tag{10.41}$$

In order to unify these two formulations, I re-write equation (10.39) in terms of “free surface equivalent” parameters:

$$h_{eq} = \frac{\rho_w h}{\rho_{w,0}} \quad ; \quad q_{x,eq} = \frac{\rho_w u_w h}{\rho_{w,0}} \quad ; \quad q_{y,eq} = \frac{\rho_w v_w h}{\rho_{w,0}} \tag{10.42}$$

Physically, we obtain these parameters if we suppose that the flow is incompressible but that the flexibility of the walls accounts for the compressibility of the fluid. By using these equivalent parameters, we obtain for equation (10.39):

$$\begin{aligned}
&\frac{\partial h_{eq}}{\partial t} + \frac{\partial q_{x,eq}}{\partial x} + \frac{\partial q_{y,eq}}{\partial y} = s_1 \\
&\frac{\partial q_{x,eq}}{\partial t} + \frac{\partial}{\partial x}\left(\frac{q_{x,eq}^2}{h_{eq}} + P_{eq} \right) + \frac{\partial}{\partial y}\left(\frac{q_{x,eq} q_{y,eq}}{h_{eq}} \right) = s_2 \\
&\frac{\partial q_{y,eq}}{\partial t} + \frac{\partial}{\partial x}\left(\frac{q_{x,eq} q_{y,eq}}{h_{eq}} \right) + \frac{\partial}{\partial y}\left(\frac{q_{y,eq}^2}{h_{eq}} + P_{eq} \right) = s_3
\end{aligned} \tag{10.43}$$

For the pressure term (10.41), we have

$$p = \rho_{w,0} a^2 \left(h_{eq} - h_{max,0} \right) / h_{max,0} \tag{10.44}$$

Except the pressure term, model (10.43) is identical to equation (10.33) that describes the free surface flows with the following notation:

$$h = h \quad ; \quad q_x = u_w h \quad ; \quad q_y = v_w h \tag{10.45}$$

Consequently, the following system of PDE’s describes in a unified framework both free surface and pressurized flows:

$$\begin{aligned}
&\frac{\partial h_{eq}}{\partial t} + \frac{\partial q_{x,eq}}{\partial x} + \frac{\partial q_{y,eq}}{\partial y} = s_1 \\
&\frac{\partial q_{x,eq}}{\partial t} + \frac{\partial}{\partial x}\left(\frac{q_{x,eq}^2}{h_{eq}} + P_{eq} \right) + \frac{\partial}{\partial y}\left(\frac{q_{x,eq} q_{y,eq}}{h_{eq}} \right) = s_2 \\
&\frac{\partial q_{y,eq}}{\partial t} + \frac{\partial}{\partial x}\left(\frac{q_{x,eq} q_{y,eq}}{h_{eq}} \right) + \frac{\partial}{\partial y}\left(\frac{q_{y,eq}^2}{h_{eq}} + P_{eq} \right) = s_3
\end{aligned} \tag{10.46}$$

By definition, the pressure term P_{eq} is the depth-integral of the pressure distribution. By using the definition (10.32) for free-surface flows and definition (10.41) for pressurized flows, we have:

$$P_{eq} = \int_0^h \rho g h \, dh = \begin{cases} \frac{1}{2}\rho g h^2 & \text{if FS} \\ \frac{1}{2}\rho g h_{max}^2 + \rho a^2 \left(h_{eq} - h_{max} \right) & \text{if PP} \end{cases} \tag{10.47}$$

which is very similar to the 1D formulation. The notation FS designates the free surface flow, while PP designates pressurized flow. If $h_{eq}>h_{max}$, the flow is obviously pressurized. If $h_{eq}<h_{max}$, the flow pattern depends on the aeration condition. Lack of aeration device prevents indeed the apparition of a free surface and a sub-atmospheric pressurized flow appears. Model (10.47) accounts for this possibility since uniform contributions can be negative. In the pressurized formulation, two terms contribute to the total pressure. The first one is the hydrostatic pressure. The second is a first order uniform contribution due to the pressurization of the flow.

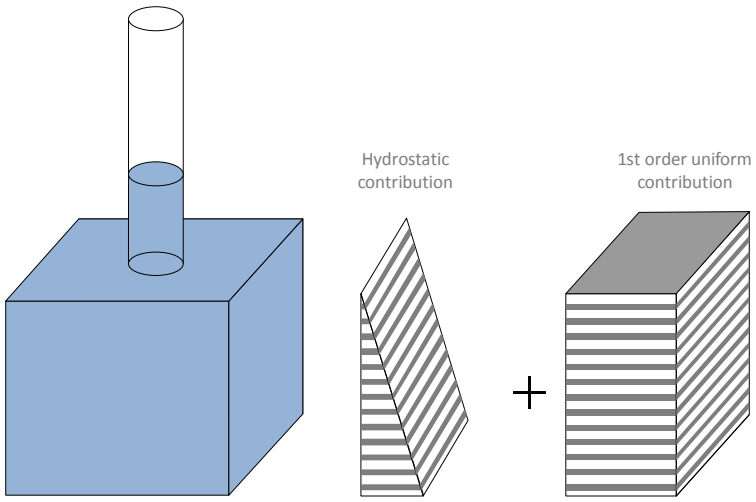

Figure 143: The Preissmann tube extends the applicability of the shallow-water equations to pressurized flows

From a physical point of view, the free surface equivalent height h_{eq} accounts for the dilatation of the walls and for the contraction of the water due to the increase in pressure. By analogy with the 1D Preissmann slot, we can define here a Preissmann tube that is added at the top of the computational mesh (Figure 143). In this case, a pressurized flow is treated as an artificial free-surface flow whose celerity is given by:

$$c^2 = g h_{eq} + a^2 \tag{10.48}$$

Developing and assessing this original model is beyond the scope of this thesis. Consequently, I have not discretized and implemented the equations into a computational code. This work will be one of the first task of my post doctoral research. For this purpose, I will rely on the Wolf flux vector splitting and on the computational code WOLF2D.

10.3.2 Multiphase Model: Mixed Flows

As introduced in section 10.2, depth-integrating the 3D drift-flux model provides a shallow-water-like model for the transport of a dispersed phase:

$$\begin{cases} \dfrac{\partial \langle \rho_m \rangle h}{\partial t} + \dfrac{\partial \langle \rho_m \rangle \tilde{u}_m h}{\partial x} + \dfrac{\partial \langle \rho_m \rangle \tilde{v}_m h}{\partial y} = s_1 \\ \dfrac{\partial \langle \alpha_d \rangle h}{\partial t} + \dfrac{\partial \langle \alpha_d \rangle \tilde{u}_m h}{\partial x} + \dfrac{\partial \langle \alpha_d \rangle \tilde{v}_m h}{\partial y} = s_2 \\ \dfrac{\partial \langle \rho_m \rangle \tilde{u}_m h}{\partial t} + \dfrac{\partial}{\partial x}\left(\langle \rho_m \rangle \tilde{u}_m \tilde{u}_m h + g P_h \right) + \dfrac{\partial}{\partial y}\left(\langle \rho_m \rangle \tilde{u}_m \tilde{v}_m h \right) = s_3 \\ \dfrac{\partial \langle \rho_m \rangle \tilde{v}_m h}{\partial t} + \dfrac{\partial}{\partial x}\left(\langle \rho_m \rangle \tilde{u}_m \tilde{v}_m h \right) + \dfrac{\partial}{\partial y}\left(\langle \rho_m \rangle \tilde{v}_m \tilde{v}_m h + g P_h \right) = s_4 \end{cases} \tag{10.49}$$

where **s** conflates all the source terms and the pressure term P_h accounts for the hydrostatic distribution of pressure:

$$P_h = \int_{h_b}^{h_s} \left(\langle \rho_m \rangle \Big|_z^{h_s} \left(h_s(x,t) - z \right) \right) dz \tag{10.50}$$

This model provides a high-fidelity description of free-surface flows that transport a dispersed phase. Nevertheless, it is useless when the flow is pressurized.

By analogy with the previous section, I may re-write model (10.49) in a quasi-linear form (10.35). The matrix of conservative unknowns is given by:

$$\mathbf{U} = \left[\langle \rho_m \rangle h \quad \langle \alpha_d \rangle h \quad \langle \rho_m \rangle \tilde{u}_m h \quad \langle \rho_m \rangle \tilde{v}_m h \right]^T \tag{10.51}$$

The Jacobian matrixes are given by:

$$\mathbf{A}(\mathbf{U}) = \begin{bmatrix} 0 & 0 & 1 & 0 \\ \tilde{u}_m \langle \alpha_d \rangle / \langle \rho_m \rangle & \tilde{u}_m & \langle \alpha_d \rangle / \langle \rho_m \rangle & 0 \\ c^2 - \tilde{u}_m^2 & 0 & 2\tilde{u}_m & 0 \\ -\tilde{u}_m \tilde{v}_m & 0 & \tilde{v}_m & \tilde{u}_m \end{bmatrix}$$

$$\mathbf{B}(\mathbf{U}) = \begin{bmatrix} 0 & 0 & 1 & 0 \\ \tilde{v}_m \langle \alpha_d \rangle / \langle \rho_m \rangle & \tilde{v}_m & 0 & \langle \alpha_d \rangle / \langle \rho_m \rangle \\ -\tilde{u}_m \tilde{v}_m & 0 & \tilde{v}_m & \tilde{u}_m \\ c^2 - \tilde{v}_m^2 & 0 & 0 & 2\tilde{v}_m \end{bmatrix} \tag{10.52}$$

where the free surface celerity is given by:

$$c^2 = \frac{\partial g P_h}{\partial \left(\langle \rho_m \rangle h \right)} \tag{10.53}$$

The celerity c is the velocity of a wave at the free surface of the mixture.

By analogy, we could depth-integrate the 3D drift-flux model under the assumptions of uniform distribution of the pressure and of a mixture density depending on the pressure. It would give the exact same formulation than equation (10.49) except that the hydrostatic pressure term is replaced by a uniform contribution.

$$\cancel{g P_h} \quad \rightarrow \quad p_h \tag{10.54}$$

This model has also the same eigenstructure than the model (10.49), except that the pressure wave celerity a replaces the free surface celerity c. By definition, a is given by:

$$a^2 = \frac{\partial ph}{\partial\left(\langle\rho_m\rangle h\right)} \tag{10.55}$$

Again, the value of the celerity a is calculated by means of continuum mechanics relations. Nevertheless, this value cannot be considered constant anymore. Indeed, the concentration in dispersed phase strongly affects the compressibility of the mixture fluid, and thus the value of the celerity. Consequently, it is necessary to compute the celerity at each time step and in each computational mesh by means of a suitable constitutive equation. For gas-liquid mixture, I showed in Chapter 7 that the celerity was given by:

$$a_m = a_0 \Big/ \sqrt{1+\alpha_0\rho_{m,0}a_0^2 p_0^{1/\beta}\Big/ p^{1+\beta/\beta}} \tag{10.56}$$

where the subscript 0 designates the reference state characterized by the atmospheric pressure. The parameter β is equal to 1.0 for isothermal processes and 1.4 for adiabatic conditions. The reference void fraction α_0 is the volume fraction of dispersed air at reference pressure and the reference density $\rho_{m,0}$ is the mixture density at the reference pressure. Integration of equation (10.55) with the formulation (10.56) gives the following equation for the pressure:

$$a_0\frac{h-h_{max}}{h_{max}} = p - p_0 + \left(p_0^{-1/\beta} - p^{-1/\beta}\right)\beta\alpha_0\rho_{m,0}a_0^2 p_0^{1/\beta} \tag{10.57}$$

which is solved iteratively with a Newton-Raphson scheme.

By analogy with the previous section, I unify the description of free-surface and pressurized flows. Since the density is already variable, I do not need to reformulate the equations in terms of “free surface equivalent parameters”. The unified model is simply:

$$\begin{cases} \dfrac{\partial\langle\rho_m\rangle h}{\partial t} + \dfrac{\partial\langle\rho_m\rangle\tilde{u}_m h}{\partial x} + \dfrac{\partial\langle\rho_m\rangle\tilde{v}_m h}{\partial y} = s_1 \\ \dfrac{\partial\langle\alpha_d\rangle h}{\partial t} + \dfrac{\partial\langle\alpha_d\rangle\tilde{u}_m h}{\partial x} + \dfrac{\partial\langle\alpha_d\rangle\tilde{v}_m h}{\partial y} = s_2 \\ \dfrac{\partial\langle\rho_m\rangle\tilde{u}_m h}{\partial t} + \dfrac{\partial}{\partial x}\left(\langle\rho_m\rangle\tilde{u}_m\tilde{u}_m h + gP_h\right) + \dfrac{\partial}{\partial y}\left(\langle\rho_m\rangle\tilde{u}_m\tilde{v}_m h\right) = s_3 \\ \dfrac{\partial\langle\rho_m\rangle\tilde{v}_m h}{\partial t} + \dfrac{\partial}{\partial x}\left(\langle\rho_m\rangle\tilde{u}_m\tilde{v}_m h\right) + \dfrac{\partial}{\partial y}\left(\langle\rho_m\rangle\tilde{v}_m\tilde{v}_m h + gP_h\right) = s_4 \end{cases} \tag{10.58}$$

where the pressure term is given by adding the hydrostatic and uniform contribution:

$$gP_h = \begin{cases} g\int_{h_b}^{h_s}\left(\langle\rho_m\rangle\Big|_z^{h_s}\left(h_s(x,t)-z\right)\right)dz & \text{if FS} \\ gP_h\left(h_{max},FS\right) + \underbrace{\int_{h_b}^{h_s} a^2 d\left(\langle\rho_m\rangle h\right)}_{=ph} & \text{if PP} \end{cases} \tag{10.59}$$

Again, the notation FS designates the free surface flow, while PP designates pressurized flow. Model (10.59) accounts also for sub-atmospheric pressurized flows since the uniform contribution can be negative.

10.4 Double-averaged Theory

In Chapter 2, the derivation of the Reynolds-averaged Navier-Stokes equations (RANS) and of the 3D drift-flux model relied on the time-integration of the Local Instant Formulation of the Navier-Stokes equations (+ jump conditions in the multiphase case). This averaging was prompted by the necessity to take into account the high-frequency variations in the temporal evolution of the flow parameters at a given point. Classical in fluid dynamics, this turbulence model accounts for the scale heterogeneities in time without requiring an important computational time like the Direct Numerical Simulation (DNS).

In some situations, time-integrated equations are however shown inadequate due to the small-scale heterogeneities in space affecting the flow. Typical examples of such situations are turbulent flows over both rough and vegetated beds. In each case, disturbing elements are randomly distributed over the whole bed. It induces a three-dimensional structure for the flow. Due to their frequent apparition in natural and anthropogenic environments, these two topics constitute challenges for scientists and engineers.

By definition, so-called rough-beds cover a large spectrum of situations that appear frequently in natural rivers and streams. The rigid beds that constitute most of the mountain torrents and fluvial rivers are a first example of rough-beds. They are naturally chaotic since they result directly from the tumultuous history of the earth [185]. Second, river bottom are frequently composed of gravels and sediments that are successively transported, dropped, dragged, and saltated according to the flow conditions [4, 13, 60, 80, 126]. Variable in time and space, sediment and gravel depots form an unpredictable roughness. Third, particular flow conditions may give birth to bigger-scale structures, called the dunes and anti-dunes, that constitute a macro-roughness [97, 219, 323]. Finally, bed roughness remains a relative notion since its effect on the flow dynamics depends strongly on the flow depth.

In a similar manner, submerged vegetations like riparian plants are also present regularly on riverbanks or floodplains, and sporadically within the riverbeds. The impact of submerged vegetation on the flow is both detrimental and beneficial. From a hydraulic point of view, vegetation increases the flow resistance and reduces the conveyance capacity of the channel [230, 322]. Consequently, vegetation has been removed for many years from channels in order to avoid flood events. Nevertheless, submerged canopies is a factor of improvement of the environmental value of rivers [230, 256]. It influences the water quality by removing nutrients and producing oxygen in stagnant regions. It also decreases the importance of bed stresses and consequently promote sedimentation and retention of particles [209]. Finally, vegetation increases the habitat diversity, and thus species diversity [230]. For these reasons, some researchers now advocate for an ecological management of channel vegetation instead of a systematic elimination [310].

Obviously, it is essential to integrate the effect of the subgrid spatial heterogeneities due to the presence of bed-roughness and vegetation into the mathematical model describing the flow dynamics. The most obvious method consists in performing a local simulation with grid cells lower than the scale of the smallest mechanism affecting the flow. This “microscopic approach” [274] is computationally intense such that it cannot be realistically applied on practical cases. A second classical method consists in spatially-averaging the bed-roughness (roughness coefficient) and the vegetation distribution (vegetation density). Nevertheless, coupling these averaged parameters with the local flows properties may become difficult, and even intractable in presence of important spatial heterogeneities.

To integrate the effect of spatial heterogeneities into the computation, various researchers lead by V.Nikora [235, 237] have proposed to supplement the time-averaging of equations by a volume-averaging within a thin slab, or an area-averaging in a plane parallel to the mean bed surface. This approach provides new double-averaged (in both time and space) equations that relate to the time-averaged equations as the time-averaged equations relate to the local instant formulation. Important additional terms appear in the double-averaged equations and account for spatial heterogeneities. The use of Double-Averaged Models (DAM) for streams affected by scale heterogeneities like turbulent flows over rough-beds and canopies is growing. It has been already successfully used by a number of research groups worldwide for developing numerical models, designing experiments, data analysis and interpretation, and guiding conceptual developments and parameterizations [237]. Since the current research trend suggests that DAM may soon become a standard tool, I investigate in this section the main features of the approach, and their implications with respect to the objectives of the research. For this purpose, I give in sub-section 10.4.1 the mathematical formulation of the Double-Averaged Navier-Stokes (DANS) equations as established in the literature [235]. As pointed in sub-section 10.4.2, DANS equations have been used to study gravel-beds flows, sand-bed streams, vegetated-bed flows, and sediment transport in macro-roughness and canopies. Finally, I underline the major interest that applying the DAM to the multiphase drift-flux model would have (sub-section 10.4.3).

From an historical point of view, the DAM originates from the study of water flows in porous-media [7, 69] and airflows over forests and bushes [252, 253, 319]. Application of the approach to turbulent flows in and above vegetation canopies is reviewed by Finnigan and Shaw in [103]. In a similar manner, de Lemos reviewed in [68] the literature treating of spatial- and double-averaging in porous media.

In fluvial hydraulics, Smith and McLean [271] were the first to use spatial averaging for analyzing velocity profiles in a flow over a wavy bed. After that, a series of publications followed the meteorological approach where averaging was implemented within Cartesian coordinates [118, 208, 209, 234]. However, the real onset of DAM in hydraulics occurred in 2002 with the beginning of the DAM workshops[237].

10.4.1 DOUBLE-AVERAGED NAVIER-STOKES EQUATIONS

The Reynolds-averaged equations (2.19) and the time-averaged advection-diffusion equation for passive substance (2.21) are the starting point of the classical double-average approach. As this classical model is not practical in some situations involving highly 3D small-scale structures of the flow, the idea of the DAM is to supplement the time-averaging by a subsequent spatial-averaging in order to capture the spatial heterogeneities.

In this section, I perform the volume-averaging of the equations within a thin slab parallel to the mean slope of the bottom. As pointed by Nikora [235], volume-averaging has several advantages over area-averaging. First, volume-averaging better suits real measurement. Second, transformations of the equations are simpler and more transparent. Third, volume-averaged equations can be applied indistinctly to surface and subsurface flows. Naturally, the dimensions of the averaging domain should be much larger than the dominant turbulent scales, but much smaller than large-scale features in bed topography.

In order to volume-average the RANS equations, we define the intrinsic volume average of the parameter f(**x**,t), which is a scalar, a vector, or a tensor component, as follows:

$$\langle f \rangle(\mathbf{x},t) \triangleq \frac{1}{V_f}\int_{V_f} f(\mathbf{x},t)\,dV \tag{10.60}$$

where V_f is the volume occupied by the fluid within the fixed region of total volume V_0. In addition, we define the superficial volume average of f(**x**,t) as follows:

$$\langle f \rangle_s(\mathbf{x},t) \triangleq \frac{1}{V_0}\int_{V_f} f(\mathbf{x},t)\,dV \tag{10.61}$$

Obviously, these two volume-averaged parameters relate to each other through the roughness geometry function ϕ_s defined as [234]:

$$\phi_s \triangleq \frac{V_f}{V_0} \quad \text{such that} \quad \langle f \rangle_s = \phi_s \langle f \rangle \tag{10.62}$$

If volume-averaging the hydrodynamic equations in a continuous fluid domain (region above the roughness crests or vegetation tops) does not pose any difficulties, the same procedure in the discontinuous domain (region below the roughness crests or vegetation tops) requires to make use of transport theorems. Indeed, volume-averaging in a continuous domain follows the classical Reynolds rules presented in Chapter 2:

$$\langle f+g \rangle = \langle f \rangle + \langle g \rangle,\quad \langle af \rangle = a\langle f \rangle,\quad \langle a \rangle = a,\quad \left\langle \frac{\partial f}{\partial s} \right\rangle = \frac{\partial \langle f \rangle}{\partial s},\quad \text{and} \left\langle \langle f \rangle g \right\rangle = \langle f \rangle \langle g \rangle \tag{10.63}$$

where f and g are variables in the time-space domain, s is a spatial or temporal coordinate, and a is a constant. In a discontinuous domain, relationships (10.63) do not hold anymore because operators (10.60) and (10.61) do not always commute with time and spatial differentiation. I already mentioned this problem when deriving the 3D drift-flux model. Indeed, the interfaces between each phase constituted discontinuities across which time-average operators did not commute. On account of this, demonstration of the 3D drift-flux model relied on transport theorems presented and proved by Ishii [154]. To perform the

volume-averaging of the time-averaged hydrodynamic equations, two transport theorems are also available in the literature. As shown in [235, 270, 315], the volume-average of a time-derivative is linked to the time-derivative of a volume-average as follows:

$$\left\langle \overline{\frac{\partial f}{\partial t}}^{s} \right\rangle_s \triangleq \frac{\partial}{\partial t}\left\langle \bar{f}^{s} \right\rangle_s + \frac{1}{V_0}\overline{\int_{S_{int}} f\mathbf{v}.\mathbf{n}dS}^{s} \quad \text{and} \quad \left\langle \phi_t \overline{\frac{\partial f}{\partial t}} \right\rangle \triangleq \frac{1}{\phi_s}\frac{\partial}{\partial t}\left(\phi_s \left\langle \phi_t \bar{f} \right\rangle\right) + \frac{1}{V_f}\overline{\int_{S_{int}} f\mathbf{v}.\mathbf{n}dS}^{s} \tag{10.64}$$

where $\phi_t = T_f/T_0$ is the time analog of the roughness geometry function, **v** is the bed-surface velocity, **n** is the inwardly directed unit vector normal to the bed surface (into the fluid), and S_{int} is the extent of water-bed interface bounded by the averaging domain. By analogy, the transport theorems for the volume-average of a spatial derivative is given by:

$$\left\langle \overline{\frac{\partial f}{\partial x_i}}^{s} \right\rangle_s \triangleq \frac{\partial}{\partial x_i}\left\langle \bar{f}^{s} \right\rangle_s - \frac{1}{V_0}\overline{\int_{S_{int}} f n_i dS}^{s} \quad \text{and} \quad \left\langle \phi_t \overline{\frac{\partial f}{\partial x_i}} \right\rangle \triangleq \frac{1}{\phi_s}\frac{\partial}{\partial x_i}\left(\phi_s \left\langle \phi_t \bar{f} \right\rangle\right) - \frac{1}{V_f}\overline{\int_{S_{int}} f n_i dS}^{s} \tag{10.65}$$

For deriving the double-averaged Navier-Stokes equations, time-averaged parameters are decomposed in a spatially-averaged value and a spatial fluctuation as follows:

$$\bar{f} = \left\langle \bar{f} \right\rangle + \tilde{f} \tag{10.66}$$

We also assume that flow variables are sufficiently smooth for ensuring that:

$$\left\langle \left\langle \bar{f} \right\rangle \right\rangle = \left\langle \bar{f} \right\rangle, \quad \left\langle \tilde{f} \right\rangle = 0, \quad \overline{\left\langle \bar{u}_i \right\rangle \left\langle \bar{u}_j \right\rangle} = \left\langle \bar{u}_i \right\rangle \left\langle \bar{u}_j \right\rangle, \quad \text{and } \phi_s \left\langle \phi_t \right\rangle = \phi \tag{10.67}$$

Based on the previous definitions, assumptions, and theorems, Nikora [235] proposed the following formulation for the double-averaged continuity equation:

$$\frac{\partial \rho_w \phi}{\partial t} + \frac{\partial}{\partial x_i}\left(\rho_w \phi \left\langle \bar{u}_{w,i} \right\rangle\right) = 0 \tag{10.68}$$

In a similar manner, the double-averaged momentum equation for pure water is given by:

$$\begin{aligned} \frac{\partial \rho_w \phi \left\langle \bar{u}_{w,i} \right\rangle}{\partial t} + \frac{\partial}{\partial x_j}\left(\rho_w \phi \left\langle \bar{u}_{w,i} \right\rangle \left\langle \bar{u}_{w,j} \right\rangle\right) &= \rho_w \phi g_i - \frac{\partial}{\partial x_j}\left(\phi \left\langle \bar{p} \right\rangle\right) - \frac{\partial}{\partial x_j}\left(\rho_w \phi \left\langle \tilde{u}_{w,i} \tilde{u}_{w,j} \right\rangle\right) \\ &- \frac{\partial}{\partial x_j}\left(\rho_w \phi \left\langle \overline{u'_{w,i} u'_{w,j}} \right\rangle\right) + \frac{\partial}{\partial x_j}\left(\rho_w \phi \left\langle \nu \overline{\frac{\partial u_{w,i}}{\partial x_j}} \right\rangle\right) \\ &+ \frac{\phi}{\left\langle \phi_t \right\rangle}\frac{1}{V_f}\overline{\int_{S_{int}} p n_i dS}^{s} - \frac{\phi}{\left\langle \phi_t \right\rangle}\frac{1}{V_f}\overline{\int_{S_{int}} \rho_w \nu \frac{\partial u_{w,i}}{\partial x_j} n_j dS}^{s} \end{aligned} \tag{10.69}$$

For the advection diffusion equation, the double averaging procedure gives:

$$\begin{aligned} \frac{\partial \rho_d \phi \left\langle \bar{C} \right\rangle}{\partial t} + \frac{\partial}{\partial x_j}\left(\rho_d \phi \left\langle \bar{C} \right\rangle \left\langle \bar{u}_{w,j} \right\rangle\right) &= \frac{\partial}{\partial x_j}\left(\rho_d \phi \left\langle \overline{D\frac{\partial C}{\partial x_j}} \right\rangle\right) - \frac{\partial}{\partial x_j}\left(\rho_d \phi \left\langle \tilde{C} \tilde{u}_{w,j} \right\rangle\right) \\ &- \frac{\partial}{\partial x_j}\left(\rho_d \phi \left\langle \overline{C' u'_{w,j}} \right\rangle\right) - \rho_d \frac{\phi}{\left\langle \phi_t \right\rangle}\frac{1}{V_f}\overline{\int_{S_{int}} D\frac{\partial C}{\partial x_j} n_j dS}^{s} + \rho_d \left\langle \bar{S} \right\rangle \end{aligned} \tag{10.70}$$

As discussed by Nikora [235], equations (10.68), (10.69), and (10.70) contain additional terms in comparison with the conventional RANS. These terms include dispersive or form-induced stresses $\left\langle \tilde{u}_{w,i} \tilde{u}_{w,j} \right\rangle$, dispersive or form-induced concentration fluxes $\left\langle \tilde{C} \tilde{u}_{w,j} \right\rangle$. It also

includes the form drag per unit fluid volume $f_{p_i} = -\frac{1}{\langle \phi_t \rangle V_f} \overline{\int_{S_{int}} p n_i dS}^s$, the viscous drag per unit fluid volume $f_{v_i} = -\frac{1}{\langle \phi_t \rangle V_f} \overline{\int_{S_{int}} \rho_w \nu \partial u_{w,i} / \partial x_j n_j dS}^s$, and the diffusive flux at the water-bed surface interface $J = -\frac{1}{\langle \phi_t \rangle V_f} \overline{\int_{S_{int}} D \partial C / \partial x_j n_j dS}^s$ (including plant surfaces,…). Another important feature of these equations is the presence of the roughness geometry function which accounts for the reduction of the flow domain in presence of bed-roughness and vegetation.

Another option for deriving a double-averaged model would have been to first perform the volume-averaging of the local instant formulation, and then to apply the time averaging to the resulting equations [7, 69]. This method is usually referred as space-time averaging, by opposition to the time-space averaging method as proposed above. The time-space averaging seems however to be more suitable for environmental hydraulics, as this approach is consistent with traditional methods in turbulence research. It is indeed possible to exploit the results of one century of research in turbulence. In contrast, the space-time averaging option has no such strong experimental support.

In any case, the discrepancy appearing between the equations obtained by “time-space” averaging and “space-time” averaging is confusing and has recently initated several debates in literature [232]. However, recent works [68, 235] have overcome this apparent discrepancy by using the so-called double decomposition. In conclusion, the difference between individual terms should be only considered when developing closures or parameterization for these terms.

10.4.2 Applications of the Method

The DANS model has been used in several ways in literature and has already provided very interesting results in the field of environmental hydraulics. As the following literature review shows, DANS model underpins the development of numerical models, the design of laboratory and field experiments, the analysis of data and their interpretation, the development of conceptual formulations and parameterizations, and finally the development of closure relationships. In particular, the DANS approach has been used to investigate flows over vegetated bed, flows over gravel-beds or artificial elements simulating gravels, flows over sand-bed, and the transport of sediments.

Numerical models based, intuitively or explicitly, on DANS have been mainly applied for modelling vegetated channels [208, 209, 229, 314]. In [229], Nearly modified the RANS with a k-ω turbulence model by including vegetative drag terms. In [208, 209], Lopez and Garcia transformed the 3D problem of water flows in vegetated channel into a more tractable 1D problem by averaging the conservation laws over space and time. Hoffmann [146] developed a space–time averaged form of the Navier–Stokes equations, in order to

improve modelling of flow in densely obstructed channels. With a different approach, Coceal et al. [54] performed DNS computation of the flow over regular arrays of cubes simulating large bluff bodies of vegetation, compared the results with experiments [55], and derived double-average of the numerical parameters in order to investigate the effects of the cubes on the flow. The same approach was used by Souliotis and Prinos [274] for investigating vegetated flows. In a similar manner Stoesser and Nikora [279] used a LES numerical model for investigating the effect of bar spacing on flow dynamics. In all cases, the conjugated use of the DANS model and the numerical approach gave interesting insight into the flow mechanisms.

In many papers, the double-averaged approach helps in improving hydraulic definitions and exploiting experimental data. For instance, V.Nikora et al. used DANS to precise the definition of an uniform flow in [235] and to identify four specific types of rough-bed flows [236]. Aberle et al. [4], Cooper and Tait [60], as well as Cameron et al. [37] performed interesting analyses of spatial flow heterogeneity over rough gravel beds in terms of form-induced stresses. In addition, Mignot et al. [222] characterize near-bed turbulence tanks to double-averaged turbulent kinetic energy budget. In [251] and [185], DANS approach helped to investigate experimentally the sediment transport process on a flat bed. On the other hand, the effect of dunes was analyzed in [219]. Finally, DANS model underpinned the analysis of experimental measures on flows and transport phenomena over vegetated flows in [116, 117, 230, 247, 256]. In this respect, H. Nepf made major contributions to the field in [199, 230, 231, 282, 283].

10.4.3 PERSPECTIVES

In view of these recent successes, it is very tempting to apply double-average approach on the multiphase strategy proposed in this thesis. Indeed, the 3D drift-flux model was derived in chapter 2 by time-integrating the local instant formulation of the Navier-Stokes equations. By introducing the concepts of mixture parameters and drift-velocity, this multiphase approach provided a high-fidelity description of transport phenomena in water flows (air, sediments, and pollutants). Applying a subsequent volume-averaging to the drift-flux model should provide a new double-averaged drift-flux model particularly suited to transport phenomena over vegetation, bed-roughness and porous media. By analogy with the DANS, applying DAM to the drift-flux model should indeed make appear additional terms in the equations: dispersive or form-induced stresses, dispersive or form-induced concentration fluxes, form drag terms, viscous terms, and the diffusive fluxes at the water-bed surface interface. This new model would be a very interesting framework to analyze experimental data and develop numerical models in the field of eco-hydraulics and environmental hydrodynamics.

Summary and conclusion

My investigations of one-dimensional transient air-water flows led me to use both a new pressure gradient in the free surface equations and the multiphase theory called drift-flux model. At the end of my doctoral research, I had however every reasons to believe that these two propositions would provide a fruitful theory to investigate various phenomena in environmental hydrodynamics and eco-hydraulics. Consequently, I identified four gaps and inconsistency in literature that results of this thesis should help to correct in future works.

In section 10.1, classical models for sediment transport and pollutants diffusion are reviewed. Consequently, I extended the applicability of the original multi-layer one-dimensional drift-flux model to all transport phenomena in free surface flows. The multiphase approach enhanced the fidelity of the description of these environmental flows.

In section 10.2, I showed that transversal velocities arising in many applications make ineffective the one-dimensional approach. Consequently, I developed an original shallow-water-like drift-flux model that is an intermediate model between 1D and 3D models. From a theoretical point of view, the model was shown able to simulate 2D free-surface flows and even 3D intricate streams when using methods to accommodate the depth-integration with vertical distribution of the flow parameters.

In section 10.3, applicability of both the shallow-water model for pure water flows and the shallow-water-like model for two-phase flows was extended to pressurized flows as well. For this purpose, I developed an original Preissmann tube that is placed at the top of the computational model.

Finally, time-integrated models were shown inadequate when applied to streams affected by scale heterogeneities like turbulent flows over rough-beds and canopies (section 10.4). For overcoming this flaw of classical approaches, the use of Double-Averaged Models (DAM) seemed popular for developing numerical models, designing experiments, data analysis and interpretation, and guiding conceptual developments and parameterizations. Since the current research trend suggested that DAM may soon become a standard tool, I investigated in section 10.4 the main features of the approach and their implications with respect to the objectives of the research.

All the results presented in this chapter were clearly preliminary and had various degree of maturation. All of them have not yet been implemented in a computational code. However, some theoretical results have already been published in a book [173], a chapter book [172], a journal paper [171] and a conference paper [170]. In any case, they provide promising perspective of research.

Conclusions and Perspectives

Environmental flows crop up in various situations of the daily lives. This observation is particularly true for civil and environmental engineers, which face such phenomena in many practical cases, like rivers, pipe networks, and hydraulic structures. Since these situations are crucial for economical, ecological, and safety reasons, scientists and engineers have devoted a lot of efforts to understand and predict natural and anthropogenic occurrences of such flows. In this respect, transient phenomena and air-water interactions are still today sources of uncertainties that require further investigation. In addition, the classical distinction between free surface and pressurized flows appears unsuitable in situations where mixed patterns and multiphase behaviors appear.

The present thesis aimed at improving the understanding and description of air-water interactions in transient flows. In view of the recent successes of the Computational Fluid Dynamics in engineering, I chose this particular path to explore the behavior of environmental flows. To be more precise, the objective of my doctoral research was to develop an unified computational code for simulating a wide range of air-water flows. Seven conditions were sought in the development of this model. The approach had to:

- account for the multiphase character of flows;
- handle transient features of the flow;
- account for the scale heterogeneities in time and space;
- unify the description of pressurized and free surface flows;
- remain affordable from a computational point of view;
- be implementable under the form of a computational code;
- be validated on academic problems and applied on real cases.

As shown all along this thesis, reaching this ambitious objective required originality and novelty in many respects.

LITERATURE REVIEW

In Chapter 2, I reviewed the state-of-the-art results in Computational Fluid Dynamic (CFD) for environmental and civil engineering. In this process, I identified both the published results on which I can rely and the knowledge gaps I need to fill in order to meet the objectives of my thesis. Since CFD is a highly interdisciplinary activity, I successively analyzed the fundamentals of continuum fluid mechanics, the mathematical models for single- and multi-phase flows, the numerical methods for hyperbolic problems, and the HACH-ULG homemade modelling system WOLF.

In order to derive a mathematical model from real world observations, the continuum assumption, the continuity principle, and the law of momentum conservation have been proven very effective. For handling environmental flows, hydraulic engineers principally derived from the previous assumptions single-phase models coupled with an advection-diffusion equation. Describing 3D, 1D and mixed flows, these models gave interesting results to date. However, close scrutiny of these models revealed weaknesses. First, they failed to describe rigorously the impact of the dispersed phase on the water flow. Second, they failed to characterize the mechanism of dispersion within the water flow and to give an unambiguous definition of the concentration. Third, mixed flow formulations were shown unable to account for the presence of air in the pressurized flow and present spurious oscillations at the transition bore. Contrary to single-phase flows, the use of multiphase flow in civil and environmental engineering has remained circumscribed to very few attempts. They gave interesting results but the theory was still in its infancy. Instead, a more thorough two-phase theory originated from chemical and mechanical engineering. In particular, the drift-flux model seemed a reliable alternative to RANS equations. Drift-flux model addressed indeed most of the shortcomings identified in the single-phase approach. Nevertheless, a lot of work was required to adapt this theory to environmental flows since it has never been used in the field of environmental and civil engineering, especially for free surface flows. In addition, no analytical solution existed in most of the cases for these models. It appeared then necessary to discretize the equations and the computational domain. Review of basic discretisation techniques available in literature underlined the performance of “numerical shock-capturing” schemes over structured grid and the ability of the Finite Volume Method to handle discontinuities, to ensure conservation of the physical quantities, and to enable an easy integration into the modelling system WOLF.

Based on this literature review, I split my work in two parts. In Part I, I investigated the development of a computational code based on a single-phase model for simulating pure water mixed flows. In Part II, I derived a multiphase model for describing air-water mixed flows. In both parts, I aimed at overcoming shortcomings identified in literature.

SINGLE-PHASE FLOWS: SUMMARY

Chapter 3 of the present thesis was dedicated to the establishment of an improved “mathematical shock-capturing model” for pure water mixed flows. For this purpose, I investigated the mathematical foundations of the Preissmann slot, which extends the applicability of the Saint-Venant equations to pressurized flows. In particular, an original negative Preissmann slot was proposed to simulate sub-atmospheric pressurized flows. Next, a comparative discussion of the Preissmann, TPA, and Dual models gave a state-of-the art mathematical model for the Preissmann slot.

In Chapter 4, the previous mathematical model was discretised for an easy implementation into the computational code WOLF. For this purpose, the linear and non-linear analyses of the new model gave insight into the information propagation properties and the required boundary conditions. Based on the structure of the solution, an adapted numerical scheme

analogous to the FVS Wolf was derived. In addition, a pseudo-unsteady strategy drastically reduced the computation time for steady flows. Von Neumann analysis proved the stability of both models. Nevertheless, oscillations appear at the transition bore. Classical of mixed flow models, they originate from the discretization of both the equations and the computational domain. Their amplitude is directly linked to the variation of celerity within a computational mesh such that they appear only at the transition bore. By introducing alternative numerical schemes (the Roe solver, the AUSM scheme, an original Exact Riemann solver, and the Lax-Friedrichs scheme), I proved that oscillations do not disappear as long as a "numerical shock-capturing schemes" are used. In my opinion, only "numerical shock-tracking approaches" could successfully diminish these oscillations. However, such development went beyond the scope of this thesis.

In the course of this doctoral research, more than 50 validation benchmarks have been considered for validating the mathematical model, its discretization, as well as its implementation. As pointed in Chapter 5, this campaign of validation confirmed the ability of the new mathematical model to simulate consistently pure water mixed flows, including sub-atmospheric pressurized flows. Comparison between the six previous solvers underlined advantages and backwards of each method. In this thesis, I chose to use exclusively the Wolf splitting. Indeed, Wolf splitting proposed the best compromise between simplicity, robustness, and accuracy for the treatment of convective, pressure and source terms. A key argument in this choice was the easy treatment of source terms.

Once validated, the modified module WOLF1D served for assessing the hydraulic design of two different sewer systems: the storm water gravity drainage system of an airport, and a city low-pressure sewer network. In the first case, frequent inundations of the airport's parking facilities prompted authorities to assess the design of the gravity sewer network. Based on the performance criteria prescribed by the norm prEN752-4:1997, WOLF1D was shown to be an efficient tool to make the hydraulic design. In the second case, the sewer system was very different since it involved low-pressure pipes. Pumping stations intercepted waters from the old drainage system and injected them into a pressurized pipe. Consequently, both steady and transient phenomena were critical in the assessment of its hydraulic design. In this respect, the use of WOLF1D enabled to identify various defects in the first design of the low-pressure pipe.

MULTI-PHASE FLOWS: SUMMARY

Since the literature review showed that single-phase models coupled with an advection diffusion equation suffer various shortcomings, I chose to investigate multiphase theories in order to develop an improved model for air entrainment. In this respect, the drift-flux model seemed to me a good candidate even if its use in civil and environmental engineering has remained circumscribe to a very few attempts. In particular, one-dimensional drift-flux models available in the literature only described pressurized flows. This prompted me to develop an original formulation of the drift-flux model adapted to applications in civil en environmental engineering.

In Chapter 6, the 3D Drift-flux model was area-integrated over a general cross section presenting a free surface. In order to accommodate the model with a vertical distribution of the flow parameters, the cross-section was divided into sub-layers. The whole development resulted in a very original mathematical model for free surface stratified two-phase flows. The model included three partial differential equations for each layer. The first equation expressed the mixture continuity. The diffusion equation complemented this first equation in order to ensure the mass conservation of both phases on their own. Finally, a single equation accounted for the momentum conservation of the mixture (water and dispersed phase) taken as a whole. The simplicity of the original model directly resulted from suitable definitions of the area-average operator and of the mixture velocity.

Thanks to an original unification of all the air-water flows likely to appear in civil and environmental engineering, Chapter 7 proposed a single conceptual model describing multiphase mixed flows. The stratified part of the mixed flow was broken down into two layers. The upper layer was a pure airflow, while the lower layer was a mixture of water and dispersed air. The flow included then three phases: a water phase, a dispersed air phase, and a pure air phase above the free surface. Particularization of the multi-layer drift-flux model to air-water mixed flows resulted in five partial differential equations. By complementing the hydrostatic pressure term with an original uniform contribution that takes into account the presence of air, applicability of the lower layer equations was further extended to pressurized flows as well.

Based on this original mathematical model, chapter 8 was dedicated to the discretization of equations and their implementation into a new academic code called WOLF IMPack (Integrated Multi-Phase Pack). For this purpose, the wave structure of the solution was established by performing both linear and non-linear analyses of the equations. Next, the Wolf flux vector splitting was applied to the equations and the stability of the scheme was proven.

In order to assess the actual fidelity and usefulness of WOLF IMPack, chapter 10 presented the results of the validation campaign of the code and its application on a real case. The validation results proved that WOLF IMPack was an efficient and useful tool for investigating air water flows in open channels and closed conduits. The code gave indeed accurate results for pure water flows and air entrainment. To some extent, computation of the upper layer dynamics enabled also to account for air entrapment in closed conduits. However, post-transition oscillations appear in the solution like for WOLF1D. They contaminate the upper layer and compromise very rapidly the stability of the computation. Except this restriction, WOLF IMPack could be considered as a success with respect to the objectives of this thesis. Consequently, the code was applied for the design of the bottom outlet of a large dam. Used in conjunction with a physical model, these investigations underlined the apparition of strong air-water interactions that affected the flow dynamics. The use of WOLF IMPack gave insight into the measured data and enabled to predict

accurately the effect of design modification on both the discharge capacity of the gallery and the pressure profile along the structure.

CONCLUSIONS

By questioning the traditional distinction between free surface and pressurized flows in both parts of the thesis, I underlined the possibility to create a unified mathematical framework for all kinds of flows relevant in civil and environmental engineering. Thanks to a modified pressure gradient, the so-called "mathematical shock-capturing approach" described indeed both free surface and pressurized flows with the free surface equations. However, application of the "numerical shock-capturing approaches" to this original set of equations made appear the occurrence of instabilities in the computation. I inferred from the analysis of post-transition oscillations that only a "numerical shock-tracking approach" or a mobile grid could satisfactorily solve such a mathematical model with highly variable celerities. This mathematical model and the shortcoming of the numerical approach associated to it constitute the first scientific conclusion or proposition of this thesis. Nevertheless, using an artificially low pressure wave celerity enabled to overcome the previous problem. Efficiency of this trick was shown in the validation of WOLF1D.

As second scientific conclusion or proposition of this thesis, I proved that multiphase models were powerful and rigorous tools for developing computational codes in civil and environmental engineering. In particular, the drift-flux theory was shown an adequate alternative to the Navier-Stokes equations in order to derive mid- and large-scale free surface multiphase models. The original mathematical model developed in this thesis provided an improved description of environmental flows affected by air entrainment. Applied to practical cases, the new computational code WOLF IMPack was proved indeed very useful and efficient.

Along these two main propositions, series of innovations and original results have been established during the doctoral research. Indeed, I identified a negative Preissmann slot, the mathematical formulation associated to the Preissmann slot, a two-phase Preissmann slot, and a Preissmann tube for shallow-water like models. In my opinion, this constitutes a major contribution to the field of mixed flows simulations. From a numerical point of view, I have developed an original exact Riemann solver for Saint-Venant equations and their extension to pressurized flows. Coupled with the Godunov approach, this scheme presented interesting shock-capturing properties. I also implemented and published a pseudo-unsteady strategy to reduce drastically the computational effort for solving steady cases. In the field of multiphase flows, this thesis suggests many innovations like the derivation of free-surface drift-flux models, like the methods to accommodate cross-sectional and depth-integrated models with non-uniform distribution of the flow parameters, and like the bi-layer three-phase conceptual model. All these originalities and improvements attest of the novelty of this doctoral research.

Obviously, the computational codes resulting from these propositions and innovations meet the objectives of this thesis. First, WOLF IMPack accounts for the multiphase character of flows thanks to the notion of drift velocities and mixture parameters. Second, the use of unsteady equations and suitable shock-capturing numerical schemes enables to handle transient features of the flow in both WOLF1D and WOLF IMPack. Third, the rigorous time-integration of the Local Instant Formulation makes appear Reynolds stresses that account for the scale heterogeneities in time. Subsequent space-integration captures space heterogeneities of the flow parameters. This last issue could be even more rigorously treated by deriving a double-averaged drift-flux model. Fifth, the description of pressurized and free surface flows is unified thanks to an original mathematical formulation of the pressure gradient. Sixth, using a one-dimensional approach keeps the computation affordable with classical personal computers. Finally, both WOLF1D and WOLF IMPack have been validated on academic problems and applied on real cases. The hydraulic design of actual cases with WOLF1D and WOLF IMPack proved the industrial interest of the approach.

Finally, the original models proposed in this thesis constitute an improvement by comparison with classical single-phase models. First, mixture parameters account for the adverse impact of the dispersed air on the water flow. Second, the rigorous derivation of the model provided a very general diffusion equation for the transport of the dispersed phase. The concentration is rigorously defined and the drift velocity may account for all kinds of diffusion. Third, the new mixed flow model accounts for the presence of air below and above the free surface. This clearly constitutes a progress in the field of environmental flows.

PERSPECTIVES

Original concepts successfully applied on air-water flows in this thesis pave the way for further research on environmental flows. From a theoretical point of view, the four main perspectives of this thesis were briefly introduced in Chapter 10. This choice to integrate some element of perspective right in the doctoral research was prompted by the strong believe that multiphase theories and “mathematical shock-capturing models” provide a a fruitful theory to investigate various phenomena in environmental engineering.

Consequently, the multiphase drift-flux model was proven an elegant framework to investigate all kinds of environmental flows that interest civil en environmental engineering. In particular, it was shown well-suited to describe sediment and pollutant transport. In addition, I showed that depth-integration of the 3D drift-flux model over a multilayer flow depth including a free surface would provide a shallow-water like model for two-dimensional environmental flows. Furthermore, I have easily extended the applicability of such a 2D free-surface model to pressurized flows by introducing an original Preissmann tube. Finally, the effect of the vegetation and other macro-roughness was investigated by assessing the interest of the recent double-averaged approach. Mathematical formulation of these original concepts was provided in Chapter 10 without validation nor application.

These promising conclusions and perspectives closed this text but open my research to other horizons. What is more, these concepts and ideas are not the only perspective of research.

In Computational Fluid Dynamics, a lot of work is still necessary to handle mobile transitions in mixed flows. As already pointed, I have every reason to believe that only mobile grids or “numerical shock-tracking approaches” could successfully tackle this problem. From a more general point of view, the problem of the computation of highly variables celerities constitutes an important topic of research.

The original idea to use multiphase models in civil and environmental engineering may be taken a step further by investigating the applicability of the two-fluid model. Derived by time-integrating the local instant formulation, the two-fluid model keeps a separate set of equations for each phases. Describing very precisely interactions between each phase, this approach requires however to explicit very precisely all the interactions’ terms between each phase. It is clearly a promising avenue worth to explore.

Finally, there remains a strong need for fundamental research in order to supply the drift-flux model in terms of suitable constitutive equations. Indeed, constitutive laws specify the values of the drift velocity, the turbulent and viscous stresses both inside the fluid and at its boundaries, the exchange in volume between each phase,… Providing simple laws adapted for the most important applications would greatly improve the fidelity of the multiphase approach.

References

1. *www.hydro-international.com*. 2009.
2. *http://www.uleth.ca/vft/Oldman_River/OldmanDam.html*. 2010.
3. Abad, J.D., G.C. Buscaglia, and M.H. Garcia, *2D stream hydrodynamic, sediment transport and bed morphology model for engineering applications.* Hydrological Processes, 2008. **22**(10): p. 1443-1459.
4. Aberle, J., K. Koll, and A. Dittrich, *Form induced stresses over rough gravel-beds.* Acta Geophysica, 2008. **56**(3): p. 584-600.
5. Aldrighetti, E. and P. Zanolli, *A high resolution scheme for flows in open channels with arbitrary cross-section.* International Journal for Numerical Methods in Fluids, 2005. **47**(8-9): p. 817-824.
6. Andre, S., *High Velocity Aerated Flows on Stepped Chutes with Macro-Roughness Element*. Communications du laboratoire de constructions hydrauliques, ed. Ecole Polytechnique Fédérale de Lausanne. 2004, Lausanne. p. 270.
7. Antohe, B.V. and J.L. Lage, *A general two-equation macroscopic turbulence model for incompressible flow in porous media.* International Journal of Heat and Mass Transfer, 1997. **40**(13): p. 3013-3024.
8. Arbenz, K. and O. Bachmann, *Eléments d'analyse numérique et appliquée*. 1992: Presses Polytechniques et Universitaires Romandes (PPUR).
9. Archambeau, P., *Contribution à la modélisation de la genèse et de la propagation des crues et inondations*, in *Applied Hydrodynamics and Hydraulic Constructions*. 2006, Liège University: Liège. p. 410.
10. Archambeau, P., B. Dewals, S. Erpicum, T. Mouzelard, and M. Pirotton, *Wolf software: a fully integrated device applied to modelling gradual dam failures and assessing subsequent risks*, in *Advances in Fluid Mechanics IV*, M. Rahman, R. Verhoeven, and C.A. Brebbia, Editors. 2002, WIT Press.
11. Aris, R., ed. *Vectors, Tensors and the Basic Equations of Fluid Mechanics*. 1962, Prentice-Hall: Englewood Cliffs, N.J.
12. Arora, M. and P.L. Roe, *On Postshock Oscillations Due to Shock Capturing Schemes in Unsteady Flows.* Journal of computational physics, 1997. **130**: p. 25-40.
13. ASCE, *Sedimentation engineering : processes, measurements, modeling, and practice*, ed. M.H. García. 2008, Reston, Va.: American Society of Civil Engineers. p. 1132.
14. ASCE Task Committee on Turbulence Models in Hydraulic Computations, *Turbulence modeling of surface water flow and transport: Part I.* J. Hydraul. Eng.-ASCE, 1988. **114**: p. 970-991.
15. Audusse, E., *A Multilayer Saint-Venant Model*. 2004, HAL - CCSd - CNRS.
16. Audusse, E. and M.-O. Bristeau, *Finite-Volume Solvers for a Multilayer Saint-Venant System.* International Journal of Applied Mathematics and Computer Science, 2007. **17**(3): p. 311-320.
17. Audusse, E., M.-O. Bristeau, B. Perthame, and J. Sainte-Marie, *A multilayer Saint-Venant system with mass exchanges for Shallow Water flows: Derivation and numerical validation.* Modélisation Mathématique et Analyse Numérique, 2009: p. 1-30.
18. Audusse, E., M.O. Bristeau, and A. Decoene, *3D Free Surface Flows Simulations Using a Multilayer Saint-Venant Model. Comparisons with Navier-Stokes Solutions*, in *Numerical Mathematics and Advanced Applications*. 2006. p. 181-189.
19. Awad, M.M. and Y.S. Muzychka. *Bounds on Two-Phase Flow - Part 1 - Frictional Pressure Gradient in Circular Pipes*. in *ASME International Mechanical Engineering Congress and Exposition*. 2005. Orlando, Florida.

20. Awad, M.M. and Y.S. Muzychka, *Effective property models for homogeneous two-phase flows.* Experimental Thermal and Fluid Science, 2008. **33**(1): p. 106-113.
21. Balayn, P., *Contribution à la modélisation numérique de l'évolution morphologique des cours d'eau aménagés lors de crues*. 2001, Université Claude-Bernard: Lyon 1. p. 139.
22. Benkhaldoun, F., I. Elmahi, and M. Seal, *Well-balanced finite volume schemes for pollutant transport by shallow water equations on unstructured meshes.* Journal of computational physics, 2007. **226**(1): p. 180-203.
23. Bergant, A., A.R. Simpson, and A.S. Tijsseling, *Water hammer with column separation: A historical review.* Journal of Fluids and Structures, 2006. **22**(2): p. 135-171.
24. Bestion, D., *The physical closure laws in the CATHARE code.* Nuclear Engineering and Design, 1990. **124**(3): p. 229-245.
25. Betamio de Almeida, A. and E. Koelle, *Fluid Transients in Pipe Networks*. International Series on Computational Engineering, ed. C.M. Publications. 1992, Boston.
26. Bombardelli, F. and H. Chanson, *Progress in the observation and modeling of turbulent multi-phase flows.* Environmental Fluid Mechanics, 2009. **9**(2): p. 121-123.
27. Bombardelli, F. and S. Jha, *Hierarchical modeling of the dilute transport of suspended sediment in open channels.* Environmental Fluid Mechanics, 2009. **9**(2): p. 207-235.
28. Bourdarias, C., M. Ersoy, and S. Gerbi, *Air entrainment in transient flows in closed water pipes: a two-layer approach*. 2009.
29. Bourdarias, C., M. Ersoy, and S. Gerbi, *A kinetic scheme for pressurized flows in non uniform closed water pipes.* Monograf´ıas de la Real Academia de Ciencias de Zaragoza, 2009. **31**: p. 1-20.
30. Bourdarias, C. and S. Gerbi, *A Finite Volume Scheme for a Model Coupling Unsteady Flows in Open Channels and in Pipelines.* Journal of Computational and Applied Mathematics, 2007. **209**(1): p. 109-131.
31. Bourdarias, C. and S. Gerbi, *A Conservative Model for Unsteady Flows in Deformable Closed Pipes and Its Implicit Second Order Finite Volume Discretisation.* Computers & Fluids, 2008. **37**(10): p. 1225-1237.
32. Bourdarias, C., S. Gerbi, and M. Gisclon, *A kinetic formulation for a model coupling free surface and pressurized flows in closed pipes.* Journal of Computational and Applied Mathematics, 2008. **218**(2): p. 522.
33. Brennen, C.E., *Fundamentals of Multiphase Flows*. 2005: Cambridge University Press.
34. Brockmeier, U., A. Schaffrath, and H. Unger, *Verification of the two-phase stratified-flow model in by separate effect tests.* Nuclear Engineering and Design, 1995. **154**(1): p. 43-50.
35. Butterworth, D., *A comparison of some void-fraction relationships for co-current gas-liquid flow.* International Journal of Multiphase Flow, 1975. **1**(6): p. 845-850.
36. Caleffi, V., A. Valiani, and A. Zanni, *Finite volume method for simulating extreme flood events in natural channels.* Journal of Hydraulic Research, 2003. **41**(2): p. 167-177.
37. Cameron, S., V. Nikora, and S. Coleman, *Double-averaged velocity and stress distributions for hydraulically-smooth and transitionally-rough turbulent flows.* Acta Geophysica, 2008. **56**(3): p. 642-653.
38. Candel, S., *Mécanique des fluides*, ed. Dunod. Vol. 1-2. 1990, Paris. p. 450.
39. Capart, H., *Dam-break induced geomorphic flows and the transitions from solid- to fluid-like behaviour across evolving interfaces*. 2000, Université catholique de Louvain. p. 208.
40. Cardle, J. and C. Song, *Mathematical Modeling of Unsteady Flow in Storm Sewers.* International Journal of Engineering Fluid Mechanics, 1983. **1**(4): p. 495-518.
41. Cardle, J. and C. Song, *Measurement of Mixed Transient Flows.* Journal of Hydraulic Engineering, 1988. **115**(2): p. 169-182.
42. Castro, M.J., A. Garcia-Rodriguez, J.M. Gonzales-Vida, J. Macias, C. Pares, and M.E. Vazquez-Cendon, *Numerical simulation of two-layer shallow water flows through channels with irregular geometry.* J. Comput. Phys., 2004. **195**(1): p. 202-235.
43. Chahed, J., V. Roig, and L. Masbernat, *Eulerian-Eulerian two-fluid model for turbulent gas-liquid bubbly flows.* International Journal of Multiphase Flow, 2003. **29**(1): p. 23-49.
44. Chanson, H., *Environmental Hydraulics For Open Channel Flows*, ed. Elsevier. 2004. p. 420 pages.

45. Chanson, H., *Bubbly flow structure in hydraulic jump.* European Journal of Mechanics - B/Fluids, 2006. **26**(3): p. 367-384.
46. Chanson, H., *Solutions Analytiques de l'Onde de Rupture de Barrage sur Plan Horizontal et Incliné.* Houille Blanche-Rev. Int., 2006(3): p. 76-86.
47. Charney, J.G., R. Fjörtoft, and J. Neumann, *Numerical Integration of the Barotropic Vorticity Equation.* Tellus, 1950. **2**(4): p. 237-254.
48. Chassaing, P., *Turbulence en Mécanique des Fluides - Analyse du phénomène en vue de sa modélisation à l'usage de l'ingénieur*. Polytech, ed. Cepadues. 2000. p. 660.
49. Chen, Q., G. Dai, and H. Liu, *Volume of Fluid Model for Turbulence Numerical Simulation of Stepped Spillway Overflow.* Journal of hydraulic Engineering, 2002. **128**(7): p. 683-688.
50. Cheng, X., Y. Chen, and L. Luo, *Numerical simulation of air-water two-phase flow over stepped spillways.* Science in China Series E: Technological Sciences, 2006. **49**(6): p. 674-684.
51. Chinnayya, A. and A. Leroux, *A new general Riemann solver for the shallow-water equations with friction and topography,*. 1999.
52. Chisholm, D., *Influence of pipe surface roughness on friction pressure gradient during two-phase flow.* Journal of Mechanical Engineering Science, 1978. **20**(6): p. 353-354.
53. Cicchitti, A., C. Lombaradi, M. Silversti, G. Soldaini, and R. Zavattarlli, *Two-phase cooling experiments - pressure drop heat transfer burnout measurements.* Energia Nucleare, 1960. **7**(6): p. 407-425.
54. Coceal, O., T. Thomas, and S. Belcher, *Spatially-averaged flow statistics within a canopy of large bluff bodies: Results from direct numerical simulations.* Acta Geophysica, 2008. **56**(3): p. 862-875.
55. Coceal, O., T. Thomas, I. Castro, and S. Belcher, *Mean Flow and Turbulence Statistics Over Groups of Urban-like Cubical Obstacles.* Boundary-Layer Meteorology, 2006. **121**(3): p. 491-519.
56. Coddington, P. and R. Macian, *A study of the performance of void fraction correlations used in the context of drift-flux two-phase flow models.* Nuclear Engineering and Design, 2002. **215**(3): p. 199-216.
57. Colebrook, C.F., *Turbulent flow in pipes, with particular reference to the transition region between smooth and rough pipe laws.* Jour. Ist. Civil Engrs., 1939.
58. Collier, J.G. and J.R. Thome, eds. *Convective Boiling and Condensation*. Oxford Engineering Science Series, 38. 1996, Oxford University Press. 640.
59. Cools, B.M., *Procès verbal de la réunion d'expertise du 3/12/2009 concernant le comportement hydraulique du parking C3*. 2010.
60. Cooper, J. and S. Tait, *The spatial organisation of time-averaged streamwise velocity and its correlation with the surface topography of water-worked gravel beds.* Acta Geophysica, 2008. **56**(3): p. 614-641.
61. Corradini, M.L., *Fundamentals of Multiphase Flow*, ed. Department of Engineering Physics University of Wisconsin. 1997.
62. Crank, J. and P. Nicolson, *A practical method for numerical evaluation of solutions of partial differential equations of the heat-conduction type.* Advances in Computational Mathematics, 1996. **6**(1): p. 207-226.
63. Cunge, J.A., F.M. Holly, and A. Verwey, *Practical Aspects of Computational River Hydraulics*. Monographs and surveys in water resources engineering. 1980, Boston: Pitman Advanced Pub. Program.
64. Cunge, J.A. and M. Wegner, *Intégration numérique des équations d'écoulement de Barré de Saint Venant par un schéma implicite de différences finies.* La Houille Blanche 1964: p. 33-39.
65. Daniels, L.C., C. Guardino, and C.P. Thompson, *An Implicit Two-Phase Compressible Flow Solver For Pipelines.* Multiphase Science and Technology, 2002. **14**(2): p. 96.
66. De Henau, V. and G.D. Raithby, *A transient two-fluid model for the simulation of slug flow in pipelines--I. Theory.* International Journal of Multiphase Flow, 1995. **21**(3): p. 335-349.
67. De Henau, V. and G.D. Raithby, *A transient two-fluid model for the simulation of slug flow in pipelines--II. Validation.* International Journal of Multiphase Flow, 1995. **21**(3): p. 351-363.

68. De Lemos, M., *Analysis of turbulent flows in fixed and moving permeable media.* Acta Geophysica, 2008. **56**(3): p. 562-583.
69. de lemos, M. and M. Pedras, *Recent mathematical models for turbulent flow in saturated rigid porous media*. Vol. 123. 2001, New York, NY, ETATS-UNIS: American Society of Mechanical Engineers.
70. Delhaye, J.M., *Jump conditions and entropy sources in two-phase systems. Local instant formulation.* International Journal of Multiphase Flow, 1974. **1**(3): p. 395-409.
71. Detrembleur, S., *No Title*, in *HACH-ARGENCO*. 2010, University of Liège.
72. Detrembleur, S., B.J. Dewals, P. Archambeau, S. Erpicum, and M. Pirotton, *Modélisation numérique et gestion du risque inondation en milieu urbain sur base de modèles topographiques à haute résolution.* Techniques - Sciences - Méthodes, 2009. **Accepted**.
73. Detrembleur, S., B.J. Dewals, S. Erpicum, P. Archambeau, and M. Pirotton, *A 2D vertical finite volume solver using a level set approach for simulating free surface incompressible flows.* European Journal of Mechanical and Environmental Engineering, 2009. **2009**(3): p. 4-9.
74. Dewals, B., P. Archambeau, S. Erpicum, T. Mouzelard, and M. Pirotton. *Coupled computations of highly erosive flows with WOLF software*. in *Proc. 5th Int. Conf. on Hydro-Science & -Engineering*. 2002. Warsaw.
75. Dewals, B.J., *Une approche unifié pour la modélisation d'écoulements à surface libre, de leur effet érosif sur une structure et de leur intéraction avec divers constituants*, in *Applied Hydrodynamics and Hydraulic Constructions*. 2006, Liège University: Liège. p. 630.
76. Dewals, B.J., S. Andre, M. Pirotton, and A. Schleiss. *Quasi 2D-numerical model of aerated flow over stepped chutes*. in *30th IAHR Congress*. 2003. Greece.
77. Dewals, B.J., S. André, A. Schleiss, and M. Pirotton. *Validation of a quasi-2D model for aerated flows over stepped spillways for mild and steep slopes*. in *Proc. 6th Int. Conf. of Hydroinformatics*. 2004. Singapore.
78. Dewals, B.J., J. Ernst, S. Detrembleur, P. Archambeau, S. Erpicum, and M. Pirotton, *Micro-scale flood risk analysis based on detailed 2D hydraulic modelling and high resolution geographic data.* Nat. Hazards, 2009. **published online**.
79. Dewals, B.J., S. Erpicum, P. Archambeau, S. Detrembleur, and M. Pirotton, *Depth-Integrated Flow Modelling Taking into Account Bottom Curvature.* Journal of Hydraulic Research, 2006. **44**(6): p. 787-795.
80. Dewals, B.J., S. Erpicum, P. Archambeau, S. Detrembleur, and M. Pirotton, *Hétérogénéité des échelles spatio-temporelles d'écoulements hydrosédimentaires et modélisation numérique.* Houille Blanche-Rev. Int., 2008: p. 109-114.
81. Dewals, B.J., S.A. Kantoush, S. Erpicum, M. Pirotton, and A. Schleiss, *Experimental and numerical analysis of flow instabilities in rectangular shallow basins.* Environmental Fluid Mechanics, 2008. **8**(1): p. 31-54.
82. Diener, R. and L. Friedel, *Reproductive accuracy of selected void fraction correlations for horizontal and vertical upflow.* Forschung im Ingenieurwesen, 1998. **64**(4): p. 87-97.
83. Djordjevic, S. and G.A. Walters. *Mixed free-surface/pressurized flows in sewers*. in *WaPUG Meting from Scotland and Northern Ireland*. 2004. Dunblane.
84. Drew, D.A., *Mathematical Modeling of Two-Phase Flow.* Annual Review of Fluid Mechanics, 1983. **15**(1): p. 261-291.
85. Drew, D.A. and S.L. Passman, *Theory of Multicomponent Fluids. Applied Mathematical Sciences*, 1999. **135**.
86. Dubois, J., *Comportement hydraulique et modélisation des écoulements de surface*. Communication, ed. Laboratoire de Constructions Hydrauliques Ecole Polytechnique Fédérale de Lausanne. 1998. p. 199.
87. Dufresne, M., M. Pirotton, B.J. Dewals, S. Erpicum, and P. Archambeau, *Experimental investigation of flow and deposit patterns in rectangular shallow reservoirs: preliminary analysis*, in *Proc. International Workshop on Environmental Hydraulics - Theoretical, Experimental and Computational Solutions*. 2009, Taylor & Francis: Valencia, Spain.

88. Dukler, A.E., Moye Wicks III, and R.G. Cleveland, *Frictional pressure drop in two-phase flow: A comparison of existing correlations for pressure loss and holdup.* AIChE Journal, 1964. **10**(1): p. 38-43.
89. Dukler, A.E., M. Wicks, and R.G. Cleveland, *Frictional pressure drop in two-phase flow: B. An approach through similarity analysis.* AIChE Journal, 1964. **10**(1): p. 44-51.
90. Durst, F., D. Miloievic, and B. Schönung, *Eulerian and Lagrangian predictions of particulate two-phase flows: a numerical study.* Applied Mathematical Modelling, 1984. **8**(2): p. 101-115.
91. Dyke, V., *An album of fluid motion*, ed. P. Press. 1982.
92. E. Audusse, M. O. Bristeau, and A. Decoene, *Numerical simulations of 3D free surface flows by a multilayer Saint-Venant model.* International Journal for Numerical Methods in Fluids, 2008. **56**(3): p. 331-350.
93. Erpicum, S., *Optimisation objective des paramètres en écoulements turbulents à surface libre sur maillage multibloc*, in *Applied Hydrodynamics and Hydaulic Construction*. 2006, University of Liège: Liège. p. 356.
94. Erpicum, S., B.J. Dewals, P. Archambeau, S. Detrembleur, and M. Pirotton, *Detailed inundation modelling using high resolution DEMs.* Engineering Applications of Computational Fluid Mechanics, 2010. **2**(4).
95. Erpicum, S., B.J. Dewals, P. Archambeau, and M. Pirotton, *Dam-break flow computation based on an efficient flux-vector splitting.* J. Comput. Appl. Math., 2009(published online).
96. Erpicum, S., F. Kerger, P. Archambeau, B.J. Dewals, and M. Pirotton. *Experimental and numerical investigation of mixed flow in a Gallery*. in *Multiphase Flow V*. 2009. New Forest: WIT Press.
97. Erpicum, S., T. Meile, B.J. Dewals, M. Pirotton, and A.J. Schleiss, *2D numerical flow modeling in a macro-rough channel.* Int. J. Numer. Methods Fluids, 2009. **61**(11): p. 1227-1246.
98. Estrada, O.P., *Investigation on the Effects of Entrained Air in Pipelines*, in *Eigenverlag des Instituts für Wasserbau der Universität Stuttgart*. 2007, Universität Stuttgart. p. 200.
99. Eykhoff, P., *System Identification: Parameter and State Estiamtion*, ed. W. Sons. 1974.
100. Falvey, H.T., *Air-Water Flow in Hydraulic Structures*. Engineering Monogaph. Vol. 41. 1980: United States Department of the Interior.
101. Ferrand, P. and S. Aubert, *A New Mixed AUSM+ Liou Scheme : an Extension of th Mixed Van Leer Flux Splitting.* Comptes rendus de l'Académie des sciences, 1998. **326**(2b): p. 5-11.
102. Ferziger, J.H. and M. Peric, *Computational methods for fluid dynamics*. 3° ed. 2002, Berlin: Springer. p. 423.
103. Finnigan, J. and R. Shaw, *Double-averaging methodology and its application to turbulent flow in and above vegetation canopies.* Acta Geophysica, 2008. **56**(3): p. 534-561.
104. Fischer-Antze, T., N. Rüther, N. Olsen, and D. Gutknecht, *Three-dimensional (3D) modeling of non-uniform sediment transport in a channel bend with unsteady flow.* J. Hydraul. Res., 2009. **47**(5): p. 670-675.
105. Fjelde, K.K. and K.H. Karlsen, *High-resolution hybrid primitive-conservative upwind schemes for the drift flux model.* Computers & Fluids, 2002. **31**(3): p. 335-367.
106. Flåtten, T. and S.T. Munkejord, *The approximate Riemann solver of Roe applied to a drift-flux two-phase flow model.* M2AN, 2006. **40**(4): p. 735-764.
107. Fraccarollo, L. and A. Armanini. *A semi-analytical solution for the dam-break problem over a movable bed*. in *Proc. XXVIII IAHR Congress*. 1999. Graz, Autriche.
108. França, F. and R.T. Lahey Jr, *The use of drift-flux techniques for the analysis of horizontal two-phase flows.* International Journal of Multiphase Flow, 1992. **18**(6): p. 787-801.
109. Froehlich, D.C. *IMPACT Project field tests 1 and 2: "blind" simulation by DaveF*. in *2nd IMPACT Project Workshop*. 2002. Mo-i-Rana.
110. Fuamba, M., *Contribution on Transient Flow Modelling In Storm Sewers.* Journal of Hydraulic Research, 2003. **40**(6): p. 685-693.
111. Gallouët, T., J.-M. Hérard, and N. Seguin, *Some approximate Godunov schemes to compute shallow-water equations with topography.* Computers & Fluids, 2003. **32**(4): p. 479-513.
112. García-Cascales, J.R., *Conservative Numerical Schemes for Unsteady 1D Two Phase Flow*. 2001, Universidad Politécnica de Valencia, Spain.

113. Garcia-Navarro, P., F. Alcrudo, and A. Priestley, *An implicit method for water flow modelling in channels and pipes.* Journal of Hydraulic Research, 1994. **32**(5): p. 721-742.
114. Ghamry, H.K. and P.M. Steffler, *Effect of applying different distribution shapes for velocities and pressure on simulation of curved open channels.* J. Hydraul. Eng.-ASCE, 2002. **128**: p. 969-982.
115. Ghamry, H.K. and P.M. Steffler, *Two dimensional vertically averaged and moment equations for rapidly varied flows.* J. Hydraul. Res., 2002. **40**: p. 579-587.
116. Ghisalberti, M. and H. Nepf, *Shallow Flows Over a Permeable Medium: The Hydrodynamics of Submerged Aquatic Canopies.* Transport in Porous Media, 2009. **78**(2): p. 309-326.
117. Ghisalberti, M. and H.M. Nepf, *The limited growth of vegetated shear layers.* Water Resour. Res., 2004. **40**(7): p. W07502.
118. Giménez-Curto, L.A. and M.A.C. Lera, *Oscillating turbulent flow over very rough surfaces.* J. Geophys. Res., 1996. **101**(C9): p. 20745-20758.
119. Glaister, P., *Approximate Riemann solutions of the shallow water equations.* Journal of Hydraulic Research, 1988. **26**(3): p. 293-306.
120. Glimm, J., J. Grove, X.L. Li, and N. Zhao, *Simple Front Tracking.* Contemporary Mathematics, 1999. **238**.
121. Glimm, J., X.L. Li, Y.J. Liu, Z.L. Xu, and N. Zhao, *Conservative front tracking with improved accuracy.* SIAM Journal on Numerical Analysis, 2003. **41**(5): p. 1926-1947.
122. Glimm, J., X.L. Li, Y.J. Liu, and N. Zhao, *Conservative front tracking and level set algorithms.* Proceedings of the National Academy of Sciences of the United States of America, 2001. **98**(25): p. 14198-14201.
123. Godunov, S.K., *Different Methods for Shock Waves*. 1954, Moscow State University.
124. Godunov, S.K., *A Difference Scheme for Numerical Solution of Discontinuous Solution of Hydrodynamic Equations. Math. Sbornik*, 1959. **47**: p. 271-306.
125. Goutal, N. and F. Maurel, *A finite volume solver for 1D shallow-water equations applied to an actual river.* International Journal for Numerical Methods in Fluids, 2002. **38**(1): p. 1-19.
126. Graf, W.H. and M.S. Altinakar, *Hydraulique fluviale. Tome 1 : Ecoulement permanent uniforme et non uniforme*. 1ère ed. Traité de Génie civil de l'Ecole polytechnique fédérale de Lausanne, ed. W. René. Vol. 16. 1993, Lausanne: Presses Polytechniques et Universitaires Romandes. p. 259.
127. Graf, W.H. and M.S. Altinakar, *Fluvial Hydraulics: flow and transport processes in channels of simple geometry*, ed. Wiley. 1998, NY.
128. Greimann, B.P., M. Muste, and F.M.J. Holly, *Two-phase Formulation of Suspended Sediment Transport* Journal of Hydraulic Research, 1999. **37**(4): p. 479-500.
129. Gudmunson, R.L., *A Numerical Study of The Two-Fluid Models for Dispersed Two-Phase Flow*, in *Numerical Analysis and Computer Science*. 2005, Royal Institute of Technology, Stockholm: Stockholm. p. 40.
130. Guinot, V., *The discontinuous profile method for simulating two-phase flow in pipes using the single component approximation.* International Journal for Numerical Methods in Fluids, 2001. **37**(3): p. 341-359.
131. Guinot, V., *Numerical simulation of two-phase flow in pipes using Godunov method.* International Journal for Numerical Methods in Engineering, 2001. **50**(5): p. 1169-1189.
132. Guinot, V., *Godunov-type Schemes: An introduction for engineers*, ed. E. Science. 2003, Amsterdam. p. 480.
133. Guinot, V., *Wave propagation in fluids: models and numerical techniques*. 2008: ISTE. p. 400.
134. Guo, Q.-C. and Y.-C. Jin, *Modeling Sediment Transport Using Depth-Averaged and Moment Equations.* J. Hydraul. Eng.-ASCE, 1999. **125**(12): p. 1262-1269.
135. Guo, Q. and C. Song, *Surging in Urban Storm Drainage Systems.* Journal of Hydraulic Engineering, 1990. **116**(12): p. 1523-1537.
136. Hager, W.H., *Blasius: A life in research and education.* Experiments in Fluids, 2003. **34**(5): p. 566-571.
137. Harlow, B.L. and K. Welch, *The SMAC method: A numerical Technique for Calculating Incompressible Fluid Flows*. 1970, Los Alamos Laboratory Report

138. Harten, A. and J. Hyman, *Self Adjsuting Method for One Dimensional Hyperbolic Conservation Laws.* Journal of computational physics, 1983. **50**(2): p. 235-269.
139. Harten, A. and J.M. Hyman, *Self adjusting grid methods for one-dimensional hyperbolic conservation laws.* Journal of computational physics, 1983. **50**(2): p. 235-269.
140. Hibiki, T., H. Goda, S. Kim, M. Ishii, and J. Uhle, *Structure of vertical downward bubbly flow.* International Journal of Heat and Mass Transfer, 2004. **47**(8-9): p. 1847-1862.
141. Hibiki, T. and M. Ishii, *Distribution parameter and drift velocity of drift-flux model in bubbly flow.* International Journal of Heat and Mass Transfer, 2002. **45**(4): p. 707-721.
142. Hibiki, T. and M. Ishii, *One-dimensional drift-flux model and constitutive equations for relative motion between phases in various two-phase flow regimes.* International Journal of Heat and Mass Transfer, 2003. **46**(25): p. 4935-4948.
143. Hibiki, T. and M. Ishii, *One-dimensional drift-flux model for two-phase flow in a large diameter pipe.* International Journal of Heat and Mass Transfer, 2003. **46**(10): p. 1773-1790.
144. Hirsch, C., *Numerical Computation of Internal and External Flows - Fundamentals of Numerical Discretization*. Vol. 1. 1988, Chichester: Wiley. p. 515.
145. Hirsch, C., *Numerical Computation of Internal and External Flows - Computational Methods for Inviscid and Viscous Flows*. Vol. 2. 1990, Chichester: Wiley. p. 691.
146. Hoffmann, M.R., *Application of a Simple Space-Time Averaged Porous Media Model to Flow in Densely Vegetated Channels.* 2004. **7**(3): p. 10.
147. Hsu, T.-J., J.T. Jenkins, and P.L.-F. Liu, *On two-phase sediment transport: sheet flow of massive particles.* Proceedings of the Royal Society of London. Series A: Mathematical, Physical and Engineering Sciences, 2004. **460**(2048): p. 2223-2250.
148. Hsu, T.-J., J.T. Jenkins, and P.L.F. Liu, *On two-phase sediment transport: Dilute flow.* J. Geophys. Res., 2003. **108**(C3): p. 3057.
149. http://www.worksongs.com/archives/2006/11/dear_mom_i_fina.php.
150. Hyman, J., *Numerical Methods For Tracking Interfaces*, in *Physica 12D*, North-Holland, Editor. 1984: 396-407. p. 396-407.
151. Idelcik, I.E., ed. *Mémento des pertes de charge. Coefficients de perte de charge singulières et de pertes de charge par frottement*. 1969, Eyrolles.
152. Irgens, F., *Continuum Mechanics*, ed. Springer-Verlag. 2008, Berlin-Heidelberg.
153. Ishii, M., *One-dimensional drift-flux model and constitutive equations for relative motion between phases in various two-phase flow regimes*. 1977. p. Medium: X; Size: Pages: 62.
154. Ishii, M. and T. Hibiki, *Thermo-fluid dynamics of two-phase flow*. First ed. 2006: Springer Science, USA. p. 430.
155. Issa, R.I., M. Bonizzi, and S. Barbeau, *Improved closure models for gas entrainment and interfacial shear for slug flow modelling in horizontal pipes.* International Journal of Multiphase Flow, 2006. **32**(10-11): p. 1287-1293.
156. Issa, R.I. and M.H.W. Kempf, *Simulation of slug flow in horizontal and nearly horizontal pipes with the two-fluid model.* International Journal of Multiphase Flow, 2003. **29**(1): p. 69-95.
157. J. I. Ramos, *One-dimensional, time-dependent, homogeneous, two-phase flow in volcanic conduits.* International Journal for Numerical Methods in Fluids, 1995. **21**(3): p. 253-278.
158. Jeffrey, A., *Quasilinear Hyperbolic Systems and Waves*. Research Notes in Mathematics, ed. P. Publishing. 1976, London-San Francisco-Melbourne.
159. Jeffrey, A. and T. Taniuti, *Non-Linear Wave Propagation with Applications to Physics and Magnetohydrodynamics*. Mathematics in Science and Engineering, ed. A. Press. 1964, New-York - London.
160. Jha, S. and F. Bombardelli, *Two-phase modeling of turbulence in dilute sediment-laden, open-channel flows.* Environmental Fluid Mechanics, 2009. **9**(2): p. 237-266.
161. Jha, S.K. and F.A. Bombardelli, *Toward two-phase flow modeling of nondilute sediment transport in open channels.* J. Geophys. Res., 2009. **115**(F3): p. F03015.
162. Jin, Y.-C. and P.M. Steffler, *Predicting flow in curved open channels by depth-averaged method.* J. Hydraul. Eng.-ASCE, 1993. **119**: p. 109-124.
163. Jing-xin and Hua, *A vertical 2-D numerical simulation of suspended sediment transport.* Journal of Hydrodynamics, Ser. B, 2007. **19**(2): p. 217-224.

164. Johansen, S.T., N.M. Anderson, and S.R. de Silva, *A two-phase model for particle local equilibrium applied to air classification of powders.* Powder Technology, 1990. **63**(2): p. 121-132.
165. Keller, U., *Intermittent flow in hydraulic conduits*, in *Versuchanstalt für Wasserbau, Hydrologie und Glaziologie der Eidgenössichen*. 2006, ETH Zürich: Zürich. p. 250.
166. Kerger, F., P. Archambeau, S. Erpicum, B.J. Dewals, and M. Pirotton, *A Fast Universal Solver for 1D Continuous and Discontinuous Steady Flows in Rivers and Pipes.* International Journal for Numerical Methods in Fluids, 2009. **Published online**.
167. Kerger, F., P. Archambeau, S. Erpicum, B.J. Dewals, and M. Pirotton, *Simulation numérique des écoulements mixtes hautement transitoire dans les conduites d'évacuation des eaux.* Houille Blanche-Rev. Int., 2009. **2009**(5): p. 159-167.
168. Kerger, F., P. Archambeau, S. Erpicum, B.J. Dewals, and M. Pirotton, *Exact Riemann Solver and Godunov Scheme for Simulating Highly Transient Mixed Flows.* Journal of Computational and Applied Mathematics, Submitted.
169. Kerger, F., S. Detrembleur, P. Archambeau, S. Erpicum, B.J. Dewals, and M. Pirotton, *An Experimental and Numerical Analysis of Effects Induced by Moving Bodies in Free Surface Water*, in *Hydraulic Structures*, S. Pagliara, Editor. 2009, Pisa University Press. p. 179-189.
170. Kerger, F., B.J. Dewals, P. Archambeau, S. Erpicum, and M. Pirotton, *Transport of Dispersed Phase in Civil Engineering: How to unify the Mathematical Description?*, in *Third International Junior Researcher and Engineer Workshop on Hydraulic Structures*. 2010.
171. Kerger, F., B.J. Dewals, P. Archambeau, S. Erpicum, and M. Pirotton, *A Multiphase Model for the Transport of Dispersed Phases in Environmental Flows: Theoretical Contribution.* European Journal of Mechanical and Environmental Engineering, Accepted.
172. Kerger, F., B.J. Dewals, S. Erpicum, P. Archambeau, and M. Pirotton, *An Extended Shallow-water-like Model Applied to Flows in Environmental and Civil Engineering*, in *Hydraulic Engineering: Structural Applications, Numerical Modeling and Environmental Impacts*, G. Hirsch and B. Kappel, Editors. 2010, Nova Science Publishers: New-York. p. 1-85.
173. Kerger, F., B.J. Dewals, S. Erpicum, P. Archambeau, and M. Pirotton, *Modelling Flows in Environmental and Civil Engineering*. 2010, New-York: Nova Science Publishers p. 155 pages.
174. Kerger, F., B.J. Dewals, S. Erpicum, P. Archambeau, and M. Pirotton, *Modelling Flows in Environmental and Civil Engineering*. 2010, Nova Science Publishers New-York. p. 155.
175. Kerger, F., B.J. Dewals, S. Erpicum, P. Archambeau, and M. Pirotton, *Modelling Flows in Environmental and Civil Engineering: Unification of the Mathematical Theory and Application to Practical Cases*. 2010, Nova Science Publishers New-York. p. 155.
176. Kerger, F., S. Erpicum, B.J. Dewals, P. Archambeau, and M. Pirotton, *1D Unified Mathematical Model For Environmental Flow Applicated to Aerated Mixed flows.* Advances in Engineering Software, 2010. **Accepted**.
177. Khan, A.A. and P.M. Steffler, *Modelling overfalls using vertically averaged and moment equations.* J. Hydraul. Eng.-ASCE, 1996. **122**: p. 397-402.
178. Khan, A.A. and P.M. Steffler, *Vertically averaged and moment equations model for flow over curved beds.* J. Hydraul. Eng.-ASCE, 1996. **122**: p. 3-9.
179. Khuat Duy, B., P. Archambeau, S. Erpicum, B.J. Dewals, and M. Pirotton, *Modélisation hydrologique à grande échelle des zones imperméables égouttées.* Houille Blanche-Rev. Int., 2009. **5**: p. 167-173.
180. Kolev, N.I., *Multiphase Flow Dynamics*. 2007: Springer. p. 308.
181. Kolev, N.I., *Multiphase Flow Dynamics 2*. 2007: Springer. p. 692.
182. Krüger, S., *Computational Contribution to Highly Supercritical Flows*. Mitteilungen der Versuchsanstalt für Wasserbau, Hydrologie un Glaziologie, ed. H.E. Minor. Vol. 167. 2001, Zürich: ETHZ. p. 171.
183. Lafaurie, B., C. Nardone, R. Scardovelli, S. Zaleski, and G. Zanetti, *Modeling Merging and Fragmentation in Multiphase Flows with Surfer.* Journal of computational physics, 1994. **113**(1): p. 134-147.
184. Lahey Jr, R.T. and D.A. Drew, *Three Dimensional Time and Volume Averaged Conservation Equations of Two-Phase Flow*, in *Advance in Nuclear Science and Technology*. 1988. p. 1-69.

185. Lanzoni, S., *Mathematical modelling of bedload transport over partially dry areas.* Acta Geophysica, 2008. **56**(3): p. 734-752.
186. Lax, P.D., *Hyperbolic Systems of Conservation Laws II.* Communications on Pure and Applied Mathematics, 1957. **X**: p. 537-566.
187. Leal, J.G.A.B., R.M.L. Ferreira, and A.H. Cardoso, *Dam-break wave propagation over a cohesionless erodible bed*, in *Proc. 30rd IAHR Congress*, J. Ganoulis and P. Prinos, Editors. 2003, IAHR: Thessaloniki, Grèce. p. 261-268.
188. Lemineur, M., *Collecte et traitment des eaux usées - la plante - rencontre riverains.* 2009.
189. Lemineur, M., *Géotechnique et assainissement à Namur: Presentation du plan d'assainissement de la vile de Namur*. 2009.
190. Lemineur, M., *Géotechnique et assinissement à Namur: le choix technique des vortex*. 2009.
191. Lemineur, M., *Le système de collecte des eaux usées mis en place par la ville de Namur.* Journal des Ingénieurs, 2009. **123**.
192. Leon, A., *Improved Modeling of Unsteady Free Surface, Pressurized and Mixed Flows in Storm-Sewer Systems.* 2007, University of Illinois at Urbana-Champaign: Urbana. p. 194.
193. Leon, A., M. Ghidaoui, A. Schmidt, and M. Garcia, *Application of Godunov-Type Schemes to Transient Mixed Flows.* Journal of Hydraulic Research, 2008. **47**(2).
194. Leon, A.S., M.S. Ghidaoui, A.R. Schmidt, and M.H. Garcia, *Efficient second-order accurate shock-capturing scheme for modeling one- and two-phase water hammer flows.* Journal of Hydraulic Engineering, 2008. **134**(7): p. 970-983.
195. Leroux, A., *Discrétisation des termes sources raides dans les problèmes hyperboliques*. 1998.
196. LeVeque, R.J., *Balancing Source Terms and Flux Gradients in High-Resolution Godunov Methods: The Quasi-Steady Wave-Propagation Algorithm.* Journal of computational physics, 1998. **146**(1): p. 346-365.
197. Leveque, R.J., *Finite Volume Methods for Hyperbolic Problems*. Cambridge texts in Applied Mathematics. 2002: Cambridge University Press. p. 540.
198. Li, J. and A. McCorquodale, *Modeling Mixed Flow in Storm Sewers.* Journal of Hydraulic Engineering, 1999. **125**(11): p. 1170-1180.
199. Lightbody, A.F., H.M. Nepf, and J.S. Bays, *Modeling the hydraulic effect of transverse deep zones on the performance of short-circuiting constructed treatment wetlands.* Ecological Engineering, 2009. **35**(5): p. 754-768.
200. Lin, S., C.C.K. Kwok, R.Y. Li, Z.H. Chen, and Z.Y. Chen, *Local Frictional Pressure-Drop during Vaporization of R-12 through Capillary Tubes.* International Journal of Multiphase Flow, 1991. **17**(1): p. 95-102.
201. Liou, M.-S., *A Continuing Search for a Near-Perfect Numerical Flux Scheme - Part I : AUSM+*, NASA, Editor. 1994, Lewis Research Center: Cleveland, Ohio. p. 43.
202. Liou, M.-S., *A Sequel to AUSM : AUSM+.* Journal of computational physics, 1996. **129**: p. 364-382.
203. Liou, M.-S., *Ten Years in the Making AUSM-Family*, NASA, Editor. 2001, Glenn Research Center.
204. Liou, M.-S., *A sequel to AUSM, Part II: AUSM+up for all speeds.* Journal of computational physics, 2006. **214**: p. 137-170.
205. Liou, M.-S. and J.R. Edwards, *Numerical Speed of Sound and its Application to Schemes for all Speeds*, NASA, Editor. 1999, Glenn Research Center.
206. Liou, M.-S. and C.J. Steffen, *A New Flux Splitting Scheme : AUSM.* Journal of computational physics, 1993. **107**: p. 23-39.
207. Lockhart, R.W. and R.C. Martinelli, *Proposed correlation of data for isothermal two-phase, two-component flow in pipes.* Chemical Engineering Progress, 1949. **45**: p. 39-48.
208. López, F. and M. García, *open-channel flow through simulated vegetation: Suspended sediment transport modeling.* Water Resour. Res., 1998. **34**(9): p. 2341-2352.
209. Lopez, F. and M.H. Garcia, *Mean Flow and Turbulence Structure of Open-Channel Flow through Non-Emergent Vegetation.* Journal of hydraulic Engineering, 2001. **127**(5): p. 392-402.
210. Lyn, D.A. and M.S. Altinakar, *Saint-Venant-Exner Equations for Near-Critical and Trenscritical Flows.* Journal of hydraulic Engineering, 2002. **128**(6): p. 579-590.

211. Machiels, O., S. Erpicum, P. Archambeau, B.J. Dewals, and M. Pirotton, *Analyse expérimentale du fonctionnement hydraulique des déversoirs en touches de piano.* Houille Blanche-Rev. Int., 2009.
212. Manninen, M., V. Taivassalo, and S. Kallio, *On the mixture model for multiphase flow*, V.t.u. (VTT), Editor. 1996, Technical Research Center of Finland: Espoo. p. 67.
213. Martinelli, R.C. and D.B. Nelson, *Prediction of pressure drop during forced-circulation boiling of water.* Transactions of the ASME, 1948. **70**(6): p. 695-702.
214. Masella, J.M., Q.H. Tran, D. Ferre, and C. Pauchon, *Transient simulation of two-phase flows in pipes.* International Journal of Multiphase Flow, 1998. **24**(5): p. 739-755.
215. Mathers, W., R.L. Ferch, W.T. Hancox, and B.H. McDonald. *Equations For Transient Flow-Boiling In A Duct*. in *2nd CSNI Specialist Meeting on Transient Two-Phase Flow*. 1978. Paris, France.
216. Mays, L., ed. *Stormwater collection systems design handbook*. ed. McGraw-Hill. 2001. 1008.
217. McAdams, W.H., W.K. Woods, and L.C. Heroman, *ASME Int. Develop. Heat Transf. Part II* Transactions of the ASME, 1942. **64**(3): p. 193-200.
218. McCorquodale, A. and M.A. Hamam, *Modeling Surcharged Flow in Sewers.* Journal of hydraulic Engineering, 1983. **125**(11): p. 1170-1180.
219. McLean, S., V. Nikora, and S. Coleman, *Double-averaged velocity profiles over fixed dune shapes.* Acta Geophysica, 2008. **56**(3): p. 669-697.
220. Méchiouta, N., B. Jennesson, J.-P. Schneider, M. Luck, and E. Valette, *Assessment of Neptune_CFD code for some Free Surface Flows interesting Fluvial Hydraulic*, in *7th International Conference on Multiphase Flow* 2010: Tamp, Fl.
221. Meyer-Peter, E. and R. Müller, *Formulas for bed-load transport*, in *2nd Meeting of the International Association for Hydraulic Structures Reserach*. 1948. p. 39-64.
222. Mignot, E., E. Barthélemy, and D. Hurther, *Turbulent kinetic energy budget in a gravel-bed channel flow.* Acta Geophysica, 2008. **56**(3): p. 601-613.
223. Moody, L.F., *Friction factors for pipe.* Transactions of the ASME, 1944. **66**(8): p. 671-684.
224. Mori, Y., K. Huikata, and T. Ohmori, *Propagation of a pressure wave in two-phase flow with very high void fraction.* International Journal of Multiphase Flow, 1976. **2**(4): p. 453-464.
225. Morooka, S., T. Ishizuka, M. Iizuka, and K. Yoshimura, *Experimental study on void fraction in a simulated BWR fuel assembly (evaluation of cross-sectional averaged void fraction).* Nuclear Engineering and Design, 1989. **114**(1): p. 91-98.
226. Mouzelard, T., *Contribution à la modélisation des écoulements quasi tridimensionnels instationnaires à surface libre*. 2002, Université de Liège: Liège. p. 253.
227. Müller-Steinhagen, H. and K. Heck, *A simple friction pressure drop correlation for two-phase flow in pipes.* Chemical Engineering and Processing, 1986. **20**(6): p. 297-308.
228. Näf, D.R., *Numerische Simulation von Stosswellen in Freispiegelströmungen*. Mitteilungen der Versuchsanstalt für Wasserbau, Hydrologie un Glaziologie, ed. D. Vischer. Vol. 148. 1997, Zürich: ETHZ. p. 175.
229. Neary, V.S., *Numerical Solution of Fully Developed Flow with Vegetative Resistance.* Journal of Engineering Mechanics, 2003. **129**(5): p. 558-563.
230. Nepf, H. and M. Ghisalberti, *Flow and transport in channels with submerged vegetation.* Acta Geophysica, 2008. **56**(3): p. 753-777.
231. Nepf, H., M. Ghisalberti, B. White, and E. Murphy, *Retention time and dispersion associated with submerged aquatic canopies.* Water Resour. Res., 2007. **43**(4): p. W04422.
232. Nield, D.A. and V.S. Travkin, *Alternative models of turbulence in a porous medium, and related matters. Discussion. Author's reply*. Vol. 123. 2001, New York, : American Society of Mechanical Engineers.
233. Nigmatulin, R.I., *Spatial averaging in the mechanics of heterogeneous and dispersed systems.* International Journal of Multiphase Flow, 1979. **5**(5): p. 353-385.
234. Nikora, V., D. Goring, I. McEwan, and G. Griffiths, *Spatially Averaged Open-Channel Flow over Rough Bed.* Journal of hydraulic Engineering, 2001. **127**(2): p. 123-133.
235. Nikora, V., I. McEwan, S. McLean, S. Coleman, D. Pokrajac, and R. Walters, *Double-Averaging Concept for Rough-Bed Open-Channel and Overland Flows: Theoretical Background.* Journal of hydraulic Engineering, 2007. **133**(8): p. 873-883.

236. Nikora, V., S. McLean, S. Coleman, D. Pokrajac, I. McEwan, L. Campbell, J. Aberle, D. Clunie, and K. Koll, *Double-Averaging Concept for Rough-Bed Open-Channel and Overland Flows: Applications.* Journal of hydraulic Engineering, 2007. **133**(8): p. 884-895.
237. Nikora, V. and P. Rowiński, *Rough-bed flows in geophysical, environmental, and engineering systems: Double-Averaging Approach and its applications.* Acta Geophysica, 2008. **56**(3): p. 529-533.
238. Omgba-Essama, C., *Numerical Modelling of Transient Gas-Liquid Flows (Application to Stratified & Slug Flow Regimes)*. 2004, Cranfield University. p. 272.
239. Owens, W.L., *Two-phase pressure gradient.* ASME Int. Develop. Heat Transf. Part II 1961: p. 363-368.
240. Paquier, A. *Sediment transport models used by Cemagref during Impact project*. in *Proc. 1st IMPACT Project Workshop*. 2002. Wallingford.
241. Perthame, B. and C. Simeoni, *A kinetic scheme for the Saint-Venant system with a source term.* CALCOLO, 2001. **38**: p. 201-231.
242. Pirotton, M., *Modelisation des dicontinuités en ecoulement instationnaire à surface libre*, in *LHCN*. 1994, Liège University: Liège.
243. Pirotton, M., P. Archambeau, and F. Kerger, *Aéroport Bruxelles Sud - Expertise du réseau d'égouttage relatif au parking à étages*. 2008.
244. Pirotton, M., P. Archambeau, and F. Kerger, *Aéroport Bruxelles Sud - Expertise du réseau d'égouttage relatif au parking à étages - prestations complémentaires*. 2008.
245. Pirotton, M., P. Archambeau, and F. Kerger, *Aéroport Bruxelles Sud - Expertise du réseau d'égouttage relatif au parking à étages - Etude instationnaire*. 2010.
246. Planck, M., *Where is Science Going ?* 1932.
247. Poggi, D. and G. Katul, *Micro- and macro-dispersive fluxes in canopy flows.* Acta Geophysica, 2008. **56**(3): p. 778-799.
248. Politano, M., A.J. Odgaard, and W. Klecan, *Numerical Evaluation of Hydraulic Transients in a Combined Sewer Overflow Tunnel System.* Journal of Hydraulic Research, 2007. **133**(10): p. 1103-1110.
249. Preissmann, A. *Propagation des intumescences dans les canaux et rivieres*. in *First Congress of the French Association for Computation*. 1961. Grenoble, France.
250. Quick, C.M., *Efficiency of Air-Entraining Vortex Formation at Water Intake.* Journal of the Hydraulics Division, Proceedings of the American Society of Civil Engineers, 1970. **96**(7): p. 1403-1416.
251. Radice, A. and F. Ballio, *Double-average characteristics of sediment motion in one-dimensional bed load.* Acta Geophysica, 2008. **56**(3): p. 654-668.
252. Raupach, M.R., J.J. Finnigan, and Y. Brunei, *Coherent eddies and turbulence in vegetation canopies: The mixing-layer analogy.* Boundary-Layer Meteorology, 1996. **78**(3): p. 351-382.
253. Raupach, M.R. and R.H. Shaw, *Averaging procedures for flow within vegetation canopies.* Boundary-Layer Meteorology, 1982. **22**(1): p. 79-90.
254. Région wallone. *http://voies-hydrauliques.wallonie.be/opencms/opencms/fr*. 2010.
255. Rhyming, G.L., *Dynamique des fluides*, ed. P.p. romandes. 1985, Lausanne.
256. Righetti, M., *Flow analysis in a channel with flexible vegetation using double-averaging method.* Acta Geophysica, 2008. **56**(3): p. 801-823.
257. Roe, P.L., *Approximate Riemann Solvers, Parameter Vectors, and Difference Schemes.* Journal of computational physics, 1981. **43**: p. 357.
258. Roe, P.L., *Sonic flux formulae.* SIAM J. Sci. Stat. Comput., 1992. **13**(2): p. 611-630.
259. Roe, P.L. and J. Pike, *Efficient construction and utilisation of approximate riemann solutions*, in *Proc. of the sixth int'l. symposium on Computing methods in applied sciences and engineering, VI*. 1985, North-Holland Publishing Co.: Versailles, France.
260. Roger, S., B.J. Dewals, S. Erpicum, D. Schwanenberger, H. Schüttrumpf, and J. Köngetter, *Experimental und numerical investigations of dike-break induced flows.* Journal of Hydraulic Research, 2009. **47**(3): p. 349-359.
261. Romate, J.E., *An approximate Riemann solver for a two-phase flow model with numerically given slip relation.* Computers & Fluids, 1998. **27**(4): p. 455-477.

262. Rosatti, G., J. Murillo, and L. Fraccarollo, *Generalized Roe schemes for 1D two-phase, free-surface flows over a mobile bed.* Journal of computational physics, 2008. **227**(24): p. 10058-10077.
263. Rottman, J.W. and J.E. Simpson, *Gravity currents produced by instantaneous releases of a heavy fluid in a rectangular channel*. 1983, Cambridge Journals Online.
264. Rouhani, S.Z. and M.S. Sohal, *Two-phase flow patterns: A review of research results.* Progress in Nuclear Energy, 1983. **11**(3): p. 219-259.
265. Sagaut, P., S. Deck, and M. Terracol, *Multiscale and multiresolution approaches in turbulence*. 2006: Imperial College Pr.
266. Sanders, R.H. and K.H. Prendergast, *The Possible Relation of the 3-KILOPARSEC Arm to Explosions in the Galactic Nucleus.* Astrophysical Journal, 1974. **188**: p. 489-500.
267. Sethian, J., *Level Set Methods and Fast Marching Methods : Evolving Interfaces in Computational Geometry, Fluid Mechanics, Computer Vision, and Materials Science*, ed. C.U. Press. 1999.
268. Sethian, J.A., *Evolution, implementation, and application of level set and fast marching methods for advancing fronts.* Journal of computational physics, 2001. **169**(2): p. 503-555.
269. Sharma, Y., J.M.W. Scoggins, O. Shoham, and J.P. Brill, *Simulation of transient two-phase flow in pipelines*, in *The 2nd International Conference on Multiphase Flow*. 1985: London, UK.
270. Slattery, J.C., *Advanced transport phenomena*. 1999, Cambridge: Cambridge University Press.
271. Smith, J.D. and S.R. McLean, *Spatially Averaged Flow Over a Wavy Surface.* J. Geophys. Res., 1977. **82**(12): p. 1735-1746.
272. Song, C., J. Cardle, and K.S. Leung, *Transient Mixed-flow models for Storm Sewers.* Journal of hydraulic Engineering, 1983. **109**(11): p. 1487-1503.
273. Soria, A. and H.I. de Lasa, *Averaged Transport Equations for Multophase Systems with Interfacial Effects*. Vol. 46. 1991, Oxford, ROYAUME-UNI: Elsevier. p. 19.
274. Souliotis, D. and P. Prinos, *Turbulence in vegetated flows: Volume-average analysis and modelling aspects.* Acta Geophysica, 2008. **56**(3): p. 894-917.
275. Steffler, P.M. and Y.-C. Jin, *Depth averaged and moment equations for moderately shallow free surface flow.* J. Hydraul. Res., 1993. **31**: p. 5-17.
276. Steger, J.L. and R.F. Warming, *Flux vector splitting of the inviscid gasdynamic equations with application to finite-difference methods.* Journal of computational physics, 1981. **40**(2): p. 263-293.
277. Stewart, J., *Analyse, concepts et contextes : Volume 1, Fonctions d'une variable*, ed. D. Boek. 2001. p. 790.
278. Stockie, J.M., J.A. MacKenzie, and R.D. Russell, *A moving mesh method for one-dimensional hyperbolic conservation laws.* SIAM Journal on Scientific Computing, 2001. **22**(5): p. 1791-1813.
279. Stoesser, T. and V. Nikora, *Flow structure over square bars at intermediate submergence: Large Eddy Simulation study of bar spacing effect.* Acta Geophysica, 2008. **56**(3): p. 876-893.
280. Streeter, V.L., E.B. Wylie, and K.W. Bedford, *Fluid Mechanichs*. Ninth ed, ed. McGraw-Hill. 1998.
281. T. B. Moodie, J. P. Pascal, and G. E. Swaters, *Sediment Transport and Deposition from a Two-layer Fluid Model of Gravity Currents on Sloping Bottoms.* Studies in Applied Mathematics, 1998. **100**(3): p. 215-244.
282. TANINO, Y. and H.M. NEPF, *Lateral dispersion in random cylinder arrays at high Reynolds number.* Journal of Fluid Mechanics, 2008. **600**(-1): p. 339-371.
283. Tanino, Y. and H.M. Nepf, *Laboratory investigation of lateral dispersion within dense arrays of randomly distributed cylinders at transitional Reynolds number.* Physics of Fluids, 2009. **21**(4): p. 046603.
284. Toro, F.E., *Riemann problems and the WAF method for solving two-dimensional shallow water equations.* Philosophical Transactions : Physical Sciences and Engineering, 1991. **338**: p. 43-68.

285. Toro, F.E., *Riemann Solvers and Numerical Methods for Fluid Dynamics*. Springer-Verlag ed. 1997. p. 600.
286. Toro, F.E., *Shock-Capturing Methods for Free-Surface Shallow Flows*, ed. John Wiley and Sons Ltd. 2000, Chichester - NY - Weinheim - Brisbane - Singapore - Toronto. p. 310.
287. Trajkovic, B., M. Ivetic, F. Calomino, and A. D'Ippolito, *Investigation of Transition From Free Surface to Pressurized Flow in a Circular Pipe.* Water Science and Technology, 1999. **39**(9): p. 115-112.
288. Truesdell, C. and R. Toupin, *The Classical Field Theories*. Handbuch der Physik, ed. Springer-Verlag. 1960, Berlin-Heidelberg.
289. Ullmann, A. and N. Brauner, *Closure relations for two-fluid models for two-phase stratified smooth and stratified wavy flows.* International Journal of Multiphase Flow, 2006. **32**(1): p. 82-105.
290. Ullmann, A., A. Goldstein, M. Zamir, and N. Brauner, *Closure relations for the shear stresses in two-fluid models for laminar stratified flow.* International Journal of Multiphase Flow, 2004. **30**(7-8): p. 877-900.
291. Ungarish, M., *On the modeling and investigation of polydispersed rotating suspensions.* International Journal of Multiphase Flow, 1995. **21**(2): p. 267-284.
292. Val-Matic, *Dynamic Characteristics of Check Valves*. 2008.
293. Van Leer, B., *Towards the Ultimate Conservative Difference Scheme V. A Second-Order Sequel to Godunov's method.* Journal of computational physics, 1979. **32**: p. 101-136.
294. Van Leer, B. *Flux-vector splitting for the Euler equations*. in *International Conference on Numerical Methods in Fluid Dynamics, 8th*. 1982. Aachen, West Germany.
295. Van Leer, B., *Flux-Vector Splitting for the 1990s*, NASA, Editor. 1991, Lewis Research Center: Cleveland. p. 203-214.
296. van Rijn, L.C., *Mathematical modelling of morphological processes in the case of suspended sediment transport*, in *Delft Hydraulic Laboratory Communication*. 1987, Delft Technological University.
297. Various, *Numerical Recipes in Fortran : The Art of Scientific Computation*. Second Edition ed, ed. Cambridge University Press. 1992, Cambridge. p. 1500.
298. Vasconcelos, J., *Dynamic Approach to the Description of Flow Regime Transition in Stormwater Systems*, in *Environmental Engineering*. 2005, University of Michigan. p. 386.
299. Vasconcelos, J. and S. Wright, *Numerical Modeling of the Transition Between Free Surface and Pressurized Flow in Storm Sewers*, in *Innovative Modeling of Urban Water Systems, Monograph 12*, J. W., Editor. 2003: Ontario, Canada.
300. Vasconcelos, J. and S. Wright, *Applications and Limitations of Single-Phase Models to the Description of theRapid Filling Pipe Problem*, in *Effective Modeling of Urban Water Systems, Monograph 13.* 2004.
301. Vasconcelos, J. and S. Wright, *Experimental Investigation of Surges in a Stormwater Storage Tunnel.* Journal of Hydraulic Engineering, 2005. **131**(10): p. 853-861.
302. Vasconcelos, J. and S. Wright, *Comparison between the Two-Component Pressure Approach and Current Transient Flow Solvers.* Journal of Hydraulic Research, 2007. **45**(2): p. 178-187.
303. Vasconcelos, J., S. Wright, and P.L. Roe, *Current Issues on Modeling Extreme Inflows in Stormawater Systems*, in *Effective Modeling of Urban Water Systems, Monograph*, I. James, McBean&Pitt, Editor. 2005. p. 53-71.
304. Vasconcelos, J., S. Wright, and P.L. Roe, *Improved Simulation of Flow Regime Transition in Sewers : The Two-Component Pressure Approach.* Journal of Hydraulic Engineering, 2006. **132**(6): p. 553-562.
305. Vasconcelos, J. and S.J. Wright, *Discussion : Comparison between the two-component pressure approach and currenttransient flow solvers.* Journal of Hydraulic Research, 2007. **45**(2): p. 178-187.
306. Vasconcelos, J.G. and S.J. Wright, *Investigation of rapid filling of poorly ventilated stormwater storage tunnels.* Journal of Hydraulic Research, 2009. **47**(5): p. 547 - 558.
307. Vasconcelos, J.G., S.J. Wright, and P.L. Roe, *Numerical Oscillations in Pipe-Filling Bore Predictions by Shock-Capturing Models.* Journal of Hydraulic Engineering-Asce, 2009. **135**(4): p. 296-305.

308. Vazquez-Cendon, M.E., *Improved treatment of source terms in upwind schemes for the shallow water equations in channels with irregular geometry.* J. Comput. Phys., 1999. **148**(2): p. 497-526.
309. Vazquez-Cendon, M.E. and E.F. Toro, *Exact solution of some hyperbolic systems with source terms.* Proceedings of the Royal Society of London. Series A: Mathematical, Physical and Engineering Sciences, 2003. **459**(2029): p. 263-271.
310. Vereecken, H., J. Baetens, P. Viaene, F. Mostaert, and P. Meire, *Ecological management of aquatic plants: effects in lowland streams.* Hydrobiologia, 2006. **570**(1): p. 205-210.
311. Verloop, W.C., *The inertial coupling force.* International Journal of Multiphase Flow, 1995. **21**(5): p. 929-933.
312. Wada, Y. and M.-S. Liou, *An Accurate and Robust Flux Splitting Scheme for Shock and Contact Discontinuities.* SIAM Journal on Scientific Computing, 1997. **18**(3): p. 633-657.
313. Wallis, G.B., *One-dimensional Two-phase Flow*, ed. M.-H.B. Company. 1969. p. 410 pages.
314. Walters, R.A. *From River to Ocean: A Unified Modeling Approach*. 2001: ASCE.
315. Whitaker, S., *Introduction to fluid mechanics*, ed. M. Krieger. 1992.
316. Whitham, G.B., *Linear and Nonlinear Waves*. 1974, New York: John Wiley & Sons. p. 636.
317. Wiggert, D., *Transient Flow in Free-Surface, Pressurized systems.* Journal of the Hydraulics Division, Proceedings of the American Society of Civil Engineers, 1972. **98**(1): p. 11-26.
318. Wilcox, C.D., *Turbulence modeling for CFD*, ed. C. Industries. 1994, La Canada, California.
319. Wilson, N.R. and R.H. Shaw, *A Higher Order Closure Model for Canopy Flow.* Journal of Applied Meteorology, 1977. **16**(11): p. 1197-1205.
320. Woldesemayat, M.A. and A.J. Ghajar, *Comparison of void fraction correlations for different flow patterns in horizontal and upward inclined pipes.* International Journal of Multiphase Flow, 2007. **33**(4): p. 347-370.
321. Woodward, P. and P. Colella, *The numerical simulation of two-dimensional fluid flow with strong shocks.* Journal of computational physics, 1984. **54**(1): p. 115-173.
322. Wu, F.-C., W.S. Hsieh, and Y.-J. Chou, *Variation of roughness coefficients for unsubmerged and submerged vegetation*. Vol. 125. 1999, Reston, VA, ETATS-UNIS: American Society of Civil Engineers.
323. Wu, W., *Computational River Dynamics*. 2008, London: Taylors and Francis.
324. Wu, W. and S. Wang, *Mathematical Models for Liquid-Solid Two-Phase flow.* International Journal of Sediment Reserach, 2000. **15**(3): p. 288-298.
325. Wylie, E.B. and V.L. Streeter, *Fluid Transients*. Première ed, ed. M.-H. Inc. 1978. p. 385.
326. Yadigaroglu, G. and R.T. Lahey Jr, *On the various forms of the conservation equations in two-phase flow.* International Journal of Multiphase Flow, 1976. **2**(5-6): p. 477-494.
327. Yan, L. and M. De-kang, *Further Development of a Conservative Front-Tracking Method for Systems of Conservation Laws in One Space Dimension.* Journal of Scientific Computing, 2006. **28**(1): p. 85-119.
328. Yang, R., W. Zhou, K. Fukuda, Z. Ju, and Z. Shang, *Modified Diffusion Flux Model for Analysis of Turbulent Gas-Particle Two-Phase Flows.* Tsinghua Science & Technology, 2005. **10**(2): p. 189-195.
329. YiH, C.S., *Dynamics of nonhomogeneous fluids*. Macmillan series in advanced mathematics and theoretical physics, ed. Macmillan. 1965.
330. Yulistiyanto, B., Y. Zech, and W.H. Graf, *Flow around a Cylinder: Shallow-Water Modeling with Diffusion-Dispersion.* J. Hydraul. Eng.-ASCE, 1998. **124**: p. 419-429.
331. Zhou, F., F.E. Hicks, and P.M. Steffler, *Effects of Trapped Air during Rapid Filling of Partially Full Pipes*, in *Annual Conference of the Canadian Society for Civil Engineering*. 2002.
332. Zhou, F., F.E. Hicks, and P.M. Steffler, *Transient Flow in a Rapidly Filling Horizontal Pipe Containing Trapped Air.* Journal of Hydraulic Engineering, 2002. **128**(6): p. 625-634.
333. Zuber, N. and J.A. Findlay, *Average volumetric concentration in two-phase flow systems.* Journal Name: Journal of Heat Transfer (U.S.); Journal Volume: Vol: 87; Other Information: Orig. Receipt Date: 31-DEC-66, 1965: p. Medium: X; Size: Pages: 453-68.
334. Zuber, N., F.W. Staub, G. Bijwaard, and P.G. Kroeger, *Steady state and transient void fraction in two-phase flow systems.*, in *Other Information: Work Performed under United*

States--Euratom Joint Research and Development Program. UNCL. Orig. Receipt Date: 31-DEC-68. 1967. p. Medium: X; Size: Pages: 422.

University of Liège

Faculty of Applied Science

Department of Architecture, Geology, Environment and Construction

Hydrology, Applied Hydrodynamics and Hydraulic Constructions

The present text, submitted to the University of Liège in fulfillment of the requirements for the degree of “Docteur en Sciences de l’Ingénieur”, aims at improving the understanding and description of air-water interactions in transient flows. A particular emphasis is set on phenomena relevant in civil and environmental engineering, like rivers, pipes, and hydraulic structures.

Theoretical results of this doctoral research may be summarized in two main propositions. First, I show that any mathematical model for free surface flows can be extended to pressurized flows. Second, the multiphase drift-flux model is proven an adequate alternative to Navier-Stokes equations in civil and environmental engineering. These propositions underpin the development of original mathematical models and new computational codes (WOLF1D and WOLF IMPack). Validation and application on actual cases prove the efficiency of the new approach.

Original concepts introduced in this thesis pave the way for further research on environmental flows, especially on the mathematical description of transport phenomena (pollutants, sediments) and heterogeneous interactions (vegetation, rough bed).